Loughborough University

Loughborough University
Institutional Repository

Damage resistance and tolerance investigation of carbon/epoxy skinned honeycomb sandwich panels

This item was submitted to Loughborough University's Institutional Repository by the/an author.

Additional Information:

- A Doctoral Thesis submitted in partial fulfilment of the requirements for the award of Doctor of Philosophy of Loughborough University.

Metadata Record: https://dspace.lboro.ac.uk/2134/10072

Publisher: © Michelle Hill

Please cite the published version.

Loughborough University

University Library

Author/Filing Title ..... HILL, M.D. .....

.....

Class Mark ..... T .....

Please note that fines are charged on ALL overdue items.

0403694655

Loughborough University

Thesis Access Form

Copy No.....**Location**.....

Author MICHELLE DENISE HILL

Title DAMAGE RESISTANCE AND TOLERANCE INVESTIGATION OF CARBON/EPOXY SKINNED HONEYCOMB SANDWICH PANELS

Status of access OPEN / ~~RESTRICTED~~ / ~~CONFIDENTIAL~~

Moratorium Period:.....years,ending...../.....200.....

Conditions of access proved by (CAPITALS):.....

Director of Research (Signature)..... J. S. Loughlan

Department of AERONAUTICAL AND AUTOMOTIVE ENGINEERING

Author's Declaration: *I agree the following conditions:*

OPEN access work shall be made available (in the University and externally) and reproduced as necessary at the discretion of the University Librarian or Head of Department. It may also be copied by the British Library in microfilm or other form for supply to requesting libraries or individuals, subject to an indication of intended use for non-publishing purposes in the following form, placed on the copy and on any covering document or label.

The statement itself shall apply to ALL copies:

This copy has been supplied on the understanding that it is copyright material and that no quotation from the thesis may be published without proper acknowledgement.

Restricted/confidential work: All access and any photocopying shall be strictly subject to written permission from the University Head of Department and any external sponsor, if any.

Author's signature.... MDHill .....**Date**.... 12th November 2007 .....

users declaration: for signature during any Moratorium period (Not Open work): ***I undertake to uphold the above conditions:***			
Date	Name (CAPITALS)	Signature	Address

Damage Resistance and Tolerance Investigation of Carbon/Epoxy Skinned Honeycomb Sandwich Panels

By

Michelle Denise Hill

A Doctoral Thesis Submitted in Partial Fulfilment of the Requirements for the Award of Doctor of Philosophy of Loughborough University

November 2007

Department of Aeronautical and Automotive Engineering
Loughborough University
Leicestershire
United Kingdom

© by Michelle Hill, 2007

Loughborough University
Date 19/2/09
Class T
Acc No. 0403694655

Research Student Office. Academic Registry
Loughborough University Leicestershire LE11 3TU UK
Switchboard: +44 (0)1509 263171 Fax: +44 (0)1509 223938

Loughborough University

CERTIFICATE OF ORIGINALITY

This is to certify that I am responsible for the work submitted in this thesis, that the original work is my own except as specified in acknowledgments or in footnotes, and that neither the thesis nor the original work contained therein has been submitted to this or any other institution for a degree.

N O'Neill ..... (Signed)

12th November 2007 ..... (Date)

Damage Resistance and Tolerance Investigation of Carbon/Epoxy Skinned Honeycomb Sandwich Panels

Abstract

This thesis documents the findings of a three year experimental investigation into the impact damage resistance and damage tolerance of composite honeycomb sandwich panels. The primary area of work focuses on the performance of sandwich panels under quasi-static and low-velocity impact loading with hemispherical and flat-ended indenters. The damage resistance is characterised in terms of damage mechanisms and energy absorption. The effects of varying the skin and core materials, skin thickness, core density, panel boundary conditions and indenter shape on the transverse strength and energy absorption of a sandwich panel have been examined. Damage mechanisms are found to include delamination of the impacted skin, core crushing, limited skin-core debonding and top skin fibre fracture at high loads. In terms of panel construction the skin thickness is found to dominate the panel strength and energy absorption with core density having a lesser influence. Of the external factors considered the indenter nose-shape has the largest effect on both failure load and associated damage area. An overview of existing analytical prediction methods is also included and the most significant theories applied and compared with the experimental results from this study. The secondary area of work expands the understanding obtained from the damage resistance study and assesses the ability of a sandwich panel to withstand in-plane compressive loading after sustaining low-velocity impact damage. The importance of the core material is investigated by comparing the compression-after-impact strength of both monolithic carbon-fibre laminates and sandwich panels with either an aluminium or nomex honeycomb core. The in-plane compressive strength of an 8 ply skinned honeycomb sandwich panel is found to be double that of a 16 ply monolithic laminate, with the type of honeycomb also influencing the compressive failure mechanisms and residual compressive strength. It is concluded that under in-plane loading the stabilising effect of the core opposes the de-stabilising effect of any impact damage.

Keywords: Sandwich panel, honeycomb, carbon fibre, composite, low-velocity impact, damage mechanisms, energy absorption, in-plane compression, compression-after-impact.

ACKNOWLEDGEMENTS

Firstly I would like to express my deepest gratitude to my supervisor Dr. Gang Zhou for his constant guidance, support and understanding over the past four years, especially during the difficult times. I would also like to thank the Department of Aeronautical and Automotive Engineering at Loughborough University for their financial support, without which I would not have been able to undertake this research. I am also grateful for the assistance of the undergraduate masters students Mr P. Walker, Mr P. Fenner, Mr A. Dakars, Mr A. Khanna and Mr I. Gracey in helping me obtain the experimental data required for this research. Although it seems almost an eternity ago I would also like to acknowledge the encouragement and excellent grounding my A-level teachers Mr. D. Ford, Mr I. Gray and Mrs L. Redhead at Bideford College gave me in my early years, without which I would never have made it to university.

I would like to thank my family in Devon for their continuous support and provision of my second home and retreat away from the bustle of life. I also wish to express my appreciation for all my friends, in particular fellow researchers Pratap Rama, Paul Osei-Owusu and Mark Wood for their friendship, encouragement and sympathetic ear irrespective of their own PhD troubles. Finally I must express my most sincere gratitude to Roger for not only his never ending support and patience but also for allowing me in to his life and giving me his everlasting love.

"Energy and persistence conquer all things" – Benjamin Franklin

TABLE OF CONTENTS

1. INTRODUCTION 1

1.1. Key issues in the applications of sandwich structures 2

1.2. Review of damage resistance 3
1.2.1. Basic damage characteristics under transverse loading 3
1.2.2. Intrinsic variables affecting damage resistance 7
1.2.3. Extrinsic variables affecting damage resistance 14

1.3. Review of damage tolerance 20
1.3.1. CAI methods 21
1.3.2. Damage characteristics under in-plane compression 31
1.3.3. Factors affecting damage tolerance 38

1.4. Outline of the thesis 41

2. SANDWICH MATERIAL SYSTEMS AND PANEL MANUFACTURE 55

2.1. Panel configuration and nomenclature 56

2.2. Skin material and manufacture 60
2.2.1. Skin material properties 60
2.2.2. Lay-up and curing procedures 64

2.3. Core materials 69
2.3.1. Honeycomb properties 69
2.3.2. Honeycomb preparation 69

2.4. Sandwich panel manufacture 71
2.4.1. Adhesive properties 71
2.4.2. Adhesive preparation 74
2.4.3. Skin - honeycomb bonding 74

3. EXPERIMENTAL PROCEDURES FOR DAMAGE RESISTANCE 77

3.1. Specimen preparations 77

3.2. Experimental set-up for quasi-static tests 79
3.2.1. Quasi-static bending tests 80
3.2.2. Quasi-static indentation tests 84
3.2.3. Effect of clamping force 85

3.3. Experimental set-up for impact testing 86

4. DAMAGE CHARACTERISATION OF TRANSVERSELY LOADED SANDWICH PANELS 95

4.1. Overview of non-destructive damage detection methods for sandwich structures 95

4.2. Identification and measurement of damage 98
4.2.1. Surface visual inspections of damage resistance panels 99
4.2.2. Cross-sectional microscopic investigation 100
4.2.3. Specimen polishing 102

4.3. Response and damage analysis of sandwich panel constituents under transverse loading 103
4.3.1. Skin plate test results 104
4.3.2. Core crush and indentation test results 113

4.4. General behaviour characteristics of sandwich panels under transverse loading 118
4.4.1. Initial damage and response 120
4.4.2. Secondary damage and response 127
4.4.3. Ultimate failure 131
4.4.4. Panels with embedded delamination in the top skin 133

4.5. Concluding remarks 140

5. OVERVIEW OF EXISTING MODELS FOR TRANSVERSE LOADING OF SANDWICH PANELS 151

5.1. Overview of existing analytical modelling methods 151
5.1.1. Equivalent single layer theories 152
5.1.2. Layerwise theories 153
5.1.3. Contact laws and elastic foundations 154
5.1.4. Spring-mass and energy balance models 156

5.2. Review of the major published models for transverse loading of sandwich panels 157
5.2.1. Models from Frostig and co-workers 158
5.2.2. Model from Wierzbicki et al. 159
5.2.3. Models from Hoo Fatt and co-workers 162
5.2.4. Model by Sburlati 166
5.2.5. Model by Wen and Reid et al. 168

5.3. Concluding remarks 173

6. DISCUSSION OF RESULTS FOR DAMAGE RESISTANCE 175

6.1. Effects of varying the major parameters on damage mechanisms 176
6.1.1. Effect of varying skin thickness on damage mechanisms 176
6.1.2. Effect of varying core density on damage mechanisms 181

6.1.3. Effect of indenter nose-shape on damage mechanisms 185
6.1.4. Effect of skin material on damage mechanisms 186
6.1.5. Effect of core material on damage mechanisms 189
6.1.6. Effect of panel size on damage mechanisms 194
6.1.7. Effect of boundary conditions on damage mechanisms 198

6.2. Effects of varying the major parameters on energy absorption 201
6.2.1. Effect of varying skin thickness on energy absorption 203
6.2.2. Effect of varying core density on energy absorption 206
6.2.3. Effect of indenter nose-shape on energy absorption 208
6.2.4. Effect of core material on energy absorption 209
6.2.5. Effect of panel size and boundary conditions on energy absorption 211

6.3. Mechanical behaviour of panels under impact loading 213
6.3.1. Effect of varying IKE on damage mechanisms 213
6.3.2. Effect of skin thickness on damage mechanisms and energy absorption 221
6.3.3. Effect of core material on damage mechanisms and energy absorption 225
6.3.4. Quasi-static vs. impact testing 229

6.4. Damage resistance assessment 232

6.5. Concluding remarks 235

7. EXPERIMENTAL PROCEDURES FOR IMPACT DAMAGE TOLERANCE 250

7.1. Design methodology for CAI of sandwich panels 250
7.1.1. Design consideration 250
7.1.2. CAI rig design and modification 253
7.1.3. Test matrix 254

7.2. Specimen preparations 255
7.2.1. End-potting 256
7.2.2. Strain gauge locations 257

7.3. Experimental set-up for in-plane compression 259

8. DISCUSSION OF RESULTS FOR IMPACT DAMAGE TOLERANCE 263

8.1. Damage tolerance assessment of monolithic laminate panels 263
8.1.1. Compressive response of undamaged laminate panels 264
8.1.2. Compressive response of impact damaged laminate panels 273

8.2. General behavioural characteristics of sandwich panels under in-plane compression 279

8.3. Compressive response of impact damaged aluminium honeycomb sandwich panels 286

8.4. Compressive response of impact damaged nomex honeycomb sandwich panels....295

8.5. Damage tolerance assessment of impact damaged panels 300

8.6. Concluding remarks 305

9. CONCLUSIONS AND RECOMMENDATIONS....310

REFERENCES....314

APPENDIX A 325

APPENDIX B 336

APPENDIX C 348

APPENDIX D 354

LIST OF FIGURES

Figure 1.1 SACMA compression after impact test rig 23
Figure 1.2 NASA compression-after-impact rig 24
Figure 1.3 Test set-up for ASTM C364 25
Figure 1.4 Compression support conditions 27
Figure 1.5 Various failure modes of sandwich panels under in-plane compression with unloaded edges simply-supported [127]: (i) skin compressive failure (ii) inward local buckling (dimpling) (iii) outward local buckling (wrinkling) (iv) Panel shear failure 32
Figure 1.6 Test procedures involved in the determination of damage resistance and damage tolerance of composite sandwich panels 44
Figure 2.1 Panel identification scheme 58
Figure 2.2 Sample of load-displacement curves obtained from flexural tests on T700/LTM45-EL cross-ply $(0/90)_{8S}$ specimens 63
Figure 2.3 Sample of load-displacement curves obtained from flexural tests on IM7/8552 cross-ply $(0/90)_{8S}$ specimens 63
Figure 2.4 Lay-up table with fibre orientation identified 65
Figure 2.5 Tick sheet for 8 ply laminate 65
Figure 2.6 Autoclave configuration 66
Figure 2.7 Autoclave curing cycles for T700/LTM45-EL and IM7/8552 67
Figure 2.8 Diamond edged tile cutter 67
Figure 2.9 Location of the artificial delamination within the laminate 68
Figure 2.10 Consolidated cells in nomex specimen cured in the autoclave (a) Damage in L-direction (b) Damage in W-direction 70
Figure 2.11 Honeycomb element terminology 73
Figure 3.1 Strain gauge position markings 78
Figure 3.2 Quasi-static bending test set-up 80
Figure 3.3 Variation in LVDT reading with position relative to the panel centre for a 4 ply 70kg/m^3 panel loaded with the HS indenter 81
Figure 3.4 Load vs. displacement plot for a sandwich panel with 12 ply carbon fibre skins and 50kg/m^3 aluminium honeycomb loaded with the flat-ended indenter 83
Figure 3.5 Load-displacement curves for 8 ply 70kg/m^3 panels loaded to ultimate failure with different torques used for clamping bolts 85
Figure 3.6 Impact rig set-up 87
Figure 3.7 Comparison of measured and theoretical free fall velocity at impact 88
Figure 3.8 Volts-time plot of impact test on 8 ply 70kg/m^3 panel at an IKE of 20.6J 89
Figure 3.9 Load-time plot of impact event on 8 ply 70kg/m^3 panel at an IKE of 20.6J 90
Figure 3.10 Load-time plot of impact event on 8 ply 70kg/m^3 panel at an IKE of 25.2J 90
Figure 3.11 Acceleration-time plot of impact event on 8 ply 70kg/m^3 panel at an IKE of 20.6J 92
Figure 3.12 Velocity-time plot of impact events on 8 ply 70kg/m^3 panel at IKE of 20.6J (no fibre fracture) and 25.2J (fibre fracture and subsequent core crushing) 93
Figure 3.13 Displacement-time plot of impact events on 8 ply 70kg/m^3 panel at IKE of 20.6J (no fibre fracture) and 25.2J (fibre fracture and subsequent core crushing) 93
Figure 3.14 Load-displacement plot of impact events on 8 ply 70kg/m^3 panels at 20.6J (no fibre fracture) and 25.2J (fibre fracture) compared with 8/70/HS(ult) quasi-static test 94
Figure 4.1 Determination of internal damage through various measurements 101
Figure 4.2 Load-displacement response of 8, 12 & 16 ply T700/LTM45-EL laminate plates loaded with both HS and FE indenters 105
Figure 4.3 Photo of 12 ply plate loaded with FE indenter 106

Figure 4.4 Load-strain response of 8, 12 & 16 ply T700/LTM45-EL laminate plates loaded with the HS indenter 107
Figure 4.5 Load-strain response of 8, 12 & 16 ply T700/LTM45-EL laminate plates loaded with the FE indenter 108
Figure 4.6 Comparison of load-displacement curves for T700/LTM45-EL and IM7/8552 plates loaded with (a) HS indenter (b) FE indenter 110
Figure 4.7 Load-strain response of 8 & 16 ply IM7/8552 laminate plates loaded with (a) HS indenter (b) FE indenter 111
Figure 4.8 Comparison of damage in 16 ply plate loaded with FE indenter Top: T700/LTM45-EL Bottom: IM7/8552 112
Figure 4.9 Load-displacement response for stabilised compression of 50 and 70kg/m^3 aluminium honeycomb crushed to ASTM C365 (two results shown for each density) 114
Figure 4.10 Load-displacement for aluminium and nomex honeycombs crushed with (a) 20mm FE indenter (b) 20mm HS indenter 116
Figure 4.11 Four cases of interaction between a HS indenter and honeycomb cells 117
Figure 4.12 Effect of indenter location on initial response of aluminium honeycomb crushed with HS indenter 118
Figure 4.13 Identification of threshold and failure loads from load-displacement curves of 16 ply 50kg/m^3 honeycomb panels loaded with HS and FE indenters 119
Figure 4.14 Initial damage threshold for sandwich panels with 70kg/m^3 aluminium honeycomb loaded with (a) HS indenter (b) FE indenter 120
Figure 4.15 Illustration of variation between top and bottom skin bending for 12/90/HS panel throughout loading range 121
Figure 4.16 Determination of damage thresholds from load-strain curves for 16 ply 50kg/m^3 panels loaded with (a) HS indenter (b) FE indenter 123
Figure 4.17 Cross-section of 8 ply 50kg/m^3 panel loaded to initial damage threshold with FE indenter 124
Figure 4.18 Effect of honeycomb crushing on top strain gauge when using the FE indenter .. 124
Figure 4.19 Cross-section of 16 ply 50kg/m^3 panel loaded with HS indenter (a) loading ceased prior to initial damage threshold (b) initial damage threshold 125
Figure 4.20 Distribution of delaminations through the thickness of the 12 ply 50kg/m^3 specimen loaded with the HS indenter to initial damage threshold 126
Figure 4.21 Illustration of panel relaxation after secondary damage propagation in panels with 4 ply skins or 90kg/m^3 honeycomb 128
Figure 4.22 Effect of core density on secondary damage load for 16 ply panels loaded with the FE indenter 128
Figure 4.23 Cross-section of 12 ply 70kg/m^3 panel loaded to secondary damage with HS indenter 129
Figure 4.24 Cross-section of 16 ply 70kg/m^3 panel loaded to secondary damage with FE indenter 131
Figure 4.25 Cross-section of panels loaded to ultimate failure (a) 12 ply 70kg/m^3 HS indenter (b) 16 ply 70kg/m^3 FE indenter 132
Figure 4.26 Comparison load-displacement curves of 8 ply 70kg/m^3 and 16 ply 70kg/m^3 panels with and without embedded delamination loaded with (a) HS indenter (b) FE indenter 134
Figure 4.27 Comparison of internal damage in 16 ply 70kg/m^3 panels loaded to secondary damage with the HS indenter (a) Panel with embedded delamination (b) Normal panel 136
Figure 4.28 Comparison of internal damage in 16 ply 70kg/m^3 panels loaded to secondary damage with the FE indenter (a) Panel with embedded delamination (b) Normal panel 137

Figure 4.29 Comparison load-strain curves of 8/70 & 16/70 panels with 16/70 panel with embedded delamination (a) HS indenter (b) FE indenter 139
Figure 5.1 Comparison of Hoo Fatt's analytical theory with experimental data from indentation testing (a) 4/50/HS(ind) & 4/70/HS(ind) with Eq. 5.10 (b) 4/50/FE(ind) & 4/70/FE(ind) with Eq. 5.10 (c) 8/50/HS(ind) & 16/50/HS(ind) with Eq. 5.12 + 5.13 (d) 8/50/FE(ind) & 16/50/FE(ind) with Eq. 5.12 + 5.13 165
Figure 5.2 Comparison of Sburati's analytical theory (Eqs. 5.16 and 5.17) with experimental data for top skin indentation of a panel loaded in bending (a) 4/50/HS&FE (b) 8/70/HS&FE (c) 12/90/HS&FE (d) 8/64/HS&FE 168
Figure 5.3 Comparison of theoretical and experimental load-displacement curves for 70kg/m^3 aluminium honeycomb sandwich panels with various skin thicknesses loaded with hemispherical indenter 173
Figure 6.1 Variation of threshold loads with the number of plies in the skins (a) initial damage threshold for HS and FE indenter (b) expanded view of previous plot for HS indenter only (c) ultimate failure for HS and FE indenter.. 178
Figure 6.2 Variation of core crushing length with skin thickness (a) initial damage threshold (b) ultimate failure 179
Figure 6.3 Variation of gradient of load-displacement curve with skin thickness (a) prior to initial damage (b) prior to ultimate failure 180
Figure 6.4 Variation of damage/failure load with honeycomb density: (a) Initial threshold HS indenter (b) Initial threshold FE indenter (c) Ultimate failure HS indenter (d) Ultimate failure FE indenter 183
Figure 6.5 Variation of panel stiffness with core density: (a) Initial stiffness HS indenter (b) Initial stiffness FE indenter (c) Ultimate stiffness HS indenter (d) Ultimate stifffness FE indenter 184
Figure 6.6 Load-displacement response of 12 ply 50kg/m^3 sandwich panels with different skin materials loaded with the HS indenter 188
Figure 6.7 Load-strain response of 12 ply 50kg/m^3 sandwich panels with different skin materials loaded with the FE indenter 188
Figure 6.8 Comparison of load-displacement curves for 8 ply panel with 70kg/m^3 aluminium or 64kg/m^3 nomex core loaded with FE indenter 190
Figure 6.9 Initial threshold region of load-displacement curves (a) 8 ply HS indenter (b) 16 ply HS indenter (c) 8 ply FE indenter (d) 16 ply FE indenter 191
Figure 6.10 Photo of 12 ply panel loaded with FE indenter to initial damage threshold (a) 70kg/m^3 aluminium (b) 64kg/m^3 nomex 193
Figure 6.11 Photo of 12 ply panel loaded with FE indenter to secondary damage (a) 70kg/m^3 aluminium (b) 64kg/m^3 nomex 193
Figure 6.12 Photo of 12 ply panel loaded with FE indenter to ultimate failure (a) 70kg/m^3 aluminium (b) 64kg/m^3 nomex 194
Figure 6.13 Comparison of 100mm and 220mm panel response - 16/70/HS (a) Load-displacement (b) Load-strain 195
Figure 6.14 Comparison of 100mm and 220mm panel response - 16/70/FE (a) Load-displacement (b) Load-strain 196
Figure 6.15 Comparison of panel response for 12 ply 50kg/m^3 panels loaded with HS indenter resting on a solid foundation (clamped & unclamped) and under bending 198
Figure 6.16 Comparison of panel response for 8 ply 64kg/m^3 nomex panels loaded with FE indenter resting on a solid foundation and under bending 200
Figure 6.17 Photo of 8/70/HS panel loaded to ultimate failure (a) resting on a solid foundation (b) in bending 201
Figure 6.18 Graphical representation of incident energy (IE) and absorbed energy (AE) 202
Figure 6.19 Variation of incident energy with number of plies in the skins at (a) initial threshold (b) secondary damage (c) ultimate failure 205

Figure 6.20 Variation of incident energy with honeycomb density: (a) Initial threshold HS indenter (b) Initial threshold FE indenter (c) Ultimate failure HS indenter (d) Ultimate failure FE indenter 207
Figure 6.21 Variation of load and energy with skin thickness for nomex panels: (a) Initial damage load (b) Incident energy at initial damage (c) Ultimate failure load (d) Incident energy at ultimate failure 210
Figure 6.22 Photographs of cross-sectioned 8 ply 70kg/m^3 panels impacted at 1.5-30.5J 215
Figure 6.23 Load vs. Displacement for 8/70/IMP panels for (a) Low IKE (b) High IKE 216
Figure 6.24 Variation of maximum load with IKE for all 8 ply 70kg/m^3 impact and QS tests 217
Figure 6.25 (a) Damage length vs. IKE for 8 ply 70kg/m^3 impact and QS tests (b) Damage area vs. IKE for 8 ply 70kg/m^3 impact and QS tests 219
Figure 6.26 Variation of absorbed energy with IKE for 8 ply 7kg/m^3 panels under impact and QS loading 220
Figure 6.27 Load-displacement curves from quasi-static and impact tests on 16 ply 70kg/m^3 panels 221
Figure 6.28 Comparison of variation in maximum load with IKE for 8 & 16 ply 70kg/m^3 panels for all impact and QS tests 222
Figure 6.29 Internal damage area in 16 ply 70kg/m^3 panels for varying IKE levels 222
Figure 6.30 Comparison of internal damage length in 8 & 16 ply 70kg/m^3 panels for varying IKE levels (damage regions based upon 16 ply data only) (a) top skin delamination length (b) core crushing length 223
Figure 6.31 Variation of absorbed energy with IKE for 8 and 16 ply 70kg/m^3 panels 225
Figure 6.32 Comparison of internal damage in 8 ply 64kg/m^3 panels and 8 ply 70kg/m^3 panels at various IKE levels using (a) damage length (b) damage area 226
Figure 6.33 Comparison of variation in maximum load with IKE for 8 ply panels with 64kg/m^3 nomex and 70kg/m^3 aluminium cores 227
Figure 6.34 Comparison of variation in maximum impactor displacement with IKE for 8 ply panels with 64kg/m^3 nomex and 70kg/m^3 aluminium cores 228
Figure 6.35 Variation of absorbed energy with IKE for 8 ply 64kg/m^3 panels 228
Figure 6.36 Photograph of the internal damage in comparable 8 ply 70kg/m^3 panels (a) Impact at 3.7J (b) Quasi-static secondary diagnostic test 230
Figure 6.37 Photograph of the internal damage in 8 ply 70kg/m^3 panels (a) Impact at 20.6J (no fibre fracture) (b) Impact at 25.2J (fibre fracture) (c) Quasi-static ultimate failure test 231
Figure 7.1 Design of compression jig 254
Figure 7.2 Location of strain gauges on front and back faces of compression panels 258
Figure 7.3 Test arrangement in Denison machine 260
Figure 7.4 Load vs. longitudinal and in-plane transverse displacement for a compression test on 8/70/CAI(14J)-1 panel 261
Figure 8.1 Compressive load vs. longitudinal and in-plane transverse displacement for 16 ply laminates with and without impact damage 264
Figure 8.2 Photograph of 16/CAI(0)-1 control panel loaded under in-plane compression 265
Figure 8.3 Variation of Poisson's ratio with load, calculated from SG2 strain gauge pair and LVDT readings for 16/CAI(0J)-1 panel 266
Figure 8.4 Load-strain response for 16/CAI(0)-1 panel under in-plane compression (a) individual strain response in 0° fibre direction (b) individual strain response in 90° fibre direction 267
Figure 8.5 Load-strain response for 16/CAI(0)-1 panel under in-plane compression (a) Mean strain (b) Bending strain 268
Figure 8.6 The deformation sequence of the compressive and buckling behaviour of 2-mm thick quasi-isotropic preconditioned carbon/epoxy panels in the (a) longitudinal direction (b) in-plane transverse direction [101] 270

Figure 8.7 Illustration of buckling sequence and strain response of 2mm thick cross-ply panels in longitudinal (loading) direction 272
Figure 8.8 Mean and bending strain at far-field (SG1) and local (SG2) locations on undamaged and impacted 16 ply laminates in in-plane compression 274
Figure 8.9 Strain variation at central (SG3) location in on undamaged and impacted 16 ply laminates in in-plane compression 275
Figure 8.10 Mode II buckling shape of damaged and undamaged laminate panels 276
Figure 8.11 Photograph of 16/CAI(20J) panel after compression loading (a) front view (impacted side) (b) back view 278
Figure 8.12 Variation of compressive strength with impact energy level for 16 ply monolithic laminates 278
Figure 8.13 Variation of Poisson's ratio with load, calculated from SG2 strain gauge pair and LVDT readings for 16/CAI(20J) panel 279
Figure 8.14 Load-displacement response of undamaged 8 ply sandwich panels with aluminium and nomex honeycomb under in-plane compression 280
Figure 8.15 Photographs of 8/70/CAI(0)-2 panel after in-plane compression: (a) Left external edge (b) Front (c) Right external edge (d) Cross-section of internal damage on longitudinal mid-section (e) Transverse mid-section view of right hand side top quadrant (f) Transverse mid-section view of right hand side bottom quadrant .. 282
Figure 8.16 Load-strain response for undamaged 8/70/CAI(0)-3 panel under in-plane compression (a) individual strain response (b) mean and bending strain response 283
Figure 8.17 Variation of Poisson's ratio with load, calculated from SG2 strain gauge pair and LVDT readings for 8/70/CAI(0J)-1 panel 284
Figure 8.18 Illustration of the deformation process of undamaged control panels under in-plane compression 285
Figure 8.19 Variation of load vs. vertical displacement for panels impacted from 0-25J and loaded in compression on the Mand machine 287
Figure 8.20 Mean and bending strain response for (a) 8/70/CAI(3J)-1 (failure located at mid-section of panel) (b) 8/70/CAI(3J)-2 (failure located at mid-section of panel) 288
Figure 8.21 Mean and bending strain response for 8/70/CAI(25J)-2 loaded on Denison with failure located at loaded end of panel 289
Figure 8.22 Photographs of 8/70/CAI(3J)-2 panel after in-plane compression: (a) Left external edge (b) Front (c) Right external edge (d) Cross-section of internal damage on longitudinal mid-section (e) Cross-section of internal damage on transverse mid-section top right quarter and (f) bottom right quarter 290
Figure 8.23 Photographs of 8/70/CAI(25J)-1 panel after in-plane compression: (a) Left external edge (b) Front (c) Right external edge (d) Cross-section of internal damage on longitudinal mid-section (e) Cross-section of internal damage on transverse mid-section top left quarter and (f) bottom left quarter 291
Figure 8.24 Photographs of 8/70/CAI(25J)-2 panel after in-plane compression: (a) Left external edge (b) Front (c) Right external edge (d) Cross-section of internal damage on longitudinal mid-section (e) Cross-section of internal damage on transverse mid-section top right quarter and (f) bottom right quarter 292
Figure 8.25 Mean and bending strain at far-field (SG1) and local (SG2) locations and load-vertical displacement response of undamaged and impacted 8 ply nomex sandwich panels under in-plane compression 296
Figure 8.26 Photographs of 8/64/CAI(9J) panel loaded under in-plane compression: (a) Front view... (b) Rear view (c) Right hand external edge (d) Cross-section of internal damage on longitudinal mid-section (e) Cross-section of internal damage on transverse mid-section top left quarter and (f) bottom left quarter 298
Figure 8.27 Photographs of 8/64/CAI(16J) panel loaded under in-plane compression: (a) Left hand external edge (b) Front view (c) Rear view (d) Cross-section of internal

damage on longitudinal mid-section (e) Cross-section of internal damage on transverse mid-section top right quarter and (f) bottom right quarter..... 299
Figure 8.28 Damage tolerance maps for 8 ply 70kg/m^3 aluminium or 64kg/m^3 nomex sandwich panels and 16 ply monolithic panels based upon compressive strength retention factor (a) Impact energy (b) Absorbed energy (c) Delamination length..... 303
Figure 8.29 Damage tolerance maps for 8 ply 70kg/m^3 aluminium or 64kg/m^3 nomex sandwich panels and 16 ply monolithic panels based upon residual compressive strain (a) Impact energy (b) Absorbed energy (c) Delamination length 304

LIST OF TABLES

Table 1.1 Review of literature concerning damage resistance testing.....45
Table 1.2 Review of literature concerning damage tolerance testing.....50
Table 1.3 Summary of compression after impact testing methods 26
Table 2.1 Material constitution of each sandwich panel system..... 57
Table 2.2 Test matrix for all loading conditions..... 59
Table 2.3 Test matrix for QS testing only..... 59
Table 2.4 Basic material properties of T700/LTM45-EL and IM7/8552 UD laminates..... 60
Table 2.5 Effective mechanical properties of T700/LTM45-EL and IM7/8552 cross-ply laminates $(0/90)_{ns}$..... 61
Table 2.6 Flexure of T700/LTM45-EL cross-ply specimens..... 61
Table 2.7 Flexure of IM7/8552 cross-ply specimens..... 62
Table 2.8 ILSS of IM7/8552 cross-ply specimens..... 62
Table 2.9 Mechanical properties of 5052 aluminium and HRH-10 nomex honeycombs..... 69
Table 2.10 Supplied mechanical properties of adhesives 71
Table 2.11 Honeycomb Geometrical Data..... 74
Table 2.12 Adhesive curing cycles 76
Table 4.1 Data for 8,12 & 16 ply T700/LTM45-EL plates loaded with HS indenter..... 106
Table 4.2 Data for 8,12 & 16 ply T700/LTM45-EL plates loaded with FE indenter 106
Table 4.3 Data for 8 and 16 ply IM7/8552 plates loaded with HS and FE indenters..... 109
Table 4.4 Individual data for 50 and 70kg/m^3 aluminium honeycomb stabilised compression tests..... 114
Table 4.5 Average data for 50, 70 and 90kg/m^3 aluminium and 64 and 96kg/m^3 nomex honeycomb bare compression tests with 20mm diameter FE loading area..... 115
Table 4.6 Average data for 50 and 70kg/m^3 aluminium honeycomb bare compression tests with 50mm diameter FE loading area..... 115
Table 4.7 Comparison of data for 8/70 & 16/70 panels and 16/70 panels containing embedded delamination loaded with HS and FE indenters 135
Table 4.8 Internal and external damage of cross-sectioned T700/LTM45-EL aluminium honeycomb panels from quasi-static bending tests.....141
Table 4.9 Internal and external damage of cross-sectioned T700/LTM45-EL nomex honeycomb panels from quasi-static bending tests.....146
Table 4.10 Internal and external damage of cross-sectioned T700/LTM45-EL aluminium honeycomb panels from quasi-static bending tests: Special cases – 220mm panels and panels containing embedded delamination.....148
Table 4.11 Internal and external damage of cross-sectioned IM7/8552 aluminium and nomex honeycomb panels from quasi-static bending tests.....149
Table 5.1 Theoretical (Eq. 5.9) and experimental values of absorbed energy for panels resting on a solid foundation loaded to ultimate failure..... 161
Table 5.2 Theoretical (Eqs. 5.22-5.25) and experimental values of absorbed energy and failure load for panels loaded in bending with the HS and FE indenters..... 172
Table 6.1 Comparison of panel stiffness increase prior to initial threshold, experimental (slope of load-displacement curve) & theoretical (flexural rigidity)..... 181
Table 6.2 Comparison of percentage increase in panel strength and stiffness with core density 182
Table 6.3 Increase in threshold values when changing from HS to FE indenter $(\frac{FE\ value}{HS\ value})$. 185
Table 6.4 Comparison of critical loads and damage within IM7/8552 and T700/LTM45-EL sandwich panels..... 187
Table 6.5 Comparison of initial damage and ultimate failure loads and stiffnesses for nomex and aluminium panels (64kg/m^3 ÷ 70kg/m^3 and 96kg/m^3 ÷ 90kg/m^3) 190

Table 6.6 Comparison of internal damage in panels resting on a solid foundation and under bending at ultimate failure 199
Table 6.7 Percentage increase in incident energy at initial damage and ultimate failure when changing from HS to FE indenter ($\frac{FE\ value - HS\ value}{HS\ value} \times 100\%$) 208
Table 6.8 Comparison of incident energy for nomex and aluminium panels 209
Table 6.9 Ultimate failure load for each panel design under quasi-static loading 233
Table 6.10 Maximum load per gram for each panel design at ultimate failure under quasi-static loading 233
Table 6.11 Energy absorption for each panel design at ultimate failure under quasi-static loading 234
Table 6.12 Energy absorption per gram for each panel design at ultimate failure under quasi-static loading 234
Table 6.13 Critical load & displacement values of T700/LTM45-EL skins / aluminium core sandwich panel quasi-static bending tests 236
Table 6.14 Slopes of load-displacement curves of T700/LTM45-EL skins / aluminium core sandwich panel quasi-static bending tests 237
Table 6.15 Incident, IE, and absorbed, AE, energies for T700/LTM45-EL skins / aluminium core sandwich panel quasi-static bending tests 238
Table 6.16 Critical load & displacement values of T700/LTM45-EL skins / nomex core sandwich panel quasi-static bending tests 240
Table 6.17 Slopes of load-displacement curves of T700/LTM45-EL skins / nomex core sandwich panel quasi-static bending tests 240
Table 6.18 Incident, IE, and absorbed, AE, energies for T700/LTM45-EL skins / nomex core sandwich panel quasi-static bending tests 241
Table 6.19 Critical load & displacement values of IM7/8552 skins / aluminium & nomex core sandwich panel quasi-static bending tests 242
Table 6.20 Slopes of load-displacement curves of IM7/8552 skins / aluminium & nomex core sandwich panel quasi-static bending tests 243
Table 6.21 Incident, IE, and absorbed, AE, energies for IM7/8552 skins / aluminium and nomex core sandwich panel quasi-static bending tests 243
Table 6.22 Critical load, displacement, incident, IE, & absorbed, AE, energy values of T700/LTM45-EL skins / aluminium and nomex core sandwich panel indentation tests 244
Table 6.23 Slopes of load-displacement curves of T700/LTM45-EL skins / aluminium and nomex core sandwich panel indentation tests 245
Table 7.1 CAI panels to be tested for damage tolerance 255
Table 7.2 Epoxy formulation for end potting for 1 mould with a volume of 84cm^3 257
Table 8.1 Summary of damage and failure loads of cross-sectioned T700/LTM45-EL monolithic laminate panels loaded under in-plane compression 307
Table 8.2 Summary of damage and failure loads of cross-sectioned T700/LTM45-EL honeycomb sandwich panels loaded under in-plane compression 307

NOMENCLATURE

AE – Absorbed energy
BI – Ballistic impact
BS – Bottom skin
BVID – Barely visible impact damage
C – Clamped boundary
CAI – Compression-after-impact
CC – Core crushing
CLT – Classical lamination theory
Cir. – Circular testing area
D – Delamination
Dia. – Diameter
DUTS – Directly under top skin
DW – Drop weight testing
EAF – Edge of adhesive fillet
ESLT – Equivalent single layer theory
F – Unsupported boundary
FAA – Federal Aviation Authority
FE – Flat ended indenter
FEP - fluonnate ethylene propylene
FF – Top skin fibre fracture
FSDT – First-order shear deformation
HS – Hemispherical indenter
HSAPT – High-order sandwich panel theory
HSDT – Higher-order shear deformation theory
IE – Incident energy
IKE – Impact kinetic energy
ILSS – Interlaminar shear strength
LVDT – Linear variable displacement transformer
LVI – Low velocity impact
M – Major
MC – Matrix cracking
NDT – Non-destructive testing
PTFE – Polytetrafluoroethelyne
QS – Quasi-static
RCS – Residual compressive strength
S – Shearing to
SDOF – Single-degree of freedom
SG – Strain gauge
Sl – Slight
Sq – Square testing area
SS – Simply-supported boundary
T_g – Glass transition temperature
TS – Top skin
TT – Through the thickness
UD – Unidirectional
VID – Visible impact damage

A – Acceleration of impactor
A_{ij} – Laminate extensional stiffnesses
b – Panel width or radius if circular
b_w – Honeycomb cell size
c – Core thickness
C_1 – Laminate constant
D_1 – Total sandwich panel bending stiffness
D_{ij} – Sandwich panel bending stiffnesses
E_c – Young's modulus of core
E_{comp} – Compressive modulus
E_f – Flexural modulus
E_i – Young's modulus of indenter
E_p – Young's modulus of panel
E_s – Young's modulus of skin
E_x – Tensile modulus
G_c – Shear modulus of core
H_0 – Constant
K – Constraint factor
k – Elastic foundation stiffness
k_b – Bending stiffness
k_{bs} – Bending-shear stiffness
k_c – Contact stiffness
K_g – Global stiffness of clamped sandwich panel
k_m – Membrane stiffness
k_s – Shear stiffness
L – Panel length
m – Impactor mass
n – Constant of indentation
p – Contact pressure distribution
P – Load
P_{init} – Initial threshold load
P_{ult} – Ultimate failure load
r – Radial location
R – Radius of indenter
R_e – Effective radius of hemispherical indenter
T – Time (impact)
t – Skin thickness
t_w – Honeycomb cell wall thickness
v – Impact velocity
v_0 – Initial impact velocity
w – Total deflection
w_e – Effective width

α – Indentation
α_c – Indentation of core
α_s – Indentation of skins
a_w – Honeycomb cell wall length
δ – Global deflection
ε_b – Bending strain
ε_m – Mean strain
η_{max} –Energy efficiency ratio
θ_w – Honeycomb expansion angle
Φ – Dynamic enhancement factor
ν_c – Poisson's ratio of core
ν_i – Poisson's ratio of indenter
ν_p – Poisson's ratio of panel
ν_s – Poisson's ratio of skin
ξ – Deformation in radial direction
ρ – Contact radius
σ_{comp} – Compressive strength
σ_{crush} – Honeycomb crushing strength
σ_{dyn_crush} – Dynamic honeycomb crushing strength
σ_f – Flexural strength
σ_x – Tensile strength
σ_y – Yield strength
τ_{dyn} – Dynamic honeycomb shear strength
τ_{13} – Shear strength of skin

PUBLICATIONS

1. Zhou, G, Hill, M and Hookham, N, Investigation of parameters dictating damage and energy absorption characteristics in sandwich panels, *7th International Conference on Sandwich Structures - Aalborg University*, Denmark, 2005.

2. Zhou, G, Hill, M, Loughlan, J and Hookham, N, Damage characteristics of composite honeycomb sandwich panels in bending under quasi-static loading, *Journal of Sandwich Structures and Materials,* 8, 55-90, 2006.

3. Zhou, G, Hill, M and Hookham, N, Investigation of parameters governing the damage and energy absorption characteristics of honeycomb sandwich panels, *Journal of Sandwich Structures and Materials,* 9(4), 309-342, 2007.

4. Zhou, G, Hill, M, Damage characteristics and residual compressive strength of composite honeycomb sandwich panels, *16th International conference on composite materials*, Japan, 2007.

1. INTRODUCTION

Composite materials have been extensively used in secondary aeronautical, automotive and marine structures since the latter part of the 20th century. Their outstanding specific strength, stiffness and design flexibility are responsible for their success, which has led to these materials becoming the desirable choice for primary structures in the past 20 years. In addition to the use of composite laminates in the place of traditional metals, composite sandwich structures are becoming common place in areas where good strength and bending stiffness-to-weight ratios and energy absorption are required.

Sandwich structures consist of two relatively strong skins bonded or co-cured to a lightweight core material. The skins are constructed from relatively thin, high strength materials such as carbon fibre, glass fibre or aluminium and are designed to provide a damage resistant layer with high in-plane strength. The core is used to separate the skin layers, increasing the panel thickness and therefore flexural rigidity without greatly increasing the weight, giving the panel strength in the transverse direction as well as providing an effective energy absorption medium. Materials used for the core are of lower stiffness and strength than those used in the skins, typical examples include aluminium and nomex honeycombs, synthetic PVC and aluminium foams, balsa wood and corrugated materials.

During the last two decades attention has been given to the damage resistance against local loads, and to a lesser extent the damage tolerance, of composite sandwich structures. Damage resistance is the ability of a structure to resist damage during loading, whilst damage tolerance is the ability of a structure to withstand loading after sustaining damage and retain its undamaged strength. Both damage resistance and tolerance are of vital importance in operational structures as it is not uncommon for accidental damage to occur during manufacture and maintenance through dropped tools, whilst in transit and during normal operation through impacts with runway debris and hailstones. This chapter reviews the most relevant work over the past two decades, with a factual summary of the most significant experimental work presented in Tables 1.1 and 1.2. From this review the main aims and objectives of the research project have been identified, as discussed at the end of the chapter.

1.1. Key issues in the applications of sandwich structures

Impact damage can seriously degrade the in-service performance of a composite sandwich panel as it is most vulnerable through-the-thickness. Extensive internal damage can be induced by even minor impacts, resulting in a significant loss of local strength despite little visual evidence on the external surface of the panel. The internal damage sustained by a composite sandwich panel under transverse loading is generally a combination of several damage mechanisms. These damage mechanisms can be identified using both non-destructive and destructive inspection techniques, though the effectiveness of techniques such as ultrasonic scanning in characterising the separate damage mechanisms is impeded by the core material. In addition to the typical damage mechanisms associated with composite laminates such as matrix cracking, delamination and fibre fracture, the presence of the core material also leads to core crushing, core shear and skin-core debonding as fundamental damage mechanisms. Any combination of these damage mechanisms can lead to failure of the panel under transverse loading.

As damage mechanisms are a key issue in damage resistance, studies are primarily concerned with the performance of both the skin and core materials, typically assessed in terms of stiffness, strength and energy absorption. The variation of the skin and/or core material, thickness and density, termed intrinsic variables, has formed a major area of interest in previous damage resistance studies. Other salient parameters considered, classified as extrinsic variables, include indenter size, nose-shape and loading speed, the panel boundary conditions and geometric size of the panel. The effect of the impact damage on the residual strength of the structure is the primary focus of damage tolerance studies. The presence of internal damage, often accompanied by a local indentation of the impacted skin, not only weakens the material in the vicinity of the impact but also causes the structure to become asymmetrical. Both factors can lead to panel failure at a stress well below that for an intact sandwich panel. Therefore it is important to understand not only how the type and extent of damage affects the residual strength, but also the effect of the skin and core configuration, panel size and boundary conditions on the in-plane compressive response.

The interaction and complexity of the damage mechanisms makes prediction and analysis of both damage resistance and tolerance extremely complicated. In addition the damage mechanisms associated with the core, namely core crushing, shear and debonding, inhibit the application of existing analysis for laminate plates to the case of sandwich structures. Many experimental studies have been completed on the damage resistance of composite sandwich panels [1-8] but often too few variables are considered such that the observations are very specific to the sandwich configuration used and conflicting conclusions are drawn by different researchers [9]. The first significant piece of analytical work on sandwich structures was completed by Allen [10] and forms the basis for most modern analytical studies. A large proportion of theoretical analysis has used mathematical prediction models such as finite element analysis. Due to the complex damage mechanisms these models tend to be very involved as failure occurs on a highly localised basis, and the success of these models is often limited.

1.2. Review of damage resistance

1.2.1. Basic damage characteristics under transverse loading

The basic damage mechanisms of a sandwich panel under transverse loading consist of skin damage, core damage and skin-core debonding. The relationship between each damage mechanism is complex and often depends on both intrinsic and extrinsic variables. However, general failure types and processes have been observed for both honeycomb and foam core sandwich panels, as illustrated graphically and discussed in [8,11-16]. In a honeycomb sandwich panel subjected to a local load, damage begins with a small amount of indentation around the indenter contact point due to crushing of the core. Core crushing reduces the support offered to the skin by the core, which leads to the onset of matrix cracking and delaminations in the loaded face sheet. These delaminations spread as the impact energy or loading force is increased which, then causes fibre failure of the top skin. Skin-core debonding is also common in co-cured sandwich panels where the excess resin from the skin is used to bond the skin to the core. If loading is continued densification of the core occurs, leading to damage and eventual penetration of the back skin.

Despite a variety of damage mechanisms occurring within a sandwich panel most research has focused on the panel response at top skin failure with damage prior to this dismissed as core crushing alone. In the significant parametric study of sandwich panels by Wen et al. [7] top skin fibre fracture was considered to be the first damage type, with focus on indenter penetration through the entire panel thickness. Although damage prior to top skin fibre fracture is sometimes difficult to identify from the impact response it is often clearly represented by variations in the quasi-static load-displacement curves. However, only a few studies have focused on the damage mechanisms relating to these variations [4,6,16-18].

The initiation of internal damage is signified by a change in gradient of the load-displacement curve, which may also be accompanied by a load drop. This transition point is observable in sandwich panels with both honeycomb and foam cores. Prior to the transition point the response can be considered as elastic. After the transition point the response becomes generally non-linear with panel stiffness increasing until top skin failure [4]. Within this non-linear region damage propagates and includes both skin delamination and core crushing. Signs of damage propagation in the form of load drops are observed within this region; however, little report has been made on which damage mechanisms these load drops are related to.

Tsotsis et al. [6] focused on the initiation of internal damage and attributed the change in slope to cracking of the phenolic resin on the cell walls of nomex honeycomb panels and plastic cell wall buckling next to the skin-core interface in aluminium honeycomb panels. Core damage was only present in close proximity to the indenter contact point and formed shear cracks in the phenolic resin on the nomex cores at 45° to the panel surface around the circumference of the flat-ended indenter. Resin cracking has also been observed in fibreglass cores and the elastic nature of nomex cores seen to allow the buckled cell walls to regain their original shape after unloading [3,19].

Delamination does not appear to occur in the tests by Tsotsis, and core crushing is stated by Williamson et al. [8] to always occur prior to skin damage, which shifts from matrix cracking to delamination. Herup et al. [2] observed core damage to occur first and then delamination when contact between the hemispherical indenter and panel

surface was fully established. However, this trend was identified for thin skins and may vary for thicker skins which distribute the load over a larger area of core. In the work by Davies et al. [17] and Rizov et al. [18] delamination is suggested to occur in conjunction with core crushing in foam panels tested with a hemispherical indenter. Although it appears that core damage is directly related to the transition point, the conflicting research in this area makes it impossible to conclude on how this is linked to delamination initiation and if changing any of the intrinsic and extrinsic variables alters the damage mechanisms.

The skin damage propagation sequence for a hemispherical indenter is illustrated by Kepler [12], starting with matrix cracking and ending with fracture of the individual plies. For a honeycomb panel skin delamination is seen to initiate directly above the cell walls beneath the indenter contact point. This then spreads along neighbouring cell walls and towards the centre of the cells before coalescing into skin fracture [4]. Delaminations are observed to increase in size through the thickness of the top skin, and are largest between the furthest two plies from the impact point [1,20-22]. Use of the de-ply technique shows delaminations to be elliptical or hourglass shaped and follow the direction of the ply directly beneath it. Delamination patterns follow the trends commonly observed in monolithic laminates [23], though delamination sizes are typically smaller in the sandwich skins, with small and medium sized delaminations situated around the mid-plane [22]. Once the delaminations become of significant size fibre fracture of the top skin soon occurs.

Barely Visible Impact Damage (BVID)

The visual assessment of damage within a structure relies on the residual dent left on the panel surface following an impact event. Accurate identification of existing damage is not only important in terms of damage resistance but also in terms of damage tolerance. The concept of barely visible impact damage (BVID) was initially created to simplify maintenance engineers' non-destructive-testing (NDT) inspection efforts when assessing in-service components. BVID is defined as the damage level corresponding to the lower limit of detectable damage during a visual inspection. The relationship

between damage detection and damage tolerance in relation to the Federal Aviation Authority (FAA) regulations is summarised by Tomblin et al. [24], and states that impacts that cause non-visible or barely visible damage must not impair aircraft operation and the damaged structure must withstand ultimate design loads. However, the way in which BVID is physically defined varies within the literature reviewed. Two popular definitions have been identified. The first states that BVID is characterised by the level of energy required to cause indentation and associated damage from the impact to be just visible to the naked eye from a distance of 1.2m [25, 26]. Typically damage is only represented by an indentation with no fibre breakage. The second definition states that the residual dent depth at the impact site should be greater than or equal to a set depth. In the work by McGowan et al. [27-29] and Palm [3] this depth was set to 0.05 inches (1.27mm), compared to 0.04 inches (1.02mm) by Cvitkovich et al. [30] and 0.02 inches (0.51mm) by Tomblin et al. [5]. A larger depth of 2mm (0.08 inches) was used in the work by Levin [31], similar to the 0.1 inch (2.54mm) dent depth used in existing criterion for thick monolithic laminates [27].

Clearly, the applicability of using dent depth as a reliable indication of internal damage is questionable. Different levels of energy could be associated with the same dent size in different sandwich panel constructions and both dent depth and internal damage are known to vary with intrinsic variables. This is especially true for different types of core material and density where large variations in dent depth can occur despite similar amounts of internal damage [3,31]. Indenter size and impact velocity are also seen to affect the residual dent depth [5,27]. The semi-empirical model by Lacy et al. [32] showed that the combinations of intrinsic and extrinsic variables which led to maximum internal damage were not the same as those which led to the greatest residual indentation. In addition when using a set dent depth criterion the required dent size may not occur until fibre fracture of the top skin, which corresponds to visible rather than barely visible damage [20,33,34]. Finally, it has also been observed that dent depth decreases with time [18,35,36], which could render the dent undetectable if there is considerable time between maintenance checks.

1.2.2. Intrinsic variables affecting damage resistance

Skin material

It is widely recognised that composites manufactured from carbon fibre or glass fibre offer the best all round performance. Although both are used extensively in forming the skins of sandwich structures carbon fibre is most common in aeronautical applications, whilst E-glass fibre is often selected for applications where the high cost associated with carbon fibre cannot be justified. The use of Kevlar and polyethylene skins are typically restricted to ballistic applications as they have very good tensile strength but have poor compressive properties and have high associated costs. A variety of fibre arrangements can be used to construct the composite skins, with UD layers or woven fabrics the most common, as shown in Table 1.1. Other fibre arrangements such as chopped strand mat (CSM) [21] are less common. Despite the wide range of carbon and glass fibres, resin systems and fibre arrangements available very few studies have investigated the effect of the skin material system on damage resistance.

Limited studies focusing on the skin material system have been published [6,19,22, 34,37-39]. Rhodes [34] in a comparison of carbon fibre and Kevlar skins, found the Kevlar skins to offer better damage resistance for a given IKE. Shih et al. [39] found skins made of polyethylene and polyester to outperform both carbon and Kevlar skins in terms of the load required for fibre fracture and absorbed energy. Roach et al. [37,38] studied the effect of using heavier E-glass woven fabrics and found the load required for top skin fracture to be higher for the heavier fabrics, though the corresponding damage area was similar. Kim et al. [22] looked at the effect of ply orientation and found the skins with plies at 90° to each other had greater delamination levels. In the study by Tsotsis et al. [6], despite a large range of skin materials including CFRP, GFRP (S-glass and E-glass) and aluminium being used, very few conclusions could be drawn regarding the effect of skin material as no direct comparisons were made.

There have been a small number of investigations into hybrid skins consisting of carbon/kevlar [34,40] and glass/aluminium [41]. The introduction of kevlar layers into a carbon fibre skin increases damage resistance primarily by introducing different damage

mechanisms to those seen for carbon fibre alone, but does induce a weight penalty as Kevlar does not have the load bearing performance of carbon fibre [34]. The addition of UHMWPE (ultra high molecular weight polyethylene) fibres [42] and glass fibres [43] to the external surfaces of the sandwich panel also offer increased impact resistance, but more beneficially provide a useful indication of impact damage having occurred.

Skin thickness

The effect of skin thickness is the parameter most considered in the damage resistance of sandwich panels [2-8,16,19,24,25,30,31,33,37,42,44,45]. Skin thicknesses studied in previous research range from 0.25mm to 7mm, as shown in Tables 1.1 & 1.2, though the most common skin thickness is from 1mm to 2mm or 4 to 8 plies, used primarily for stiffness dominated applications. The majority of research only considers two or three different skin thicknesses and often only limited conclusions can be drawn. Two of the most significant pieces of work were completed by Williamson et al. [8] who compared 2, 3, 5 and 20 ply skins and Herup et al. [2] who compared 4, 8, 16, 32 and 48 ply skins.

It is widely recognised that increasing the skin thickness causes an increase in both the damage initiation load and the load required for top skin fracture [2,4-8,16,19,33,37,42]. This trend applies equally to quasi-static and impact loading and for a given IKE level the peak contact force increases with skin thickness [2,5,44,45], whilst the duration of the impact decreases [44]. In terms of damage, increasing the skin thickness increases the IKE for BVID [5,25,30,31,33] and associated internal damage area [25,31,33]. The internal damage area at top skin fibre fracture is also seen to increase [2]. However, this comparison can be misleading as BVID and fibre fracture occur at different IKE levels for varying skin thicknesses. If the IKE level is fixed the skin delamination area is seen to reduce for thicker skins prior to the occurrence of fibre fracture in [33]. Conversely delamination area is unaffected for CFRP/nomex honeycomb panels in [3,8], whilst the accompanying core damage area increases in [3] and decreases in [8].

The increase in performance of thicker skin panels is directly attributed to the increased bending stiffness. The thicker skin distributes the applied load over a larger area,

consequently reducing the localised stresses [8]. In panels with thin skins made of 4 plies or less the low bending stiffness causes the load to be highly concentrated over a small area such that the contact pressure is transferred almost directly to the core [2]. The contact area may correspond to one or two cells, and consequently the core dominates the panel response and transverse strength rather than the skins as in the case of thicker skinned panels. Due to the localised nature of the transverse response it is also suggested that unbalanced sandwich panel constructions might provide the most efficient design when designing for minimum weight as the bottom skin has little effect on the panel response to loading [6].

Core material

Two types of core structure are used in the majority of modern sandwich panels, namely honeycomb and foam. Metallic honeycomb cores are typically made from aluminium or titanium if the structure is to be used in areas of high temperature. Popular non-metallic honeycombs included nomex (aramid paper coated with phenolic resin, common designation HRH) and fibreglass (E-glass fabric coated with phenolic resin, common designation HFT or HRP). Foam materials include polyvinyl chloride (PVC), polymethacrylimide (PMI), polystyrene (PS), polyurethane (PUR) and aluminium, manufactured in a closed-cell formation with common trade names such as Divinycell, Rohacell, Klegcell and Airex. Other less common core materials used in previous sandwich panel research include Cormat made from polyester/felt/epoxy [13], balsa wood [46,47], Vermiculux made from calcium silicate [7] and integrated core hollow glass fibre sandwich panels, also called woven sandwich fabric preforms [48-50].

Whilst both foam and honeycomb cored panels have been used predominantly in damage resistance testing, a foam core is often the more popular choice due to it being inexpensive in comparison to honeycombs and because it can be considered as homogeneous and isotropic, simplifying accurate representation of the core structure in theoretical models. Also the continuous surface of foam cores can assist in skin-core bonding, compared to the small cell wall surface area in honeycomb cores. However, honeycombs generally offer better strength and stiffness-to-weight ratios. The effect of

combining both materials to have panels with cores constructed of foam-filled honeycomb [40,51-56] or foam with corrugated or metallic insertions [57-59] has been studied by various researchers. These core structures have the strength of honeycomb cores whilst the foam stabilises the honeycomb walls and provides a continuous surface area for skin-core bonding, though the associated weight penalty is significant.

Very limited research exists for the direct comparison of foam and honeycomb cores in terms of damage resistance, with the few studies reviewed in Table 1.1. In a comparison of nomex honeycomb and Rohacell foam it has been found that for a given IKE the honeycomb sandwich panels have a slightly higher peak force than foam sandwich panels [45], though the overall response is similar. The amount of core damage is slightly greater in the foam panels than the honeycomb panels [1], though the reverse is observed for skin damage [60]. This is primarily due to the variation of core damage mechanisms and the anisotropic nature of honeycomb cores. Aluminium honeycomb cores undergo cell wall buckling leading to extensive plastic crushing under transverse loading, which is irreversible upon unloading. Foam cores are much more elastic and at low to medium loads can regain their shape leaving small residual dents on the impacted surface of the panel. Damage in foam cores is typically localised crushing and shear cracks. This leads to a variation in the panel response at higher loads and renders some of the observations regarding panel behaviour to be not directly applicable to honeycomb sandwich structures.

A small amount of literature has made comparisons between nomex and aluminium honeycomb. Whilst CFRP skins have often been combined with nomex honeycomb, as on the Beech Starship aircraft [24,61], due to moisture degradation and corrosion problems with aluminium honeycomb [62], modern day aluminium honeycombs with improved protective coatings are still popular. As the brittle resin coating on the nomex cores determines the strength of the honeycomb, with greater thicknesses of resin providing greater strength, the brittle resin has been linked to reduced damage resistance and tolerance [63]. The majority of research comparing nomex and aluminium honeycombs gives a similar damage resistance for a common core density and thickness [1,3,6,19]. Tsotsis et al. [6] reported a similar load required for initial core damage. In terms of internal damage Palm [3] who considered several core materials, observed the

skin delamination area to be comparable in nomex and aluminium cores whilst Bernard et al. [1] reported a larger number of buckled cell walls in the aluminium honeycomb for a given IKE.

Core density

As core density is calculated from the volume of the honeycomb sheet rather than cell wall material, it is regulated by both the cell wall thickness and cell size. In metallic honeycomb the cell wall thickness is directly dependent on the foil thickness of the metal used to form the cell walls. In nomex honeycomb the cell wall thickness is controlled by the amount of resin covering the aramid paper. Whilst much research has focused on the effect of core density on damage resistance via varying the cell wall thickness [1,3, 6,16,19,22,24,31,39,44,45,60,63], no significant research has been found for the effect of varying the cell size. Core densities studied ranged from 30 to 200kg/m^3 for honeycomb and 30 to 400kg/m^3 for foam, with the average density of the foam cores higher than for the honeycomb cores due to the lower strength of foam for a given density. Typically the effect of core density was studied using only two or three different densities, with 48kg/m^3 nomex honeycomb being the most common type of honeycomb core used in damage resistance studies, as shown in Tables 1.1 and 1.2.

Many researchers have studied the behaviour, performance and modelling of honeycomb core materials, the most significant work by Gibson et al. [64], Goldsmith et al. [65], Wierzbicki [66], Becker [67] and Mohr et al. [68-71]. The compressive strength and stiffness of the bare core material is directly related to core density. Therefore it follows that increasing the core density will proportionally increase the load required for the initiation of core damage in a sandwich panel [6], especially when the skin thickness is low and the loading area is large as the core dominates the response. Subsequently the peak force for a given IKE also increases with core density [39,45] as does the IKE required for BVID [31].

In terms of the effect of core density on the internal damage of a sandwich panel existing research shows varied findings. Goswami et al. [72] found that increasing the

core stiffness caused a reduction in the total energy released by the structure during impact and therefore reduced the tendency for delaminations to initiate and propagate. This is supported by Anderson et al. [45] who found that panels with a high density core had better damage resistance than those with a low density core and that the impact damage was more localised. In a study into the effect of the core on the overall sandwich structure performance Wierzbicki [73] concluded that a sandwich panel designed for maximum energy absorption should have a honeycomb core with a low crush strength, provided failure of the top skin, full densification of the core and excessive spread of the crushed zone towards the panel boundaries do not intervene.

Increasing the density of the fibreglass honeycomb core from 88 to 192kg/m^3 caused a reduction in total damage area in [24] but gave no clear correlation in the work by Ambur et al. [44] where 48, 88 and 128kg/m^3 core densities were considered. The core damage area was found to decrease by both Palm [3] and Caldwell et al. [63] for honeycomb cores. The effect of increasing the core density on skin damage caused a reduction in delamination area in [22,31,60] but a definite increase in delamination area in [3]. Whilst the former relationship is expected the latter is not, though the reason for this discrepancy is difficult to identify due to many differences in the intrinsic and extrinsic variables used within each study.

Core thickness

The effect of core thickness has been studied by [1,4,5,8,13,44,60,74]. Typically only two or three different thicknesses are compared with the most common thicknesses being 12.7 or 25.4mm, though thicknesses ranging from 6.35 to 60mm have been used in previous damage resistance studies, shown in Tables 1.1 & 1.2. Gibson et al. [64] highlighted the importance of the core to the sandwich structure as a whole, with its purpose being not only to maintain the distance between the top and bottom skins but also to contribute to the overall stiffness of the panel. The existence of a coupling between the core and skin displacements means the stiffness contribution of the core is not purely proportional to the total core thickness, but is a function of the core

thickness, varying with core height and dependent on the skin. This phenomenon is known as the skin effect [75] or core thickness effect [67].

Williamson et al. [8] performed the largest study into the effect of core thickness on damage resistance. In this study it was found increasing the core thickness increased the amount of skin and core damage. This observation has also been repeated in other research [1,44,60], though the opposite was found in [5]. The larger damage area is caused by the increased bending stiffness of the thicker core. Thinner panels undergo a larger level of global bending which leads to less local damage for a given load. Local core crushing and buckling may also occur easier in panels with thicker cores due to the lower local buckling load of the longer of the cell walls, thus reducing the through-the-thickness stiffness of the panel [4,8]. This has also been observed in the determination of bare honeycomb crush strength by Wu et al. [76] where some increase in crush strength occurred with decreasing honeycomb thickness.

In addition to increasing the damage area increasing the core thickness decreases the loads required for both damage initiation and top skin fibre fracture when the support span is moderate or the specimen is resting on a solid base [4,8]. If the support span is large global bending dominates the response and the thicker cored panel can sustain a higher load before fibre fracture [13]. Energy absorption prior to fibre fracture increases slightly when the core thickness changes from thin to moderate [4]. Any larger increases in core thickness do not cause any further increase in energy absorption, suggested to be due to local rigidity dominating the response [20].

Comparisons have also been made between sandwich panels and laminate plates of the same construction as the sandwich panel skins [20,22,37,38,42,44]. These studies have found damage to initiate at a lower IKE in sandwich panels than laminate plates [42,44]. This leads to larger delaminations in the sandwich panels at low IKE levels. However, at medium to high IKE levels the total delamination area is greater in the laminate plates [22,42], with significant delaminations located at the back face of the laminate plates but near the mid-plane of the top skin of the sandwich panels. The presence of the core increases the IKE required for fibre fracture and reduces the associated delamination size, whilst also slightly increasing the amount of absorbed energy [20].

1.2.3. Extrinsic variables affecting damage resistance

Specimen dimensions

A large amount of research into the quasi-static transverse response of sandwich structures has used three-point bending of two-dimensional sandwich beams rather than point loading of three-dimensional panels for ease of analysis. However, sandwich panels rather than beams are used in the majority of modern engineering applications, and estimations of both transverse strength and failure mechanisms from beam testing are not the same as obtained from panel testing due to the finite width of the beam and the existence of a one-dimensional state of stress. Therefore the focus of this literature review is on panels rather than beams.

A significant range of specimen sizes have been used in previous sandwich panel studies, as shown in Tables 1.1 and 1.2. As damage resistance is often studied as a precursor to damage tolerance testing, the specimen dimensions are commonly dictated by the requirements for damage tolerance testing. The majority of specimens are square with dimensions ranging from 80mm × 80mm to 850mm × 850mm, though most are between 100mm × 100mm and 200mm × 200mm. A lesser number of studies have used circular panels with diameters ranging from 70mm to 337mm. Although rectangular panels are more representative of panels found in practical applications, during loading the corners of the panel tend to lift from the support causing an uneven stress distribution at the panel edges. Furthermore, when the damage area is relatively large the rectangular support could interfere with the development of damage mechanisms. This cannot happen with circular panels and consequently the stress distribution is even across the panel surface, allowing the testing area to dominate the response without the interference of the support geometry. However, no comparison of the impact response of square and circular sandwich panels has been made in the literature reviewed. Hazizan et al. [74] compared the peak impact force of sandwich beams of varying length with circular sandwich panels and found the peak impact force in the panels to be higher for a given IKE, due to the higher flexural rigidity of the panel. It was also suggested that the panels contained larger levels of internal damage at lower IKE levels than in the beams.

The few studies on the effect of specimen size for square sandwich panels draw limited conclusions. Ambur et al. [44] considered the effect of doubling the panel length from 114mm to 240mm on impact response and found the deflection profile in the lengthwise direction to be identical when subjected to a 4J impact, implying a similar amount of global bending. This is corroborated by Tomblin et al. [77] who also found increasing only one panel dimension to have no effect on either impact force, duration or damage area. However, increasing both width and length dimensions caused the peak impact force for a given IKE to reduce, whilst the impact duration increased and the resulting damage area and dent depth decreased. Despite an extensive range of tests completed by Wen et al. [7] on 200mm × 200mm and 850 × 850mm panels, only limited conclusions were made. Broadly speaking increasing the specimen size typically gave a similar load for fibre fracture of the top skin, though the damage mechanisms did alter from shear failure in small panels to global bending failure in some of the large panels, whilst others failed in a mixed mode.

Davies et al. [17], and Anderson et al. [45], highlighted the possible dangers in using small specimens when assessing damage resistance. Davies suggested that the extent of the damage caused during loading may extend outside the panel boundaries and the forces induced during clamping may affect the results obtained. Comparisons were made between the impact damage of small 200mm × 400mm panels and large 800mm × 800mm panels. For the same level of impact energy the smaller panels were seen to suffer fibre fracture and delamination of the top skin whilst the larger panels had some delamination and core damage but no fibre breakage. This is suggested to be due to more energy being absorbed elastically through the greater amount of global deflection and induced membrane action in the large panels, leaving less energy to be absorbed through creating permanent damage. This highlights the need for caution when comparing the transverse response of panels of different sizes.

Support conditions

Three types of support are commonly used in damage resistance testing, namely clamped, simply-supported or resting on a rigid foundation. The latter is used to

ascertain the indentation response of a sandwich panel as global bending deformation is prevented, whilst clamped and simply-supported support conditions are used to represent the fixings found in practical applications. Although both clamped and simple supports constrain vertical and horizontal translation and have similar levels of contact force and strain at the impact point for a given IKE, the prevention of rotation by the clamped support induces higher strains away from the impact point for a larger duration [44]. Therefore it is intuitive to suggest that the internal damage area may also be greater in clamped panels.

The indentation response of panels resting on a solid foundation and loaded in bending has been compared by Williamson et al. [8] and Zhou et al. [19]. The indentation of the panels in bending, calculated by subtracting the bottom skin displacement from the top skin displacement, shows a close correlation with the level of indentation measured for the panel resting on a solid foundation. The peak force for a given IKE and load required for fibre fracture are also comparable. This is attributed to the local contact and bending stresses induced by the indentation at the loading point dominating both the panel response and damage mechanisms. It is also noted that this may not be applicable to thin panels where membrane stresses dominate the panel response and damage to the back surface of the panel can be induced [8,78].

Despite the above discussion Williamson did not make a comparison of the internal damage in panels for each support system. Caldwell et al. [63] found simply-supported panels in bending to contain a larger area of core damage than those resting on a solid foundation, though the accompanying skin delamination area was smaller. Tomblin et al. [24,77] found the panels on a rigid foundation to undergo a high contact force over a shorter duration for a given IKE, with a similar planar damage area and greater residual dent depths compared to those with clamped supports. It is also suggested that the panels resting on a solid base are representative of the sections of aircraft panels that are sited directly above a frame or bulkhead [77]. The presence of the core has also been considered to affect the constraint conditions. Aymerich et al. [20] found in the comparison of clamped circular laminate plates and sandwich panels that the top skin of the sandwich panel reacted more like a plate on a deformable foundation. Hoo Fatt et al.

[79,80] also recognised the effect of support conditions on global and local deformation, with the development of separate equations for each support condition.

Indenter geometry

Typical indenter geometries used in damage resistance testing include hemispherical, flat-ended and conical nose-shapes. Other less common indenters included pyramid shapes [81] and deformable water filled membranes [82]. Indenter diameters, traditionally measured in inches, varied from 6.35mm (1/4") to 76mm (3") in the literature reviewed. As can be seen from Tables 1.1 and 1.2, by far the most common indenter was a 12.7mm (1/2") or 25.4mm (1") diameter steel hemispherical indenter, as it is representative of the operational damage caused by dropped tools and stones. The largest studies into the effect of indenter size on impact response have been carried out by Wen et al., Raju et al. and Chen et al. [4,7,83] where a minimum of four different indenter sizes were used.

The effect of indenter shape on damage propagation and associated energy absorption is discussed in-depth by Kepler [12,21] for hemispherical, flat-ended and conical indenters. In high energy impact tests the panels impacted with the hemispherical indenter were found to contain considerably more skin and core damage than the panels impacted with conical indenters. However, the force relating to fibre fracture and penetration of the top skin was much lower. Wen et al. [7] also found this to occur, with the top skin failure load highest for the flat-ended indenter and lowest for the conical indenter. This is as a direct result of the reducing indenter contact area, from flat ended to hemispherical to conical indenters.

Decreasing the size of a hemispherical indenter has a similar effect to changing the indenter shape in that the load becomes concentrated over a smaller area. Therefore the localised stresses become larger for a given load, and the force required for both the initiation of damage [4,6,27] and top skin fibre fracture [4,5,7,8] reduces accordingly. The increase in magnitude of the damage initiation load does not increase at the same rate as contact area. Doubling the indenter diameter increased the contact area fourfold

but only increased the indentation load by 2.5 in the research by Tsotsis et al. [6]. This is attributed to an interaction between the honeycomb cell walls and the indenter, with the area of the cell walls beneath the indenter controlling the indentation load rather than the actual indenter area. Interestingly, it has also been found that for a given IKE below that required for fibre fracture, the maximum contact force is comparable for different indenter sizes even though the damage area varies, due to a larger area of panel undergoing a lower contact pressure during the impact [8,27].

It is generally found that increasing the indenter diameter decreases the dent depth [5,8,24,27,84]. The variation of damage area with increasing indenter size is unclear. However, both Williamson et al. [8] and McGowan et al. [27] found increasing the indenter size to decrease the damage area for a given IKE level, whilst the opposite is reported by Chen et al. [83], Meo et al. [84] and Tomblin et al. [5,24]. As the transverse response is dependent on a number of both intrinsic and extrinsic variables it is difficult to identify why the opposing trends occurred. The variations in both the load required for failure and damage size appear to be most affected by a change from 1/2" (12.7mm) to 1" (25.4mm) diameter indenters. Chen et al. [83] studied indenter diameters from 6.25mm to 50.8mm for a fixed IKE of 4J. For indenter sizes up to 38mm damage area increased with increasing indenter size. After 38mm the damage area reduced slightly for further increases in indenter size. For a given indenter size both the skin and core damage areas reach a maximum value that is not exceeded with further increases in load, though this value does increase with increasing indenter size [8].

Impact kinetic energy level

The impact kinetic energy can be varied by either varying the impact speed or indenter mass. The variation of impact speed is the most common method, typically using a drop weight rig for low velocity impacts. Quasi-static loading and high velocity ballistic impacts are also used to assess impact response at either end of the velocity spectrum. At all loading speeds it is widely recognised that increasing the impact energy will increase the level of damage within a sandwich panel until fibre fracture of the top skin occurs. As seen from Table 1.1 the majority of research into the damage resistance of

sandwich panels focuses on low velocity impacts as it is representative of the operational impacts which occur during manufacture and maintenance through dropped tools etc. High velocity impacts using an airgun, with speeds up to 300m/s, have been considered to a lesser extent.

Quasi-static testing, typically at loading rates between 1-10mm/min, is generally only used as an introduction to impact testing. The controlled loading speed allows the test to be stopped at any moment, facilitating the identification of damage mechanisms and propagation. Accurate data for the load-displacement response is also obtained much easier than in impact testing. However, as the loading speed is very slow the analogy of the quasi-static response to the impact response is often questioned due to strain rate sensitivity. It is stated that if the duration of the indenter being in contact with the panel is much longer than the duration required for the elastic stress waves to propagate through the panel then the impact can be treated as quasi-static [85].

The strain rate sensitivity of a sandwich panel depends on the constituent materials. Both epoxy resin and E-glass fibre are reported to be strain rate sensitive, as is foam due to its visco-elastic properties. Sandwich panels consisting of glass fibre and foam cores have been found to be rate sensitive in many instances [7,17,21,37,38] under both low velocity, less than 10m/s, and high velocity, 30 to 160m/s, impacts. Carbon fibre/foam core panels have also shown an amount of strain rate sensitivity [43,86]. Whilst the effect on damage area is inconsistent, the critical loads required for top skin fracture and panel penetration were frequently underestimated when using quasi-static testing compared to impact testing. The increase in panel stiffness under impact loading induced an increase in load, which in turn led to a higher level of absorbed energy for perforation of the panel [7,21,37]. Wen et al. [7] define a dynamic enhancement factor, Φ, to measure the increase in perforation energy for impact loading over quasi-static loading, with Φ increasing with impact velocity.

The effect of impact velocity on honeycomb sandwich panels has received less attention. The study of glass fibre/aluminium honeycomb panels by Mines et al. [13] found an increase in the energy required for perforation under impact. Panels made from carbon fibre skins and aramid honeycomb showed limited strain rate effects. In the

study by McGowan et al. [27] for a set IKE small increases in peak contact force were only seen at impact velocities above 7m/s and the damage induced by airgun impacts initiated at a slightly lower IKE than for drop weight impacts, but gave a similar damage area once damage had occurred. Williamson et al. [8] reported similar panel stiffness under both quasi-static and low velocity impacts with comparable amounts of skin and core damage for a given load. Conversely, Herup et al. [2] stated that the amount of internal damage at a given load varied for quasi-static and low velocity impacts, though the damage at fibre fracture was comparable. Increases in panel stiffness and top skin fracture load were also reported, and concluded to be due to the inertial stiffening effect, which is more prominent for thicker skins because of their greater mass.

A number of direct studies into the performance of aluminium and nomex honeycomb under quasi-static and impact loading have also found the core materials to be strain rate sensitive. Increases in crush strength have been found for low velocity impacts, though there is conflicting reports on the level of increase. Both Goldsmith et al. [65] and Zhao et al. [87] found crush strength of aluminium honeycomb to increase by 30-50% from the quasi-static value at velocities from 2 to 28m/s. Contrastingly Wu et al. [76] obtained similar levels of increase for some core types but showed crush strength to increase linearly with impact speed for velocities from 9 to 26m/s. For an impact at 10m/s Yamashita et al. [88] show a 20% increase for peak compressive strength and only a 10% increase in crush strength. For nomex honeycomb the increase in crush strength is reduced to 10% at an impact velocity of 20m/s [65].

1.3. Review of damage tolerance

The assessment of the impact damage tolerance and residual strength of a sandwich panel can be carried out in a number of ways. In-plane compression-after-impact (CAI) is the most common method used for both monolithic laminates and sandwich structures [5,26,27,30,36,77,89-91]. In-plane compression testing is generally chosen over tensile testing as the compressive strength of a sandwich panel is lower than the tensile strength and in-plane compression represents the most critical loading scenario. Other methods

of evaluating damage tolerance include three or four point bending of impacted beams [31,33-35,42,43,92-94] and shear testing [83,95]. Whilst three or four point bending is comparatively simple, it is only applicable to beams rather than panels and shear testing requires a complex loading rig.

An amount of experimental studies have been completed on both the in-plane compression of undamaged panels and compression-after-impact testing of impacted panels, as summarised in Table 1.2. In addition impact damage has been simulated by the introduction of artificial delaminations, holes and notches. Irrespective of the internal damage state factors such as panel size and support conditions have a large bearing on the values of compressive strength determined experimentally. The intrinsic variables discussed previously for damage resistance are also of interest in damage tolerance testing. The variation of any of these factors can affect not only the panel strength but also the failure mechanisms involved. In an attempt to understand the key issues in the damage tolerance of sandwich panels firstly the existing testing methods are reviewed then the case of undamaged panels is discussed prior to the assessment of panels containing impact and artificial damage.

1.3.1. CAI methods

At present there are no industry wide standards for the compression-after-impact of sandwich panels. However, a number of methods have been developed by the aerospace industry to determine the CAI performance of monolithic laminates [96]. The common feature of all methods is the introduction of low-velocity impact damage using a hemispherical indenter to simulate the in-service impacts caused by dropped tools, runway debris, etc. onto a flat panel. The specimen geometry, impact energy, and compression support conditions vary between each method. The two most common methods are those developed by Boeing (commonly referred to as SACMA) [97] and NASA [98], both reviewed below. A less common method was created by the Composites Research Advisory Group (CRAG) [96]. The impact aspect of this method is similar to the aforementioned methods but the original specimen is subjected to multiple impacts then sectioned to form multiple coupons which are loaded in

compression. One other alternative method specific to the compression testing of sandwich specimens is ASTM C364 [99]. Although this method is for compression rather than compression-after-impact it is relatively common in the CAI testing of sandwich panels, so is also reviewed briefly below. An amount of CAI testing has previously been completed at Loughborough University on monolithic laminates [100-102]. The methods used were based upon and developed from those used at Imperial College [96]. A summary of the LU/IC method is contained in Table 1.3, along with the SACMA, NASA, CRAG and ASTM C364 methods.

SACMA SRM 2-88: Compression-after-impact properties of oriented fibre-resin composites

This method was developed by Boeing and has been adopted by the Suppliers of Advanced Composite Materials Association (SACMA) [97] and is the basis of the Airbus Industries test method and ASTM D7137 [103]. It is currently the most popular method for the compression-after-impact of monolithic laminates. A test specimen measuring 152mm × 102mm × 4.6-5.6mm is clamped to an aluminium support base, with a 76mm × 127mm cut out area, using 4 rubber tipped toggle clamp fixings. The specimen is impacted using a drop weight impact rig equipped with a 5kg, 16mm diameter hemispherical indenter. The drop height can be adjusted to give the required impact energy of 6.7J/mm, which is specified in terms of panel thickness. The impact energy can be determined using the potential or kinetic energy, the latter value providing more accuracy as friction losses are accounted for.

As the size of the specimen used in both the impact and compression test phases is identical the test specimen does not need to be trimmed prior to compression testing. A specially designed compression rig is used to support the specimen, shown in Fig. 1.1. The specimen is clamped at the loaded ends and simply-supported along the longer unloaded edges, with loading at a rate of 1.27mm/min. Four axial strain gauges are used to measure the strain. An ultrasonic C-scan should be performed on the test specimen prior to impact to ensure no irregularities are present. After impact a visual inspection of the panel is needed to identify any external damage and a second ultrasonic C-scan

should be conducted to determine the level of internal damage (delamination). A minimum of 5 specimens should be tested to ensure consistency of results.

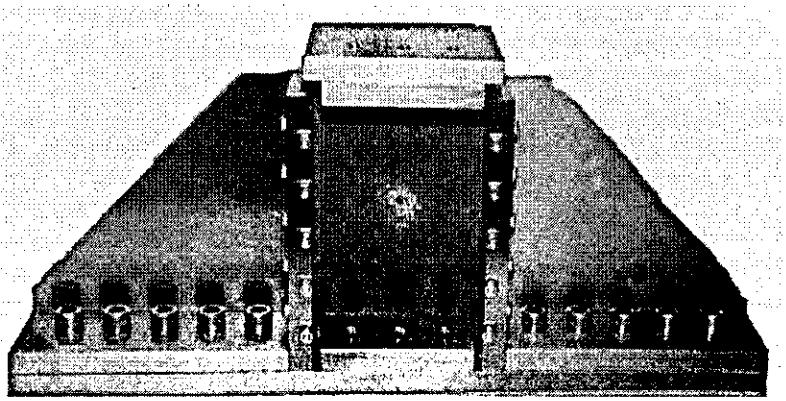

Figure 1.1 SACMA compression after impact test rig

NASA 1092: Standard tests for toughened resin composites

An alternative method has been developed by NASA [98]. This method is similar to the SACMA method but utilises bigger test specimens, making it less popular due to the larger associated testing costs. The test specimens measure 254-317mm × 178mm and are 6.35mm thick. Specimens are clamped centrally between a steel base plate and top plate with 127mm × 127mm cut-outs. Impact damage is induced using a drop weight impact rig with a 4.55kg, 12.7mm diameter hemispherical indenter. The indenter drop height is 508mm, producing a fixed impact energy of 27J. As with the SACMA method the test specimens should be visually checked and C-scanned before and after the impact, with the testing of three specimens for verification of results.

The impacted specimen must be trimmed to 178mm × 125mm to fit into the compression rig, shown in Fig. 1.2. This also removes any damage to the panel induced through the clamping supports used in the impact phase and ensures each loading edge is perfectly square and flat. The 125mm loading edges of the specimen are clamped between two steel plates to prevent local buckling of the specimen ends, whilst the 178mm edges are simply-supported. The load is applied through the clamped edges at a

crosshead speed of 1.27mm/min and back to back axial strain gauges are used to monitor the load-strain response.

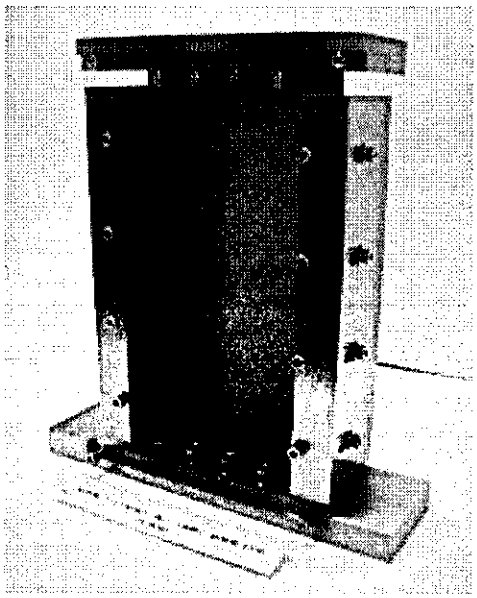

Figure 1.2 NASA compression-after-impact rig

ASTM C364: Edgewise compressive strength of sandwich constructions

ASTM C364 is the standard test method for edgewise compressive strength of sandwich constructions [99]. This procedure is for in-plane compression only and does not include or consider impact damage. Unlike the other test methods reviewed above ASTM C364 does not offer support to the unloaded edges of the panel, so 'column compression' is induced. The dimensions of the test specimens are set as ratios of the overall panel geometry. The specimen width must be at least twice the panel thickness, greater than 50mm, with a minimum of four complete honeycomb cells across the width. The length of the unsupported gauge section must be less than eight times the panel thickness. The experimental set-up is illustrated in Fig. 1.3.

The load is applied directly to the specimen ends, therefore requiring the loading ends of the panel to be flat and parallel to each other and perpendicular to the unloaded panel edges. During compression the loaded edges must be laterally supported to prevent

early buckling failure due to separation of the skins from the core at the point of contact with the loading plates. This can be done by either using steel bars clamped to the specimen and support rig or by potting the specimen ends in resin or equivalent material. The loading speed is suggested as 0.5mm/min but can be varied as required. The compressive stress in the panel at failure is found by dividing the ultimate load by the cross-sectional area of both skins.

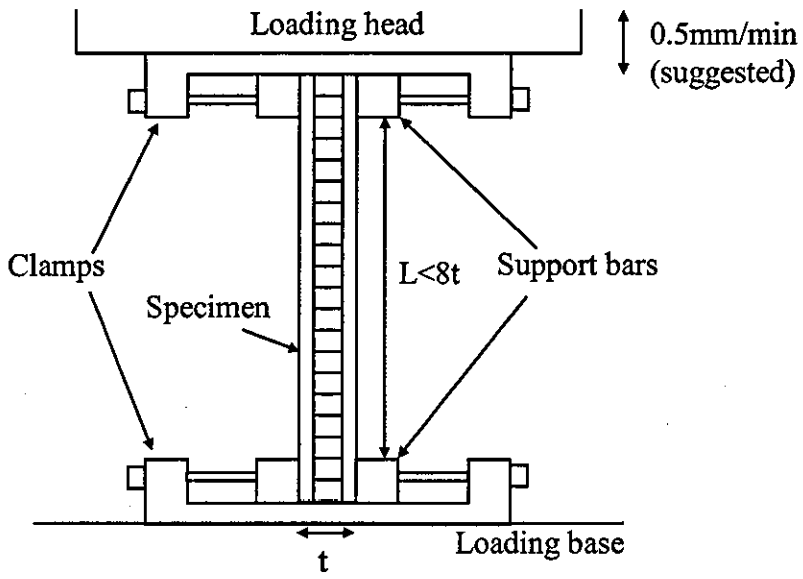

Figure 1.3 Test set-up for ASTM C364

From the literature reviewed and summarised in Table 1.2 it is immediately apparent that very few experimental studies have followed any of the CAI methods discussed above, although many similarities were seen in the methods used. Of those that did two followed the SACMA method [40,57] whilst several others used ASTM C364 even though it is designed for in-plane compression rather than compression-after-impact of sandwich panels [95,104-107]. In terms of inflicting impact damage the majority of studies used the BVID criterion or varying low impact energy levels applied with a HS indenter, in a manner similar to the NASA and SACMA procedures. Therefore it is necessary to review the boundary conditions and panel geometries used in previous CAI studies of sandwich panels, in order to ascertain an appropriate test method to use in the current research project.

Table 1.3 Summary of compression after impact testing methods

Parameter	Unit	NASA	SACMA	CRAG	ASTM C364*	LU/IC
Specimen dimensions	mm	254-317 × 178 × 6.35	152 × 102 ×4.6-5.6	Dia. ≥ 140 t ≤ 3	-	100-500 × 100-500 × 10-25
Impact test area	mm	127 × 127	127 × 76	Dia. 100	-	Dia. 100-500
Boundary conditions	-	C	C at four corners	C	-	C
Impactor mass	kg	4.55	5	Variable	-	Variable
Impactor size	mm	HS Dia. 12.7	HS Dia. 16	HS Dia. 10	-	HS Dia. 10
Impact energy/ drop height	J / m	27 / 0.508	Variable	Variable / 1	-	Variable
Specimen dimensions	mm	254 × 125 × 6.35	152 × 102 × 4.6-5.6	180 × 50 × 3 (gauge length 100)	L ≤ 8t W ≥ 50 & ≥ 2t t undefined	350 × 250 × 10-25 or 150 × 100 × 1-6.4
End fixings	-	C between steel plates	C between steel plates	C using end tabs	C between steel bars	C with epoxy end pots
Side fixings	-	SS	SS	SS	F	SS
Loading rate	mm/ min	1.27	1.27	To cause failure within 30-90 secs	0.5 or for failure in 3-6 mins	1

Note:

Specimen size given by length × width × thickness ($L \times W \times t$) for rectangular geometries or diameter × thickness ($d \times t$) for circular geometries.

* Standard specifically for sandwich panels

LU/IC – Loughborough University/Imperial College method

Compression Fixings

As seen in Table 1.3 a clamped support condition is typically used for the loaded ends of a panel within a compression rig. Clamped conditions prevent panel rotation and horizontal movement of the panel ends. This is created by either clamping the panel directly with metal blocks, as seen in the SACMA and NASA methods or potting the panel ends in epoxy resin. The potting material prevents direct rotation of the panel ends in a similar way to clamping the panel ends with metal blocks. However, as the potting material is not fixed to the loading head a minimal amount of rotation of the potting material can occur. Potting the panels in epoxy resin or setting the panel ends into metal

blocks eliminates the possibility of inflicting damage to the panel ends, as can occur when mechanically clamping or gripping the panel ends. Potting the panel ends also helps to prevent end brooming and the occurrence of delaminations at the loaded panel ends. Irrespective of which method is used to clamp the loading ends it is vital that the ends are completely flat and parallel to the loading surface. If the loading ends and loading head are not in parallel an uneven stress distribution can be induced at the panel ends, which may lead to premature failure of the panel at the loaded ends. In a small number of the previous studies reviewed in Table 1.2 simple supports were used for the loaded ends. However, this type of support condition is more difficult to create as horizontal panel movement is constrained but rotation of the panel ends is permitted. The three variations of boundary condition are shown in Fig. 1.4.

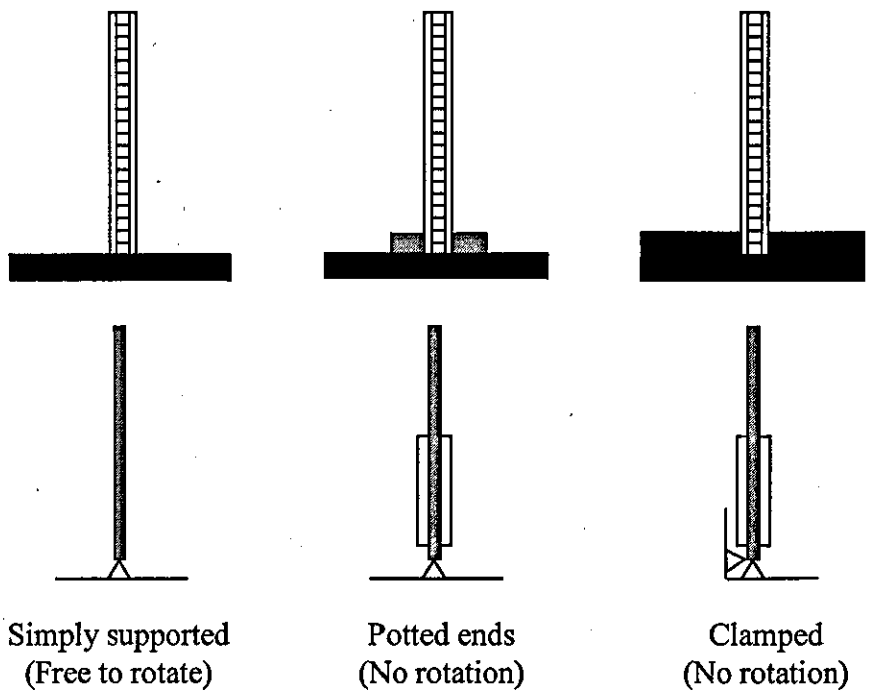

Figure 1.4 Compression support conditions

The unloaded edges of the panel can be free, simply-supported or clamped. If the edges are free then compression of the panel can be compared to compression of a wide column. If the edges of the panel are simply-supported or clamped then the panel must be treated as a plate. Clearly in the two-dimensional beam case the buckling modes and associated analysis is much simpler than for the three-dimensional plate case, with

Timoshenko or Euler beam theory often applied in the former case. Additionally if the unloaded edges are free and the panel aspect ratio is moderate to large, global buckling of the specimen is likely to occur and the load required for failure will be much less than for that of a panel with simply-supported or clamped unloaded edges. Hence the simple or clamped supports used on the unloaded edges are often termed anti-buckling supports, although contrary to what the name suggests local panel buckling can still occur but will be at a much higher load.

In the literature reviewed clamped loaded ends were achieved in a number of ways. Mechanical clamping of the ends is typically used for specimens with free unloaded edges. To overcome the problem of crushing the weak core material when trying to grip the specimen tight enough to prevent slipping, the loaded ends of the sandwich panel can be reinforced. Reinforcement is commonly in the form of high density aluminium honeycomb such as 350kg/m^3 [90,108] or solid metal blocks [109,110] used to replace the low density core in the clamping region. Glass epoxy or aluminium tabs can also be bonded to the outer surface in the clamping region.

Setting the specimen in U or C shaped aluminium or steel blocks [47,111-114] and potting the loaded panel ends in epoxy resin [83,106,115] were used as popular alternatives to mechanical clamping of the loaded ends. In addition to the traditional method of potting as used for monolithic laminates [100-102], an alternative method is to remove the core from the loading end and fill the clamping region with epoxy resin and/or chopped glass fibre. Once set the specimen can then be mechanically clamped or the ends machined to provide a flat parallel load surface and loaded directly when the panel thickness is sufficient [27,29,47,116]. Moody, Vizzini and co-workers [26,117, 118] used a variation on these methods by potting the sandwich panel in a Bismuth metal alloy with a very low melting temperature. This method allowed the specimens to be removed whole from the potting material after testing and the potting material to be reused. In addition it was not necessary to machine the ends before testing, as required for traditional potting methods.

In previous experimental studies, as shown in Table 1.2, the majority of researchers used clamped loaded ends and free unloaded edges, with a lesser number of studies

using clamped loaded ends and simply-supported unloaded edges. Very little research has considered the effect of the panel constraints. The importance of accurately representing the boundary conditions seen in operational situations has been highlighted by Nokkentved et al. [119]. Panels are typically fixed to a framework and each other and therefore are constrained in both length and width directions. McGowan et al. [27] investigated the effect of edge supports on the compressive response by testing sandwich panels with both simply-supported and unsupported unloaded edges. It was found that the removal of the simple supports only affected the panel just before the point of failure when the panel suddenly bent, increasing the compressive strain in the impacted skin. The global axial stiffness of the panel was not affected by the absence of edge supports, and the panel failed in a similar way to the panel with simply-supported edges tested under the same conditions. Despite this observation caution must be taken when comparing panels with supported and free edges and all subsequent discussion will distinguish between the two support conditions, with focus on panels with supported unloaded edges where possible.

Panel Geometry

Due to the lack of established CAI test standards for sandwich panels the geometry of the panels used in existing research varies immensely, as shown in Table 1.2. For the impact testing phase the overall specimen geometry is irrelevant if the panel is clamped as only the area inside the clamped region responds to the impact. However, when the panel is tested in compression the diameter of the impact damage should not be greater than half the specimen width and penetration of the panel should not have occurred. If the damage is in excess of these limits then it is too extensive to meaningfully evaluate damage tolerance with a subsequent compression test. In these circumstances a bigger panel or lower energy level should be used.

In the references reviewed the general trend was to use a square panel for the impact testing phase which was then trimmed to make a smaller sized rectangular panel for the compression testing phase, in line with the NASA CAI testing method. This removed any damage induced by the clamps during impact testing and allowed for machining of

the panel edges to obtain the flat and parallel/perpendicular edges required for compression testing. The typical size of the panels used in the compression testing phase had length and width dimensions between 100-300mm and overall thicknesses of 25-30mm. Large panels were less common due to the higher costs involved. Small panels with lengths and/or widths below 100mm combined with large thicknesses were more comparable to coupons or columns [60,95,104,105,107,109,120-123]. These are not representative of panels so consequently are not considered further in this review.

The panel dimensions used in previous research also seemed to be dependent on the specimen boundary conditions. As shown in Table 1.2 the length-to-width ratio otherwise known as the panel aspect ratio was typically 1 to 2.5, irrespective of the support conditions. However, the width-to-thickness ratio was generally below 5 for panels with clamped loaded edges and free unloaded edges but above 5 for panels with clamped loaded edges and simply-supported unloaded edges. As the width-to-thickness ratio approaches unity or the aspect ratio drops below 1 panel buckling becomes less likely. Therefore dimensions with these ratios should be avoided when studying the impact damage tolerance of realistic structural panels.

The effect of varying the panel aspect ratio has been studied by only a small number of researchers. For undamaged panels with simply-supported unloaded edges increasing the aspect ratio from 1 to 2 [124] and 1.33 to 2 [47] reduced the failure load despite the failure mechanisms being the same. In panels containing impact or artificial damage often very few comparisons could be made for panels with different aspect ratios, as despite a reduction in failure load with increasing aspect ratio, the level of impact/artificial damage also increased [26,125,126]. One exception to this was in the study by Tomblin et al. [77] where the effect of panel aspect ratio was compared by normalising the panel length and width by the damage diameter. Both length and width were varied for impact damaged panels with clamped loaded edges and simply-supported unloaded edges. Increasing the width to give an aspect ratio between 1.6-0.64 tended to marginally increase the compressive strength, as was also observed by Moody et al. for panels with unsupported side edges [26], whilst increasing the panel length to give an aspect ratio between 0.84-1.32 caused a minor reduction in compressive strength. The latter was suggested to be due to an interaction between global buckling

and the local indentation as a result of the impact damage. In addition the narrow specimens had higher strain levels within the damaged region, indicating a higher level of load was carried through the damaged region which resulted in higher levels of bending. Different failure mechanisms were also observed in narrow and wide panels, with wide panels exhibiting a dimple-growth arrest mechanism.

Overall the review of panel support conditions and geometry shows both variables to be of extreme importance in the compression-after-impact testing of sandwich panels. Both variables can affect not only the compressive failure loads but more importantly can determine the type of failure modes encountered. Therefore extreme caution must be taken when selecting suitable testing conditions to accurately represent the loading conditions the structure would be exposed to in operational conditions. If this is not achieved the results obtained from experimental testing may not be representative. For all reasons considered above it is believed the LU/IC method is suited to the CAI testing in this project.

1.3.2. Damage characteristics under in-plane compression

Failure modes of intact panels

The response of undamaged panels in in-plane compression has been studied both directly and as a part of wider studies into the damage tolerance of sandwich panels. Before the more complicated case of impact damaged panels can be understood the basic failure modes and strength of undamaged sandwich panels must be identified. A variety of failure modes have been identified for panels under in-plane compression; namely compressive failure of the skins, skin wrinkling or local buckling, skin dimpling and panel shear failure, all applicable to panels with both supported and unsupported unloaded edges [104,123,127]. Global or Euler buckling is restricted to columns or panels with unsupported unloaded edges. Failures that occur at or close to the supports, such as end crushing or brooming [40,105], are not true compressive failure modes, and are not representative when assessing residual compressive strength. The failure modes of sandwich panels under in-plane compression are much more dependent on the

intrinsic and extrinsic variables, in particular the panel boundary conditions, than for transverse loading. The most common failure modes are discussed below and depicted in Fig. 1.5, taken from [127].

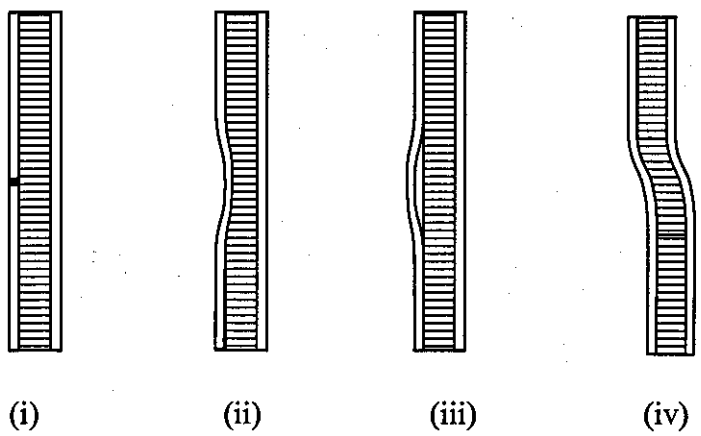

Figure 1.5 Various failure modes of sandwich panels under in-plane compression with unloaded edges simply-supported [127]: (i) skin compressive failure (ii) inward local buckling (dimpling) (iii) outward local buckling (wrinkling) (iv) Panel shear failure

The first failure mode, applicable to panels with both supported and unsupported unloaded edges is compressive failure of the skins, as shown in Fig. 1.5(i). Compressive skin failure, often incorrectly termed microbuckling in previous research, depends purely upon the strength of the skins and will be the dominant failure mode provided the core is of sufficient stiffness and gives adequate support to the skins. Although for compressive skin failure the skins are assumed to support the entire load, the failure strength is generally lower than the compressive strength of the skin material as attained during mechanical property testing. The failure location can vary but ideally should be close to the panel mid-section. The compressive failure of one skin can lead to failure of the second skin nearly simultaneously in undamaged panels [30]. In addition compressive skin failure often occurs in conjunction with local buckling type failure modes.

Local buckling can take a number of forms, namely symmetric, asymmetric or single-sided. The latter is most common in experimental studies so forms the focus of the

following discussion. Single-sided buckling is a local instability failure with a short wavelength of the same order of magnitude as the core thickness [123,128], and can occur such that the skin either buckles into or away from the core. The terminology used in existing literature for these types of failure varies, often with no real distinction between them. In this research inward buckling will be termed 'dimpling' whilst outward buckling will be termed 'wrinkling'. Under compressive loading the most common type of local buckling is dimpling, which occurs when one of the panel skins is depressed inwards into the core, causing crushing of the core which then spreads in the width-wise direction, shown in Fig. 1.5(ii). Dimpling is typically associated with cores of low compressive strength and stiffness and when the crush strength of the core is less than the interfacial tensile strength. The second form of local buckling, termed wrinkling, occurs when the skin debonds from the core and bends outwards, depicted in Fig. 1.5(iii). Wrinkling is caused by either poor interfacial tensile strength or low core tensile strength permitting core tearing, as indicated by a thin layer of core remaining on the debonded skin.

Another type of buckling failure specific to honeycomb or corrugated cores is termed intra-cell buckling [129], where the skin buckles into each individual honeycomb cell, leading to panel failure via core crushing or skin-core debonding. This type of failure is comparatively uncommon compared to the other types of wrinkling failure, so is not depicted in Fig. 1.5. Intra-cell buckling generally only occurs in panels with very thin skins and large honeycomb cells, though it has also been linked to the sagging of the uncured laminate skins over the honeycomb cells prior to co-curing of the sandwich panel [108].

Both global buckling and panel shear failure are typically seen in columns or coupons with unsupported unloaded edges [105,122,123,130], though wide columns can still fail in global buckling [110]. Shear failure of panels with supported edges, as depicted in Fig. 1.5(iv), typically occurs after global or local buckling if the core material has a relatively low shear strength and modulus [47,51].

Failure modes of damaged sandwich panels

The failure modes established above for intact sandwich panels form the basis of the failure modes seen in impact damaged panels. Whilst it is widely recognised that increasing the impact energy and/or damage area reduces the RCS, the variation of either factor can also cause a change in failure mode. At low impact energies where the internal damage area is small the failure modes of the impact damaged panels were expected to be similar to those of the undamaged panels [36,106]. However, in the majority of cases the introduction of even a low level of impact damage generated stress concentrations at the impact site, leading to failure of the impacted skin. Failure of the back skin due to global buckling, debonding or compressive failure often occurred if loading was continued [26,29,106,117].

The way in which the damage propagates under compressive loading can either be progressive or catastrophic depending on the level of impact energy and size of the impact damage area. Catastrophic failure is characterised by a sudden dramatic failure of the panel, often accompanied by a loud noise, with an abrupt loss of load carrying capability. Although this in itself implies the existence of an unstable failure mode the damage propagation in the early stages of loading is often stable. Progressive failure is signified by partial load loss or suspension of load increase prior to complete panel failure through the growth of delaminations or core crushing emanating from the impact damaged region. The nature of the impact damage growth leading to failure is often a combination of the failure modes identified for the undamaged panels. Although it is often just referred to as a local buckling or compressive failure [5,26], three varying types of impact damage propagation were identified, all of which were applicable to panels with both unsupported and simply-supported unloaded edges.

Firstly, in panels with skin delamination caused by the impact the delamination was seen to propagate, which in turn led to compressive failure of the skin across the panel width [110]. The second and most common failure mode was due to growth of the residual indentation inwards causing further core crushing, leading to compressive skin failure across the panel width [5,30,40,77,81,89,115,117,131]. In the study by Shipsha et al. [36] whilst the residual indentation grew inwards the area surrounding the impact

damaged area buckled outwards and it was this that led to a catastrophic skin-core debonding failure. Thirdly, in addition to the residual indentation buckling inwards it was also seen to propagate perpendicular to the loading direction with failure due to the indentation spreading across the entire panel width [89,90,115].

Each of the above failure modes initiates with the propagation of the impact damage. However, whether or not this develops into a compressive skin failure or dimpling/ wrinkling failure depends upon the ability of the panel to resist the spread of the damage. In some instances for honeycomb sandwich panels the impact damage never spread and failure was purely due to the initiation of compressive skin failure emanating from the edge of the impact damage. In other instances although the residual indentation initially grew, upon reaching a certain distance from the impact centre the dimple was arrested until the energy in the skin became large enough to either cause an unstable propagation of the existing dimple or compressive skin failure [26,77,89]. Conversely, this dimple arrest mechanism did not appear to exist in the foam cored panels tested by Tomblin et al. [89] and the indentation spread progressively.

The use of strain gauges at various locations across the panel skins can provide valuable information regarding the nature of the damage growth in impact damaged panels. It has been shown that the compressive load can be carried by the damage region at low loads but is redistributed around the impact damage location at higher loads, with large local stress concentrations forming around the impact site [5,27,30,77]. Strain gauges positioned away from the damage site at a far-field location often show a linear stress-strain response until failure, indicating that the effect of the impact damage on the compressive response is insignificant away from the damage site [5,27,30,115]. Despite this even for low levels of impact damage where the impact damaged panels failed in a similar mode to the undamaged panels a reduction in residual compressive strength still occurred. This is contrary to monolithic laminates where there is often no reduction in RCS for low impact energies. In the sandwich panels as the impact energy and damage size increases a definite reduction in RCS occurs, with reductions up to 60% common [5,27,83]. Further increases in impact energy can lead to a RCS of just 40% of the undamaged sandwich panel strength [5,40,115].

Compression of panels containing simulated damage

The compressive response of sandwich panels containing simulated impact damage has been studied by a number of researchers over the past decade, the major work reviewed in Table 1.2. Damage has been simulated in three different ways; using holes or notches [28-30,90,108,125,126,131-133], embedded delaminations at the skin-core interface [46,114,119,134] and preconditioned indentations [90,118]. By introducing one or a combination of the artificial damage types listed above, either part or several aspects of the damage seen in impacted panels can be reproduced. As the size, location and construction of these artificial damage states are known they are generally much easier to model than actual impact damage. The results of these models can then be compared with experimental results to ascertain the accuracy of the model in simulating the compressive response of panels with both artificial and impact damage.

Notches can be used to simulate skin fracture or other failure modes that are long and thin rather than circular, whereas circular holes can be used to represent impact damage as well as being representative of the holes used for structural attachments. The correct size of the equivalent hole is not easily defined, as the damage caused by impact is intense at the impact centre but decreases towards the panel edges. In the research by Bull et al. [132] the radius of the equivalent hole is taken as the radius of the circle inscribing the area in which all the delaminations throughout the impacted skin overlap.

Notches or holes within a structure introduce large local stress concentrations at and slightly away from the notch site. When loaded in compression damage zones form around the stress intense regions at the notch/hole. The damage zones, which consist of fibre microbuckling, cracking and sometimes delamination, spread as load is increased and eventually result in a catastrophic compressive failure of the panel [125,126,131, 132]. The way in which the damage zone propagates towards the panel edge is not too dissimilar to that seen in impact-damaged panels under compressive loading. In a number of studies compressive skin failure was identified as the cause of failure in both impacted panels and panel with holes under in-plane compression, though the extent of the failure was less in panels with holes [131,132]. However, panels with notches/holes

tend to exhibit a larger reduction in RCS than equivalent impact damaged panels [29] and ply orientation can affect the sensitivity of a panel to the presence of a hole/notch [108]. It is concluded that holes alone cannot accurately model impact damage as the skin-core debonding and core crushing often seen in impact damaged panels are neglected [90,133].

The introduction of an artificial delamination using a Teflon insert at the skin-core interface is commonly used to simulate skin-core debonding. The failure mechanisms of panels containing skin-core debonds regularly consisted of wrinkling of the debonded region which led to propagation of the debond and then global buckling, core shear or compressive failure of the skins depending on the support conditions [114,134]. This differs to the trends seen in impact damaged panels where the skin often underwent dimpling, due to the residual dent and weakened core. The use of Teflon inserts to simulate delamination in the laminate skin of a sandwich panel loaded in in-plane compression has not been properly considered. In the few studies completed [135-137] focus was on the performance of the laminate skin with the core/sandwich structure arrangement only used as an anti-buckling support. Analysis of the problem was as for a laminate plate ignoring the presence of the core structure.

Core damage has also been simulated in a few instances [90,118] by creating a permanent indentation during manufacture. To simulate core damage the honeycomb core was crushed to a predefined depth and diameter prior to flat skin-core bonding. The depth and diameter of the crushed region are designed to give a similar geometric profile to impact damaged panels. Dimple propagation perpendicular to the loading direction was found to be the key damage mechanism, instigated by the geometrical imperfection of the indentation. However, the inclusion of core indentation alone was not sufficient to model impact damaged panels as the residual compressive strength was significantly higher than for panels with equivalent impact damage areas [90,118].

1.3.3. Factors affecting damage tolerance

The effect of both intrinsic and extrinsic variables on the compressive strength of sandwich panels is not well documented. The most comprehensive pieces of research into these issues are those by Tomblin and co-workers [5,77,89]. In this research the effect of skin thickness, core thickness, indenter size and skin and core material were considered. However, the number of variations for each parameter was typically restricted to two, such that only limited conclusions could be drawn. In other published research often two parameters were changed simultaneously, again restricting the identification of the individual effects of each variable [115].

As expected thicker skinned panels have a higher compressive strength than thinner skinned panels [3,5116,138], with the compressive strength approximately doubling for 2 to 4 ply skins [5] and trebling for 8 to 24 ply skins [116]. In addition to affecting the compressive strength the failure modes also changed, with thinner skinned panels typically failing due to compressive failure of the skins as the skins were not strong enough to crush the core, whilst thicker skinned panels failed due to the catastrophic inward growth and propagation of the residual indentation [89,115].

The effect of core thickness and core density were often studied simultaneously. Increasing the core thickness generally gave a noticeable increase in the compressive strength [5,124,138]. Panels with thick low density cores were often prone to local buckling, whilst high density cores provided greater stability to the skins and consequently failed due to compressive skin failure. The increase in compressive strength with core density was significant for low to medium density cores but was minimal for further increases in core density [128]. This is likely to be due to the change in failure mode from local buckling to compressive skin failure.

Comparison of different skin materials for panels in compression has only been made by Gustin et al. [40] who found panels with Kevlar or carbon/Kevlar hybrid skins to have a lower undamaged compressive strength than panels with carbon skins. This trend was not seen in the impacted panels due to the lower amount of impact damage in the Kevlar or hybrid panels for a given IKE. Tsang et al. [90] tested panels with different

skin lay-ups but constant thickness and found that the basic failure mechanism did not change though the compressive strength did vary. Panels with cross-ply skins had a higher compressive strength than those with angle ply skins.

Tomblin et al. [89] compared the performance of impacted panels with carbon fibre skins/nomex cores and glass fibre skins/foam cores with similar core density and skin thickness. Although the compressive strength of the foam panels was higher the dimple arrest mechanism exhibited by the nomex honeycomb panels was not present in the foam cored panels. This is due to the elastic-plastic nature of the foam cores being unable to constrain the propagation of the residual indentation. Comparisons of various foam and honeycomb core materials with respect to the compressive response have been made to a limited extent [3,30,130]. For the studies into the effect of the honeycomb core material only limited conclusions were drawn due to the variation of several factors simultaneously. In the comparison of impact damaged nomex and aluminium cored panels [30] generally the aluminium panels showed less sensitivity to the impact damage with lower local strain concentrations and a slightly higher residual compressive strength than the nomex panels. Although the failure modes for both types of panel were similar, the nomex panels did show some growth of the residual indentation whereas the aluminium panels did not.

Other variables found to affect the residual compressive strength (RCS) include the size of the indenter and impact velocity used in the impact phase, the effect of specimen curvature and testing at elevated temperatures. For a 4J impact energy level Chen et al. [83] found the RCS to decrease when the indenter diameter was increased up to a diameter of 12.7mm. Further increases in indenter diameter above 12.7mm marginally increased the RCS. This trend was suggested to be due to indenter diameters of 12.7mm and below causing fibre fracture of the impacted skin, whereas larger indenters only caused residual indentation of the skin. Tomblin et al. [5] found the failure modes associated with 25.4mm and 76.2mm indenters to be different and panels loaded with the small indenter to generally have a higher RCS for a given IKE. The small indenter was found to cause a large residual dent but small damage area, which led to a compressive skin failure emanating from the damage site under in-plane compression. For the large indenter although the residual indentation was small the associated

damage area was large, which permitted dimpling of the skin at the damage site under in-plane compression, with failure due to the indentation propagating across the panel width. This demonstrates the importance of accurately representing the impact conditions the panel structure will be exposed to in service if a true representation of the compressive response is to be obtained.

The effect of impact velocity was considered by both Zenkert et al. [81] and McGowan et al. [27]. Zenkert found panels subjected to quasi-static indentation whilst resting on a solid base to suffer propagation of the residual dent prior to compressive skin failure. However, for unsupported panels subjected to low velocity impact there was no growth of the residual indentation with catastrophic compressive skin failure. In the study by McGowan where impact damage was inflicted by both drop weight and airgun apparatus, a subsequent variation in RCS could be seen. Below the BVID threshold this difference was small but above the threshold the RCS of the panels impacted with the airgun was 14% lower than for the panels impacted with drop weight rig despite the residual dent depths being similar. This variation was due to the internal damage caused by the airgun impact being more severe and highlights the problems of using dent depth alone as a measure of impact damage and subsequent RCS.

Panels with an amount of curvature in the widthwise direction were studied by Moody et al. [26] and McGowan et al. [28,29] to simulate aircraft fuselage structures. However, no discussion of the effect of the curvature was given by McGowan and in the study by Moody both flat and curved panels were seen to have similar residual compressive strengths, though growth of the impact damage was slightly delayed in the curved panels. Research into other issues affecting in-service panels such as environmental effects is very limited. Walker [116] tested panels in in-plane compression at both room and elevated temperatures. Increasing the temperature from room temperature (70°F/ 21°C) to 300°F (150°C) did not affect the failure load or mechanims in sandwich panels with 8 ply skins though a reduction in strength was observed for panels with 24 ply skins. Very limited conclusions could be drawn from the research due to the small number of specimens tested. No experimental studies into the effect of moisture on the in-plane compressive response of sandwich panels were found.

1.4. Outline of the thesis

The principle aims of this research project are to investigate experimentally first the damage resistance and second the damage tolerance of composite sandwich panels. The primary aims of the damage resistance study are to identify the key damage mechanisms involved in the transverse loading of sandwich panels and to ascertain the effects of varying a number of the intrinsic and extrinsic variables as identified from the literature review on the performance of a sandwich panel and identify which variables are most dominant. The performance will be assessed in terms of strength, stiffness, internal damage and energy absorption. Focus will be on the panel response up to fibre fracture of the top skin, as these damage levels correspond to BVID and VID. Damage levels exceeding this are not representative of low-velocity impact damage and therefore are beyond the scope of damage tolerance assessment. To aid identification of the key damage mechanisms and critical loads, mechanical property testing and transverse loading of the individual skin and core materials will also be completed.

The intrinsic and extrinsic variables to be studied in the damage resistance phase include skin thickness, core density, skin and core materials, specimen support conditions, indenter geometry and loading speed. The reasons behind the choice of these variables are as follows. Although skin thickness has been widely studied in previous research it is regarded as a primary factor in the design of sandwich structures and often only two or three skin thicknesses were compared. This study aims to compare four skin thicknesses ranging from 4 to 16 plies, arranged in a cross-ply lay-up. A cross-ply lay-up has been chosen as it is a balanced symmetric simple lay-up and provides good strength in both the transverse and in-plane directions.

Core density is suggested to be closely linked to energy absorption, though the literature reviewed gave conflicting reports on the relationship with internal damage. A large proportion of the existing research has used foam cores with less information available for honeycomb sandwich panels, despite honeycomb cores being more popular in aerospace applications due to their superior strength and stiffness-to-weight ratios. Therefore an aluminium honeycomb core and a nomex honeycomb core have been

selected for this study. Very limited information has been found for the direct comparison of these two honeycomb types. Also few studies have considered skin material type so a limited comparison of skin material will be made as a part of this research for two types of carbon fibre. The low temperature cure carbon/epoxy T700/ LTM45-EL has been extensively used in previous research carried out at Loughborough University and a large database of mechanical properties is available. This is compared with the high temperature cure second generation composite system IM7/8552.

The effect of specimen support condition is considered by comparing panels with a clamped circular testing area in bending with those resting on a solid foundation. This comparison in addition to a small amount of testing on larger panels should allow the global and local responses to be pin-pointed, and their effect on the sandwich panel behaviour identified. Panels will be loaded with both hemispherical and flat-ended indenters of a fixed diameter. Hemispherical indenters are the most common in existing research but the few studies into indenter geometry suggest indenter shape to have a significant effect on the damage mechanisms, with flat ended indenters simulating much larger hemispherical indenters. Finally the effect of loading speed will be assessed by using both quasi-static and low velocity impact testing. Quasi-static testing will be used to identify the key damage mechanisms with the aid of load-displacement and load-strain responses. Internal damage will be assessed using diagnostic testing and destructive cross-sectioning of the loaded panels. The knowledge obtained from quasi-static testing will then be used in the assessment of the effect of impact energy on the internal damage, studied using a drop weight rig with impact energies up to the level required for top skin fibre fracture. Damage resistance maps will then be constructed for the following study of damage tolerance.

The second study area focuses on the damage tolerance of sandwich panels, with the key aim to assess the effect of the core on the in-plane compressive response. Compression-after-impact testing has been selected to assess damage tolerance as compressive loading represents the most critical loading scenario. From the literature reviewed it is clear that the effect of both intrinsic and extrinsic variables has received limited attention. The focus of much of the previous research was to determine the basic compressive behaviour of one sandwich panel configuration. The comparison of

aluminium and nomex honeycomb cores has only been briefly considered by two researchers. In addition none of the research reviewed made direct comparisons between the damage tolerance of monolithic laminate plates and sandwich panels. Therefore these two issues will be the focus of this study. Although there is also the need for more research into the effect of the other intrinsic and extrinsic variables on damage tolerance it is not feasible as part of this project due to both time and financial constraints.

The method and equipment used for compression testing will be adapted from previous research completed at Loughborough University. The specimen dimensions will be fixed to give an aspect ratio of 1.33, which lies within the common range of 1-2.5 as established from the literature reviewed. The unloaded edges of the panel will be simply-supported rather than unsupported as in the majority of previous damage tolerance studies of sandwich panels. Simple supports have been chosen as unsupported 'wide columns' are not representative of the actual panels used in aircraft structures which are supported on all sides. The panels will be impacted at various impact energy levels and contain damage ranging from BVID to top skin fibre fracture. This will allow the determination of damage tolerance maps and the assessment of sandwich panel sensitivity to impact damage. The use of strain gauges to help identify the occurrence of impact damage propagation and ensuing failure modes has been chosen over other techniques such as shadow moiré interferometry due to restricted access to the panel during loading. The compressive response of undamaged panels will also be assessed to provide a basis for comparison with impact damaged panels and the determination of the compressive strength retention factor.

A spider diagram of the experimental processes used in the study of damage resistance and tolerance of composite sandwich panels is shown in Fig. 1.6. The materials used within this study and their respective properties are presented in Chapter 2 along with the manufacturing processes used to construct the sandwich panel specimens. Chapter 3 summarises the experimental procedures used for damage resistance testing and Chapter 4 discusses the key damage mechanisms involved in transverse loading. A review of existing analytical models for the transverse loading of sandwich panels is the focus of Chapter 5. The effect of the intrinsic and extrinsic variables on damage resistance and energy absorption is discussed in Chapter 6. The experimental procedures for damage

tolerance testing are summarised in Chapter 7 with the findings of the study presented in Chapter 8. The main findings and conclusions of the entire research project are given in Chapter 9, along with possible areas for future work.

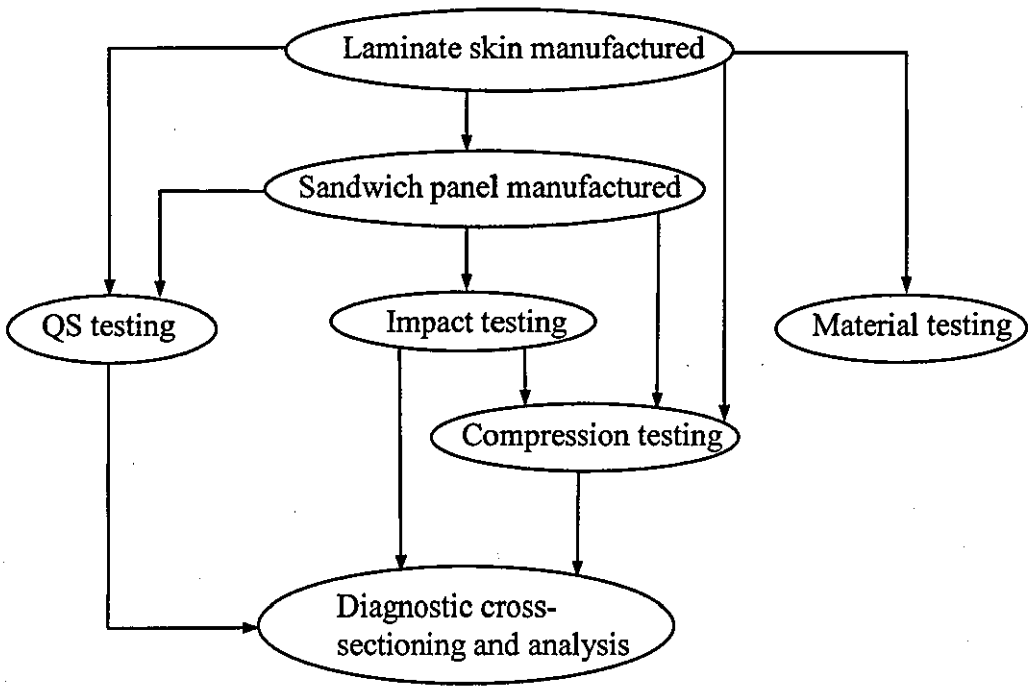

Figure 1.6 Test procedures involved in the determination of damage resistance and damage tolerance of composite sandwich panels

Table 1.1 Review of literature concerning damage resistance testing

Authors (ref no.)	Testing conditions					Composite System							Energies			Damage detection methods	Damage types	Paper focus
						Skin			Core									
	Test type	Boundary Conditions	Specimen Size	Indenter	Loading speed	Material	Lay-up	thickness	material	density	cell size	thickness	IKE (J)	AE (J)	Critical loads			
Bernard, Lagace 1989 (1)	I	C, sq. 127 x 127	152 x 178	HS 12.7	Air gun	CFRP AS4/3501-6	$(45/-45/0)_s$	?	Aluminum honeycomb	80	?	6.4 & 9.6	<10J	?	DI 0.4J	X-ray with dye, X-sectioning, visual	BVID 1-4J, debonding, CC, FF for IKE>7J, D max area reached by 2J	Effect of core thickness and core type, Damge vs. energy plots
									Nomex honeycomb	80	?	3.2, 6.4, 9.6						
									Rohacell foam	80	n/a	3.2 & 9.6						
Herup, Palazotto 1997 (2)	QS, I	SS, sq. 127 x 127	178 x 178	HS 12.7	QS - ? I - 0.06-25J	CFRP AS4/3501-6	$(0/90)_{ns}$	4, 8, 16, 32, 48 ply	HRH-10-1/8-9.0 nomex	144	3.175	12.7	0.34J-8.5J	40%-69%	Max. 780-1300N	C-scan, photomicrographs	D hour glass and cross hour glass shape and MC, CC	QS vs. I studying damage initiation and skin thickness
Raju, Tomblin, 2001 (4)	QS	F, resting on rigid base	?	HS 6.35, 25.4, 50.8 & 76.2	1.27mm/min	CFRP woven fabric, plain weave	QI $[90/45]_s$ (s=1,2,3)	ply thickness 0.216mm	Nomex honeycomb	48	4.76	9.525 & 19.05	?	AE about 60-70% before FF AE > 80% at FF	Initial damage <1kN FF 2-8kN depending on panel/ indenter	Visual, X-sectioning, C-scan	CC, D, FF total penetration of back face	Indentation response. Effect of indenter diamater on failure modes and energy absorption
						E-glass woven fabric, plain weave	QI $[90/45]_2$	ply thickness 0.228mm										
Tsotsis, Lee, 1996. (6)	QS, I	QS - SS 279 x 279, I resting on solid base with cir hole diameter of indenter	10 x 305 x 305	QS - FE 6.35 & 12.7, I - HS 15.88	3.8mm/min + other speeds for loading rate effect	S2-glass UD	CP	2, 3, 4 plies	Nomex honeycomb	nomex 80, 144, 184	3-4	overall panel thickness 10	3-27J	?	CC 0.37-1.7kN	Visual, X-sect, microscopy	Core buckling in al. and resin cracking in nomex (core cracking)	Effect of material type and indenter size. Focus on intial failure modes
						Aluminium	n/a	n/a	Nomex honeycomb	48	6.35		-		CC 0.34-0.53kN			
						S2-glass UD	CP	2, 3, 4 plies	Aluminium honeycomb	96, 136	3-4		-		CC 0.4-1.6kN			
						CFRP woven roving IM mod	plain weave	1 ply	Nomex honeycomb	60, 144	3-4		-		CC 0.33-1.6kN			
Wen, Reddy, Reid, and Soden. 1998 (7)	QS, I	C, sq. 850 x 850 & 20 x 20	900 x 900, & 300 x 300	HS, FE & con - QS & LVI 5.25 -150, BI 10.5 & 45	QS - 3mm/min, I - LVI 4.8-9.5m/s and BI <305m/s	E-glass woven roving	woven roving	1.75mm (3 plys), 3.25mm (6 plys), 7mm (12 plys)	Divinycell foam & vermiculux	Divinycell 130 & 400 Vermiculux 475	n/a	20-25	500-2000J	AE>80%	FF 2-57kN depending on panel materials	Visual, X-sect	X-shaped, CC, FF, SF, lower skin debonding, total penetration of back face.	Energy absorption under QS, LVI and BI. Effect of skin thickness and core density
Williamson, Lagace 1994 (8)	QS, I	2C & 2F or resting on rigid base 89 x 102 or 203	89 x 356	HS 12.7, 25.4, 38.1	QS 1.1mm/min I - 1.2-3.45m/s	CFRP AS4/3501-6	(0/90), (0/90/0), (0/90/0/90) or $(0/90)_{10}$	?	Nomex honeycomb	48	3.2	none, 6.4, 9.5, 25.4	?	?	FF: (0/90) 25mm core - 1.75kN 6mm core - 2.25kN (0/90/0/90) 25mm core 2.25kN	Visual, x-ray with dye penetrant, x-sectioning, microscopy	D, FF, CC, MC, debonding	Effect of skin thickness and core thickness, laminate vs. sandwich and bending vs. indentation
Mines, Worrall, Gibson 1998 (13)	QS, I	C, in-plane movement allowed	500 x 500	HS 50	QS 10mm/min I <8m/s	GFRP plain weave	(0/90/90/0)	0.48 (2 ply)	Coremat polyester felt/epoxy	640	n/a	10	QS 213J I 393J	QS 97J	QS - FF bottom skin 14kN	Visual	Bottom skin FF with core damage	Energy and failure mode plots, effect of impact velocity and effect of constituent materials on panel behaviour
						GFRP satin weave	(0/90/90/0)	0.55 (2 ply)	Aeroweb 3003 honeycomb	94	6.35	13 & 28	QS 142 & 129J I 196 & 230J	QS 67J & 85J	QS - FF top skin 7 & 8kN		Top skin FF with core damage	
Davies, Choqueuse et al. 1995 (17)	QS, I	2 SS 2F QS & I 200 x 400 I 800 x 800	500 x 200, 1000 x 800	HS 25.4	2 & 5 & 100 mm/min	E glass woven roving polyester resin	2 plies	2mm	PVC foam	80	n/a	20	?	?	Small panel QS DI 1kN FF 4kN I FF 5kN Large panel 5.3kN no FF	?	D, CC, FF top skin, FF back skin	QS vs. I studying damage initiation and effect of panel size

Aymerich, Priolo, and Vacca. 1998 (20)	I	C, cir. 70 dia.	? (> 70mm dia)	HS 12.5	1.3-5m/s	CFRP UD	$(0_4/45/0_4/-45/0_4)_s$	2.5mm	Rohacell foam or no core	71	n/a	47.3	2-22J sandwich FF 16J plate FF 7J	60% then >75% after FF	DI 2KN FF 3.73kN for plate, 5.25kN for sandwich	Visual, X-sectioning, X-ray, photomicrographs, C-Scan using pulse-echo .	Laminate: FF, D, MC. Sand: CC, FF, D, MC	Energy absorption, cause of failure. Laminates vs. sandwich
Kepler 2004 (21)	QS, I	SS	500 x 500 x 46	50mm HS, low cone, tall cone	QS - 50mm/min I - air gun 70 & 93 m/s	Chopped strand mat and E glass	[CSM/(90/0)$_3$] or [CSM/(90/0)/(-30/60)/(30/-60)]	3-3.5mm	PVC foam one with aramid internal layer	60	n/a	40	?	QS tests 710-1010J I tests 1250-2170J	?	Visual, x-sectioning	D, debonding, FF, core cracking, pluging, entire pentration	Effect of indenter nose shape and impact speed, introduction of aramid layer in middle of core
Kim, Jun 1992 (22)	I	SS on ring support 50.8mm dia	76.2 x 76.2	HS 12.7	DW	CFRP	$(0/45/90/-45)_s$ or $(45/-45/0/90)_s$	?	Nomex honeycomb or none	48 or 128	3.175	?	2.1, 3.78, 5.03J	1-4.5J	?	Deply technique	MC, D in two-lobed shape, CC	Laminate vs. sandwich for energy absorption and damage extent
Tomblin, Lacy et al. 1999 (24)	I	SS or resting on rigid base	100 x 100?	25.4 and 50mm	DW	CFRP AS4/8553-40	$(45/90/0/-45/0)_s$	2mm	glass /polyimide honeycomb	88	4.76	22.86	135-678J?	?	?	through transmission C-scan	?	Review of work completed for Advanced technology composite fuselage program
									glass /phenolic honeycomb	192								
							$(45/90/0/-45/0)_{3s}$	6mm		88								
Levin 1989 (31)	I	C, 140 x 140	1000 x 160	HS 30	DW	CFRP T300/914C	$(45/-45/0/90)_{2s}$ and another	8 ply or 28 plies	Aluminium honeycomb	72, 130, 192	3.2	50mm total thickness	1-60J		BVID 11J for 8 ply skin 72 core	Visual, X-sectioning, C-scan	CC, D, FF	Effect of skin thickness and core density on BVID and dmage size. Also RCS in 4-point bending
Gottesman, Bass, Samuel 1987 (33)	I	SS 100 x 100 ?	405 x 100	HS 25.4	DW	CFRP AS4/3502	(45/-45/0/-45/45)	0.675	Aluminium honeycomb	130	3.175	20mm total thickness	5-12.5J	?	FF 12.5J	C-scan through transmission	D, FF, CC	Determination of FF loads for different skin thickness, core density. Also residual strength using 4-point bending
							(45/-45/0/90/0/-45/45)	0.945		130			10-17J		FF 17J			
							$(45/-45/0_3/90/0_3/-45/45)$	1.485		354			10-27J		FF 27J			
Rhodes 1975 (34)	I	80 x 80	80 x 150 or 560 x 80 impact in 4-point bending	HS 12.7	Air gun and DW 16 - 67m/s	CFRP (two types) and/or kevlar/epoxy (hybrids)	(0/90)s or (45/-45)s or hybrid combination	0.14-0.165mm cured ply thickness	Nomex honeycomb or none	48	?	25	0.11-6.51J	?	Sandwich BVID 1.2J FF 2.7J in CFRP Laminate BVID 0.4J	Visual, x-sectioning	CC, D, FF	Effect of skin material and hybrids. Effect of impact under loading and RCS in 4-point bending
Auerkari, Pankakoski, Kauppinen, 1995. (35)	I + 4-point bending after I	F, resting on a tubular anvil 40mm dia.	60 or 80 x 800	HS 20	0.4 to 2.3m/s	CFRP, UD	CP, sym	1.4 or 2.1mm	Divinycell H-100 foam	100	n/a	20 & 24	1.5-20J	?	DI 0.7J thin skin 1.4J thin skin	Visual, ultrasonic B and C-scans	CC diameter smaller than D	Effect of face defects/damage from a LVI on face buckling load (RCS).
Roach, Evans, Jones 1998 (37,38)	QS, I	C 200 x 200 laminates un-supported sandwich on rigid base	300 x 300?	FE 20	QS - 2mm/min I - 30, 60, 120m/s	E glass woven roving (two types) polyester resin (top skin only)	3, 5 or 10 plies	2.64-16mm	Divinycell H grade or none	130	n/a	25	35-1500J	?	thin sandwich top skin FF QS 40J 30m/s 90J 60m/s 144J	Visual, back lighting, x-sectioning, c-scan	D, CC, FF top skin penetration of skin and core	Effect of loading rate, QS vs. Impact. Laminates compared with laminate bonded to core (single skin sandwich)
Kiratisaevee, Cantwell 2005 (41)	I	Resting on 135mm dia. Ring	170 x 170	HS 12.7	DW 1-3m/s?	UD or woven glass fibre and aluminium layers	Al/glass/Al/glass/Al	2mm?	Aluminium foam	?	n/a	10	0.5-28J	?	?	Visual, x-sectioning	CC	Determination of force vs. IKE curve to use with energy balance model

Nettles, Hodge 1990 (42)	I	4-pont bending set-up	292 x 76	HS 12.7 1.2kg	DW	CFRP T300/fiberlite934	$(0/45/-45/90)_{ns}$	8 & 16 ply	Glass/ phenolic honeycomb	32	4.76	35	1-10J		8 ply BVID 2.4J FF 3.3J 16 ply BVID 7J FF 9.7J	X-sectioning, photomicrographs	D initiates at 1J, CC initiates at 0.65J maximum reached at 2J, FF, penetration	Effect of skin thickness and laminate vs sandwich. Also RCS through 4 point bending
		C, cir. 76 dia.	114 x 114						None	n/a	n/a	n/a			BVID 2J FF 4.2J		Back skin split, D initiates at 1.5J, MC, FF	
Hiel, Ishai 1992 (43)	I + 4-point bending after I	Beam SS support length 203mm	356 x 102	HS 16	DW 2.4-6m/s Airgun 40-160m/s	CFRP G40-600/5245C with inner and outer layer GFRP fabric 7781/5245C	18 plies CFRP $(0/30/-30)_{3s}$	CFRP 2.52 GFRP 0.25	Syntac foam 350C	?	n/a	24.8	DW 47-201J Airgun 156-201J	?	?	Visual, x-sectioning	CC, debonding, skin damage	Effect of loading speed on damage. Also different manufacturing techniques for sandwich bonding
Ambur, Cruz 1995 (44)	I	C or SS 114 x 241 or 102 x 127	127 x 254	HS 12.7	DW	IM7/5260 (BMI resin)	$[(45/0/-45/90/0)_{2,3 \text{ or } 6}/90]_{ns}$	26, 32, 52 ply	Glass/ phenolic honeycomb or none	48, 88, 128	?	6.35, 9.5, 12.7	1-40J	?	DI - 26 ply sandwich 3.4J plate 5.4J	C-scan, x-sectioning, photomicrographs	D, CC, FF, debonding. Bottom skin FF at high IKE	Effect of skin and core thickness, core density, boundary conditions
Anderson, Madenci, 2000. (45)	I	SS	76.2 x 76.2	HS 25.4	Drop heights 0.2-1.2m	CFRP, 4x4 twill weave - CF0111/LTM45-EL	(0/90/0) & $(0_2/90_2/0_2)$	0.79 (3 plys) or 1.58 (6 plys)	Rohacell foam	51 or 110	n/a	12.7	3.5-21.5J	-	Max. 5.78kN	Visual, X-sectioning, Moire shadow interferometry	CC, D, SF, facesheet cracking/tearing	Residual dent as measure of internal damage. Effect of resin pooling
									HRH-10 Nomex	48 or 96	3.175	12.7	3.5-26J	-	Max. 6.6kN			
Freeman et al. 2005 (53)	I followed by fatigue testing	C, cir. 76.2 dia.	304.8 x 76.2	HS 12.7	DW mass 7.25, 12.25, 22.25kg	Plain weave carbon fibre F-62 epoxy resin	2 plies	0.61	Honeycomb filled with foam	106, 164	?	25.6 total thickness	10, 20, 30J	?	FF 106 - 0.7kN & 164 - 1kN	C-scan	FF, pentration front skin D, FF, penetration back skin	Effect of varying IKE level, impactor mass, core density, skin thickness on critical loads
							4 plies	1.22		106					FF 1.1 to 1.4kN			
Torre, Kenny 2000 (58)	I	2C & 2F	250 x 450, 450 x 250, 450 x 450	HS	0-12.5	GFRP	$(0/45/90/-45)_s$	?	Phenolic foam some with corrugated GRFP	?	n/a	?	0-2000J	95-99%	Max. 8-19.5kN	Visual	FF, debonding, CC	Energy absorption performance quantification, effect of adding corregated GRFP
Nguyen et al. 2005 (62)	I	C to rigid base	152 x 101	HS 25	DW	Aluminiun 2024-T8	n/a	0.813 top 0.508 bottom	Aluminium honeycomb 5056	?	?	25.4	1-15J	?	?	Visual, x-sectioning	CC	Few impacts for comparison with FE model
Caldwell, Borris, Falabella 1990 (63)	I	SS 178 x 178 or resting on solid base	203 x 203	HS 12.7	2.4m/s	E-glass fabric 7781/F185	6 plies	1.52mm	Honeycomb - Nomex, glass, carbon	48, 64, 80, 88, 96	3.2, 4.8, 6.4	12.7	5.4J and 8.1J	?	?	Visual, x-sectioning, C-scan	MC, D, FF, CC,	Effect of core type and density. Also residual strength testing
Akil Hazizan, Cantwell 2003 (74)	QS, I	Beam SS 20 x 170-200 or 25 x 200-500	?	HS 10	DW	glass fibre/epoxy	woven roving	0.6	Aluminium honeycomb 3003	84	6	13, 25	<2J	AE from bending 60% 12-15% core	?	Visual, x-sectioning	CC	Effect of skin and core, contact & shear & bending effects. Used in analytical modelling
		Plate F 136 dia ring	?		DW									AE 50% contact effects				
		200 x 20 resting on solid base	?		QS 0.1, 1, 10, 100 mm/min								Indent-ation					
Horrigan, Aitken et al. 2000 (82)	I	C	720 x 320	Deformable water filled membrane 100mm dia.	20-40m/s at 15deg incidence angle	Glass epoxy 8 harness satin	2 plies of (0/90)	0.59	NomexHRH-10-1/8-3.0	48	3.175	25.4	170-300J?	?	?	Visual, x-sectioning	D, CC	Large soft body impact compared with smaller solid body impact. Experiment compared with FE model
				HS 69	15.3m/s													
Meo, Vignjevic, Marengo 2005 (84)	I	resting on ring, 100mm dia.	381 x 305 multiple impacts on one specimen	HS 16 or 50mm	DW	CFRP 69/GFE 3105 H	(90/45/45/90) for 4 ply	2 or 4 ply	Nomex HRH10-1/8	29, 96	3.175	6.35, 15.24	5-20J	?	?	Pulse echo C-scan, visual	D, MC, FF, CC	Effect of skin thickness, material, core thickness, density, indenter size. Assessed by dent depth and delam
						AS4/8552		3 & 2 ply or 4 & 3 ply	Nomex HRH10-1/8	64, 96	3.175	6.35, 25.4						

Sburlati, 2002. (85)	QS	SS	76.2 x 76.2	HS 25.4	?	CFRP CF011/LTM45 EL 4x4 twill	$(0_2/90_2/0_2)$	1.586	Rohacell foam	110WF	n/a	12.7	?	?	Initial core damage 0.7kN	Visual, x-sectioning	CC	Determine indentation produced by impact
Ferri, Sankar, 1997. (86)	QS, I	SS, 240 x 240 & 115 x 115	250 x 250 & 125 x 125	HS 24.5	QS - 1.2mm/min I - 1-5m/s	CFRP woven roving, T300/BMI resin	five harness satin weave	1.43mm (4 plies) and 2.65mm (8 plies)	Divinycell H60 foam or no core	60	n/a	16	?	Plate FF QS 28.5J I 38.5J Sandwich FF QS 11.3J I ?	Plate FF QS 5.6kN I 6.7kN Sandwich FF QS 3.3kN I 4kN	Photo-microscopy, X-sectioning, X-ray, C-scan using pulse-echo mode to get damage at skin/core interface.	Laminate: X-shape, FF, MC, fibre tow separation. Sand: CC, FF of top and back skin	Energy absorption and damage resistance. QS vs I Laminates vs. sandwich
Schubel, Luo, Daniel 2005 (109)	QS, I	2 SS 2F 254 x 279	279 x 279	HS 12.7	QS ? DW 1.6-5m/s	CFRP AS4 carbon five harness satin weave	4 plies	1.37	Divinycell PVC foam	250	n/a	25.4	7.8-108J	?	QS FF 17.3kN?	Visual, C-scan, B-scan	D	QS vs. impact, variation of damage, force with IKE
Wu, Sun 1996 (148)	I	2 SS 2 F beam 50mm support length	25 x 101	HS 7.9	DW 0.5-3.1m/s	CFRP AS4/3501-6	$(0_2/90_2/0_2)$	0.76	Rohacell foam	205	n/a	12.7	0.13-4.95J	?	1.8J no damage 2.2J MC, D, CC	X-ray, optical microscopy	MC, D, CC, debonding	Determination of damage states, used in formulation of FE model
Besant, Davies, Hitchings, 2001	I	C_1F 500 length	600 x 175 x 16	FE 20 2.1kg 5.38kg 5.38kg	 1.94m 1.52m 2.27m	CFRP fiberite 7714D/XAS	$(0/+45/90/-45/0/0)_s$	0.25 ply thickness	Aluminum 4.5 1/8-10(5052)T	72	3.2	10?	 40J 80J 120J	?	 7.5kN 10kN 13kN	?	CC, core through thickness shear yielding	Comparison of FE model with experimental data
Zheng, Li, Wu, 1998.	QS	C or SS on 60 diameter ring	?(>60 dia)	HS 20	QS - 1mm/s or 0.1mm/s	Glass plain weave and T300/QY8911	$(0/90)_G/45/45/0/-45/45)$	?	NRH-2-60-(0.08) Nomex honeycomb	80?	2?	Overall panel thickness 9.5	-	-	Initial damage 0.45kN FF 1.5kN	Thermal aminating, C-scan	D, dumbbell shaped, CC, top skin penetration	Comparison of FE model for impact with QS experimental data
Belingardi, Cavatorta, duella, 2003.	QS, I	resting on flat base with 76.2 dia cutout	100 x 100	HS 20 20kg	QS and DW 0.02, 4, 6 m/s	Glass UD + fabric layer	$(random/-45/45/0/0)_2$	2.79	Foam	80	n/a	30	up to 220J	?	FF 8-10kN depending on speed	Visual, X-sectioning	top and bottom facesheet penetration, CC	Effect of strain rate and core strength on performance
Charles, Guedra-Degeorges 1991	I	resting on 2 supports 100mm apart. Also some resting on solid base	?	HS 16	DW	CFRP fabric & UD T300/914	4 plies fabric/UD/UD/fabric	?	Nomex honeycomb	?	?	15	1-30J	?	visible damage 2.5J FF 30J	C-scan, visual	D, FF, CC	Effect of skin type on damage levels. Also residual strength through 4-point bending
						Kevlar fabric 1457 resin	2 plies							?	visible damage 1J FF 13J			
Sharma, Murthy, Krishna 2004	I	C, sq. 20 x 20?	63.5 x 12.5	HS 20	15m/s?	E-glass/resin - epoxy or polyester	woven roving	2	PU foam	400	n/a	16	7.5-37.5J	?	0.2kN FF 23J FF back skin	Visual	FF, D, CC	Effect of resin on impact, compared with FE
Compston, Styles et al. 2006	I	80 x 80	200 x 200?	HS 10	1.4-3.1m/s	glass fibre/ polypropylene	woven roving	1 ply 0.35mm?	Aluminium foam	230	n/a	5.2	5-25J	AE 40%	25J no FF	Optical microscopy, laser scanning	MC, CC, FF	Effect of skin and core material on impact response/ damage
						glass fibre/ vinylester	woven roving	1 ply 0.5mm?	PVC foam	200		5.2			15J FF			
Robinson, Davies 1992	I	C, cir dia. 102 or 337	?	HS 6.35	<6m/s with varying mass	CFRP	woven roving	2mm (10 plies)	None	n/a	n/a	n/a	1-11J	?	FF 9J, 2.2kN	Visual, lighting, c-scan	MC, D, FF, CC, pentration?	Laminate vs. sandwich for energy absorption and damage extent.Sandwich used to protect back (load bearing) skin
				HS 19.05		CFRP and GFRP	woven roving	0.33mm top skin 0.93mm back skin	Nomex honeycomb	?	?	5	1-8J		Back skin damage 8J, 1.1kN			
				HS 6.35		GFRP	woven roving	2mm (12 plies)	None	n/a	n/a	n/a	2-11J		?			
Anderson, Madenci, 2000.	QS	2 SS 2 F beam 70mm support	76.2 x 76.2	HS 25.4	QS	CFRP, 4x4 twill weave - CF0111/LTM45-EL	(0/90/0)	0.79 (3 plys)	Rohacell foam	110	n/a	12.7	-	-	Initial CC 0.3kN	?	CC, debonding	Looking at initial damage threshold and comparing with FE model
							$(0_2/90_2/0_2)$	1.58 (6 plys)							Initial CC 0.75kN			

Sburlati, 2002. (85)	QS	SS	76.2 x 76.2	HS 25.4	?	CFRP CF011/LTM45 EL 4x4 twill	$(0_2/90_2/0_2)$	1.586	Rohacell foam	110WF	n/a	12.7	?	?	Initial core damage 0.7kN	Visual, x-sectioning	CC	Determine indentation produced by impact
Ferri, Sankar, 1997. (86)	QS, I	SS, 240 x 240 & 115 x 115	250 x 250 & 125 x 125	HS 24.5	QS - 1.2mm/min I - 1-5m/s	CFRP woven roving, T300/BMI resin	five harness satin weave	1.43mm (4 plies) and 2.65mm (8 plies)	Divinycell H60 foam or no core	60	n/a	16	?	Plate FF QS 28.5J I 38.5J Sandwich FF QS 11.3J I ?	Plate FF QS 5.6kN I 6.7kN Sandwich FF QS 3.3kN I 4kN	Photo-microscopy, X-sectioning, X-ray, C-scan using pulse-echo mode to get damage at skin/core interface.	Laminate: X-shape, FF, MC, fibre tow separation. Sand: CC, FF of top and back skin	Energy absorption and damage resistance. QS vs I Laminates vs. sandwich
Schubel, Luo, Daniel 2005 (109)	QS, I	2 SS 2F 254 x 279	279 x 279	HS 12.7	QS ? DW 1.6-5m/s	CFRP AS4 carbon five harness satin weave	4 plies	1.37	Divinycell PVC foam	250	n/a	25.4	7.8-108J	?	QS FF 17.3kN?	Visual, C-scan, B-scan	D	QS vs. impact, variation of damage, force with IKE
Wu, Sun 1996 (148)	I	2 SS 2 F beam 50mm support length	25 x 101	HS 7.9	DW 0.5-3.1m/s	CFRP AS4/3501-6	$(0_2/90_2/0_2)$	0.76	Rohacell foam	205	n/a	12.7	0.13-4.95J	?	1.8J no damage 2.2J MC, D, CC	X-ray, optical microscopy	MC, D, CC, debonding	Determination of damage states, used in formulation of FE model
Besant, Davies, Hitchings, 2001	I	C,F 500 length	600 x 175 x 16	FE 20 2.1kg 5.38kg 5.38kg	 1.94m 1.52m 2.27m	CFRP fiberite 7714D/XAS	$(0/+45/90/-45/0/0)_s$	0.25 ply thickness	Aluminum 4.5 1/8-10(5052)T	72	3.2	10?	 40J 80J 120J	?	 7.5kN 10kN 13kN	?	CC, core through thickness shear yielding	Comparison of FE model with experimental data
Zheng, LI, Wu, 1998.	QS	C or SS on 60 diameter ring	?(>60 dia)	HS 20	QS - 1mm/s or 0.1mm/s	Glass plain weave and T300/QY8911	$(0/90)_0/45/45/0/-45/45)$	?	NRH-2-80-(0.08) Nomex honeycomb	80?	2?	Overall panel thickness 9.5	-	-	Initial damage 0.45kN FF 1.5kN	Thermal aminating, C-scan	D, dumbbell shaped, CC, top skin penetration	Comparison of FE model for impact with QS experimental data
Belingardi, Cavatorta, duella, 2003.	QS, I	resting on flat base with 76.2 dia cutout	100 x 100	HS 20 20kg	QS and DW 0.02, 4, 6 m/s	Glass UD + fabric layer	$(random/-45/45/0/0)_2$	2.79	Foam	80	n/a	30	up to 220J	?	FF 8-10kN depending on speed	Visual, X-sectioning	top and bottom facesheet penetration, CC	Effect of strain rate and core strength on performance
Charles, Guedra-Degeorges 1991	I	resting on 2 supports 100mm apart. Also some resting on solid base	?	HS 16	DW	CFRP fabric & UD T300/914	4 plies fabric/UD/UD/fabric	?	Nomex honeycomb	?	?	15	1-30J	?	visible damage 2.5J FF 30J	C-scan, visual	D, FF, CC	Effect of skin type on damage levels. Also residual strength through 4-point bending
						Kevlar fabric 1457 resin	2 plies							?	visible damage 1J FF 13J			
Sharma, Murthy, Krishna 2004	I	C, sq. 20 x 20?	63.5 x 12.5	HS 20	15m/s?	E-glass/resin - epoxy or polyester	woven roving	2	PU foam	400	n/a	16	7.5-37.5J	?	0.2kN FF 23J FF back skin	Visual	FF, D, CC	Effect of resin on impact, compared with FE
Compston, Styles et al. 2006	I	80 x 80	200 x 200?	HS 10	1.4-3.1m/s	glass fibre/ polypropylene	woven roving	1 ply 0.35mm?	Aluminium foam	230	n/a	5.2	5-25J	AE 40%	25J no FF	Optical microscopy, laser scanning	MC, CC, FF	Effect of skin and core material on impact response/ damage
						glass fibre/ vinylester	woven roving	1 ply 0.5mm?	PVC foam	200		5.2			15J FF			
Robinson, Davies 1992	I	C, cir dia. 102 or 337	?	HS 6.35	<6m/s with varying mass	CFRP	woven roving	2mm (10 plies)	None	n/a	n/a	n/a	1-11J	?	FF 9J, 2.2kN	Visual, lighting, c-scan	MC, D, FF, CC, pentration?	Laminate vs. sandwich for energy absorption and damage extent.Sandwich used to protect back (load bearing) skin
				HS 19.05		CFRP and GFRP	woven roving	0.33mm top skin 0.93mm back skin	Nomex honeycomb	?	?	5	1-8J		Back skin damage 8J, 1.1kN			
				HS 6.35		GFRP	woven roving	2mm (12 plies)	None	n/a	n/a	n/a	2-11J		?			
Anderson, Madenci, 2000.	QS'	2 SS 2 F beam 70mm support	76.2 x 76.2	HS 25.4	QS	CFRP, 4x4 twill weave - CF0111/LTM45-EL	(0/90/0)	0.79 (3 plys)	Rohacell foam	110	n/a	12.7	-	-	Initial CC 0.3kN	?	CC, debonding	Looking at initial damage threshold and comparing with FE model
							$(0_2/90_2/0_2)$	1.58 (6 plys)							Initial CC 0.75kN			

Nomenclature: QS - quasi-static, I - impact, LVI - low velocity impact, BI ballistic impact, DW drop weight
C - clamped, SS - simply supported, F - free, cir -circular, sq - square, dia - diameter, HS - hemispherical, FE - flat ended

CC - core crushing, FF top skin fibre fracture, MC - matrix cracking, D - delamination
BVID - barely visible impact damage, IKE - impact kinetic energy, AE - absorbed energy

Table 1.2 Review of literature concerning damage tolerance testing

Authors (ref. no.)	Compression testing conditions (test standard where available)			Materials							Impact testing conditions			Delamination area (mm^2)	Dent depth (mm)	Notch size (mm)	Damage detection method	Residual compressive strength	Notes
	Load speed mm/min	Specimen size mm (AR)	Bndry cndtns	Skin			Core				Loading speed	Indenter	IKE (J)						
				material	Lay-up	thckns	material	density	cell size	thckns									
Palm. 1991 (3)	?	127 x 76 (1.67)	?	CFRP IM8/8551	0 & ±45 fibres	8 ply 1.02mm 4 ply 0.51mm	aluminium honeycomb Nomex honeycomb	32 61 29 48 48	?	12.7	DW	HS 12.7	0, 1.4-8.1 0, 1.4-5.4	skin 0-310 core 0-2500mm + skin 0-500 core 0-skin 0-240 skin 0-450 skin 0-375 core 0-175mm	0-2.7 0-2.0 0-1.1 2.2 3.8	-	C-scan and cross-sectioning	0J - 207MPa 8.1J - 292MPa 0J -352MPa 8.1J - 128MPa 0J - 167MPa 8.1J - 90MPa 0J - 287MPa 8.1J - 244MPa 0J - 175MPa 5.4J - 110MPa	fibreglass reinforced thermoset and thermoplastic core also tested. Effect of core type and density studied (and skin thickness to small extent)
Tomblin. 2001 (5)	NASA 1.27mm/min	267 x 216 (1.24)	C, SS	Carbon plain weave	$(90/45)$ $(90/45)_2$ $(90/45)_3$	0.4, 0.8, 1.2	Nomex honeycomb	48	4.76	9.5 & 19.05	DW	HS 25.4mm or 76.2mm	undmgd & 5.6-37J	0-16129	0-5.84	-	Ultrasonic C-scan	undmgd 700kN/m damaged CSRF 0.38-0.83	Varying IKE levels. Effect of skin thickness, core thickness and indenter size. Many test results
Kassapoglou 96 (25)	?	152.4 x 152.4 (1)	C, F?	CFRP plain weave IM7/8552	(±45)/(0/90)/(±45) (±45)/(0/90)2/(±45) (±45)/(0/90)	0.571 0.762 0.381	HFT-3/16-3.0	48	4.76	25.4	DW	HS 12.7	BVID 3.03 4.98 1.84	295 470 272	1.14 ? 1.52	-	Ultrasonic inspection, sectioning and micrographs	(MPa) 201 181 254	Contains data from other refs. Model quite accurate.
Moody, Harris, Vizzini. 2002 (26)	1.52	356 x 83 (4.3) 356 x 152 (2.3) 356 x 305 (1.2)	C, F	CFRP AS4/3501-6	$(90,0)_8$	?	Nomex honeycomb	48	3.2	25.4	DW	HS 25.4	5.88J BVID	100-200 600-750 825-975	<0.5mm	-	C-scan (pulse echo)	130-200MPa 150-225Mpa 160-210MPa	flat and curved panels with 1.1m radius of curvature. Only flat results included here
McGowan, Ambur. 98 (27)	?	254 x 127 (2)	C, SS C, SS C, SS C, SS C, SS C, F C, SS C, SS C, SS C, SS C, SS	CFRP ud and woven AS4/8552	QI 8 ply [0/45/-45/0/90/-45/45/0]$_f$ (f indicates fabric ply)	1mm skin thickness	korex honeycomb	72	3.175	12.7	undmgd DW DW DW Air Air Air Air Air Air Air	HS 12.7 (HS 25.4mm limited indenter size testing)	- 2.034 5.424 9.492 1.4916 5.1528 5.6952 9.3564 9.7632 10.17 9.6276	- 18.38706 56.322468 165.48354 10.32256 73.54824 114.902996 194.19316 - - -	- 0.0762 0.3429 1.27254 0.05588 0.5334 0.5842 1.143	-	C-scan, shadow moire interferometry	(kN) 171.2 116.5 100.1 92.1 122.8 92.5 90.7 81 81.4 (37.8) 76.5 (56.9) 80.7 (80.7)	12.7 and 25.4mm indenters used in impact, show damage initiation and BVID occurs at lower energy for smaller indenter. Airgun causes greater internal damage than drop weight and lower RSC at high energy levels. Dent depth is not reliable indication of internal damage. CAI shows global response not effected by impact. Small number of panel put under preload during impact. Amount of preload shown in brackets in RCS column.
McGowan, Ambur. 97 (28)	?	1676 x 254-356 (4.7-6.6)	C, F for undmgd C, S for notched and impact	CFRP tow AS4/8552	0,90,45 & -45 plies used 36-50 plies	39mm overall panel thickness	Phenolic (HRP) honeycomb	192	4.76	varying	DW	HS 25.4	undmgd - BVID 135.6J 6.78-155.6	- - 58.42 & 68.58mm dia 0-1550mm^2	- - 0.33 & 1.52 0-1.52	- notch in skins 50.8 x 4.8	shadow moire interferometry, C-scan	311kN loading stopped 898.5kN failure 778.4kN loading stopped -	Varying thickness skins, panel thickness constant as honeycomb thickness increased accordingly. Notched panels tested aswell as CAI. Varying width panels - tapered and impacted at two points
McGowan, Ambur. 97 (29)	?	254 x 127 (2)	C, F	CFRP tow AS4/8552	50 plies 50/46 plies 50/46 plies 36 36 36 36 43/38plies 43/38plies 43/38plies	39mm overall panel thickness	Phenolic (HRP) honeycomb	192	4.76	varying	DW	HS 25.4	135.6 undmgd 81.36 135.6 81.36 54.24 undmgd - - -	2585 - 1225 2126 1597 1090 - - - -	0.3302 - 0.2159 1.4097 0.2794 0.2413 - - - -	notch in 2 skins - - - - - - - 50.8 38.1 25.4	shadow moire interferometry, C-scan	(kN/normalised) 620.9/0.497 1249/- 771.7/0.618 460.4/0.469 533.6/0.544 584/0.595 981.7/- 346.1/0.352 387.9/0.395 496.8/0.506	Varying thickness skins, panel thickness constant as honeycomb thickness increased accordingly. Notched panels tested aswell as CAI
Cvitkovich, Jackson. 1999 (30)	0.5	152 x 152 (1)	C, F	IM7/8552 plain weave	(±45/0/90) (±45/0/90/±45) (±45/0/90/0/90/±45)	0.19 ply thickness	Nomex Aluminium	48 98	3.18 3.18	25.4	DW	HS 12.7 also undmgd and notched	1.11-2.06 1.75-3.25 2.82-5.26 2.2-4.11	-	0.64-1.35 0.51-1.8 0.4-2.97 0.81-1.85	notched specimens with 6.35 dia hole front skin only	cross-sectioning of replica panels and shadow moire inferometry	234-324MPa 207-290MPa 186-266MPa 228-359MPa	Skin thickness and core type tested, strain gauge results. Undamaged, notched and impact panels compressed

Shipsha, Zenkert. 2005 (36)	1	270 x 180 (1.5)	C, F?	GFRP	?	2.4	Rohacell foam	?	-	50	DW	HS 25	10 60	BVID skin 18mm²	0.5 1.2	-	Visual, cross-sectioning, digital speckle photography	116.5kN 91.3kN	undamaged and 10, 20, 30, 40, 50, 60J impacts studied
Gustin, Joneson et al. 2005 (40)	Boeing?	100 x 100 (1)	C, SS?	CFRP & Kevlar mix	plain weave, twill 4 layers in all skins	0.3048, 0.254, 0.305 ply thickness	foam filled paper honeycomb	112	12.7	25.4	DW	HS 12.7	0-45	-	-	-	-	15MPa-5MPa	effect of adding kevlar to skins studied
Avilles, Carlsson, 2006 (46)	0.8mm/min	200 x 150 (1.33)	C, SS	S2- glass/ epoxy plain weave fabric	3 layers	2	PVC foam Balsa	48 100 200 150	n/a	25 12.5 50 25 25 25	Skin-core debond	-	-	-	-	Debonds circ. 60, 62.5, 75, 100mm dia. Sq. 45, 56, 68, 90mm	shadow moire interferometry	32-62kN 27-55kN 40-70kN 40-75kN 50-95kN 52-108kN	Effect of debond size on RCS also square debonds given lower RCS but two debonds (one at each interface) gives has similar RCS to single debond
Boyle et al. 2001 (47)	2.54	122 x 92 (1.3) 183 x 92 (2) 122 x 92 (1.3) 183 x 92 (.2)	C, SS	E glass plain weave	?	3.2	Balsa Divinycell HT-70 foam	150 70	-	12.7	undmgd	-	-	-	-	-	-	(kN) 400, 694 334, 592 267, 347 240, 334	Compression only. First number is for loading through buckling until post buckling. Second number is for loading until total failure.
Christopherson, Mahinfalah et al. 2005 (51)	?	127 x 127 (1)	C, F	CFRP plain weave	2 skins 1 skin on impact side 1 skin on non-impacted side	4 ply	foam filled honeycomb	?	?	15.9 25.4	Airgun 80-150m/s	HS 12.7	30-80 49-120 24-67 24-53	-	-	-	-	7.5-31MPa 5.9-8.5MPa 4.6-6.4 2.6-10	small mass high velocity impact. Assessing effect of skin and core presence. Also impact on 4 ply laminate
Palazotto, Gummadi, Valdya, Herup. 1998 (57)	SACMA 0.254mm/min	101.6 x 101.6? (1)	?	CFRP	$(0/45/90/-45)_{2s}$	?	steel Z-pin core	-	-	?	pendulum	HS 12.7	1.27J 1.27J 3 impacts static indent	-	-	-	Acoustic emissions, C-scan, cross sectioning	38.6kN 32.2kN 36.6kN	Z-pin core used with different agles for pins - hollow truss configuration
Akay, Hanna. 1990 (60)	0.5	127 x 76 (1.67) 27mm gauge section	C, F (27mm gauge section)	CFRP plain & 8 harness weave	5 ply front (45/90/90/90/45) 3 ply back (90/45/90)	1.97 front 0.63 back	Rohacell foam Nomex honeycomb Rohacell foam Rohacell foam Rohacell foam	51 48 71 71 110	- 3.1 - - -	12.5 25	DW	HS 12.7	1.5-10	0-75 0-125 0-50 - 0.-145	-	-	C-scan	38-15kN 45-30kN 49-31kN 64-31kN 69-33kN	Impact on clamped and unclamped samples. CAI failure load same for both cases. Increasing foam thickness increases skin damage and no increase in CAI strength
Zenkert, Shipsha, Bull, Hayman.	1	300 x 300 (1)	C, F?	CFRP	$(0/90/45/-45)_{3s}$ $(0/90/45/-45)_{3s}$	1.8 5.4	Divinycell H80 Divinycell H200	80 200	-	60 50	DW	HS 25, also pyramid shaped	30 50 100 250	15mm dia 20mm dia 20mm dia 30mm dia	0.8 0.4	-	C-scan plus surface damage and digital speckle	216kN	blunt and sharp impactors used (hole and crack damage shapes) - only results from blunt impactor included here. Also compression after indentation tests
Chen, Chen, Chen. 1991 (83)	0.5	127 x 76.2 (1.67)	?	CFRP	$(0/90)_{2s}$	0.14 ply thickness	Aluminium	70	6.35	?	DW	HS 12.7 HS 6.25-50.8	0-9 4	200-430mm² 120-380mm²	-	-	C-sen, X-ray	38.6-24.1MPa 38.36-22.1MPa	effect of varying IKE and indenter size
Tomblin. 2002 (89)	NASA 1.27mm/min	268 x 216 (1.24)	C, SS	Carbon plain weave E-glass satin weave	(90/45) $(90/45)_2$	0.4 0.8 0.8	Nomex honeycomb Divinycell	48 70	4.76 -	19.05	DW	HS 76.2mm	14.1J 9.9J 40.7J	Dia. 57.91mm Dia. 58.67mm ?	0.43 0.18 1.02	-	Ultrasonic C-scan	140kN/m 306kN/m 368kN/m	Other panels including undamaged panels tested and results plotted in RCS diagrams for all panel types
Tsang, Lagace. 94 (90)	3	356 x 89 - 203mm gauge section (2.28)	C, F	CFRP plain weave AS4/3501-6	CP CP CP CP CP CP CP CP AP (±45) AP (±45) AP (±45) AP (±45) AP (±45) AP (±45) AP (±45) AP (±45)	0.350 : 0.175 ply thickness	Nomex honeycomb	48	3.18	25.4	Undmgd QS QS QS Sim skin Sim core Sim core Sim core Undmgd QS QS QS Sim skin Sim core Sim core Sim core	HS 12.7 HS 25.4 HS 38.1 HS 12.7 HS 25.4 HS 38.1 HS 12.7 HS 25.4 HS 38.1 HS 12.7 HS 25.4 HS 38.1	delam width - ? - 10 14 20 - ? - 10 14 20	- ? - 1 0.75 0.2 - ? - 1 0.75 0.2	- 10x10 X along fibre tows - 10x10 X along fibre tows -	Visual, X-ray, cross-sectioning, microscopy, shadow moire,dial gage measurement of indentation and deply via pyrolysis.	(MPa) 400 275 255 280 290 350 320 310 250 220 215 205 220 240 230 235	Damage inflicted through QS loading and simulated core and skin damage. RCS of CP affected more than AP by damage type. RCS lower for AP. Simulated core damage affects RCS least

Mouritz, Thomson. 1999 (95)	ASTM C364 0.5	50-225 x 75 (0.7-3) 225 x 75 (3)	C,F	GFRP	chopped strand mat and woven roving	2.8	Divinycell HT-90 foam	90	-	30	undmgd DW Interfacial crack	- HS 25	- 20 30 -	-	-	-	scanning electron microscope	220-150Mpa 90% undmgd 50% undmgd 40mm: 50% undmgd	compression strength reduces with increase in gauge length and causes change in failure mode. Short specimens not representative.multiple impacts 15mm apart
Fleck, Sridhar. 2002 (104)	ASTM C364 0.06	20-79 x 36-28 (0.7-2.2) 19-386 x 34-15 (0.6-25.7) 21-439 x 35-20 (0.6-22)	C, F	Woven E-glass	4 layers 8 harness satin	1?	Divinycell	30 100 200	-	10	undmgd	-	-	-	-	-	-	21.1-13.8MPa 42.7-27.6MPa 65-23.5MPa	Compression only. Varying specimen width and length to see different failure modes.
Mamalis, Manolakos et al. 2005 (105)	ASTM C364 5	140 x 70 (2)	SS, F ?	GFRP	3 or 5 layers using quadriaxial reinforcement and chopped mat	3.6 or 3.3	Rohacell foam PVC foam PVC foam Polyurethane foam	75 100 80 80	-	total panel thickns 40mm	undmgd	-	-	-	-	-	-	88.0 / 89.15 kN 91.22 / 91.95 kN 71.36 / 63.14 kN 22.77 / 15.83 kN	Compression only. Varying core and skin materials. RCS first number skin type 1 second number skin type 2.
Mouring, Barton, Joyce. (106)	ASTM C364 0.762	228.6-254 x 152.4 (1.5-1.67)	C, F	Astroquartz AQII/977-3	?/5 ply	1.19/0.81	HRP/F50-5.5 flexcore honeycomb	88	?	27.94	?	undmgd 12.7 25.4 12.7 25.4	- 8.136 27.12 47.46 9.6276				Visual	(MPa) 227.53-284.06 215.12-247.52 206.84-237.87 184.78-232.35 128.93-177.88	Expresses importance of not having eccentricity during loading. Global buckling proved not to be a factor in experimental results and failure. RCS reduces as IKE increases. Increasing indenter size marginally reduces RCS
Vadakke, Carlsson. 2004 (107)	ASTM C364	25-250 x 37.5 (0.67-6.67)	C, F	E-glass/ vinylester S-glass/ vinylester	? plain weave (0/90)	3.6 2 (2 plies)	PVC foam	100 200 75	n/a	50 50 12.5	undmgd	-	-	-	-	-	-	80kN 88.5-105kN 8.8-22kN	Effect of gauge length on strength and failure mode. Short gauge - skin failure, medium gauge - face wrinkling, long gauge - global buckling
Lagace, Mamorini. 2000 (108)	2.67	350 x 89 (170mm gauge section) (1.91)	C, F	CFRP plain weave AS4/3501-6	CP CP CP CP CP CP CP AP (±45) AP (±45) AP (±45) AP (±45) AP (±45) AP (±45) AP (±45)	0.350 (0.175 ply thickness)	Nomex honeycomb	48	3.18	25.4	notched	-	-	-	-	O hole 1 skin - 3.18 3.18 3.18 6.35 6.35 9.53 9.53 - 3.18 6.35 6.35 6.35 9.53	Visual examination during and after test	approx (MPa) av. 3 tests 447 450 405 351 290 260 265 250 av. 3 tests 239 av. 3 tests 228 225 220 216 av. 2 tests 220	Failure defined as10% or greater reduction in load carrying ability. Specimens with notches had load reduction for CP but not for AP. CP strains are linear. AP strains are non-linear, similar to monolythic composites. No signs of wrinkling or local instability.
Schubel, Luo, Daniel 2005 (109)	?	175 x 25.4 (73.1 gauge section) (2.88)	C, F	CFRP AS4 carbon five harness satin weave	4 plies	1.37	Divinycell PVC foam	250	n/a	25.4	QS ? DW 1.6-5m/s	HS 12.7	undmgd 108J	- >25..4 dia	- 0.9	- -	Visual, C-scan, B-scan	679MPa 269MPa	Only 1 impacted panel compressed, RCS loss 60%
Kassapoglou Jonas, Abbott 1988 (110)	1.27	gauge section 229 x 154 (1.48)	C, F	CFRP AS4/E7K8 UD, plain, 5 & 8 harness satin weave	various lay-ups	various	Nomex honeycomb	14.7 14.7 29	?	25.4 19.05	pendulum	HS 12.7, 38.1	0, 2.69-11.93	23-55mm dia	-	-	C-scan	0J - 466.6-544.1 N/m x10^{-3} 6.51-1.93J - 329.3-470.4 N/m x10-3 0J - 298.5N/m x10^{-3} 5.42J - 191.6N/m x10^{-3} 0J - 313.4 N/m x10^{-3} 4.61J - 234.2N/m x10^{-3}	compression on panels impacted to threshold of detectability
Bull, Hallstrom 2004 (113)	1mm/min	650 x 650 with necking in centre to 550 width (1.18)	C/SS, F	E-glass fabric	$(0/0/45/-45)_s$	6 plies	Divinycell foam	200	n/a	50	QS Airgun 1000m/s undmgd Drilled Drilled Drilled Repaired	Cone shape 40mm dia. - - - - -	AE 2.9-3.8kJ AE 5.8-6.9kJ - - - - -	debond 61 x 78 debond 82 x 104 - - - - -	- - - - - - -	- - - 60mm dia. 80mm dia. 100mm dia. -	Visual, cross-sectioning	670-710kN 560-611kN 1804kN 879kN 886kN 822kN 1316kN	Drilled holes cannot simulate impact damage as no skin or debonding damage. Repaired panel performs nearly as good as undamaged panel. Ballistic impact slightly more damaging than QS

Davies et al. 2004 (115)	?	490 x 496 (0.99)	C,SS	Fiberite 7714 D/XAS UD CFRP	QI QI QI CP CP CP	2 2 2 1 1 1	aluminium 4.5-1/8-10(5052) honeycomb	72	3	10 10 10 25 25 25	DW	FE 20	- 80 120 - 20 80	approx skin indentation area - 15525 24650 - 4500 6800	- 2.77 3.43 - 1.93 front face penetrated	-	C-scan	(kN) 770 535 505 600 495 190	Effect of skin/core thickness studied. Thick skin thin core was best. C-scans revealed core crushing rather than skin delam.
Walker. 1998 (116)	0.5	889 x 305 (2.92) 914 x 305 (3)	C, F?	IM7/5260	8 plies (45/-45/0/90)$_s$ 24 plies (45/90/-	?	Titanium honeycomb HFT-G honeycomb	96	4.76	25.4	undmgd	-	-	-	-	-	-	259kN 208kN 290kN 861kN 883kN	Compression only. Tests also completed at elevated temperatures (results not included here)
Turner, Vizzini. 2004 (117)	1.524	356 x 152 (2.34)	C,F	IM7/8552	[90/0]s front facesheet with integral stiffeners		Nomex	48	3.1	25.4	DW	HS 25.4	5.88		<0.5mm			200-275MPa	Integral stiffeners through use of extra 0 degree plies on front facesheet, varying number of stiffeners
Macdonald, Vizzini. 2002 (118)	1.5	356 x 83 (4.3)	C, F?	IM7/8552	(90/0)s	-	Nomex honeycomb	48	3.1	25.4	indented prior to curing	HS 25	-	-	0.1-0.33 0.89-1.1 1.49-1.53	-	-	231-263MPa 254-319MPa 171-278MPa	Uncured panel crushed 1.6, 3.2 & 4.8mm. Measured depth after cure in dent depth column. Repeat tests for
Nokkentved, Lundsgaard-Larsen, Berggreen. 2005 (119)	0.82mm/min	700 x 500 (1.4)	C, C with in-plane movement allowed	Glass fibre mats	2 chopped strand mats, 2 quadro-axial mats	3.2 (4 plies)	Divinycell PVC foam	80 200	n/a	45	undmgd undmgd Debond Debond Debond Debond Debond Debond undmgd Debond	-	-	-	-	- - 100mm dia. 100mm dia. 200mm dia. 200mm dia. 300mm dia. 300mm dia. - 200mm dia.	Visual, coin tap test, air-coupled ultrasonic scanning	Failure/buckling 248kN / - 286kN / - 307kN / 260kN 318kN / - 180kN / 168kN 171kN / 113kN 167kN / - 173kN / 99kN 333kN / - 195kN / -	Failure loads decrease with debond size. Failure mechanisms vary from fast debond propagation to wrinkling induced face compression failure
Glinecki, Kodali, Curley 1982 (120)	ASTM C364	12.7 guage length x 50.8 (0.25)	C, F	CFRP UD, plain and 8 harness weave	(0/90/45/-45) (0/45/-45/0) (90/-45/45/90)	?	Nomex honeycomb	48	3.18	8.38	debond + crushing	-	-	-	-	0-25.4mm debonds	Ultrasonic inspection.	310-120MPa 530-290MPa 255-120MPa	Compression with debonds and core crushing of varying size
Vadakke, Carlsson. 2004 (123)	ASTM C364 1.5	100 gauge length x 37.5 (2.67)	C, F	Plain weave S-glass Carbon plain weave	6 layers	2 1.75	PVC foam	45 80 100 130 75	-	50 25 12.5	debond	-	-	-	-	0, 25, 50mm debonds 0 & 50mm debond	-	kN 21.5, 16.4, 14.5 23.5, 18.4, 15.5 26.5, 19.4, 17.0 25.0, 23.0, 20.2 20.1, 11.1	Compression with debonds. Effect of debond size studied. RCS - first number no debond, second & third numbers 25 & 50mm debonds
Paik, Thayamballi Kim. 1999 (124)	?	500 x 500 (1) 500 x 250 (2) 500 x 500 (1)	SS, SS	A5083-H321 aluminium	-	3	A3003-H19 aluminium honeycomb	54.5 83.2	6.35	25.4 12.7 25.4 12.7	undmgd	-	-	-	-	-	-	725kN 330kN 312kN 371kN	Compression only. Core thickess and panel aspect ratio affect strength, honeycomb density has little effect
Soutis, Spearing. 2002 (125)	0.13	? 152 x 51 (3) 305 x 102 406 x 203 ? 152 x 51 (3) 305 x 102 406 x 203	C, F?	CFRP T-300/BMS8 plain weave fibres	(0/90) (±45/0/90)	0.211 ply thickness	Nomex	?	?	25.4	notched	-	-	-	-	undamaged 6.35 x 12.7 6.35 x 25.4 6.35 x 50.8 undamaged 6.35 x 12.7 6.35 x 25.4 6.35 x 50.8	Visual through sectioning and micrographs	(MPa) 300 147 121.8 87.5 215 105.3 87.9 72	Damage inflicted through notch through both skins. Damage modelled as crack growth. Results displayed poorly and have possible mistakes.
Toribio, Spearing. 2001 (126)	0.25 reduced to 10-30micro m/min at 80% of failure load	152 x 51 (3) 305 x 102 (3) 406 x 203 (2) 152 x 51 (3) 305 x 102 (3) 406 x 203 (2)	C, ?	E glass (0/90) satin weave - 8 4 harness	2 plys 3 plys	0.49 0.28	Nomex honeycomb	48	?	25.4	notched	-	-	-	-	12.7 25.4 50.8 12.7 25.4 50.8	Visual Inspection and cross-sectioning, micrographs, X-ray	84, 85.4 65.6, 65.9 66.1, 66.8 64.8, 84.8 55.3, 68.7 50.8, 54.8	First number is LDZ initiation load second number is ultimate failure load. Hole to specimen width ratio 0.25 for all tests
Wadee 1999 (128)	?	322 x 70 322x152 (2.1) 500 x 90 (5.6) 210 x 102 (2.06)	SS, F C, F	Aluminium alloy Pure aluminium	n/a	0.25 0.25 0.9 1	Polystyrene foam Stiff foam - polyurethane Soft foam - polyurethane Rubber foam	?	n/a	25	undmgd	-	-	-	-	-	-	2.9kN 5.65kN 3.59kN 0.56kN 0.59-0.605kN 0.872-1.01kN	Global and local buckling of end loaded beams. Experimental compared with theoretical work. Discusses effect of initial imperfections on response.

Fagerberg, 2004 (129)	0.5	200 x 150 (1.33) 200 x 100 (2)	C, F	CFRP	(0/90)s or (90/0)s	1	Divinycell H-grade	30 45 60 80 100 130 200	-	?	undmgd	-	-	-	-	-	-	kN/m each skin 183 / 135 265 / 190 320 / 277 442 / 298 499 / 374 472 / 434 482 / 472	Compression only. Tests effect of core density and ply orientation. RCS - first value is for 0/90 second value is for 90/0. Ply orientation affects strength as does density to a point
Thomsen, Banks. 2004 (130)	?	150 x 100 (1.5)	C, F	CFRP ud	5 plys (±10/0/±10) (±45/0/±45) (±25/0/±25)	0.25	Aluminium 3/8-5056-0.0007	?	9.53	10	undmgd	-	-	-	-	-	-	N/mm 108.6 (64.1) 94.2 (60.5) 125.8 (89.0)	Compression only. Intra-cell buclliking seen to occur for panels with very thin skins prior to ultimate failure. Loads for intra-cell buckling are in brackets.
Edgren, Asp, Bull. 2004 (131)	1mm/min	300 x 300 (1) 150 x 150 (1)	C, F	CFRP NCF 0/90 & ±45	$(0/90/45/-45)_s$ $(0/90/45/-45)_{ss}$ $(0/90/45/-45)_{ss}$	1.8 5.4 5.4	Divinycell H-80 foam Divinycell H-200 foam Divinycell H-200 foam	80 200 200	-	60 50 50	undmgd DW hole notch	- HS 12.5 -	- 30 50 100 250 -	- 32 x 54 36 x 69 ? 63 x 68 69 x 72 -	- 0.8 (28 dia) ? ? 0.4 (16 dia) ? -	- in 1 skin: 50mm hole notch 50x1.5	C-scan, Polishing (some stepwise in thickness direction), microscopy	Failure strain -0.9 -0.58 -0.6 -0.47 -0.48 -0.49 -0.49 0.42	Focus on kink band formation. No RCS given. (kinking = microbuckling!) Panel compressed in 90 fibre direction Concludes holes/notches cannot be compared to CAI panels as specimen size is diferent from CAI panels.
Bull, Edgren. 2004 (132)	?	300 x 300 (1) (220mm gauge section) 150 x 150 (1)	C, F	CFRP	QI $[0/90/45/-45]_{ss}$	1.8 5.4 1.8 5.4	Divinycell foam	80 200 80 200	-	60 50 60 50	DW notched	HS 12.5	30 50 100 250 -	15mm dia 20mm dia 20mm dia 30mm dia -	-	- 30mm hole 30mm crack 30mm hole 30mm crack	C-scan, digital speckle photography	212.5MPa 205.4MPa 187.9MPa 176.0MPa 192.6MPa 167.6MPa 184.2MPa 156.5MPa	Also impacts with pyramid shape impactor, not included here.
Mahfuz et al. 2005 (134)	0.25	520 x 254 (2)	SS, F	Plain weave S-glass	3 layers	16.5mm panel thckns	Klegcell PVC foam	75 130 260	-	12.7	debond	-	-	-	-	50.8mm debond	-	33.4kN (34.3kN) 36.1kN (37.8kN) 40.9kN (45.4kN)	Compression with debonds. Number in brackets is strength of undamaged panel
Lacy, Hwang. 2003	?	203.2 x 203.2 (1)	C, F	CFRP plain weave NB321/3K70P	(90/45) (90/45) $(90/45)_2$ $(90/45)_2$ $(90/45)_2$ $(90/45)_2$ $(90/45)_3$ $(90/45)_3$	0.4 0.4 0.8 0.8 0.8 0.8 1.2 1.2	Nomex PN2-3/16-3.0	48.1 (for all??)	4.76	19.1	DW	HS 25.4 HS 76.2 HS 25.4 HS 25.4 HS 76.2 HS 76.2 HS 25.4 HS 76.2	6.7 7.2 6.7 20.3 7.2 28.2 6.7 11.1	core crush area 362.9167833 1013.414956 397.1130194 739.6722823 1284.848563 3725.44194 573.042208 1284.848563	2.3 0.4 0.8 3.2 0.4 4.2 0.6 0.6	-	(TTU) ultrasonic C-scan, sectioning	(MPa) 185.6 165.5 356 317.5 354.5 236.9 482.6 429.6	FEM based on Tomblins results. Focuses on strain data

Nomenclature: QS - quasi-static, I - impact, DW drop weight, Air - air gun, Sim - simulated, Undmgd - undamaged
C - clamped, SS - simply supported, F - free, dia - diameter, HS - hemispherical, FE - flat ended

Note: Panel size quoted is the nominal panel size. Where available dimensions of the panel gauge section have been included in brackets. Value in (_) is the panel aspect ratio

2. SANDWICH MATERIAL SYSTEMS AND PANEL MANUFACTURE

To allow the effect of skin thickness on damage resistance and tolerance to be determined sandwich panels with 4, 8, 12 and 16 $(0/90)_{ns}$ cross-ply laminate skins are studied. The effect of core density is investigated by using 50kg/m^3, 70kg/m^3 and 90kg/m^3 density 5052 aluminium honeycomb as the core material. T700/LTM45-EL carbon/epoxy is selected for the skin material, as previous studies completed at the university have used this material for studies on monolithic laminates and therefore a large database of material properties is available. Despite this composite system being used on the F/A-18 E/F Super Hornet wing and tailplane structures and other small aircraft such as the X35-RLV and X-36 launch vehicles, it is not typically found in modern aeronautical structures, as the low T_g value of the skin material is not best suited for high strength applications. Additionally, problems with moisture ingression and honeycomb degradation in sandwich panels are accentuated when aluminium honeycomb is used in conjunction with carbon/epoxy skins. The severity of the degradation dramatically increases with carbon/epoxy skins as the material chemical formulation and conductivity of carbon fibre can increase the rate of galvanic corrosion when in contact with aluminium. Therefore a more typical aeronautical composite system consisting of IM7/8552 carbon/epoxy skins combined with 64kg/m^3 and 96kg/m^3 nomex honeycomb is used in addition to the aforementioned materials. IM7/8552 carbon/epoxy has a much greater T_g, and therefore high temperature performance than T700/LTM45-EL, as it is cured at a higher temperature. This makes it suitable for use on aircraft structural parts such as in fighter wings and fuselages, and consequently it is currently used in a wide range of aerospace applications. Nomex is increasingly being used in the place of aluminium honeycomb due to its high mechanical properties, low density and good long-term stability. Because nomex is made from aramid paper and phenolic resin it does not degrade when in contact with moisture and does not react with carbon fibre.

A cross-ply lay-up is selected for the skins rather than a UD or quasi-isotropic lay-up as cross-ply skins provide the most efficient design in terms of in-plane strength and stiffness of thin laminates where interlaminar shear is negligible. The thickness of the

skins is either 0.5mm (4 plies), 1mm (8 plies), 1.5mm (12 plies) or 2mm (16 plies). All core materials are 12.7mm thick. Therefore the overall panel thickness changes slightly with each configuration. Clearly an increase in panel thickness will increase the flexural rigidity and therefore alter the bending response. Similarly increasing the core thickness will have the same effect but to a greater extent. However, the amount of skin thickness variation compared to overall panel thickness is minimal and therefore deemed negligible so is not considered as part of this project.

The manufacture of a composite sandwich panel involves two principal steps: the laying-up and curing of the laminate skins, and the bonding of the laminate skins to the honeycomb core. Co-curing of the laminate to the core is not used as the bond line strength can be considerably less than with the use of a separate adhesive, and skin-core debonding can become a major issue, especially under in-plane loading. The sandwich panel test specimens measure 150mm × 150mm for the damage resistance tests and 200mm × 150mm for the damage tolerance tests. However, to reduce the curing and bonding time, panels of size 300mm × 300mm are made, which are then cut to produce either four 150mm × 150mm panels or two 200mm × 150mm panels. This also allows better quality control. A summary of the manufacturing procedures employed is discussed below, with in-depth manufacturing instructions included in Appendix D.

2.1. Panel configuration and nomenclature

Four composite systems comprised of the aforementioned materials, described in Table 2.1, are used to identify the effects of the sandwich materials on the overall performance of a sandwich structure. System 1 is used predominantly in this research and is the baseline configuration. Systems 2, 3 & 4 are used to investigate the effect of core and skin material respectively on sandwich panel performance. System 1 is used extensively in both damage resistance and damage tolerance testing, with limited testing on system 2. Systems 3 & 4 are only considered in the quasi-static aspect of damage resistance testing.

Table 2.1 Material constitution of each sandwich panel system

	Skin type	Honeycomb type	Adhesive type
System 1	T700/LTM45-EL	50, 70, 90kg/m^3 Aluminium 5052	VTA260
System 2	T700/LTM45-EL	64, 96kg/m^3 HRH Nomex	VTA260
System 3	IM7/8552	50, 70, 90kg/m^3 Aluminium 5052	Redux 312
System 4	IM7/8552	64, 96kg/m^3 HRH Nomex	Redux 312

Two types of adhesive are used in this project, namely VTA260 from Advanced Composites Group (manufacturers of T700/LTM45-EL) and Redux 312 from Hexcel Composites (manufacturers of IM7/8552). Each adhesive is compatible with the resin system used within the carbon fibre prepreg it is paired with, such that VTA260 is specifically designed for use with the LTM45-EL resin system and likewise Redux 312 is for use with the 8552 resin system. Both are high-strength film adhesives suitable for use in bonding both metal-metal and metal-composite sandwich structures. The maximum curing temperature of 120° permits the adhesives to be used in sandwich structures operating up to 100°C, which is important when testing in high temperature/ humidity environments. As the T_g of T700/LTM45-EL is only 75°C without post-curing the VTA260 adhesive with a variable curing temperature of 65-120°C is particularly suited for use with T700/LTM45-EL skins.

Due to the extensive number of tests completed as part of this PhD project a concise panel identification scheme has been devised, as illustrated in Fig. 2.1. A test matrix showing which panel configurations to be tested under each loading condition, shown in Table 2.2, has been made to facilitate planning and understanding. This can be further separated to identify individual quasi-static tests as shown in Table 2.3.

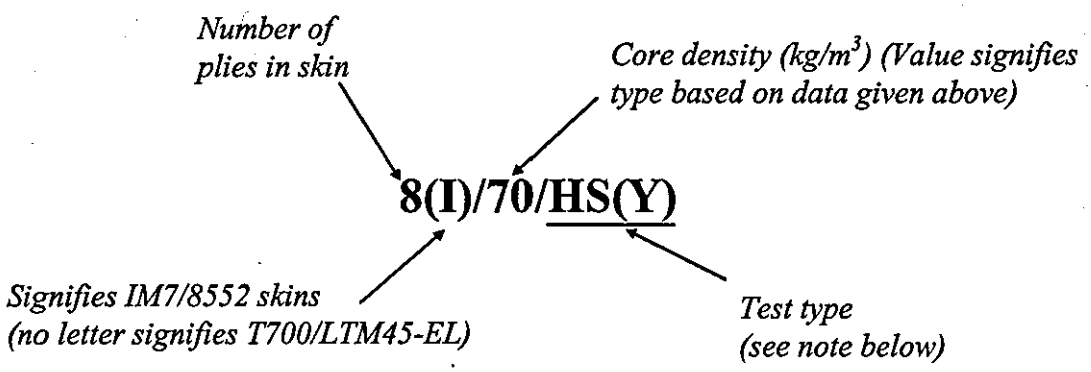

Test Type:

HS(**Y**) = Quasi-static (QS) with hemispherical indenter

FE(**Y**) = QS with flat-ended indenter

(**Y**) = initial (init), secondary (sec) or ultimate (ult) failure when discussing specific quasi-static bending test results OR (ind) for indentation test to ultimate failure

IMP(**X**) = impact test, using HS indenter

CAI(**X**) = compression-after-impact

(**X**) = impact energy in Joules,

(0) represents control panel test with compression test only

Example:

16/64/IMP(5) = 16 ply T700/LTM45-EL skins with 64kg/m^3 nomex honeycomb impacted at 5J

Figure 2.1 Panel identification scheme

Table 2.2 Test matrix for all loading conditions

Core density (kg/m³) & type			Skin thickness and material type							
			T700/LTM45-EL				IM7/8552			
			4	8	12	16	4	8	12	16
	Aluminium	50								
		70								
		90								
	Nomex	64								
		96								

= QS tests only

= QS and impact tests

= QS, impact and CAI tests

Table 2.3 Test matrix for QS testing only

		T700/LTM45-EL				IM7/8552			
		4	8	12	16	4	8	12	16
Aluminium	50	I	I	I	I				
	70	*HS* I *FE* I	I	I	I				
	90		I	I					
Nomex	64		I	I					
	96		I	I					

= Panel loaded to ultimate failure under bending conditions with HS & FE indenter

= Diagnostic tests under bending conditions

I = Panel loaded to ultimate failure under indentation conditions with HS & FE indenter

2.2. Skin material and manufacture

2.2.1. Skin material properties

Basic material data for IM7/8552 UD laminates have been obtained from manufacturer's data for 0.125mm thick unidirectional tape material, as shown in Table 2.4. The properties of T700/LTM45-EL UD laminates were determined in-house as part of a previous PhD project within the department using 16 ply laminates [139]. Effective mechanical properties (namely tensile, compressive, flexural and in-plane properties) of T700/LTM45-EL cross-ply laminates have been determined experimentally during previous research, using the respective ASTM standards D3039 [140], D3410 [141], D790 [142] and D3518 [143]. The above tests have only been completed in full for 8 ply T700/LTM45-EL cross-ply laminates. All values determined are summarised in Tables 2.4-2.5.

Table 2.4 Basic material properties of T700/LTM45-EL and IM7/8552 UD laminates

		T700/LTM45-EL		IM7/8552
Mechanical property		Tested [105]	Manf. Data [a]	Manf. data [b]
0° tensile strength	MPa	1956.3±89.5	4900	2724
90° tensile strength	MPa	48.0±5.1	-	111
0° tensile modulus	GPa	126.7±4.0	230	164
90° tensile modulus	GPa	9.1±0.3	-	12
0° compression strength	MPa	1032.0±5.9	-	1690
0° compression modulus	GPa	120.3±2.3	-	150
0° ILSS (short beam shear)	MPa	66.3±1.2	-	137
In-plane shear strength	MPa	72.5±1.8	-	120

[a] T700 fibre data supplied by manufacturer Toray Industries Inc.

[b] IM7/8552 data supplied by manufacturer Hexcel Composites, Duxford, UK

As both flexural strength and interlaminar shear strength (ILSS) are the dominating factors in transverse loading, tests to ASTM standards D790 [142] and D2344 [144] have been completed on IM7/8552 $(0/90)_{8S}$ and $(90/0)_{8S}$ laminates to compare with existing data within the department for T700/LTM45-EL $(0/90)_{8S}$ laminates, results shown in Tables, 2.7-2.8 and Figs. 2.2-2.3. Flexure tests have also been repeated for both $(0/90)_{8S}$ and $(90/0)_{8S}$ T700/LTM45-EL laminates as existing data was limited, with

results given in Table 2.6. Due to the nature of the ILSS tests requiring very small specimens with a length-to-depth ratio of 4 it is difficult to test beams with less than 16 plies. However, on the basis of previous research [145,146] it is suggested that the variation in ILSS with ply thickness will be small for laminates of this thickness. Also laminates with fewer plies actually have a slightly higher ILSS than those with a larger number of plies. Therefore the value for ILSS obtained for a 16 ply laminate can be used as a lower bound approximation for the 4, 8 and 12 ply laminates.

Table 2.5 Effective mechanical properties of T700/LTM45-EL and IM7/8552 cross-ply laminates $(0/90)_{ns}$

Property			8 plies	12 plies	16 plies	
			T700/ LTM45-EL	T700/ LTM45-EL	T700/ LTM45-EL	IM7/8552
Tensile modulus, E_x	CLT	GPa	68.5	-	-	-
	Experimental	GPa	68.69	-	-	-
Tensile strength		GPa	1.06	-	-	-
Compressive modulus, E_{comp}		GPa	78.04	-	-	-
Compressive strength		MPa	548.78	-	-	-
Flexural modulus, E_f	CLT	GPa	90.5	83.1	79.4	-
	Experimental	GPa	76.55±2.7	76.78±9.3	104.06±3.8	109.37±3.9
Flexural strength		GPa	1.14±142	1.32±184	1.16±1.0	1.25±0.8
Interlaminar shear strength		MPa	-	-	61.75±8.5	81.03±6.2
Poisson's ratio, v_{xy}	tensile	-	0.040	-	-	-
	compressive	-	0.063	-	-	-

Table 2.6 Flexure of T700/LTM45-EL cross-ply specimens

	$(0/90)_{8S}$				$(90/0)_{8S}$			
Specimen	Width (mm)	Thickness (mm)	Stress (MPa)	E_f (GPa)	Width (mm)	Thickness (mm)	Stress (MPa)	E_f (GPa)
1	2.42	1.86	1173.70	100.92	2.41	1.92	1132.01	71.82
2	2.48	1.88	1293.36	107.47	2.47	1.94	1151.88	71.44
3	2.46	1.83	1007.18	104.67	2.48	1.93	1267.78	72.61
4	2.37	1.86	1232.13	105.41	2.42	1.92	1201.16	74.43
5	2.44	1.83	1154.48	103.33	2.47	1.92	1322.59	75.61
6	2.49	1.89	1163.12	96.06	2.44	1.9	1258.46	75.73
7	2.38	1.84	1163.95	106.15	2.51	1.91	1287.62	75.73
8	2.44	1.87	965.98	105.71	2.45	1.9	1300.25	77.79
9	2.47	1.87	1167.37	109.22	2.38	1.91	1382.32	76.22
10	2.43	1.86	1253.52	101.70	2.43	1.92	1286.49	75.66
		Av.	1157.48 ±101.63	104.06 ±3.76		Av.	1259.06 ±77.14	74.71 ±2.09

Table 2.7 Flexure of IM7/8552 cross-ply specimens

	$(0/90)_{8S}$				$(90/0)_{8S}$			
Specimen	Width (mm)	Thickness (mm)	Stress (MPa)	E_f (GPa)	Width (mm)	Thickness (mm)	Stress (MPa)	E_f (GPa)
1	2.39	1.97	1240.46	102.81	2.42	1.86	1170.74	88.77
2	2.30	1.97	1165.21	106.40	2.38	1.82	1297.67	89.47
3	2.04	1.97	1243.23	109.97	2.45	1.86	1082.62	84.10
4	2.21	1.96	1237.34	110.72	2.44	1.88	1108.14	82.07
5	2.24	1.94	1435.37	110.83	2.37	1.87	1105.25	85.23
6	2.45	1.96	1331.74	109.23	2.61	1.86	1216.44	84.40
7	1.97	1.96	1242.88	117.74	2.21	1.86	1238.29	89.33
8	2.46	1.95	1160.51	108.33				
9	2.34	1.96	1208.25	110.67				
10	2.39	1.96	1253.47	106.95				
11	2.00	1.97	1170.32	102.19				
12	1.98	1.95	1251.24	103.79				
13	2.39	1.97	1136.06	104.80				
14	2.5	1.94	1235.49	100.26				
		Av.	1251.85 ±80.49	109.37 ±3.87		Av.	1174.16 ±80.26	86.20 ±2.97

Table 2.8 ILSS of IM7/8552 cross-ply specimens

	$(0/90)_{8S}$				$(90/0)_{8S}$			
Specimen	Load (kN)	Thickness (mm)	Width (mm)	Stress (MPa)	Load (kN)	Thickness (mm)	Width (mm)	Stress (MPa)
1	0.56	1.96	2.62	81.88	0.54	1.87	2.49	87.40
2	0.60	1.98	2.46	92.05	0.62	1.83	2.7	93.81
3	0.46	1.97	2.24	79.00	0.60	1.87	2.67	89.99
4	0.59	1.99	2.47	89.60	0.53	1.9	2.43	86.58
5	0.52	1.98	2.2	89.46	0.60	1.87	2.71	88.95
6	0.54	1.97	2.62	78.45	0.59	1.86	2.68	88.17
7	0.53	1.98	2.57	78.73	0.59	1.86	2.68	88.47
8	0.49	2.01	2.52	72.66	0.54	1.89	2.43	87.53
9	0.48	1.92	2.44	77.31	0.57	1.83	2.68	86.86
10	0.56	1.97	2.68	80.17	0.55	1.9	2.53	85.03
11	0.56	1.93	2.69	81.24	0.60	1.88	2.6	91.45
12	0.52	1.93	2.68	76.12	0.57	1.79	2.48	96.81
13	0.57	1.97	2.53	85.73	0.62	1.87	2.68	92.78
14	0.49	1.97	2.59	71.96	0.56	1.83	2.65	86.30
			Av.	81.03 ±6.18			Av.	89.29 ±3.32

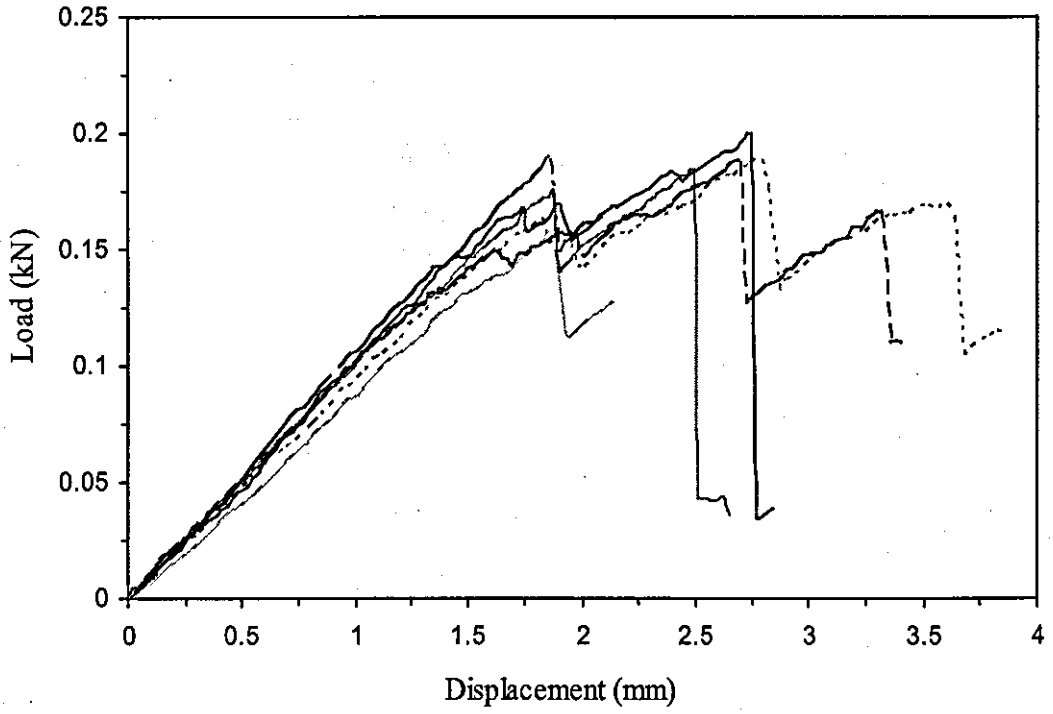

Figure 2.2 Sample of load-displacement curves obtained from flexural tests on T700/LTM45-EL cross-ply $(0/90)_{8S}$ specimens

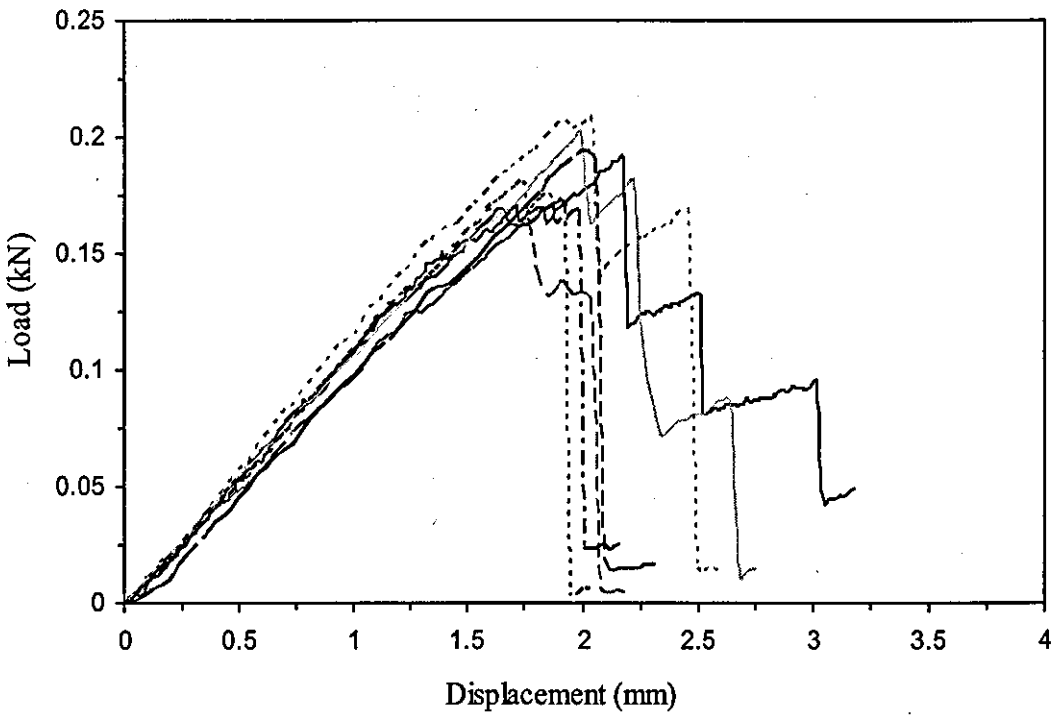

Figure 2.3 Sample of load-displacement curves obtained from flexural tests on IM7/8552 cross-ply $(0/90)_{8S}$ specimens

2.2.2. Lay-up and curing procedures

Cross-ply laminates of 4, 8, 12 or 16 plies were manufactured from UD prepreg and cured in an autoclave. Both the T700/LTM45-EL and IM7/8552 prepregs were supplied in the form of unidirectional tape wound on to a big drum, stored under frozen conditions when not in use. Before any part of the manufacturing process was begun all work surfaces were cleaned with acetone to remove any grease and dust particles which could contaminate the sandwich panel materials and impair their performance.

Individual plies measuring 300mm × 300mm were cut from the roll of prepreg on a cutting table using a ruler and Stanley knife. Once cut each ply was returned to the freezer to maintain a frozen state. During cutting the prepreg drum was also returned to the freezer intermittently as it became tacky when left at room temperature, making it difficult to produce a good clean cut. Once all the plies were cut they were laid up on a glass lay-up table with a metal guide in the form of a right angle. The guide indicated the 0° and 90° directions and was used to ensure each ply was aligned correctly, see Fig. 2.4. The prepreg tape was sandwiched in between two backing sheets. The first ply was removed from the freezer and one backing sheet removed. This was then placed on the lay-up table face up with the fibres aligned along the 0° direction. A second ply was then removed from the freezer and one backing sheet removed. This was placed facedown, directly above the first ply with the fibres aligned in the 90° direction. This process was repeated until the desired lay-up was obtained, $(0/90)_{ns}$ with $n = 1, 2, 3$ or 4 representing a 4, 8, 12, or 16 ply laminate. A tick sheet, as shown in Fig. 2.5, was used to help ensure the correct positioning of each ply with special attention to aligning the two central plies in the same 90° direction to produce a balanced symmetric laminate.

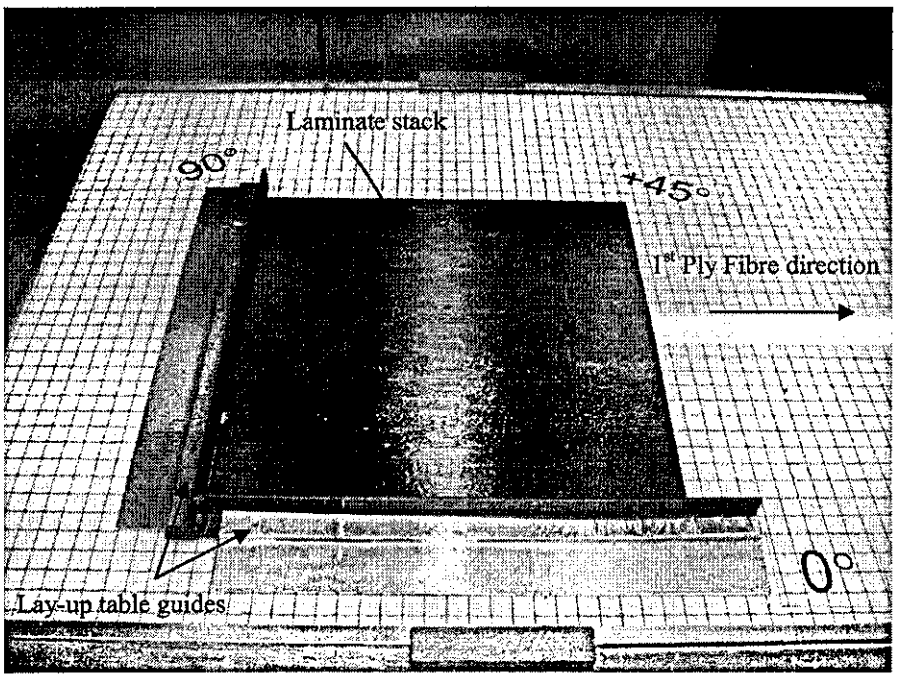

Figure 2.4 Lay-up table with fibre orientation identified

Layer	Ply orientation	Completed
1.	0°	
2.	90°	
3.	0°	
4.	90°	
5.	90°	
6.	0°	
7.	90°	
8.	0°	

Figure 2.5 Tick sheet for 8 ply laminate

The completed laminate stack was then ready for curing in an autoclave. The laminate stack was removed from the freezer and the backing sheets peeled off in turn and a porous layer of PTFE placed on each side of the bare laminate. This arrangement was then placed in the autoclave in between 4 layers of nylon bleeder fabric, all on top of a sheet of non-porous PTFE. A piece of vacuum bagging film was placed on top of the

bleeder fabric to prevent resin contacting the steel caul plate, which had the same dimensions as the laminate stack and was situated on top of the laminate-fabric arrangement. A piece of breather fabric was placed on the caul plate to cover the sharp metal edges, and a large piece of vacuum bagging film used to cover the entire autoclave base to provide the vacuum environment necessary for curing. A diagram of the autoclave laminate-fabric arrangement is shown in Fig. 2.6. The autoclave was then closed up and set to run for the desired cure time. The cure cycle for each type of carbon fibre prepreg is shown in Fig. 2.7. Once cured the laminate was removed from the autoclave and the rough edges trimmed using the diamond-edged tile cutter to a finished size of 300mm × 300mm, Fig. 2.8. The specimen was then cleaned with acetone ready to bond to the honeycomb core material.

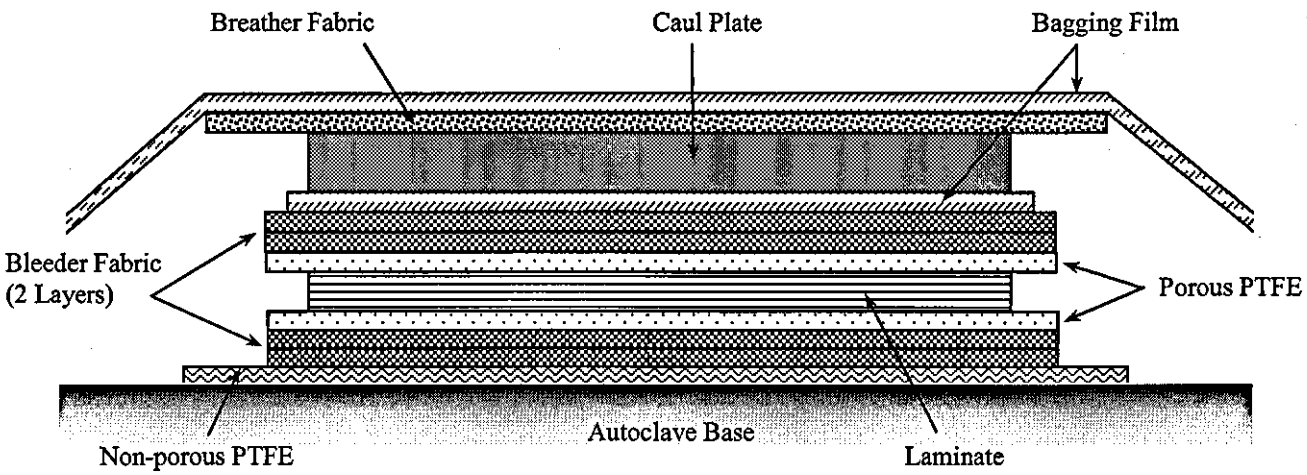

Figure 2.6 Autoclave configuration

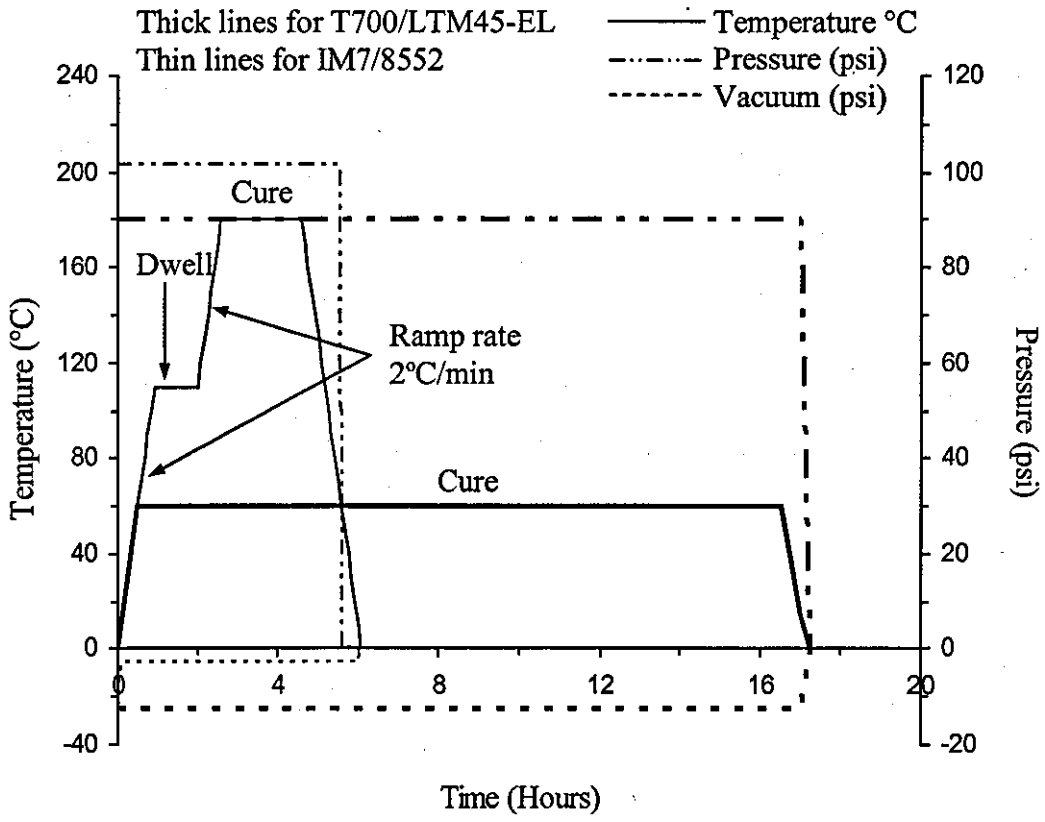

Figure 2.7 Autoclave curing cycles for T700/LTM45-EL and IM7/8552

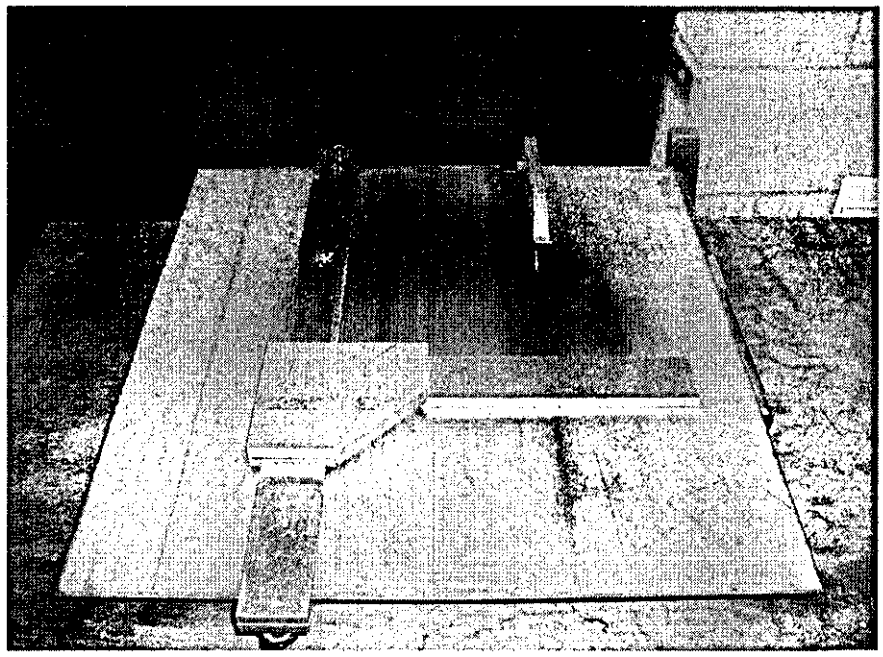

Figure 2.8 Diamond edged tile cutter

Artificial delaminations

A small number of laminates containing artificial delaminations were also manufactured (see Section 4.4). The procedure used for laying up these laminates was the same as above but single specimen 150mm × 150mm laminates were made rather than the bigger 4-specimen 300mm × 300mm laminates. This was primarily for quality control with precise location of the embedded delamination but also because only a small number of 'delaminated' panels were required. The 0.051mm thick delamination was cut from a large sheet of thermoplastic fluonnate ethylene propylene (FEP) film using a 40mm diameter circular steel cutting ring. The delamination was located between the two central 90° plies in the centre of the specimen, Fig. 2.9. Accurate positioning was essential and was achieved using a template made from a laminate backing sheet and a ruler.

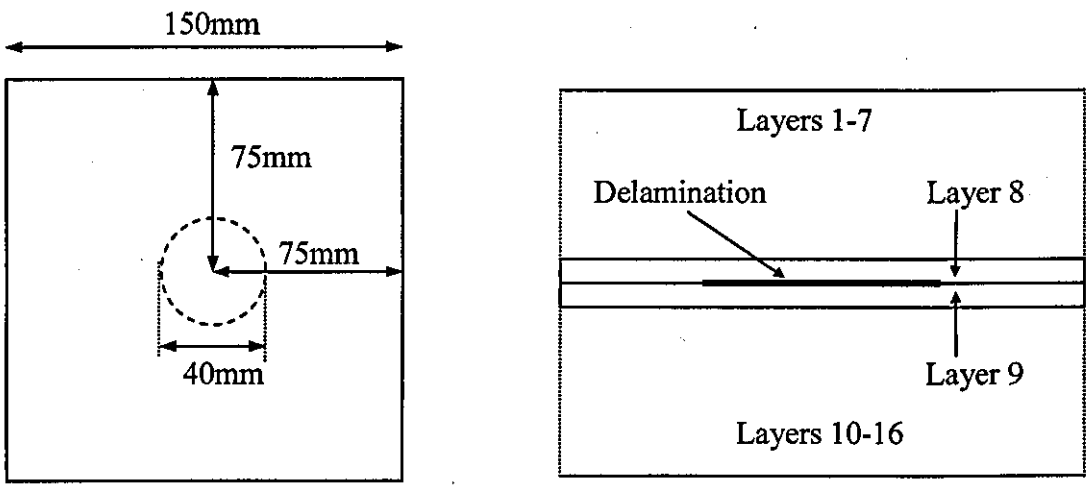

Figure 2.9 Location of the artificial delamination within the laminate

2.3. Core materials

2.3.1. Honeycomb properties

Basic mechanical properties for 12.7mm thick Aluminium 5052 and Nomex HRH-10 core materials of varying density have been obtained from the manufacturer's datasheets and through experimental tests carried out within the department to ASTM C365 [147]. A full discussion of the experimental test methods and results are included in Section 4.3.2. A summary of the key values obtained from the manufacturer are quoted here for reference in Table 2.9.

Table 2.9 Mechanical properties of 5052 aluminium and HRH-10 nomex honeycombs

Honeycomb Designation	Density (kg/m^3)	Compressive					Plate Shear			
		Bare		Stabilised		Crush strength (MPa)	L direction		W direction	
		Strength (MPa)	Modulus (MPa)	Strength (MPa)	Modulus (MPa)		Strength (MPa)	Modulus (MPa)	Strength (MPa)	Modulus (MPa)
3.1-3/16-10	50	2.00	-	2.30	517	0.90	1.45	310	0.90	152
4.4-3/16-15	70	3.59	-	4.10	1000	1.72	2.25	470	1.48	210
5.7-3/16-20	90	5.65	-	5.80	1520	2.69	3.15	620	2.05	265
HRH-10-3/16-3.0	48	2.07	-	2.40	140	-	1.20	40	0.70	25
HRH-10-3/16-4.0	64	3.45	-	3.90	190	-	1.80	60	1.00	35
HRH-10-3/16-6.0	96	6.45	-	7.70	400	-	2.60	85	1.50	50

2.3.2. Honeycomb preparation

When preparing the honeycomb a minimal amount of handling and pressure was applied to the honeycomb surface as it could be easily damaged and grease on the surface of the honeycomb could not be removed without a chemical bath. Any grease left on the surface could contribute to a poor bonding quality and any damage such as cell wall buckling or distortion will weaken the honeycomb and impair its performance.

The honeycomb core material was supplied in 1400mm × 3000mm × 12.7mm sheets, and cut into 320mm × 320mm pieces for aluminium or 350mm × 350mm pieces for

nomex, using a Stanley knife and ruler. The aluminium honeycomb pieces were cut 20mm wider than the required 300mm panel width to ensure good laminate-core bonding at the panel edge and to prevent any damaged or distorted cells at the cut edge being used within the panel structure. For the nomex cores which were bonded using the autoclave, this excess width was increased to 50mm due to the problem of consolidation at the panel edges caused by the pressure inside the autoclave pressing on the honeycomb edge, shown in Fig. 2.10. Although this problem could not be eliminated, using a larger excess of core around the specimen edge minimised the problem.

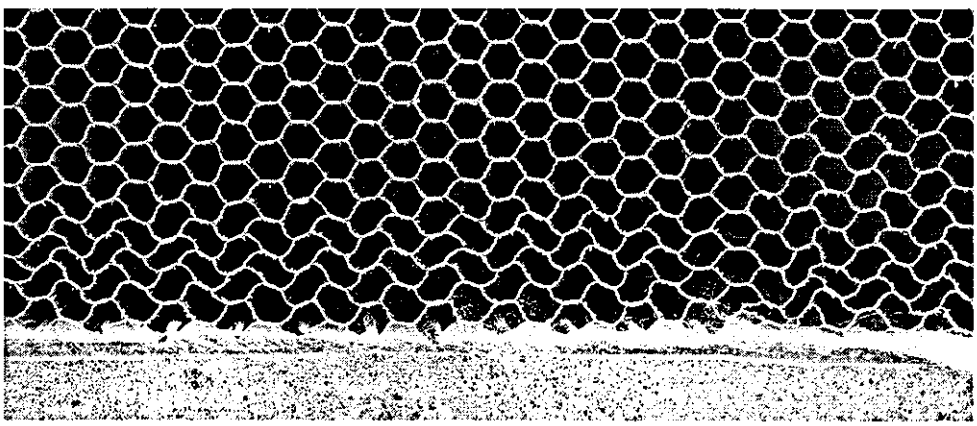

(a)

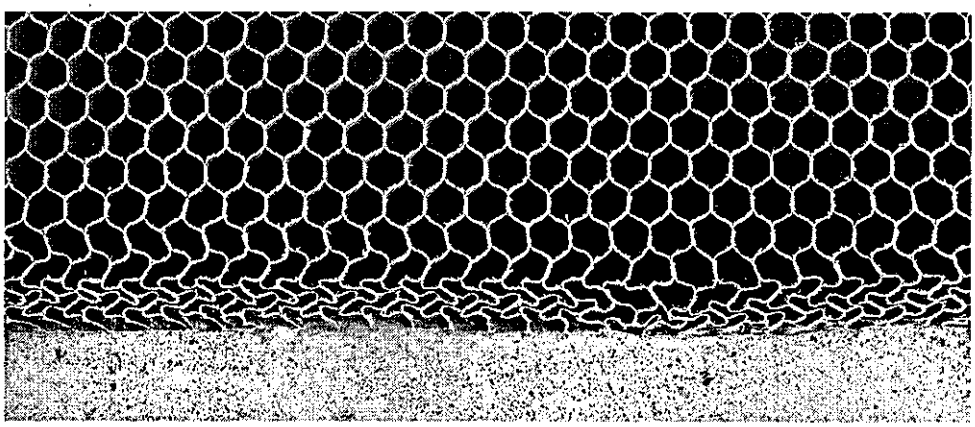

(b)

Figure 2.10 Consolidated cells in nomex specimen cured in the autoclave
(a) Damage in L-direction (b) Damage in W-direction

The pieces of nomex honeycomb were also dried in an oven before bonding, as nomex absorbs moisture from the air over time. This moisture was removed before the nomex was bonded to form a sandwich panel because excess moisture can affect the bonding

process. As no clear guidelines for exact drying time were quoted in the product data sheets and after informal consultations with the manufacturer suggesting an overnight cure at medium temperature, the nomex was dried for approximately 16 hours at 65°C immediately before bonding.

2.4. Sandwich panel manufacture

2.4.1. Adhesive properties

Three types of adhesive have been used in the sandwich panels manufactured as part of this work. All sandwich panels with IM7/8552 skins have been bonded using Redux 312 supplied by Hexcel Composites. Initial specimens containing T700/LTM45-EL skins were bonded using XLTA225. However, this product was taken out of production and replaced with a similar but improved adhesive VTA260 by the manufacturer (ACG). The curing process and properties for these three adhesives are very similar and as skin-core debonding is not expected the effects of the change in adhesive have not been investigated. The strength of the adhesive must be adequate to prevent skin-core debonding during testing. Strength values are obtained through various peel tests requiring specialist equipment which is not available at Loughborough University. Therefore all strength data has been taken from the manufacturers datasheets and is shown in Table 2.10.

Table 2.10 Supplied mechanical properties of adhesives

Mechanical property	ACG XLTA225	ACG VTA260	Redux 312
Areal weight (g/m^2)	313	313	300
Lap shear strength (MPa)	18.8-21.0	28-36	43
Bell peel strength (N/mm)	-	-	9.1
T-peel strength (N/mm)	2.55	-	-
Climbing drum peel strength	52.4-61.5 Nm/m	58-78 Nm/m	710 N/76mm
Flatwise tensile (MPa)	4.8-6.1	7.4-7.8	9.1

Note: Values quoted are for tests at room temperature. Adherends were Alclad 2024-T3 aluminium skins and 7.9-1/4-40 5052-T aluminium honeycomb. Values quoted for VTA260 are for curing at 65-120°C

Adhesive Bonding Pressure

The laminate-core bonding process required both temperature and pressure to cure the adhesive. For XTA225 and VTA260 adhesives a minimum bond pressure of 0.1MPa was used during curing as recommended by the manufacturer. For Redux 312 this was increased to 0.18MPa. Although these were minimum values and higher pressures could be used, it was not advisable due to the comparatively low crushing strength of the core materials.

When curing in the oven the pressure was applied using weights spread over the upper surface of the skin-core assembly via a 1cm thick 8.9kg steel caul plate. The steel caul plate was used to distribute the weight evenly over the entire surface with additional weights placed on top to obtain the required pressure. The total amount of weight required to obtain the minimum pressure was calculated using Eq. 2.1:

$$Pressure\ (MPa) = \frac{Force\ (N)}{Honeycomb\ cell\ wall\ surface\ area\ (mm^2)} \tag{2.1}$$

The honeycomb cell wall area was estimated from the number of honeycomb elements within the panel. The honeycomb elements used were assumed to be regular hexagons with an expansion angle θ_w of 60° and consisting of 6 cell walls of uniform length a_w. The cell walls not parallel to the L-direction, represented by thin lines in Fig. 2.11, are free walls shared with the adjoining cells and have a web thickness of t_w. Therefore the area of these walls is halved when considering an array of cells rather than an individual cell. The cell walls parallel to the L-direction, represented by thick lines in Fig. 2.11, are double walls and have a total thickness of $2t_w$, giving a thickness of t_w for the individual cell wall area. The cell wall area of a single honeycomb element contained in an array is given by Eq. 2.2:

$$\begin{aligned} A_{element} &= 0.5 \times (4t_w a_w) + 2t_w a_w \\ &= 4t_w a_w \end{aligned} \tag{2.2}$$

An array of honeycomb cells is shown in Fig. 2.11, where it can be seen that the number of cells in the W-direction is equal to the width of the array divided by the cell size, b_w. In the L-direction one row of cells has a width of $2a_w$ whist the next row has a width of only a_w. Hence the number of cells in the L-direction is given by the length of the array divided by the average cell width of $1.5a_w$. From this the surface area of the entire 300mm^2 honeycomb sheet was found by multiplying the area of each element by the total number of elements contained in the sheet. The honeycomb geometry, surface area and required weight for each honeycomb and adhesive type used are summarised in Table 2.11.

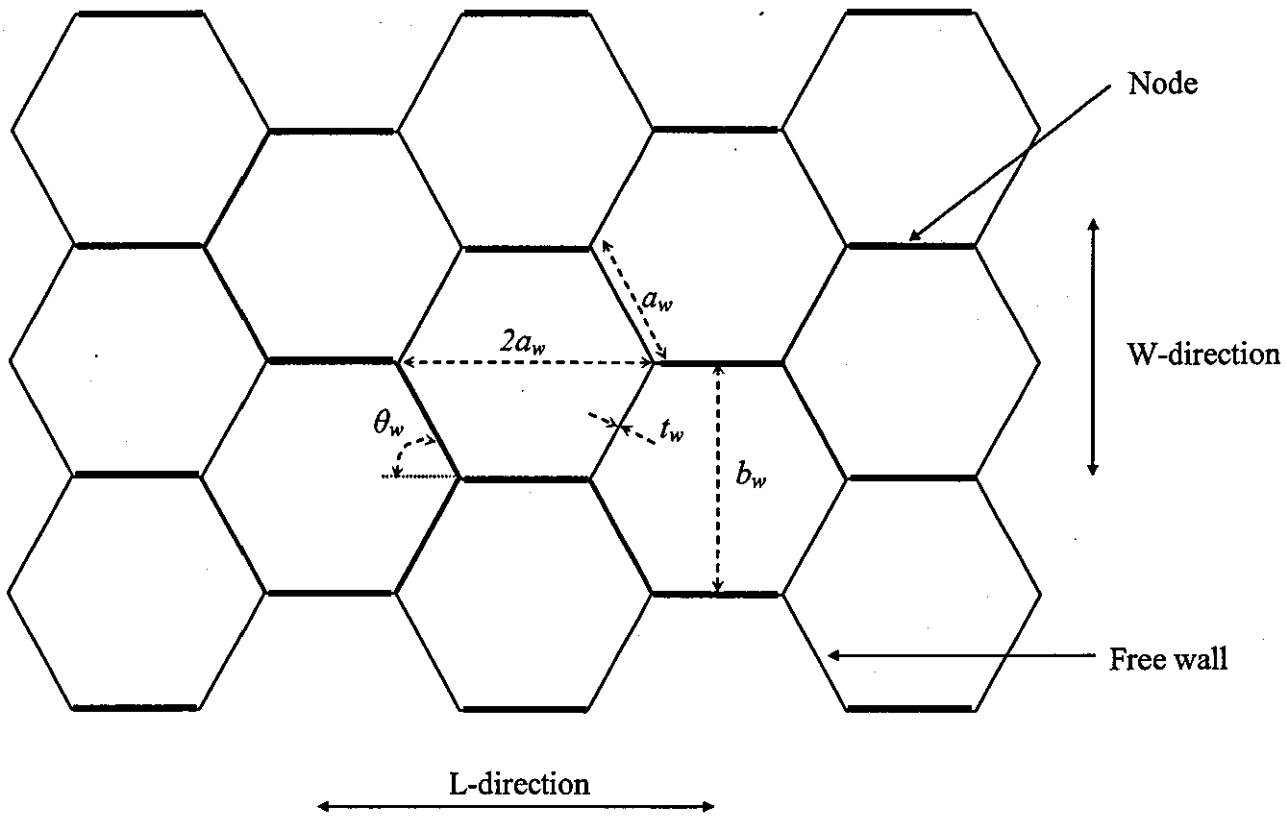

Figure 2.11 Honeycomb element terminology

Table 2.11 Honeycomb Geometrical Data

	Aluminium 5052			HRH Nomex	
	3.1-3/16-10	4.4-3/16-15	5.7-3/16-20	HRH-10-3/16-4.0	HRH-10-3/16-6.0
Cell wall length, a_w (mm)	2.72	2.72	2.72	2.83	2.83
Cell size, b_w (mm)	4.76	4.76	4.76	5.00	5.00
Expansion angle, θ_w (°)	60	60	60	60	60
Web thickness, t_w (mm)	0.0254	0.0381	0.0508	0.1	0.15
Elements in 300mm^2 sheet	4634	4634	4634	4327	4327
Element Area, $A_{element}$ (mm^2)	0.2764	0.4145	0.5527	1.132	1.698
Total surface area (mm^2)	1280.8	1920.8	2561.2	4898.2	7347.2
Required load (VTA260) (N)	128.08	192.08	256.12	489.82	734.72
Required load (Redux) (N)	217.7	326.5	435.4	832.7	1249.0
Equivalent Mass (VTA260) (kg)	13.06	18.58	26.11	49.93	74.90
Equivalent Mass (Redux) (kg)	22.2	33.3	44.4	84.9	127.3
Caul Plate Mass (kg)	8.9	8.9	8.9	8.9	8.9
Additional Mass (VTA260) (kg)	4.16	10.68	17.21	41.03	66.00
Additional Mass (Redux) (kg)	13.3	24.4	35.5	76.0	118.4

2.4.2. Adhesive preparation

The adhesives were supplied on large rolls which required frozen storage. The rolls were removed from the freezer and allowed to defrost thoroughly before use to prevent the bonds and supporting mesh material within the adhesive, which were brittle when frozen, fracturing when the adhesive was unrolled. Sheets measuring 310mm × 310mm were cut from the rolls using a sharp pair of scissors. The adhesive sheets were cut 20mm larger than the skins to ensure good bonding at the skin-core edges. One sheet of adhesive was used for each skin-core bond, so a total of 2 sheets were needed per sandwich panel. The protective backing sheets on the adhesive were kept in place until the adhesive was ready to use to prevent dirt and grease sticking to the adhesive surface, and the sheets were returned to the freezer until required for bonding.

2.4.3. Skin - honeycomb bonding

Bonding the laminate skins to the honeycomb core was completed in two stages using an adhesive film. Each skin was bonded separately to ensure the thickness of each bond

line was uniform, as gravitational forces can cause the adhesive to run down the honeycomb cell walls before it is fully cured when bonding both skins simultaneously. A process of co-curing the skins to the core without the use of an adhesive film was not used for a number of reasons. Co-curing of the skins and core often leads to poor bond quality unless a prepreg with a very high resin weight is used. Additionally there is a large mismatch between the pressure required to cure the laminate skins and the crushing strength of the core materials. Lastly due to the nature of the honeycomb walls only providing intermittent support to the uncured skin, dimpling of the skin can occur during curing, which in turn can lead to poor panel performance under in-plane compression.

Curing was carried out using either an oven or autoclave depending on the amount of weight needed to achieve the required pressure when curing in the oven, see Table 2.11. For weights above 25kg the autoclave had to be used for practical reasons.

Each skin was cleaned with acetone to remove any grease and particles left from trimming the edges on the tile cutter. The 0° fibre direction was marked on the side of the skin not to be bonded with a permanent marker. A sheet of adhesive was removed from the freezer and one backing sheet peeled off. The adhesive was then placed face down on top of the skin. The second backing sheet was removed and the honeycomb sheet carefully positioned such that the honeycomb L-direction was aligned with the 0° fibre direction. The second skin was rested on top of the honeycomb directly above the lower skin being bonded and the steel caul plate placed on top of the second skin. The purpose of the second skin was to prevent accidental damage being caused to the honeycomb cell walls when applying/removing the heavy steel caul plate.

The skin-core lay-up was then placed on a piece of non-porous release fabric to prevent any excess adhesive contacting with the oven shelf/autoclave. This arrangement was placed in the front loading oven and extra weights distributed evenly over the caul plate to obtain the required pressure, as given in Table 2.11. The oven was then switched on and allowed to reach the required curing temperature before starting timing. This allows the heat to spread through the skin, core and caul plate and reach the bond line at the centre of the panel before the outer regions reach the curing temperature. The slow heat-

up rate also prevents the formation of bubbles in the adhesive which can occur if the adhesive heats up too rapidly. For curing in the autoclave a ramp rate of 2°C/min was selected and a pressure of 0.1MPa and full vacuum applied. The autoclave was then set to run through the required dwell cycle, then left to cool under pressure and vacuum until a temperature below 30°C was reached. The required curing conditions for each adhesive are given in Table 2.12.

Once cured the skin-core assembly was left in the oven/autoclave to cool gradually as rapid cooling can cause cracking and residual stresses in the adhesive through the adhesive shrinking too quickly. The excess adhesive and honeycomb around the bonded skin edge were then trimmed with a Stanley knife. The second skin was then bonded by repeating the above process. Once the entire panel was bonded it was trimmed and cut into either 4 equal specimens measuring 150mm × 150mm or 2 specimens measuring 205mm × 150mm using the diamond edged tile cutter. Each specimen was then cleaned with water and acetone to remove trimmed particles and dust.

Table 2.12 Adhesive curing cycles

	ACG XLTA225	ACG VTA260	Redux 312
Curing temperature	60°C	65 °C (120°C)	120 ± 5°C
Curing pressure	0.1MPa	0.1-0.21MPa	0.1-0.35MPa
Curing time	16hrs	16hrs (1hr)	30mins
Ramp rate	-	-	5°C per min
Cool down	-	Drop temp below 70°C whilst maintaining pressure	

3. EXPERIMENTAL PROCEDURES FOR DAMAGE RESISTANCE

Currently no precise testing procedures exist for evaluating the damage resistance of composite sandwich panels. A number of test standards for the transverse testing of laminate plates have been created, however, these are not directly applicable to sandwich panels and generally do not conform with compression-after-impact methods. The QS/ impact testing procedure chosen for this study is in line with the requirements for CAI testing, as discussed in Section 1 and defined in Section 7, and closely follows other research within the department on the CAI response of laminate plates. Like manufacturing all testing was completed in house. An in-depth description of all test procedures is included in Appendix D, with a summary given below for each process.

3.1. Specimen preparations

To help identify the deformation pattern on the top and bottom skins during quasi-static loading strain gauges were bonded to the top and bottom panel surfaces. The panels loaded to ultimate failure provided information about the entire loading cycle so benefited most from having strain gauges. Where necessary the panels tested to secondary damage were also strain gauged to support the results obtained from the ultimate test. Strain gauges were not required on the panels loaded to initial damage.

The strain gauges used were FLA-5-11 single element gauges with a gauge length of 5mm, supplied by Technimeasure Ltd. The strain gauges were orientated parallel to the 0° fibres, the fibre direction on the external surfaces. The gauge bonded to the top surface was positioned 20mm away from the loading centre to prevent the indenter contacting the gauge during loading. Due to the gauge being located away from the centre of the panel the strain readings collected were less than if the gauge was bonded directly under the loading point, but still close enough to provide a measure of the local deformation. A second strain gauge was located on the top skin of the panel 20mm away from the loading centre at 45° to the 0° fibres in a small number of early tests. The readings from this gauge did not provide any additional information about the interaction of the 0° and 90° plies as was anticipated. Therefore it was omitted in all

later tests. The gauge bonded to the bottom surface was located at the centre of the bottom surface of the panel, directly inline with the loading point. This gauge was used to provide information regarding the global deformation of the panel.

The centre of both the top and bottom panel surfaces on each specimen were located by drawing two diagonal lines joining each corner with a permanent marker pen. The point at which these lines crossed marked the centre point for the bottom strain gauge. On the top surface a line 30mm in length was drawn away from the centre of the panel parallel with the 0° fibres. A line 20mm from the centre of the panel was drawn perpendicular to the previous line. The crossing point of these two lines marked the centre point for the top strain gauge. A 100mm diameter circle was also drawn around the centre of the top surface of the panel, outlining the clamping region used during quasi-static and impact testing. A diagram of the panel marking is shown in Fig. 3.1. The regions marked for strain gauging were then lightly sanded to remove any undulations and cleaned with acetone to provide a smooth clean surface, as required for good adhesion. Each strain gauge was then bonded in turn.

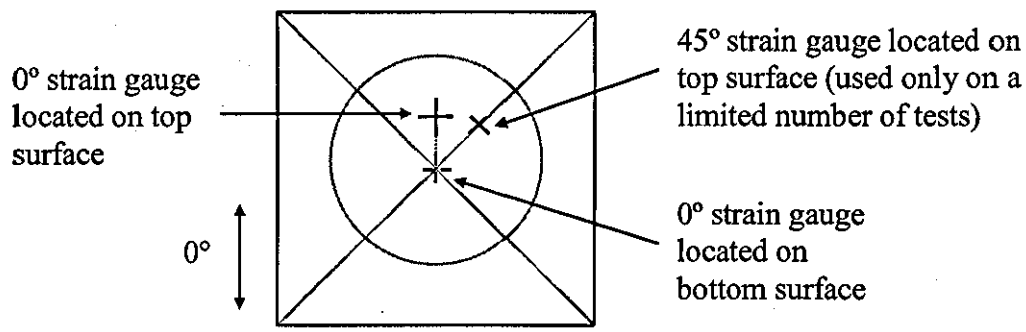

Figure 3.1 Strain gauge position markings

The strain gauge was removed from the protective plastic sheath and placed face down on the panel surface. A piece of non-stick paper supplied with the strain gauge was positioned between the strain gauge legs and the panel surface to prevent the legs becoming glued to the panel. A piece of sellotape was then placed over the gauge and paper to allow the gauge to be moved and accurately aligned with the location marks.

Once in position the sellotape was peeled back to reveal the underside of the gauge and a small drop of isocianate adhesive, a quick-drying superglue, spread over the gauge. The sellotape was then stuck back down and a small amount of pressure applied to the gauge to remove any trapped air bubbles, with care taken not too apply too much pressure as this could induce pre-strain into the gauge. The glue was allowed to dry before peeling off the sellotape, leaving the gauge firmly stuck to the panel surface. The strain gauge legs were carefully lifted up and a pair of copper terminals glued onto the panel surface, such that the terminals butted up to the strain gauge. The strain gauge legs were bent back down and trimmed to the same length as the terminal to prevent unwanted contact with the panel surface. Both the strain gauge legs and 0.5m long electrical wires were then soldered to the copper terminals. The resistance across the electrical wires was measured to check the circuit was good with no bridging of the terminals. A good circuit gave a resistance of approximately 120Ω±1Ω. The electrical wires were then coiled up, labelled with the gauge location and taped down until ready for use.

3.2. Experimental set-up for quasi-static tests

All quasi-static tests on skin, core and panel specimens were completed using a Mand universal testing machine. The Mand machine has a load range of 0-100kN and is displacement controlled. This type of control system lends itself to investigations into damage characteristics especially when used in conjunction with an impact test rig. Loads were applied to the panel at a constant loading rate of 5mm/min using either a hemispherical or flat-ended indenter, which could be interchanged as required. Load and displacement data from the Mand machine were captured and recorded using an Orion delta 353D data acquisition system (data logger). Strain gauge and LVDT data were also recorded through the data logger. This set-up was used for both quasi-static bending and quasi-static indentation tests, which are discussed in Sections 3.2.1. and 3.2.2 respectively.

3.2.1. Quasi-static bending tests

Quasi-static bending tests were completed on skin plates and sandwich panels. The test set-up used in each case was identical. Fully clamped boundary conditions were used in all bending tests. The 150mm × 150mm test specimen was firmly clamped between two steel plates, with 100mm diameter central circular cut-outs. A small number of tests were also completed on 300mm × 300mm sandwich panels with a 220mm loading area to investigate the effect of specimen size and edge effects. In this instance two steel plates with a 220mm diameter circular cut-out were used in the place of the 100mm diameter clamping plates. The clamping plates and specimen were then placed onto two steel box supports and secured to the Mand machine base. The box supports were used to raise the specimen off the base as machine accuracy was only obtained over a selected ±25mm range of travel. Outside the selected range of travel the loading head oscillated slightly such that loading was no longer steady state and poor load-displacement results were collected. A diagram of the test set-up is shown in Fig. 3.2.

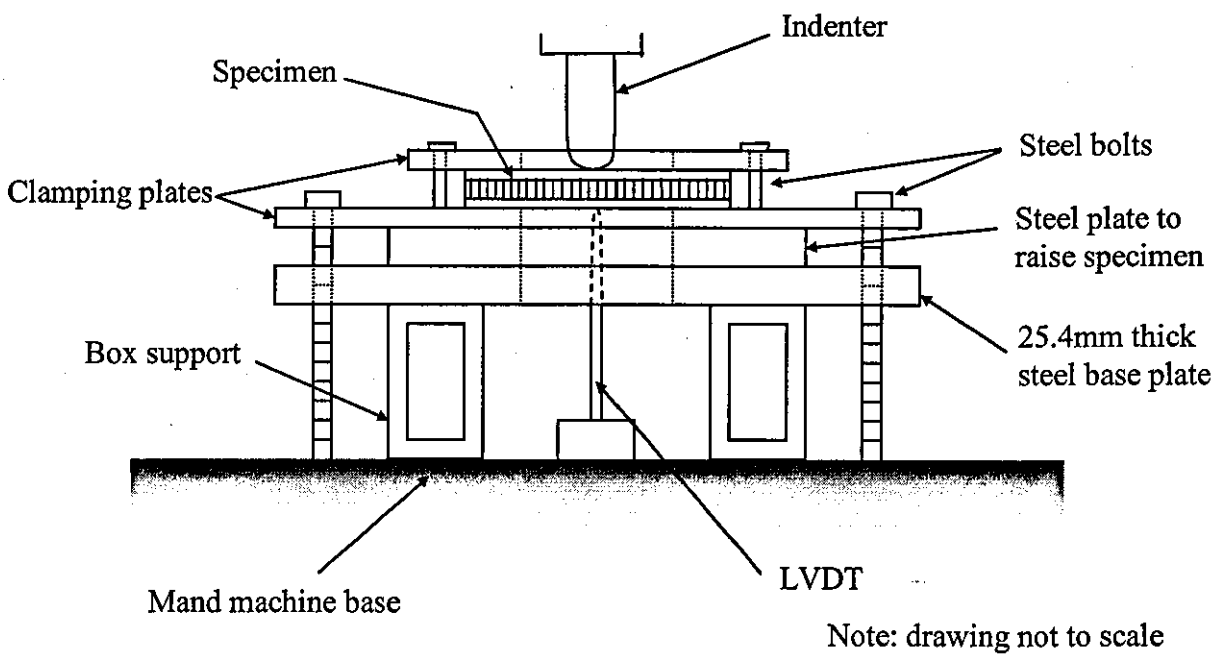

Figure 3.2 Quasi-static bending test set-up

Raising the specimen above the base also conveniently allowed an LVDT (linear variable differential transformer) to be positioned underneath the specimen. The indenter displacement and corresponding load data measured by the Mand machine only provided information on the top surface displacement when testing a sandwich panel. This accounts for local deformation through both panel flexing and core crushing. By locating the LVDT underneath the panel the bottom surface displacement could also be measured, which provided information on the global bending of the panel. By subtracting the LVDT displacement from the indenter displacement an estimate of the amount of core crushing was obtained. Ideally the LVDT would have been positioned at the centre of the panel. However, the strain gauge located at the centre of the bottom surface of the panel prevented this so instead the LVDT was offset from the panel centre by 5-10mm whenever strain gauges were present. Consequently the amount of global bending was slightly underestimated and hence the core crushing overestimated, see Fig 3.3, although the effect of this offset was small in comparison to the total top skin displacement.

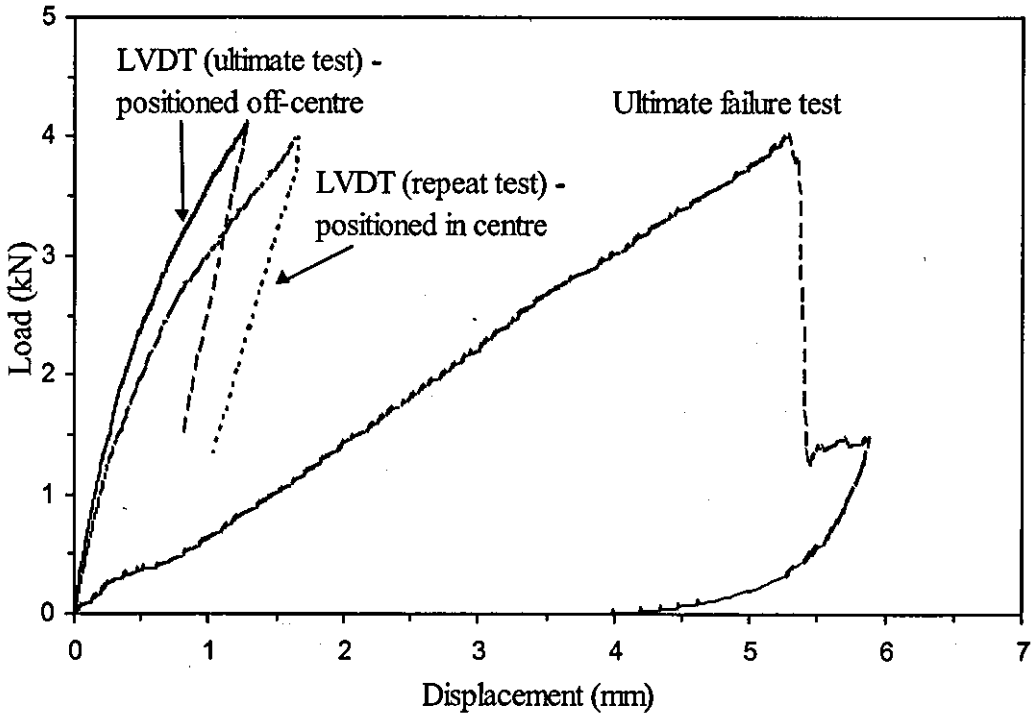

Figure 3.3 Variation in LVDT reading with position relative to the panel centre for a 4 ply 70kg/m^3 panel loaded with the HS indenter

The specimen was clamped between the two steel clamping plates and the bolts tightened just past finger-tightness, to 4Nm using a torque wrench. On specimens with strain gauges the electrical wires were connected to the Orion delta 353D acquisition system via a dummy gauge board for temperature compensation. The load, displacement and LVDT output cables were also connected to this system, which had a sampling rate of 0.5 Hz. Two types of indenter were used for bending tests, namely hemispherical (HS) and flat-ended (FE), both 20mm in diameter. The required indenter was attached to the loading head and lowered to 1-2mm above the specimen. The specimen was loaded at a rate of 5mm per minute and loading stopped either when the top skin of the panel failed, signified by a sudden large load drop accompanied by a loud bang, or at a predetermined load. The predetermined load was used for diagnostic tests with the specimen being loaded to a point just after either initial or secondary damage had occurred. These predetermined loads were identified from the load-displacement plots of previous ultimate failure tests, as discussed in the following sub-section.

Once the test was finished the specimen was carefully removed from the clamps and inspected for damage, as discussed in the following chapter. The data captured through the Orion data logger, recorded either in volts or microstrain, was transferred to a computer for analysis. The computer program EXCEL was used to convert and analyse the data. The load, displacement and LVDT data were converted to either kN or mm using Eqs. 3.1-3.3. The strain data was recorded directly in microstrain so did not require conversion. Load-displacement and load-strain plots were then produced.

$$True\ load = \left(-\frac{mand\ output\ voltage + 0.0013}{0.9927}\right) \times \left(\frac{load\ range\ (kN)}{10}\right) \text{ (kN)} \qquad (3.1)$$

$$True\ displacement = \left(-\frac{mand\ output\ voltage + 0.0362}{0.4362}\right) \text{ (mm)} \qquad (3.2)$$

$$True\ LVDT\ displacement = \frac{LVDT\ output\ voltage}{0.5532} \text{ (mm)} \qquad (3.3)$$

Diagnostic tests

To determine the cause of failure under quasi-static loading a panel was loaded until ultimate failure, (C), signified by a loud bang and large drop in load during testing. This corresponded to failure of the top skin due to the indenter penetrating the skin. A load-displacement plot produced from an ultimate failure test is shown in Fig. 3.4. The occurrence of any damage prior to ultimate failure was then identified from the load-displacement curve. From the curve shown below two points of damage propagation can be identified at points (A) and (B), hereon referred to as initial damage and secondary damage. Diagnostic tests were then completed by loading similar panels to the respective reference loads for initial and secondary damage. The diagnostic panels were then cross-sectioned to reveal the cause of initial damage (A) and secondary damage (B). This process was completed extensively on the T700/LTM45-EL panels with both aluminium and nomex cores to gain a thorough understanding of the damage mechanisms. A very limited number of diagnostic tests were completed on the IM7/8552 panels as the damage mechanisms were considered similar.

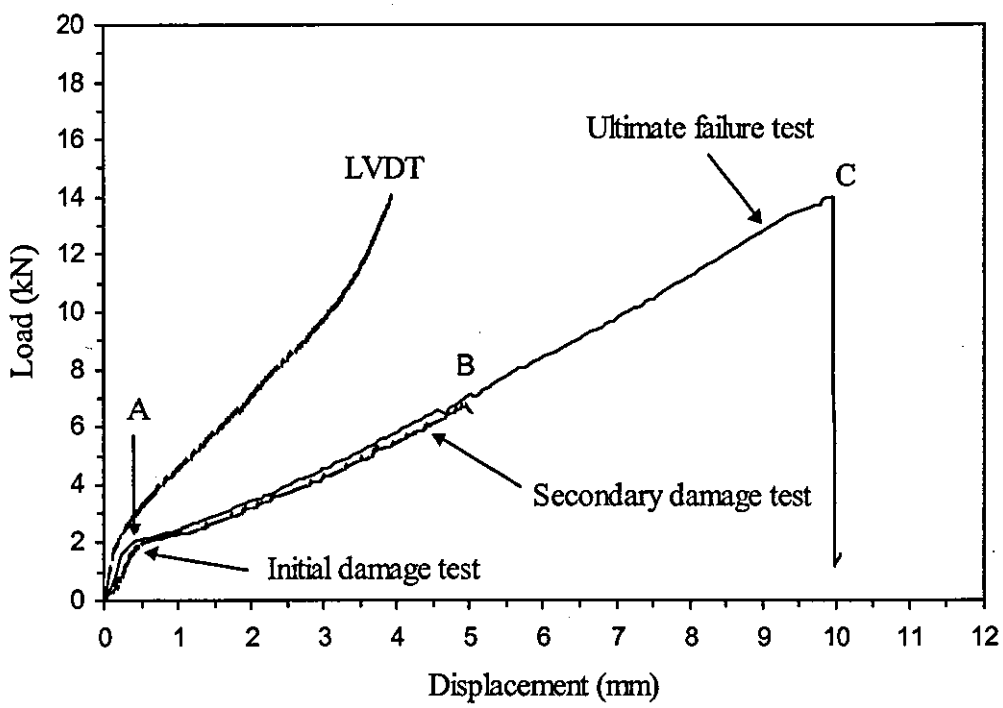

Figure 3.4 Load vs. displacement plot for a sandwich panel with 12 ply carbon fibre skins and 50kg/m^3 aluminium honeycomb loaded with the flat-ended indenter

3.2.2. Quasi-static indentation tests

Quasi-static indentation tests were completed on both sandwich panels and honeycomb core specimens. The procedure used for sandwich panel indentation tests was identical to that for the bending tests except the support conditions were changed and consequently the LVDT was redundant. The specimen was clamped to a solid base using one of the 100mm diameter circular cut-out steel clamping plates from the bending test arrangement. As the bottom surface of each specimen was in contact with the solid base no global deformation could occur, therefore no strain gauges were required on the bottom surface of the sandwich panel specimens.

Two types of indentation test were completed on honeycomb specimens to identify peak compression and crushing strengths and provide an understanding of the crushing behaviour. The first type of crush test was through stabilised compression, following ASTM C365 [147]. Aluminium skins were bonded to the top and bottom surfaces of a bare honeycomb specimen measuring 76.5mm × 76.5mm using VTA260 adhesive. The specimen was then placed onto a solid base and crushed over the entire surface using a flat plate loader. The aluminium skins were used to give the honeycomb cell walls stability under loading. As loading is over the entire specimen surface it is of vital importance that the loading surface is parallel to the honeycomb surface. If the loading surface is not parallel the honeycomb will not be crushed evenly and low values of strength and modulus may be obtained. The displacement was taken directly from the indenter and although this had no bearing on the strength values obtained it was not regarded reliable enough to determine the modulus.

The second type of honeycomb indentation test used a 150mm × 150mm bare honeycomb specimen. The specimen was placed on a solid base and clamped using the circular 100mm diameter cut-out steel plate as described for a sandwich panel. Load was applied at the centre of the specimen using either a 20mm diameter hemispherical or flat-ended indenter. A small number of tests were also completed using a 50mm diameter flat-ended indenter to assess the effect of loading area. In each test case loading was applied until the indenter had crushed the honeycomb specimens to at least half their original thickness of 12.7mm. No strain gauges were used in any of the

honeycomb indentation tests so all results are presented in terms of load-displacement graphs. The results of the honeycomb indentation tests are included in Section 4.3.

3.2.3. Effect of clamping force

The effect of the clamping force on the panel response under bending has been acknowledged. The clamping force used must be enough to prevent horizontal panel movement during loading, but not crush the honeycomb. During the majority of quasi-static tests a torque wrench was not available so the clamping bolts used to secure the clamping plates were tightened to finger tightness plus quarter of a turn with a spanner. This level of tightness corresponds to approximately 8Nm of torque. In a small number of initial tests the clamping bolts were tightened past this level. Also one 8/70/HS panel was tested with a clamping torque of 1Nm.

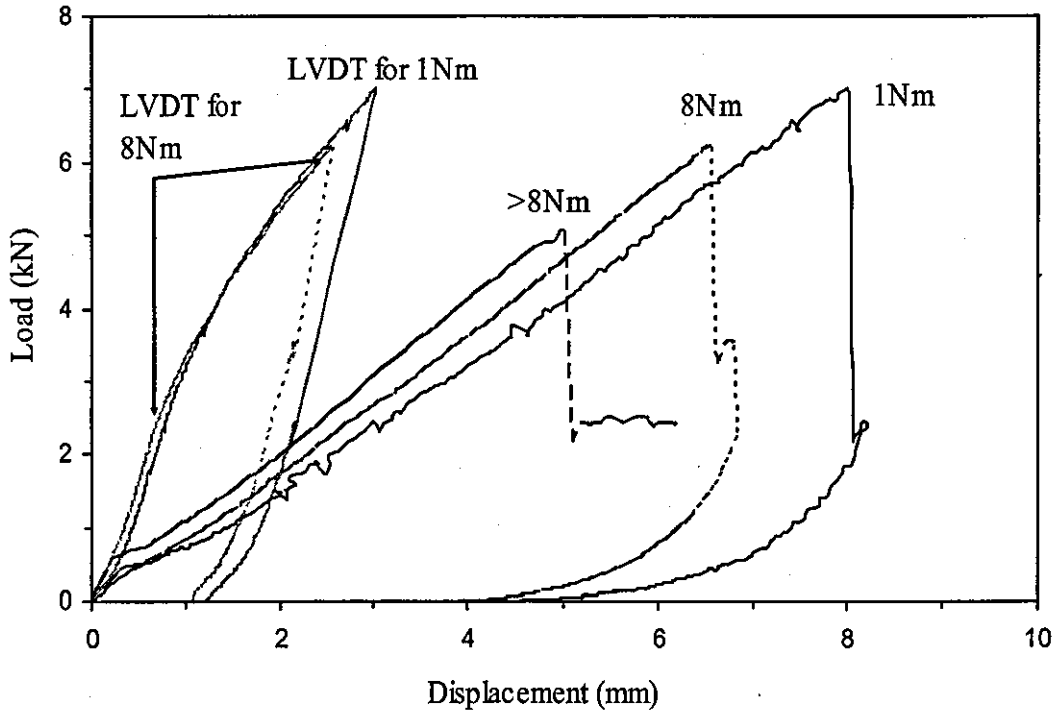

Figure 3.5 Load-displacement curves for 8 ply 70kg/m^3 panels loaded to ultimate failure with different torques used for clamping bolts

The load-displacement curves for three 8/70/HS panels loaded to ultimate failure are shown in Fig. 3.5. It can clearly be seen that the level of torque used to clamp the panel affects the panel strength. The stiffness of all three panels after the initial damage threshold is exceeded is very similar, but the ultimate failure load and displacement increases when the clamping torque is reduced. This is because of membrane effects and top skin stretching. If a panel is not clamped firmly horizontal movement can occur and the panel is able to relax by sagging within the unsupported region. When this happens the top skin membrane forces are greatly reduced. Therefore the top skin displaces further and is able to withstand a higher load level due to reduced in-plane stresses. Consequently an amount of variation in the load-displacement response of panels loaded in quasi-static bending can be expected due to uncontrolled levels of torque used in the clamping of many panels.

3.3. Experimental set-up for impact testing

Impact testing was carried out using a drop-weight impact testing rig and WINDSPEED WAVECAP computer software. The impact drop-weight tower consisted of: (a) a hemispherical nosed impactor 20mm in diameter with an overall mass for the unit of 1.49kg, (b) a strain-gauged load cell which was mounted within the impactor unit and used to measure force through four strain gauges mounted on to a load cell cylinder, (c) an impactor guide rail to ensure the impactor remained vertical during flight and was perpendicular to the specimen at contact, (d) two photodiodes located on the guide rail just above the specimen 50.1mm apart to obtain the incident and rebound velocities of the impactor via measurement of time, Fig. 3.6. The time data was recorded directly using two timer counters which were activated when the steel flag bolted to the impactor unit passed through the photodiode gates. The strain gauge load cell data was recorded using a Microlink 4000 data acquisition unit with a sampling rate of 50μs controlled by the WAVECAP software. As the signals received from the strain-gauged load cell were very weak they were passed through a strain gauge amplifier prior to entering the Microlink unit.

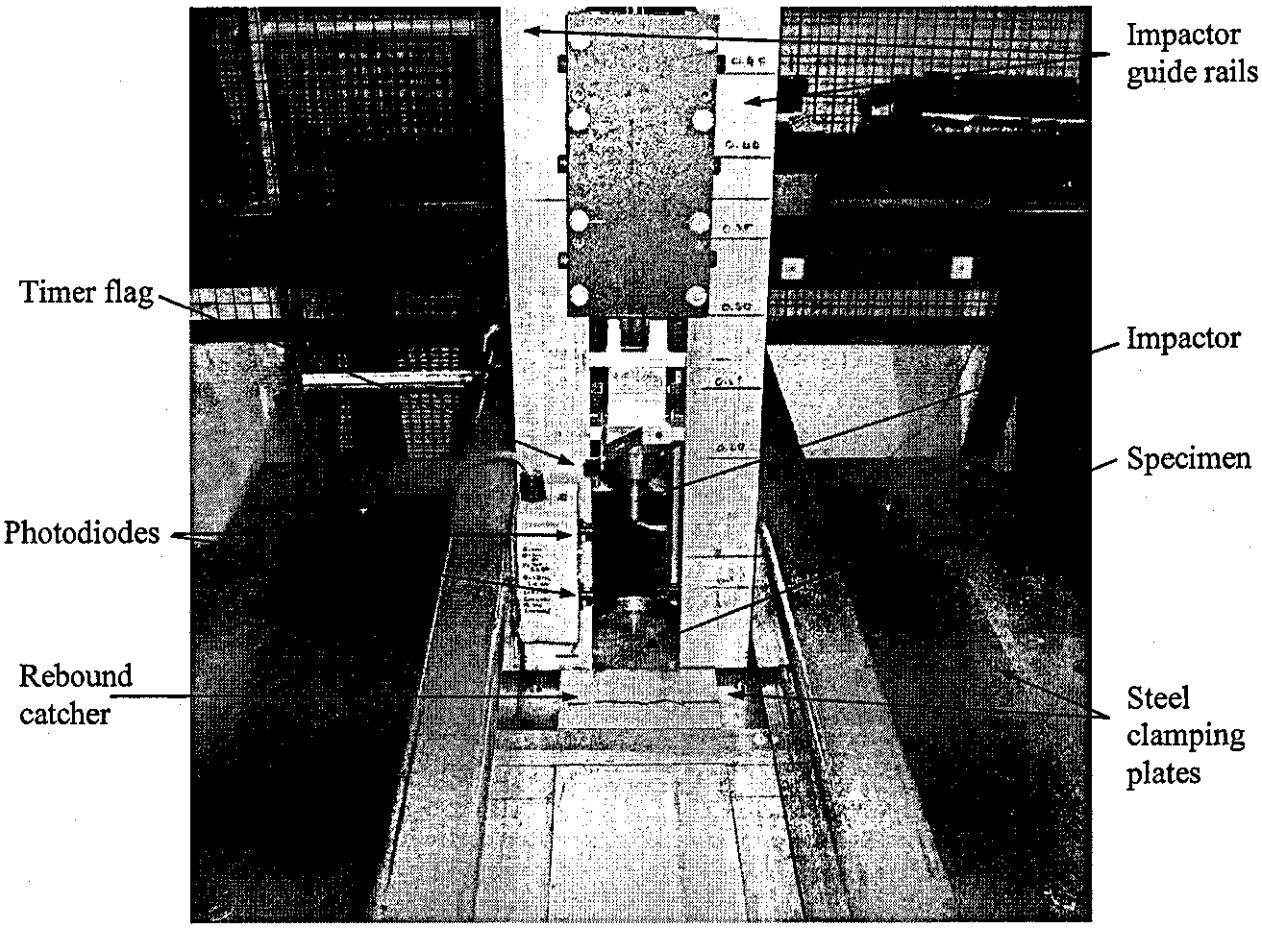

Figure 3.6 Impact rig set-up

Fully clamped support conditions were used for all impact tests. As in the quasi-static tests two steel clamping plates with 100mm diameter holes were used to fix the specimen to the impact rig base. As in the quasi-static case the clamping bolts were tightened to 4Nm using a torque wrench. The impactor was lowered to ensure the specimen was aligned such that the impactor contacted with the centre of the specimen, then the impactor was raised to the desired height. The impact energy was varied by increasing or decreasing the drop height of the impactor. Theoretically all potential energy should be converted to kinetic energy provided that the system is without any losses. However, friction forces present between the impactor and the guide rail and the effect of gravitational acceleration on the impactor meant that this assumption could not be made, Fig. 3.7. Therefore practice drop tests were completed on plywood specimens to determine the exact drop height required to achieve the desired energy level upon

impact for each individual test. The maximum drop height of the tower was 4.2m, which approximately corresponded to an impact energy of 55J. Once the drop height was set the impactor was released manually and the time and load cell data captured. Multiple impacts on the specimen were prevented by manually sliding a piece of wood between the specimen and the rebounding impactor. At very low and high levels of impact energy the impactor did not rebound high enough to prevent a second impact. However, in this instance due to the residual energy not even being enough to trigger the rebound timer it could be assumed that the absorbed energy was almost equal to the applied impact energy.

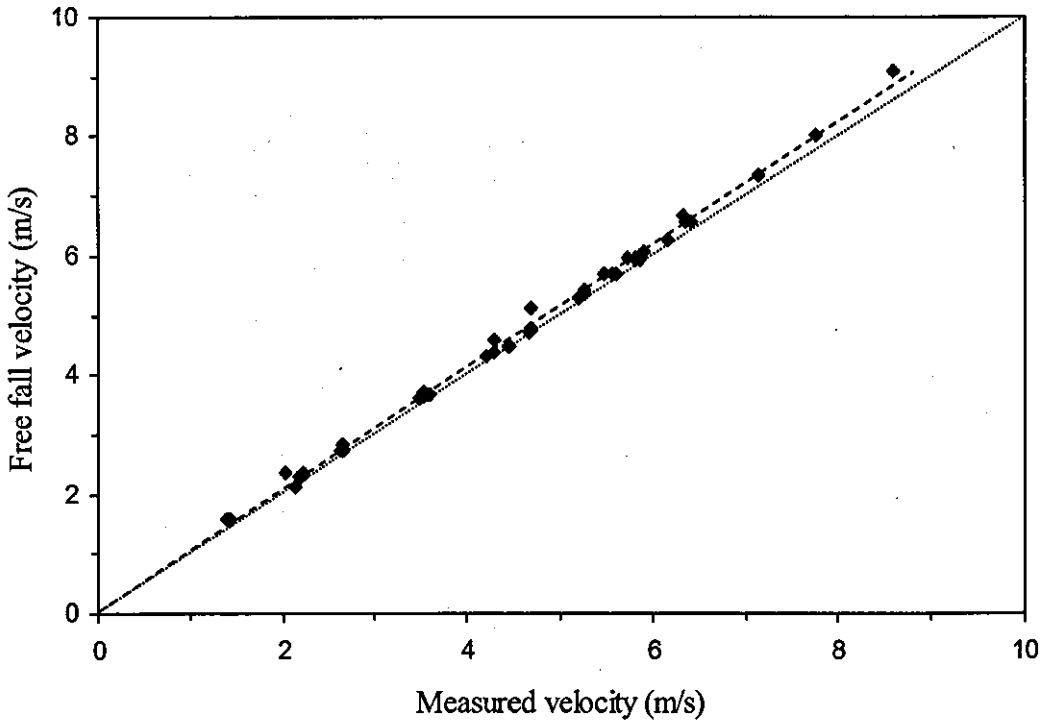

Figure 3.7 Comparison of measured and theoretical free fall velocity at impact

The data recorded by the Microlink system represented load in terms of volts. The time data was also known as the Microlink system was set up to record load data every 50μs. From this a volts-time plot was produced of the entire test, Fig. 3.8 for a 20.6J impact on an 8 ply 70kg/m^3 panel, which was then trimmed to focus only on the section where the impactor was in contact with the panel. From calibration tests it was known that

1kN corresponded to 7.79mV, allowing calculation of the load in kN using Eq. 3.4. A load-time plot was then produced, showing the loading and unloading phase of the panel, Fig. 3.9. Any fibre fracture of the top skin and ensuing core crushing could easily be identified on the load-time plot. As shown in Fig. 3.10 for a 25.2J impact on an 8 ply 70kg/m^3 panel.

$$Load = 0.128 \times (Volts \times 1000) + 0.19 \tag{3.4}$$

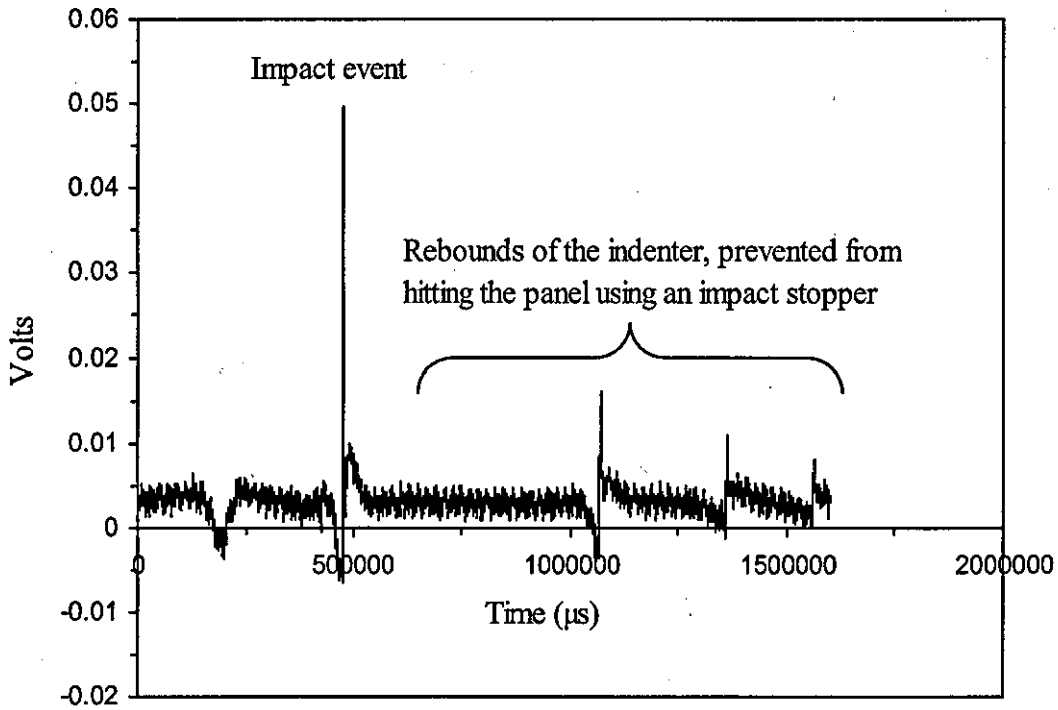

Figure 3.8 Volts-time plot of impact test on 8 ply 70kg/m^3 panel at an IKE of 20.6J

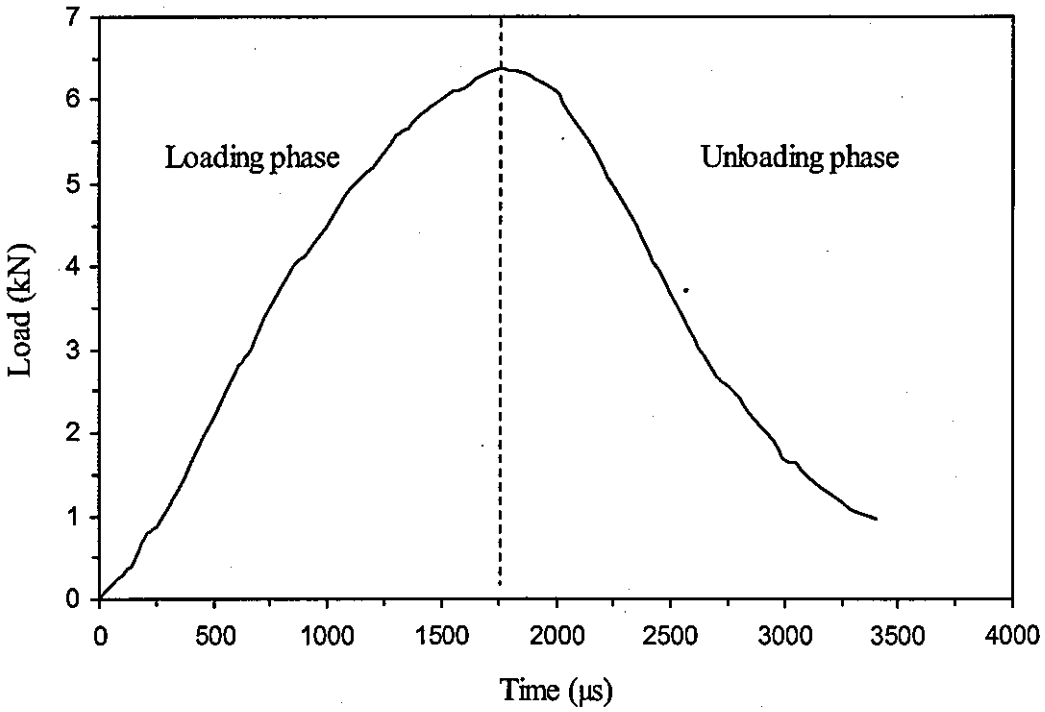

Figure 3.9 Load-time plot of impact event on 8 ply 70kg/m^3 panel at an IKE of 20.6J

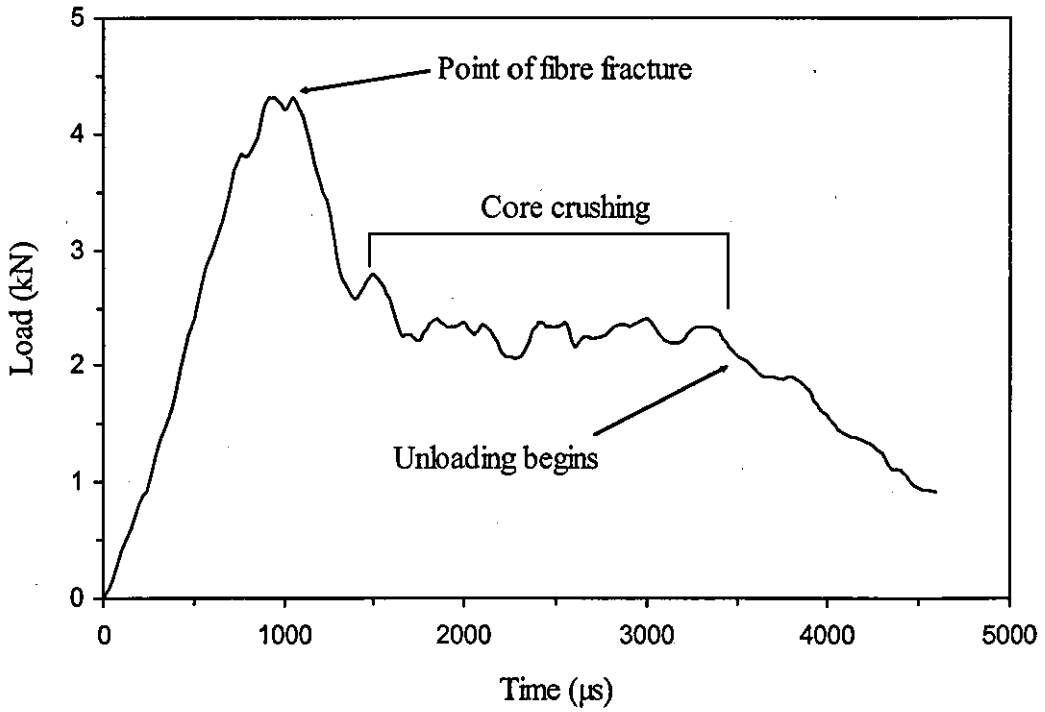

Figure 3.10 Load-time plot of impact event on 8 ply 70kg/m^3 panel at an IKE of 25.2J

The acceleration of the impactor during the impact event was calculated by dividing the load by the impactor mass of 1.49kg and an acceleration-time plot produced, Fig. 3.11. The area under this curve, found through integration, represented the velocity of the impactor, Eq. 3.5. The velocity at the onset and cessation of loading was checked to match the values obtained from the photodiodes for impact and rebound velocities. Velocity was then plotted against time, Fig. 3.12 and the process repeated to calculate displacement, Eq. 3.6. In cases of very low IKE or impacts causing fibre fracture the impactor often did not rebound high enough to pass through the photodiode capturing the rebound time. This is reflected in the velocity-time curves which show a very small rebound velocity. The displacement-time curve never returns completely to zero due to core crushing within the panel. In panels with fibre fracture and subsequent core crushing the displacement-time curve shows very little recovery following maximum deflection, Fig. 3.13.

$$v = v_0 - \int_0^T A.dT = v_0 - \frac{1}{m}\int_0^T P.dT \tag{3.5}$$

$$w = \int_0^T v.dT = v_0 T - \frac{1}{m}\int_0^T\int_0^T P.dT^2 \tag{3.6}$$

Finally a load-displacement plot can be produced to compare with the quasi-static test results, Fig. 3.14. The energy absorbed during the test was found in both the impact and quasi-static cases by calculating the area underneath the load-displacement curve, Eq. 3.7. Alternatively for the impact case a more accurate way used the incident and rebound times to find the absorbed energy through Eq. 3.8. The incident and rebound velocities were found by dividing the incident and rebound times by the distance between the photodiodes, 50.1mm. In cases of very low IKE levels and very high IKE levels where fibre fracture occurred, the impactor did not rebound high enough to trigger the rebound timer. In these instances the absorbed energy was calculated from the final impactor velocity derived from the raw strain and time data captured during the impact. This method is not as accurate due to the data processing procedure, but does provide a reasonable indication of energy absorption.

$$Absorbed\ energy,\ AE = \int_0^s P.dw \tag{3.7}$$

$$Absorbed\ energy,\ AE = \frac{1}{2}mv_{incident}^2 - \frac{1}{2}mv_{rebound}^2 \tag{3.8}$$

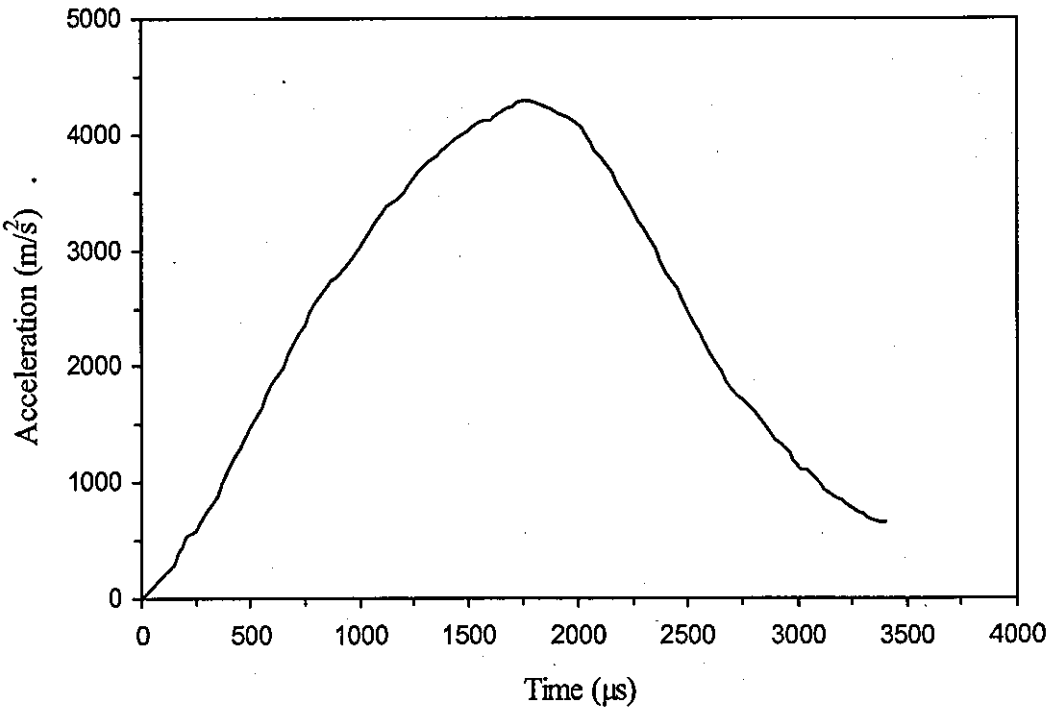

Figure 3.11 Acceleration-time plot of impact event on 8 ply 70kg/m^3 panel at an IKE of 20.6J

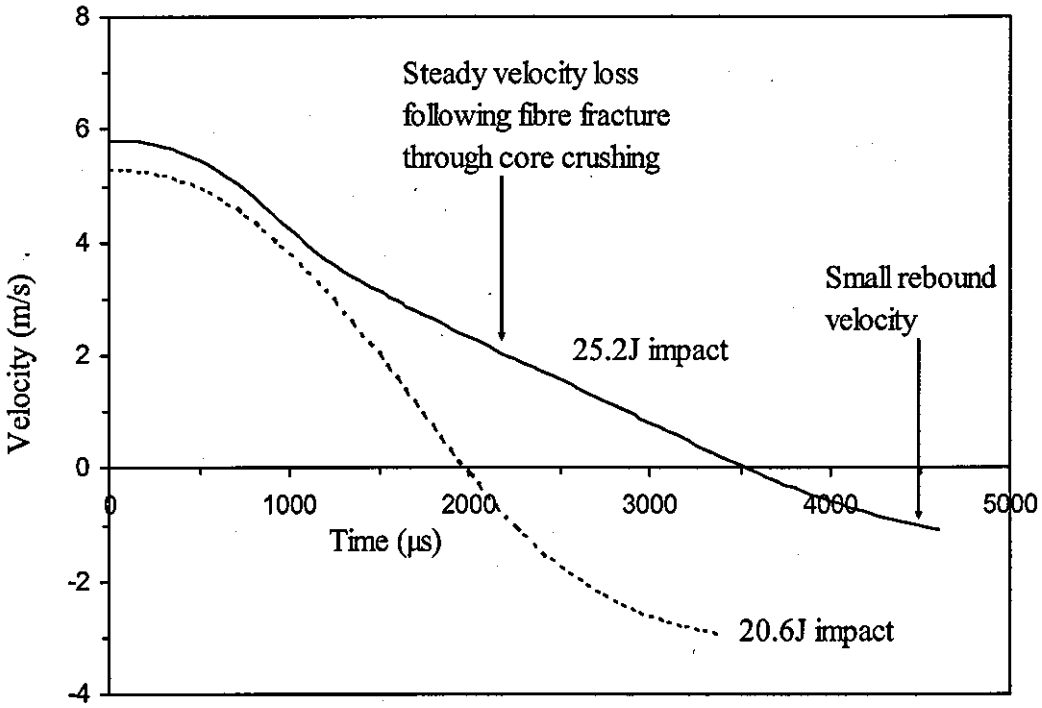

Figure 3.12 Velocity-time plot of impact events on 8 ply 70kg/m^3 panel at IKE of 20.6J (no fibre fracture) and 25.2J (fibre fracture and subsequent core crushing)

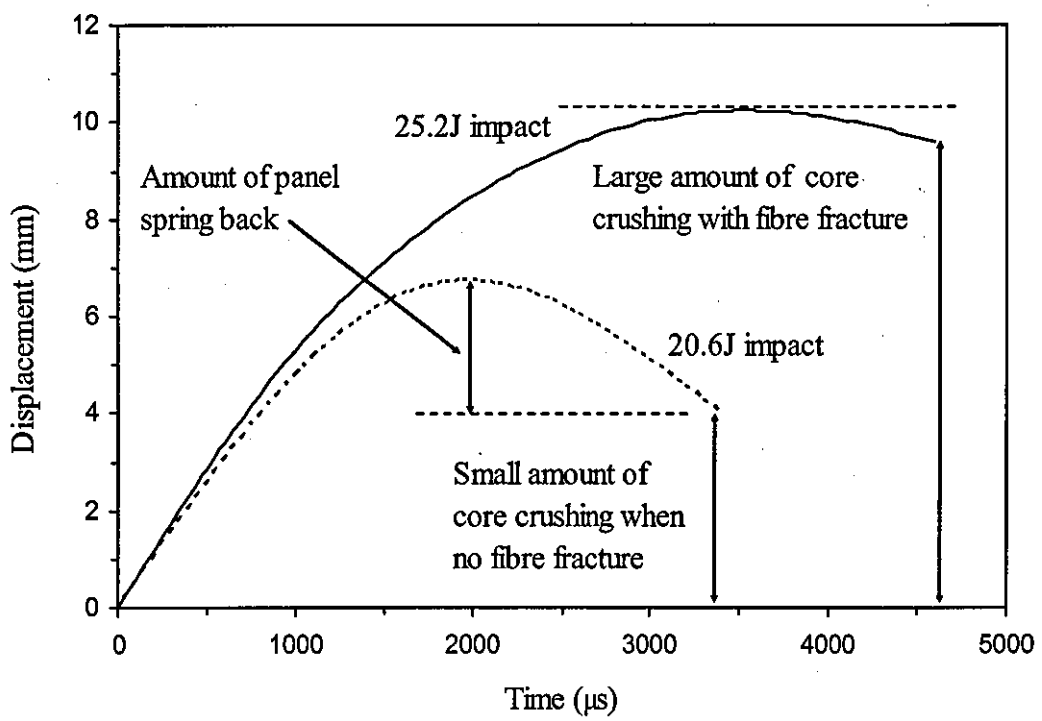

Figure 3.13 Displacement-time plot of impact events on 8 ply 70kg/m^3 panel at IKE of 20.6J (no fibre fracture) and 25.2J (fibre fracture and subsequent core crushing)

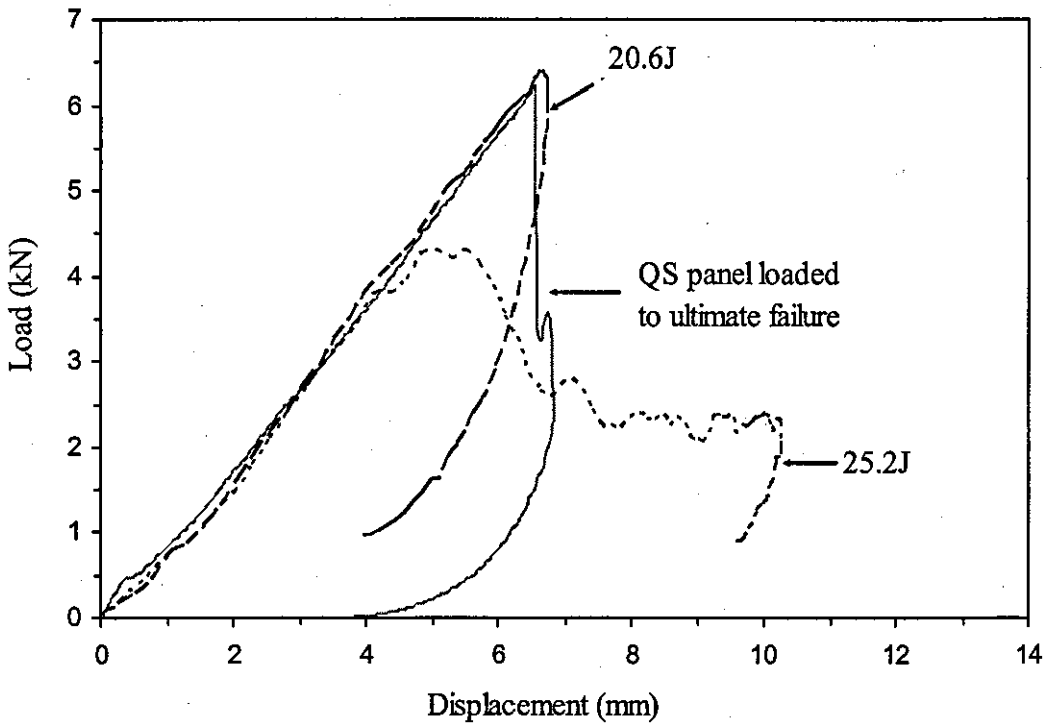

Figure 3.14 Load-displacement plot of impact events on 8 ply 70kg/m^3 panels at 20.6J (no fibre fracture) and 25.2J (fibre fracture) compared with 8/70/HS(ult) quasi-static test

4. DAMAGE CHARACTERISATION OF TRANSVERSELY LOADED SANDWICH PANELS

For an in-depth understanding of how a sandwich panel responds to transverse loading and to obtain the most efficient design for energy absorption it is necessary to identify the damage mechanisms induced during loading and how these damage mechanisms propagate to cause ultimate failure of the panel. In addition to examining the physical damage caused to sandwich panels through destructive and non-destructive techniques, tests have been carried out on the individual skin and core materials used to form the sandwich panels. These tests provide an understanding of how each constituent works within the sandwich panel and identify which factors are likely to have the greatest effect on the loading response and damage mechanisms of a sandwich panel. The existence of damage within a sandwich panel has also been identified using the measurements taken during loading via strain gauges, combined with the load-displacement response curves. A combination the aforementioned methods has been used to determine the cause of damage propagation and failure within a transversely loaded sandwich panel.

4.1. Overview of non-destructive damage detection methods for sandwich structures

Seven different techniques for detecting damage in a sandwich structure have been established from the literature reviewed in Section 1. These are tap test, ultrasonic C-scan, X-ray radiography, thermography, shadow moiré interferometry, shearography and visual inspection with a microscope.

The most basic non-destructive testing method is the tap test. Internal damage can be detected by lightly tapping the surface of the panel with a coin or tapping hammer. A defect is signified by a change in tone of the ringing sound resulting from tapping. This method has been used for in-service inspection of both laminates and sandwich structures. A trained ear is required to identify a change in tone, which can be difficult

to distinguish for small areas of damage. Additionally it is not possible to distinguish between different types of damage or obtain an accurate measurement of damage size.

The most popular and effective method for detecting damage in composite laminates is the ultrasonic C-Scan. A C-Scan can be done in one of two ways, scanning for damage through the entire thickness of the panel (through transmission) or scanning at predetermined positions by setting the scanning depth (pulse echo). Whilst the former method is the most straightforward when applied to a sandwich panel, the resulting C-scan will show damage to both the laminate skins and honeycomb core as well as any skin-core debonding, with it being impossible to distinguish between each type of damage. Research has shown that the damage area detected using through transmission C-Scanning corresponds well with the honeycomb cell wall crushing area obtained through specimen cross-sectioning, but generally overestimates skin delamination [4,89].

The pulse echo method depends on manually setting the scanning depth and therefore can be very inaccurate if the selected scan depth does not match that of a ply interface. It is common for undulations to exist in each ply layer, such that the distance which corresponds to a ply interface at one point may be in the middle of a ply at a different point. An additional problem with sandwich panels is the uneven surface created by the adhesive at the skin-core interface. The adhesive fillets in the honeycomb cells not only make it difficult to set the distance to the skin-core interface but also can affect the amplitude of the returning ultrasonic waves giving the impression of internal damage when viewed on the C-scan image. Consequently neither C-scan technique used alone is suitable for accurate identification of the individual damage mechanisms in sandwich panels. Utilising both techniques to allow comparison of the data obtained from the pulse echo and through transmission scans will aid identification of different damage types, but will also increase both the inspection time and costs.

X-ray radiography provides another means of examining the internal damage and is particularly useful in determining core defects and damage [1,8,20,83,86,90,126,148]. The X-rays easily pass through the thin, low density composite skins and can detect irregularities in the core structure and skin-core debonding. Consequently conventional

X-ray techniques cannot detect planar defects, such as delaminations. Detection of core crushing is possible, but as the X-rays are reflected by the vertical cell walls, unless the crushing is quite extensive it is difficult to identify on the radiograph. Additionally to obtain a clear picture of damage the X-ray needs to be collimated and motor driven, as the X-ray radiograph has a 3D distortion effect away from the damage sight.

Shadow moiré interferometry can be used to measure dimple propagation during quasi-static testing and out-of-plane deformation/local buckling during compression loading. Typically a light-reflective line-grid film is adhered onto the panel surface and is calibrated prior to testing with a light source directed at the panel surface. During the test the moiré fringe patterns associated with grid distortions are recorded with a camcorder. Selected images from the videotape can then be digitised and measured after the test. This method can only provide a measure of out-of-plane deformation, but does give a good indication of the deformation sequence with respect to load and time. For a sandwich panel indentation of the top skin is an important type of damage mechanism but still needs to be related to internal damage for complete understanding. Additionally this technique is only suited to compression tests where the face of the panel is unobstructed from the camera, therefore it is not compatible with the compression rig used in this study.

Laser shearography is an advancement of shadow moiré interferometry, using lasers to detect minute changes in surface strain during loading. A reference picture of the structure is compared to pictures taken during the application of a low pressure, thermal or vibration load. It is very applicable to sandwich structures and can detect internal damage including delamination, core crushing and skin-core debonding. However, like the shadow moiré technique it cannot distinguish between multiple types of internal damage.

Pulse thermography uses infrared imaging to monitor the thermal response of a material, and is particularly useful in detecting the presence of moisture within a structure. A pulse of heat is sent via a flash or quartz lamp to the surface of material, which causes instantaneous heating of the material surface. As the heat flows through the thickness of the material variations in the local surface temperature can be seen

using an infrared camera. These variations are due to defects and discontinuities in the internal material structure which affect the heat flow through the material. Single-sided or through transmission measurements can be taken and a thermal diffusivity image produced. This response must then be fitted to a theoretical model for a quantitative measurement of thermal diffusivity to interpret the spread of damage through the thickness. All imaging is produced using an infrared camera and associated kit, which is quite expensive to purchase.

A popular destructive testing technique is visual inspection of the damage through cross-sectioning of the damaged structure. This is the most basic method of damage evaluation and can provide quick initial estimations of panel damage. However, internal damage can only be seen through cross-sectioning of the panel, with visual inspection assisted by the use of a microscope, and is only able to provide information at the cut-surface. Therefore this method is not compatible with CAI testing as the panel cannot be cut in between the impact and compression stages of the test. Micrographs of the internal damage revealed through sectioning are useful when performing detailed damage analysis and when the damage area is very small. A three-dimensional picture of the damage can be produced by cutting the specimen at numerous locations across the specimen width. Visual inspection does not require expensive equipment though being a destructive testing technique the cost of composite samples can become high.

4.2. Identification and measurement of damage

From the methods reviewed visual inspection of the panel damage through destructive cross-sectioning was chosen for damage resistance analysis. This method was selected based upon its ability to clearly distinguish between skin, core and debonding type damages. The information obtained through destructive sectioning was combined with the non-destructive damage characterisation gained from the analysis of load-displacement and load-strain data collected during testing. A variety of measurements of physical damage have been taken from the cross-sectioned panels and tabulated in Tables 4.8-4.11 & 6.24-6.26 for QS and impact specimens respectively.

4.2.1. Surface visual inspections of damage resistance panels

External visual inspections of the panel surface provided a non-destructive assessment of panel damage following loading. In cases of high energy/load levels fibre fracture of the top skin occurred, which could be easily identified on the panel surface. For lower energy/load levels skin dishing occurred on the loaded face around the impact point. The shape of the dishing was generally circular but spread to give a cross shape aligned with the 0° and 90° fibres as load levels increased. In a few instances regarding panels loaded to ultimate failure (12/50/HS & 16/70/HS) cracks also appeared on the top skin surface, aligned with the 90° fibres. The depth of the dishing, generally referred to in published literature as residual dent depth, increased with energy/load and was measured with respect to the undamaged panel surface. Due to the small distances being measured accuracy was limited to 0.25mm at best. The length of the residual dent was also measured with a ruler along the 0° fibres, with accuracy limited to 1mm due to the small levels of bending towards the periphery of the dent. All external dent measurements are shown in Tables 4.8-4.11 & 6.24-6.26.

An additional problem with using dent depth as a measurement of internal damage was observed for nomex panels. Unlike aluminium panels which display a dent even at low loads, nomex panels often contain no dent following loading, especially under impact conditions. This is due to the elastic nature of the nomex core, which although containing irreversible damage, elastically returns to shape upon load removal. This is prevented in the aluminium specimens due to the plastic cell wall folding of the aluminium honeycomb. Until fibre fracture occurs there is no external sign of the nomex panel having sustained damage. This gives cause for concern in terms of damage assessment of in-service nomex panels and highlights the need for the use of other non-destructive methods.

An examination of the back skin did not reveal any information regarding internal damage. As loading was limited to that required for top skin failure, fibre damage of the back skin did not occur in any test. The only evidence of loading was seen through residual bending of the back skin. For the aluminium honeycomb panels tested at low loads the back skin remained almost flat, with noticeable circular deformation forming

at higher loads directly under the loading point. For the nomex honeycomb panels residual bending of the back skin was negligible. Even at load levels corresponding to fracture of the top skin the bottom skin had only very minor residual bending. In all damage resistance tests no precise measure of back skin bending was taken, instead the extent of bending was just noted as either none, slight, medium or extensive in Tables 4.8-4.11.

4.2.2. Cross-sectional microscopic investigation

The process selected to determine the internal damage caused to panels was via destructive cross-sectioning. Panels were sectioned using a diamond coated tile cutter, such that the diametric cross-section was aligned parallel to the 0° fibres and displayed the damage at the centre of the loading point. In some cases the panels were also sectioned parallel to the 90° fibres to provide an understanding of how the non-symmetric nature of the honeycomb core affected damage progression. The cut surfaces of the specimens were polished using a Lapping polisher and SiC 220 grade abrasive paper. The specimen was manually held against the abrasive paper with a medium amount of pressure to ensure even polishing across both skin surfaces. A minimal amount of material was removed during polishing across the entire cut surface of the specimen to remove the rough surface left by the tile cutter and assist in identification of delamination and fibre damage.

The internal damage was analysed by measuring parameters such as core crushing depth and length across the cut section, delamination length/number and position, and existence of fibre damage/fracture, all illustrated in Fig. 4.1 and Tables 4.8-4.11 & 6.24-6.26. The extent of core crushing was measured by counting the number of damaged cells, with damage defined as cell wall distortion or buckling as well as cell wall folding or tearing. The measurement of delamination length was determined both with the naked eye and using a microscope. However, the visual interpretation and measurement of skin delamination length and number of delaminations is not as accurate as for core crushing, since it depends highly on whether or not the delamination is held open after load removal and panel sectioning, as the skin tries to spring back to its original

location. Examining the panels with a microscope reduced this problem but did not eliminate it, though also allowed more localised failures such as matrix cracking and small delaminations to be identified.

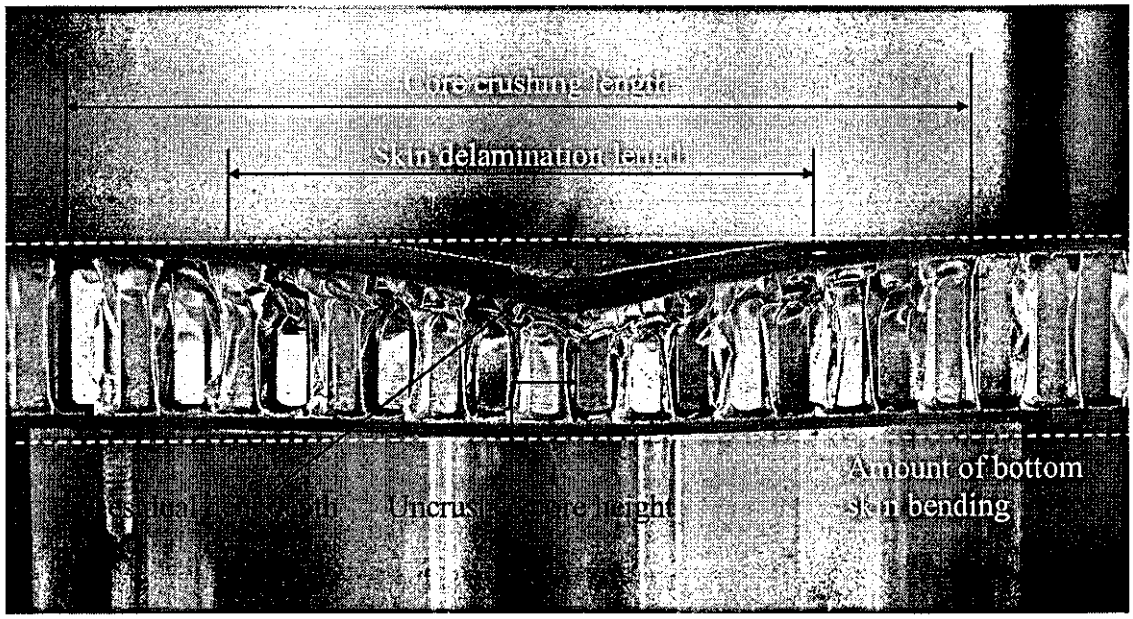

Figure 4.1 Determination of internal damage through various measurements

The measurement of internal damage within the nomex cored panels was inhibited by the elastic recovery of the nomex core. At lower load levels delaminations became almost completely closed and the cell walls did not maintain a buckled shape as in the aluminium honeycomb specimens. At low to medium energy levels damage to the nomex core was represented by cracks in the phenolic resin covering the aramid paper. At higher energy levels where top skin fibre fracture occurred excessive cracking and flaking of the resin combined with minor tearing of the aramid paper was identified. Only under loading with the flat-ended indenter to ultimate failure did the nomex core maintain a buckled shape. These issues are discussed with the aid of illustrations in Section 6.1.5.

Of all the parameters measured the number of crushed cells/core crushing length was the most representative measure of QS/impact damage. Core crushing length was the easiest parameter to measure and provided consistent results when comparing both similar and increasing load levels. Core crushing was present for all levels of load and

was measurable even at the lowest load levels applied. Unlike core crushing, delaminations were not always visible in some of the panels subjected to low loads. The overall length of delamination was generally smaller than core crushing length, the exception to this being in some of the QS test panels loaded to ultimate failure with the FE indenter, (4/70/FE, 16/50&70&90/FE, 8/96/FE, 12/96/FE, 16/64&96/FE). In these cases ultimate failure of the panel, through the indenter shearing through the top skin, caused massive skin relaxation and stress transfer, which in turn caused the unstable rapid propagation of a major delamination.

Additionally it has been found for all aluminium panels that core crushing length is generally similar or slightly greater than the external dent length, with agreement increasing with load level. This means that external dent length, measured relatively soon after loading has occurred, can be used as a good measure of the extent of internal damage, be it core crushing alone or core crushing with delaminations. In the instances where major top skin delamination was present, fibre fracture also occurred, which itself is a clear sign of major internal damage.

4.2.3. Specimen polishing

In order to assess the nature of damage in panels with small amounts of skin damage it was necessary to finely polish the damaged section for microscopic investigation of the top skin. This generally only applied to panels loaded to initial damage and panels loaded to secondary damage with the FE indenter. This involved extracting the section of the specimen containing damage (maximum dimensions of 27mm × 15mm) and setting it in epoxy resin using a rubber mount. The specimen was positioned in the mould with the damaged surface face down. The epoxy mixture was the same as that used to pot the CAI panels without the slate powder (described in Section 7.2.1). Once set the epoxy specimen was polished using a Lapping polisher. The polishing process consisted of four stages starting with grinding using SiC 220 grade abrasive paper and water at 300rpm for 2-3 minutes. The specimen was then subjected to fine grinding using an MD-Largo disc and DP-Spray with an aluminium particle size of 6μm at 150rpm for 6 minutes. The third step consisted of polishing with an MD-Dur (fine satin

fabric) disc and the 6μm DP-Spray at 150rpm for 4 minutes, finishing with fine polishing using the same type disc and rotation speed but with a 1μm DP-spray for 3 minutes. Once polished the specimen was observed through a microscope and any delaminations, matrix cracks or fibre fractures could be identified. Micrographs could then be taken of the damaged area if required.

One issue with polishing the aluminium honeycomb sandwich panel specimens was that some of the DP-Spray polishing media contained aluminium particles. Clearly it is not possible to polish the aluminium honeycomb using aluminium particles. An additional problem with polishing aluminium sandwich panels involved the occasional detachment of large aluminium particles from the honeycomb core during polishing, creating a deep scratch on the polished surface. Once a scratch occurred the only way to remove it was to repeat the polishing process from the beginning, which removed more of the specimen than desired. To minimise these problems as much of the aluminium honeycomb core as possible was removed from the specimen before potting using a Stanley knife. However, it was very difficult to remove the core at the skin/core interface due to the strength of the adhesive, and consequently some minor scratching occurred on a small number of specimens, though this did not adversely affect the clarity of the damage.

4.3. Response and damage analysis of sandwich panel constituents under transverse loading

Plate bending and core indentation tests have been completed on the sandwich panel skin and core materials respectively. These tests provided additional information regarding the deformation and damage mechanisms attributed to each individual material. The performance of each skin and core material was analysed, and any major variations in load response identified. The procedures used in the plate bending tests were identical to those used for the quasi-static sandwich panel bending tests, to eliminate any issues regarding testing conditions. Two types of indentation test were completed on the core materials, one to ASTM C365 [147] and the other aimed at replicating the contact conditions seen in the sandwich panel bending tests.

4.3.1. Skin plate test results

Plate tests have been completed on 4, 8, 12 and 16 T700/LTM45-EL cross-ply laminates and 8 and 16 ply IM7/8552 laminates. All plates were loaded to ultimate failure, no diagnostic tests have been completed. The 150mm × 150mm specimens were identical to the skins used in the sandwich panels and were tested using the same 100mm clamping ring arrangement and strain gauge locations as for the quasi-static sandwich panel bending tests, discussed in Section 3.2.1. Both hemispherical and flat-ended indenters were used in the plate tests to provide an understanding of the effect of the indenter nose-shape on the plate response. The load-displacement and load-strain curves are shown in Figs. 4.2-4.7.

T700/LTM45-EL plate tests

The load-displacement response for all plates loaded to ultimate failure is shown in Fig. 4.2. The response is almost linear at small levels of deflection, 0.5mm to 1mm for all plate thicknesses and shows a similar amount of deflection for both HS and FE loading cases. The amount of deflection is approximately equal for both loading cases up until a deflection of 1mm, 1.5mm and 2mm for the 16, 12 and 8 ply plates respectively. The plate response then becomes highly non-linear and the plate stiffness increases at a much greater rate for the FE case than the HS case. This is as expected as the FE indenter spreads the load over a larger area than the HS indenter. The loading area of the HS indenter can almost be compared to a point load which induces greater localised stresses than the distributed FE load. Consequently the ultimate failure load for the HS case is much lower than seen for the FE case.

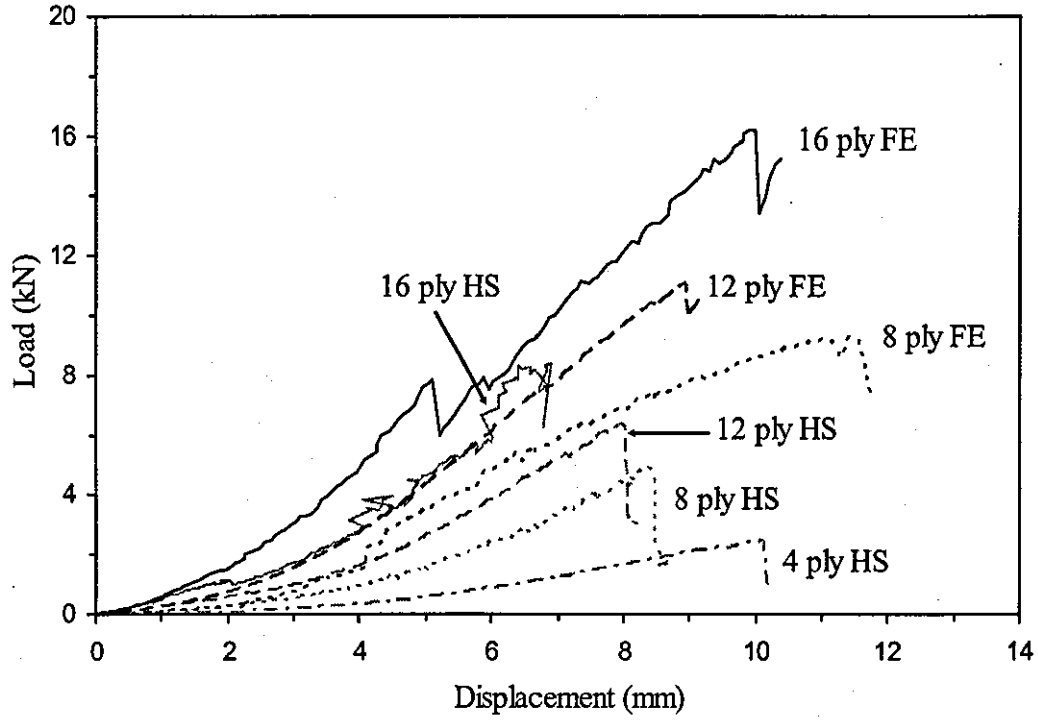

Figure 4.2 Load-displacement response of 8, 12 & 16 ply T700/LTM45-EL laminate plates loaded with both HS and FE indenters

For both loading cases increasing the plate thickness increases the ultimate failure load whilst reducing the deflection for a given load. In all tests ultimate failure is due to fibre fracture, with the indenter shearing through the entire plate thickness in the 8 and 12 ply plates loaded with the FE indenter, Fig. 4.3. Cross-sectioning of the plates reveals multiple delaminations through the thickness of the plate, concentrated around the indenter contact area, generally with one or two major delaminations extending over at least 50mm. In the plates loaded with the FE indenter these major delaminations spread over almost the entire plate length. The location of the major delaminations is generally in the lower half of the plate, with the second largest delamination generally occurring between the outermost plies.

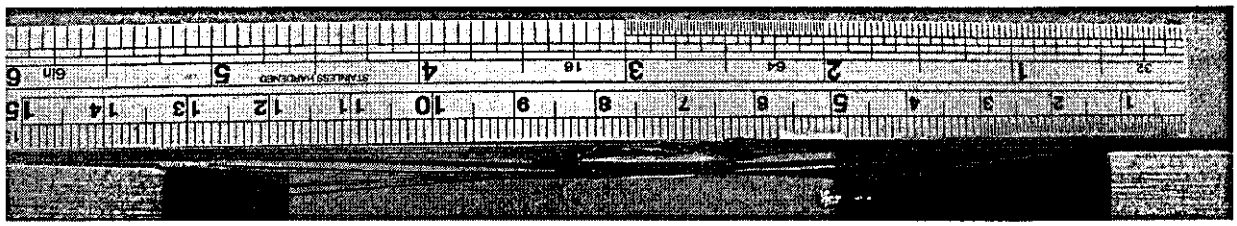

Figure 4.3 Photo of 12 ply plate loaded with FE indenter

Damage initiation and propagation cannot easily be identified on the load-displacement curves, excluding the 16/FE plate, as it is represented by fluctuations in the load-displacement response which can easily be confused with fluctuations occurring due to the testing machine oscillation, emphasised in the 16/HS response. Analysis of the load-strain curves in conjunction with the load-displacement curves allows identification of the initial damage threshold and ultimate failure points, Tables 4.1-4.2.

Table 4.1 Data for 8,12 & 16 ply T700/LTM45-EL plates loaded with HS indenter

	Initial damage threshold				Ultimate failure			
	4 ply	8 ply	12 ply	16 ply	4 ply	8 ply	12 ply	16 ply
Load (kN)	0.31	0.43	0.71	1.13	2.45	4.89	6.37	8.36
Displacement (mm)	3.83	2.57	2.46	2.04	10.10	8.36	7.92	6.89
Top strain (με)	-	750	387	208	-	5243	5156	3407
Bottom strain (με)	-	9128	10198	7880	-	23063	18519*	13592
Energy (J)	0.39	0.42	0.83	1.17	8.54	13.35	18.03	20.77

* Point at which strain gauge broke/stopped recording

Table 4.2 Data for 8,12 & 16 ply T700/LTM45-EL plates loaded with FE indenter

	Initial damage threshold			Ultimate failure		
	8 ply	12 ply	16 ply	8 ply	12 ply	16 ply
Load (kN)	0.32	0.50	1.34	9.32	11.09	16.17
Displacement (mm)	2.30	1.58	1.70	11.43	8.92	9.98
Top strain (με)	-248	-474	-484	1341	4120	4112
Bottom strain (με)	2171	2192	3232	8341	7633	8383
Energy (J)	0.23	0.33	1.04	49.39	38.25	70.26

For the HS case both the top and bottom load-strain curves show significant changes in gradient at the load at which the load-displacement curves become non-linear, Fig. 4.4. This is a clear indication of internal damage initiating within the plate. As both strain gauges detect changes the most likely damage mechanism is delamination. Once delamination has occurred the laminate is split into several sub-laminates, such that increased membrane stretching of the sub-laminates causes the plate to effectively stiffen. The large drops in both strain and load in the 16 ply plate represent the sudden unstable growth of the delaminations within the plate, supporting the above theory.

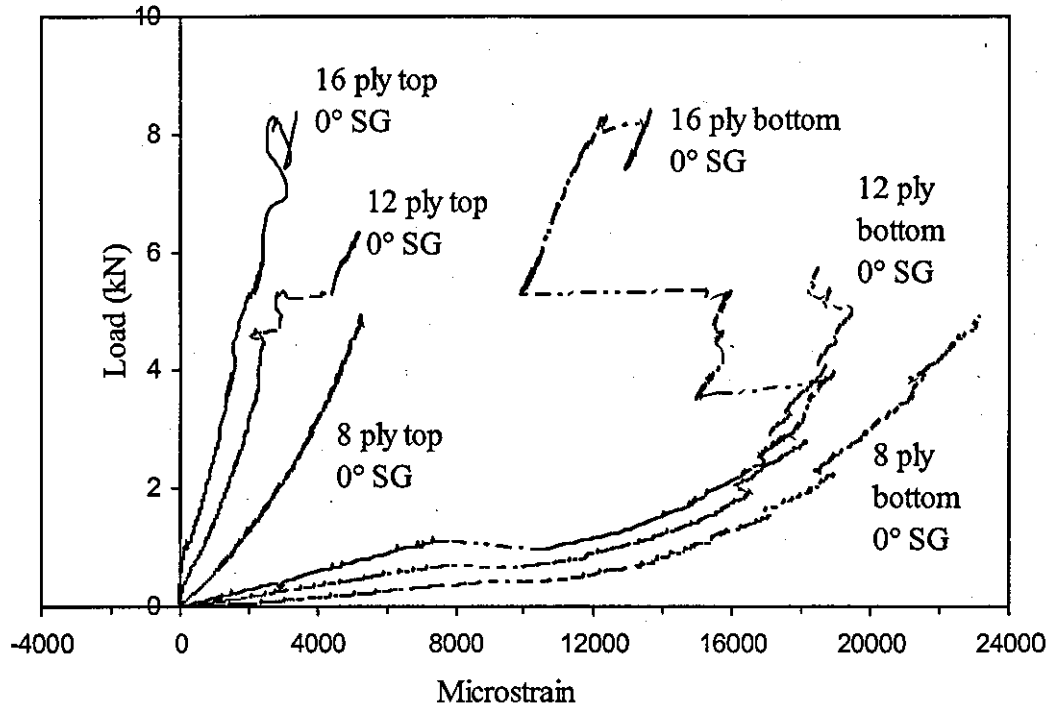

Figure 4.4 Load-strain response of 8, 12 & 16 ply T700/LTM45-EL laminate plates loaded with the HS indenter

The initial strain response of the 8 ply plate loaded with the HS indenter varies from that of the thicker plates. The strain gauge on the top surface shows the top surface to be in compression for less than 0.1kN of load. From then on both the top and bottom surfaces are in tension and both strain gauges show a steady increase in strain up to ultimate failure. The stiffening effect seen in the load-displacement curves of the thicker plates at the point of delamination is minimal in both the 4 and 8 ply plates. This

suggests that membrane stretching dominates the response of the thinner plates from the onset of loading, such that the thinner plates behave more like a membrane with no flexural rigidity than a rigid plate. This could be significant when trying to model the response for sandwich panels with 4 or 8 ply skins.

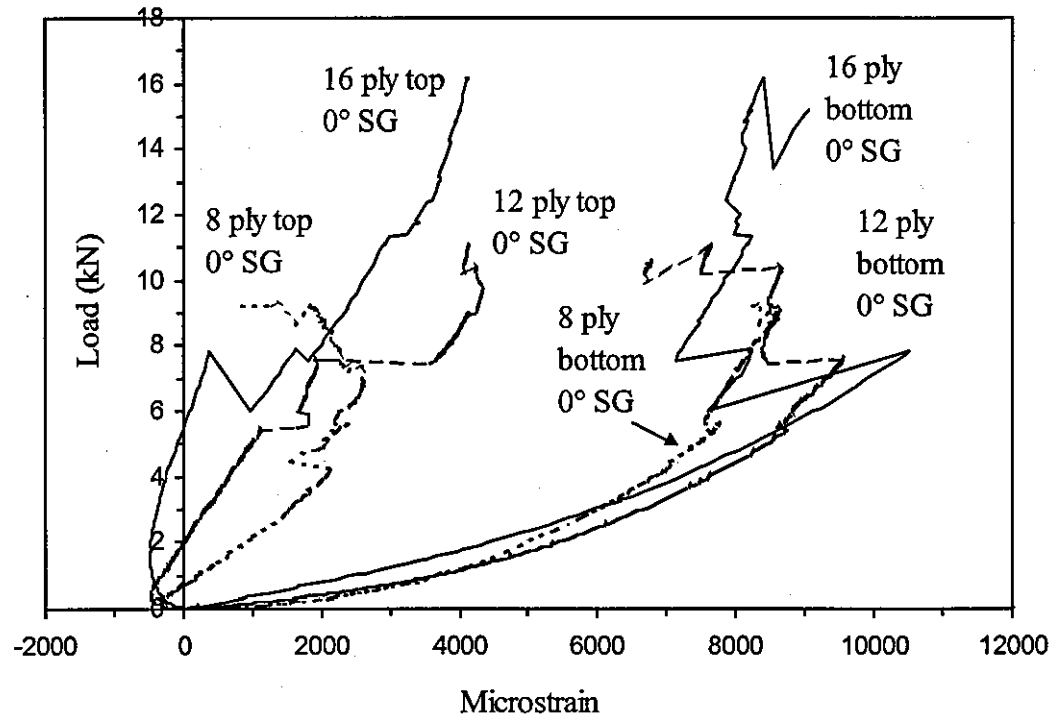

Figure 4.5 Load-strain response of 8, 12 & 16 ply T700/LTM45-EL laminate plates loaded with the FE indenter

The load-strain curves for the plates loaded with the FE indenter are very similar to those for the HS case, Fig. 4.5. The initial compressive region of the top surface is much greater for FE loading. This is as expected as the load is spread over a larger region causing more global bending and less local indentation/damage. The spread of the delaminations has a more dramatic effect on the load and strain response than in the HS case. Drops in both top and bottom strain are present for all plate thicknesses tested. Despite the sudden strain drop the 8 ply plate again shows membrane like behaviour.

IM7/8552 plate tests

The major difference seen between the IM7/8552 and T700/LTM45-EL plates was in the load required to cause ultimate failure. The IM7/8552 plates failed at a load approximately 42% and 68% of that required for the T700/LTM45-EL plates loaded by the HS and FE indenters respectively. The load-displacement curves for the IM7/8552 plates are otherwise very similar to those of the T700/LTM45-EL plates, with the majority of the trends identified for the T700/LTM45-EL plates being applicable, Fig. 4.6. The curves for plates of the same lay-up/loading case have similar gradients up to 2kN for the 16 ply plates and 4kN for the 8 ply plates. After this point the curves deviate due to the T700/LTM45-EL plates exhibiting a sudden fluctuation in load whilst the slope of the IM7/8552 plates remains unaltered almost up to the point of ultimate failure. Unlike the T700/LTM45-EL plates there are no clear signs of damage initiating and spreading within the IM7/8552 plates and there are no load drops during loading of the plates with the FE indenter. This suggests ultimate failure occurs immediately after the point of damage initiation.

The load-strain curves for the IM7/8552 plates are shown in Fig. 4.7. These curves again show similar trends to the T700/LTM45-EL results in terms of strain magnitude and direction. As ultimate failure of the IM7/8552 plates occurs rapidly at a moderate load the distinct jumps in strain, which were indicative of sudden damage propagation in the T700/LTM45-EL plates, do not occur for the IM7/8552 plates. The initial damage threshold, quoted in Table 4.3, for the IM7/8552 plates is identified from small fluctuations in the load-strain curves only, though these changes are minute and open to question.

Table 4.3 Data for 8 and 16 ply IM7/8552 plates loaded with HS and FE indenters

	Initial damage threshold				Ultimate failure			
	8 ply		16 ply		8 ply		16 ply	
	HS	FE	HS	FE	HS	FE	HS	FE
Load (kN)	0.63	0.27	0.81	1.12	1.98	6.13	3.64	11.54
Displacement (mm)	3.55	1.89	1.63	1.63	6.72	7.97	5.93	6.73
Top strain (με)	876	-80	-3	-528	3783	1980	3474	9288
Bottom strain (με)	11106	1917	5355	3005	43527	6963	12462	12442
Energy (J)	0.80	0.20	0.562	0.83	5.13	16.31	10.66	29.16

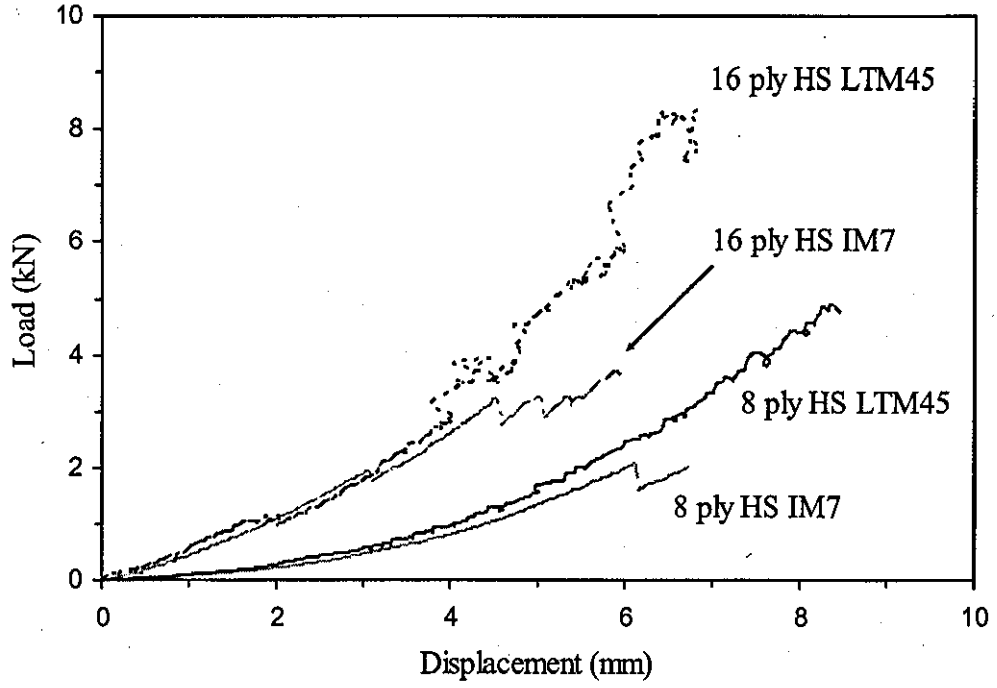

(a)

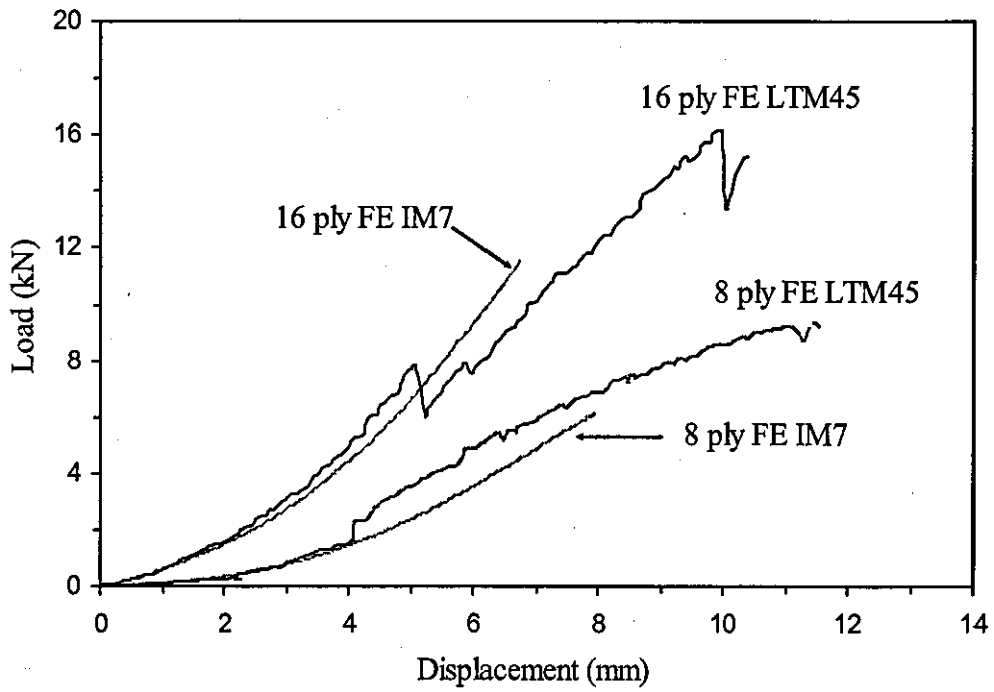

(b)

Figure 4.6 Comparison of load-displacement curves for T700/LTM45-EL and IM7/8552 plates loaded with (a) HS indenter (b) FE indenter

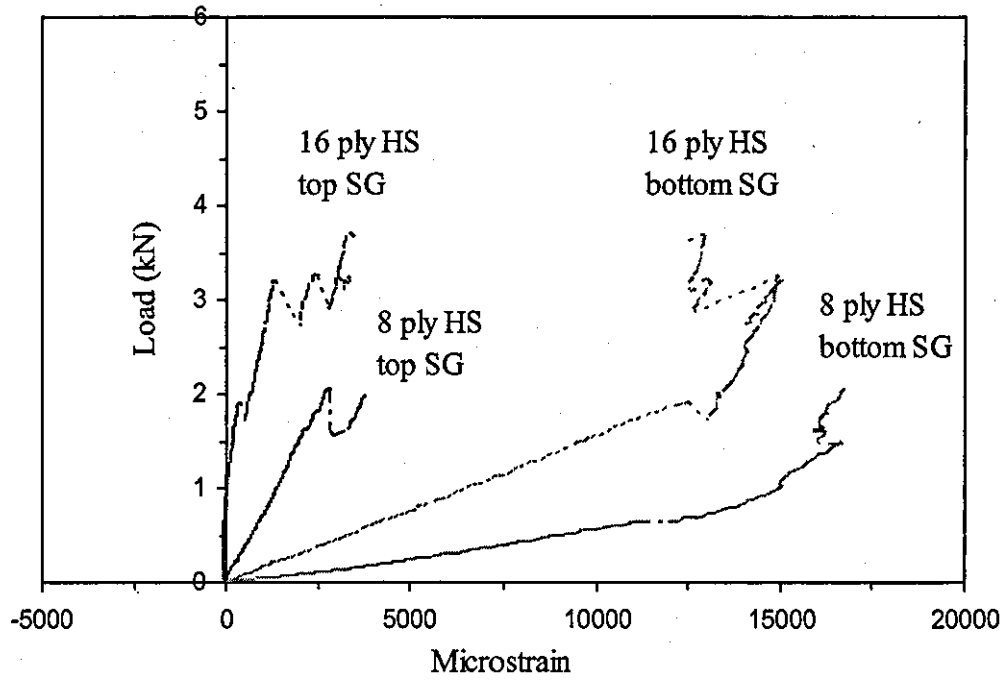

(a)

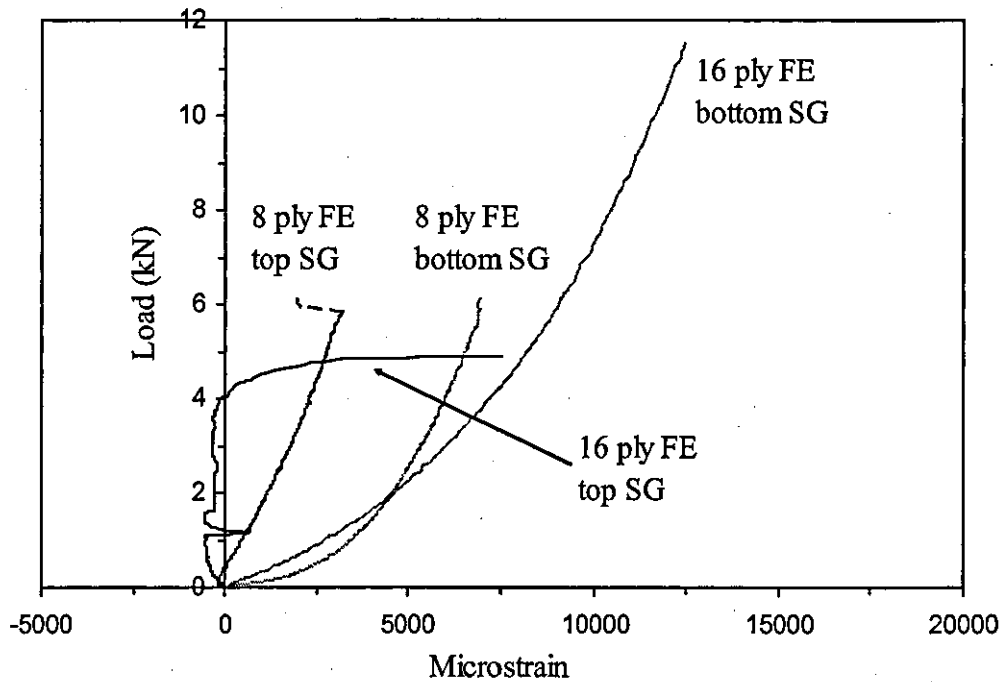

(b)

Figure 4.7 Load-strain response of 8 & 16 ply IM7/8552 laminate plates loaded with (a) HS indenter (b) FE indenter

Cross-sectioning the plates to reveal the internal damage showed the extent of the delaminations at ultimate failure to be much less than in the T700/LTM45-EL plates of the same lay-up and loading condition, Fig. 4.8. In both material types delaminations were present through the thickness of the plate around the indenter contact point. However, unlike in the T700/LTM45-EL plates the delaminations did not propagate away from the loading centre in either the HS or FE loading cases. At the centre of the IM7/8552 plates the FE indenter not only caused fibre fracture but also sheared through the top layers of the plate. This was also the case to a lesser extent for the plates loaded with the HS indenter. This suggests that the IM7/8552 plates do not dissipate the load throughout the entire loading area as well as the T700/LTM45-EL plates and consequently failure becomes very concentrated about the loading contact area.

The reduction in ultimate failure load of the IM7/8552 plates is due to the flexural performance of the IM7/8552 skin material. Although the flexural strength and modulus of each skin material are similar, Tables 2.6 & 2.7, the failure mechanisms involved vary. In the flexural tests completed to determine the mechanical properties, Section 2.2, the failure in the IM7/8552 specimens resulted in complete loss of load resistance, visible from the load-displacement curves in Fig. 2.3, and in a number of cases the specimen snapped in half. Contrary to this the T700/LTM45-EL specimens were able to withstand an equal or higher load following failure prior to complete failure of the specimen, shown in Fig. 2.2. Delaminations in these specimens were extensive, often splitting the specimen into two separate sublaminates.

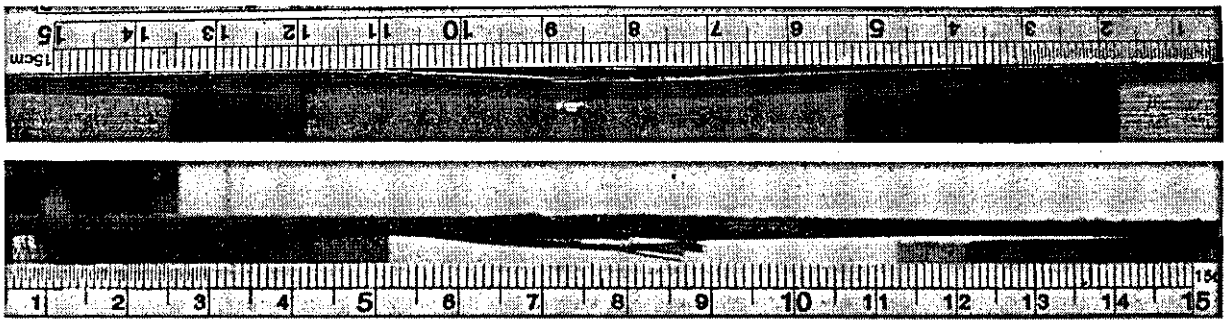

Figure 4.8 Comparison of damage in 16 ply plate loaded with FE indenter

Top: T700/LTM45-EL Bottom: IM7/8552

4.3.2. Core crush and indentation test results

The mechanical properties of aluminium and nomex honeycombs under compression have been obtained through crush tests following ASTM C365 [147] and from data supplied by the manufacturer. Two types of crush test exist, namely bare compression and stabilised compression [147,149]. Both tests require specimens measuring 76.5mm × 76.5mm, which are crushed using a flat plate loader. Bare compression tests are used to obtain a quick estimate of compressive strength and for quality control. For stabilised compression thin aluminium skins are bonded to the top and bottom surfaces of the honeycomb specimen with adhesive. Stabilised compression tests provide higher values of compressive strength as the loaded edge of the cell walls are supported by adhesive fillets. In both test cases it is of vital importance that the loading surface is parallel to the honeycomb surface. If the loading surface is not parallel the honeycomb will not be crushed evenly and low values of strength and modulus will be obtained.

Stabilised compression tests have been completed on 50 and 70 kg/m^3 aluminium honeycomb, Fig. 4.9. The values obtained for the stabilised compression load and crush load are much lower than those quoted by the manufacturer. This could be due to the above problem of parallel loading or due to irregularities in the honeycomb structure. In many of the aluminium honeycomb sheets an amount of cell distortion was present such that the honeycomb cells were not perfect hexagons. Values of modulus have not been determined as only the displacement of the loading head was measured. ASTM C365 states that an LVDT inserted through a hole in the specimen should be used to accurately measure the specimen displacement. Determination of the specimen modulus via the loading head displacement can lead to modulus values as small as one third of the actual value [149]. Test data for the stabilised compression tests on 50 and 70 kg/m^3 aluminium honeycomb are given in Table 4.4. Data supplied by the manufacturer for both aluminium and nomex are quoted in Table 2.9 in Section 2.

Table 4.4 Individual data for 50 and 70kg/m^3 aluminium honeycomb stabilised compression tests

Core type/test number		Peak load (kN)	Peak displac. (mm)	Av. Crush load (kN)	Stabilised strength (MPa)	Crush strength (MPa)
3.1-1/16-10 (50kg/m^3)	50 test 1	8.88	1.36	6.04	1.58	1.07
	50 test 2	8.59	1.08	6.15	1.53	1.09
	50 test 3	8.97	1.26	6.06	1.59	1.07
	50 test 4	8.42	1.33	5.52	1.50	0.98
	50 test 5	7.60	1.57	5.64	1.35	1.00
	50 test 6	7.96	1.46	5.63	1.42	1.00
	50 - Average	8.40	1.34	5.84	1.49	1.04
4.4-3/16-15 (70kg/m^3)	70 test 1	13.71	1.80	10.39	2.44	1.85
	70 test 2	15.04	-	10.47	2.67	1.86
	70 test 3	14.51	1.14	9.82	2.58	1.75
	70 - Average	14.42	1.47	10.23	2.56	1.82

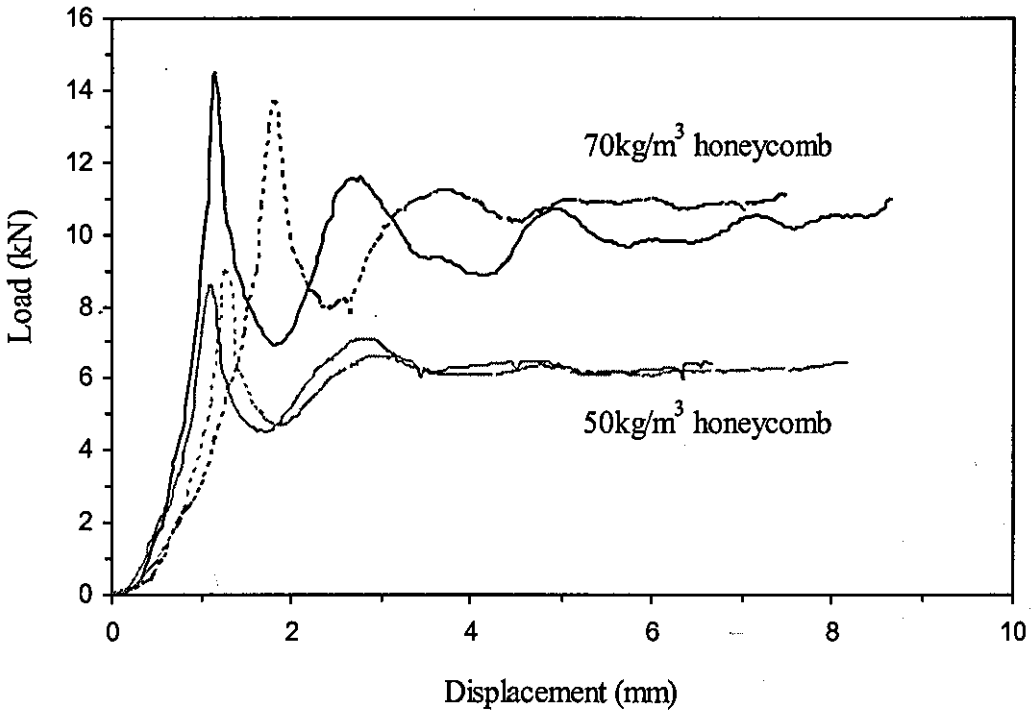

Figure 4.9 Load-displacement response for stabilised compression of 50 and 70kg/m^3 aluminium honeycomb crushed to ASTM C365 (two results shown for each density)

To gain a better understanding of how the honeycomb is crushed within the sandwich panel indentation tests have also been completed on 76.5mm × 76.5mm bare specimens with 20mm diameter HS and FE indenters. Also two tests have been completed using a 50mm FE indenter. The stabilised strength and crush strength for each honeycomb density loaded with the FE indenter are summarised in Tables 4.5-4.6. Peak and crush loads are not determinable for HS loading so the results from the HS tests are shown only in graphical form. Under FE loading the load-displacement curve produced is similar to that produced during stabilised compression, though the bare compression load is lower, see Fig. 4.10(a). The load-displacement curve from HS loading does not have the typical characteristics of a honeycomb crush test, Fig 4.10(b). It does not contain a peak load followed by steady oscillations in load representing core crushing. Instead the curve has a gradual increase in gradient with irregular oscillatory characteristics. This is due to the way in which the indenter contact area steadily increases during the early stages of loading, causing a gradual increase in the number of cells being crushed and hence increasing the resistance to loading.

Table 4.5 Average data for 50, 70 and 90kg/m^3 aluminium and 64 and 96kg/m^3 nomex honeycomb bare compression tests with 20mm diameter FE loading area

Core type/test number		Peak load (kN)	Peak displac. (mm)	Av. crush load (kN)	Stabilised strength (MPa)	Av. crush strength (MPa)
3.1-1/16-10	(50kg/m^3)	0.59	0.38	0.47	2.08	1.66
4.4-3/16-15	(70kg/m^3)	1.18	0.41	0.75	4.16	2.64
5.7-3/16-20	(90kg/m^3)	1.63	0.43	1.01	5.77	3.57
HRH-10-3/16-4.0	(64kg/m^3)	1.15	0.63	0.92	4.04	3.25
HRH-10-3/16-6.0	(96kg/m^3)	2.55	0.66	1.34	8.98	4.73

Table 4.6 Average data for 50 and 70kg/m^3 aluminium honeycomb bare compression tests with 50mm diameter FE loading area

Core type/test number		Peak load (kN)	Peak displac. (mm)	Av. Crush load (kN)	Stabilised strength (MPa)	Av. Crush strength (MPa)
3.1-1/16-10	(50kg/m^3)	3.13	0.51	2.40	1.66	1.28
4.4-3/16-15	(70kg/m^3)	7.58	1.08	3.75	4.02	1.99

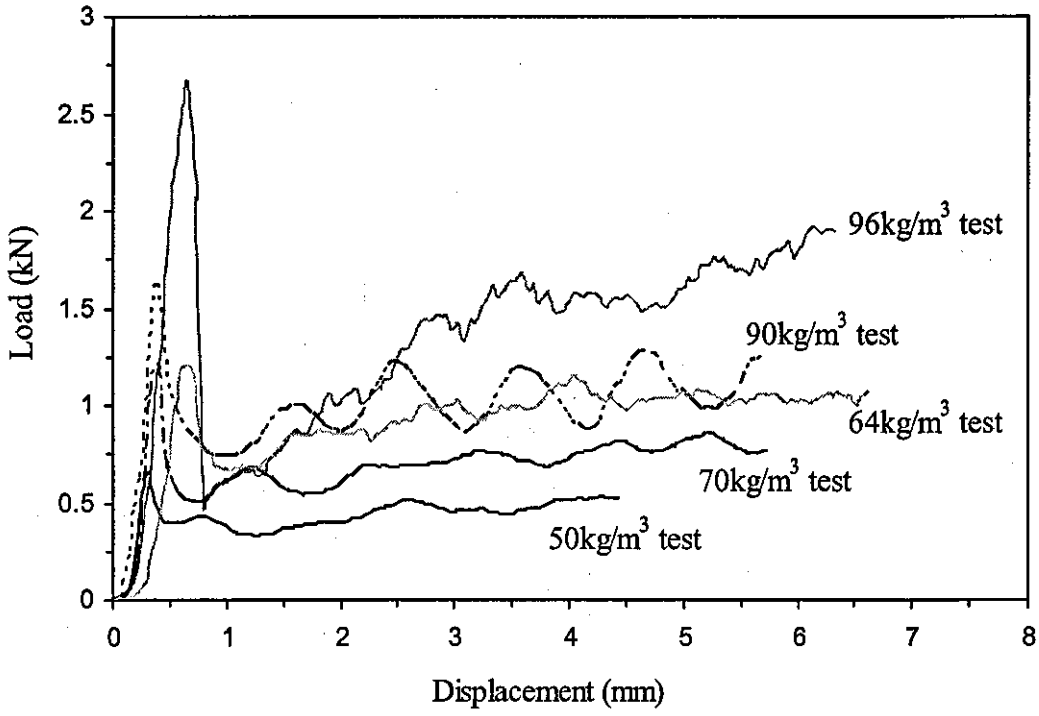

(a)

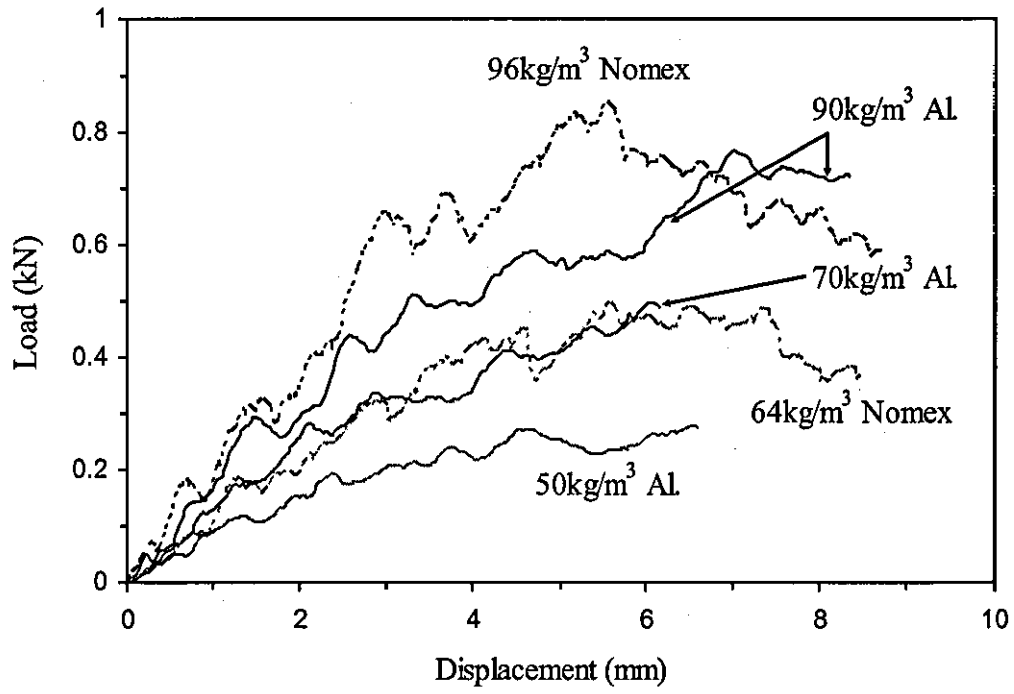

(b)

Figure 4.10 Load-displacement for aluminium and nomex honeycombs crushed with (a) 20mm FE indenter (b) 20mm HS indenter

When loading with the HS indenter the initial contact area is very small. Therefore the location of the indenter with respect to the cell could affect the initial load-displacement response. Four possible indenter contact points exist, Fig. 4.11 each with a different amount of material directly below the loading centre. To identify if the location of the loading centre with respect to the cell influenced the HS loading response two loading cases were considered. Cases 1 and 3 were chosen as they represented the extreme conditions, case 1 with no material under the loading centre and case 3 with the loading centre at the apex of a cell where three walls meet. The effect of the loading centre location is illustrated in Fig. 4.12 for 50 and 70kg/m^3 aluminium honeycomb. The load-displacement curves suggest the indenter contact point with respect to the cell has little effect on the response as all curves are very similar. However, the accuracy of the results are limited as although the indenter was aligned with the cell visually using a ruler it was difficult to identify the exact indenter and cell centres and not all cell walls in the honeycomb structure formed perfect hexagons, as discussed previously.

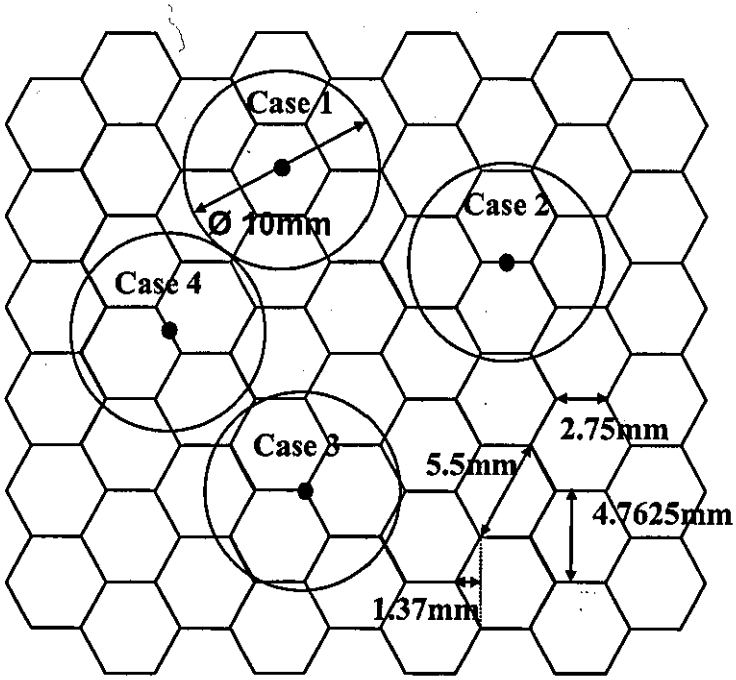

Note: Diagram not to scale

Figure 4.11 Four cases of interaction between a HS indenter and honeycomb cells

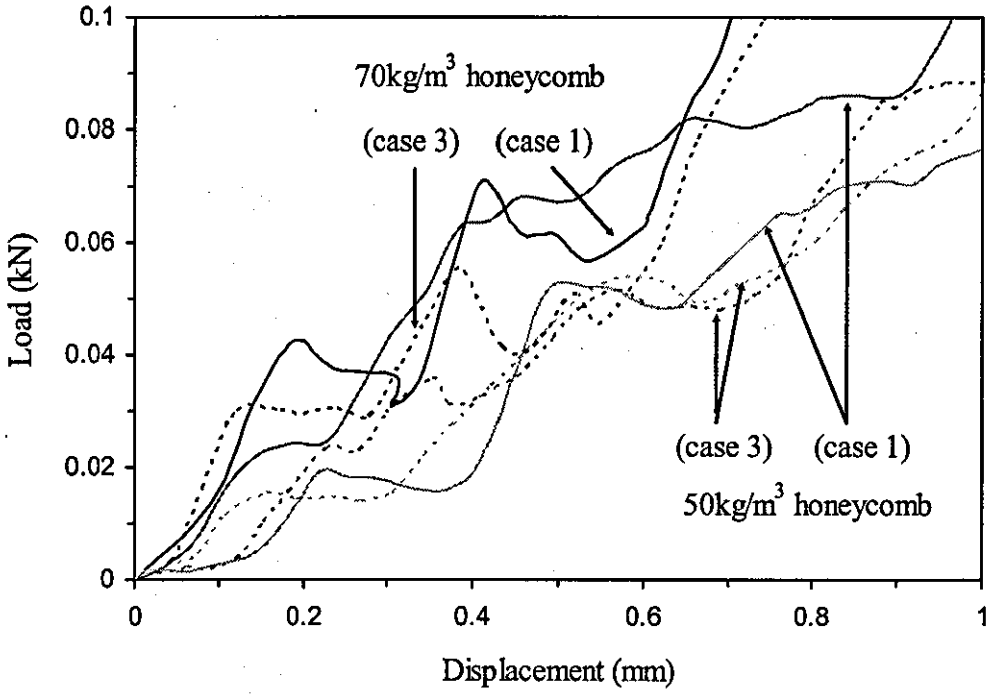

Figure 4.12 Effect of indenter location on initial response of aluminium honeycomb crushed with HS indenter

4.4. General behaviour characteristics of sandwich panels under transverse loading

Determination of the response and corresponding failure modes of sandwich panels subjected to quasi-static loading using both HS and FE indenters has been based on visual observations of the physical damage and experimental data via load-displacement and load-strain plots, with consideration of the previous findings from the laminate plate and honeycomb tests. Diagnostic tests have been conducted for a number of panel configurations to help in the determination of damage modes and progression. The different stages of damage initiation and propagation, shown in Fig. 4.13, are identified and classified as the 'initial damage threshold', followed by 'secondary damage' representing sudden damage propagation and finally 'ultimate failure' when the indenter causes fibre fracture of the top skin. At this point the panel has lost a significant portion of its load carrying capability and although the bottom skin can still provide resistance the panel is classified as having failed and loading is stopped.

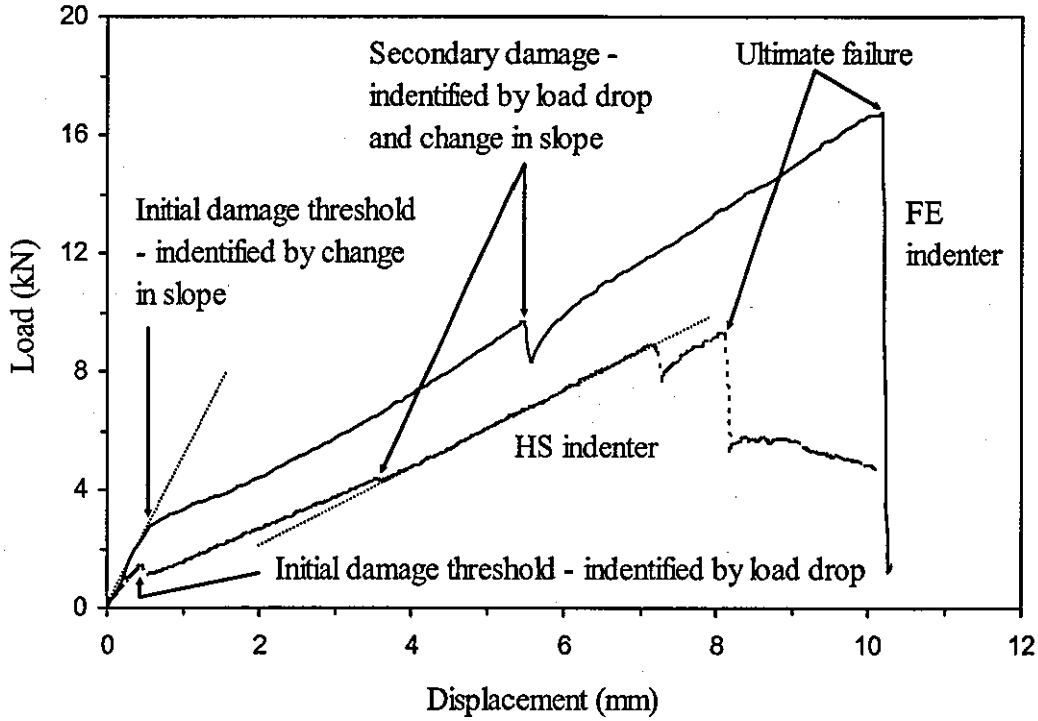

Figure 4.13 Identification of threshold and failure loads from load-displacement curves of 16 ply 50kg/m^3 honeycomb panels loaded with HS and FE indenters

The findings are based on tests on the baseline panels with 4, 8, 12 and 16 ply T700/LTM45-EL skins and 50, 70 and 90 kg/m^3 aluminium honeycomb. The general behaviour of all panel configurations for each indenter nose-shape is similar, with variations based on changes in skin thickness or core density discussed where applicable. The individual load-displacement and load-strain curves for each panel test are included in Appendix A in Figs. A1-A32. The critical values corresponding to damage propagation and failure determined from the load-displacement and load-strain curves are summarised in Tables 6.13-6.23 at the end of Section 6.

4.4.1. Initial damage and response

The first sign of damage initiation within a sandwich panel under quasi-static loading has been termed the 'initial damage threshold'. The initial damage threshold occurs at relatively low loads and can be identified from both the load-displacement and load-strain curves. On the load-displacement curve the initial damage threshold is represented by a change in panel stiffness, shown by a decrease in the gradient of the curve, which is also accompanied by a drop in load in some instances, Fig. 4.14. When loading with the HS indenter there is a clear load drop in panels with thick skins, 12 or 16 ply, but not for those with thin skins, 4 or 8 ply, which show a smooth transition in gradient at the initial damage threshold. Conversely, for loading with the FE indenter the reverse trend is observed.

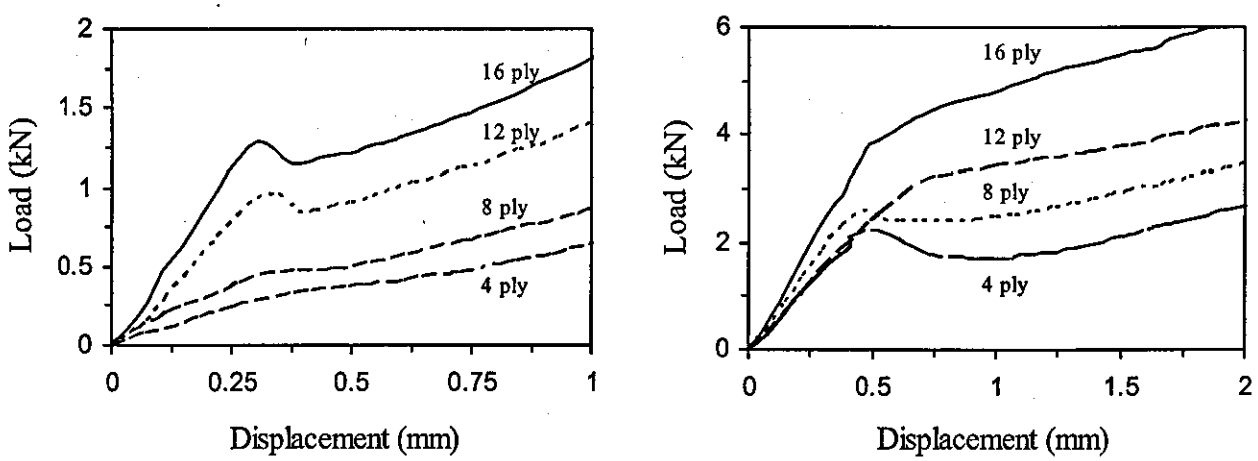

Figure 4.14 Initial damage threshold for sandwich panels with 70kg/m^3 aluminium honeycomb loaded with (a) HS indenter (b) FE indenter

When damage initiates within the panel the resistance of the panel reduces but as the Mand machine is displacement controlled the indenter continues to move downwards at a steady rate, causing the effective 'load drop' witnessed in a number of the load-displacement curves. The variation in the shape of the load-displacement curves at the initial damage threshold could appear to be due to different failure mechanisms dominating the response. The LVDT readings shown on the load-displacement curves

in Appendix A (an example also included in Fig. 4.15) indicate bending of the bottom skin to occur from the onset of loading with only a slight decrease in bending rate after the initial threshold. The difference between the LVDT reading and the indenter displacement (i.e. panel indentation) increases dramatically at the initial damage threshold, indicating core crushing to have occurred.

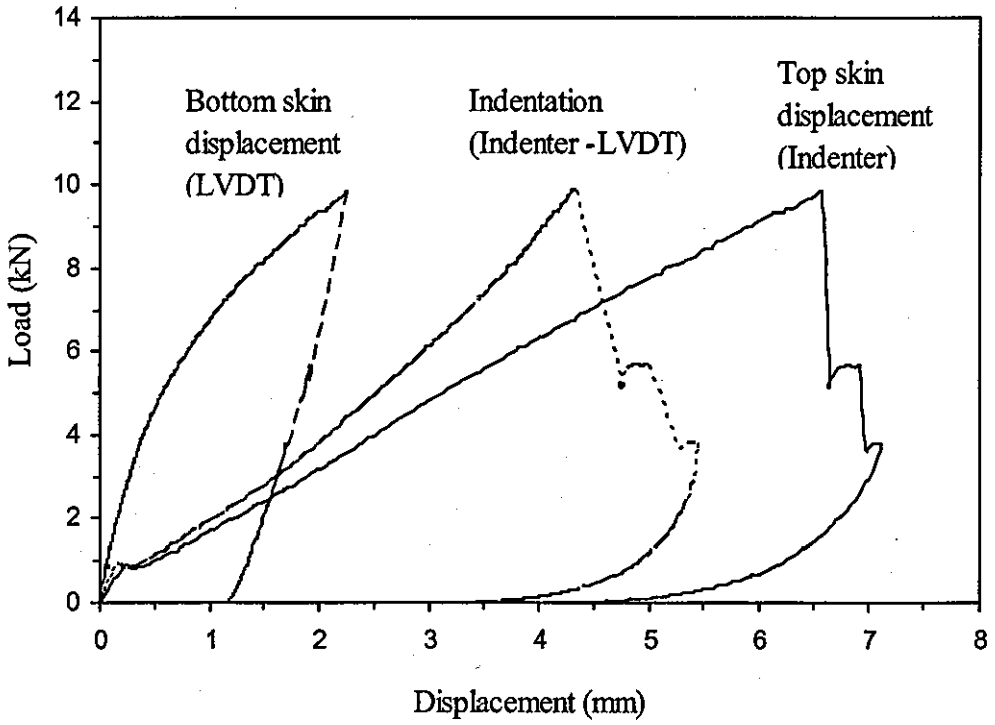

Figure 4.15 Illustration of variation between top and bottom skin bending for 12/90/HS panel throughout loading range

The variation in the shape of the load-displacement curves is due to the way in which the honeycomb interacts with the skin. In the thin skinned 4 and 8 ply panels the skins act as a membrane, conforming to the shape of the indenter, so the honeycomb dominates the local response. Hence, the sandwich panel load-displacement curves reflect the trends witnessed in the honeycomb crush test load-displacement graphs, Section 4.3.2. These graphs contained a clear peak load in the 20mm FE indenter bare crush tests, whilst the 20mm HS indenter curves showed no load drop but a steady, though non-linear, increase in load with displacement. In the thick skinned panels the skins have greater resistance to bending and control the response by distributing the

load over a larger area. When the honeycomb under the FE indenter starts to yield the surrounding skin distributes the load over adjoining undamaged cells and the stiffness of the skin prevents it from conforming to the shape of the indenter/crushed honeycomb. In the HS case the effect is still localised due to the nature of the small indenter contact area, and the local core strength still has a dominant effect on the panel response.

The strain data supports the above theories, load-strain graphs shown in Appendix A with an example shown in Fig. 4.16. Prior to the initial threshold the strain on the top surface is either marginally compressive for the thinner skinned panels or fluctuates around zero, whilst the bottom skin shows a steady increase in tensile strain from the onset of loading. These results are typical of this type of loading configuration, clearly indicating simple global bending of the panel. At the initial damage threshold there is a sudden large increase in tensile strain on the top surface for only a marginal increase in load, indicating local stretching of the top skin due to the lack of support from the core. This is much more pronounced for the FE case where the top surface strain begins to increase just prior to the initial threshold being reached, and rapidly continues through the initial threshold, shown by the zero load-strain gradient. At the initial threshold the bottom strain gauge is relatively unaffected, only showing a short relaxation when a load drop occurs. This is a clear indication that the initial damage is situated either in or close to the top skin and is local rather than global in nature. There is a definite initiation and propagation of core crushing, which extends over a larger area for the FE loading case, and therefore has a greater effect on the strain response than in the HS loading case.

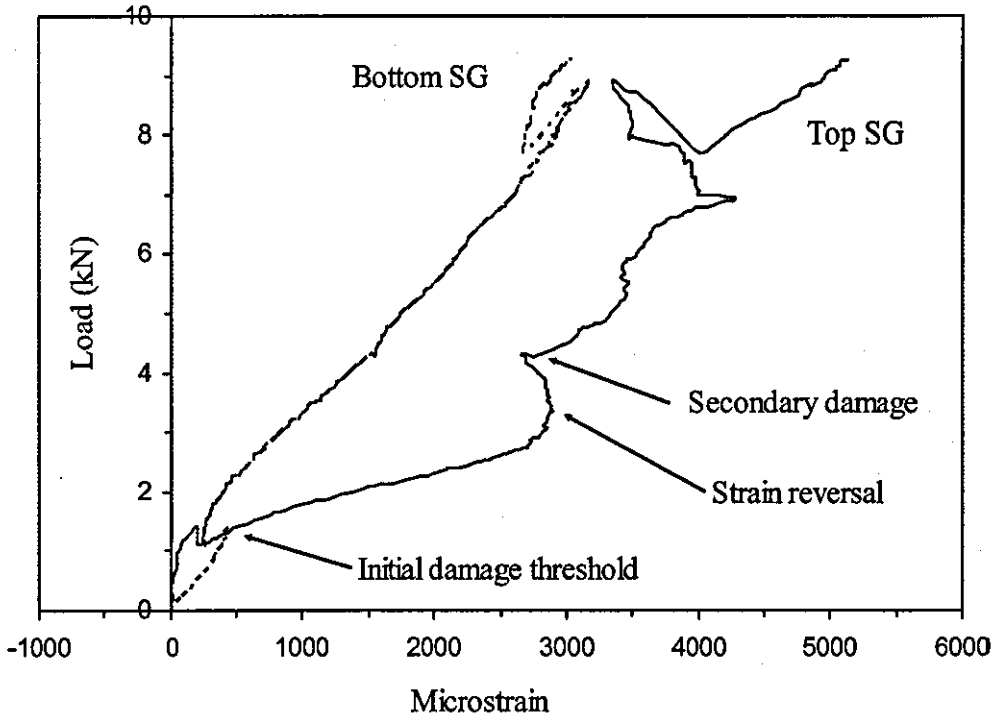

(a)

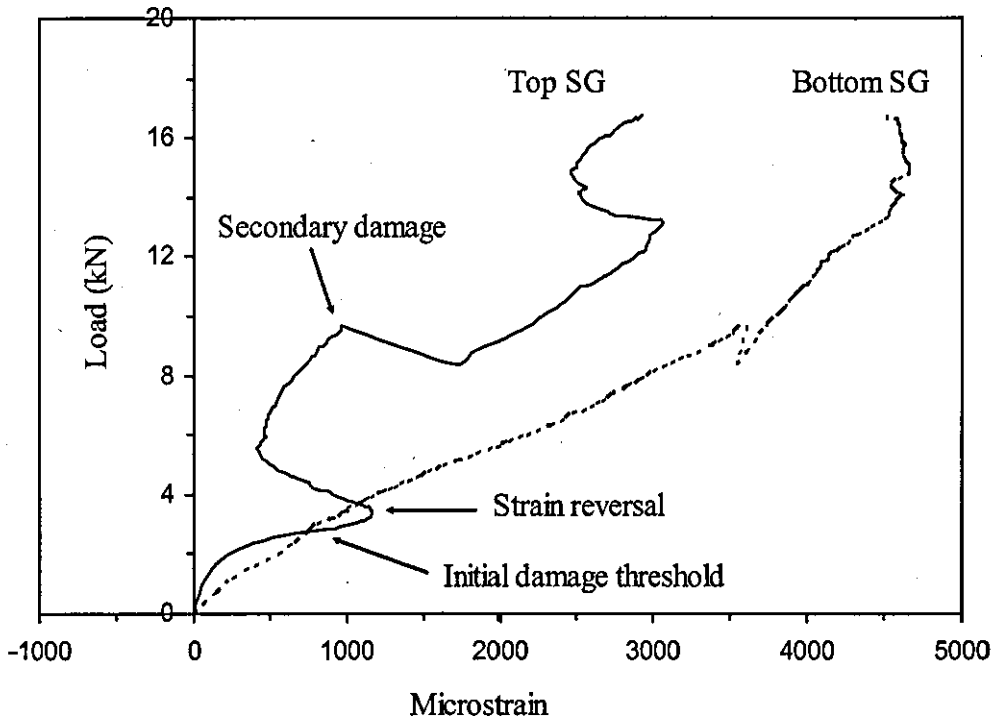

(b)

Figure 4.16 Determination of damage thresholds from load-strain curves for 16 ply 50kg/m^3 panels loaded with (a) HS indenter (b) FE indenter

The increase in top surface strain ends when the load-strain gradient reverses from positive to negative. In the FE case the load at this point corresponds with the maximum load applied to many of the diagnostic panels loaded to just past the initial damage threshold. An internal examination of the FE diagnostic panels shows core crushing to extend to the location of the top strain gauge, Fig. 4.17. Therefore it becomes clear that the top strain reversal occurs when core crushing reaches and passes underneath the top strain gauge. A diagram of this process is shown in Fig. 4.18. This highlights the dependency of strain readings on local response, which is not the same at the panel centre as at the top strain gauge location due to the response of the honeycomb, but can still provide a useful measure of local damage propagation.

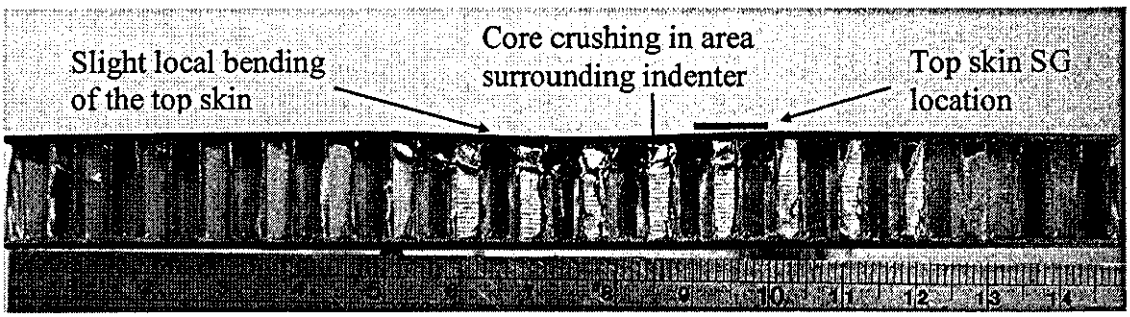

Figure 4.17 Cross-section of 8 ply 50kg/m^3 panel loaded to initial damage threshold with FE indenter

Slight tension	*Just prior to initial damage*: honeycomb crushing just reaches gauge. Strain begins to increase as top skin stretches where honeycomb is crushed under indenter.
Tension	*Just after initial damage*: crushing spreads under gauge. Large amount of top skin stretching as gauge is 'bent' around deformed honeycomb.
Increased tension followed by Relaxation 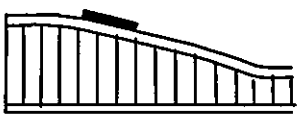	*At load-strain curve reversal*: crushing spread past gauge so upward force from honeycomb greatly reduced allowing skin to deflect easily and shrink back, effectively compressing itself.

Figure 4.18 Effect of honeycomb crushing on top strain gauge when using the FE indenter

Sectioning of the panels loaded to the initial damage threshold reveals core crushing in both the HS and FE cases. Core crushing is very slight in the HS case, often occurring in only two to three cells directly under the indenter, Fig. 4.19. Contrary to some findings core damage has been found to initiate from the very onset of loading in the form of cell wall distortion. This was identified from loading a 16/50/HS panel to a load just below the initial damage threshold, Fig 4.19(a). Sectioning of this panel revealed cell wall distortion and the formation of initial buckling lines in two cells directly under the indenter contact point. No signs of skin damage were present. In the 16/50/HS(init) panel, loaded past the initial damage threshold, multiple small delaminations were present through the top skin and cell wall buckling under the indenter contact point was prominent with core damage spread over 9 cells.

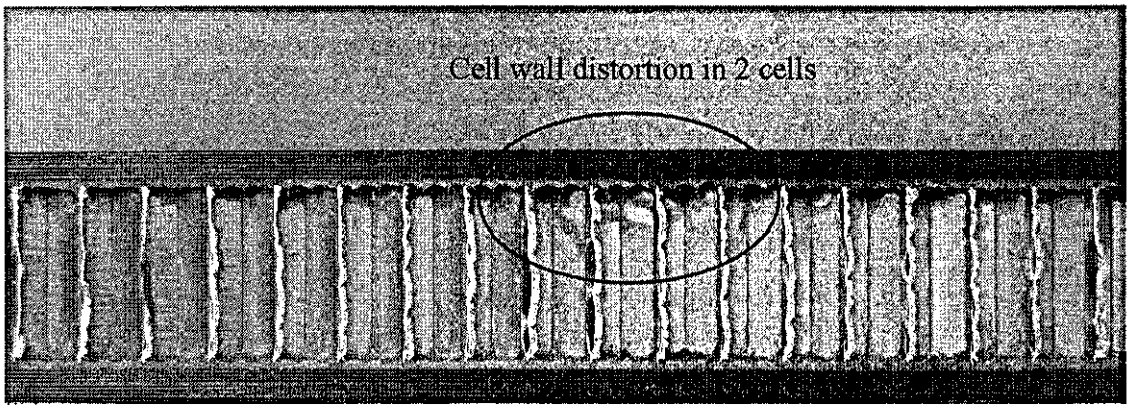

(a)

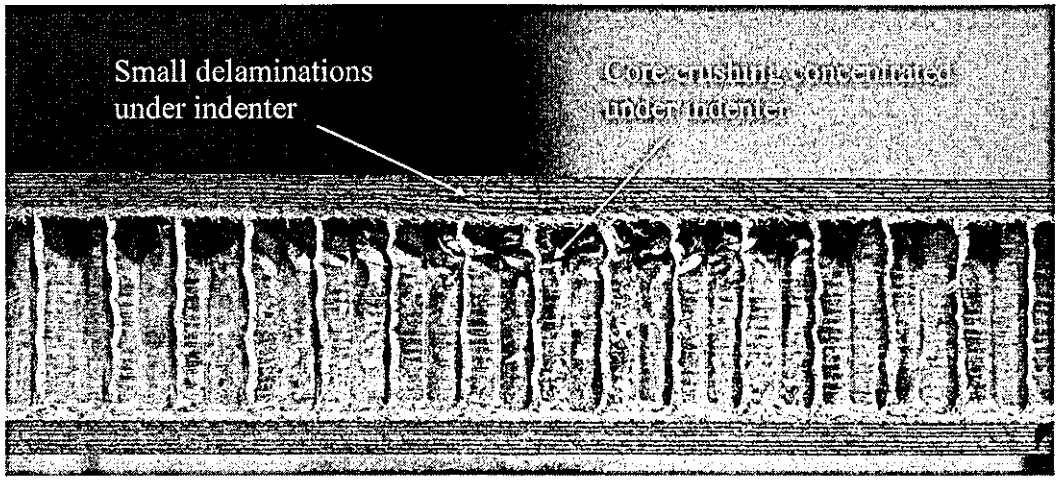

(b)

Figure 4.19 Cross-section of 16 ply 50kg/m^3 panel loaded with HS indenter
(a) loading ceased prior to initial damage threshold (b) initial damage threshold

Small delaminations are often present in the panels loaded with the HS indenter, directly under the indenter loading point, sometimes forming a shear cone as illustrated in Fig. 4.20. Although a number of these panels contain delaminations many of the panels were loaded past the initial damage threshold to ensure that initial damage had occurred. Therefore it is highly possible that core failure occurred first with skin delamination following in quick succession as the skin suddenly lost its support when the core collapsed under the indenter. In the panels loaded only marginally past the point of initial damage the delaminations are very small and often only one or two in number. These small delaminations are induced by the very high local interlaminar shear stresses. These type of delaminations spread in a stable manner and are not critical to the panel performance until they become unstable, and rapidly spread in a dramatic nature. In the panels loaded with the FE indenter no delaminations are visible under the microscope, even after applying the fine polishing process described in Section 4.2.3. Therefore core failure is the only damage mechanism present in the FE loading case.

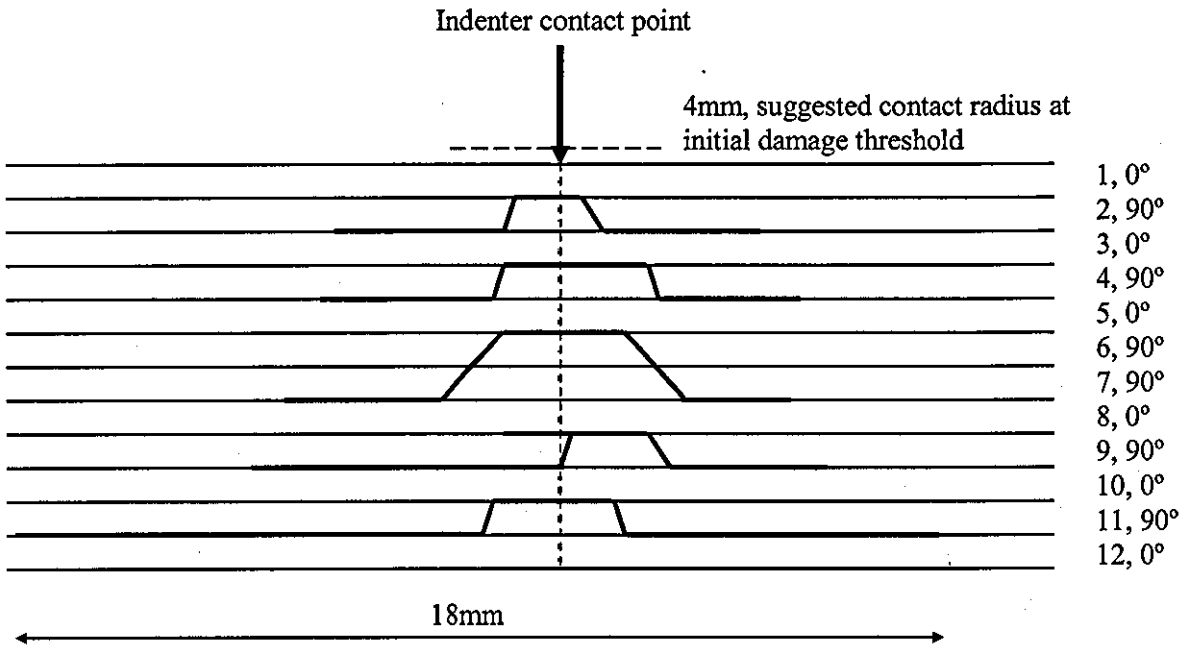

Figure 4.20 Distribution of delaminations through the thickness of the 12 ply 50kg/m^3 specimen loaded with the HS indenter to initial damage threshold

(Observations taken from a polished specimen disc through a microscope along the 0° fibre direction. Overall features would look the same in the 90° fibre direction though the locations of the delaminations may vary slightly)

4.4.2. Secondary damage and response

Secondary damage can be identified from the load-displacement curves by a change in gradient, which may also be accompanied by one large load drop or several smaller load fluctuations occurring between the initial damage threshold and ultimate failure, as seen in Fig. 4.13. Secondary damage is clearly displayed on the load-displacement curves of thicker skinned panels loaded with the FE indenter, through distinct load drops and panel stiffening. Only a small number of panels loaded with the HS indenter experienced a load drop or fluctuation, but most show a clear stiffening of the panel at higher loads.

The panels with thin 4 ply skins or dense 90kg/m^3 honeycomb do not follow the above trend for secondary damage. In these cases the panels show a relaxation rather than stiffening at higher loads, Fig. 4.21. This is because the honeycomb dominates the response, either due to the membrane like behaviour of the thin skins or in the case of the 90kg/m^3 core due to the increased support offered to the skins. In the 12/90/FE and 16/90/FE panels secondary damage occurs soon after initial damage, Fig. 4.22. The load required for core failure in the 90kg/m^3 honeycomb is very high and not much lower than the critical load required for delamination propagation. Therefore when the core fails at the initial threshold the skin is immediately under a high level of stress and delamination propagation occurs soon after. The load required for delamination propagation is similar for all three core densities, therefore becoming closer to the initial threshold load as density increases. This trend suggests if core density is increased further skin delamination would occur either before core failure or simultaneously. Tests on 144kg/m^3 honeycomb would help to prove this point but have not been undertaken in this research.

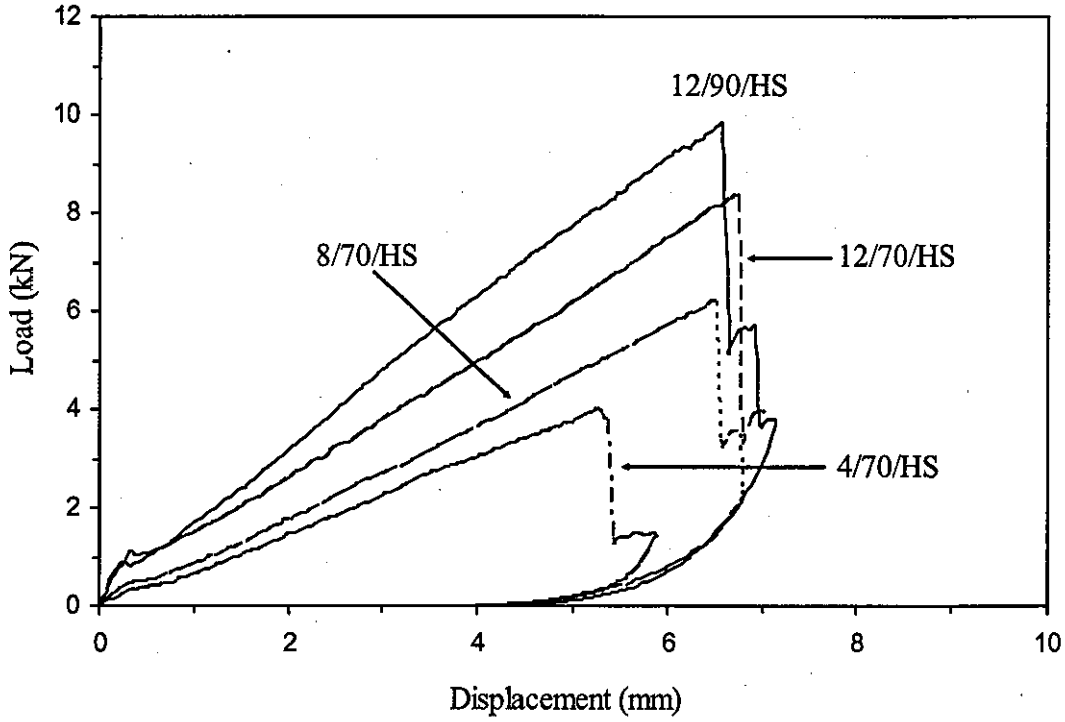

Figure 4.21 Illustration of panel relaxation after secondary damage propagation in panels with 4 ply skins or 90kg/m^3 honeycomb

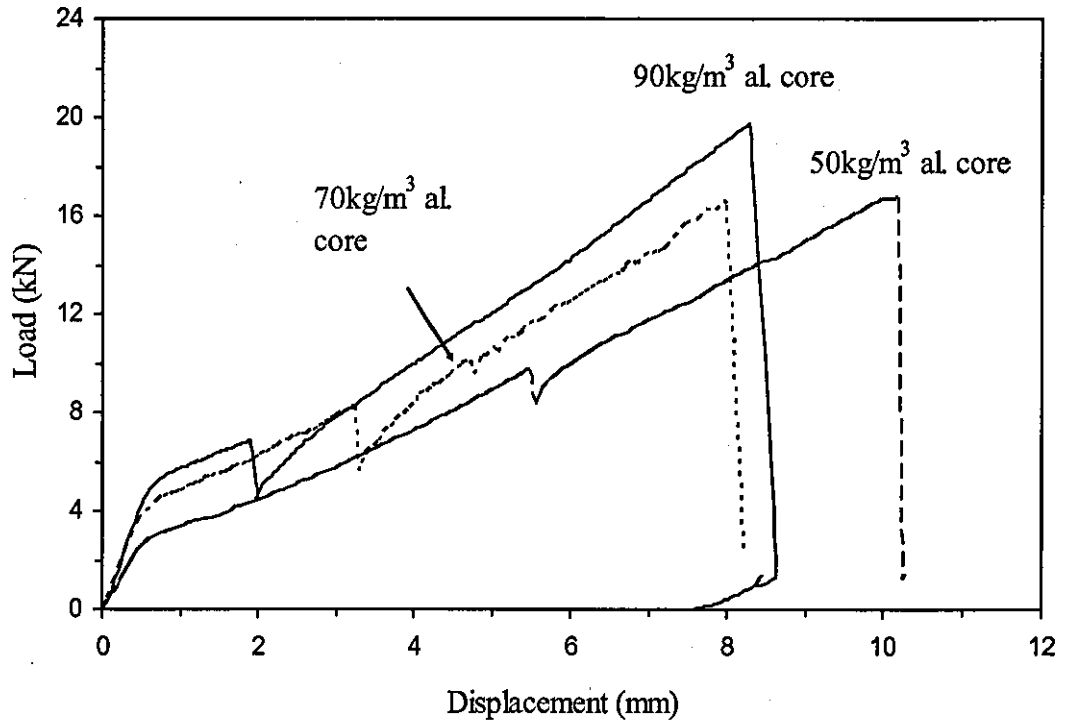

Figure 4.22 Effect of core density on secondary damage load for 16 ply panels loaded with the FE indenter

Secondary damage propagation is also indicated on the load-strain curves in Appendix A, an example shown in Fig. 4.16. The bottom strain response shows clear stiffening of the bottom skin at secondary damage in the majority of panels. The lack of major fluctuations in strain indicates any damage propagation to be located in or near the top skin. However, there is no clear trend in the top strain response, which occasionally shows no sign of damage occurrence. Signs of damage propagation are represented by either a fluctuation or an increase in strain, which maybe preceded by a sharp decrease in strain in the thinner skinned panels. The strain reversal occurring midway between initial damage and ultimate failure in the panels loaded with the HS indenter must not be confused with secondary damage. The cause of the strain reversal is due to damage passing under the top strain gauge, Fig 4.23, as described previously for the FE case, but occurs much later in the loading stage due to the localised nature of HS loading. Any other strain reversals occurring after this point are due to damage propagation. As damage maybe very localised and may not propagate equally in all directions, especially in the case of delamination, if the damage does not propagate away from the centre of the panel in the direction of the top surface strain gauge then it will not be detected by the gauge.

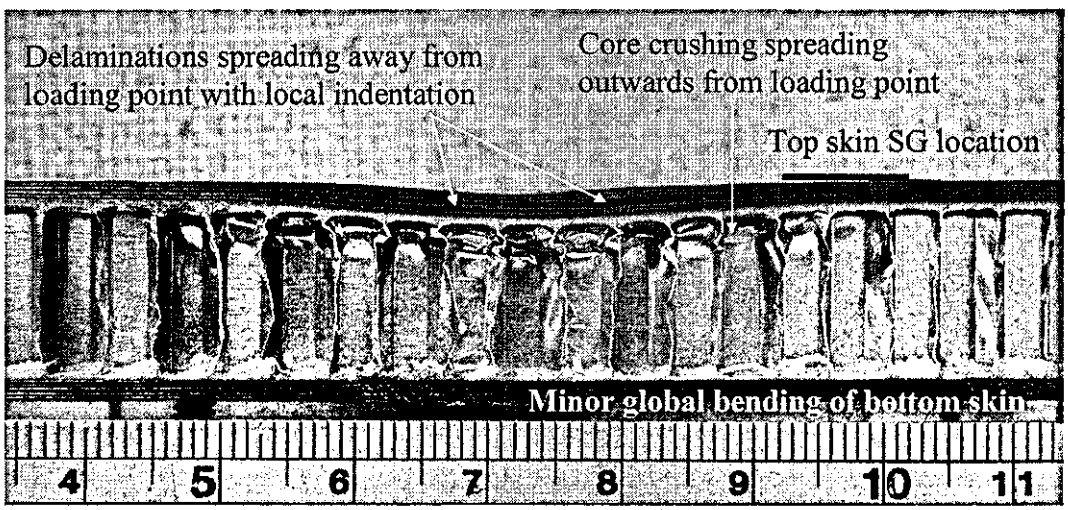

Figure 4.23 Cross-section of 12 ply 70kg/m^3 panel loaded to secondary damage with HS indenter

As the honeycomb failed at the initial threshold and is known from the honeycomb crush tests to undergo steady plastic folding after the peak load has been passed, secondary damage must be skin related. As delamination initiates soon after core failure, identified from the initial damage test, the most likely cause of secondary damage is due to the delaminations propagating. The results from the laminate plate tests showed sudden changes in strain despite almost no variation in the load-displacement curve (except for the 16 ply plate loaded with the FE indenter, which demonstrated a large drop in load with a corresponding increase in strain). These characteristics are very similar to those witnessed in the sandwich panel tests. Therefore it is most likely that secondary damage, causing stiffening of the sandwich panel, is due to delamination propagation, which maybe more dramatic in the FE panel tests due to the nature of the contact area and stresses.

A visual inspection of the internal damage in the diagnostic panels loaded to the secondary damage threshold shows core crushing and delamination in both loading cases, Figs. 4.23-4.24. Core crushing is extensive, having spread both horizontally and vertically from the initial damage state. In the HS case multiple delaminations exist directly beneath the loading centre, with several major delaminations often spreading to one side. Delamination generally occurs between the plies directly above or below the central plies of the laminate. Delaminations do not exist between the central 0° plies but often shear across them. In the panels loaded with the FE indenter delaminations are located at the edge of the indenter contact point. There are typically only one to two small delaminations with one larger delamination, which shears across the central 0° plies at or just outside of the indenter edge. This shows that the shear stress is greatest at the perimeter of the FE indenter.

In several instances where loading with the FE indenter was ceased exactly at the location of the load drop small delaminations can only be seen under a microscope. The only secondary diagnostic panel with no visible delamination was the 12/70/FE(sec) panel. This may be due to the cut plane of the specimen not corresponding with the loading centre. As delaminations are quite well established in many panels loaded with the HS or FE indenter it is unlikely that secondary damage is due to delamination initiation, even in the FE case where no delaminations were present at the initial damage

threshold. It is more likely that the load drop witnessed in many FE tests is due to sudden propagation of a delamination that initiated at some point between initial and secondary damage. This theory is supported by the panels loaded with the HS indenter, which contain significant delaminations throughout the skin thickness at secondary damage despite no signs of delamination propagation being detectable on the load-displacement curves.

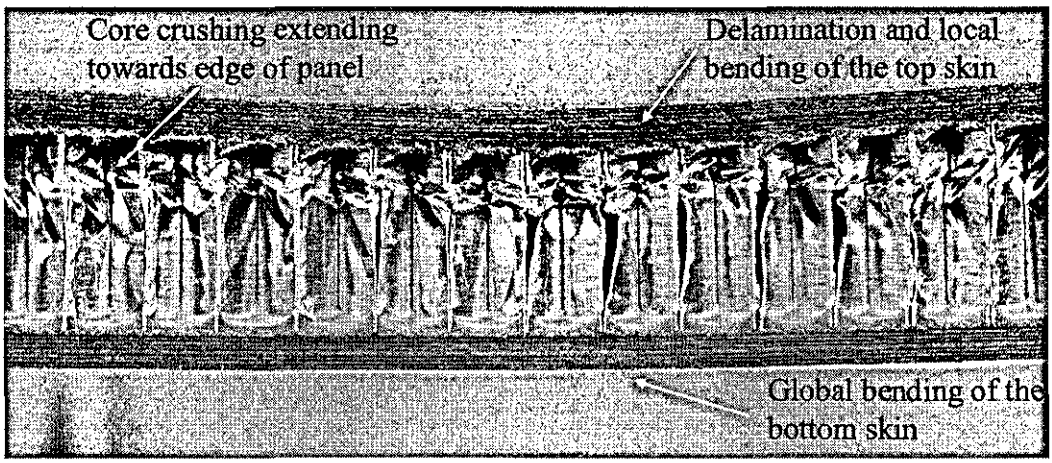

Figure 4.24 Cross-section of 16 ply 70kg/m^3 panel loaded to secondary damage with FE indenter

4.4.3. Ultimate failure

Ultimate failure in both the HS and FE loading cases occurs when the indenter shears through the top skin causing extensive fibre fracture, Fig 4.25. This is accompanied by a loud bang during testing and is represented by a sudden extensive drop in load on the load-displacement curve, illustrated in Fig. 4.13. The load supported by the panel after ultimate failure is greater in the HS case. This is because the damage caused by the HS indenter is more local and fibre fracture occurs only directly under the centre of the indenter, where the stresses are largest. The panel still provides resistance to loading as the indenter tries to force its way through the top skin. In the FE case the stresses are largest around the periphery of the indenter, which induces skin fracture at this location, effectively causing a plug in the top skin. This allows the indenter to shear through the

top skin with only minor frictional resistance, leaving the remaining uncrushed section of the core and the bottom skin to support the load.

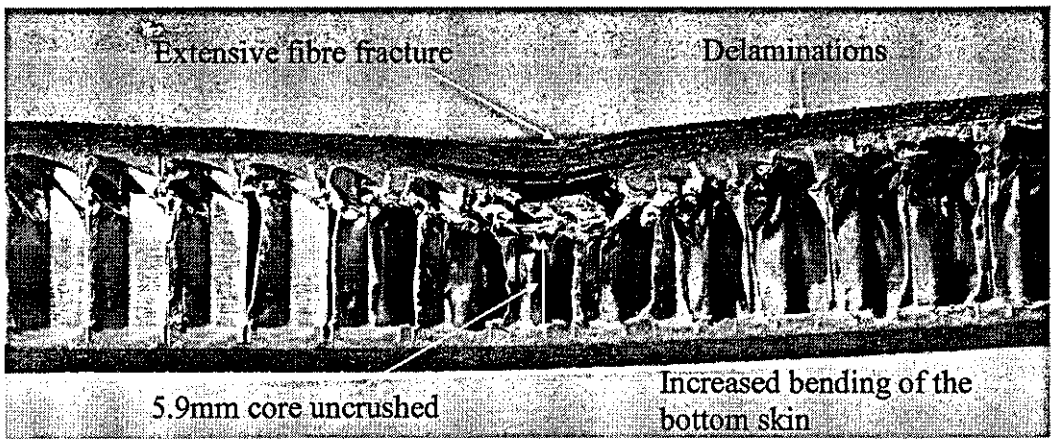

(a)

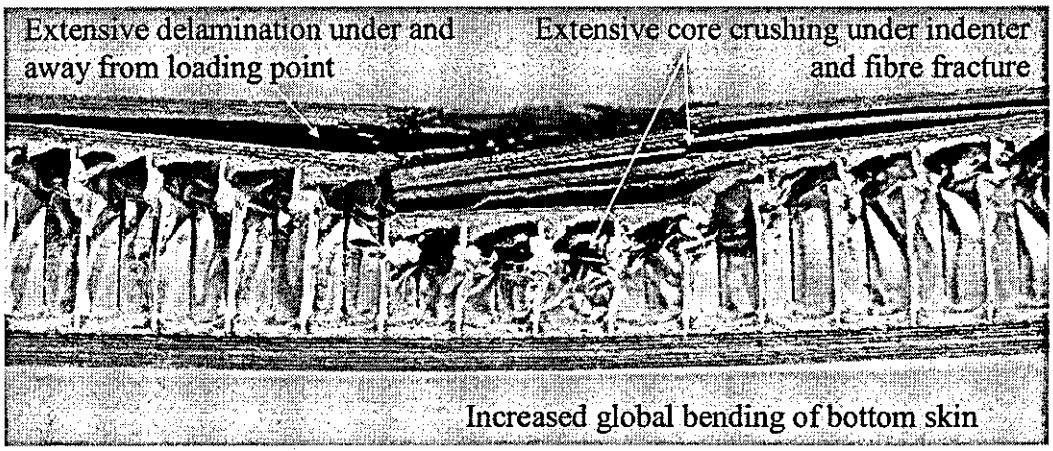

(b)

Figure 4.25 Cross-section of panels loaded to ultimate failure
(a) 12 ply 70kg/m^3 HS indenter (b) 16 ply 70kg/m^3 FE indenter

In a small number of tests the load-displacement curves contain a number of minor load drops prior to ultimate failure. It is thought that these load drops are caused by one of two things. The load drops could be due to the indenter cutting through the top skin along a section of its circumference prior to the entire indenter shearing through the skin, caused by the panel and indenter not being in parallel or the region underneath the indenter not crushing uniformly. Alternatively it is suggested that as the indenter shears through in turn each of the sublaminates created by delaminations spread through the thickness, the panel experiences a load drop. The latter explanation is applicable to both indenter shapes whereas the former is not.

4.4.4. Panels with embedded delamination in the top skin

To help establish when top skin delamination occurs and its effect on the stiffness of a sandwich panel an embedded delamination was added to the top skin of four panels with 16 ply skins and 70kg/m^3 honeycomb. The embedded delamination was 40mm in diameter and located at the mid-plane of the top skin. The delamination size was selected on the basis of results of monolithic panels and was found to be sufficient to reduce the residual compressive strength [100]. Ultimate failure and diagnostic tests were completed for both indenter types to attempt to determine the onset of delamination growth. In addition to comparing the normal 16 ply panels with the panels containing an embedded delamination a comparison has also been made with normal 8 ply panels, as by inserting a delamination the 16 ply top skin is effectively split into two 8 ply sub-laminates.

The load-displacement and load-strain curves for the HS and FE tests are shown in Figs. 4.26 and 4.29 and compared with the normal 8 and 16 ply panel curves. The initial deviation in the FE load-displacement curve in Fig. 4.26 for the 16 ply panel with embedded delamination is due to experimental bedding in effects, not effects caused by the embedded delamination. The 'expected' load-displacement curve obtained from the diagnostic test on the same panel configuration provides proof of this.

The load-displacement response of 16 ply 70kg/m^3 sandwich panels with and without embedded delamination are very similar. Between initial and ultimate failure the stiffness of the panel with embedded delamination is constant and matches that of the normal 16 ply panel following secondary damage, Fig. 4.26. Under HS loading the ultimate failure load and displacement is lower for the panel containing the embedded delamination than the normal panel and there is no sign of secondary damage on the load-displacement or load-strain response of the panel with embedded delamination. Although under FE loading the panel with embedded delamination does not undergo a load-drop signifying secondary damage like the normal 16 ply panel, the ultimate failure load and displacement are very similar.

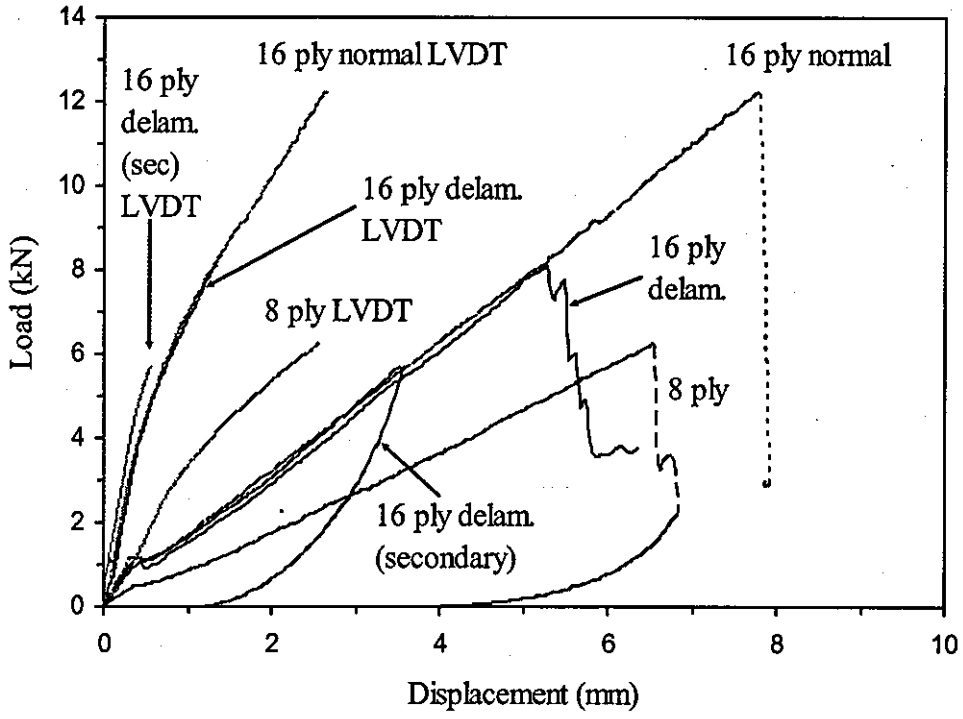

(a)

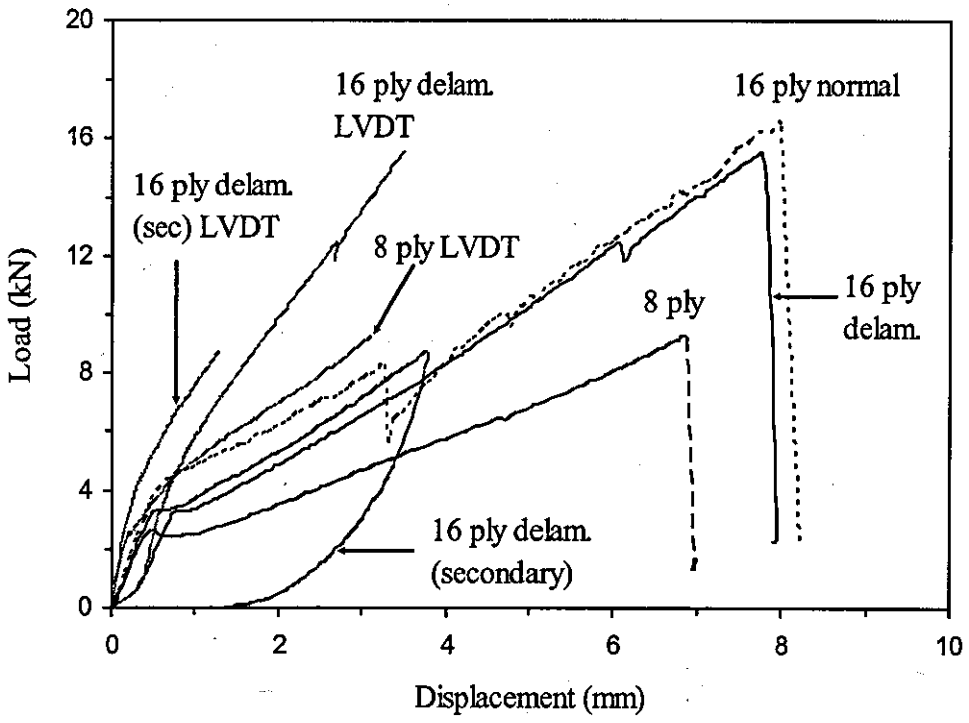

(b)

Figure 4.26 Comparison load-displacement curves of 8 ply 70kg/m^3 and 16 ply 70kg/m^3 panels with and without embedded delamination loaded with (a) HS indenter (b) FE indenter

Table 4.7 Comparison of data for 8/70 & 16/70 panels and 16/70 panels containing embedded delamination loaded with HS and FE indenters

	Parameter	Hemispherical indenter			Flat-ended indenter		
		8 ply	16 ply delam	16 ply normal	8 ply	16 ply delam	16 ply normal
Initial threshold	Load, P_{init} (kN)	0.51	1.15	1.06	2.60	3.27	3.71
	Displacement (mm)	0.18	0.42	0.42	0.46	0.51	0.47
	Gradient (kN/mm)	2.83	3.0	4.05	5.71	6.39	7.75
	Top strain (με)	-7	-73	149	591	886	213
	Bottom strain (με)	280	388	432	1154	1134	870
Secondary damage	Load, P_{sec} (kN)	2.60	5.80	8.01	4.65	8.61	8.64
	Displacement (mm)	2.83	3.52	5.18	3.05	3.78	3.24
	Delamination (mm)	35	43	47	53	70	56
	Core crushing (mm)	32	45	65	71	82	93
Ultimate failure	Load, P_{ult} (kN)	6.22	8.12	12.21	9.21	15.58	16.67
	Displacement (mm)	6.54	5.28	7.79	6.87	7.76	7.95
	Delamination (mm)	59	62	80	45	112	*96+
	Core crushing (mm)	78	69	98	114	114	*97+

* measurements taken from photograph only as original panel unavailable

A comparison of the internal damage present in the panels loaded to ultimate failure shows similar damage in both the normal and delaminated 16 ply panels. In all panels failure is by fibre fracture with multiple delaminations emanating from the loading point. A summary of the delamination and core crushing size are shown in Table 4.7, extracted from Tables 4.8 & 4.10. In both loading cases although delaminations extended further than the length of the embedded delamination, the embedded delamination did not propagate at its location between the central 90° plies. Instead the embedded delamination sheared to the adjoining 90°/0° interface at its edge then propagated outwards.

In both the embedded delamination panel and normal panel loaded with the HS indenter to secondary damage multiple delaminations are present at the loading point and extend over a similar distance. Interestingly in both panels a significant delamination was located 2-3 plies above the top skin-core interface and was bigger than the embedded delamination, Fig. 4.27. Skin core debonding was present in the normal panel. In the panels loaded with the FE indenter multiple delaminations are not present in either

panel. The normal 16 ply panel has a significant delamination between the 9^{th} - 10^{th} plies shearing to 10^{th} - 11^{th} plies, located entirely to one side of the loading centre. Again the embedded delamination has not spread at the mid-plane location but sheared across the 9^{th} ply at the edge of the embedded delamination and propagated away from the loading centre between the 9^{th} - 10^{th} plies, Fig 4.28.

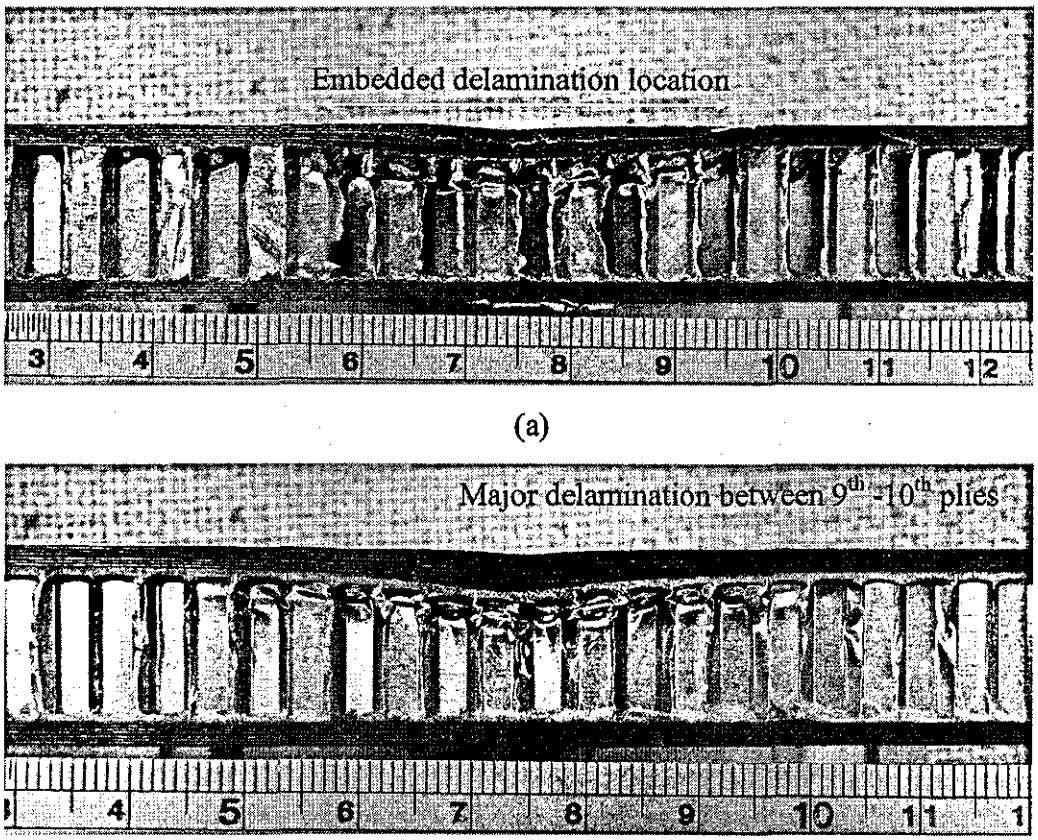

Figure 4.27 Comparison of internal damage in 16 ply 70kg/m^3 panels loaded to secondary damage with the HS indenter

(a) Panel with embedded delamination (b) Normal panel

This evidence obtained from the load-displacement response and physical panel damage suggests secondary damage in the normal panel is due to sudden delamination propagation with the formation of a large delamination in the top skin. Upon formation of this delamination the overall stiffness of the panel increases, indicating the top skin to have a large influence on the panel response. At the point of ultimate failure multiple small delaminations throughout the thickness accompanied by a large delamination between the 9^{th}-10^{th} plies nullifies the effect of the embedded delamination.

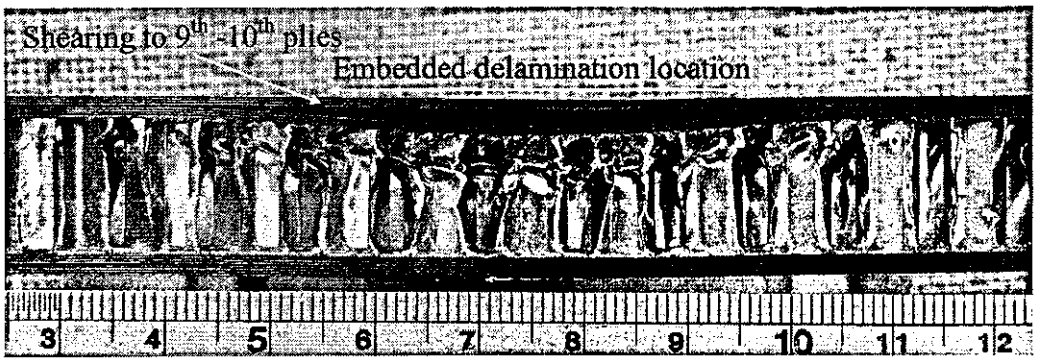

(a)

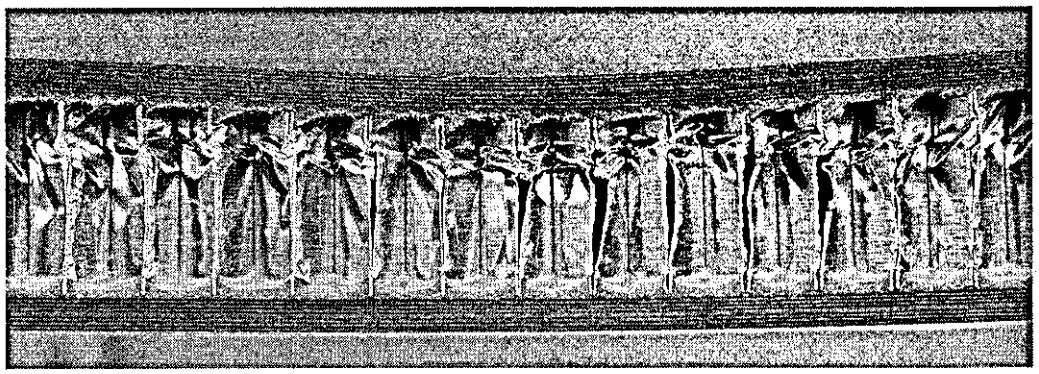

(b)

Figure 4.28 Comparison of internal damage in 16 ply 70kg/m^3 panels loaded to secondary damage with the FE indenter
(a) Panel with embedded delamination (b) Normal panel

Prior to initial damage the stiffness of the 16 ply panel with embedded delamination is lower than that of the normal 16 ply panel but higher than that of the 8 ply panel, though the 8 ply initial damage threshold occurs at a lower load. These variations are more accentuated for the HS loading case due to the larger influence of local effects on the panel response. Comparing the load-strain results up to initial damage shows a similar response on the bottom skin of the three different panels, Fig 4.29. Under HS loading the strain in the top skin of the 16 ply panel with embedded delamination and the 8 ply panel fluctuates around zero whilst the normal 16 ply panel has an increasing tensile strain response. In the FE loading case before initial damage the top strain response is slightly compressive for the 8 & 16 ply normal panels, but marginally tensile for the 16 ply panel with embedded delamination. Immediately after the initial threshold the top strain response shows strain readings with a maximum of 4700με for both the 8 ply and

16 ply delaminated panels. This shows the deformation of the top skin of the panel with embedded delamination is more like that 8 ply panel than the 16 ply panel.

The presence of the embedded delamination clearly affects the panel response at the initial threshold. Although the response of the panel with embedded delamination does not match that of the 8 ply panel, the top skin of the panel with embedded delamination is effectively responding as two 8 ply sub-laminates. After initial damage the response of the 8 ply panel and the 16 ply panel with embedded delamination is very different. This indicates delamination to occur at the initial threshold. Delamination initiates in the undamaged 8 & 16 ply panels causing the top skin to split into 2 sub-laminates. As propagation of the embedded delamination was not observed in the diagnostic panels loaded to secondary damage it is possible that the 2 sub-laminates forming the top skin of the panel with embedded delamination split to form one 8 ply sub-laminate and two thinner 4 ply sub-laminates. This theory is reflected in the panel loaded with the HS indenter to secondary damage, which contains a medium size delamination located between the 13^{th} -14^{th} plies. After delamination occurs at the initial threshold the thickness of the major sub-laminate in both the 16 ply panels will be similar, leading to a comparable load-displacement response and stiffness after initial damage. To verify this experimentally a 16 ply panel containing embedded delamination should be loaded to the initial threshold and sectioned.

The panels loaded with the HS indenter are more sensitive to the presence an embedded delamination than those loaded with the FE indenter. The smaller contact area of the HS indenter increases the effect of local discontinuities on the panel response as identified previously. The 40mm diameter embedded delamination is significantly larger than the 4mm estimated contact diameter of the HS indenter at initial damage, and consequently the area of panel reacting to the load is contained within the 40mm diameter delamination region. For the 20mm diameter FE indenter the indenter contact area is not small in comparison to the embedded delamination or overall panel area. Therefore the area affected by loading is not so localised and even at low loads will extend over 30-40mm in diameter. Hence the area of panel responding to the load will extend past the area containing the embedded delamination.

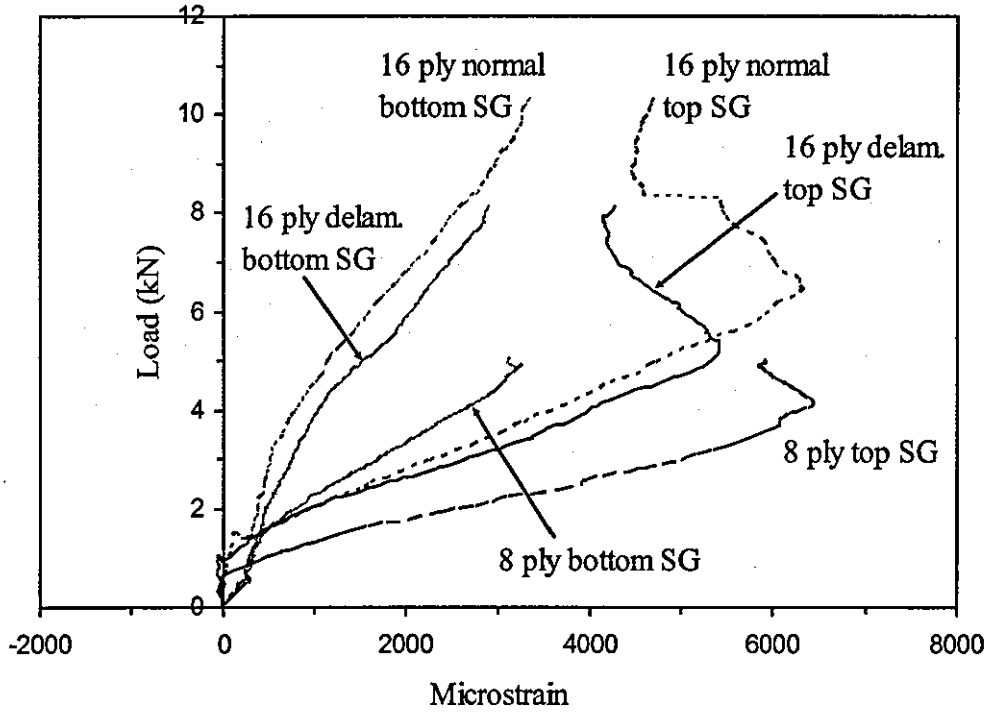

(a)

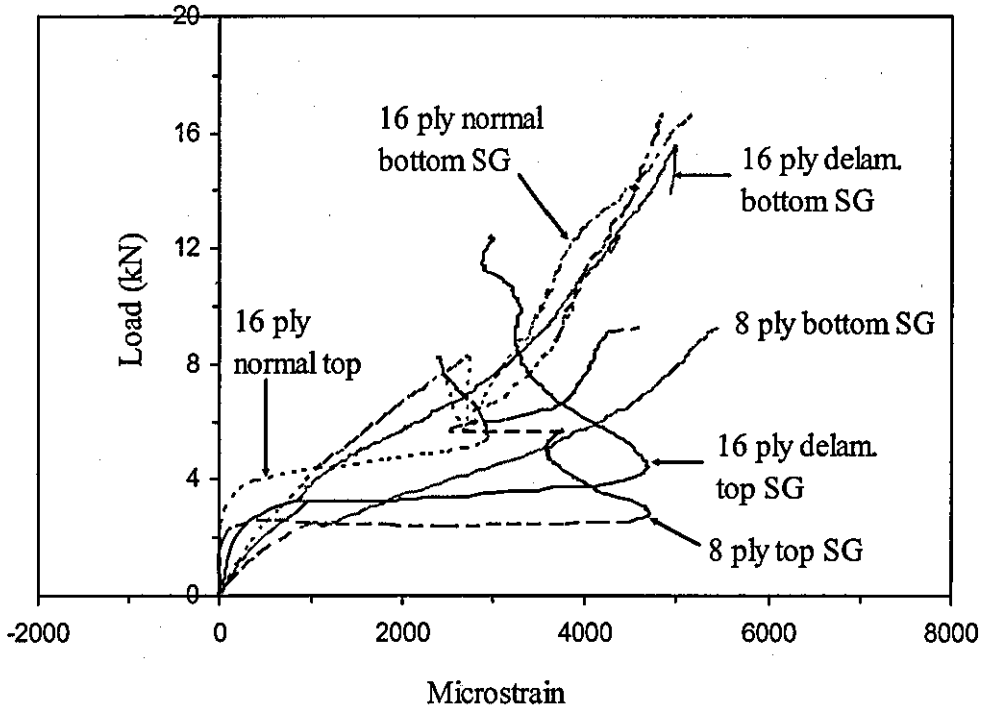

(b)

Figure 4.29 Comparison load-strain curves of 8/70 & 16/70 panels with 16/70 panel with embedded delamination (a) HS indenter (b) FE indenter

4.5. Concluding remarks

Extensive quasi-static tests have been completed on sandwich panels with aluminum and nomex honeycomb cores. Both internal and external damage has been measured through cross-sectioning of the panels and tabulated. Values such as core crushing length, skin delamination length and residual dent depth have been used as a measure of damage level. Laminate plate bending tests and honeycomb core crushing tests have also been conducted to aid identification of the causes of failure in sandwich panels.

Three critical damage levels have been identified as; the initial damage threshold, signifying core failure and the initiation of matrix cracks and minute delaminations; secondary damage through sudden propagation of delaminations within the top skin; and ultimate failure where top skin fibre fracture occurs and the indenter pierces through the top skin. These general failure mechanisms are applicable to all skin thicknesses and core densities. Variation of indenter shape does affect the load and way in which each failure occurs, but the failure mechanisms are the same in principle. All results discussed here are equally applicable to impact results, which are discussed in Chapter 6.

A small number of additional tests on panels with embedded delaminations were completed to try to identify when delamination initiates and its affect on panel performance. Embedded delaminations in 16 ply 70kg/m^3 panels reduced the panel stiffness at the onset of loading and initial threshold load, but had little effect on the panel response after initial damage occurred, except to remove any load drops or fluctuations witnessed at secondary damage. This proved delamination to initiate at the initial threshold, and the rapid unstable propagation of existing delaminations to be the cause of secondary damage. Although only limited tests were completed on panels with embedded delamination the results obtained from these panels supported the observations and conclusions made regarding damage mechanisms of sandwich panels subjected to quasi-static loading.

Table 4.8 Internal and external damage of cross-sectioned T700/LTM45-EL aluminium honeycomb panels from quasi-static bending tests

Panel ID	Core Damage				Residual external damage			Top skin damage				
	No. of damaged cells	Length of core damage	Undamaged cell height (at centre)	Damage profile	Residual dent (centre TS)		Bottom skin bending	Penet-ration	Skin/core debonding	Delamination		
					depth	length				Present	Position	Length
4/50/HS Ult ■	16	72mm	8mm	DUTS	3mm	62mm	Y	Y	N	Y	M, *3-4* 1-2 in 90° direction	53mm
4/50/FE Ult ■	27	121mm	5mm	Below TS at edge of bubbles, shearing to BS at clamps	5.5mm	103mm	Y	Y	N	Y	M, *3-4*, 1-2 -90° direction Shears at indenter edge	110mm
4/70/HS Ult ■	12	52mm	7mm	DUTS	3mm	45mm	Sl	Y	N, large gap 3-4 plies	Y	M, *3-4*, 1-2 in 90° direction (over 13mm in centre)	48mm
4/70/HS Ult REP ■	12	50mm	7.3mm	DUTS	2.5mm	50mm	Sl	Y	N, large gap 3-4 plies	Y	M, *3-4*, 1-2 in 90° direction (over 13mm in centre)	49mm
4/70/FE Init ■	7	28mm	9mm	3mm below TS in centre spreading to DUTS	0.25mm	20mm	Very slight	N	N	N	-	-
4/70/FE Ult ■	14	65mm	5mm	Below TS in centre, DUTS toward edge	5mm	53mm	Y	Y	N, large gap 3-4 plies	Y	M, *3-4*, 1-2 -90° direction Shears at indenter edge	105mm
4/90/HS Ult ■	10	44mm	8mm	DUTS	2.5mm	50mm	Y	Y	N	Y	1-2 in 90° direction, S, 3-4 in 0° direction	45mm
4/90/FE Ult ■	11	48mm	5.5mm	3mm below TS in centre to DUTS toward edge	4mm	55mm	Y	Y	N	Y	1-2 in 90° direction 3-4 in 0° direction	48mm
8/50/HS Init ■	4	12.5mm	11.5mm	EAF	None	None	N	N	N	Y	M, TT Shear cone 3-4, 5-6, 6-7, *7-8*	16mm on disc, 6.5mm on panel

8/50/HS Ult ■	26	107mm	6mm	DUTS at centre shearing one side	3.7mm	90mm	Y	Y	N, large gap 7-8 plies	Y	M, TT, 2-3, *5-*,7-8	63mm
8/50/FE Init ■	13	51mm	8.5mm	2mm below TS at edge of adhesive bubbles	1mm	47mm	Sl	N	N	N	- (matrix damage?)	-
8/50/FE Ult ■	33	137mm	4.5mm	EAF shearing to BS toward clamp	7.2mm	120mm	Y	Y	N	Y	M, TT 2-3, *5-6, 7-8*	94mm
8/70/HS Init ●	3	10.5mm	11mm	DUTS	0.4mm	5mm	N	N	N	Y	2-3 3-4, S, *5-6, 6-7*	8mm on panel, 10mm 5-6 disk
8/70/HS Sec ■	8	32mm	9.5mm	DUTS	0.9mm	30mm	Sl	N	N	Y	M 2-3, 3-4, S, *5-6* 6-7, S, 7-8	35mm
8/70/HS Ult ■	16	70mm	6mm	DUTS	3.2mm	61mm	Y	Y	N, gap 7-8 plies	Y	M, TT 2-3, *5-6*, 7-8	39mm
8/70/HS Ult (1Nm) ■	20	85mm	6mm	DUTS	4mm	70mm	Y	Y	N	Y	M, TT 2-3, *5-6*, 7-8	65mm
8/70/HS Ult (8Nm) ■	19	78mm	6mm	DUTS	3.3mm	70mm	Y	Y	N	Y	M, TT 2-3, *5-6*, 7-8	59mm
8/70/FE Init ●	10	41mm	10.5mm	DUTS	0.5mm	29mm	Sl	N	Poor TS bonding to one side of centre	N	-	-
8/70/FE Sec ■	16	71mm	9mm	DUTS	2.5mm	113mm	Y	N	N	Y	3-4, S, *5-6* (one side only)	53mm
8/70/FE Ult ■	27	114mm	7mm	DUTS shearing to BS near clamp	4.8mm	134mm	Y	Y	N, large gap 7-8 plies	Y	M, TT 2-3, *5-6, 7-8*	45mm
8/90/HS Ult ■	20	95mm	6mm	DUTS spreading level with centre damage	3.5mm	90mm	Y	Y	N, large gap 7-8 plies	Y	M, TT *2-3, 5-6, 7-8*	54mm

8/90/FE Ult ■	25	111mm	6mm	Below TS shearing to BS before clamps	5.5mm	95mm	Y	Y	N, large gap 7-8 plies	Y	M, TT *2-3, 5-6, 7-8*	74mm
12/50/HS Init ●	4	11mm	10.5mm	1.5mm below EAF	None	None	N	N	N	Y	M, TT, Shear cone *11-12*	18mm
12/50/HS Sec ■	20	83mm	9mm	DUTS	2mm	63mm	N	N	N	Y	M 2-3, 4-5, 5-6, *7-8*, 10-11	37mm (1/4 panel) 26mm (1/2panel)
12/50/HS Ult ■	29	121mm	6mm	DUTS shear to BS before clamp	4mm	110mm	Y	Y, 90° crack TS	Y TS at centre + large gap 11-12 plies	Y	M, TT, *7-8, 9-10, 11-12*	30mm
12/50/FE Init ●	12	48mm	10mm	DUTS	0.5mm	30mm	N	N	N	N	-	-
12/50/FE Sec ●	27	110mm	9mm	DUTS	8.5mm	76mm	Y	N	N	Y	5-6 on ½ panel (90°), 7-8 on epoxy disc	5-6 7mm 7-8 8mm + to disk edge
12/50/FE Ult ■	36 (to panel edge)	150mm +	2mm	DUTS shearing to BS near clamp	9.2mm	150mm +	Y	Y	N, large gap 11-12 plies	Y	M, TT *7-8, 11-12*	56mm
12/70/HS Init ■	5	19mm	10.5mm	EAF	None	None	N	N	N	Y	M 7-8, S, 8-9, 11-12	5mm
12/70/HS Sec ■	13	55mm	8mm	DUTS	1.6mm	50mm	Y	N	N	Y	M, 7-8, S, 9-10, *13-14*	43mm
12/70/HS Ult ■	19	93mm	5.7mm	EAF	3.3mm	81mm	Y	Y	N, large gap 11-12 plies	Y	M, TT *5-6*, 10-11, S, 11-12	42mm
12/70/FE Init ●	13	59mm	9.8mm	EAF	0.9mm	50mm	Sl	N	N	N	-	-
12/70/FE Sec ●	19	92mm	7.8mm	EAF (slight cell wall distortion down to BS)	2.3mm	78mm	Y	N	N	N	-	-

12/70/FE Ult ■	29	146mm	4.7mm	EAF (in centre extending straight towards edge)	4.8mm	102mm	Y	Y	N, large gap 11-12 plies	Y	M, TT 5-6, 9-10, S, 11-12	44mm
12/90/HS Ult ■	23	107mm	6mm	DUTS spreading to BS before clamps	3.5mm	85mm	Y	Y	N, large gap 11-12 plies	Y	M, TT 4-5, *6-7*, 7-8, *11-12*	61mm
12/90/FE Ult ■	26	118mm	3mm (bending to BS)	Below TS at edge of bubbles shearing to BS before clamps	6.3mm	95mm	Y	Y	N, large gap 11-12 plies	Y	M, TT *7-8*, 9-10, *11-12*	101mm
16/50/HS linear region ■	2	10mm	11mm	Cell wall distortion & formation of buckling lines	None	None	N	N	N	N	-	-
16/50/HS Init ■	9	40mm	10mm	EAF	None	None	N	N	N	Y	M, TT 2-3, S, 3-4 9-10 *13-14, S, 14-15*	10mm
16/50/HS Sec ■	20	93mm	8.5mm	EAF	1.5mm	75mm	Y	N	N	Y	M, TT 2-3, 3-4, 5-6, 7-8, 10-11	13mm
16/50/HS Ult ■	22 (more to side opposite debonding)	99mm	4mm	One side EAF, at debonding DUTS	3.5mm	95mm	Y	Y	Y, at TS to one side of indenter	Y	M, S, TT *7-8, 14-15*	55mm
16/50/FE Init ●	18	65mm	10mm	1mm below EAF	0.6mm	35mm	Sl	N	N	N	-	-
16/50/FE Sec ■	28	117mm	9mm	EAF	2mm	92mm	Y	N	Y, at BS in centre of panel	Y	At one side only *7-8*, S, *9-10*	26mm
16/50/FE Ult ■	36 (to panel edge)	150mm +	Crushed to BS EAF (1mm AF)	EAF	8.2mm	150mm +	Y	Y	Y, TS indenter edge one side	Y	M *9-10, 15-16*	15-16 56mm, 9-10 100mm to panel edge
16/70/HS Init ●	3	15mm	10.7mm	DUTS	None	None	N	N	N	Y	M, TT, Shear cone *12-13*, 14-15	9mm
16/70/HS Sec ■	15	65mm	8mm	DUTS	0.9mm	46mm	Sl	N, 90° crack TS	Y, at TS directly under indenter	Y	M, TT 2-3, 11-12, 6-7, *9-10*, *4-5*, 13-14	47mm

16/70/HS Ult ■	19	95mm	4.6mm	EAF	4.2mm	79mm	Y	Y	N large gap 14-15, 15-16 plies	Y	M, TT *7-8, 12-13*	46mm
16/70/HS Ult repeated ■	20	98mm	4.75mm	DUTS in centre shearing to BS at clamping edge	3.5mm	95mm	Y	Y	N	Y	M, TT *9-10*, 13-14, 15-16	80mm
16/70/FE Init ●	12	61mm	9.3mm	DUTS	0.8mm	54mm	Sl	N	N	N	-	-
16/70/FE Sec ■	20	93mm	7.5mm	EAF (in centre extending straight towards edge)	1.8mm	79mm	Y	Y	N	Y	clear one side *9-10, S, 10-11* other 7-8	(28mm) 56mm
16/70/FE Ult *Photo only*	20+	97mm+	3.3mm	EAF	4.7mm	92mm	Y	Y	N, large gap 14-15 plies	Y	M, *6-7*, 7-8, *10-11*, 14-15	96mm+
16/90/HS Ult ■	23	108mm	5mm	DUTS in centre shearing to BS	4mm	100mm	Y	Y	N	Y	M, TT 2-3, 9-10, 15-16	75mm
16/90/FE Ult ■	26	122mm	2.5mm	DUTS at indenter edge shearing to BS	6.5mm	100mm	Y	Y	N, large gap 14-15 plies	Y	M, TT 9-10, 11-12, 15-16	126mm

Symbols in Panel ID column:
■ = observations and measurements taken from cross-sectioned panel ● = damage observed through polished disc
No symbol = measurements taken from photograph only

Abbreviations:
EAF = Core damage starts at edge of adhesive fillets beneath top skin DUTS = Directly under top skin
BS = Bottom skin TS = Top skin
M = Major TT = Through the thickness S = Shearing to
Y = Yes N = No Sl = Slight

Table 4.9 Internal and external damage of cross-sectioned T700/LTM45-EL Nomex honeycomb panels from quasi-static bending tests

Panel ID	Core Damage				Residual external damage			Top skin damage				
	No. of damaged cells	Length of core damage	Undamaged cell height at centre	Damage profile	Residual dent (centre TS)		Bottom skin bending	Penet-ration	Skin/core debonding	Delamination		
					depth	length				Present	Position	Length
8/64/HS Ult ■	20	86mm	7.5mm	DUTS	1mm	20mm	Sl	Y	N	Y	M, TT 2-3, *5-6, 7-8*	69mm
8/64/FE Ult ■	26	110mm	5mm	DUTS spreading level with centre damage	3mm	50mm (slight)	Sl	Y	N, large gap 7-8 plies	Y	M, TT 2-3, 3-4, S, *5-6, 7-8*	100mm
8/96/HS Ult ■	17	73mm	7.5mm	Edge of adhesive half way up side of cell walls	0.8mm	13mm	Sl	Y	N	Y	M, TT 1-2, 3-4, *5-6,* 7-8	60mm
8/96/FE Ult ■	21	89mm	1.5mm	Edge of adhesive half way up side of cell walls	4mm	20mm	Sl	Y	N	Y	M, TT *5-6,* 7-8	120mm
12/64/HS Init ■	1	6.5mm	11.3mm	EAF	None	None	N	N	N	Y	M *2-3,* 3-4, 7-8, 10-11, *11-12*	14mm
12/64/HS Sec ■	9	39mm	10.5mm	DUTS	Tiny dip	5mm	N	N	N	Y	M, TT 4-5, 7-8	34mm
12/64/HS Ult ■	21	93mm	6mm	EAF epoxy cracking ½ way down cell	1.7mm	16mm	Sl	Y	N, large gap 11-12 plies	Y	M, TT *7-8,* 9-10, *11-12*	77mm
12/64/FE Init ■	7	32mm	9mm	1/3 way down cell in centre, EAF at indenter edges	None	None	N	N	N	N?	4-5??	-
12/64/FE Sec ■	16	71mm	9mm	Just below TS	None	None	N	N	N	N	-	-
12/64/FE Ult ■	28	122mm	4mm	EAF shearing straight to BS one side	No dent 4mm skin plugging at indenter	20mm	Sl	Y	N, large gap 11-12 plies	Y	M, TT 5-6, S, *7-8,* 11-12	119mm

12/96/HS Ult ■	20	85mm	6.3mm	DUTS shearing to BS	1.5mm	20mm	Sl	Y	N	Y	M, TT 2-3, *4-5, 7-8, 11-12*	53mm
12/96/FE Ult ■	21	85mm	3mm	DUTS spreading level with centre damage	6mm	20mm	Sl	Y	N, large gap 11-12 plies	Y	M, TT 5-6, S, *7-8*	110mm
16/64/HS Ult ■	25	107mm	5mm	EAF spreading level with centre damage	1.7mm	20mm	Sl	Y	N	Y	M, TT 3-4, *9-10*, 13-14	55mm
16/64/FE Ult ■	30	128mm	2mm	EAF/DUTS towards panel edges	7mm	20mm	Sl	Y	N	Y	M, TT *9-10* L direction *7-8* W direction	149mm (to panel edges)
16/96/HS Ult ■	19	81mm	7mm	DUTS/ EAF	2.5mm	21mm	Sl	Y	N	Y	M, TT 5-6, *7-8*, 9-10, 14-15	70mm
16/96/FE Ult ■	24	104m	3.5mm	DUTS/ EAF	7mm	20mm	Sl	Y	N	Y	M, TT *9-10*, 13-14, 15-16	120mm

Table 4.10 Internal and external damage of cross-sectioned T700/LTM45-EL aluminium honeycomb panels from quasi-static bending tests
Special cases – 220mm panels and panels containing embedded delamination

Panel ID	Core Damage				Residual external damage			Top skin damage				
	No. of damaged cells	Length of core damage	Undamaged cell height at centre	Damage profile	Residual dent (centre TS)		Bottom skin bending	Penet-ration	Skin/core debonding	Delamination		
					depth	length				Present	Position	Length
16/70/HS Large ■	33	141mm	3.7mm	DUTS shearing begins 45mm from centre	4.2mm	130mm	Y	Y, 90° crack TS	N, large gap 14-15-16 plies	Y	M, TT 7-8, 9-10, *11-12*, 13-14, *15-16*	74mm
16/70/FE Large ■	46	203mm	1.5mm	DUTS at centre spreading straight towards edge	10.5mm	195mm	Y	Y	N, large gap 15-16 plies	Y	M, TT 7-8, *9-10*, 15-16	93mm
16/70/HS Delam Sec ■	11	45mm	7.5mm	edge of adhesive bubbles	0.7mm	26mm	Sl	N	N	Y	M 13-14 Little spread of artificial	43mm
16/70/HS Delam Ult ■	17	69mm	4.7mm	EAF	2.4mm	57mm	Y	Y	N, large gap 14-15-16 plies	Y	M, TT Artificial shears to 9-10 at delam edge	62mm
16/70/FE Delam Sec ■	19	82mm	6mm	edge of adhesive bubbles	1mm	56mm	Sl	N	N	Y	Artificial shears to 9-10 at delam edge	70mm
16/70/FE Delam Ult ■	25	114mm	3.5mm	edge of adhesive bubbles	5mm	87mm	Y	Y	N, large gap 14-15-16 plies	Y	M, TT, Artificial shears to 9-10 at delam edge	112mm

Table 4.11 Internal and external damage of cross-sectioned IM7/8552 aluminium and Nomex honeycomb panels from quasi-static bending tests

Panel ID	Core Damage				Residual external damage			Top skin damage				
	No. of damaged cells	Length of core damage	Undamaged cell height at centre	Damage profile	Residual dent (centre TS)		Bottom skin bending	Penet-ration	Skin/core debonding	Delamination		
					depth	length				Present	Position	Length
4I/70/HS	3	8mm	10mm	More bending /flexing than buckling	1.5mm	50mm	Y	N?	Y major bottom	Y	1-2, *3-4*	38mm
4I/70/FE	11	45mm	7mm	EAF	2.8mm	50mm	Y	Y	N	Y	*3-4*	45mm
8I/70/HS	9	40mm	8mm	EAF	1.5mm	30mm	SI	Y	N	Y	*5-6*, 6-7, 7-8	35mm
8I/70/FE	18	78mm	6mm	EAF	5mm	75mm	Y	Y	N	Y	*7-8*, 5-6	53mm
12I/50/HS T1	18	82mm	4.5mm	EAF	3.5mm	75mm	SI	Y	Y top skin in centre	Y	M, TT *11-12*, 7-8	62mm
12I/50/HS T2	17	80mm	6mm	EAF	2mm	70mm	SI	Y	Y top skin in centre	Y	M, TT, *7-8, 9-10*	36mm
12I/50/HS T3	16	73mm	6.5mm	EAF	2mm	60mm	SI	Y	Y top skin in centre	Y	M, TT 7-8, *11-12*	54mm
12I/50/FE	32	148mm (to panel edge)	3mm	EAF	7mm	148mm (entire panel width)	Y	Y	N	Y	M, TT *7-8, 11-12*	75mm
12I/70/HS	12	53mm	7mm	EAF	1.3mm	80mm	Y	Y	Y extensive in centre of top skin	Y	M, TT 2-3, 5-6, *7-8*, 9-10, *11-12*	40mm

12I/70/FE	18	77mm	6mm	EAF	3.5mm	20mm	Y	Y	Y major top + bottom skin	Y	M, *7-8*, 9-10, 11-12	83mm
12I/90/HS SEC	5	25mm	9mm	EAF	0.2mm	6mm	N	N	Y top skin in centre	Y	TT 4-5, 7-8, *8-9, S, 10-11*	21mm
12I90/HS	8	37mm	4mm	DUTS no real folding of cell walls, bending + distortion	2mm	25mm	N	Y	Y extensive in centre top skin + bottom skin all detached	Y	M, TT *7-8*, 9-10, 11-12	44mm
12I/90/FE SEC	5	25mm	9mm	No real buckling but cell wall distortion	0mm	0mm	Y	N	Y major top + bottom skin all over	Y	10-11	40mm?? one half only
12I90/FE	9	41mm	5mm	EAF shearing to BS one side	2.5mm	20mm	Y	Y	Y major top + bottom skin all over	Y	M, TT *7-8*, 9-10, 11-12	46mm
16I/70/HS	13	58mm	7mm	EAF	1.6mm	50mm	Sl	Y	N	Y	M, TT *10-11*, 13-14, *15-16*	43mm
16I/70/FE	24	104mm	4.5mm	EAF	5.2mm	100mm	Y	Y	N	Y	M, TT 7-8, *9-10, 13-14*	80mm
12I/64/HS	12	52mm	8mm	EAF	0.5mm	10mm	N	Y	Y small bit in top skin centre	Y	M, TT 3-4, *7-8*, 8-9, *9-10, 11-12*	37mm
12I/64/FE	25	106mm	5mm	EAF	3.5mm	20mm	Sl	Y	Y Top skin in centre	Y	M, TT 4-5, *7-8*, 11-12	50mm
12I/96/HS	9	40mm	9mm	EAF	0.5mm	15mm	Sl	Y	Y very slight in centre top skin	Y	M, TT 2-3, 4-5, 5-6, *7-8, 9-10, 11-12*	35mm
12I/96/FE	12	50mm	7mm	EAF spreading to BS at indenter edge	2mm	20mm	Sl	Y	Y top skin in centre slight	Y	M, TT 7-8, 11-12	64mm

5. OVERVIEW OF EXISTING MODELS FOR TRANSVERSE LOADING OF SANDWICH PANELS

A variety of analytical models have been created for sandwich panels subjected to various loading conditions, as reviewed in [9,150-152]. As sandwich panels are usually much thicker than monolithic laminates analytical models are often preferred to full three-dimensional numerical models [153–155]. This is because a massive number of elements are required to accurately represent the skin and core structures within a three-dimensional model, and consequently high levels of cost and computational effort are involved in processing the model. The majority of analytical models provide an approximate solution rather than an exact solution, and a comparison is made with existing three-dimensional finite element models. The only exact analytical model is the one developed by Pagano [156] based upon the three-dimensional elasticity solution, but it is only applicable for simply-supported square sandwich panels. Analytical models can be split into various categories, with an overview of each model type and the major published works given in the following sections.

5.1. Overview of existing analytical modelling methods

The majority of published works on modelling transverse loading of sandwich panels are based upon classical two-dimensional plate theories. Classical plate theories focus on the structure rather than the loading case and model the structure such that the dynamics of the structure are fully accounted for. These two-dimensional plate models include equivalent single layer theories (ESLT), using both first and higher order theories, and layerwise theories. Two alternative methods to the classical theories are based upon the localised contact response and the impact dynamics of the structure. Modelling the sandwich panel as a plate on an elastic foundation with defined contact laws is a common method used in modelling the local quasi-static indentation response. When modelling the impact dynamics of a structure, spring-mass and energy balance models which treat the sandwich panel as a set of masses and springs are more suited.

5.1.1. Equivalent single layer theories

ESL theories model the sandwich panel as an equivalent single layer [157–165]. The simplest of these models uses classical laminate theory (CLT) or Kirchoff-Love theory, which assumes a continuous linear variation of displacement and therefore transverse strain through the thickness of the panel [166,167]. As there is no transverse shear stress-strain relationship present, shear stress is recovered using equilibrium equations. Because the Kirchoff-Love theory is designed for thin laminate plates rather than thick anisotropic sandwich panels with a relatively soft transverse shear modulus, the theories often over predict failure loads whilst under predicting deflections.

An alternative to the Kirchoff-Love theory is the Reissner-Mindlin or first order shear deformation theory (FSDT) [157,160,163]. FSDT accounts for transverse shear effects on the panel and assumes the normal of the panel remains straight after deformation but is no longer normal to the reference surface. This method is more applicable to sandwich panels as it is designed for thick plates, but gives an unrealistic constant variation of transverse shear stress through the thickness. Shear correction factors are introduced to improve the FSDT model. However, these correction factors are highly dependent on material properties and loading conditions, and often have to be determined by comparing the FSDT output to full 3D analyses. This makes the model very specific to the chosen loading case and panel configuration, both which may change during the design process. Better approximations can be obtained from refined or higher-order shear deformation theories (HSDT) as warpage of the panel can be accounted for since the assumptions used permit a non-linear variation in displacements, strains and stresses [158,159,161,162]. Although these theories are more complicated as they often account for 2D or 3D stresses/strains, they are more accurate than the FSDT models, but are still unable to accurately model the transverse strains and stresses that occur between two layers with extremely different stiffness properties.

The problem with all the ESL theories is that the individual properties of each layer are neglected and interlaminar stresses and strains cannot be estimated directly. Therefore it is not possible to predict when or where damage initiation and propagation between layers will occur. Additionally these theories provide solutions only in numerical forms.

5.1.2. Layerwise theories

The application of layerwise theories to sandwich panels has been attempted by a small number of researchers [168–171]. Layerwise theories use the same basic methods as the ESL theories, but rather than taking the sandwich panel as one equivalent layer each layer is considered separately so that it has its own unique displacement field and distinct material properties. As the computation proceeds layer by layer there is both stress and strain continuity at the interfaces and it is possible to analyse the mechanical interaction between layers, therefore permitting predictions of local failure. Due to the nature of layerwise theories the computational effort required for analysis is directly related to number of layers and degrees of freedom. Therefore for panels with a large number of layers the computational effort can match that required for full 3D numerical analyses.

This problem with layerwise theories can be reduced by limiting the number of degrees of freedom, regardless of the number of layers. This type of simplification is referred to as discrete layerwise theory and can provide very accurate approximations to the full three-dimensional analyses provided the number of layers is not too large. Another variation of layerwise theory is the zig-zag approach [172,173]. Here in-plane displacements are assumed to be layerwise linear and continuous through the thickness yet the total number of degrees of freedom is limited to five regardless of the number of layers.

Of all the classical theories available layerwise theories are the only ones able to accurately deal with localised loading cases and associated intense stress/strain fields around the loading point. However, despite the fact that layerwise theories have been shown to produce the most accurate predictions of sandwich panel response they are still of a numerical nature and require even greater computational efforts than the ESL theories. Therefore layerwise theories are not easy to use when making initial predictions of panel performance and basic comparisons between different sandwich panel designs.

5.1.3. Contact laws and elastic foundations

Contact laws are basic relations which link local load to local indentation. Thus, they are commonly used in indentation analysis. Hertzian contact or experimentally determined static indentation laws are used to describe the contact made between the hemispherical indenter and the panel surface [174–177]. The general form of the contact law is given in Eq. 5.1 where k_c and n are constants that need to be determined. Values for k_c and n should be determined experimentally as both constants are dependent on panel geometry and materials. For a laminate plate loaded with a hemispherical indenter, the value of n is generally taken as $^3/_2$, based on Hertz's theory of contact and k_c is calculated using Eq. 5.2. For a sandwich panel these values may not be applicable, though in many cases the value of n is taken to be the same as in the laminate plate case [7,176,178,179] and k_c is calculated through Eq. 5.2. In the small number of cases where a value of n was determined experimentally for a sandwich panel the value was always less than 1.5; Cantwell and co-workers [41,74] found n to range between 0.7 - 1.2 and k_c to range between 0.2×10^6 - 2×10^6 N/m^n and were dependent on loading rate and panel material, whilst Anderson [180] found n to range from 1.11-1.17 and k_c to range from 1.31×10^6 - 4.84×10^6 N/m^n for different panel types.

$$P = k_c \alpha^n \tag{5.1}$$

$$k_c = \frac{4}{3} \frac{\sqrt{R}}{\left(\frac{1-\nu_i^2}{E_i} + \frac{1-\nu_p^2}{E_p} \right)} \tag{5.2}$$

Coupled with the contact law the sandwich panel is commonly modelled as a plate on an elastic foundation. This enables the realistic compressible soft core characteristics to be included. The most well-known approaches are the one parameter Winkler and two parameter Pasternak or Vlasov elastic foundation models. The Winkler foundation is represented by continuously distributed independent linear tension-compression springs [177,178,181–183]. The response is linear and the intensity of the elastic foundation, q, is assumed to be proportional to the deflection, w, hence introducing the modulus of the foundation, k, representative of the core stiffness. The Pasternak foundation includes

additional shear springs to allow the effects of interfacial shear stresses to be assessed [176,184]. Both types of model provide a prediction of the indentation response of a sandwich panel resting on a solid base. There are distinct limitations with these models if used directly. As the models are linear they cannot be used after the point when the core undergoes plastic deformation and they assume all of the core material to react equally to the load.

Attempts to model the entire loading range were made by Olsson et al. who separated the indentation response of a sandwich panel into regions [178,181]. For the initial region prior to core crushing the panel was modelled using small deflection theory for a plate on an elastic foundation. After core crushing but prior to delamination occurring large deflection plate theory was employed incorporating membrane effects. After delamination initiation the panel was modelled as a membrane alone since the existence of delaminations give rise to a significant loss in bending stiffness. Although reasonable correlation with experimental data was shown the complexity of the model restricts its usefulness as a simple analytical prediction tool.

To obtain a complete model which accounts for both the local indentation and global bending response a superposition method can be used, as shown by Thomsen [184]. Thomsen's method uses the elastic foundation theory to obtain a value for local indentation of a compressible panel which is then added to the displacement obtained using classical sandwich panel theory for bending of an incompressible panel. By accounting for both local and global deformations both global and localised panel failure mechanisms can be assessed.

These theories are especially applicable to sandwich panels using cores with a very low Young's modulus. In this type of panel core failure will always occur before global failure when subjected to localised loading scenarios. The elastic foundation theory can only determine localised deformation directly around the loading point and does not take into account any effect the localised deformation may have on the unloaded skin directly below the loading point. Whilst this maybe of minor relevance, the elastic foundation theory also assumes that the core behaves elastically but there is no interaction between the vertical and shear stresses within the core. This is not an

accurate representation of the physical situation as an interaction must exist to satisfy equilibrium requirements.

5.1.4. Spring-mass and energy balance models

Whilst the classical theories are suited to quasi-static loading situations, when assessing impact performance the dynamic response of the system becomes important. An alternative approach used in modelling impacts on composite structures is the spring-mass and energy balance model. The model, which is capable of predicting the maximum impact force and the contact force history, was originally developed for monolithic laminates by Greszczuk and Shivakumar et al. [185,186] but has been adapted for use with sandwich panels by a number of researchers [7,9,178,179,187].

In a spring-mass model the stiffness and resistance of the structure to loading is represented by springs. The impactor mass is generally much larger than the mass of the sandwich panel, which sometimes leads to the terms related to the mass of the sandwich panel being neglected for simplicity [54,187]. Four separate spring stiffnesses are typically used to represent the entire system, forming a two-degree of freedom spring-mass model; k_c corresponds to the non-linear contact stiffness between the impactor and the top skin and is determined from contact laws. k_b and k_s represent the bending and shear stiffness of the entire panel, the latter term of significant importance when modelling sandwich panels with a high shear rigidity. Normally these two terms are combined analytically to form k_{bs}. Finally when the sandwich panel undergoes large deflections or has a thin top skin the membrane stiffness k_m becomes important. If the deflections are small such that the membrane stiffness can be neglected and the contact stiffness taken as linear, the system can be represented by a much simpler single-degree of freedom (SDOF) spring-mass model.

A further adaptation of the spring-mass model to incorporate the core transverse flexibility and transform the system into a three-degree of freedom system has been attempted by Malekzadeh et al. [179]. In addition to just representing the system by springs and masses, dampers are incorporated into the model. These dampers are used

to provide an energy dissipation mechanism, representing the energy absorbed in creating permanent material damage, especially through core crushing [179,180,187, 188]. Several methods have been used to calculate the various spring stiffnesses and damper coefficients. Attempts have also been made to adapt the equations for k_{bs}, k_m and k_c developed for monolithic laminates [7,41,178]. In other instances the local skin and global plate stiffnesses are derived using classical theories and the core response taken from honeycomb crushing theory [187,189]. In all cases the stiffnesses derived are applicable only within the linear elastic region and consequently the models cannot accurately predict the dynamic response once material damage has occurred, due to the irregular reductions in each individual stiffness.

Energy balance models, which are an extension of the spring-mass models, can be used to find the maximum force and deflection for a given impact kinetic energy [7,41,74]. At the point of maximum deflection the velocity of the projectile is zero and all the IKE has been absorbed in deforming the structure. The energy absorption mechanisms are the same as used in the spring-mass models and therefore employ the same stiffnesses, k_c, k_{bs} and k_m. As with the spring-mass models for small deflections the membrane stiffness may be neglected and where indentation dominates the response k_{bs} can also be ignored, providing immense simplification to the problem. As seen for the spring-mass models the accuracy of the energy balance models depend on the accuracy of the method used to calculate the stiffnesses and are not representative for panels containing permanent damage.

5.2. Review of the major published models for transverse loading of sandwich panels

The most significant research into the development of analytical prediction methods for sandwich panels subjected to transverse loading has been completed by Frostig and co-workers [164,165,190–196], Wierzbicki et al. [73], Hoo Fatt and co-workers [73,79,80,187,188,197], Sburlati [174] and Wen et al. [7]. These analytical theories incorporate several of the methods described above. The main aspects of each theory

are summarised below and values calculated using the main equations compared with experimental data from this research.

5.2.1. Models from Frostig and co-workers

Frostig and co-workers have published many papers on the analytical modelling of 'soft core' sandwich beams and panels, a selection included in [164,165,190–196]. Soft core sandwich structures are representative of panels with deformable cores typically constructed of foam or non-metallic honeycomb materials. These soft core structures undergo a large amount of local deformation when subjected to localised loads and subsequently suffer from local indentation, which is not characterised in models which assume an incompressible or 'antiplane' core. Frostig's high-order sandwich panel theory (HSAPT) is based upon classical thin plate theory for the skins and three-dimensional elasticity theory for the core. The way in which the theory is derived makes it applicable for various boundary conditions and loading scenarios, with such flexibility uncommon in many existing theories.

The governing equations are derived from a potential energy balance initially assuming linear small deformation kinematic relations for the skins [164], and later non-linear deformation kinematic relations [165,190] when attempting to model the non-linear behaviour. The core is assumed to have transverse shear and normal stiffness but negligible resistance to in-plane normal and shear stresses. As there is no constraint on core displacement fields the core height can change, representing local crushing. Unlike many theories an assumed deflection shape is not used and the higher order non-linear in-plane and transverse deformation equations are determined analytically. A solution to the governing equations can be obtained for a particular set of boundary conditions and loads using software such as Matlab. In the non-linear theory developed using the non-linear kinematic relations complex non-linear partial differential equations with no closed-form solution are obtained. To solve these equations and obtain a numerical solution requires simplifications based upon simplified non-linear or linear kinematic equations for the core.

The use of linear kinematic relations along with the assumptions of small deflections and isotropic elastic behaviour of the entire structure makes the theory only applicable to the initial region of the load-displacement curve. Frostig [165] states that the model is accurate up to the limit point load level, which represents local buckling of the skin, and the core behaves more like a Winkler foundation. In none of the Frostig papers reviewed, is a comparison made with actual experimental data for the conventional composite sandwich panels as used in the aerospace or marine industries. Several comparisons are made with full three-dimensional finite element models, generally for simply-supported structures that are often beams rather than panels. Sokolinsky et al. [199] applied Frostig's HSAPT theory to foam core sandwich beams with aluminium skins. Therefore the ability of the HSAPT theory to predict the response of the clamped carbon fibre/honeycomb sandwich panels as used in this study is unknown.

5.2.2. Model from Wierzbicki et al.

The analytical method for local indentation presented by Wierzbicki et al. in [73] is derived from the bare crushing resistance of a hexagonal honeycomb cell structure. The model is applicable to aluminium sandwich panel specimens resting on a solid foundation and loaded with a cylindrical flat-ended indenter. The resistance of the panel to loading is assumed to consist of the crushing resistance of the core directly beneath the indenter and the shear resistance of the material surrounding the periphery of the indenter, with the core modelled as a rigid-plastic foundation. The bending resistance of the top skin is assumed to be negligible when compared to the membrane resistance and the skin-core adhesion is too weak to allow the development of in-plane radial support.

Under quasi-static loading the extent of the plastic deformation in the radial direction ξ is related to the indentation force P by Eq. 5.3.

$$P = \pi \sigma_{crush} \xi^2 \tag{5.3}$$

For punch-through shear of the skin and tensile necking of the skin Eqs. 5.4 and 5.5 are used respectively.

$$\frac{\xi_{cr}}{R} = \sqrt{1 + \frac{2}{\sqrt{3}} \frac{\sigma_y}{\sigma_{crush}} \frac{t}{R}} \tag{5.4}$$

$$\frac{\xi_{cr}}{R} = \sqrt{1 + 2\sqrt{2\varepsilon_c} \frac{\sigma_y}{\sigma_{crush}} \frac{t}{R}} \tag{5.5}$$

The energy absorbed by the panel during punch indentation is given by Eq. 5.6

$$AE = \frac{\pi \zeta_{crush}{}^2 R^4}{16 \sigma_y t} \left\{ \left(\frac{\xi}{R} \right)^4 \left[\ln \left(\frac{\xi}{R} \right)^4 - 1 \right] + 1 \right\} \tag{5.6}$$

An energy efficiency ratio is calculated using Eq. 5.7

$$\eta_{\max} = 1 + \frac{1}{2} \frac{\sigma_y t}{\sigma_{crush} R} \tag{5.7}$$

Under impact loading the dimensionless kinetic energy can be related to the radial deformation through Eq. 5.8 derived using the energy balance method.

$$\overline{IKE} = \bar{\xi}_f^4 \left[\ln \bar{\xi}_f^4 - 1 \right] + 1 \tag{5.8}$$

The accuracy of Eq. 5.8 was stated to be within 5% of experimental data for low velocity tests and 16% for higher impact velocities. However, the analytical approximations relating to quasi-static indentation, given in Eqs. 5.3-5.7, were not compared with experimental data.

If Eqs. 5.3 and 5.6 are combined the energy absorbed at ultimate failure can be calculated for panels resting on a solid foundation and loaded with a flat-ended indenter.

$$AE = \frac{\pi \sigma_{crush}{}^2 R^4}{16 \sigma_y t} \left\{ \left(\frac{P^2}{\pi^2 R^4 \sigma_{crush}^2} \right)^4 \left[2 \ln \left(\frac{P}{\pi R^2 \sigma_{crush}} \right) - 1 \right] + 1 \right\} \quad (5.9)$$

A comparison of the absorbed energy calculated using Eq. 5.9 and the experimental absorbed energy from the indentation tests as reported in Chapter 6 is shown in Table 5.1. A value of 265MPa has been taken for the aluminium yield strength, σ_y, and the honeycomb crush strength, σ_{crush}, is as given in Table 2.9. Although Eq. 5.9 applies to loading with an FE indenter an approximation can be made for the HS loading case, where the indenter radius at ultimate failure is assumed to be 5mm. Reasonable agreement is seen between the theoretical and experimental values with a maximum error of 18% for aluminium honeycomb panels loaded with the FE indenter. For the HS indenter the absorbed energy at failure is overestimated by up to 40% when an equivalent contact radius of 5mm is assumed. As Eq. 5.9 is highly dependent on contact radius this inaccuracy for the HS loading case is most likely due to a poor estimate of the contact radius, which may vary with skin thickness and core density. No prediction could be made for the panels with a nomex honeycomb core as the yield strength of the nomex material is unknown.

Table 5.1 Theoretical (Eq. 5.9) and experimental values of absorbed energy for panels resting on a solid foundation loaded to ultimate failure

	HS indenter				FE indenter			
Specimen ID	Load (kN)	AE (J)	E_{theory} (J) Eq. 5.9	% Error	Load (kN)	AE (J)	E_{theory} (J) Eq. 5.9	% Error
4/50	3.00	7.75	8.78	32.22	5.21	17.87	19.69	10.18
4/70	3.14	6.72	7.84	38.71	5.39	13.80	15.75	14.13
8/50	5.27	16.69	15.89	3.28	9.78	43.48	43.72	0.55
8/70	6.33	16.85	20.14	28.19	9.28	31.99	30.32	5.22
8/90	7.11	17.83	22.90	36.53	9.23	25.75	24.24	5.86
12/50	8.16	28.37	28.32	9.17	14.40	79.30	71.21	10.20
12/70	7.89	21	22.23	16.63	13.20	47.93	47.03	1.88
12/90	10.86	35.84	40.61	22.17	13.88	47.53	44.37	6.64
16/50	9.18	36.2	27.63	-19.72	16.46	88.01	72.50	17.62
16/70	10.61	34.33	32.65	1.25	17.68	78.73	70.13	10.92

5.2.3. Models from Hoo Fatt and co-workers

The first significant work by Hoo Fatt and co-workers derived an analytical model for the local quasi-static indentation of a sandwich panel resting on a solid foundation [197]. The model was derived using the principle of minimum potential energy and employed an assumed deflection shape function. A number of assumptions were made in the analysis, taken from the earlier piece of work with Wierzbicki [73]; the skin was assumed to rest on the rigid-plastic foundation rather than being bonded to it, the initial peak present in the crushing of bare honeycomb was ignored such that a constant crush force was assumed, and as the levels of transverse skin deformation were several times the skin thickness the bending resistance was neglected with the skin response purely represented by membrane stretching. In addition the hemispherical indenter was approximated as a flat-ended indenter with an effective radius of 0.4R and an even contact pressure distribution to allow the minimisation of the potential energy without requiring numerical processing. The approximate analytical solution for a membrane on a rigid foundation, shown in Eq. 5.10, was seen to over predict the experimental load-displacement response by up to 15%. An attempt was also made to predict the top skin cracking load using maximum stress and Tsai-Hill criteria. However, the predicted loads did not correlate well with experimental data.

$$\alpha = \sqrt[3]{\frac{9\left(P - \pi\sigma_{crush}R_e^2\right)^2}{64C_1\sigma_{crush}}}$$

where (5.10)

$$C_1 = 8\left[\frac{1}{45}\left(A_{11} + A_{22}\right) + \frac{1}{49}\left(2A_{12} + 4A_{66}\right)\right]$$

An attempt was made to predict the work done in causing top skin perforation, core crushing and bottom skin perforation of metallic skinned honeycomb sandwich panels under impact loading in [198]. The top skin perforation analysis was an extension of the work in [73], with the incorporation of core-shear effects caused by the skin-core bond into the relationship between P and ξ given in Eq. 5.11. However, the bottom skin was assumed to remain undeformed until top skin penetration had occurred and assumptions

had to be made for the dynamic crushing/shearing strengths of the honeycomb and estimations of the effective radius of hemispherical indenters. A reasonable estimation of the ballistic limit was made, though the analytical values of deformation depth and width were significantly underestimated.

$$P = \pi \tau_{dyn} \xi^2 + \pi \sigma_{dyn\ crush} \left(\xi^2 - R^2 \right) \tag{5.11}$$

The methods used in [197] were extended in [79,80,187] and used in conjunction with a spring-mass-damper model to represent impact loading. The local membrane response was as derived in [197] with a similar method used to derive the local plate bending response for a plate on a rigid-plastic foundation, Eq. 5.12.

$$P = \frac{32}{15} \sqrt{2 D_1 \sigma_{crush} \alpha} + \pi \sigma_{crush} R^2$$

where (5.12)

$$D_1 = \frac{16384}{11025} \left(7D_{11} + 7D_{22} + 4D_{12} + 8D_{66} \right)$$

The global panel response for clamped or simply-supported panels was also modelled, using a FSDT process to include the effects of both bending and shear. The general solution is shown in Eq. 5.13, where the value of K_g was determined from the minimisation of potential energy, employing equations for the flexural stiffness of a sandwich panel taken from [200], and is dependent on the boundary conditions. Fully clamped, simply-supported and two edges clamped boundary conditions were considered and the effect of local deformations causing non-symmetry in the panel were neglected. The panels with two edges clamped were treated as wide beams whilst in the fully clamped case a transverse deformation shape was obtained from fitting functions to numerical solutions obtained from LS-DYNA. In the simply-supported case the deflection shapes were taken from exact series solutions for a simply-supported panel subjected to a central point load.

$$P = K_g \delta \tag{5.13}$$

The equations derived for the static loading case were used in calculating the dynamic response through the use of spring-mass-damper systems. Single-degree of freedom systems were used to represent panels resting on a solid foundation whilst two-degree of freedom systems were used for clamped panels, with a simplified linear local spring response for ease of analysis. Dynamic material properties were used to replace static properties where necessary. In addition to the prediction of the top skin tensile failure load in [197] equations were also generated for the core shear failure load, assuming a rigid-plastic foundation, and the bottom skin fracture load, using Timoshenko plate bending theory and maximum tensile strains. The analytical load-displacement response and associated failure loads were compared with experimental data from [2,7,8] and a 10-25% variation between analytical and experimental results was observed. The errors in the analytical values were primarily due to the assumed deflection shapes and methods used to obtain dynamic material properties.

In the more recent paper [188] a different deflection shape function was employed in forming the local membrane response and the contact pressure under the hemispherical indenter was defined as a function of contact radius rather than being approximated as a flat-ended indenter of an effective radius and constant pressure, Eq. 5.14.

$$p = \frac{3P}{2\pi\rho^2}\sqrt{1-\left(\frac{r}{\rho}\right)^2} \tag{5.14}$$

Bottom skin failure load and deflection were derived though the minimisation of potential energy and membrane stretching with global deflection shapes taken from LS-DYNA. Although these equations appear to correlate reasonably well with the experimental data from [13] closed form solutions for the local response cannot be obtained without the use of numerical methods, in this case the Monte Carlo numerical method. Additionally the model still requires assumptions for the deflection shapes, a skin-core constrain factor and dynamic material properties.

The accuracy of Hoo Fatt's theory has been assessed by comparing the above theory with the experimental data obtained from indentation testing. In [187] experimental data for sandwich panels with 0.325mm skins indented with a HS indenter and resting on a solid foundation was within 15% of analytical predictions when the panel was modelled as a membrane on a rigid plastic foundation, Eq. 5.10. Similarly for clamped square panels with 3.5mm thick skins loaded with a FE indenter and modelled as a plate on an elastic foundation considering both the local and global responses the analytical predictions were found to be within 10% of the experimental data.

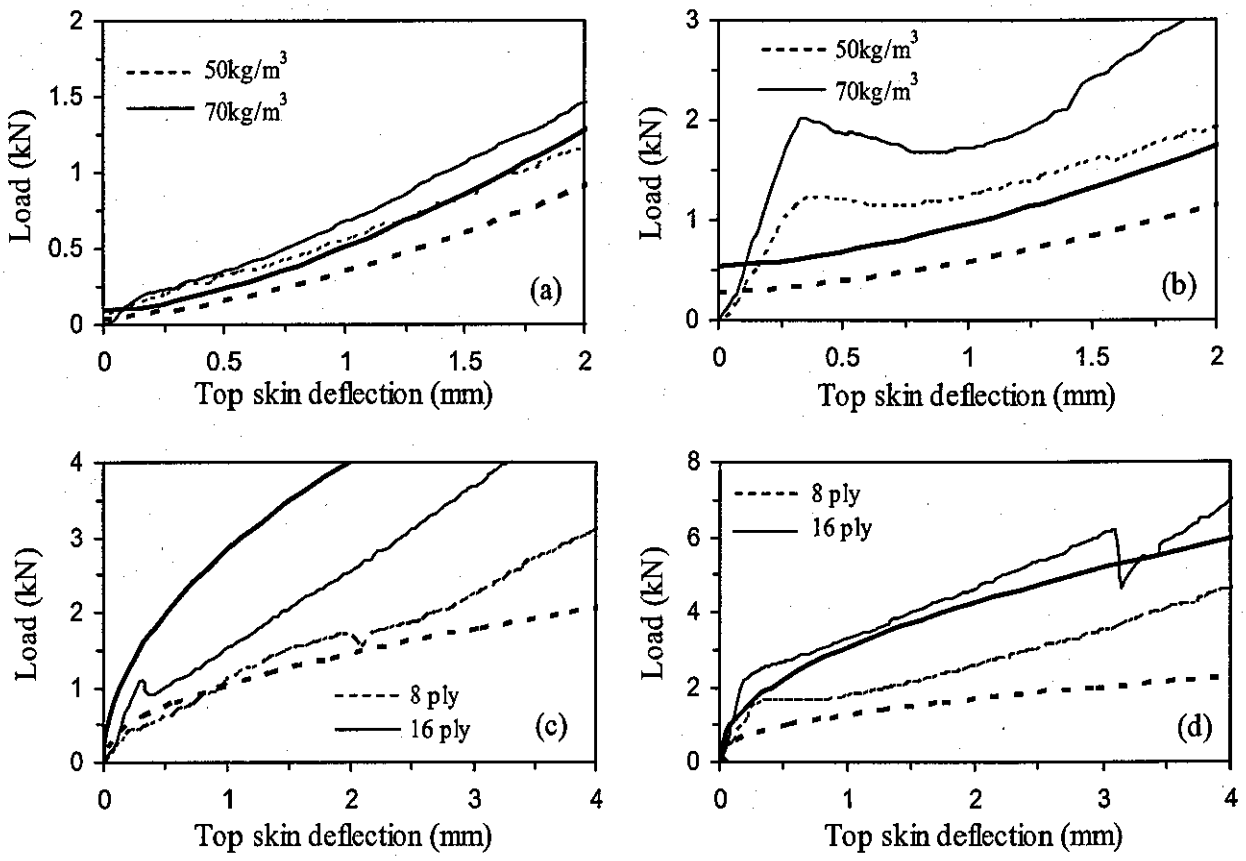

Legend: Thick line – Analytical prediction Thin line – Experimental data

Figure 5.1 Comparison of Hoo Fatt's analytical theory with experimental data from indentation testing (a) 4/50/HS(ind) & 4/70/HS(ind) with Eq. 5.10 (b) 4/50/FE(ind) & 4/70/FE(ind) with Eq. 5.10 (c) 8/50/HS(ind) & 16/50/HS(ind) with Eq. 5.12 + 5.13 (d) 8/50/FE(ind) & 16/50/FE(ind) with Eq. 5.12 + 5.13

In the indentation tests completed as part of this research the response of the sandwich panels with 4 ply skins and both 50kg/m^3 and 70kg/m^3 aluminium honeycomb cores was more comparable to a membrane than a plate. However, the correlation between the analytical prediction obtained from Eq. 5.10 and the experimental data was poor for the HS loading case and terrible for the FE loading case, as shown in Fig. 5.1(a & b). The thicker 8 and 16 ply panels with a 50kg/m^3 core were modelled as a plate on a rigid plastic foundation, Eq. 5.12, and in both cases the correlation between the analytical prediction and the experimental data was poor, as shown in Fig. 5.1(c & d). Due to the poor correlations obtained the application of Hoo Fatt's theory to other indentation cases and the more complicated indentation response of panels loaded in bending, has not been attempted.

5.2.4. Model by Sburlati

Sburlati [174] presents an analytical model for the indentation of a foam core sandwich panel. A Hertzian pressure distribution is assumed and the panel treated as an elastic half space. Each skin is assumed to act as a membrane with negligible bending and transverse shear resistance and an antiplane core is assumed. The plate stiffness is assumed to be composed of skin membrane stiffness and core shear stiffness. In determination of the membrane response both skins are assumed to deflect by the same amount. Analytical solutions are given for both clamped and simply-supported circular sandwich panels loaded with either flat-ended or hemispherical indenters. The solution is separated to give the individual contributions of both the core and skins, Eq. 5.15. The equations for panels with a clamped boundary and loaded with a hemispherical or flat-ended indenter are given in Eqs. 5.16 and 5.17 respectively.

$$\alpha = \alpha_c + \alpha_s \tag{5.15}$$

$$\alpha_c^{HS} = \frac{P}{2\pi c G_c}\left(\left(\ln 2 + \ln\frac{R_e}{b}\right) - \frac{5}{6}\right)$$
$$\alpha_s^{HS} = \frac{P}{2\pi c^2 t E_s}\left(\frac{1}{4}b^2\left(\nu_s^2 - 1\right) - \frac{23}{75}R_e^2\left(\nu_s^2 - 1\right) + \frac{1}{5}R_e^2\left(\nu_s^2 - 1\right)\left(\ln 2 + \ln\frac{R_e}{b}\right)\right) \quad (5.16)$$

$$\alpha_c^{FE} = \frac{P}{2\pi c G_c}\left(\left(\ln 2 + \ln\frac{R}{b}\right) - \frac{1}{2}\right)$$
$$\alpha_s^{FE} = -\frac{P}{2\pi c^2 t E_s}\left(\frac{1}{4}b^2\left(\nu_s^2 - 1\right) - \frac{4}{9}R^2\left(\nu_s^2 - 1\right) + \frac{1}{3}R^2\left(\nu_s^2 - 1\right)\left(\ln 2 + \ln\frac{R}{b}\right)\right) \quad (5.17)$$

As the model is based upon linear theory and does not account for damage it is only applicable prior to the initiation of core crushing at the initial threshold. Good correlation was seen between the analytical solution, FEM analysis and experimental data obtained from Anderson et al. [154] for the load-indentation response of simply-supported panels loaded in bending with a hemispherical indenter. A comparison of Eqs. 5.16 and 5.17 with data from bending tests completed as a part of this research also shows reasonable accuracy. Although the theory was developed for foam core sandwich panels it is very accurate for sandwich panels with aluminium honeycomb and thicker skins when the honeycomb shear modulus, G_c, is taken for the weaker 'W direction'. For the panels with 4 ply skins, which are known to behave more like a membrane than a plate, the theory slightly underestimates the indentation for a given load. However, the predicted indentation for the nomex honeycomb core panels is closer to the total top skin deflection than the top skin indentation. The inability of the theory to accurately predict the indentation may in part be due to the very low shear modulus of nomex, which permits large amounts of panel bending at low loads and is accentuated when using a larger contact area as in the case of the flat-ended indenter. Therefore the model should only be applied to panels of sufficient shear stiffness that offer adequate resistance to global bending at low loads.

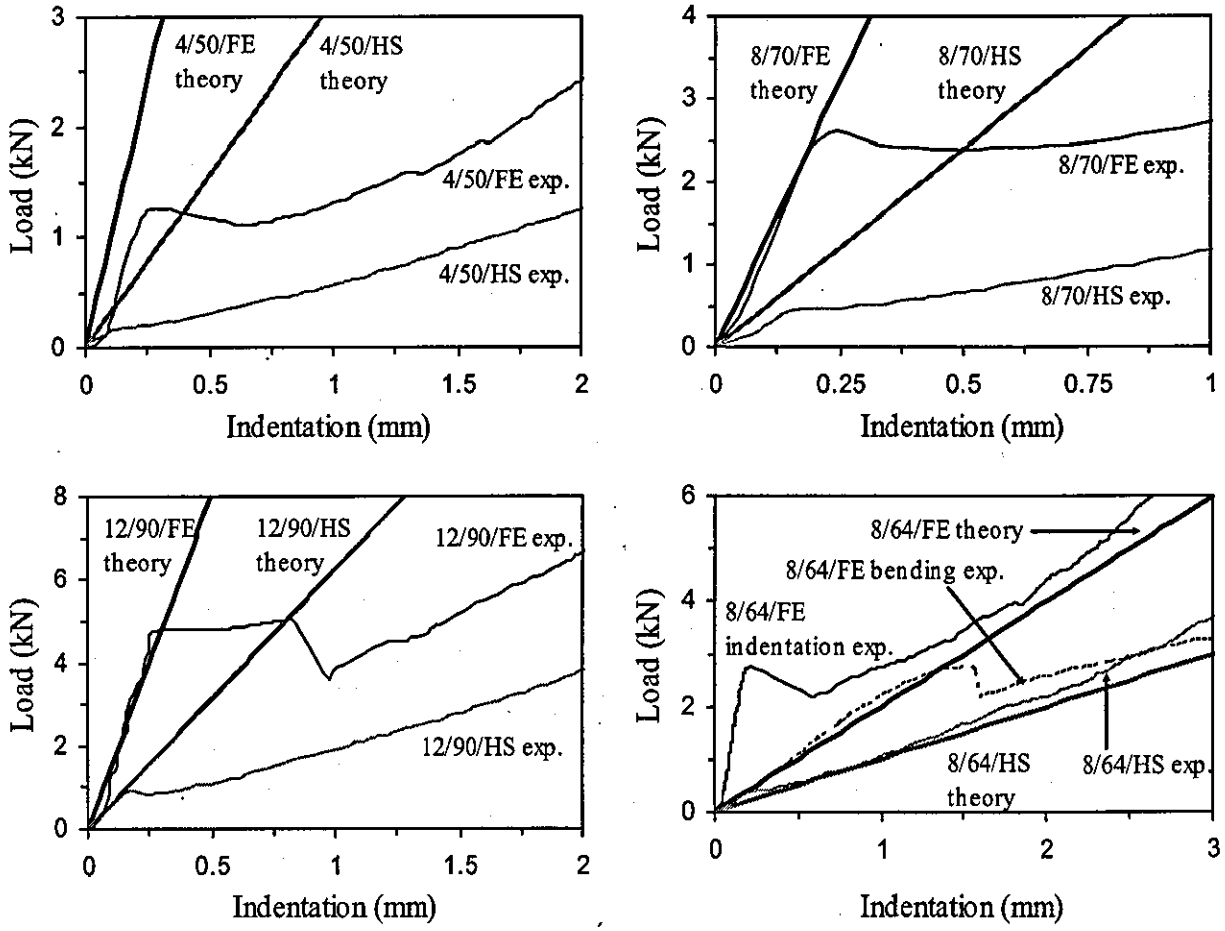

Legend: Thick line – Analytical prediction Thin line – Experimental data

Figure 5.2 Comparison of Sburati's analytical theory (Eqs. 5.16 and 5.17) with experimental data for top skin indentation of a panel loaded in bending (a) 4/50/HS&FE (b) 8/70/HS&FE (c) 12/90/HS&FE (d) 8/64/HS&FE

5.2.5. Model by Wen and Reid et al.

The analytical method proposed by Wen et al. [7] to predict the top skin failure load and absorbed energy of square foam core sandwich panels loaded with both hemispherical and flat-ended indenters is an adaptation of the energy balance model for circular monolithic laminates created by Shivakumar et al. [186]. Equivalent stiffnesses for k_c, k_b and k_s are formulated for a square sandwich panel. The membrane stiffness, k_m, is neglected as the top skin deflection is stated to be small at the point of top skin failure.

This assumption is questionable as deflections greater than the top skin thickness have been observed not only in this research but also in numerous other experimental studies.

The contact stiffness, k_c, has been derived for a hemispherical indenter in the same way as Shivakumar, with a slight modification for the panel modulus used in the calculation. The shear stiffness, k_s, is as defined by Shivakumar for a circular plate in Eq. 5.18, whilst the bending stiffness, k_b, is quoted for a square sandwich panel, said to be taken from Timoshenko [201], Eq. 5.19. The value of E_p in the equations for k_b and k_s is defined as the equivalent modulus for a sandwich panel, calculated through Eq. 5.20. For a flat-ended indenter the contact equations used are those developed by Fabrikant et al. [202,203] for isotropic plates, Eq. 5.21. To find the elastic constant, H_0, in Eq. 5.21 elasticity theory and the rule of mixtures for composite laminates is employed. However, in the derivation of the stiffness equations a one-dimensional stress-strain relationship is assumed whereas it should be at least two-dimensional for a plate, forming one of the major limitations of this model.

$$k_s = \frac{4\pi}{3} G_c c \left(\frac{E_p}{E_f - 4\nu_{12} G_c} \right) \left(\frac{4}{3} + \log \frac{L}{2R} \right)^{-1} \tag{5.18}$$

$$k_b = \frac{86.2 E_p (c+2t)^3}{12\left(1-\nu_{12}^2\right) L^2} \tag{5.19}$$

$$E_p = E_c r^3 + E_s \left(1 - \left[\frac{c}{c+2t} \right]^3 \right) \tag{5.20}$$

$$P^{FE} = \frac{2R}{\pi H_0} \alpha \tag{5.21}$$

To allow a value of absorbed energy to be obtained along with failure mode maps some assumptions are made for the load required for top skin failure. In the HS loading case the maximum force at top skin failure is calculated using the Hertzian contact law given in Eq. 5.22 with an assumed indentation depth of 1mm, taken from experiments. This assumption is highly questionable as it is known from the experimental data collected in this research that the indentation depth at top skin failure varies with the intrinsic variables, especially skin thickness. Also the force contribution resulting from both

panel bending and shear is ignored, although both bending and shear stiffness are included in the calculation of absorbed energy at top skin failure, Eq. 5.23. For loading with an FE indenter the top skin failure load is assumed to be directly related to the transverse shear strength of the skin and core crushing, given in Eq. 5.24. This equation for failure load is then combined with a previously defined energy equation to give the absorbed energy for top skin failure, AE^{FE}, in Eq. 5.25. Normalised experimental values for maximum load and energy are compared with the analytical predictions, which show the accuracy of these equations to be quite poor, especially when applied to low density cores. No graphical prediction is given for the load-displacement response despite a theoretical relationship between load and displacement being given.

$$P_{ult}^{HS} = k_c \alpha^{1.5} \tag{5.22}$$

$$AE^{HS} = \frac{2}{5}\left(\frac{\left(P_{ult}^{HS}\right)^5}{k_c^2}\right)^{1/3} + \frac{\left(P_{ult}^{HS}\right)^2}{2k_{bs}} \tag{5.23}$$

$$P_{ult}^{FE} = 2\pi R t \tau_{13} + \pi R^2 K \sigma_c \tag{5.24}$$

$$AE^{FE} = \frac{\left(P_{ult}^{FE}\right)^2}{2}\left(\frac{1}{k_c} + \frac{1}{k_{bs}}\right) + \pi \tau_{13} R t^2 \tag{5.25}$$

Although this model is limited and makes some questionable assumptions in analytical terms it is comparatively simple and sections of the model have been adopted by other researchers [41,187]. Inclusion of the membrane effects may improve the model, especially when applied to sandwich panels with thin skins. Additionally as the method is based upon elastic spring constants, which as discussed previously for spring-mass models are only applicable prior to permanent material damage occurring, the model may be more accurate when applied to the initial linear region rather than being used to predict the top skin failure load, which only occurs after extensive core crushing.

To apply the model to the experimental results obtained from the panel bending tests requires minor modification to the bending stiffness, k_b, as Wen developed the model for square sandwich panels. An equivalent equation for a clamped circular sandwich panel loaded at the centre can be adapted from Shivakumar [186] using the equivalent

flexural modulus of a sandwich panel, E_p, developed by Wen, given in Eq. 5.26. The shear and contact stiffnesses used in Wen's model are applicable to circular panels so do not require modification.

$$k_b = \frac{4\pi E_p (c+2t)^3}{3(1-\nu_{12}^2)b^2} \tag{5.26}$$

The top skin failure load for panels loaded in bending with both hemispherical and flat-ended indenters has been predicted using Eqs. 5.22 and 5.24 respectively. The predicted and experimental values, which are compared in Table 5.2, show the load to be under predicted for the FE loading case but massively over predicted for the HS loading case. As the predicted values of the ultimate failure load are not correct the experimental values for load are used in calculating the absorbed energy, using Eqs. 5.23 and 5.25. For the panels with an aluminium honeycomb core the absorbed energy is underestimated by 35-75% but is largely overestimated for the panels with a nomex honeycomb core. The absorbed energy has also been calculated for the initial threshold using Eqs. 5.23 and 5.25, excluding the effects of skin shear in Eq. 5.25, and taking the experimental value for the initial threshold load. Interestingly for the panels with an aluminium honeycomb core loaded with either the HS or FE indenter the energy is underestimated for the panels with thin skins but overestimated for panels with thick skins. This trend is reflected in the predicted load-displacement response, as shown in Fig. 5.3 for panels with a 70kg/m^3 aluminium honeycomb core loaded in bending with the HS indenter.

Despite large increases in bending stiffness with small increases in skin thickness the predicted load-displacement response is almost identical for all panels with 4, 8, 12 and 16 ply skins. One factor known to have a large effect on the theoretical predictions is the contact radius of the hemispherical indenter. The theoretical values calculated in Table 5.2 were based upon the contact radius equations given by Wen though the predicted radii were often smaller than the experimental observations suggested. Additionally the contact law used in Wen's model for the hemispherical loading case is directly taken from laminate plate theory, which is known to differ for sandwich panels

[41,74,180]. This has a direct effect on both the predicted ultimate failure load for the hemispherical indenter and absorbed energy. Therefore if more accurate predictions are to be obtained a correct representation of the contact conditions in terms of both stiffness and contact area is required.

Table 5.2 Theoretical (Eqs. 5.22-5.25) and experimental values of absorbed energy and failure load for panels loaded in bending with the HS and FE indenters

Specimen	Experimental				Predicted					
	Initial threshold		Ultimate failure		Initial threshold		Ultimate failure			
	Load (kN)	Energy (J)	Load (kN)	Energy (J)	Energy (J)	% Error	Load (kN)	% Error	Energy (J)	% Error
4/50/HS	0.16	0.03	3.09	8.73	0.01	-61.97	25.33	719.73	3.17	-63.71
8/50/HS	0.37	0.06	5.41	20.09	0.05	-9.37	44.44	721.41	9.25	-53.95
12/50/HS	0.71	0.18	7.65	28.63	0.19	4.81	58.06	658.99	18.09	-36.81
16/50/HS	1.38	0.40	9.25	40.63	0.68	69.28	71.48	672.74	26.24	-35.41
4/70/HS	0.28	0.06	4.00	10.77	0.03	-57.94	27.11	577.86	3.89	-63.88
8/70/HS	0.48	0.13	6.22	19.74	0.07	-48.24	46.03	640.09	8.95	-54.65
12/70/HS	0.96	0.25	8.32	29.02	0.25	0.22	59.51	615.28	15.66	-46.04
16/70/HS	1.46	0.36	10.32	37.20	0.56	55.11	72.80	605.43	23.78	-36.08
4/90/HS	0.24	0.04	4.26	11.14	0.02	-60.74	29.03	581.41	3.58	-67.85
8/90/HS	0.42	0.05	7.86	27.90	0.04	-14.38	47.74	507.44	11.32	-59.44
12/90/HS	0.91	0.14	9.85	36.21	0.18	31.31	61.07	519.96	17.42	-51.91
16/90/HS	1.31	0.23	14.05	56.87	0.37	59.52	74.22	428.24	34.47	-39.38
8/64/HS	0.38	0.08	6.22	22.13	0.23	183.11	43.36	597.03	49.97	125.81
12/64/HS	0.76	0.20	8.17	29.64	0.88	337.70	57.08	598.64	85.91	189.86
16/64/HS	1.31	0.59	12.76	58.07	2.54	329.76	70.58	453.15	205.58	254.02
8/96/HS	0.31	0.08	6.44	24.44	0.11	35.48	44.05	584.02	37.66	54.10
12/96/HS	0.80	0.22	10.34	39.23	0.68	210.26	57.71	458.13	95.15	142.54
16/96/HS	1.25	0.49	13.40	53.77	1.63	233.00	71.16	431.03	158.75	195.23
4/50/FE	1.26	0.39	4.99	22.35	0.32	-18.97	3.28	-34.30	5.44	-75.65
8/50/FE	1.73	0.56	8.66	38.07	0.58	2.95	5.22	-39.74	16.39	-56.96
12/50/FE	1.68	0.48	13.94	72.74	0.54	11.85	7.16	-48.65	41.33	-43.18
16/50/FE	2.38	0.78	16.77	91.80	1.07	37.06	9.10	-45.75	60.84	-33.73
4/70/FE	2.18	0.68	5.12	17.39	0.70	2.44	4.47	-12.78	4.33	-75.12
8/70/FE	2.31	0.84	9.20	35.72	0.75	-10.43	6.41	-30.37	13.87	-61.16
12/70/FE	2.75	1.16	12.80	55.61	1.05	-9.46	8.35	-34.80	27.12	-51.23
16/70/FE	3.63	1.17	16.67	74.82	1.81	54.94	10.29	-38.30	45.99	-38.53
4/90/FE	2.93	1.41	5.36	15.26	1.01	-28.31	5.44	1.49	3.87	-74.65
8/90/FE	3.50	1.53	9.95	38.06	1.38	-9.71	7.38	-25.83	13.11	-65.57
12/90/FE	4.68	1.84	14.02	60.37	2.43	31.95	9.32	-33.53	26.15	-56.68
16/90/FE	4.71	1.55	19.75	91.79	2.43	56.95	11.26	-42.99	50.53	-44.95
8/64/FE	2.74	2.51	8.70	40.34	6.08	142.14	6.35	-27.02	63.21	56.70
12/64/FE	3.43	2.41	12.40	64.70	9.48	293.30	8.29	-33.15	128.24	98.21
16/64/FE	4.53	3.66	17.00	91.49	16.48	350.28	10.23	-39.83	239.85	162.17
8/96/FE	3.36	2.31	8.57	42.87	6.43	178.33	9.19	7.22	43.77	2.09
12/96/FE	3.94	2.22	12.04	53.86	8.79	295.91	11.13	-7.57	86.44	60.49
16/96/FE	6.46	5.81	17.55	75.48	23.54	305.10	13.07	-25.53	181.47	140.42

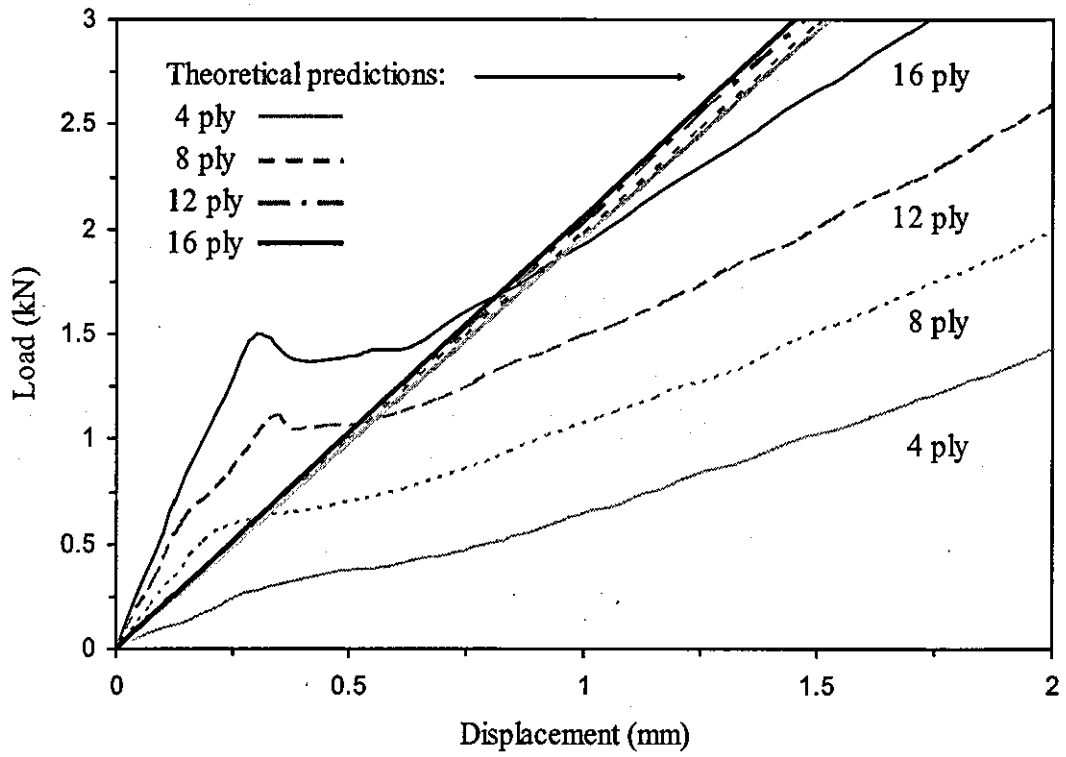

Figure 5.3 Comparison of theoretical and experimental load-displacement curves for 70kg/m^3 aluminium honeycomb sandwich panels with various skin thicknesses loaded with hemispherical indenter

5.3. Concluding remarks

An overview has been given of the various analytical prediction methods currently available for the transverse loading of sandwich panels, with the significant papers documented. Whilst a large number of papers have been published on numerical models employing higher order theories, these types of model do not lend themselves to situations where a quick estimation of panel performance is required and are too complex for the majority of composite engineers working within industry. Few papers have been published that give reasonably simple yet accurate analytical predictions of the critical values relating to transverse loading. Of the papers reviewed the most promising models that do not require numerical techniques to obtain a solution have been applied and compared with experimental data collected during this research project.

Of the models considered those from Wierzbicki et al. [73] and Sburlati [174] are the most promising. Wierzbicki's model for predicting the absorbed energy at top skin failure of a panel resting on a solid foundation loaded with an FE indenter gives values within 18% of the experimental data. However, the model is only applicable to FE indenters and also could not be applied to panels with a nomex honeycomb core as the yield strength of the nomex material is unknown. Sburlati's model for predicting the top skin indentation of panels loaded in bending shows a very good correlation with experimental data for aluminium honeycomb panels but is poor when applied to panels with nomex honeycomb. Additionally as it is based upon linear theory it is only applicable up to the initial threshold load.

Despite looking promising the models developed by Hoo Fatt and co-workers [79,80, 187,188,197,198] and Wen et al. [7] did not produce good correlations with the experimental data. The load-indentation response of sandwich panels loaded with HS and FE indenters predicted from the models by Hoo Fatt was poor for both thick and thin panels. Although the model included a number of questionable assumptions the accuracy was much worse than seen in comparisons made by Hoo Fatt. Similar was also true for the predictions made using Wen's model for top skin failure load and absorbed energy of panels loaded in bending. Top skin failure loads of aluminium honeycomb panels loaded in bending with the FE indenter were under predicted by up to 50% and even when the experimental loads were used to calculate absorbed energy the predicted values had an error of up to 75%. As with all the other models the predictions for the nomex honeycomb panels were much worse than for the aluminium honeycomb panels. Although the accuracy of Wen's model seems to be poor this may in part be due to needing to determine a large number of constants, many of which were highly based on both experimental and theoretical values. In addition both Hoo Fatt and Wen's models require an estimate of the contact radius of the hemispherical indenter. Both models appear to be highly sensitive to changes in this value, which highlights the need to accurately represent the actual contact conditions that occur between the hemispherical indenter and the sandwich panel. If this can be modelled both Hoo Fatt and Wen's models may be improved.

6. DISCUSSION OF RESULTS FOR DAMAGE RESISTANCE

The damage resistance performance of sandwich panels can be evaluated both in terms of the specific damage mechanisms, associated load and stiffness levels and the energy absorption capacity. The basic damage mechanisms involved in quasi-static transverse loading have been assessed in Section 4.4. Building upon the findings of Chapter 4 the focus of this chapter is on the effect of varying skin thickness, core density, indenter nose-shape and loading rate. A number of tests have also been completed on panels with varying skin material, core material, size and support conditions and the results compared to the baseline 100mm diameter sandwich panels with an aluminium core and T700/LTM45-EL skins. These tests provide additional insight into the factors most affecting the sandwich panel response under transverse loading. The effect of loading rate has been studied through comparison of quasi-static test results with low-velocity impact test results for a variety of panel configurations.

It is very important in structural design to understand how changing parameters such as skin thickness, core material and density, indenter nose-shape and panel boundary conditions affect the performance of a panel under transverse loading. In some instances determination of the initial and secondary damage load thresholds was compounded if the specimen did not undergo a load drop. This combined with an amount of normal experimental variation in the results led to substantial variation in some of the values. Consequently average values have been taken where possible and a full listing of the critical loads, displacements and stiffnesses are contained in Tables 6.13-6.23 at the end of this section. Numerous graphs illustrating the effects of changing each variable are also included in Appendix B for completeness.

6.1. Effects of varying the major parameters on damage mechanisms

6.1.1. Effect of varying skin thickness on damage mechanisms

Load-displacement curves comparing the response of panels with different skin thicknesses are shown in Figs. B1-B5 in Appendix B, with the critical loads representative of initial damage and ultimate failure directly compared in Fig. 6.1(a-c). Also included in Fig. 6.1(a-c) where applicable is the peak load of the bare honeycomb loaded with the FE indenter (values taken from Table 4.5). The damage mechanisms witnessed at initial damage and ultimate failure were similar for all skin thicknesses. Although internal damage length does typically increase with skin thickness as seen from Table 4.8, no general trends can be identified for delamination growth but core crushing length does appear to increase with skin thickness in Fig. 6.2.

There seem to be a linear relationship between skin thickness (number of plies in the skin) and initial damage load when loading with the FE indenter as shown in Fig. 6.1(a). The variation in the experimental data from the line of best fit may be due to the initial threshold sometimes being indicated by a smooth change in gradient rather than a clear load drop, such that the variation associated with defining the threshold is greater. For loading with the HS indenter the variation of initial damage load with skin thickness is of a polynomial form, Fig. 6.1(b). The function of $y \propto x^4$ is possibly better suited than the function of $y \propto x^2$, in which x and y denote the skin thickness and initial threshold load respectively.

The relationship between skin thickness and ultimate failure load in Fig. 6.1(c) is linear for both the HS and FE indenters. The good correlation is assisted by the point of ultimate failure being clearly defined by a large load drop in all cases. On average doubling the skin thickness causes the ultimate failure load to increase by 80%, corresponding to a 3.5 and 4kN load increase for every 0.5mm thickness increase for the HS and FE loading cases respectively.

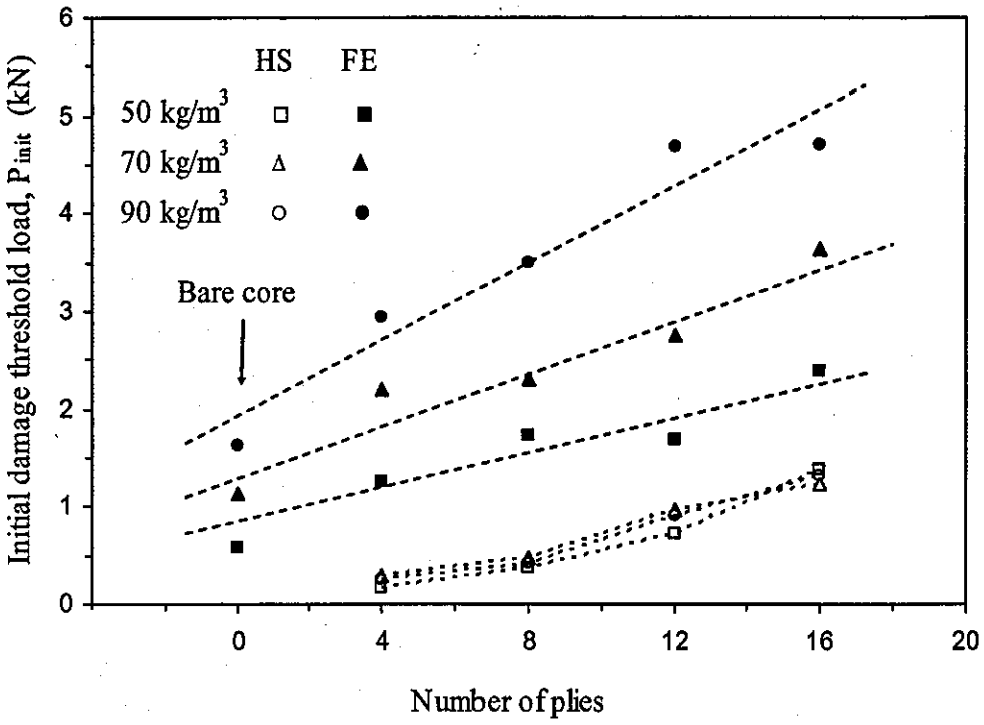
HS
FE
50 kg/m3
70 kg/m3
90 kg/m3
Bare core
Initial damage threshold load, Pinit (kN)
Number of plies
0
1
2
3
4
5
6
0
4
8
12
16
20

(a)

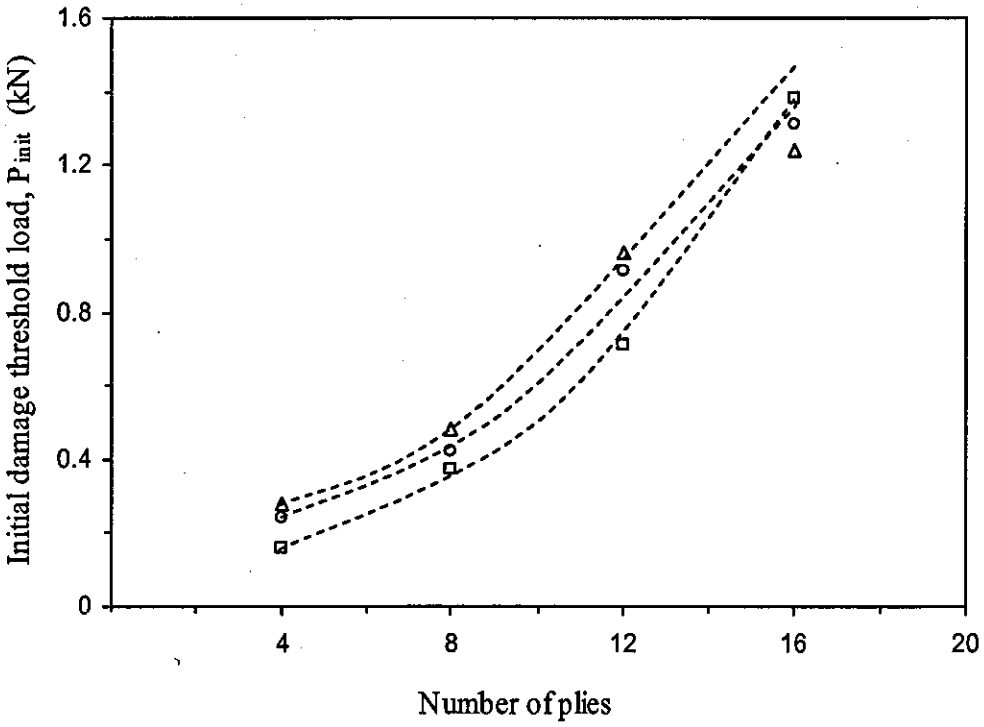
Initial damage threshold load, Pinit (kN)
Number of plies
0
0.4
0.8
1.2
1.6
4
8
12
16
20

(b)

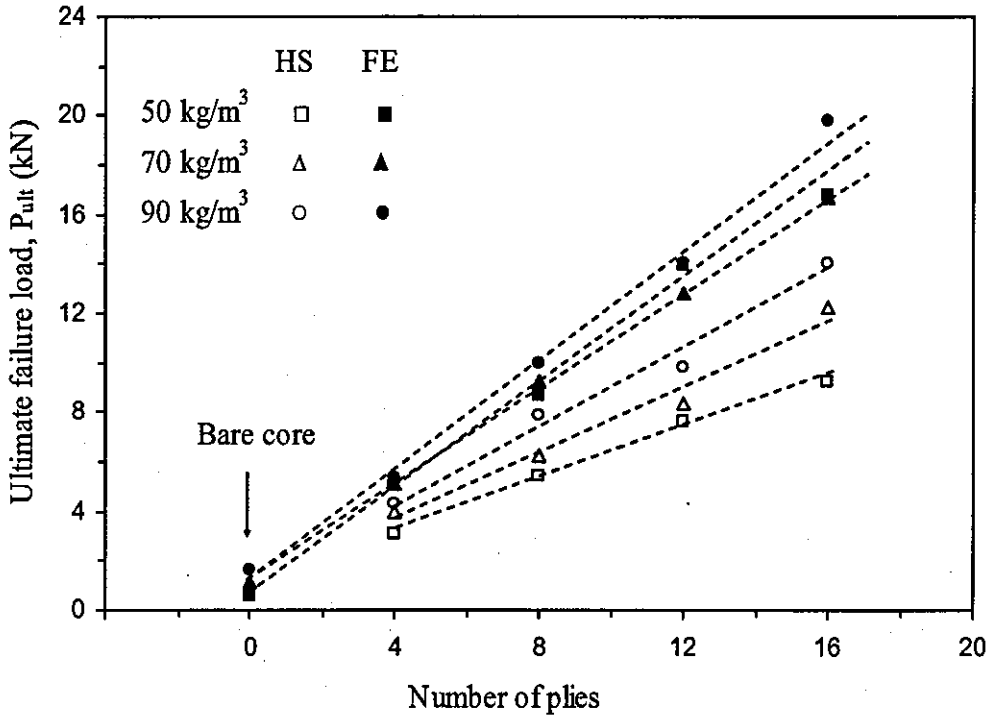

(c)

Figure 6.1 Variation of threshold loads with the number of plies in the skins (a) initial damage threshold for HS and FE indenter (b) expanded view of previous plot for HS indenter only (c) ultimate failure for HS and FE indenter

The gradient of the load-displacement curve both prior to initial damage and ultimate failure, summarised in Table 6.14, also increases linearly with skin thickness in Fig. 6.3. Doubling the skin thickness causes a 90% and 30% increase in panel stiffness prior to initial damage in the HS and FE loading cases respectively. Prior to ultimate failure this becomes 50% and 60% respectively. A comparison of the panel stiffness prior to the initial threshold determined experimentally is compared with the theoretical flexural rigidity of a wide sandwich beam, calculated using Eq. 6.1 taken from [204], in Table 6.1. Typically the theoretical value of flexural rigidity overestimates the increase in panel stiffness determined experimentally.

$$D = \frac{E_s b t^3}{6(1-\nu_{xy}\nu_{yx})} + \frac{E_s b t (c+t)^2}{2(1-\nu_{xy}\nu_{yx})} + \frac{E_c b c^3}{12(1-\nu_c^2)} \tag{6.1}$$

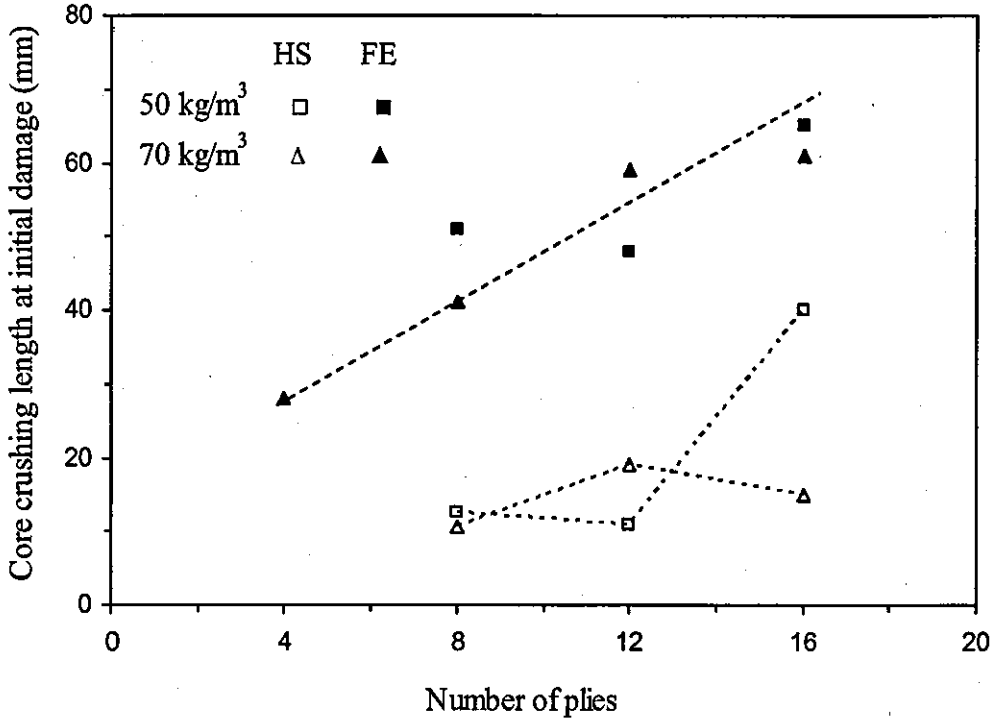

(a)

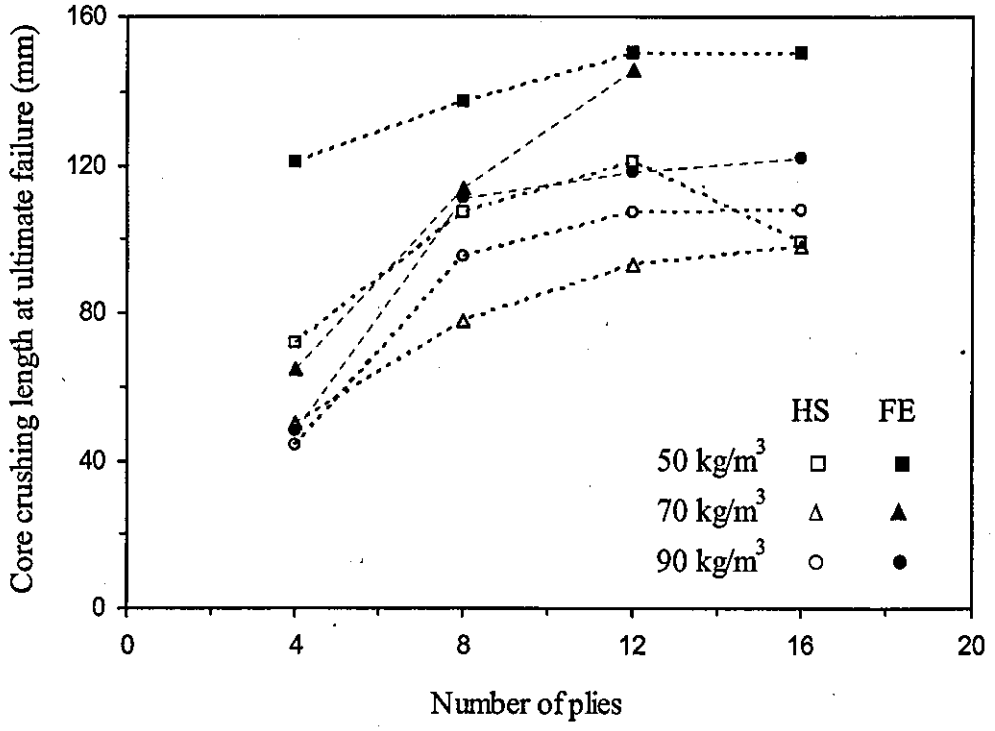

(b)

Figure 6.2 Variation of core crushing length with skin thickness

(a) initial damage threshold (b) ultimate failure

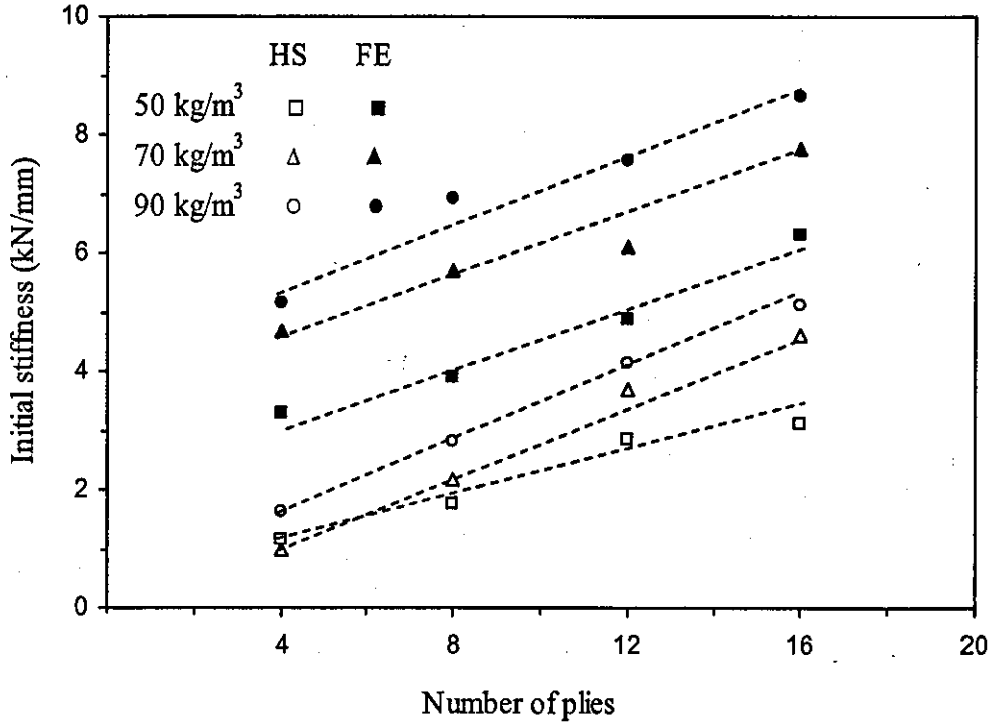

(a)

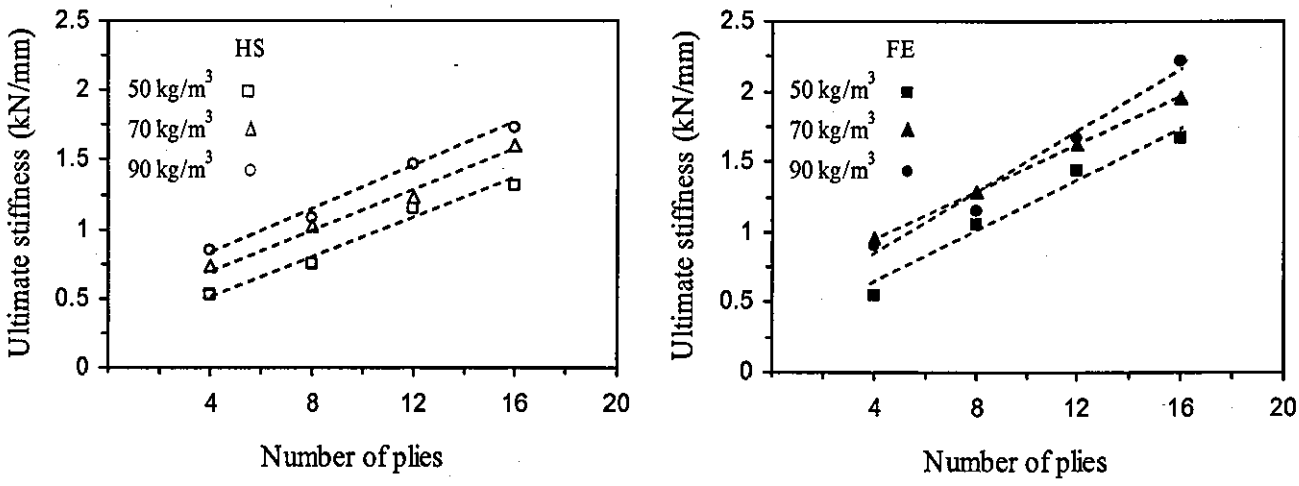

(b)

Figure 6.3 Variation of gradient of load-displacement curve with skin thickness
(a) prior to initial damage (b) prior to ultimate failure

Table 6.1 Comparison of panel stiffness increase prior to initial threshold, experimental (slope of load-displacement curve) & theoretical (flexural rigidity)

	Parameter	4 ply	8 ply	12 ply	16 ply
	Skin thickness, t, (mm)	0.5	1	1.5	2
	Increase in t	-	2	1.5	1.33
50kg/m^3 core	Flexural rigidity MNmm^2)	353	749	1151	1651
	Increase in flexural rigidity	-	2.12	1.54	1.43
	Increase in stiffness - HS indenter	-	1.55	1.60	1.10
	Increase in stiffness - FE indenter	-	1.19	1.25	1.29
70kg/m^3 core	Flexural rigidity (MNmm^2)	362	758	1160	1660
	Increase in flexural rigidity	-	2.09	1.53	1.43
	Increase in stiffness - HS indenter	-	2.23	1.70	1.25
	Increase in stiffness - FE indenter	-	1.22	1.07	1.27
90kg/m^3 core	Flexural rigidity (MNmm^2)	372	768	1170	1670
	Increase in flexural rigidity	-	2.06	1.52	1.43
	Increase in stiffness - HS indenter	-	1.75	1.46	1.23
	Increase in stiffness - FE indenter	-	1.34	1.09	1.15

6.1.2. Effect of varying core density on damage mechanisms

Load-displacement plots comparing the effect of honeycomb density for each skin thickness on load response are shown in Figs. B6-B12 in Appendix B, with the critical loads representative of initial damage and ultimate failure directly compared in Fig. 6.4. The ultimate failure load of the laminate plates has also been included where available. The damage mechanisms witnessed at initial damage and ultimate failure were similar for all core densities. There is no correlation between core density and internal damage size for a given skin thickness/indenter nose-shape.

At initial damage core density does not affect the threshold load when loading with the HS indenter but does cause a linear increase in threshold load when loading with the FE indenter, Fig. 6.4. This is expected as loading with the HS indenter is very localised and dominated by the skin resistance, as shown in the previous sub-section, Fig. 6.1(b). In the latter case the load is reacted by a much larger area of the panel and core crushing is the primary damage mechanism present at the initial damage threshold, Table 4.8. The similarity in the increase in bare core crushing strength and initial threshold load reflects

this in Table 6.2. The increase in core density of 40% for 50 to 70kg/m^3 and 30% for 70 to 90kg/m^3 also causes an increase in the initial panel stiffness in both the HS and FE loading cases, between 17-34%.

Table 6.2 Comparison of percentage increase in panel strength and stiffness with core density

	Parameter	Core density increase, HS loading		Core density increase, FE loading	
		50 to 70kg/m^3	70 to 90kg/m^3	50 to 70kg/m^3	70 to 90kg/m^3
Average percentage increase	Core density	40%	29%	40%	29%
	Bare core strength	-	-	97%	43%
	Crush strength	-	-	60%	35%
	Core modulus	-	-	93%	52%
	Initial load, P_{init}	32%	-6%	56%	46%
	Initial stiffness	22%	30%	34%	17%
	Ultimate load, P_{ult}	22%	17%	0%	10%
	Ultimate stiffness	26%	12%	33%	0%

At ultimate failure increasing the core density has a minimal effect on panel stiffness for both loading cases, shown in Fig. 6.5. For the HS loading case the ultimate strength of the panel increases with core density to a slightly larger extent than for the FE loading case, shown in Fig. 6.4. Even though the honeycomb undergoes cell wall buckling failure at the initial threshold it still provides crushing resistance throughout the loading range. As honeycomb crush strength increases with density, Table 6.2, it is therefore expected that this will cause an increase in the ultimate failure load of the panels. This increase will be small in comparison to that seen when increasing the skin thickness, as the skins dominate the panel response following initial damage. The increased effect of core density on the ultimate failure load of the panels loaded with the HS indenter is due to the smaller area of damaged honeycomb, meaning there is more undamaged core to resist loading. The effect of core density on panel stiffness is expected to be minimal as the increase in the flexural rigidity with core density is negligible, as shown in Table 6.1.

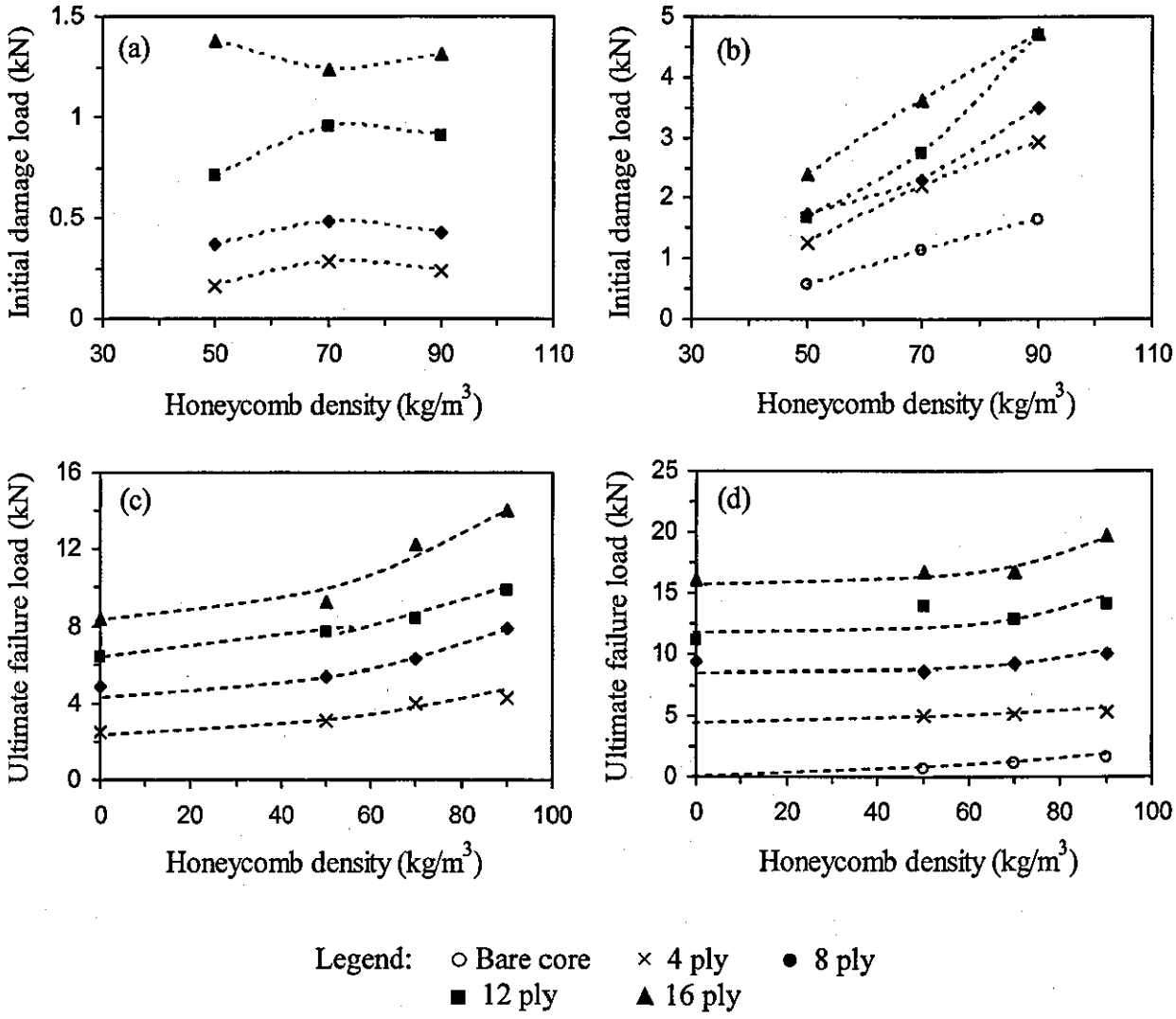

Figure 6.4 Variation of damage/failure load with honeycomb density:

(a) Initial threshold HS indenter (b) Initial threshold FE indenter

(c) Ultimate failure HS indenter (d) Ultimate failure FE indenter

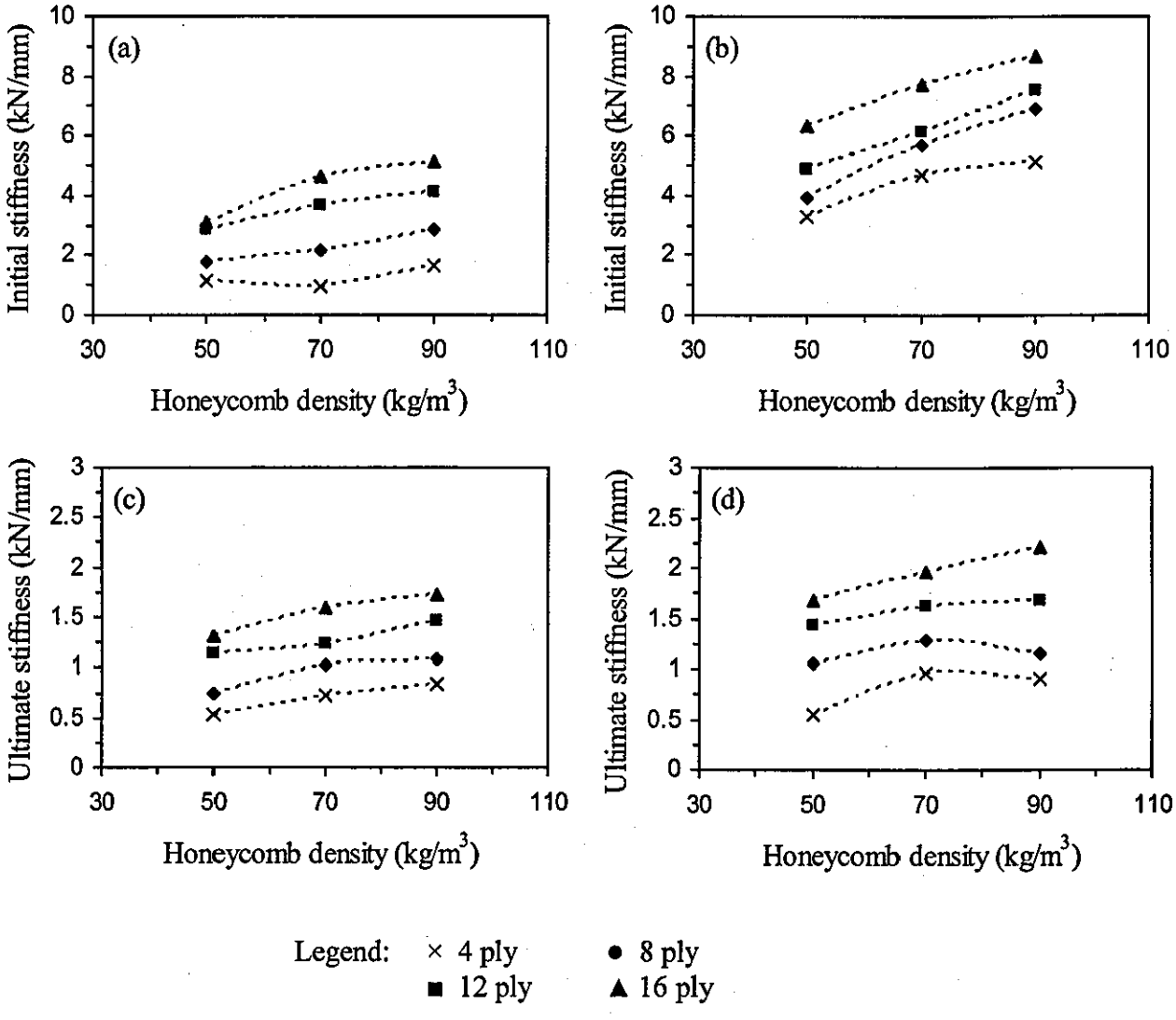

Figure 6.5 Variation of panel stiffness with core density:

(a) Initial stiffness HS indenter (b) Initial stiffness FE indenter

(c) Ultimate stiffness HS indenter (d) Ultimate stiffness FE indenter

6.1.3. Effect of indenter nose-shape on damage mechanisms

The effect of the indenter nose-shape on the load-displacement response is compared for each panel configuration in Figs. B13-B21 in Appendix B. The damage mechanisms connected with each indenter nose-shape were discussed in Section 4.4. In all instances panels loaded with the 20mm diameter FE indenter withstand a much higher load for a given displacement and undergo ultimate failure at a load on average 50% higher than those loaded with the 20mm diameter HS indenter. The panel stiffness between the initial threshold and ultimate failure is on average 20% higher for the panels loaded with the FE indenter. At ultimate failure the length of the core damage is always greater for the FE indenter by 1.1-1.7 times, as shown in Table 6.3. It is not possible to make accurate comparisons of skin delamination length due to its unstable nature but delamination length in the panels loaded with the FE indenter can be double that of those loaded with the HS indenter.

Table 6.3 Increase in threshold values when changing from HS to FE indenter $(\frac{FE\ value}{HS\ value})$

Panel type	Initial threshold			Ultimate failure		
	Load	Stiffness	Core damage (length in mm)	Load	Stiffness	Core damage (length in mm)
4/50	7.88	2.88	-	1.61	1.02	1.68 (49)
4/70	7.86	4.81	-	1.28	1.32	1.30 (15)
4/90	12.2	3.17	-	1.26	1.07	1.09 (4)
8/50	4.68	2.21	4.08 (38.5)	1.60	1.40	1.28 (20)
8/70	4.82	2.63	3.90 (30.5)	1.48	1.26	1.46 (36)
8/90	8.33	2.44	-	1.27	1.06	1.17 (16)
12/50	2.37	1.72	4.36 (37)	1.82	1.25	>1.24 (29)
12/70	2.89	1.66	3.11 (40)	1.54	1.33	1.57 (53)
12/90	5.14	1.82	-	1.42	1.14	1.10 (11)
16/50	1.72	2.03	1.63[a] (25)	1.81	1.27	>1.52 (51)
16/70	2.93	1.68	4.07 (46)	1.37	1.23	-
16/90	3.60	1.69	-	1.41	1.28	1.13 (14)

[a] : HS diagnostic test stopped well past point of initial damage

> : Core damage extends over entire 150mm panel length in FE case

\- : No diagnostic tests completed (except for 16/70 panel where FE panel is missing)

At the initial threshold core damage was dominant in both loading cases and accompanied by delamination in the HS loading case, Table 4.8. As expected the core crushing length is much greater in panels loaded with the FE indenter due to the larger contact diameter of 20mm, compared to an estimated 4mm for the HS indenter. Typically the number of damaged cells at the initial threshold increases approximately 4 times when changing from the HS to FE indenter, which generally corresponds to a 30-40mm increase in length. The constant increase in core crushing length when changing from HS to FE indenter is independent of skin thickness.

The trends shown in Table 6.3 regarding initial threshold load show the amount of increase in damage load with indenter type to be dependent on skin thickness, with the level of increase varying between 1kN to 3.8kN. Panel stiffness prior to the initial threshold is always greater when loading with the FE indenter, the increase being most significant for the thinner skinned panels. It is known that the panels with thinner skins react differently to loading than those with thicker skins. The thinner skins deform directly under and around the indenter, whilst the thicker skins distribute the load over a larger area so become less sensitive to indenter shape.

6.1.4. Effect of skin material on damage mechanisms

Quasi-static tests have been completed on sandwich panels with IM7/8552 skins to determine the effect of the skin material on sandwich panel performance. Panels with 4, 8, 12 & 16 ply skins and 70kg/m^3 aluminium core and panels with 12 ply skins and 50, 70 & 90 kg/m^3 aluminium and 64 & 96 kg/m^3 nomex honeycomb have been tested. Strain gauges were only used on the 12I/50/HS&FE IM7/8552 panels. All panels were loaded to ultimate failure and no diagnostic tests were conducted. An example comparison of the load-displacement response of each panel type is shown in Fig. 6.6, with curves comparing the performance of the two materials for all panel configurations included in Figs. B22-B29 in Appendix B with critical data summarised in Tables 4.11 & 6.19-6.21. The performance of the IM7/8552 panels is compared with the T700/LTM45-EL panels in terms of the load and damage levels at critical points in Table 6.4.

The response of the IM7/8552 and T700/LTM45-EL panels is similar up to the initial threshold. Panel stiffness is comparable whilst the initial threshold load is typically higher for the IM7/8552 panels, with an average increase of 30% for the HS loading case and 9% for the FE loading case. This increase in threshold load is as a direct consequence of the 30% higher interlaminar shear strength of the IM7/8552 material as shown in Tables 2.5 & 2.8. Although no diagnostic tests were completed on the IM7/8552 panels it is believed on the basis of the response characteristics in Figs. 6.6 & 6.7 that the damage mechanisms at the initial damage threshold are due to core crushing and minor delaminations as identified for the T700/LTM45-EL panels.

Table 6.4 Comparison of critical loads and damage within IM7/8552 and T700/LTM45-EL sandwich panels

Specimen	T700/LTM45-EL							IM7/8552			
	Initial threshold load (kN)	Secondary damage			Ultimate failure			Initial threshold load (kN)	Ultimate failure		
		Load (kN)	Core crushing (mm)	Delam. (mm)	Load (kN)	Core crushing (mm)	Delam. (mm)		Load (kN)	Core crushing (mm)	Delam. (mm)
4/70/HS[a]	0.28	2.67	-	-	4.00	52	48	0.21	1.23	10	38
8/70/HS	0.50	2.60	32	35	6.22	78	59	0.60	2.96	40	35
12/70/HS[a]	0.96	4.29	55	43	8.32	93	42	1.07	4.18	53	40
16/70/HS	1.24	6.49	65	47	12.21	95	46	1.75	5.96	58	43
12/50/HS[b]	0.75	3.35	83	37	7.65	121	30	1.05	3.62	82	62
12/90/HS[a]	0.91	4.20	-	-	9.85	107	61	1.34	3.76	37	44
12/64/HS	0.76	4.20	39	34	8.17	93	77	1.12	3.93	52	37
12/96/HS	0.80	2.21	-	-	10.34	85	53	1.27	4.76	40	35
4/70/FE	2.18	3.23	-	-	5.12	65	105	1.98	3.46	45	45
8/70/FE	2.31	4.65	71	53	9.21	114	45	2.75	5.97	78	53
12/70/FE[a]	2.75	7.10	92	0	12.83	146	44	3.17	8.47	77	83
16/70/FE	3.63	8.64	93	56	16.67	97+	96+	3.88	10.98	104	80
12/50/FE	1.68	6.63	110	8	13.94	150+	56	1.84	9.46	148+	75
12/90/FE[a]	4.68	5.04	-	-	14.02	118	101	3.30	8.75	41	46
12/64/FE[b]	3.43	5.23	71	0	12.40	122	119	2.90	8.72	106	50
12/96/FE	3.94	5.57	-	-	12.04	85	110	4.40	8.36	50	64

Note: Some IM7/8552 panels had skin-core debonding, results were used with caution
[a] indicates major top and bottom skin debonding in IM7/8552 panels
[b] indicates poor top skin bonding only in centre of IM7/8552 panels
\+ indicates damage spread to panel edge or to limit of photo in 16/70/FE case

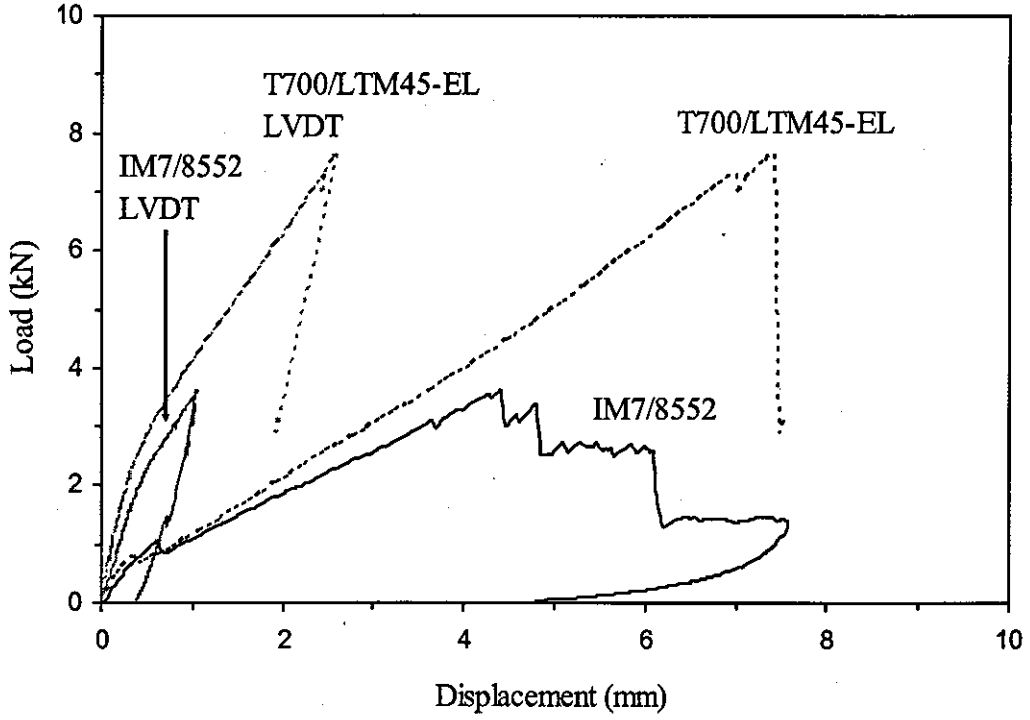

Figure 6.6 Load-displacement response of 12 ply 50kg/m^3 sandwich panels with different skin materials loaded with the HS indenter

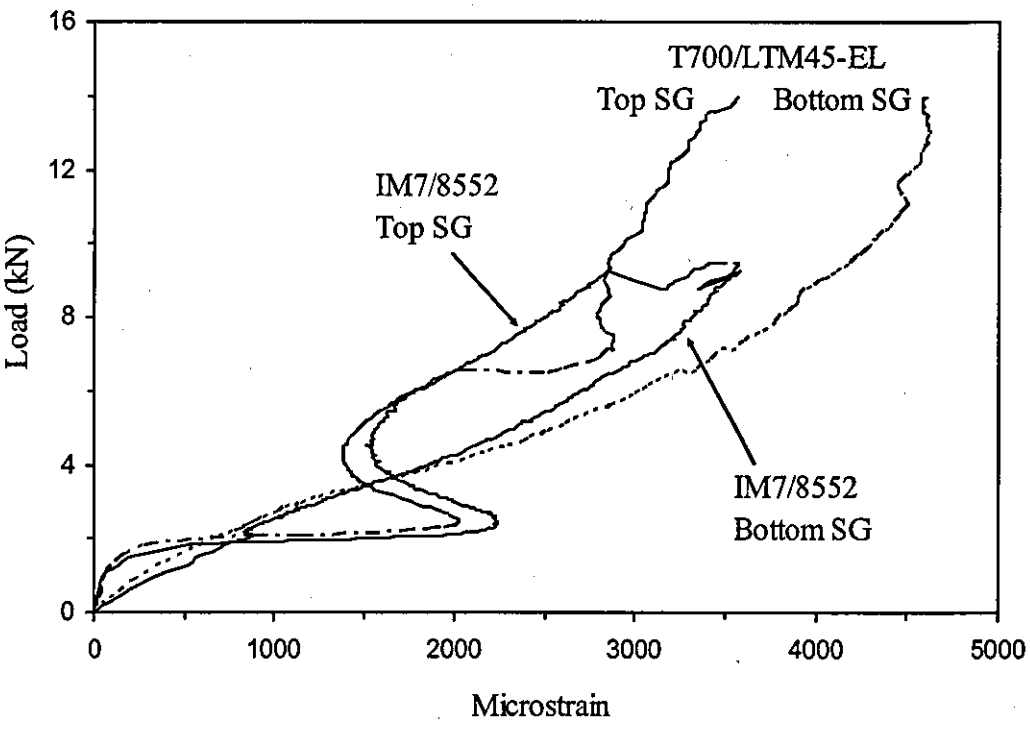

Figure 6.7 Load-strain response of 12 ply 50kg/m^3 sandwich panels with different skin materials loaded with the FE indenter

Secondary damage propagation can be seen in some of the IM7/8552 panels loaded with the FE indenter to ultimate failure, though where present it is at a lower load than in the T700/LTM45-EL panels. The strain responses of the IM7/8552 and T700/LTM45-EL panels follow the same trend up to the initiation of skin damage in the IM7/8552 panels, Fig. 6.7. Ultimate failure initiates at a much lower load and displacement in the IM7/8552 panels than in the T700/LTM45-EL panels and is generally represented by a series of load drops rather than one distinct load drop. These multiple load drops are expected to relate to fibre fracture in one sublaminate with the successive drops corresponding to fibre fracture in the remaining sublaminates.

The reduction in the ultimate failure load of the IM7/8552 sandwich panels reflects the trend seen for the IM7/8552 laminate plates, which failed at only 42% and 68% of the load sustained by the T700/LTM45-EL laminate plates when loaded by the HS and FE indenters respectively. This compares to failure loads of 46% and 67% for the sandwich panels. In addition, the earlier results from the testing of IM7/8552 cross-ply specimens to determine the flexural strength and modulus in Section 2.2, are in accordance with the observations for sandwich panels. This is a clear indication that the reduction in strength of the IM7/8552 panels is due purely to the performance of the skins.

6.1.5. Effect of core material on damage mechanisms

The effect of the core material on damage mechanisms and panel strength has been studied through a comparison of 64 and 96 kg/m^3 nomex honeycomb with 70 and 90 kg/m^3 aluminium honeycomb. In all cases the core thickness and cell size were kept constant at 12.7mm and 5mm respectively. A comparison of the two material types is shown graphically as an example in Figs. 6.8 & 6.9, with a full set of load-displacement curves shown Figs. B30-B35 in Appendix B for completeness. The damage loads and panel stiffness have also been compared at critical points, using the ratio of the nomex value divided by the aluminium value for a given skin thickness and indenter nose-shape in Table 6.5.

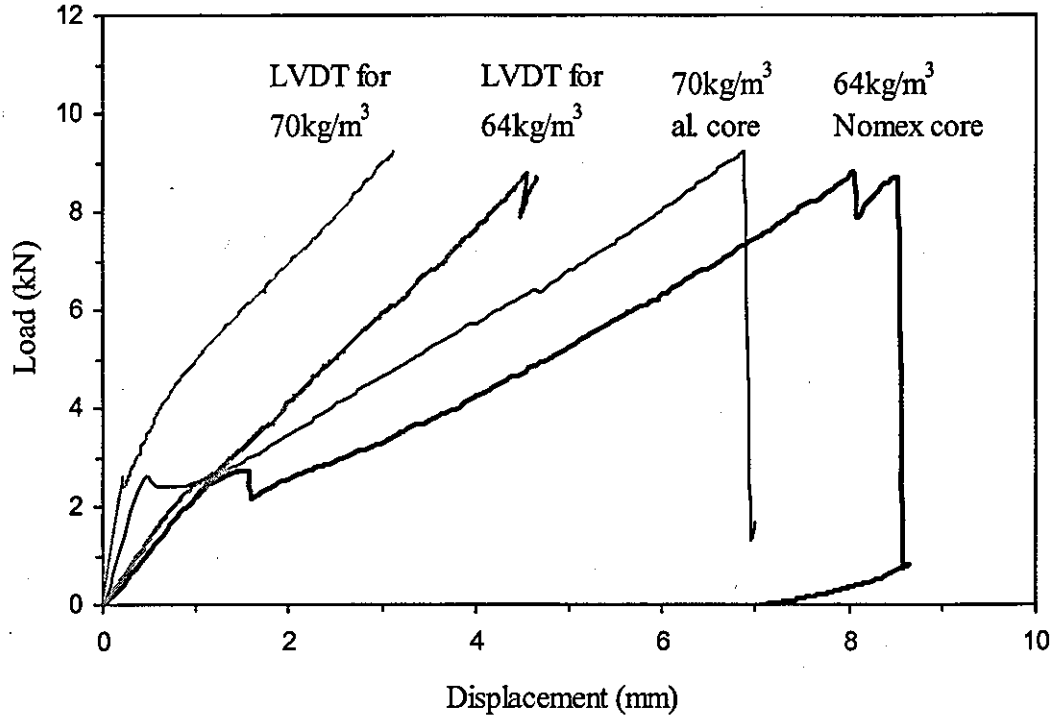

Figure 6.8 Comparison of load-displacement curves for 8 ply panel with 70kg/m^3 aluminium or 64kg/m^3 nomex core loaded with FE indenter

Table 6.5 Comparison of initial damage and ultimate failure loads and stiffnesses for nomex and aluminium panels (64kg/m^3 ÷ 70kg/m^3 and 96kg/m^3 ÷ 90kg/m^3)

	Skin thickness	Initial damage threshold				Ultimate failure			
		HS		FE		HS		FE	
		P_N/P_{AL}	E_N/E_{AL}	P_N/P_{AL}	E_N/E_{AL}	P_N/P_{AL}	E_N/E_{AL}	P_N/P_{AL}	E_N/E_{AL}
Low density cores	Bare core		0.19[b]	0.98[a]	0.19[b]			1.23[c]	
	8	0.76	0.50	1.19*	0.41	1.00	0.86	0.94	0.87
	12	0.79	0.47	1.25	0.49	0.98	0.96	0.97	0.88
	16	1.06	0.35	1.25	0.41	1.05	0.93	1.02	0.95
High density cores	Bare Core		0.26[b]	1.56[a]	0.26[b]			1.32[c]	
	8	0.74	0.31	1.18*	0.41	0.82	0.76	0.86	0.98
	12	0.88	0.49	1.19*	0.51	1.05	0.95	0.86	1.01
	16	0.95	0.29	1.37	0.52	0.95	0.96	0.89	1.05

Note:

E_N and E_{AL} represent panel stiffness estimated from gradient of load-displacement curve
* Indicates initial threshold load taken at load drop rather than change in gradient
[a] Bare compressive strength (kN) compared from bare compression tests (Table 4.5)
[b] Stabilised compressive modulus compared from manufacturers data (Table 2.9)
[c] Average crush strength (kN) compared from bare compression tests (Table 4.5)

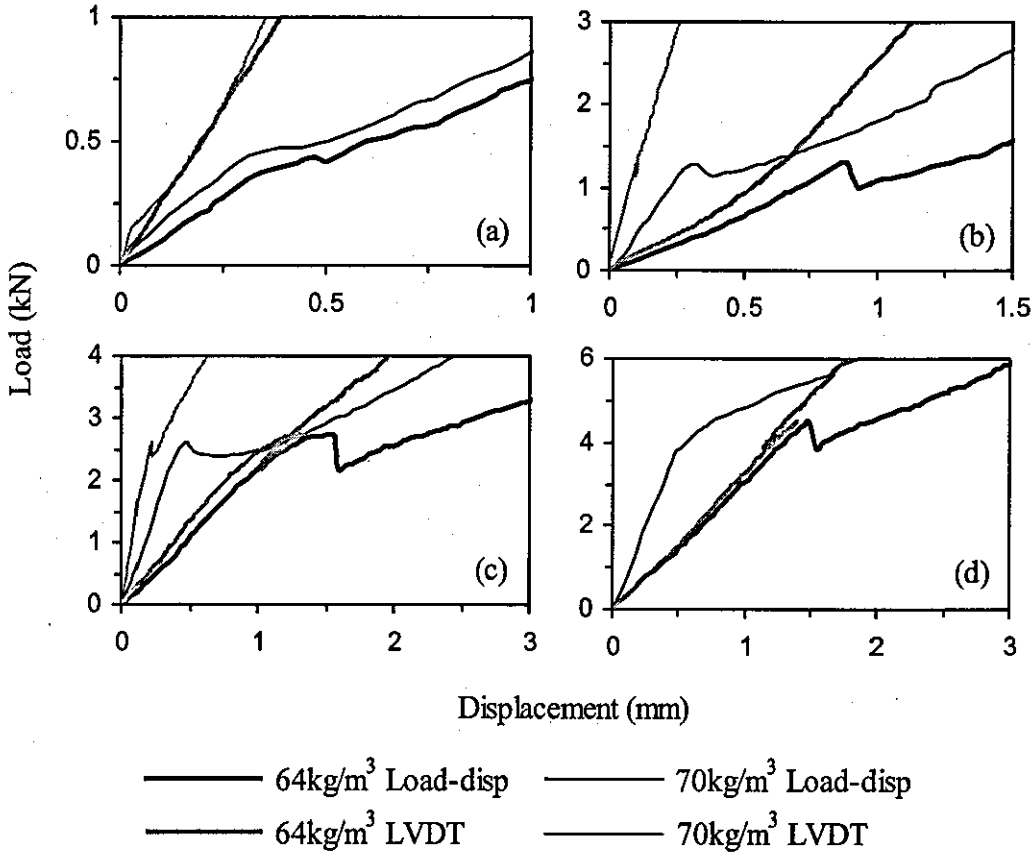

Figure 6.9 Initial threshold region of load-displacement curves

(a) 8 ply HS indenter (b) 16 ply HS indenter

(c) 8 ply FE indenter (d) 16 ply FE indenter

The key difference in the load-displacement response of the two panel types occurs at the initial threshold, as shown in Fig. 6.9. While the damage threshold loads are similar in magnitude the nomex panels exhibit a load drop in all cases. When loading with the FE indenter the load drop is sometimes preceded by a change in gradient, i.e. for the 8/64, 8/96 and 12/96 panels, though the initial threshold is still taken at the point of the load drop. For all loading cases and panel types the stiffness of the nomex panels is on average only 43% of the stiffness of the aluminium panels at the initial threshold. Ultimate failure occurs at a comparable load for both core types.

The variation in the nomex panel strength and stiffness at the initial threshold is due to the elastic nature of the nomex honeycomb. As the core dominates the panel stiffness prior to initial damage it is expected that the initial panel stiffness will be lower for the nomex panels. The amount of reduction is less than seen for the bare honeycomb due to an amount of panel stiffness associated with the resistance of the skins to bending. The lower modulus of the nomex honeycomb leads to global bending of the panel rather than local indentation. This is indicated by the close correlation of the load-displacement and load-LVDT curves in Fig. 6.9(b-d), where the LVDT was positioned directly at the centre of the bottom skin.

In terms of internal damage the nomex panels contain extensive core crushing and delamination at ultimate failure, Fig. 6.12. The extent of crushing is generally slightly less than in the aluminium panels but the delaminations are larger, especially in the 8 and 12 ply panels, Table 4.9. This is because the elastic nature of the nomex material allows the top and bottom skins to spring back to their original positions once the load is removed, opening up any delaminations in the top skin that occurred during loading. At initial and secondary damage there is no visible residual dent in any of the nomex panels and core crushing is spread over a lower number of cells than in the aluminium panels, Figs. 6.10 & 6.11. In the cross-sectioned specimens, unlike in the aluminium panels, the honeycomb cell walls are not folded plastically and damage is identified only by cracking of the resin covering the aramid paper. This combined with the lack of residual dent and surface damage prior to fibre fracture demonstrates how non-penetrative damage in nomex panels can go undetected despite the panel losing much of its local strength and stiffness.

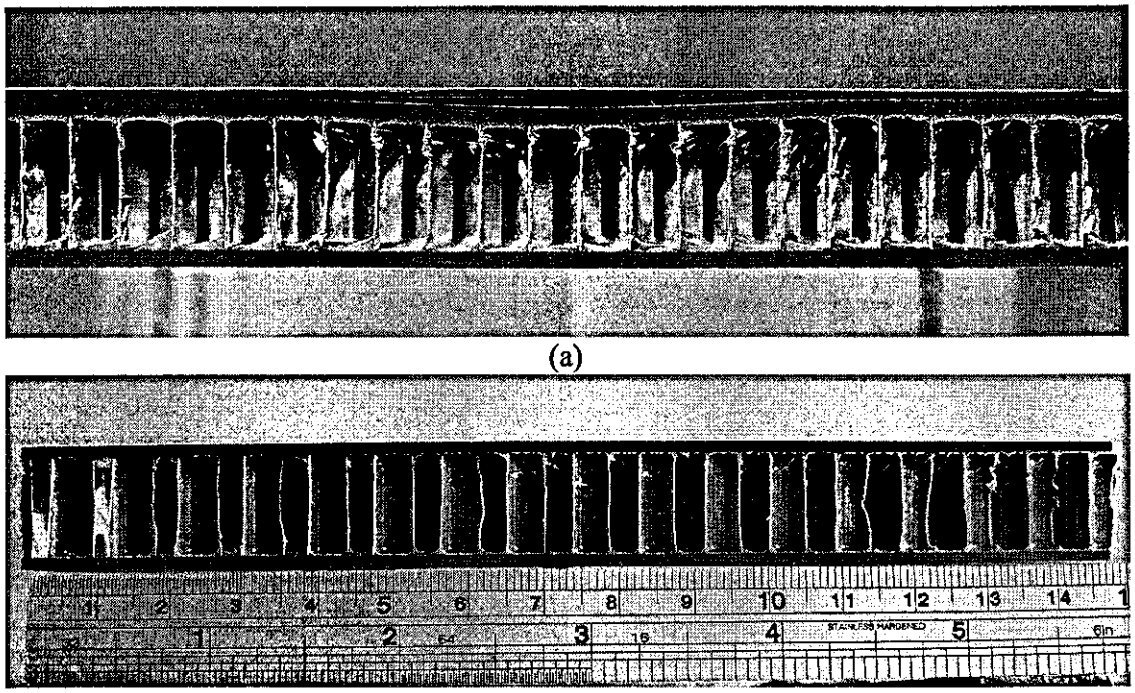

(a)

(b)

Figure 6.10 Photo of 12 ply panel loaded with FE indenter to initial damage threshold

(a) 70kg/m^3 aluminium (b) 64kg/m^3 nomex

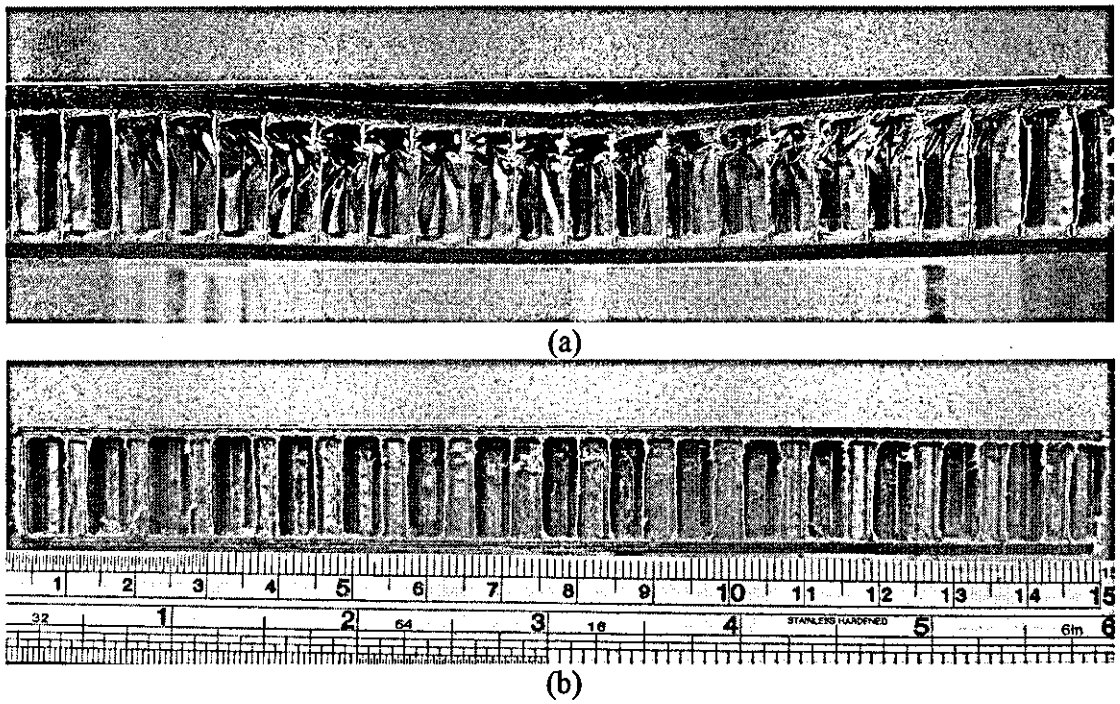

(a)

(b)

Figure 6.11 Photo of 12 ply panel loaded with FE indenter to secondary damage

(a) 70kg/m^3 aluminium (b) 64kg/m^3 nomex

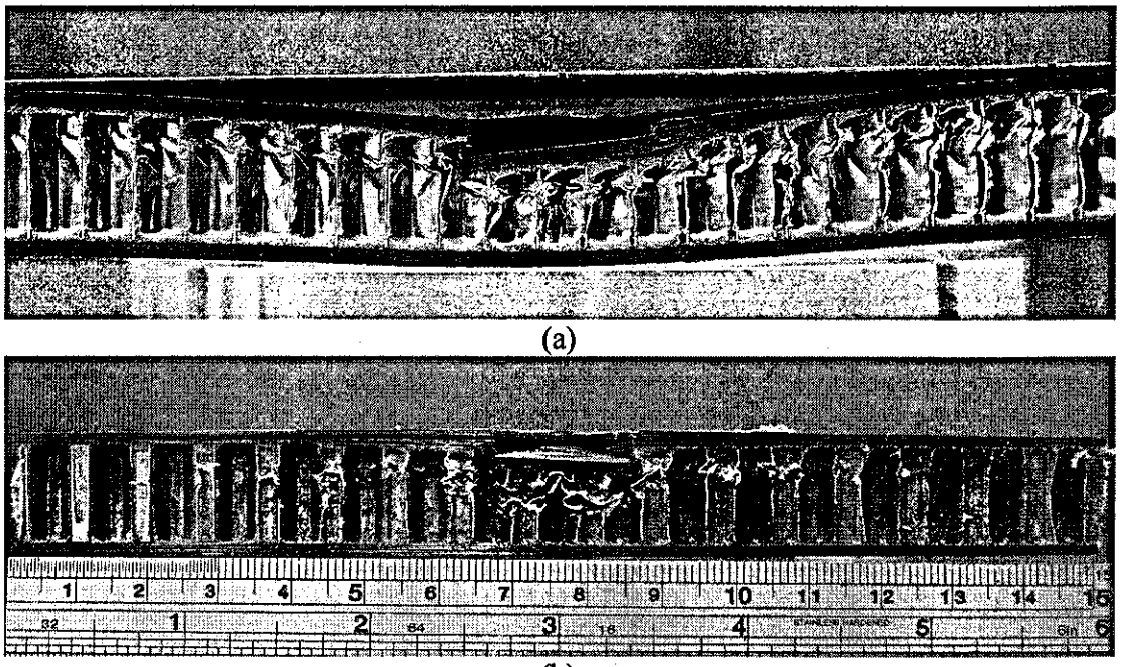

(a)

(b)

Figure 6.12 Photo of 12 ply panel loaded with FE indenter to ultimate failure
(a) 70kg/m^3 aluminium (b) 64kg/m^3 nomex

6.1.6. Effect of panel size on damage mechanisms

In a number of the quasi-static ultimate failure tests on thicker skinned panels it was noted that the damage area extended outside of the 100mm diameter clamped area, with delaminations propagating to the edge of the 16 ply 50kg/m^3 panel loaded with the FE indenter. To determine the effect of this on the damage mechanisms panels measuring 300mm × 300mm with 16 ply skins and 70kg/m^3 honeycomb were loaded to ultimate failure with the HS and FE indenters. The diameter of the testing area was increased to 220mm, 2.2 times the size of that used previously. All aspects of the testing procedure were identical to that used on the 150mm × 150mm panels, except an extra strain gauge was added to the top surface parallel to the 0 fibres on the panel centre line to give two gauges, situated 20mm and 44mm away from the loading centre respectively. The load-displacement and load-strain curves for the HS and FE tests are shown in Figs. 6.13-6.14.

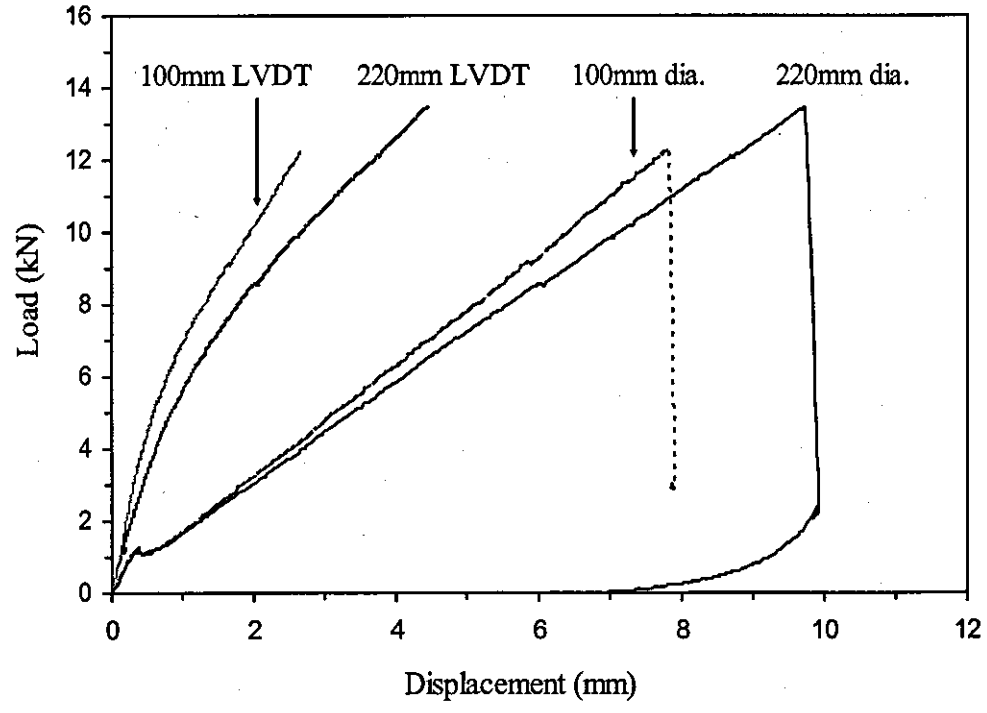

(a)

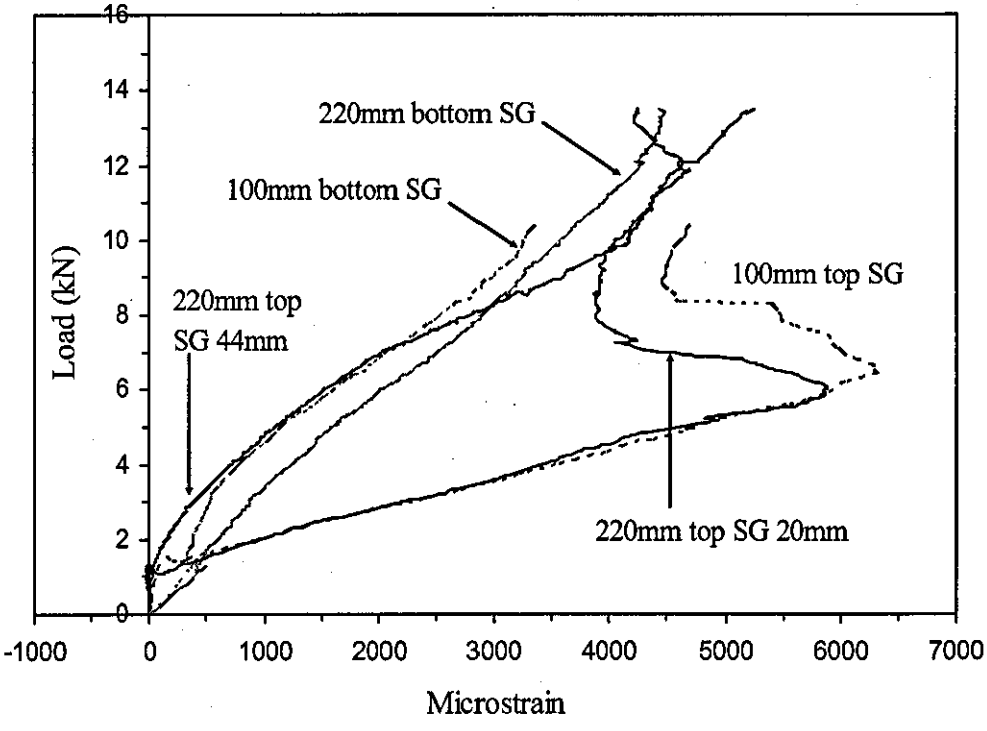

(b)

Figure 6.13 Comparison of 100mm and 220mm panel response - 16/70/HS
(a) Load-displacement (b) Load-strain

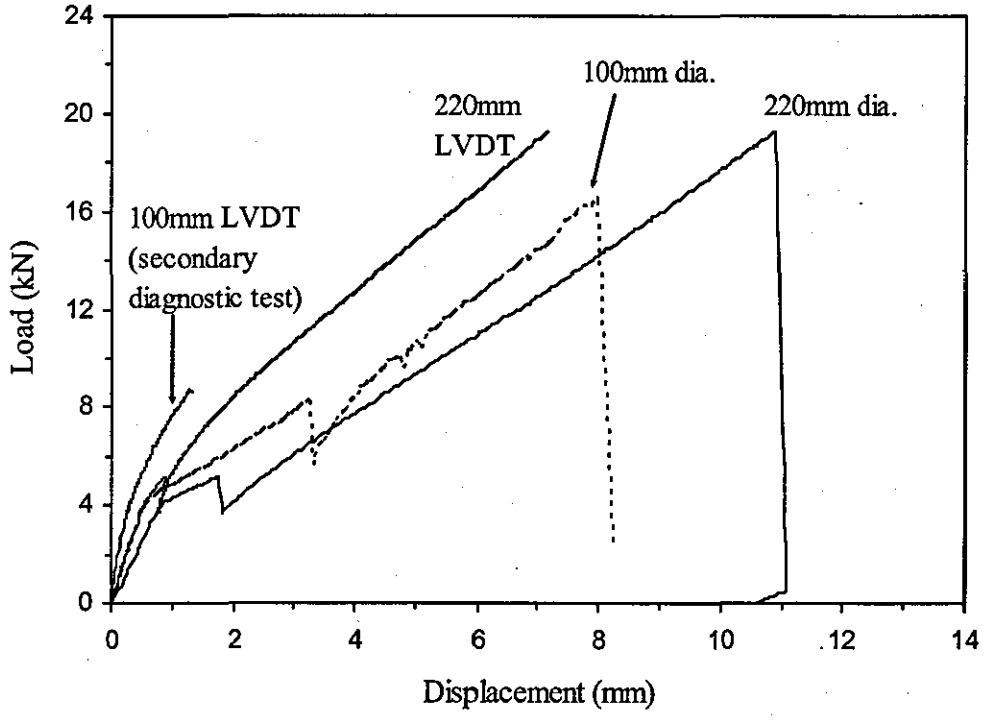

(a)

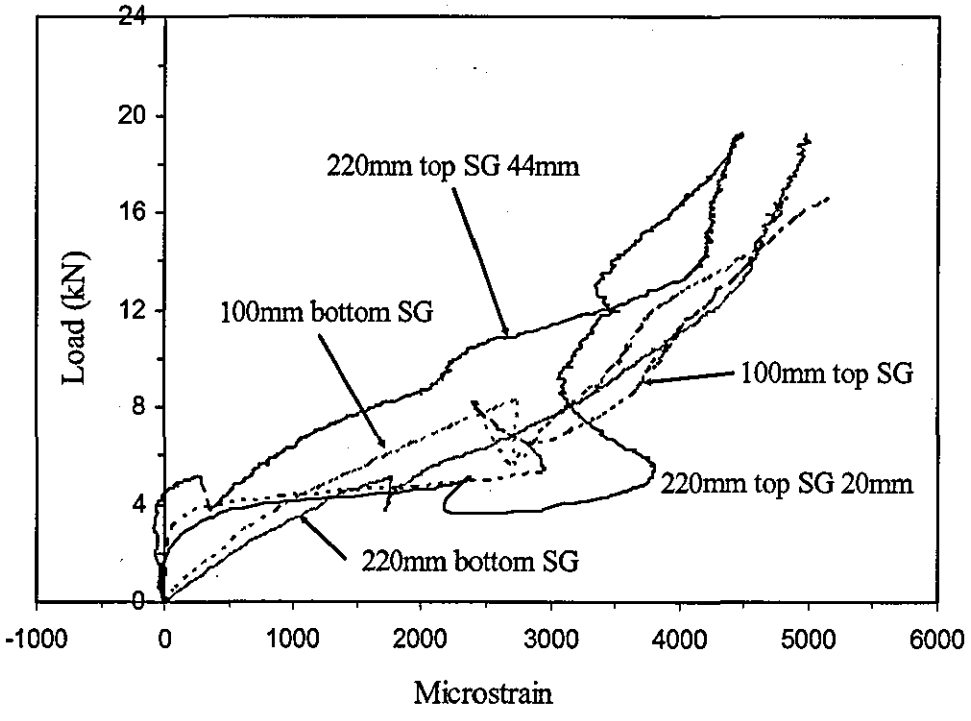

(b)

Figure 6.14 Comparison of 100mm and 220mm panel response - 16/70/FE

(a) Load-displacement (b) Load-strain

The panel response at the initial threshold is identical in terms of the strength, stiffness and strain response for the 100mm and 220mm panels loaded with the HS indenter, Fig. 6.13(a). This is expected as the loading area of the HS indenter is small compared to the panel size, causing a localised response. When loading with the FE indenter the initial threshold load is similar for both panel sizes, Fig. 6.14(a), though the amount of both top and bottom skin deflection is greater for the larger panel, leading to a 30% reduction in panel stiffness for the 220mm panel prior to initial damage. This is due to greater levels of global bending, shown by the higher level of strain on the bottom skin of the larger panel compared to the smaller panel. In both loading cases the strain gauge 20mm from the loading centre on the top surface clearly detects initial damage, whilst the additional gauge 44mm away from the loading centre does not, Figs. 6.13(b) and 6.14(b). The reduction in strain levels and sensitivity just 44mm away from the loading centre shows that initial damage and skin deformation is highly localised and supports the observations discussed in Section 4.4 regarding the localised nature of panel deformation and strain gauge sensitivity.

The ultimate failure load is higher for the larger panels due to the increased amount of global bending and membrane effects. The damage caused to the panels at ultimate failure, as recorded in Tables 4.8 & 4.10, is similar for the same indenter. In the bigger panels the damage is contained within the testing area and ultimate failure was due to fibre fracture of the top skin accompanied by multiple delaminations. In the HS loading case core crushing extends over 85mm in the larger panel compared to 90mm in the smaller panel, and the depth of uncrushed honeycomb directly under the indenter is around 4mm in both cases. In the FE loading case core crushing extends over 100mm in the smaller panel and 190mm in the larger panel, with 2mm of core uncrushed directly under the indenter in both cases. Multiple delaminations are present in each panel, in excess of 100mm in length in both cases.

It can be seen that the local response and damage mechanisms are similar for both panel sizes. The concerns raised regarding the possible interaction between the clamping supports and the panel when damage propagates past the testing area within the small panel are unwarranted. Therefore the observations made on small panels are valid for

larger panels and it is not necessary to test panels with clamped regions larger than 100mm with regards to the local response and damage mechanisms.

6.1.7. Effect of boundary conditions on damage mechanisms

As the local response of the sandwich panels was found to be significant, it is important to investigate the contribution of global bending to panel response. To this end a number of tests have been completed on panels resting on a solid base, such that all deformation is due to local indentation of the top skin into the core. The majority of panels were clamped on the top surface to give the same 100mm diameter circular testing area as for the panels tested under bending and all panels were loaded to ultimate failure. In a small number of tests the panels were not clamped to determine the effect of clamping. An example of the results obtained is shown in Fig. 6.15 for 12 ply 50kg/m^3 aluminium panels loaded with the HS indenter.

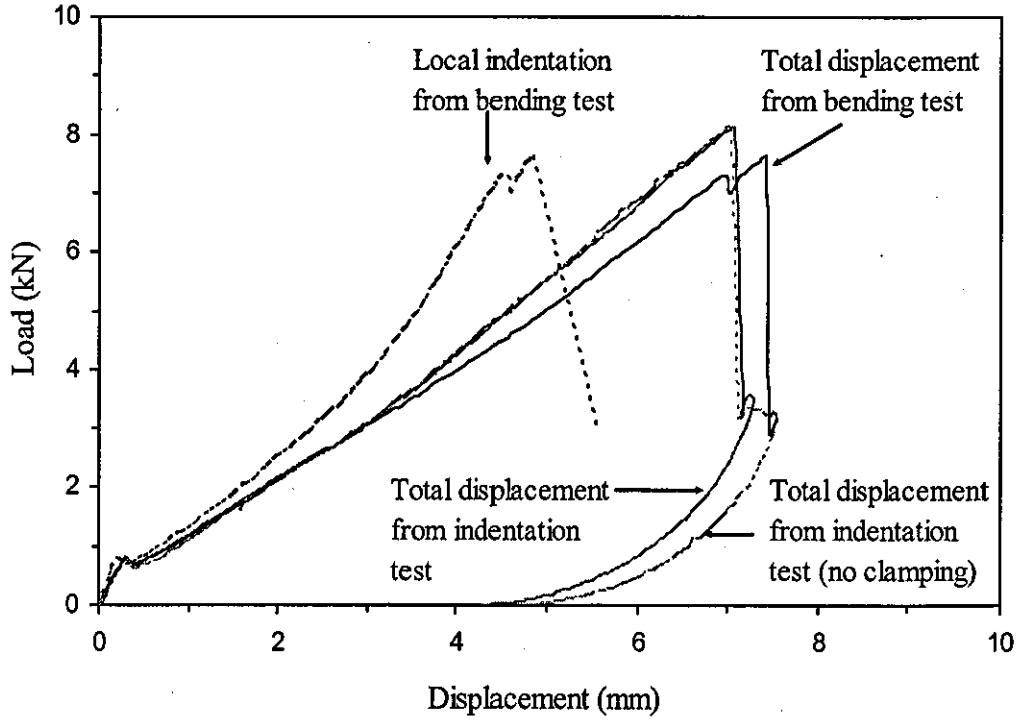

Figure 6.15 Comparison of panel response for 12 ply 50kg/m^3 panels loaded with HS indenter resting on a solid foundation (clamped & unclamped) and under bending

Table 6.6 Comparison of internal damage in panels resting on a solid foundation and under bending at ultimate failure

	Bending		Indentation	
	No. damaged cells	Delamination (mm)	No. damaged cells ( ) = difference	Delamination (mm) ( ) % increase
4/50/HS	16	53	14 (-2)	57 (8%)
4/70/HS	12	48	11 (-1)	50 (4%)
8/50/HS	26	63	22 (-4)	45 (-29)
8/70/HS	19	59	16 (-3)	72 (22%)
8/90/HS	22	54	13 (-9)	64 (19%)
12/50/HS	29	30	25 (-4)	50 (67%)
12/70/HS	19	42	19 (0)	70 (67%)
12/90/HS	22	61	19 (-3)	72 (15%)
16/50/HS	22	55	28 (6)	60 (9%)
16/70/HS	20	80	20 (0)	84 (5%)
8/64/HS	20	69	14 (-6)	60 (-13%)
12/64/HS	21	77	14 (-7)	75 (-3%)
12/96/HS	20	53	13 (-7)	65 (23%)
4/50/FE	27	110	24 (-3)	95 (-14%)
4/70/FE	14	49	14 (0)	77 (57%)
8/50/FE	33	94	30 (-3)	70 (26%)
8/70/FE	27	45	20 (-7)	97 (116%)
8/90/FE	25	74	14 (-11)	77 (4%)
12/50/FE	36	56	35 (-1)	100 (79%)
12/70/FE	23	44	23 (0)	102 (132%)
12/90/FE	26	101	19 (-7)	96 (-5%)
16/50/FE	36	100	33 (-3)	120 (20%)
16/70/FE	28	96	27 (-1)	135 (41%)
8/64/FE	26	100	17 (-9)	104 (4%)
12/64/FE	28	119	19 (-9)	104 (-13%)
12/96/FE	21	110	14 (-7)	71 (-35%)

A comparison of the load-displacement response for the aluminium honeycomb panels on a solid foundation with the local indentation response for the panels in bending, shows good correlation in terms of critical loads. At the initial threshold the panel indentation is similar as expected since initial damage is due to local core crushing. At higher loads the local indentation measured from the panel in bending is much less than for the panel resting on a solid foundation, despite ultimate failure occurring at a similar load. When a nomex honeycomb core is used the critical loads signifying initial damage, secondary damage and ultimate failure are again of a similar magnitude. In addition the slopes of the two indentation curves tend to show a better correlation than

for the aluminium honeycomb panels at high loads when loading with the FE indenter, as shown in Fig. 6.16.

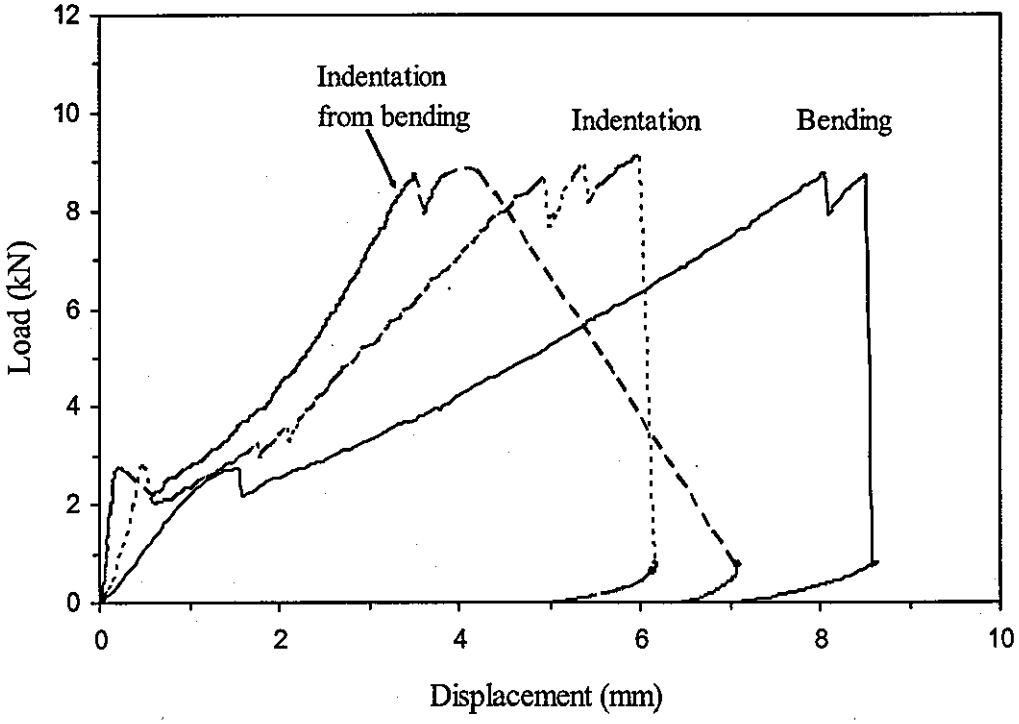

Figure 6.16 Comparison of panel response for 8 ply 64kg/m^3 nomex panels loaded with FE indenter resting on a solid foundation and under bending

The damage mechanisms present at ultimate failure are the same in both cases though typically the extent of core crushing is slightly less whilst the delamination size is slightly greater in the panels on a solid foundation, illustrated in Fig. 6.17 and Table 6.6. In terms of boundary condition effects when the clamped and unclamped panels resting on a solid foundation are compared it can be seen that there is very little difference in the panel response, Fig. 6.15.

The similarity in the critical loads for panels in bending and resting on a solid foundation is directly attributable to the localised nature of both the core and top skin damage and subsequent failure. The indentation tests highlight the extent of the global response of a sandwich panel loaded in bending and imply the local response is only partially independent of the global response. The difference in the local indentation

response measured directly from the panels on a solid foundation and indirectly from the bending tests suggests there is a coupling between the top and bottom skin deflections. This coupling means removal of the global element of the bending response, achieved through resting the panels on a solid foundation, will not provide an accurate measurement of the local response seen in the bending case.

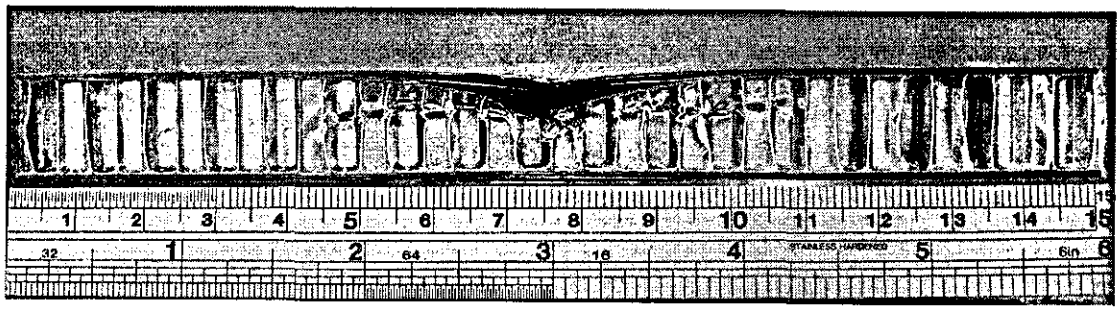

(a)

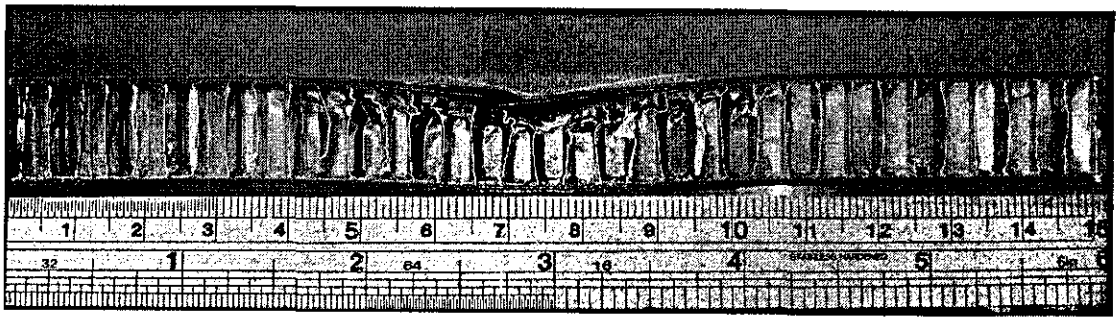

(b)

Figure 6.17 Photo of 8/70/HS panel loaded to ultimate failure
(a) resting on a solid foundation (b) in bending

6.2. Effects of varying the major parameters on energy absorption

In addition to their effect on panel strength it is equally important to know how changing parameters such as skin thickness, core density and indenter nose-shape affect the overall energy absorption capabilities of a panel. Energy absorption can be assessed both in terms of incident or applied energy and absorbed energy, as illustrated in Fig. 6.18. Incident energy in quasi-static tests is determined from the area under the load-displacement curve up to the chosen threshold and represents the total energy applied to

the panel. Consequently the incident energy is dependent on both load and displacement values. The absorbed energy is represented by the area contained within the load-displacement curve when the panel is both loaded and unloaded at the same rate after either ultimate failure or the desired load is reached in the diagnostic tests. Ideally absorbed energy would be used in comparisons rather than incident energy as it gives an accurate measure of the energy absorbed through irreversible damage and panel deformation. Unfortunately controlled unloading of the panel was only used in the latter tests, therefore only the incident energy is known for the majority of panels tested in quasi-static bending. A comparison of the incident and absorbed energies from all quasi-static panel tests show at ultimate failure typically over 90% of the incident energy is absorbed by the panel, and in many panels under FE loading the absorbed energy is 99% of the incident energy for both nomex and aluminium panels. Therefore the comparison of incident energy at ultimate failure is a good representation of the energy absorption characteristics. A full listing of the incident energies and absorbed energies where available is contained in Tables 6.13-6.23 at the end of the Section.

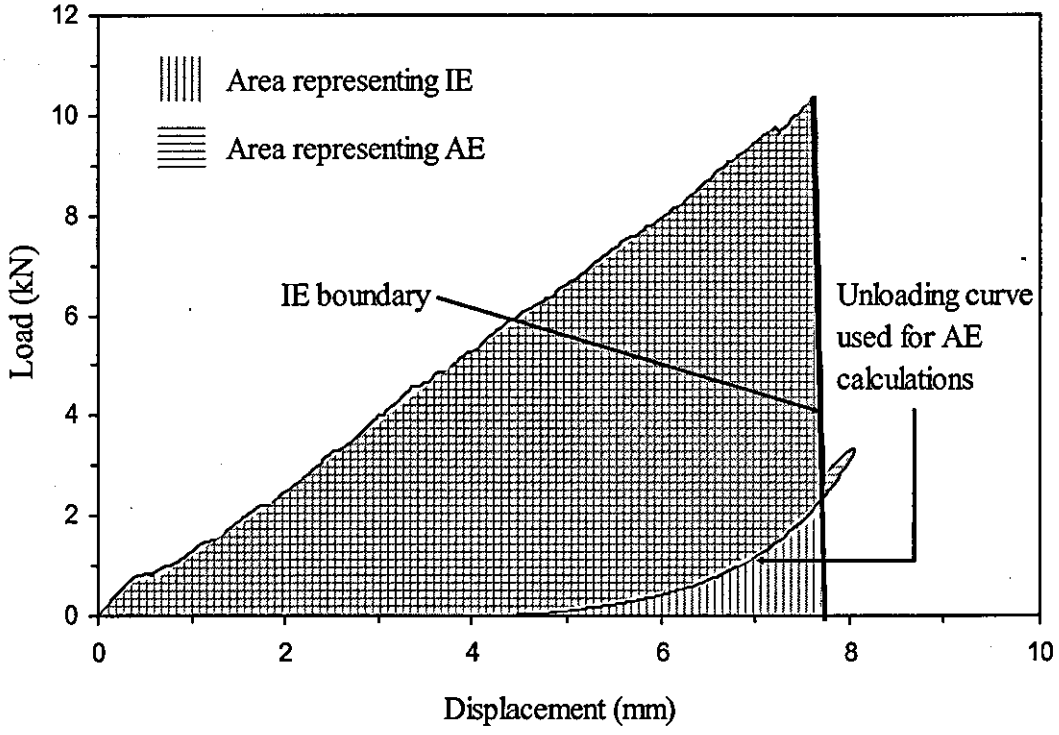

Figure 6.18 Graphical representation of incident energy (IE) and absorbed energy (AE)

6.2.1. Effect of varying skin thickness on energy absorption

The relationship between incident energy and skin thickness at initial and secondary damage and ultimate failure is shown graphically in Fig. 6.19(a-c). The variation of incident energy with skin thickness at initial damage shows a significant amount of scatter compared to the linear correlation between load and skin thickness identified previously. However, incident energy does appear to increase marginally with skin thickness. This is because there is large variation in panel displacement for a given load at load levels below that required for initial damage. The reduction in displacement for a given load with increasing skin thickness in the FE loading case counteracts the effect of the increased load. This indicates incident energy to be less dependent on skin thickness, primarily due to the dominance of the core on the panel deformation, at low loads.

The variation of incident energy with skin thickness at secondary damage is non-linear with significant fluctuations as a result of the unstable nature of delamination propagation, the cause of secondary damage. Difficulties in identifying secondary damage in cases where no load drop occurs may also introduce errors in the numerical values used in the plots. Incident energy clearly increases with skin thickness, especially at higher loads. The thicker skins contain higher levels of delamination due to the increased number of ply interfaces, which are directly responsible for energy absorption.

The ultimate failure curves are linear like those in the load-thickness plots. This is expected as load increases linearly with skin thickness at ultimate failure and the general trend at high loads shows displacement to increase with skin thickness for a given load in both HS and FE loading cases. Doubling the skin thickness more than doubles the incident energy at ultimate failure, an average percentage increase of 120% and 125% for the HS and FE loading cases respectively.

Unloading curves for the secondary damage diagnostic tests of 8, 12 and16 ply panels with a 70kg/m^3 core under HS loading are available and show the absorbed energy to be

62-63% of the incident energy in all three cases. Unfortunately the only other data available for the absorbed energy of the diagnostic tests was for the 4/70/FE panel which absorbed 60% of the incident energy at initial damage. More diagnostic test results for other panel configurations are required before any general conclusions can be made concerning the energy absorption resulting from initial and secondary damage.

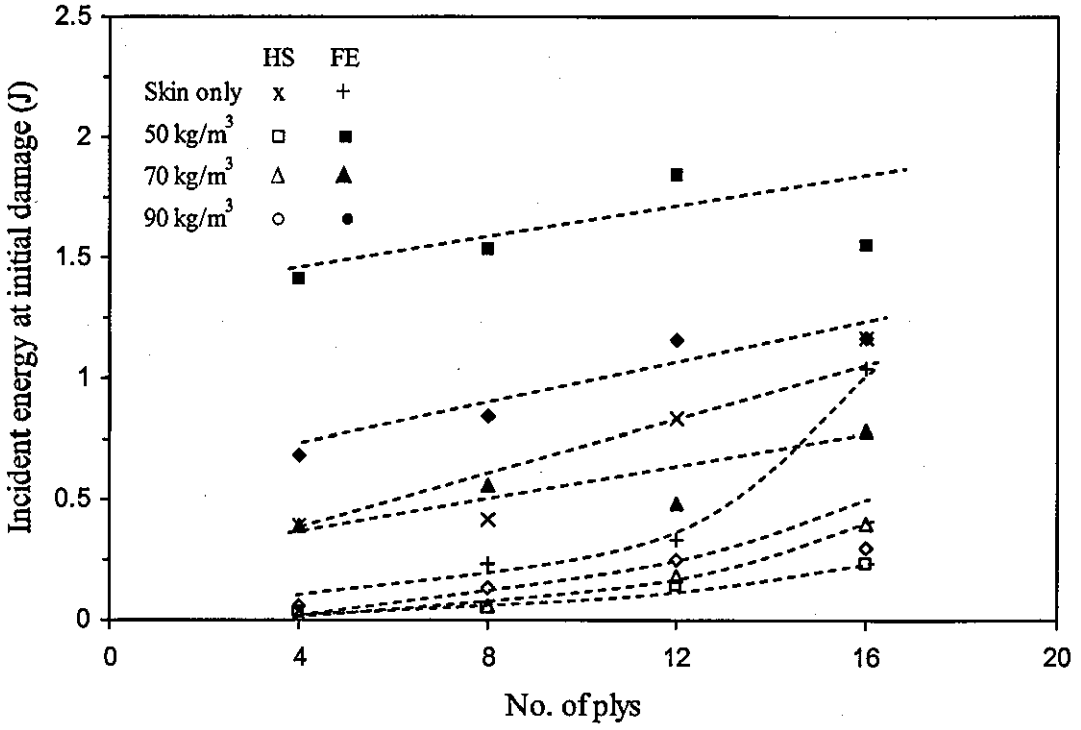

(a)

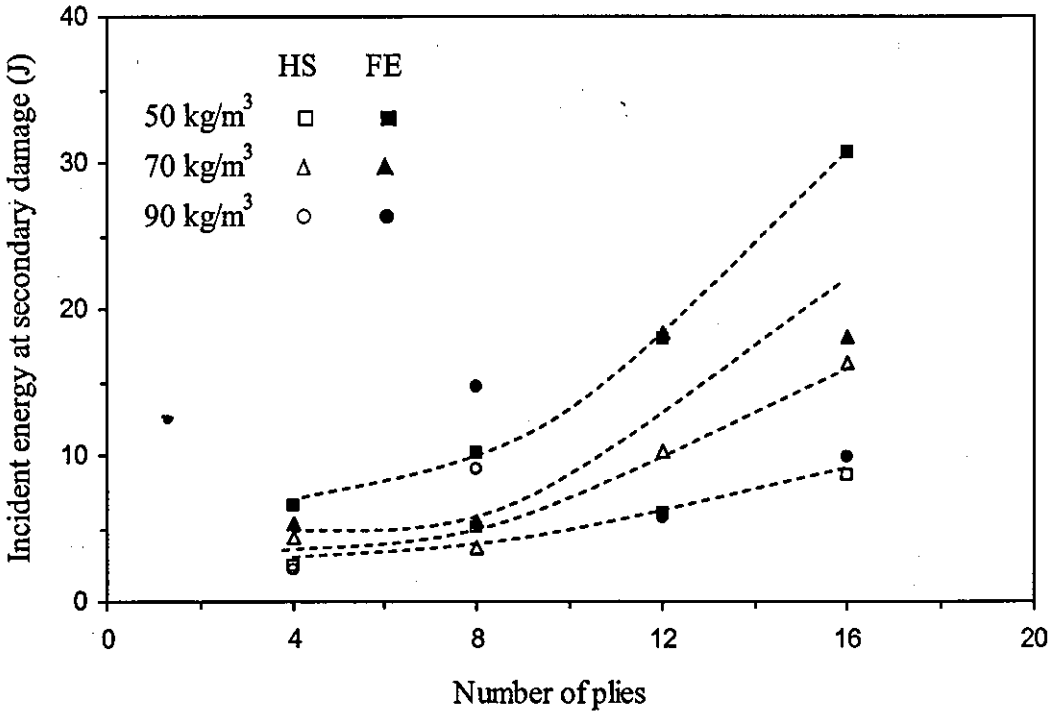

(b)

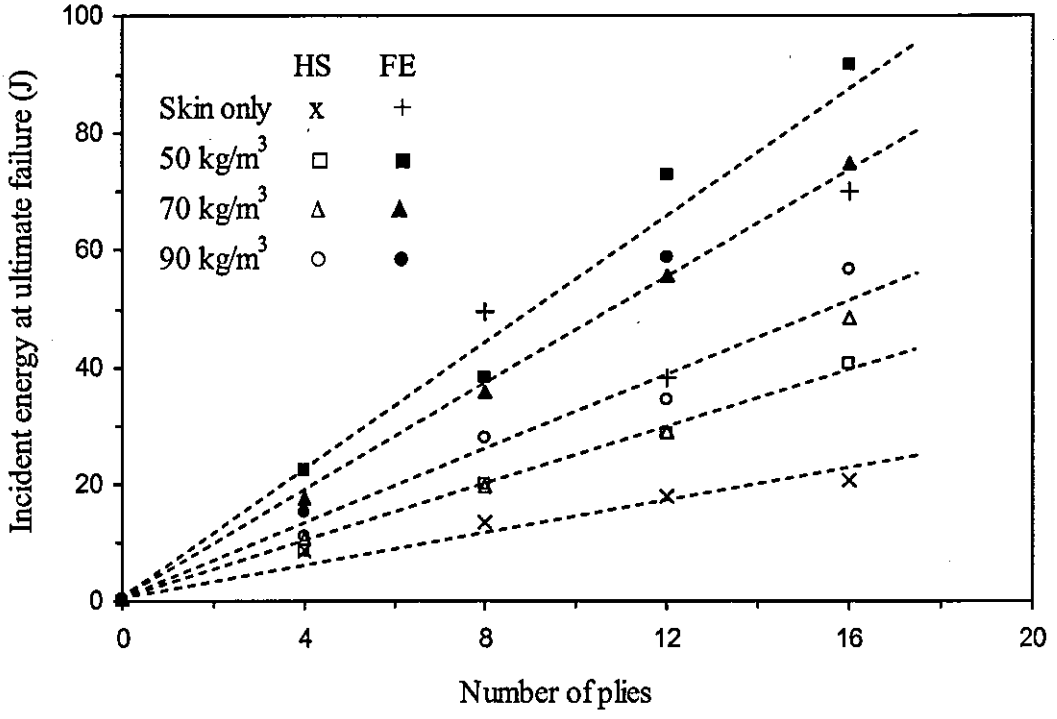

(c)

Figure 6.19 Variation of incident energy with number of plies in the skins at (a) initial threshold (b) secondary damage (c) ultimate failure

6.2.2. Effect of varying core density on energy absorption

At the initial threshold the panels loaded with the FE indenter show a linear increase in initial threshold load with core density. This leads to a clear linear increase in incident energy with core density at the initial threshold, Fig. 6.20. This is expected as the core controls the panel response up to the initial threshold with initial damage identified as local core failure. Conversely the trend for the panels loaded with the HS indenter show a decrease in incident energy with increasing core density. This is as a result of the initial threshold load remaining approximately constant whilst displacement decreases for a given load with increasing core density. Although core crushing is the primary damage mechanism the localised nature of the HS loading case means the panel response is controlled by the skins.

Although at high loads the panel displacement at a given load reduces marginally with increasing density when loading with the HS indenter, when coupled with the large increase in ultimate failure load leads to a linear increase in incident energy with core density at ultimate failure, Fig. 6.20. The localised nature of loading means core crushing extends away from the loading point right up to the point of fibre fracture, providing an additional method of energy absorption that is accentuated by higher core density and therefore strength.

In the FE loading case the ultimate failure load is approximately constant whilst at high loads displacement at a given load reduces significantly with core density. In the panels with thin skins the relationship between core density and incident energy shows incident energy to reduce with increasing core density. This is because the thin skins act as a membrane, which when coupled with a low density core allows extensive top skin deflection and core crushing combined with large amounts of global bending due to the lower core modulus, increasing the energy absorption capacity. In the thicker skinned panels there is a large level of scatter in the results, especially when including the results from the skin plate tests, and it is not possible to draw any firm conclusions regarding the variation of incident energy with core density in these panels.

From the analysis of both panel strength and energy absorption it is possible to conclude that the effect of honeycomb density on panel response is not as important as the effect of skin thickness. Testing of panels with denser honeycomb would help to clarify if the effect of the core is overshadowed by the effect of the skin thickness or if the variation in core density considered here is not great enough.

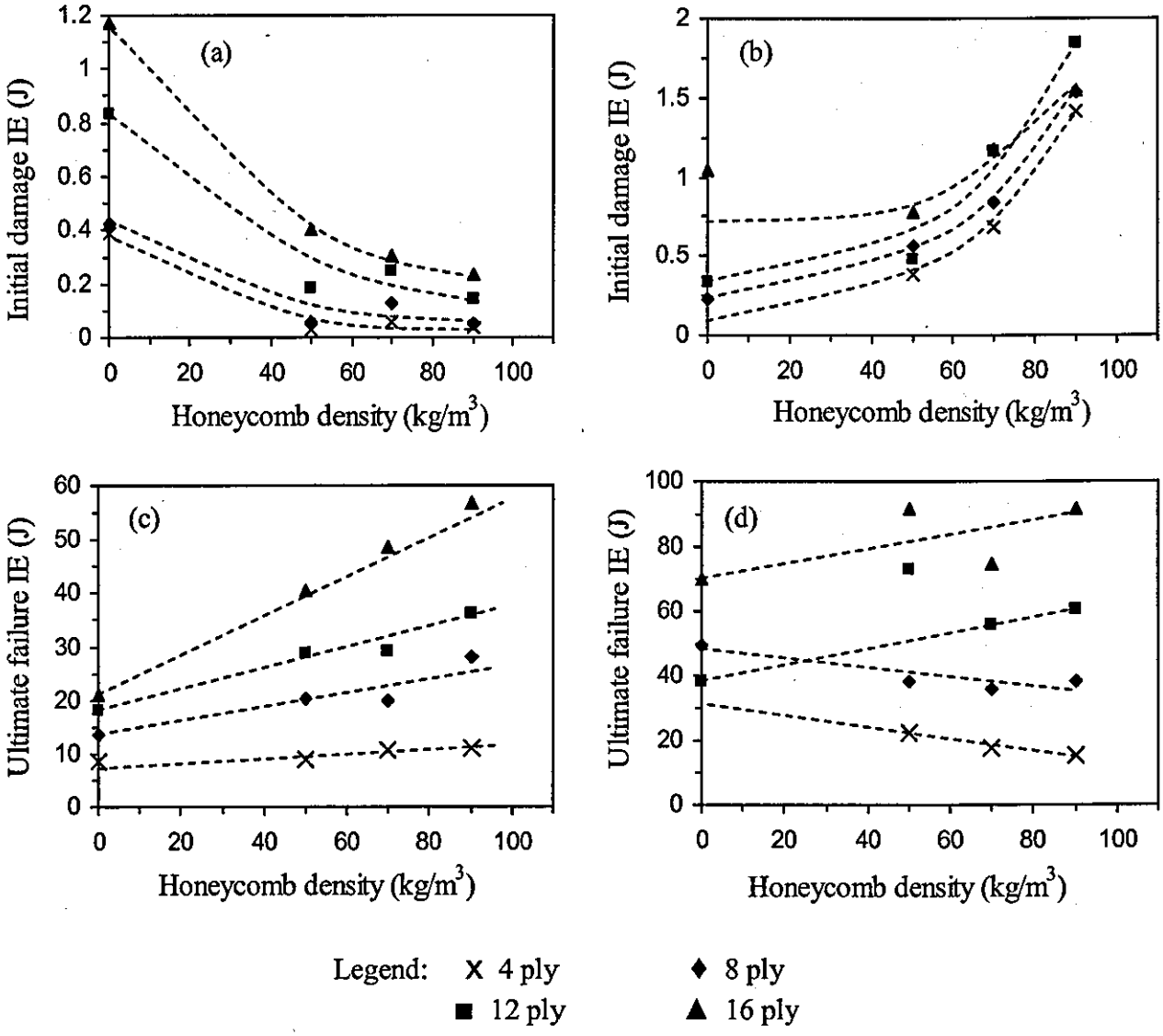

Figure 6.20 Variation of incident energy with honeycomb density:

(a) Initial threshold HS indenter (b) Initial threshold FE indenter

(c) Ultimate failure HS indenter (d) Ultimate failure FE indenter

6.2.3. Effect of indenter nose-shape on energy absorption

For a given core density and skin thickness the incident energy is clearly greater for the panels loaded with the FE indenter than those loaded with the HS indenter, Figs. 6.19 & 6.20. This is directly associated to a greater extent of core crushing in the panels loaded with the FE indenter as the panel response is less localised than in the HS loading case. The amount of increase in both threshold loads and displacement at a given load for the panels loaded with the FE indenter compared to those loaded with the HS indenter is not constant. The lowest increase in energy absorption is seen in the panels with thin skins and high density core when loaded to ultimate failure.

At initial damage the percentage increase in incident energy is greatest for panels with thin skins and a high core density, Table 6.7. This is because the thin skins provide little resistance to the FE indenter and energy is absorbed through core crushing over a large area with the denser honeycomb requiring a higher load for core crushing to occur. At ultimate failure the percentage increase in the incident energy at ultimate failure decreases with an increase in core density and there is no pattern for skin thickness, Table 6.7. Here the skins control the response with stabilised core crushing over a larger area and higher levels of indenter displacement when the core density and associated crush strength and modulus are low.

Table 6.7 Percentage increase in incident energy at initial damage and ultimate failure when changing from HS to FE indenter $\left(\frac{FE\ value - HS\ value}{HS\ value} \times 100\%\right)$

Skin thickness	Core density							
	Laminate skins		50kg/m^3		70kg/m^3		90kg/m^3	
	E_{init} %	E_{ult} %	E_{init} %	E_{ult} %	E_{init} %	E_{ult} %	E_{init} %	E_{ult} %
4			1341	156	1114	61	3711	37
8	-45	270	833	89	546	81	2960	36
12	-60	112	167	154	364	92	1214	71
16	-11	238	95	126	290	54	574	61

6.2.4. Effect of core material on energy absorption

The tests on 64kg/m^3 and 96kg/m^3 nomex panels with 8, 12 and 16 ply T700/LTM45-EL skins shows nomex to behave in a similar manner to aluminium in terms of energy absorption. When both damage load and incident energy are plotted against skin thickness, Fig. 6.21, a linear relationship can be seen for all panel densities. This matches the trends identified for the aluminium panels. With only two nomex core densities considered there is not enough data to compare the effect of core density on energy absorption for nomex. However, the position of the lower density core in relation the higher density core in Fig 6.17 is the same as for the aluminium panels, indicating the higher density core to be able to withstand a higher load but have a lower incident energy.

Table 6.8 Comparison of incident energy for nomex and aluminium panels

		64kgm^{-3} / 70kgm^{-3}		96kgm^{-3} / 90kgm^{-3}	
	Skin	HS	FE	HS	FE
	thickness	IE (J)	IE (J)	IE (J)	IE (J)
Initial damage threshold	8	0.08/0.12	2.51/0.79	0.08/0.05	2.31/1.53
	12	0.20/0.21	2.41/0.87	0.22/0.14	2.22/1.84
	16	0.59/0.31	3.66/1.21	0.49/0.23	5.81/1.55
Ultimate failure	8	22.1/19.7	40.3/35.7	24.4/27.9	42.9/38.1
	12	29.6/29.0	64.7/55.6	39.2/36.2	53.9/60.4
	16	58.1/48.6	91.5/74.8	53.8/56.9	75.5/91.8

Note: First number represents nomex, second number represents aluminium

A direct comparison of the incident energy at initial damage and ultimate failure in nomex and aluminium panels is made in Table 6.8. Typically the nomex specimens have a higher level of incident energy at the initial threshold than the aluminium panels for a given skin thickness and indenter type, despite having a comparable threshold load. This is expected as the core dominates the response at low loads and is the main source of energy absorption. The lower modulus of the nomex core allows greater global bending of the panel, which absorbs large amounts of incident energy. Once the load is removed the elastic nature of the nomex allows the specimen to spring back to

its original location, releasing an amount of the stored incident energy. This is reflected in the level of absorbed energy measured from the tests on 70kg/m^3 and 64 kg/m^3 panels loaded to secondary damage with the HS indenter. The 70 kg/m^3 aluminium panels absorbed 63% of incident energy whilst the 64kg/m^3 nomex panels absorbed just 46%. This recoverable energy mechanism means for a given level of incident energy less energy is absorbed through creating permanent damage, in effect providing a better panel design for energy absorption without having to increase the skin thickness.

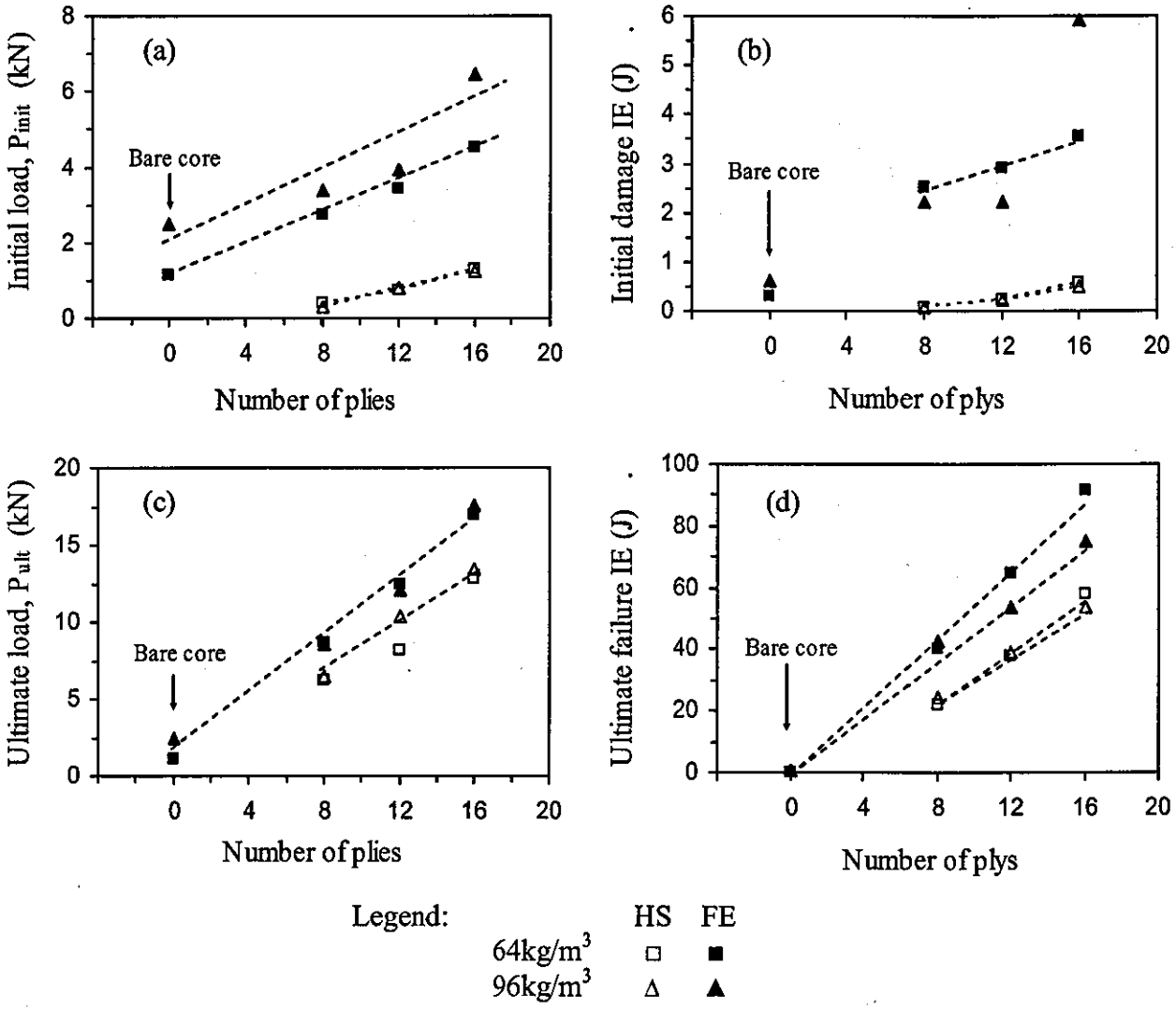

Figure 6.21 Variation of load and energy with skin thickness for nomex panels:

(a) Initial damage load (b) Incident energy at initial damage

(c) Ultimate failure load (d) Incident energy at ultimate failure

At ultimate failure the incident energy is either similar or slightly higher for the nomex panels. The corresponding absorbed energy is comparable for the aluminium and nomex panels, 92% and 90% for HS loading and 99% for FE loading in both cases. Although the lower modulus of the nomex core still permits larger levels of global bending the skin dominates the response at ultimate failure and once top skin fibre fracture occurs the recoverable energy previously released upon unloading the stretched skin fibres is consumed in creating irreversible damage.

6.2.5. Effect of panel size and boundary conditions on energy absorption

The tests completed on panels resting on a solid foundation and in bending with a 220mm diameter testing area highlight the importance of global bending within aluminium sandwich panels. In the panels resting on a solid foundation the similar ultimate failure load but typically lower displacement for a given load leads to a lower level of incident energy than for the panels loaded in bending, Table 6.22. The removal of the global bending element, especially in the panels with a lower modulus, is directly responsible for the reduction in incident energy. It could be assumed that without the recoverable energy available from global bending that a higher amount of energy would be absorbed in creating permanent damage. However, the average absorbed energy of panels resting on a solid foundation or in bending is identical, 92% for HS loading and 98% for FE loading. From the tests on panels in bending it can be seen that at ultimate failure the energy recoverable from global bending (measured by the deflection of the LVDT) is on average 35% of the incident energy taken in global bending. However, as the bottom skin and adjoining core spring back to their original position the force created by the motion causes more core crushing as the core is forced on to the indenter. This in turn absorbs more energy in creating permanent damage and leads to only 8% and 2% of total recoverable energy under HS and FE loading respectively.

In the large panels significantly more global deformation occurred during loading, leading to a 43% and 51% increase in incident energy at ultimate failure for the large panels compared to the small panels for HS and FE loading respectively. At initial damage the incident energy was very similar as local deformation rather than global

deformation was dominant. In the large panels at ultimate failure 54% and 72% of the incident energy was taken in global bending compared to 42% and 55% for the smaller panels under HS and FE loading respectively. However, the total energy absorbed by the large panels in creating permanent damage was comparable to that seen for the small panels, 97% and 98% in the HS and FE loading cases. This again is due to the relaxation of the bottom skin at top skin fracture causing core damage to propagate.

The panels resting on a solid foundation can be considered as a skin resting on an elastic foundation. Using Eq. 5.9 for absorbed energy in Section 5.2.2 based upon the work by Wierzbicki et al. [73], a prediction of the energy absorbed at ultimate failure has been made for the aluminium panels, as shown in Table 5.1. Although Eq. 5.9 was developed for FE loading an equivalent contact radius of 5mm at ultimate failure was assumed for the HS indenter, though the theoretical values overestimated the absorbed energy by up to 40%. However, for the FE loading case the predicted values were within 18% of the experimental values for all skin thicknesses and core densities. A prediction of the absorbed energy for the nomex panels could not be made as the yield strength of the nomex material is unknown.

6.3. Mechanical behaviour of panels under impact loading

Impact tests have been completed extensively on panels with 8 ply skins 70kg/m^3 aluminium core to examine how sandwich panels perform under impact conditions and identify any differences between quasi-static and impact loading. A limited amount of tests have also been completed on sandwich panels with 8 ply skins 64kg/m^3 nomex core and 16 ply skins 70kg/m^3 aluminium core. These tests will allow a brief examination of the effect of skin thickness and core material on impact performance as well as providing more information on impact response in general.

6.3.1. Effect of varying IKE on damage mechanisms

The extent and type of damage present within an impacted panel varies with the level of impact energy. The damage caused to 8 ply 70kg/m^3 panels impacted at energies up to 30J was measured in terms of external and internal damage, as in the quasi-static case discussed in Section 4. Measurements of the residual dent, internal core crushing, skin delamination and fibre fracture were taken for all impact tests, tabulated in Tables 6.24-6.27, and are illustrated in Fig. 6.22 through photographs of the panel cross-sections for 8 ply 70kg/m^3 panels. As selection of the load-(integrated)displacement plots of the impact events are shown in Fig. 6.23 to aid understanding. Where possible the data from impact tests on the compression-after-impact panels and the previous quasi-static tests has been included. For the CAI panel data in Fig. 6.24 core crushing size has been estimated from the external dent length. Dent length is a good indication of the internal damage length, generally matching or slightly underestimating the length of core crushing, shown in Tables 6.24-6.27.

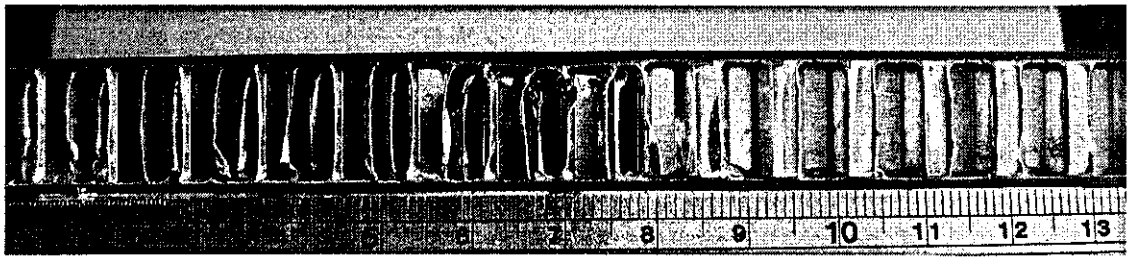

(a) IKE = 1.5J

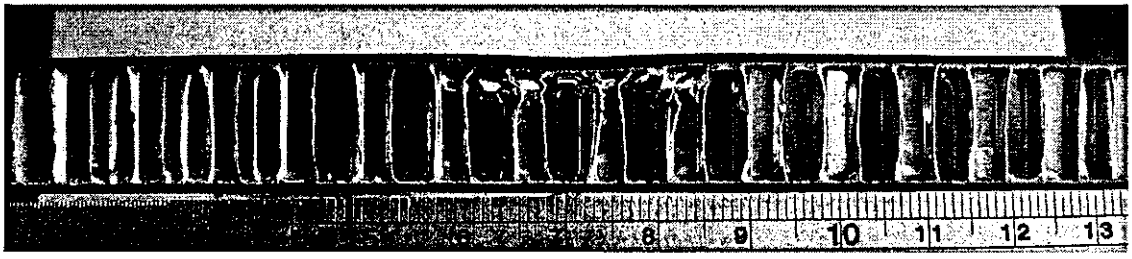

(b) IKE = 3.7J

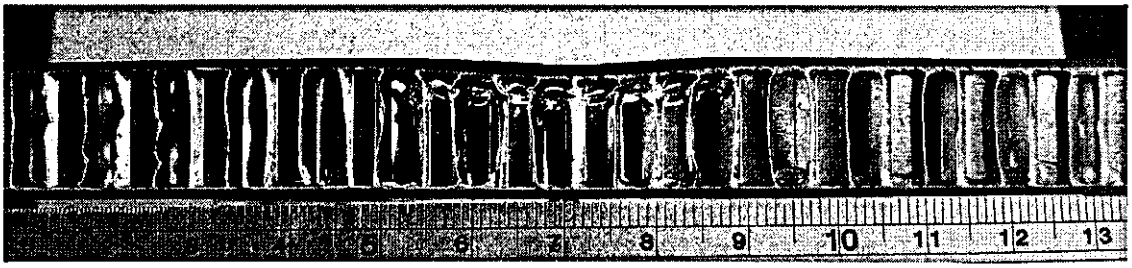

(c) IKE = 5.2J

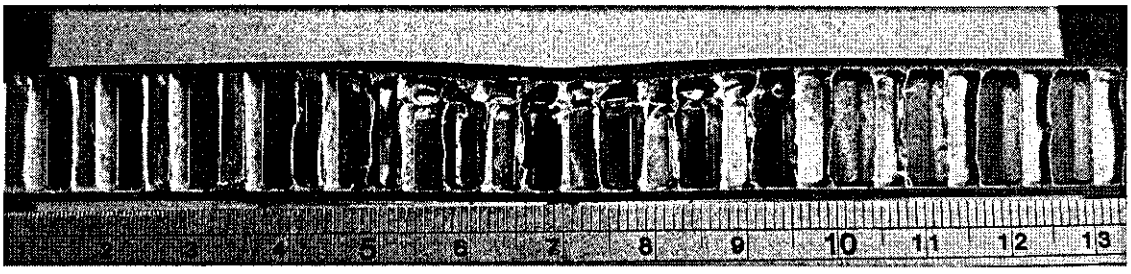

(d) IKE = 9.1J

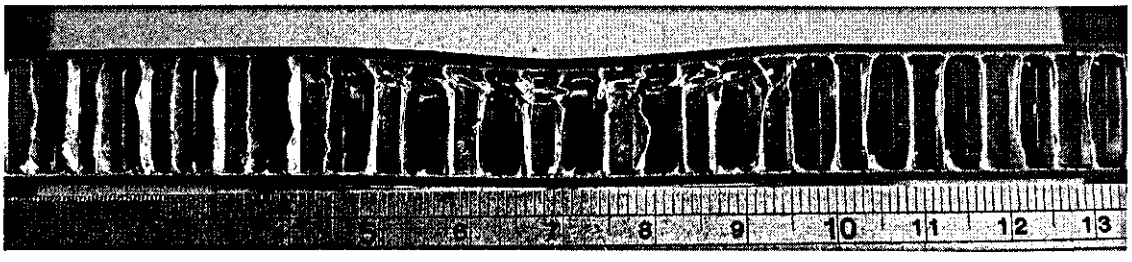

(e) IKE = 13.2J

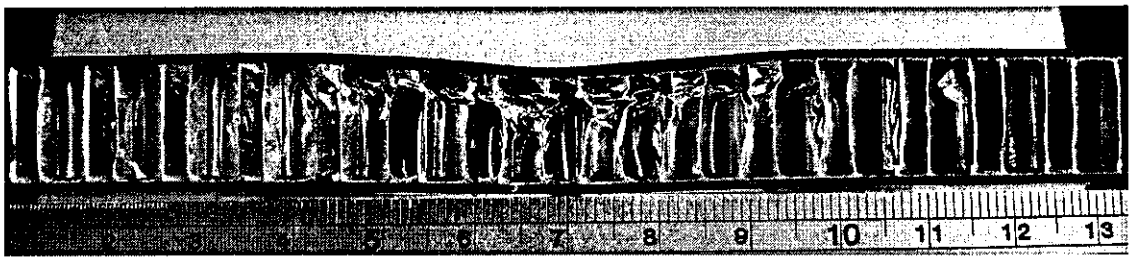

(f) IKE = 16.2J

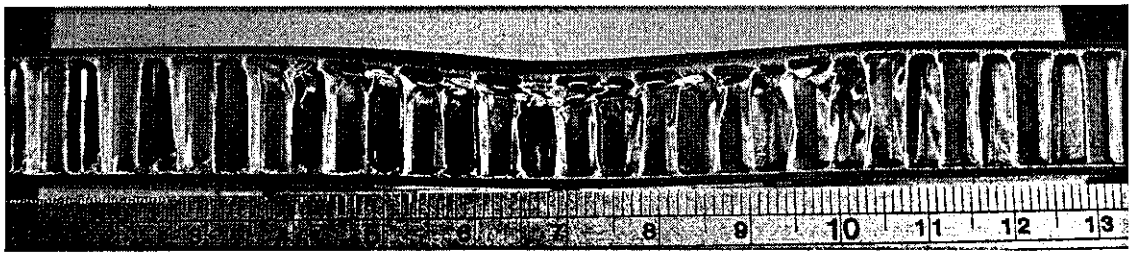

(g) IKE = 20.6J

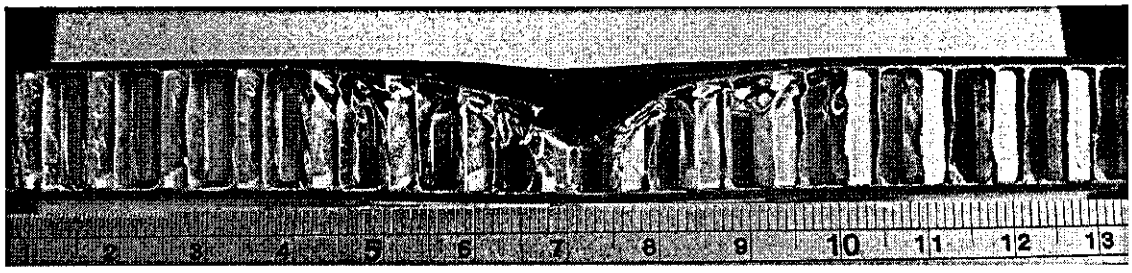

(h) IKE = 25.5J

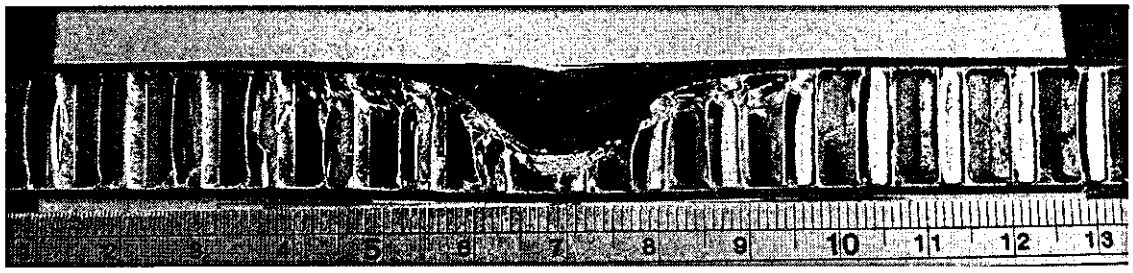

(i) IKE = 30.5J

Figure 6.22 Photographs of cross-sectioned 8 ply 70kg/m^3 panels impacted at 1.5-30.5J

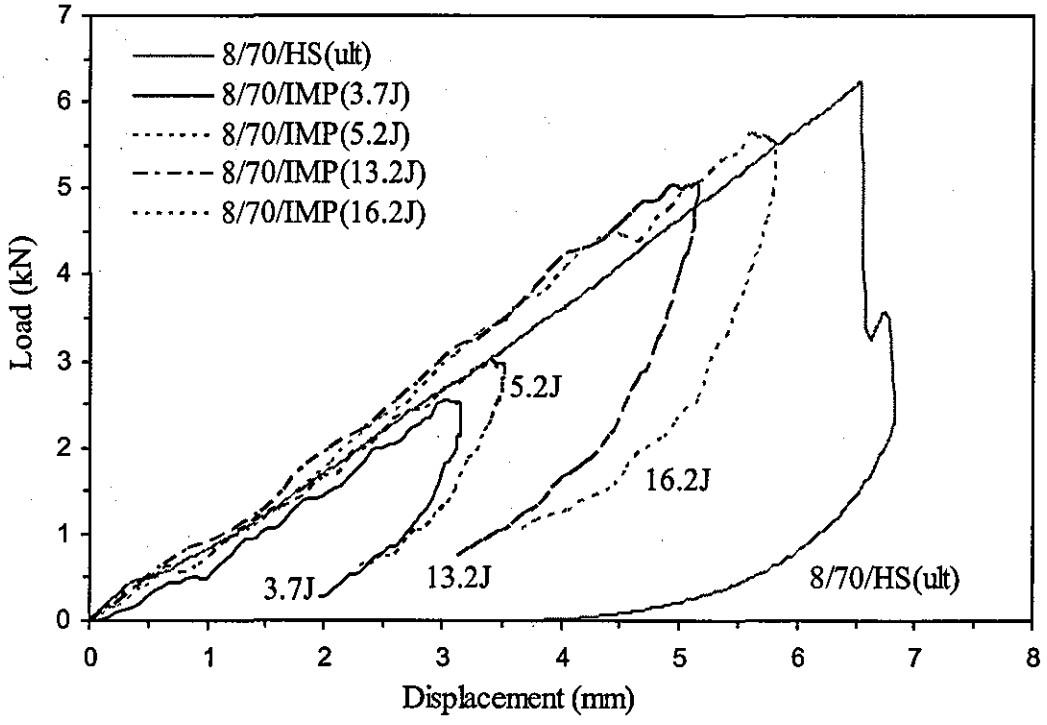

(a)

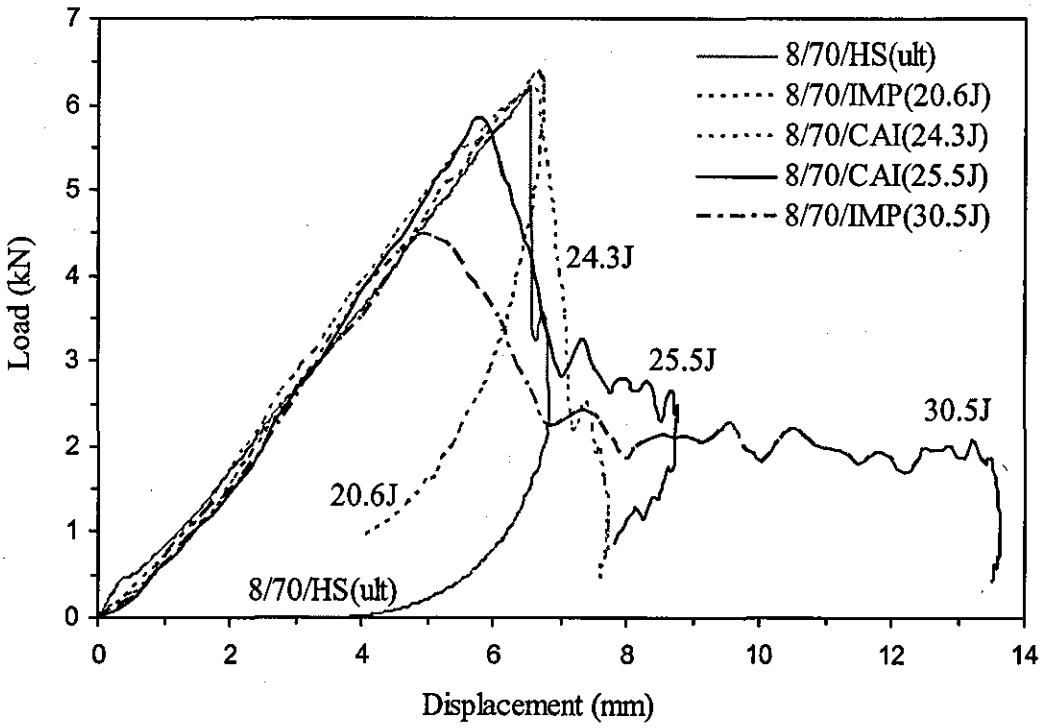

(b)

Figure 6.23 Load vs. Displacement for 8/70/IMP panels for (a) Low IKE (b) High IKE

Transitions in damage mechanisms throughout the IKE range can be identified from the maximum load vs. IKE plot, Fig. 6.24, and damage size vs. IKE plots, Fig. 6.25(a-b). Whilst damage length was measured directly from the cross-sectioned panels, damage area was estimated with the assumption of a circular shape. The increase in damage length with IKE is inherently non-linear up to 5J, whilst the increase in damage area is linear. In both cases the delamination and core crushing lengths are similar. This region, numbered 1 in Fig. 6.25(b), represents a steady increase in damage through core crushing and minor delaminations. These delaminations occur directly under the indenter between a small number of ply interfaces. As the IKE is increased these delaminations extend away from the impact centre until the stress levels triggered by the impact dominate the impact event causing it to become unstable, which in turn produces noticeable delamination growth at one of the ply interfaces.

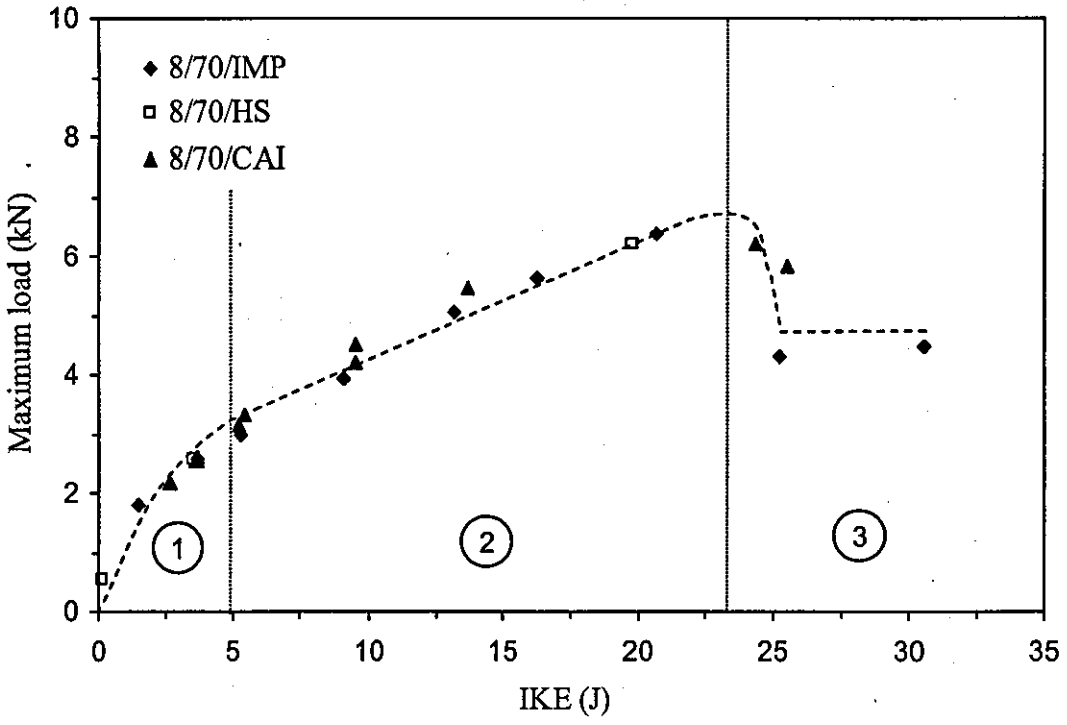

Figure 6.24 Variation of maximum load with IKE for all 8 ply 70kg/m^3 impact and QS tests

After 5J the core crushing size increases linearly with IKE until fibre fracture and is more extensive than delamination, labelled region 2. The rate of increase in delamination size with IKE reduces and plateaus from 10-16J. In this plateau region

increases in IKE do not cause further propagation of the major delamination as the stresses at the delamination tip are less than the required crack opening stresses. Consequently the smaller local delaminations propagate within the damage region. As delamination is only measured by the magnitude of in-plane damage length rather than through-the-thickness delamination levels this region is seen as a suspension of damage growth. Delamination growth then resumes once the multiple delaminations through the thickness are of similar size. The steady linear increase in core crushing is expected since the local top skin deflection steadily increases with IKE between 5-20J regardless of damage mechanisms.

Fibre fracture, accompanied by a large amount of skin delamination and core crushing, initiates at approximately 23J, the start of region 3, when the local stresses become too large and both transverse and in-plane damage propagation are at their limit. As each individual ply fractures stresses are rapidly transferred to the other intact plies and the fractured plies 'spring' back towards their relaxed state, causing existing delaminations to propagate further until entire top skin penetration at 25J. Increasing the IKE to 30.57J caused an increase in the depth of core crushed, though the area which core crushing and skin delamination was spread over decreased. At the higher IKE the stresses tend to become more localised, which in turn causes fibre fracture to occur faster and the impact is resisted by a smaller area of the panel. Consequently the corresponding maximum load during impact is reduced, Fig. 6.24, and a reduction in damage area after fibre fracture can be observed for both skin delamination and core crushing areas. A trend line was added to Fig. 6.24 based upon the available data and shows a significant load drop for a small increment of IKE at the beginning of region 3. This sharp drop maybe as a result of the limited number of data points combined with normal experimental data scatter rather than a true feature of the sandwich panel response, and could be eliminated if more data points were collected.

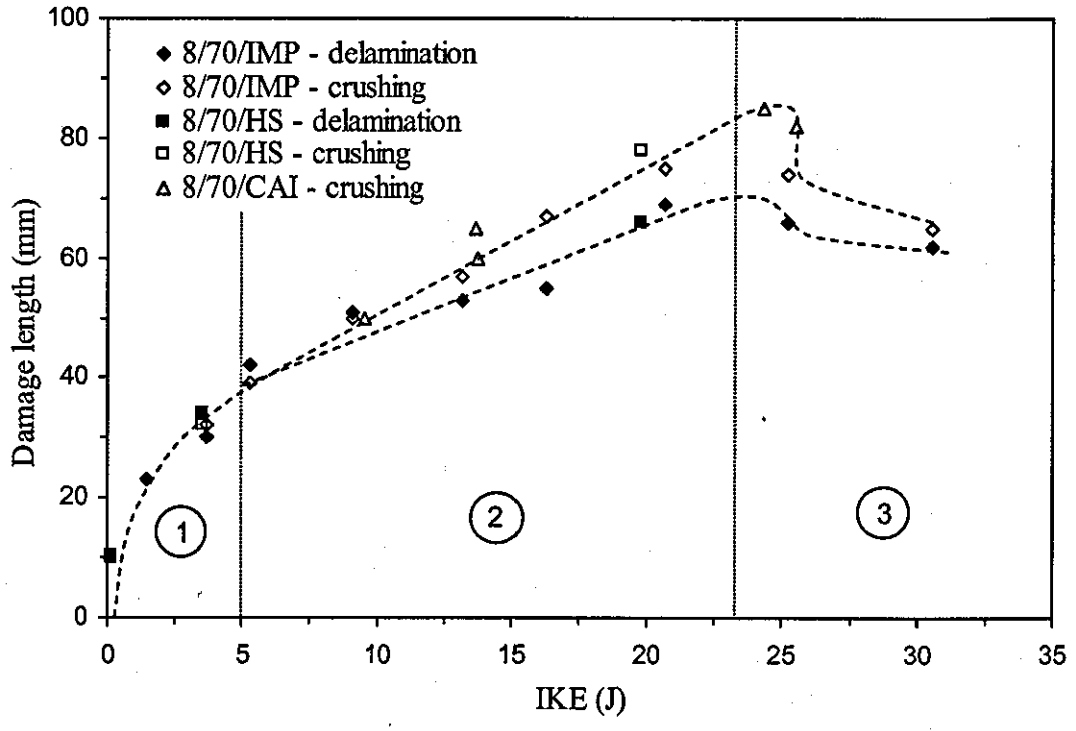

(a)

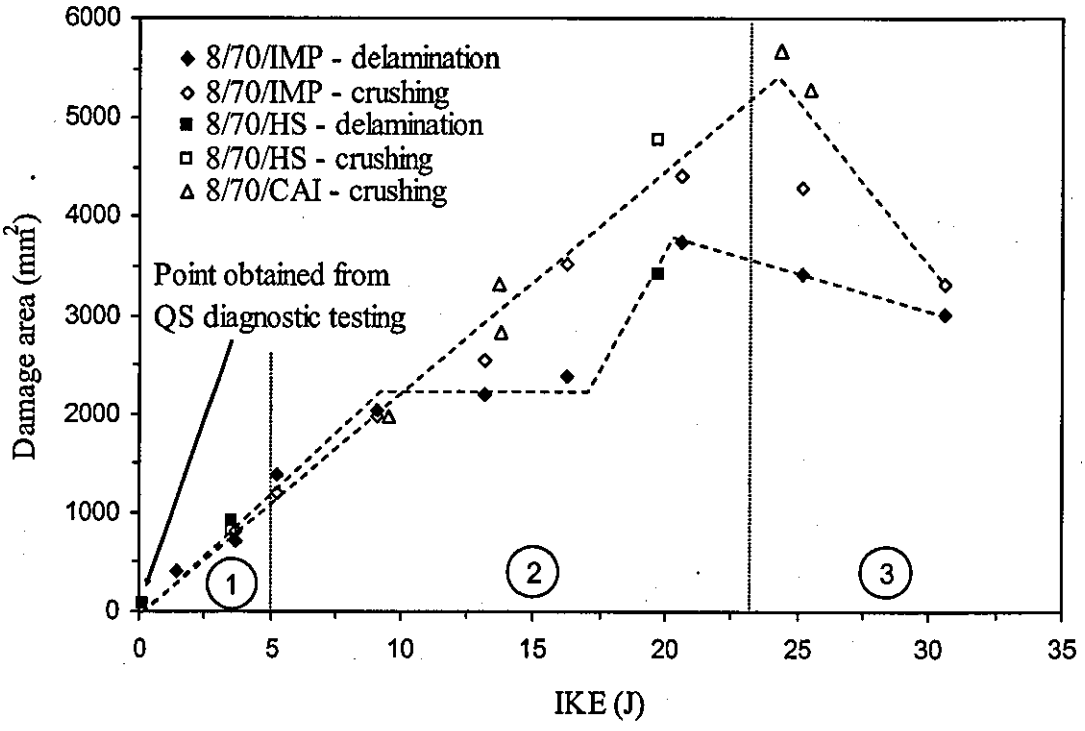

(b)

Figure 6.25 (a) Damage length vs. IKE for 8 ply 70kg/m^3 impact and QS tests

(b) Damage area vs. IKE for 8 ply 70kg/m^3 impact and QS tests

The efficiency of a panel for energy absorption purposes can be measured by dividing the absorbed energy by the impact energy. This is represented graphically by plotting AE against IKE in Fig. 6.26. Up to the point of fibre fracture absorbed energy is 64 - 69% of IKE. After fibre fracture this ratio increases to about 98%. Within regions 1 and 2 elastic deformation of the top skin, and bottom skin to a lesser extent, occurs in addition to internal damage propagation. This stretching is almost reversible upon unloading and therefore provides a recoverable mechanism of energy absorption, in this case around 30%. After top skin fibre fracture the energy absorbed through global deformation of the bottom skin is still recoverable, represented by the 2% of recoverable energy present after fibre fracture. This recoverable type of energy absorption mechanism can be very beneficial when designing a structure to resist multiple impacts and therefore it is very useful to know the location of the boundary between the two absorption regions.

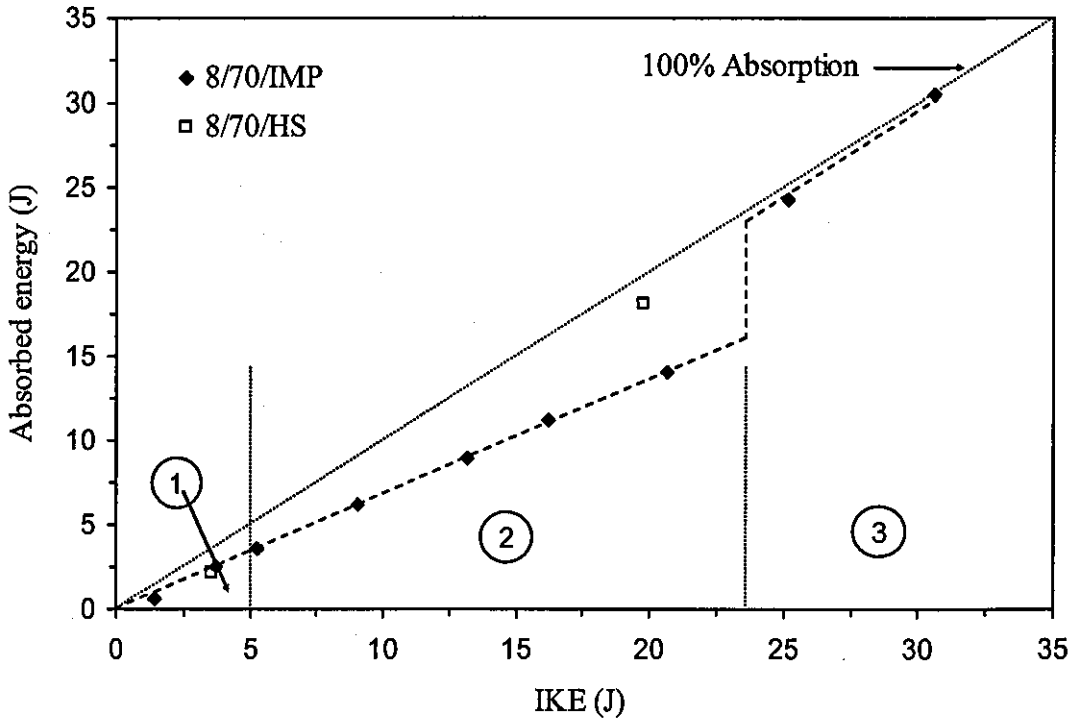

Figure 6.26 Variation of absorbed energy with IKE for 8 ply 7kg/m^3 panels under impact and QS loading

6.3.2. Effect of skin thickness on damage mechanisms and energy absorption

Panels with 16 ply skins and 70kg/m^3 aluminium honeycomb were impacted at increasing IKE levels up to 55J, just sufficient to cause fibre fracture of the top skin. An example of the load-displacement response attained from the impact tests on the 16 ply panels is shown in Fig. 6.27. The shape of the maximum load vs. IKE curve in Fig. 6.28 is similar for each panel thickness. Although the magnitude of the maximum load attained for the 16 ply panels for a given impact energy was higher than for the 8 ply panels it was not doubled. Nevertheless, it is interesting to note that both the maximum load and IKE level sustained by the panel immediately before fibre fracture doubled from 6kN at 23J to 12kN at 46J when the skin thickness was doubled.

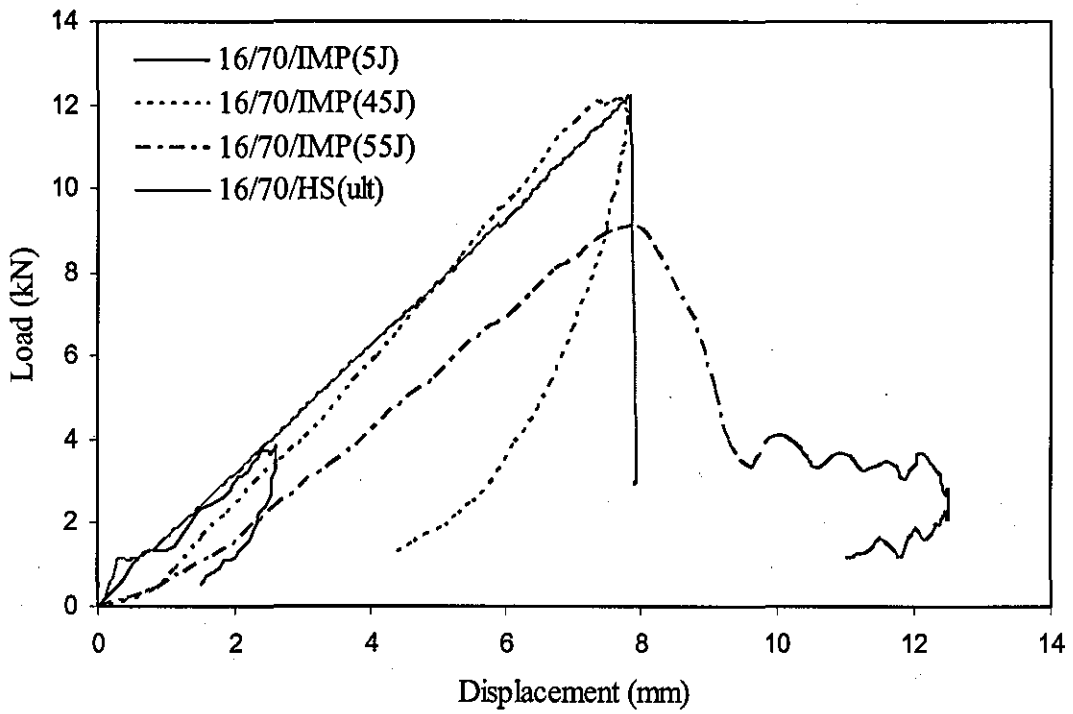

Figure 6.27 Load-displacement curves from quasi-static and impact tests on 16 ply 70kg/m^3 panels

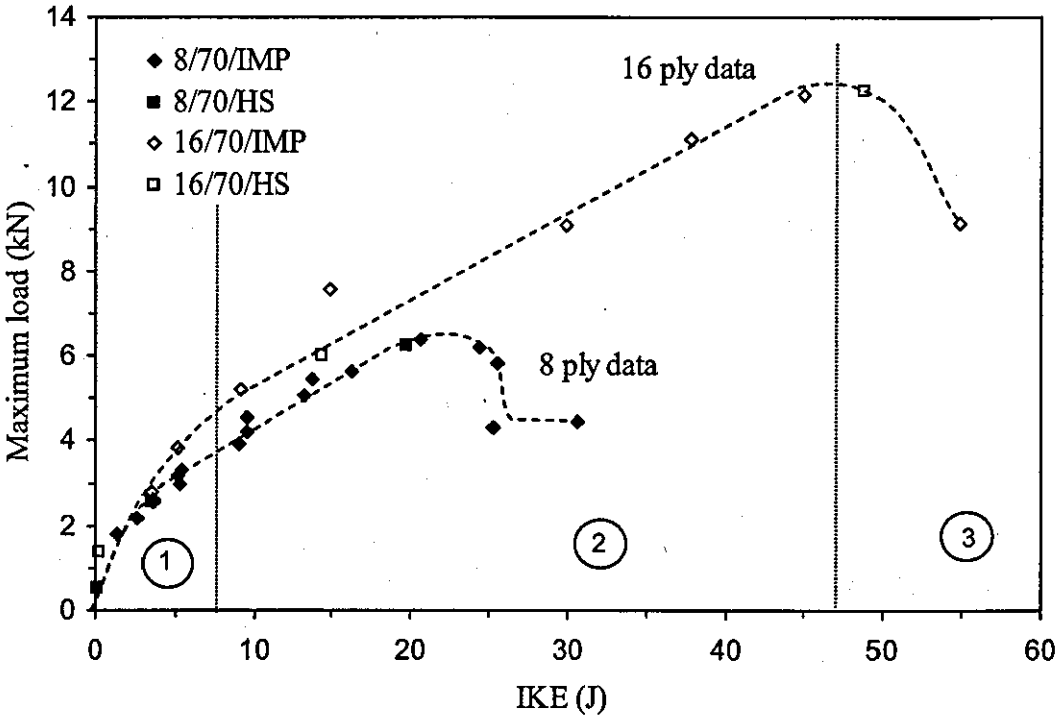

Figure 6.28 Comparison of variation in maximum load with IKE for 8 & 16 ply 70kg/m^3 panels for all impact and QS tests

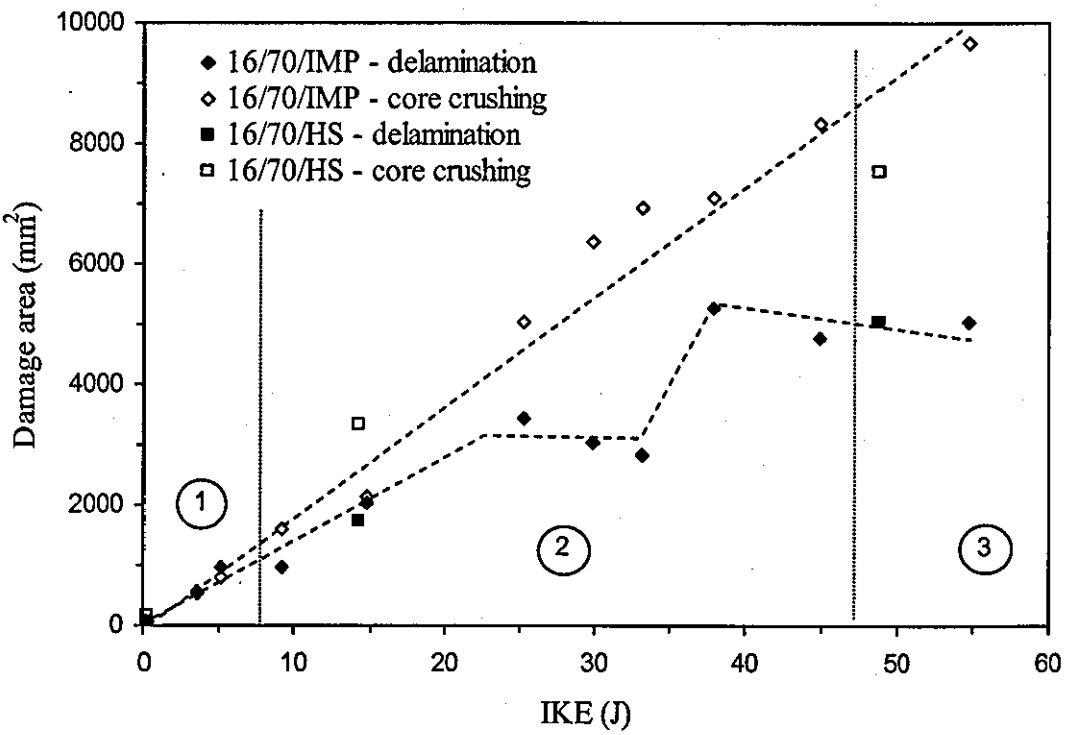

Figure 6.29 Internal damage area in 16 ply 70kg/m^3 panels for varying IKE levels

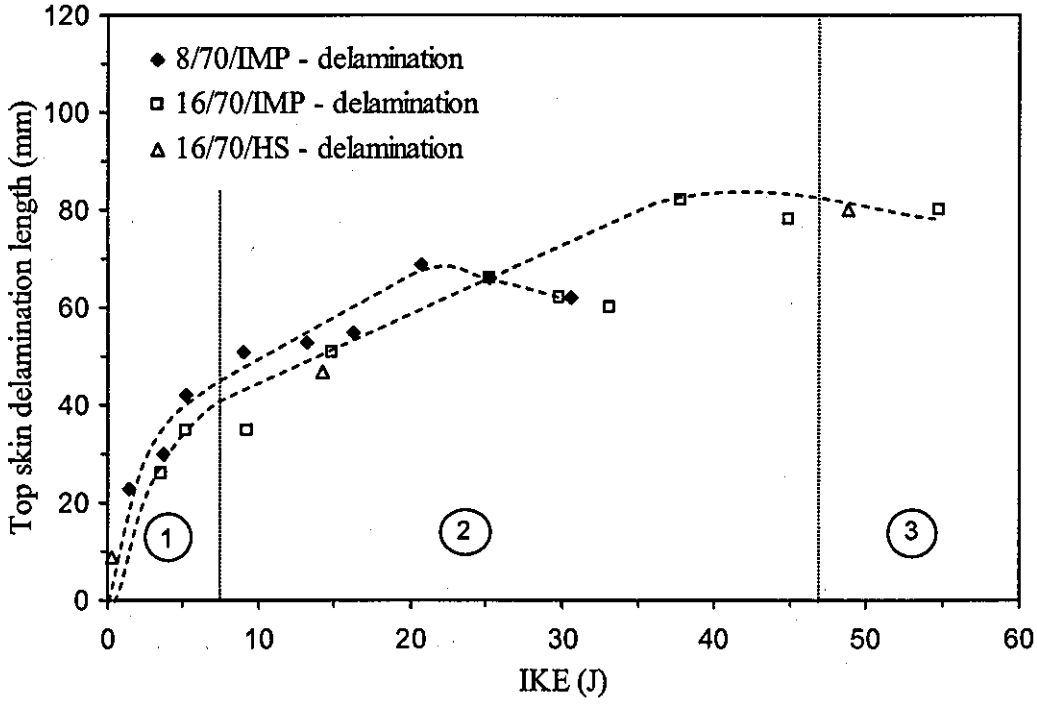

(a)

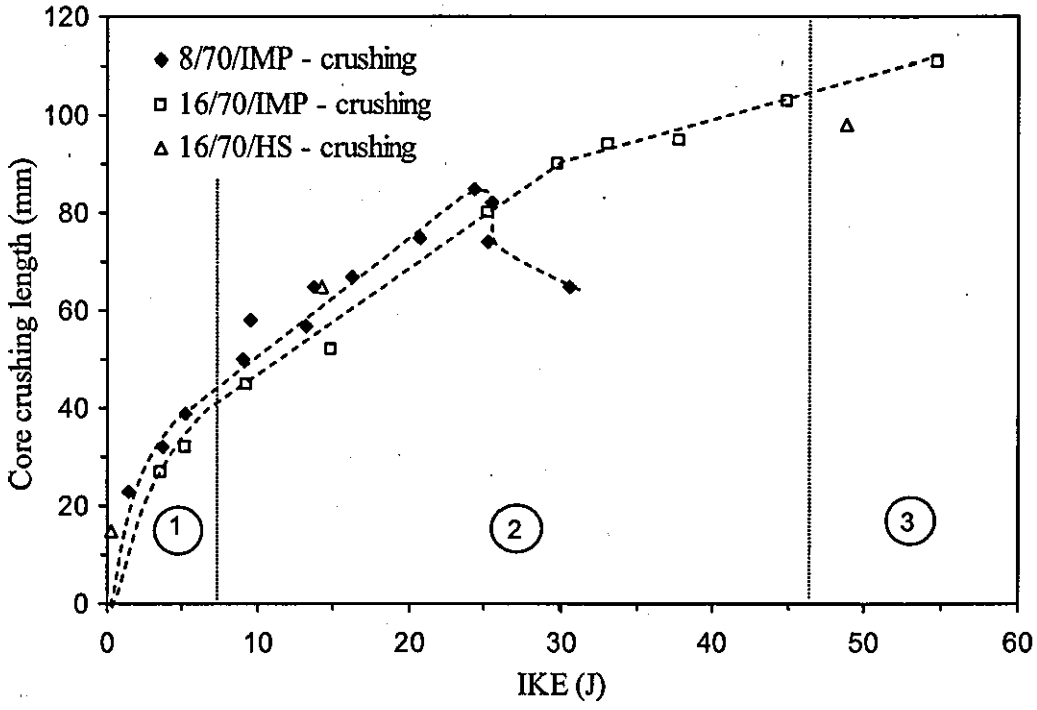

(b)

Figure 6.30 Comparison of internal damage length in 8 & 16 ply 70kg/m^3 panels for varying IKE levels (damage regions based upon 16 ply data only)
(a) top skin delamination length (b) core crushing length

The trends identified previously for the 8 ply panels regarding damage propagation and variation of damage size with IKE level, including the suspension of damage growth represented by the plateau region within region 2 in Fig. 6.29, also apply to 16 ply panels. The upper boundary of regions 1 and 2 are increased to 7.5J and 47J in the 16 ply panels compared to 5J and 23J in the 8 ply panels, Fig. 6.30. The only difference in response occurs within region 2 for the thicker panels where the rate of increase in core crushing reduces at 30J rather than increasing linearly to the point of fibre fracture, Fig. 6.30(b). There is a noticeable scatter in the core crushing data within region 2 for the thinner skinned panels, with a linear line of best fit added. However, a two part line with a reduction in gradient could also be fitted to the 8 ply data, matching the 16 ply trend.

Until the point of fibre fracture the amount of internal damage for a given IKE level is marginally lower for the thicker skinned panels. The closeness of the two sets of data suggests that the impact response is not dominated by skin thickness. The increase in skin thickness and therefore panel stiffness does cause a higher load to be applied to the panel, Fig. 6.28, due to the increased resistance to bending, but that higher load in turn causes higher stresses and therefore gives a damage area similar to that seen for the thinner skinned panel. This is supported by the ratio of absorbed energy to IKE prior to fibre fracture, generally between 65-67%, matching that seen for the 8 ply 70kg/m^3 panels, in Fig. 6.31. This indicates the major source of permanent energy absorption prior to fibre fracture to come from core crushing, with lesser involvement of skin delamination. Therefore increasing the skin thickness affects the energy absorption capacity only in a secondary manner by spreading the load over a larger area of core and allowing larger loads to be absorbed through delamination between double the number of ply interfaces before fibre fracture occurs.

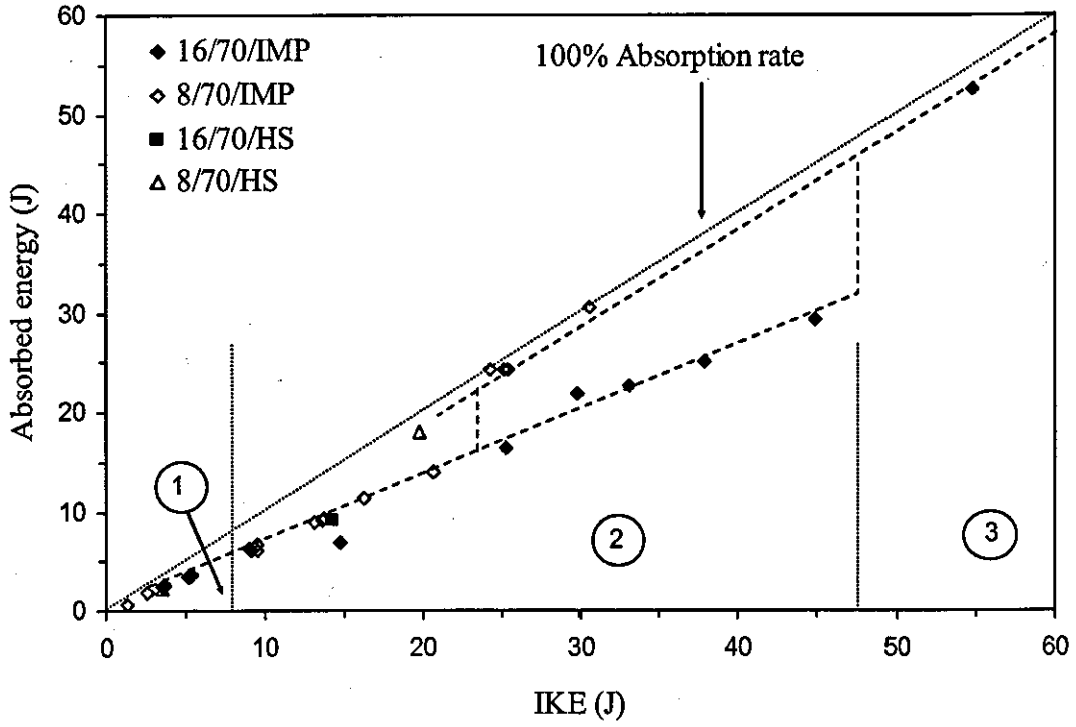

Figure 6.31 Variation of absorbed energy with IKE for 8 and 16 ply 70kg/m^3 panels

6.3.3. Effect of core material on damage mechanisms and energy absorption

To assess the effect of core material on impact response panels with 8 ply skins and a 64kg/m^3 nomex or 70kg/m^3 aluminium core were impacted at increasing IKE levels up to 30J. Fig. 6.32 shows the variation in damage size with IKE for both the panel types. The amount of delamination and core crushing and maximum load sustained by each panel type is similar within region 1. In region 2 of Fig. 6.33, the level of core crushing appears comparable for both core types, though the nomex results do show extensive scatter possibly due to the elastic nature of the nomex core. The reduced stiffness of the nomex panels, as a result of the lower core modulus, seems to result in the reduction in skin delamination size and accompanying maximum load. This is in accordance with the larger impactor displacement of the nomex panels in Fig. 6.34. The existence of the plateau region on the damage area vs. IKE plot cannot be concluded as there are no intermediate data points between 9-16J where the plateau region occurred for the aluminium cored panels.

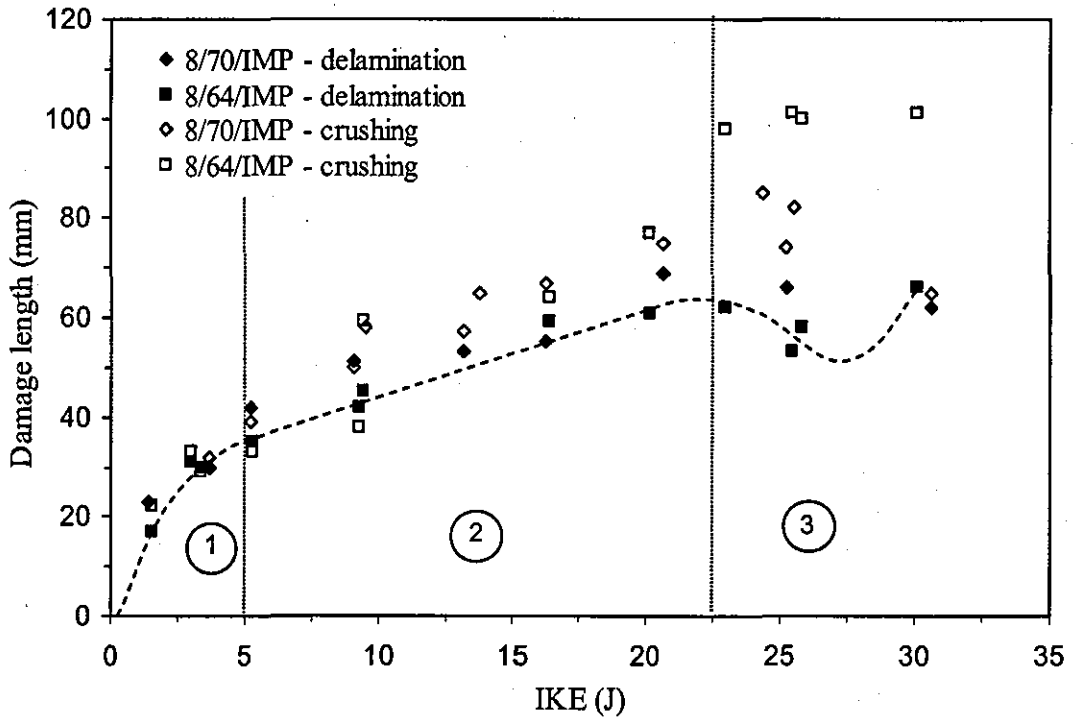

(a)

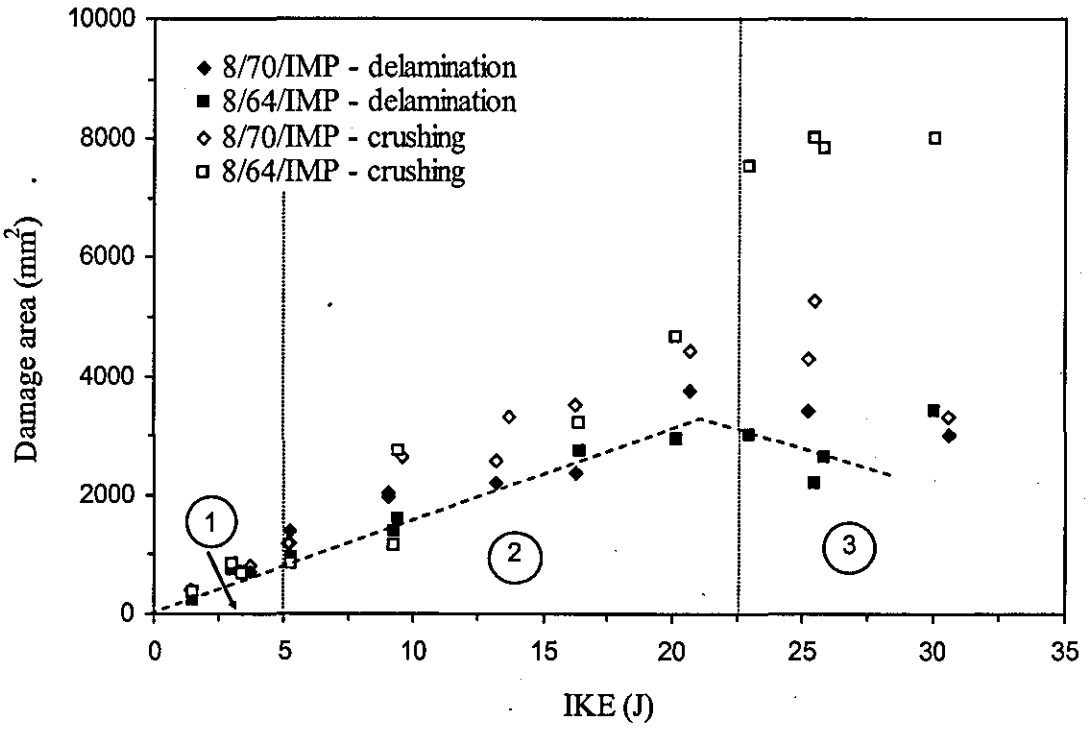

(b)

Figure 6.32 Comparison of internal damage in 8 ply 64kg/m^3 panels and 8 ply 70kg/m^3 panels at various IKE levels using (a) damage length (b) damage area (no correlation added for crushing due to extensive scatter)

Once fibre fracture initiates, around 23J for both panel types, the response of the core material becomes substantial in the nomex panels. This is shown by the core crushing area almost doubling upon fibre fracture, Fig. 6.32(b). This is also accompanied by a higher maximum load sustained by the nomex panels than the aluminium panels and an increase in impactor displacement with IKE, Fig. 6.34. When fibre fracture occurs sudden pressure is passed from the skin to the core causing extensive core damage in the brittle nomex. As loading continues past fibre fracture the higher crush strength of the nomex allows the nomex panels to sustain a higher load than the aluminium panels.

Absorbed energy, until the point of fibre fracture is 52-59% of the IKE for the nomex panels, compared to 64-69% for the aluminium panels. After fibre fracture AE increases to 96%, similar to that of the aluminium panels, shown in Fig. 6.35. The difference in the amount of absorbed energy between the two core materials is directly related to the greater ability of the nomex panels to recover elastically.

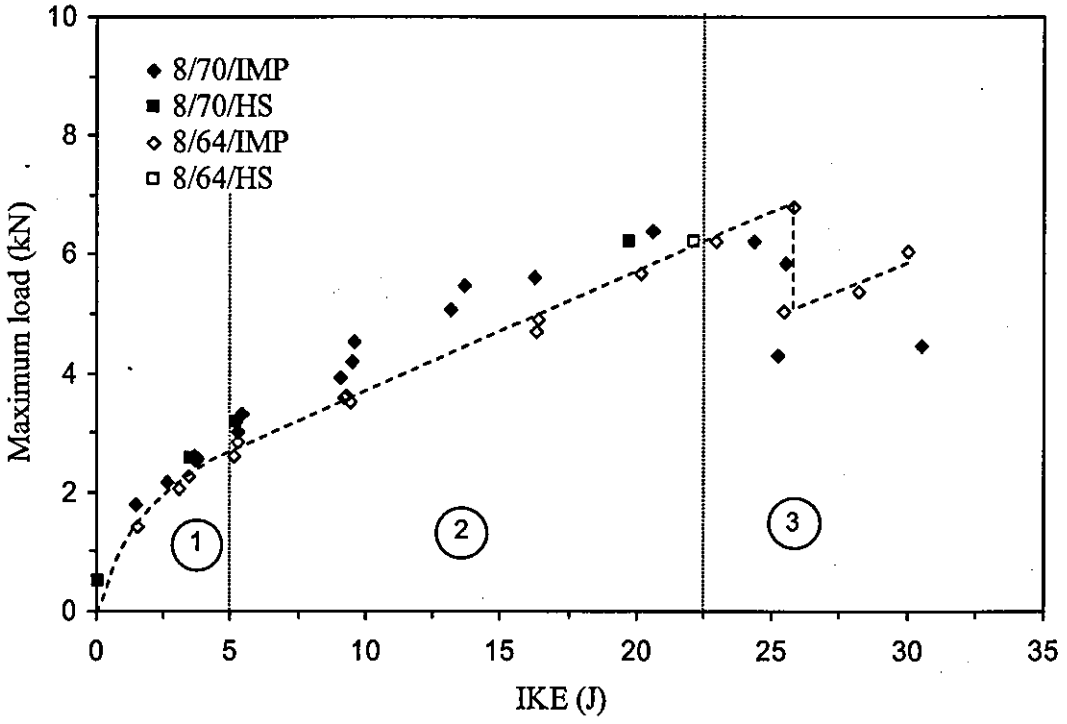

Figure 6.33 Comparison of variation in maximum load with IKE for 8 ply panels with 64kg/m^3 nomex and 70kg/m^3 aluminium cores

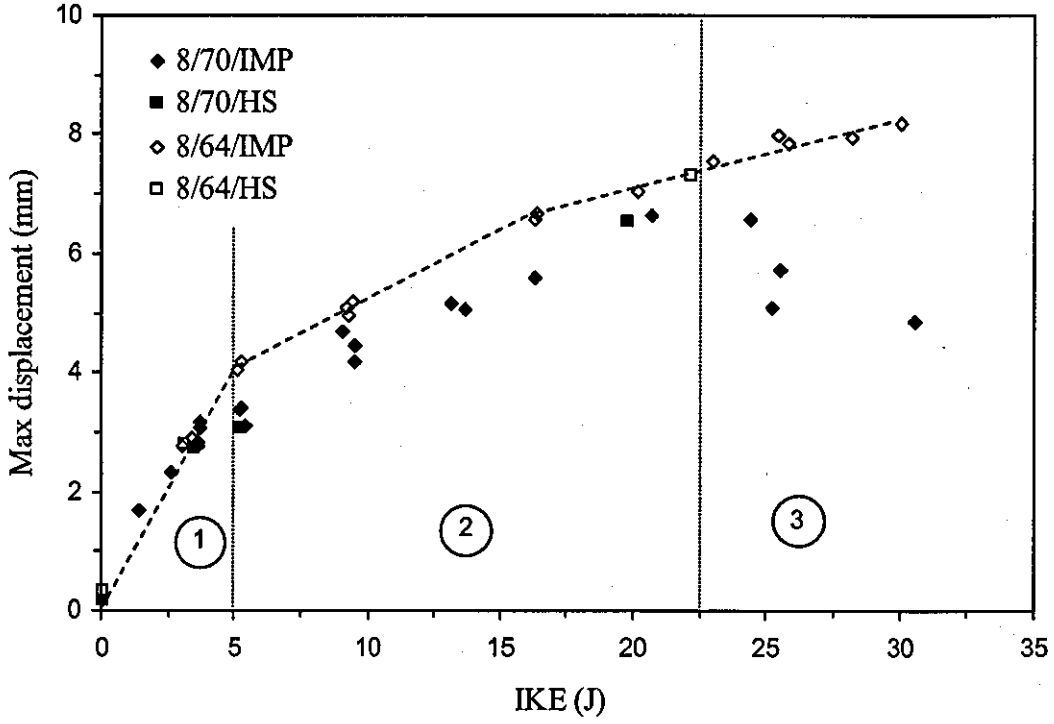

Figure 6.34 Comparison of variation in maximum impactor displacement with IKE for 8 ply panels with 64kg/m^3 nomex and 70kg/m^3 aluminium cores

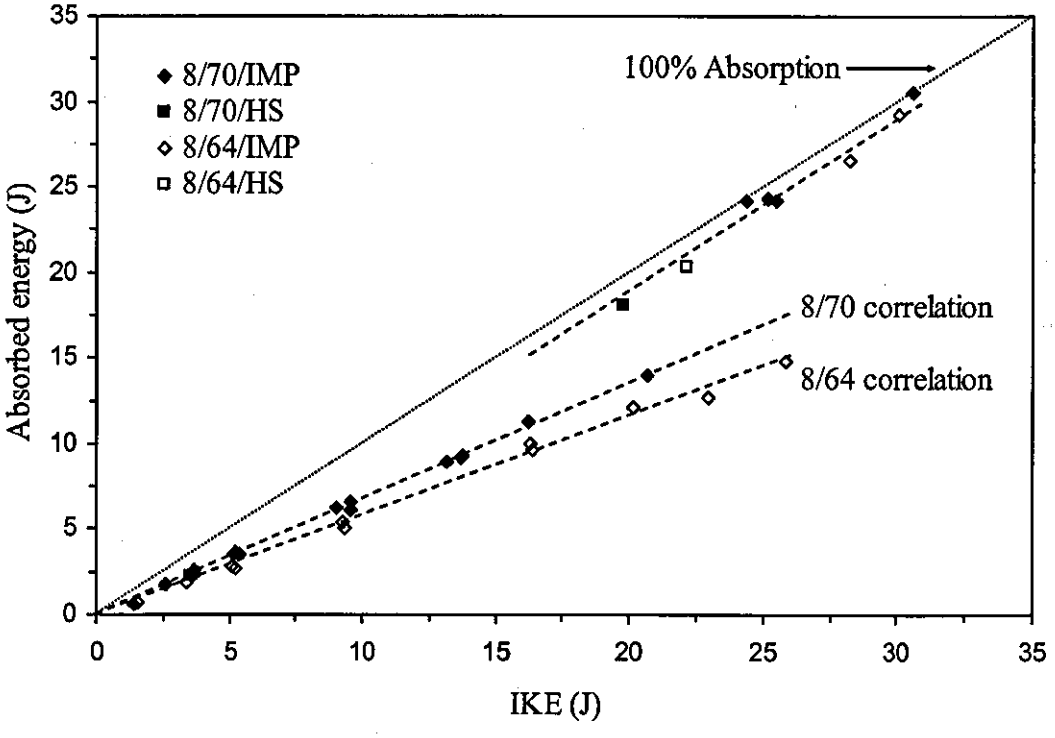

Figure 6.35 Variation of absorbed energy with IKE for 8 ply 64kg/m^3 panels

6.3.4. Quasi-static vs. impact testing

It is often desirable to use quasi-static testing rather than low-velocity impact testing when studying the response of panels to transverse loading because of its convenience, if the panels are 'rate insensitive. As the impact velocities used in the current investigation were low, the quasi-static and impact responses are expected to be similar. A comparison of the results from each test type with respect to damage mechanisms has been made for all panel types tested, with quasi-static data included where possible in Figs. 6.23-6.35 and Tables 6.24-6.27.

In the quasi-static loading case damage initiation and propagation was clearly represented on the load-displacement curves via load drops and changes in gradient. Due to the rapid nature of impact testing and inherent problems with signal interference the impact load-displacement curves contain a limited number of data points and fluctuations, which inhibit the identification of damage propagation from the curves. Although the load-displacement curves derived from the impact data show reasonable correlation with the quasi-static data, examples shown for 8 and 16 ply 70kg/m^3 panels in Figs. 6.23 and 6.27, there are no clear signs of damage propagation unless fibre fracture occurs.

In some of the lower IKE level impacts there is a clear change in panel stiffness around the quasi-static initial threshold load. This feature becomes less obvious in the higher level IKE impacts and in a number of tests the panel stiffness actually increases past the initial threshold. Typically panel stiffness between the initial threshold and ultimate failure is very similar for quasi-static and impact testing. This is to be expected as LTM45-EL and 8552 epoxies have minimal sensitivity to strain rate at low-velocities [205,206]. 5052 type aluminium honeycomb does show strain rate effects with the impact mean crushing pressure 30-50% higher than the quasi-static value when impacted at 8.5-35m/s [65,87]. This increase is reduced to 10% for nomex honeycomb.

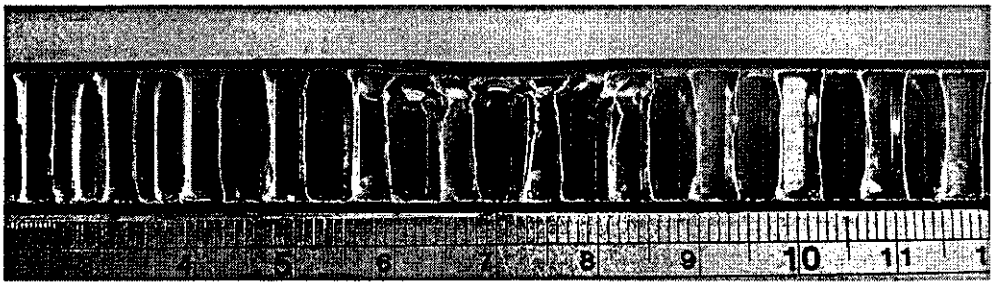

(a)

(b)

Figure 6.36 Photograph of the internal damage in comparable 8 ply 70kg/m^3 panels
(a) Impact at 3.7J (b) Quasi-static secondary diagnostic test

In all panels configurations tested the load required to cause fibre fracture under impact is comparable to the quasi-static load, though the corresponding IKE level is typically higher, illustrated in the plots of maximum load vs. IKE, Figs. 6.24, 6.28, 6.33. Whilst the slight increase in IKE is due to the increase in global bending of the impact specimens, the clear correlation of maximum load is expected as the underlying damage mechanisms are the same for both impact and quasi-static loading. The damage measured from the quasi-static diagnostic test panels has been included on the damage length/area vs. IKE curves in Figs. 6.25, 6.29, 6.30, 6.32. The amount of internal damage in terms of both core crushing and skin delamination size within the quasi-static and impact panels with a corresponding IKE is almost identical.

This is illustrated in Fig. 6.36 for the 8/70/HS(sec) panel with an applied energy of 3.5J and the 8/70/IMP(3.7J) panel. The maximum load reached in each test was almost identical (~2.56kN) along with the amount of core crushing (~32mm) and skin delamination (~33mm). It was not possible to recreate the damage level seen in the quasi-static initial diagnostic test due to the very low level of IKE required to obtain the

equivalent level of initial damage from the quasi-static tests. The internal damage in the quasi-static panel with ultimate failure at 6.22kN is compared to the 20J (no fibre fracture, maximum load 6.38kN) and 25J (fibre fracture, maximum load 4.3kN) impact panels in Fig. 6.37. All panels have similar core/skin damage lengths with fibre fracture in the 25J and QS panels.

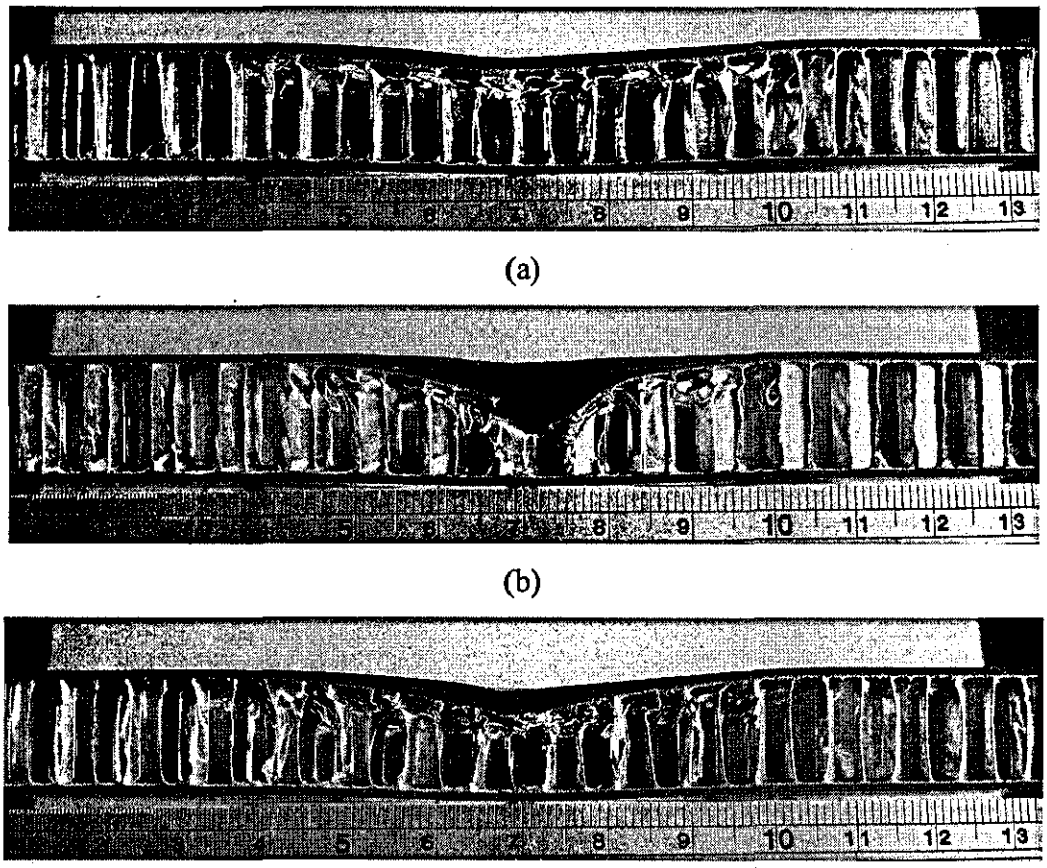

(a)

(b)

(c)

Figure 6.37 Photograph of the internal damage in 8 ply 70kg/m^3 panels
(a) Impact at 20.6J (no fibre fracture) (b) Impact at 25.2J (fibre fracture)
(c) Quasi-static ultimate failure test

As the key damage mechanisms were the same for both quasi-static and impact test cases the levels of absorbed energy were also the same, as shown in Figs. 6.26, 6.31 and 6.35. Unfortunately only a very small number of quasi-static diagnostic tests had controlled unloading of the specimen after secondary damage, namely 8, 12 and 16 ply

panels with 70kg/m^3 core and 12 ply 64kg/m^3 nomex panels. The average amount of absorbed energy at secondary damage was 63% and 46% in the aluminium and nomex panels respectively. At ultimate failure this increased to 92% for both the aluminium panels and the nomex panels. These figures match well with those of the impact specimens prior to and after fibre fracture, 64-69% increasing to 98% for aluminium panels and 52-59% increasing to 96% for the nomex panels.

Overall it can be concluded that the damage mechanisms identified in the quasi-static tests are applicable to impact testing and the sandwich panels are not strain rate sensitive. Impact testing has proved skin delamination to occur at low IKE levels and propagate at a steady rate in conjunction with core crushing. The increase in IKE required for fibre fracture is due to the increased deflection at fibre fracture in the impact specimens, allowing increased energy absorption through global bending.

6.4. Damage resistance assessment

It has been shown that panel strength typically increases with skin thickness, core density and indenter type (HS to FE). Incident energy and therefore absorbed energy also increases with skin thickness and indenter type (HS to FE), though its relationship with core density is less critical and depends on the indenter type. If the weight of the panels is also considered the most efficient structure for both damage resistance and energy absorption can be identified. As not all panels were weighed and there was a variation in actual weight due to manufacturing alterations concerning the amount of adhesive used, a theoretical weight has been used. The theoretical weight has been calculated based upon the skin and core weights measured experimentally and an adhesive weight of 6g for 1 sheet used per bond line.

For maximum strength and damage resistance clearly panels with a thick skin and high density aluminium core will provide optimum performance, as summarised in Table 6.9. However, weight is an important issue in many operational structures, so consequently a trade off often has to be made. When the weight of the panels is taken into consideration, as illustrated in Table 6.10, optimum panel performance is not so

clear cut. When the loading area is concentrated, as in the HS loading case, panels with thin skins and a high density core can often perform as well as panels with a thicker skin and lower density core. The use of panels with a thinner skin and higher density core may also be beneficial in terms of manufacturing cost as the cost of using more carbon fibre is much greater than the cost of using denser honeycomb. When the loading area is larger as in the FE case, although panels with thicker skins still perform best honeycomb density becomes less relevant such that lower density cores often perform better than higher density cores.

Table 6.9 Ultimate failure load for each panel design under quasi-static loading

Skin/Core	HS indenter - Max load (kN)				
	50	70	90	64	96
4	3.09	4.00	4.26	-	-
8	5.41	6.22	7.86	6.22	6.44
12	7.65	8.32	9.85	8.17	10.34
16	9.25	12.21	14.05	12.76	13.40
Skin/Core	FE indenter – Max load (kN)				
	50	70	90	64	96
4	4.99	5.12	5.36	-	-
8	8.66	9.21	9.95	8.70	8.57
12	13.94	12.83	14.02	12.40	12.04
16	16.77	16.67	19.75	17.00	17.55

Table 6.10 Maximum load per gram for each panel design at ultimate failure under quasi-static loading

Skin/Core	HS indenter - Max Load per gram (N/g)				
	50	70	90	64	96
4	51.02	60.58	59.66	-	-
8	58.56	63.57	76.15	62.89	59.48
12	60.75	63.32	72.02	61.68	72.91
16	56.89	72.65	81.01	75.44	75.07
Skin/Core	FE indenter - Max load per gram (N/g)				
	50	70	90	64	96
4	82.40	77.54	75.07	-	-
8	93.74	94.12	96.40	87.96	79.15
12	110.71	97.65	102.52	93.62	84.90
16	103.14	99.18	113.87	100.51	98.32

In addition to damage resistance performance, the ability of a structure to absorb energy is often of equal importance. Whilst energy absorption clearly increases with skin thickness, even when panel weight is taken into consideration core density is an important factor, as shown in Tables 6.11 and 6.12. The energy absorption per gram for panels with a low density core is often higher than for those with a high density core, especially when the loading area is of significant size as in the FE loading case. This is as a direct result of increased core crushing area in the panels with a low density core. Core crushing is the best source of energy absorption, especially prior to fibre fracture of the skins as it also causes bending of the top skin, and is optimised when the loading area is large and the core density and therefore crushing strength is low.

Table 6.11 Energy absorption for each panel design at ultimate failure under quasi-static loading

Skin/Core	HS indenter - energy absorption (J)				
	50	70	90	64	96
4	8.73	10.77	11.14	-	-
8	20.09	19.74	27.9	22.13	24.44
12	28.63	29.02	36.21	29.64	39.23
16	40.63	48.56	56.87	58.07	53.77
Skin/Core	FE indenter – energy absorption (J)				
	50	70	90	64	96
4	22.35	17.39	15.26	-	-
8	38.07	35.72	38.06	40.34	42.87
12	72.74	55.61	60.37	64.70	53.86
16	91.80	74.82	91.79	91.49	75.48

Table 6.12 Energy absorption per gram for each panel design at ultimate failure under quasi-static loading

Skin/Core	HS indenter - energy absorption per gram (J/g)				
	50	70	90	64	96
4	0.14	0.16	0.16	-	-
8	0.22	0.20	0.27	0.22	0.23
12	0.23	0.22	0.25	0.29	0.28
16	0.25	0.289	0.33	0.34	0.30
Skin/Core	FE indenter - energy absorption per gram (J/g)				
	50	70	90	64	96
4	0.37	0.26	0.21	-	-
8	0.41	0.37	0.37	0.41	0.40
12	0.58	0.42	0.43	0.49	0.38
16	0.56	0.45	0.53	0.54	0.42

6.5. Concluding remarks

The damage resistance of composite sandwich panels has been assessed in terms of damage mechanisms and energy absorption. Both quasi-static and impact loading cases have been considered along with the effect of skin thickness and material, core density and material, indenter type and panel boundary conditions. For all cases the critical damage mechanisms do not change. Skin thickness is seen to have the largest effect on panel performance both in terms of critical loads and energy absorption. Indenter nose-shape has a significant affect on the damage resistance of a panel, with panels being much more susceptible to damage when the loading area is concentrated as in the case of the HS indenter.

Panel boundary conditions studied included panels with a larger loading area in bending and panels resting on a solid foundation. The outcome of these tests showed the local response to be dominant. Although the larger panels had an increased ultimate failure load and energy absorption due to an increase in the global bending response the damage mechanisms were the same. Tests on the nomex panels showed global bending to occur to a larger extent than in the aluminium panels, which provided a useful source of recoverable energy such that the level of energy absorbed in creating permanent damage was reduced by around 10%.

The effect of loading rate, for impacts up to 8.5m/s was deemed negligible. The damage mechanisms witnessed under impact loading matched those seen in quasi-static testing and showed core crushing and delamination to both be present at low impact energies and increase until fibre fracture occurred. Absorbed energy was approximately 65% in the aluminium panels for all IKE levels up to that required for fibre fracture. The optimum design for panels in terms of both energy absorption and damage resistance was assessed with consideration of panel weight, and determined to be panels with a thick skin and low density core when the loading area is significant. For a concentrated loading area thin skin-high density core panels perform equally well, especially when material cost is taken into consideration.

Table 6.13 Critical load & displacement values of T700/LTM45-EL skins / aluminium core sandwich panel quasi-static bending tests

Specimen identity	Initial damage		Secondary damage		Ultimate failure	
	Load (kN)	Displ./LVDT* (mm)	Load (kN)	Displ./LVDT* (mm)	Load (kN)	Displ./LVDT (mm)
4/50/HS1	0.16	0.15/0.04	1.63	3.02/0.52	3.09	5.62/1.59
4/50/FE1	1.26	0.54/0.23	3.02	3.74/1.38	4.99	7.59/4.20
4/70/HS1	0.28	0.30/0.05	2.67	3.46/0.76	4.00	5.28/1.65
4/70/FE1	2.20	0.50/0.29	3.23	2.51/0.74	5.12	5.31/2.16
4/70/FE2	2.15	0.55/0.39	-	-	-	-
Average±SD	2.18±0.04	0.53±0.04/0.34	-	-	-	-
4/90/HS1	0.24	0.16/0.05	1.83	2.25/0.44	4.26	5.11/1.70
4/90/FE1	2.93	0.78/0.58	4.85	3.67/1.88	5.36	4.41/2.38
8/50/HS1	0.37	0.27/0.06	2.66	3.62/0.59	5.41	7.29/2.40
8/50/HS2	0.37	0.24/0.05	-	-	-	-
Average±SD	0.37±0.00	0.26±0.02/0.06	-	-	-	-
8/50/FE1	1.77	0.46/0.21	4.30	3.86/1.51	8.66	8.27/4.54
8/50/FE2	1.68	0.47/0.23	-	-	-	-
Average±SD	1.73±0.06	0.47±0.01/0.22	-	-	-	-
8/70/HS1	0.48	0.42/0.19	2.62	2.94/0.76	6.22	6.54/2.56
8/70/HS2	0.48	0.23/0.07	2.57	2.72/0.43	-	-
8/70/HS3	0.54	0.23/0.07	-	-	-	-
Average±SD	0.50±0.03	0.29±0.11/0.11	2.60±0.04	2.83±0.16/0.60	-	-
8/70/FE1	2.33	0.37/0.19	5.70	3.93/1.36	9.21	6.87/3.11
8/70/FE2	2.34	0.42/-	3.60	2.17/-	-	-
8/70/FE3	2.26	0.43/-	-	-	-	-
Average±SD	2.31±0.04	0.41±0.03/0.19	4.65±1.49	3.05±1.25/1.36	-	-
8/90/HS1	0.42	0.15/0.03	4.65	3.79/2.98	7.86	6.73/2.43
8/90/FE1	3.50	0.66/0.37	6.56	3.64/2.13	9.95	6.43/3.56
12/50/HS1	0.78	0.30/0.10	3.35	3.32/0.67	7.65	7.41/2.59
12/50/HS2	0.71	0.41/0.09	3.42	3.57/0.67	-	-
12/50/HS3	0.77	0.30/0.10	-	-	-	-
Average±SD	0.75±0.04	0.34±0.06/0.10	3.39±0.05	3.45±0.18/0.67	-	-
12/50/FE1	1.77	0.34/0.14	6.55	4.55/1.80	13.94	9.96/3.92
12/50/FE2	1.63	0.44/0.18	6.71	4.95/2.30	-	-
12/50/FE3	1.65	0.46/-	-	-	-	-
Average±SD	1.68±0.08	0.41±0.06/0.16	6.63±0.11	4.75±0.28/2.1	-	-
12/70/HS1	1.10	0.33/-	4.25	3.40/-	8.32	6.73/-
12/70/HS2	0.93	0.30/-	4.32	3.38/-	-	-
12/70/HS3	0.86	0.22/-	-	-	-	-
Average±SD	0.96±0.12	0.28±0.06/-	4.29±0.05	3.39±0.01/-	-	-
12/70/FE1	2.86	0.61/-	6.83	4.17/-	12.83	8.00/-
12/70/FE2	2.68	0.40/-	7.36	3.98/-	-	-
12/70/FE3	2.71	0.39/-	-	-	-	-
Average±SD	2.75±0.10	0.47±0.12/-	7.10±0.38	4.08±0.13/-	-	-
12/90/HS1	0.91	0.23/0.067	4.20	2.64/0.44	9.85	6.58/2.26
12/90/FE1	4.68	0.68/0.43	5.04	1.46/0.64	14.02	7.33/3.66
16/50/HS1	1.42	0.45/-	4.30	3.57/-	9.25	8.10/-
16/50/HS2	1.31	0.46/-	4.19	3.22/-	-	-
16/50/HS3	1.40	0.42/-	-	-	-	-
Average±SD	1.38±0.06	0.44±0.02/-	4.25±0.08	3.40±0.25/-	-	-
16/50/FE1	2.38	0.45/-	9.69	5.45/2.23	16.77	10.19/3.42
16/50/FE2	2.18	0.34/0.20	7.77	4.27/1.79	-	-
16/50/FE3	2.59	0.36/-	-	-	-	-
Average±SD	2.38±0.21	0.38±0.06/0.20	8.73±1.36	4.86±0.83/2.01	-	-

16/70/HS1	1.06	0.42/0.13	6.98	4.47/1.02	12.21	7.79/2.64
16/70/HS2	1.29	0.30/0.10	6.63	4.07/0.82	-	-
16/70/HS3	1.38	0.30/-	-	-	-	-
Average±SD	1.24±0.17	0.34±0.07/0.12	6.81±0.25	4.27±0.28/0.92	-	-
16/70/FE1	3.71	0.47/-	8.25	3.25/-	16.67	7.95/-
16/70/FE2	3.73	0.38/-	9.03	3.23/-	-	-
16/70/FE3	3.44	0.62/-	-	-	-	-
Average±SD	3.63±0.16	0.49±0.12/-	8.64±0.55	3.24±0.01/-	-	-
16/90/HS1	1.31	0.3/0.12	6.44	3.36/0.77	14.05	7.77/3.00
16/90/FE1	4.71	0.58/0.40	6.86	1.90/0.99	19.75	8.28/4.24

* Standard deviation is given only to the average displacement values.

Table 6.14 Slopes of load-displacement curves of T700/LTM45-EL skins / aluminium core sandwich panel quasi-static bending tests

Specimen identity	Linear elastic region kN/mm	Post-initial damage region kN/mm	Slope loss from initial to secondary region	Post-secondary damage region kN/mm
4/50/HS1	1.14	0.57	50%	0.53
4/50/FE1	3.28	0.70	79%	0.54
4/70/HS1	0.97	0.80	17%	0.73
4/70/FE1	5.00	1.12	-	0.96
4/70/FE2	4.33	-	-	-
Average±SD	4.67±0.47	1.12	76%	-
4/90/HS1	1.62	0.80	51%	0.84
4/90/FE1	5.14	1.10	79%	0.90
8/50/HS1	1.74	0.71	-	0.75
8/50/HS2	1.80	-	-	-
Average±SD	1.77±0.04	0.71	60%	-
8/50/FE1	4.24	0.91	-	1.05
8/50/FE2	3.58	-	-	-
Average±SD	3.91±0.47	0.91	77%	-
8/70/HS1	1.70	0.93	-	1.02
8/70/HS2	2.47	0.93	-	-
8/70/HS3	2.35	-	-	-
Average±SD	2.17±0.41	0.93±0	57%	-
8/70/FE1	6.30	1.13	-	1.29
8/70/FE2	5.57	1.07	-	-
8/70/FE3	5.26	-	-	-
Average±SD	5.71±0.53	1.10±0.04	81%	-
8/90/HS1	2.83	1.27	55%	1.08
8/90/FE1	6.90	1.54	78%	1.15
12/50/HS1	2.60	0.93	-	1.14
12/50/HS2	3.36	0.91	-	-
12/50/HS3	2.57	-	-	-
Average±SD	2.84±0.45	0.92±0.01	68%	-

12/50/FE1	5.90	1.18	-	1.43
12/50/FE2	4.41	1.15	-	-
12/50/FE3	4.34	-	-	-
Average±SD	4.88±0.88	1.17±0.02	76%	-
12/70/HS1	3.33	1.15	-	1.23
12/70/HS2	3.83	1.31	-	-
12/70/HS3	3.91	-	-	-
Average±SD	3.69±0.31	1.23±0.11	67%	-
12/70/FE1	4.69	1.09	-	1.63
12/70/FE2	6.70	1.26	-	-
12/70/FE3	6.95	-	-	-
Average±SD	6.11±1.24	1.18±0.12	81%	-
12/90/HS1	4.14	1.50	64%	1.46
12/90/FE1	7.55	0.67	91%	1.67
16/50/HS1	3.16	1.09	-	1.31
16/50/HS2	2.85	1.18	-	-
16/50/HS3	3.33	-	-	-
Average±SD	3.11±0.24	1.14±0.06	63%	-
16/50/FE1	5.29	1.45	-	1.67
16/50/FE2	6.41	1.36	-	-
16/50/FE3	7.19	-	-	-
Average±SD	6.30±0.96	1.41±0.06	78%	
16/70/HS1	4.07	1.53	-	1.60
16/70/HS2	5.17	1.68	-	-
16/70/HS3	4.60	-	-	-
Average±SD	4.61±0.55	1.61±0.11	65%	-
16/70/FE1	7.89	1.51	-	1.96
16/70/FE2	9.82	1.76	-	-
16/70/FE3	5.55	-	-	-
Average±SD	7.75±2.14	1.64±0.18	79%	-
16/90/HS1	5.11	1.91	63%	1.73
16/90/FE1	8.66	1.28	85%	2.21

Table 6.15 Incident, IE, and absorbed, AE, energies for T700/LTM45-EL skins / aluminium core sandwich panel quasi-static bending tests

Specimen identity	Initial damage		Secondary damage		Ultimate failure	
	IE (J)	AE (J) / AE/IE	IE (J)	AE (J) / AE/IE	IE (J)	AE (J) / AE/IE
4/50/HS1	0.03	-	2.46	-	8.73	7.42 / 85%
4/50/FE1	0.39	-	6.63	-	22.35	21.17 / 95%
4/70/HS1	0.06	-	4.44	-	10.77	10.26 / 95%
4/70/FE1	0.68	0.41 / 60%	5.35	-	17.39	17.20 / 99%
4/70/FE2	0.70	-	-	-	-	-
Average±SD	0.69±0.01	-	-	-	-	-
4/90/HS1	0.04	-	2.16	-	11.14	9.81 / 88%
4/90/FE1	1.41	-	11.26	-	15.26	15.00 / 98%
8/50/HS1	0.06	-	5.1	-	20.09	-
8/50/HS2	0.06	-	-	-	-	-

Average/SD	0.06±0	-	-	-	-	-
8/50/FE1	0.56	-	10.13	-	38.07	-
8/50/FE2	0.49	-	-	-	-	-
Average/SD	0.53±0.05	-	-	-	-	-
8/70/HS1	0.13	-	3.86	-	19.74	18.05 / 91%
8/70/HS2	0.07	-	3.52	2.19 / 62%	-	-
8/70/HS3	0.15	-	-	-	-	-
Average/SD	0.12±0.04	-	3.69	-	-	-
8/70/FE1	0.84	-	5.47	-	35.72	-
8/70/FE2	0.8	-	5.52	-	-	-
8/70/FE3	0.73	-	-	-	-	-
Average/SD	0.79±0.06	-	5.50	-	-	-
8/90/HS1	0.05	-	9.02	-	27.9	26.47 / 95%
8/90/FE1	1.53	-	14.71	-	38.06	37.65 / 99%
12/50/HS1	0.18	-	5.99	-	28.63	-
12/50/HS2	0.19	-	6.63	-	-	-
12/50/HS3	0.18	-	-	-	-	-
Average/SD	0.18±0.01	-	6.31	-	-	-
12/50/FE1	0.48	-	18.01	-	72.74	-
12/50/FE2	0.49	-	19.18	-	-	-
12/50/FE3	0.42	-	-	-	-	-
Average/SD	0.46±0.04	-	18.60	-	-	-
12/70/HS1	0.25	-	10.27		29.02	-
12/70/HS2	0.21	-	10.24	6.42 / 63%	-	-
12/70/HS3	0.18	-	-	-	-	-
Average/SD	0.21±0.04	-	10.26	-	-	-
12/70/FE1	1.16	-	18.34	-	55.61	-
12/70/FE2	0.71	-	19.43	-	-	-
12/70/FE3	0.75	-	-	-	-	-
Average/SD	0.87±0.25	-	18.89	-	-	-
12/90/HS1	0.14	-	5.91	-	36.21	34.45 / 95%
12/90/FE1	1.84	-	5.75	-	60.37	59.99 / 99%
16/50/HS1	0.4	-	8.61	-	40.63	-
16/50/HS2	0.39	-	7.75	-	-	-
16/50/HS3	0.35	-	-	-	-	-
Average/SD	0.38±0.03	-	8.18	-	-	-
16/50/FE1	0.78	-	30.62	-	91.8	-
16/50/FE2	0.63	-	20.67	-	-	-
16/50/FE3	0.73	-	-	-	-	-
Average/SD	0.71±0.08	-	25.65	-	-	-
16/70/HS1	0.30	-	16.36	-	48.56	-
16/70/HS2	0.25	-	14.27	9.03 / 63%	-	-
16/70/HS3	0.33	-	-	-	-	-
Average/SD	0.29±0.04	-	15.32	-	-	-
16/70/FE1	1.17	-	18.04	-	74.82	-
16/70/FE2	1.18	-	18.91	-	-	-
16/70/FE3	1.27	-	-	-	-	-
Average/SD	1.21±0.06	-	18.48	-	-	-
16/90/HS1	0.23	-	11.36	-	56.87	54.64 (96%)
16/90/FE1	1.55	-	9.87	-	91.79	90.44 (99%)

Table 6.16 Critical load & displacement values of T700/LTM45-EL skins / nomex core sandwich panel quasi-static bending tests

Specimen identity	Initial damage		Secondary damage		Ultimate failure	
	Load (kN)	Displ./LVDT* (mm)	Load (kN)	Displ./LVDT* (mm)	Load (kN)	Displ./LVDT (mm)
8/64/HS1	0.38	0.35/0.15	2.18	2.79/0.81	6.22	7.31/3.07
8/64/FE1	2.74	1.55/1.33	3.69	3.45/1.81	8.70	8.52/4.29
8/96/HS1	0.31	0.34/0.24	3.67	3.51/1.83	6.44	7.11/3.53
8/96/FE1	3.36	1.51/1.40	4.13	2.44/2.44	8.57	8.28/4.65
12/64/HS1	0.77	0.46/0.20	3.95	3.71/0.98	8.17	7.38/2.59
12/64/HS2	0.73	0.46/0.23	4.44?	4.07/1.34?	-	-
12/64/HS3	0.77	0.46/0.22	-	-	-	-
Average±SD	0.76±0.02	0.46±0.02	4.20±0.35	3.89±0.25	-	-
12/64/FE1	3.69	1.44/0.98	5.19	3.67/1.56	12.40	9.38/3.91
12/64/FE2	3.22	1.66/0.97	5.26?	3.55/1.94?	-	-
12/64/FE3	3.39	1.27/1.03	-	-	-	-
Average±SD	3.43±0.24	1.46±0.20	5.23±0.05	3.61±0.08	-	-
12/96/HS1	0.80	0.42/0.19	2.21	1.75/0.51	10.34	7.63/3.35
12/96/FE1	3.94	1.08/0.90	5.57	2.24/1.92	12.04	7.70/3.69
16/64/HS1	1.31	0.88/0.65	5.87	4.60/1.81	12.76	9.40/3.77
16/64/FE1	4.53	1.74/1.57	7.50	4.34/2.30	17.00	9.71/4.26
16/96/HS1	1.25	0.81/0.58	-	-	13.40	8.52/3.42
16/96/FE1	6.46	2.03/1.76	7.10	3.33/1.84	17.55	8.64/4.12

Table 6.17 Slopes of load-displacement curves of T700/LTM45-EL skins / nomex core sandwich panel quasi-static bending tests

Specimen identity	Linear elastic region (kN/mm)	Post-initial damage region (kN/mm)	Slope loss from initial to secondary region	Post-secondary damage region (kN/mm)
8/64/HS1	1.09	0.87	20%	0.88
8/64/FE1	2.32	0.79	66%	1.12
8/96/HS1	0.89	1.07	120%	0.82
8/96/FE1	2.80	0.76	73%	1.13
12/64/HS1	1.75	1.13	-	1.18
12/64/HS2	1.78	1.14	-	-
12/64/HS3	1.66	-	-	-
Average±SD	1.73±0.06	1.14±0.01	36%	-
12/64/FE1	2.94	1.03	-	1.44
12/64/FE2	2.99	1.01	-	-
12/64/FE3	3.07	-	-	-
Average±SD	3.00±0.07	1.02±0.01	66%	-
12/96/HS1	2.02	1.19	41%	1.39
12/96/FE1	3.88	1.42	63%	1.69
16/64/HS1	1.60	1.39	13%	1.49
16/64/FE1	3.16	1.57	50%	1.86
16/96/HS1	1.50	1.62	108%	1.66
16/96/FE1	4.52	1.48	67%	2.33

Table 6.18 Incident, IE, and absorbed, AE, energies for T700/LTM45-EL skins / nomex core sandwich panel quasi-static bending tests

Specimen identity	Initial damage		Secondary damage		Ultimate failure	
	IE (J)	AE (J) / AE/IE	IE (J)	AE (J) / AE/IE	IE (J)	AE (J) / AE/IE
8/64/HS1	0.08	-	3.13	-	22.13	20.37 / 92%
8/64/FE1	2.51	-	8.17	-	40.34	39.90 / 99%
8/96/HS1	0.08	-	6.00	-	24.44	18.86 / 77%
8/96/FE1	2.31	-	5.90	-	42.87	42.30 / 99%
12/64/HS1	0.23	-	7.49	-	29.64 [37.81]	34.70 / 92%
12/64/HS2	0.17	-	[9.04]	4.20 / 46%	-	-
12/64/HS3	0.20 [0.61]	0.26 / 43%	-	-	-	-
Average/SD	0.20±0.03	-	-	-	-	-
12/64/FE1	2.91	-	11.96	-	64.70	63.30 / 98%
12/64/FE2	1.99	-	11.36	5.48 / 48%	-	-
12/64/FE3	2.32 [2.56]	0.87 / 34%	-	-	-	-
Average/SD	2.41±0.47	-	11.66±0.42	-	-	-
12/96/HS1	0.22	-	2.10	-	39.23	36.65 / 93%
12/96/FE1	2.22	-	8.17	-	53.86	53.5 / 99%
16/64/HS1	0.59	-	12.98	-	58.07	53.65 / 92%
16/64/FE1	3.66	-	18.85	-	91.49	90.63 / 99%
16/96/HS1	0.49	-	-	-	53.77	50.42 / 94%
16/96/FE1	5.81	-	14.27	-	75.48	74.49 / 99%

Number in square brackets [] is incident energy when unloading starts

Table 6.19 Critical load & displacement values of IM7/8552 skins / aluminium & nomex core sandwich panel quasi-static bending tests

Specimen identity	Initial damage		Secondary damage		Ultimate failure	
	Load (kN)	Displ./LVDT* (mm)	Load (kN)	Displ./LVDT* (mm)	Load (kN)	Displ./LVDT (mm)
[a]4/70/HS1	0.21	0.46/0.19	0.41	1.50/0.80	1.23	3.55/2.13
4/70/FE1	1.98	0.70/0.56	2.39	2.35/1.12	3.46	3.58/1.78
8/70/HS1	0.60	0.30/0.11	-	-	2.96	3.28/0.70
8/70/FE1	2.75	0.70/0.50	-	-	5.97	4.36/2.31
[b]12/50/HS1	1.05	0.62/0.20	3.09	3.64/0.82	3.62	4.42/1.02
12/50/FE1	1.84	0.50/0.32	9.27	7.52/3.54	9.46	7.82/3.60
[b]12/70/HS1	1.07	0.43/0.16	-	-	4.18	3.37/0.77
[a]12/70/FE1	3.17	0.65/-	5.13	2.97/-	8.47	5.29/-
[a]12/90/HS1	1.31	0.47/0.22	2.73	1.86/0.43	3.76	4.91/2.76
[b]12/90/HS2	1.37	0.50/0.19	[3.21]	[2.19/0.46]	-	-
Average±SD	1.34±0.04	0.49±0.02/0.21	-	-	-	-
[a]12/90/FE1	3.12	0.54/0.63	4.13	2.05/2.32	8.75	4.99/2.44
[a]12/90/FE2	3.48	0.69/0.57	4.24	2.74/2.91	-	-
Average±SD	3.30±0.25	0.62±0.11/0.60	4.19±0.08	2.40±0.49/2.62	-	-
16/70/HS1	1.75	0.53/0.25	-	-	5.96	3.91/0.99
16/70/FE1	3.88	0.65/0.45	9.55	4.32/2.19	10.98	5.06/2.60
12/64/HS1	1.12	0.77/0.46	2.50	2.48/0.90	3.93	4.21/1.56
[b]12/64/FE1	2.90	1.26/1.07	3.17	1.59/1.25	8.72	6.91/3.62
12/96/HS1	1.27	0.85/0.39	4.76	3.86/1.35	4.76	3.86/1.34
12/96/FE1	4.40	1.54/1.33	4.45	3.11/2.93	8.36	5.56/3.64

Number in square brackets [] is incident energy when unloading starts

[a] Signifies major top and/or bottom skin debonding

[b] Signifies Top skin debonding in centre only

Table 6.20 Slopes of load-displacement curves of IM7/8552 skins / aluminium & nomex core sandwich panel quasi-static bending tests

Specimen identity	Linear elastic region (kN/mm)	Post-initial damage region (kN/mm)	Slope loss from initial to secondary region	Post-secondary damage region (kN/mm)
4/70/HS1	0.88 (0.37)	0.25	72%	0.42
4/70/FE1	3.55	0.54	85%	0.86
8/70/HS1	2.44	0.82	66%	1.02
8/70/FE1	5.00	1.18	76%	1.18
12/50/HS1	1.93	1.05	46%	0.73
12/50/FE1	3.88	0.90	77%	1.21
12/70/HS1	2.80	1.23	56%	1.11
12/70/FE1	6.37	0.97	85%	2.12
12/90/HS1	2.90	1.37	-	1.11
12/90/HS2	2.79	1.39	-	-
Average±SD	2.85±0.08	1.38±0.01	52%	-
12/90/FE1	5.88	1.25	-	2.13
12/90/FE2	6.24	1.27	-	-
Average±SD	6.06±0.25	1.26±0.01	79%	-
16/70/HS1	3.61	1.46	60%	1.40
16/70/FE1	6.32	1.31	79%	1.82
12/64/HS1	1.45	0.97	33%	0.86
12/64/FE1	2.36	0.84	64%	1.37
12/96/HS1	1.89	1.35	29%	1.15
12/96/FE1	3.47	1.20	65%	1.87

Table 6.21 Incident, IE, and absorbed, AE, energies for IM7/8552 skins / aluminium and nomex core sandwich panel quasi-static bending tests

Specimen identity	Initial damage		Secondary damage		Ultimate failure	
	IE	AE	IE	AE	IE	AE (J) / AE/IE
4/70/HS1	0.07	-	0.37	-	1.96 [3.03]	[2.03] / 67%
4/70/FE1	0.81	-	3.96	-	7.66	7.18 / 94%
8/70/HS1	0.12	-	-	-	5.36 [6.01]	[5.48] / 91%
8/70/FE1	1.12	-	-		15.77	-
12/50/HS1	0.41	-	2.63	-	8.97	-
12/50/FE1	0.63	-	-	-	39.32	39.02 / 99%
12/70/HS1	0.29	-	-	-	7.76	-
12/70/FE1	1.30	-	10.68	-	25.54 [28.61]	[27.89] / 97%
12/90/HS1	0.36	-	2.94	-	11.31	-
12/90/HS2	0.42	-	[3.85]	[2.19]	-	-
Average±SD	0.39±0.04	-	-	-	-	-
12/90/FE1	0.93	-	5.74	-	22.90 [25.47]	[24.36] / 96%
12/90/FE2	1.41	-	7.82 [10.47]	[5.57]	-	-
Average±SD	1.17±0.34		6.78±1.47	-	-	-
16/70/HS1	0.52	-	-	-	12.68 [16.44]	[15.35] / 93%
16/70/FE1	1.37	-	-	-	32.97 [41.50]	[41.03] / 99%
12/64/HS1	0.47	-	3.33	-	8.99 [11.72]	[10.22] / 87%
12/64/FE1	2.01	-	2.81	-	30.92	30.42 / 98%
12/96/HS1	0.66	-	-	-	9.76 [14.95]	[12.35] / 83%
12/96/FE1	3.60	-	9.25	-	24.28	23.81 / 98%

Number in square brackets [] based upon point at which unloading starts

Table 6.22 Critical load, displacement, incident, IE, & absorbed, AE, energy values of T700/LTM45-EL skins / aluminium and nomex core sandwich panel indentation tests

Specimen identity	Initial damage		Secondary damage		Ultimate failure			
	Load (kN)	Displ. (mm)	Load (kN)	Displ. (mm)	Load (kN)	Displ. (mm)	IE (J)	AE (J)
4/50/HS1	0.17	0.19	-	-	3.00	5.14	7.75	7.00
4/50/FE1	1.22	0.38	2.83	3.26	5.21	6.47	18.72	17.87
4/70/HS1	0.16	0.11	-	-	3.14	4.18	6.72	7.95
4/70/FE1	2.05	0.37	3.77	2.38	5.39	4.26	13.96	13.80
8/50/HS1	0.43	0.23	1.70	1.93	5.27	6.30	-	15.84
8/50/FE1	1.55	0.30	-	-	9.74	8.56	44.29	43.48
8/70/HS1	0.40	0.18	2.25	2.20	6.33	5.40	-	17.47
8/70/FE1	2.64	0.35	2.84	1.00	9.28	5.14	32.36	31.99
8/90/HS1	0.53	0.19	-	-	7.11	5.13	17.83	17.79
8/90/FE1	3.29	0.44	3.30	1.13	9.23	4.66	26.30	26.32
12/50/HS1	0.75	0.27	3.50	3.30	8.13	7.06	28.37	25.93
12/50/FE1	1.86	0.39	6.80	4.18	14.40	10.13	80.01	79.61
12/70/HS1	0.97	0.30	3.45	2.43	7.89	5.35	21.00	19.22
12/70/FE1	3.03	0.34	6.89	3.03	13.20	6.54	48.43	48.70
12/90/HS1	0.88	0.27	-	-	10.86	6.44	35.84	34.55
12/90/FE1	4.04	0.54	4.48	1.16	13.88	6.30	47.82	47.67
16/50/HS1	1.09	0.33	-	-	9.18	7.47	35.48	35.49
16/50/FE1	2.22	0.21	6.21	3.09	16.46	9.56	89.33	88.01
16/70/HS1	1.21	0.24	5.87	3.33	10.61	5.83	34.52	32.25
16/70/FE1	3.06	0.33	6.78	2.10	17.68	7.81	80.73	79.02
8/64/HS1	0.36	0.23	-	-	5.76	5.09	13.87 [15.91]	14.55
8/64/FE1	2.77	0.49	3.55	2.08	9.11	5.98	32.10	31.82
12/64/HS1	0.84	0.33	3.37	2.63	6.51	4.92	21.16	18.94
12/64/FE1	3.24	0.36	5.01	1.82	12.95	5.86	43.95	43.37
12/96/HS1	1.02	0.54	3.78	2.44	10.20	5.64	27.17	24.95
12/96/FE1	6.13	0.62	-	-	11.46	4.65	32.81	31.54

Number in square brackets [] based upon point at which unloading starts

Table 6.23 Slopes of load-displacement curves of T700/LTM45-EL skins / aluminium and nomex core sandwich panel indentation tests

Specimen identity	Linear elastic region kN/mm	Post-initial damage region kN/mm	Slope loss from initial to secondary region	Post-secondary damage region kN/mm
4/50/HS1	2.40	0.51	79%	0.55
4/50/FE1	3.93	0.67	83%	0.75
4/70/HS1	1.14	0.76	33%	0.90
4/70/FE1	6.65	1.59	76%	0.82
8/50/HS1	2.22	0.83	63%	0.95
8/50/FE1	5.36	0.94	82%	1.11
8/70/HS1	2.36	1.03	56%	1.27
8/70/FE1	18.26	0.87	95%	1.66
8/90/HS1	2.92	1.23	58%	1.38
8/90/FE1	9.62	0.00	100%	1.89
12/50/HS1	2.81	0.96	66%	1.28
12/50/FE1	5.29	1.38	74%	1.34
12/70/HS1	4.17	1.30	69%	1.70
12/70/FE1	10.09	1.65	84%	1.92
12/90/HS1	4.33	1.57	64%	1.79
12/90/FE1	10.82	0.46	96%	2.05
16/50/HS1	1.73	1.08	38%	1.25
16/50/FE1	8.09	1.41	83%	1.59
16/70/HS1	5.96	1.77	70%	1.87
16/70/FE1	9.16	2.23	76%	2.13
8/64/HS1	1.68	0.98	42%	1.24
8/64/FE1	6.99	1.11	84%	1.86
12/64/HS1	2.66	1.24	53%	1.42
12/64/FE1	13.16	1.74	87%	2.12
12/96/HS1	2.35	1.66	29%	2.07
12/96/FE1	11.61	2.29	80%	2.54

Table 6.24 Impact parameters and internal damage of T700/LTM45-EL 8 ply 70kg/m^3 aluminium honeycomb panels from QS & impact tests

Specimen	Impact Parameters								Panel damage						
									Delamination		No. of damaged cells	Core damage		Dent	
	IKE (J)	AE (J)	AE/IKE (%)	Impact velocity (m/s)	Rebound velocity (m/s)	Peak force (kN)	Peak displac. (mm)	Impact duration (μs)	Length (mm)	Area (mm^2)		Length (mm)	Area (mm^2)	Depth (mm)	Length (mm)
8/70/HS(init)	0.15	-	-	-	-	0.54	0.23	-	10	78.54	3	10.5	86.59	0.4	5
8/70/HS(sec)	3.52	2.187	0.62	-	-	2.57	2.72	-	34	907.92	8	32	804.25	0.9	30
8/70/HS(ult)	13.22	-	-	-	-	5.06	5.01	-	39	1194.59	16	70	3848.45	3.2	61
8/70/HS(ult) rep	19.74	18.05	0.91	-	-	6.22	6.54	-	66	3421.19	19	78	4778.36	3.3	70
8/70/IMP(1.4J)	1.43	0.63	0.44	1.39	-	1.78	1.7	3300	23	415.48	5	23	415.48	0.2	10
8/70/CAI(2.6J)	2.6	1.75	0.67	1.87	1.06	2.17	2.33	1600	-	-	-	-	-	0.6	20
8/70/CAI(3.6J)	3.62	2.45	0.68	2.21	1.25	2.55	2.77	1750	-	-	-	-	-	-	-
8/70/CAI(3.7J)	3.66	2.44	0.67	2.22	1.28	2.61	2.83	3300	-	-	-	-	-	0.75	28
8/70/CAI(3.7J)	3.69	2.39	0.65	2.23	1.32	2.54	3.17	3650	-	-	-	-	-	-	-
8/70/ IMP (3.7J)	3.69	2.54	0.69	2.23	1.24	2.56	3.05	3650	30	706.86	8	32	804.25	0.6	22
8/70/CAI(5.2J)	5.2	3.49	0.67	2.64	1.51	3.16	3.37	3200	-	-	-	-	-	-	35
8/70/ IMP (5.2J)	5.24	3.59	0.69	2.65	1.49	3	3.4	3400	42	1385.44	9	39	1194.59	1	36
8/70/CAI(5.4J)	5.4	3.55	0.66	2.69	1.57	3.32	3.11	1550	-	-	-	-	-	1.2	30
8/70/ IMP (9.1J)	9.06	6.2	0.68	3.49	1.96	3.93	4.69	3550	51	2042.82	12	50	1963.50	1.3	45
8/70/CAI(9.5J)	9.51	6.60	0.69	3.57	1.98	4.19	4.46	3450	-	-	-	-	-	1.5	50
8/70/CAI(9.5J)	9.54	6.11	0.64	3.58	2.15	4.52	4.16	3200	-	-	-	-	-	-	-
8/70/ IMP (13.2J)	13.18	8.92	0.68	4.21	2.39	5.06	5.14	3250	53	2206.18	14	57	2551.76	2	57
8/70/CAI(13.7J)	13.68	9.19	0.67	4.29	2.46	5.46	5.05	3100	-	-	-	-	-	2	65
8/70/CAI(13.8J)	13.76	9.22	0.67	4.30	2.47	-	-	-	-	-	-	-	-	2	60
8/70/ IMP (16.2J)	16.24	11.24	0.69	4.67	2.59	5.62	5.6	3250	55	2375.83	16	67	3525.65	2	55
8/70/ IMP (20.6J)	20.63	14.01	0.68	5.26	2.98	6.38	6.62	3400	69	3739.28	18	75	4417.86	2.5	70
8/70/CAI(24.3J)	24.34	24.24	0.995	5.72	-	6.2	6.58	3550	-	-	-	-	-	3.5	85
8/70/ IMP (25.2J)	25.18	24.32	0.97	5.82	-	4.3	5.09	4600	66	3421.19	17	74	4300.84	2	70
8/70/CAI(25.5J)	25.47	24.15	0.95	5.85	1.33	5.84	5.73	4200	-	-	-	-	-	4.5	82
8/70/ IMP (30.6J)	30.57	30.49	0.997	6.41	-	4.46	4.85	5350	62	3019.07	15	65	3318.31	2.5	60

Specimens in bold typeface had fibre fracture of top skin

Table 6.25 Impact parameters and internal damage of T700/LTM45-EL 8 ply 64kg/m^3 Nomex honeycomb panels from QS & impact tests

Specimen	Impact Parameters								Panel damage						
									Delamination		No. of damaged cells	Core damage		Dent	
	IKE (J)	AE (J)	AE/IKE (%)	Impact velocity (m/s)	Rebound velocity (m/s)	Peak force (kN)	Peak displac. (mm)	Impact duration (μs)	Length (mm)	Area (mm^2)		Length (mm)	Area (mm^2)	Depth (mm)	Length (mm)
8/64/HS(init)	0.08	-	-	-	-	0.38	0.35	-	-	-	-	-	-	-	-
8/64/HS(sec)	3.13	-	-	-	-	2.18	2.79	-	-	-	-	-	-	-	-
8/64/HS(ult)	22.13	20.37	0.92	-	-	6.22	7.31	-	69	3739.28	20	86	5808.80	1	20
8/64/IMP(1.5J)	1.54	0.7	0.45	1.44	1.06	1.42	2.15	4600	17	226.98	5	22	380.13	0	0
8/64/IMP(3.0J)	3.04	1.65	0.54	2.02	1.36	2.07	2.75	3950	31	754.77	8	33	855.30	0	0
8/64/IMP(3.4J)	3.41	1.83	0.54	2.02	1.46	2.25	2.9	1900	30	706.86	7	29	660.52	0	0
8/64/CAI(5.1J)	5.13	2.83	0.55	2.62	1.76	2.59	4.04	2050	-	-	-	-	-	0	0
8/64/IMP(5.3J)	5.28	2.74	0.52	2.66	1.84	2.83	4.18	2150	35	962.11	8	33	855.30	0	0
8/64/CAI(9.2J)	9.23	5.45	0.59	3.52	2.25	3.58	5.09	2050	-	-	-	-	-	0	0
8/64/IMP(9.3J)	9.29	5.04	0.54	3.53	2.39	3.61	4.94	1900	42	1385.44	9	38	1134.11	0	0
8/64/IMP(9.4J)	9.43	4.95	0.52	3.56	2.45	3.53	5.17	4150	45	1590.43	14	59	2733.97	0	0
8/64/CAI(16.3J)	16.29	10.03	0.62	4.68	2.90	4.69	6.56	1850	-	-	-	-	-	0	0
8/64/IMP(16.4J)	16.37	9.64	0.59	4.69	3.01	4.9	6.66	2100	59	2733.97	15	64	3216.99	0	0
8/64/IMP(20.2J)	20.15	12.12	0.60	5.2	3.28	5.68	7.03	1850	61	2922.47	18	77	4656.63	0	0
8/64/IMP(22.9J)	22.93	12.67	0.55	5.55	3.71	6.23	7.54	1850	62	3019.07	22	98	7542.96	0.25	10
8/64/IMP(25.5J)	25.45	24.54	0.96	5.85	1.11	5.04	7.99	7050	53	2206.18	24	101	8011.85	0.5	6
8/64/IMP(25.8J)	25.8	14.76	0.57	5.89	3.85	6.8	7.84	1850	58	2642.08	23	100	7853.98	0.5	30
8/64/CAI(28.2J)	28.2	26.54	0.94	6.15	1.49	5.37	7.95	1550	-	-	-	-	-	2	15
8/64/IMP(30J)	30.03	29.24	0.97	6.35	1.03	6.05	8.19	1600	66	3421.19	24	101	8011.85	1.5	16

Specimens in bold typeface had fibre fracture of top skin

Table 6.26 Impact parameters and internal damage of T700/LTM45-EL 16 ply 70kg/m^3 aluminium honeycomb panels from QS & impact tests

Specimen	Impact Parameters								Panel damage						
	IKE (J)	AE (J)	AE/IKE (%)	Impact velocity (m/s)	Rebound velocity (m/s)	Peak force (kN)	Peak displac. (mm)	Impact duration (μs)	Delamination		No. of damaged cells	Core damage		Dent	
									Length (mm)	Area (mm^2)		Length (mm)	Area (mm^2)	Depth (mm)	Length (mm)
16/70/HS(init)	0.31	-	-	-	-	1.39	0.3	-	9	63.62	3	15	176.71	0	0
16/70/HS(sec)	14.27	9.03	0.63		-	6	3.34	-	47	1734.94	15	65	3318.31	0.9	46
***16/70/HS(ult)**	36.42	-	-	-	-	10.39	6.64	-	46	1661.90	19	95	7088.22	4.2	79
16/70/HS(ult) rep	48.8	-	-	-	-	12.24	7.83	-	80	5026.55	20	98	7542.96	3.5	95
16/70/IMP(3.5J)	3.52	2.37	0.67	2.17	1.24	2.79	2.05	1150	26	530.93		27	572.56	0.25	9
16/70/IMP (5.2)	5.17	3.47	0.67	2.63	1.51	3.84	2.62	1500	35	962.11	7	32	804.25	0.5	12
16/70/IMP(9.2J)	9.2	6.01	0.65	3.51	2.07	5.2	3.91	1550	35	962.11	10	45	1590.43	0.5	20
16/70/IMP (14.8)	14.8	6.86	0.46	4.45	3.26	7.57	3.87	2650	51	2042.82	13	52	2123.72	1	40
16/70/IMP (25.3)	25.25	16.33	0.65	5.82	3.46	-	-	-	66	3421.19	18	80	5026.55	1.2	70
16/70/IMP(29.9J)	29.86	21.73	0.73	6.33	3.30	9.1	6.44	1400	62	3019.07	21	90	6361.73	1.7	80
16/70/IMP(33.1J)	33.08	22.60	0.68	-	-	-	-	-	60	2827.43	19	94	6939.78	1.7	80
16/70/IMP (37.8)	37.8	24.96	0.66	7.13	4.15	11.13	6.9	2750	82	5281.02	22	95	7088.22	2	80
16/70/IMP (44.9)	44.88	29.2	0.65	7.76	4.59	12.15	7.63	2750	78	4778.36	24	103	8332.29	2.5	95
16/70/IMP(54.8J)	54.8	52.47	0.96	8.58	1.78	9.11	7.92	1050	80	5026.55	27	111	9676.89	3.5	100

* possible premature fibre fracture due to poor skin manufacture
Specimens in bold typeface had fibre fracture of top skin

Table 6.27 Impact parameters and internal damage of T700/LTM45-EL 16 ply laminate plates from QS and impact tests

Specimen	Impact Parameters								Panel damage	
	IKE (J)	AE (J)	AE/IKE (%)	Impact velocity (m/s)	Rebound velocity (m/s)	Peak force (kN)	Peak displac. (mm)	Impact duration (μs)	Delamination	
									Length (mm)	Area (mm^2)
16/HS(ult)	20.77	-	-	-	-	8.36	6.86	-	110	9503.32
16/CAI(2.5J)	2.51	0.88	0.35	1.83	1.48	1.92	2.14	1400	-	-
16/IMP(2.5J)	2.52	0.72	0.29	1.84	1.55	1.64	2.07	1300	8	50.27
16/IMP(5.1J)	5.12	1.09	0.21	2.62	2.33	3.24	3.34	1850	27	572.56
16/CAI(5.2J)	5.15	1.35	0.26	2.63	2.26	2.92	4.1	2050	-	-
16/CAI(10.4J)	10.35	3.97	0.38	3.73	2.93	4.68	4.61	1700	-	-
16/IMP(10.4J)	10.37	2.78	0.27	3.73	3.19	4.67	4.64	1650	46	1661.90
16/IMP(19.9J)	19.86	3.74	0.19	5.16	4.65	8.18	6.23	1750	73	4185.39
16/CAI(20.3J)	20.26	6.52	0.32	5.22	4.30	8.38	5.5	1550	-	-

7. EXPERIMENTAL PROCEDURES FOR IMPACT DAMAGE TOLERANCE

The test procedures used for the damage tolerance investigation involved compression-after-impact testing of sandwich specimens and laminates. To minimise project cost focus was on panels consisting of 8 ply skins and 70kg/m^3 aluminium honeycomb. To establish the effect of the core on the compressive response panels with 8 ply skins with 64kg/m^3 nomex honeycomb and 16 ply laminates were also tested. The nomex core was selected to assess the effect of the core material, whilst the 16 ply laminates were used to determine the effect of separating one thick skin into two thinner skins with the use of a core component. For each test set a range of impact damage levels were used to obtain an accurate correlation between residual compressive strength and IKE. The level of impact damage applied to each panel was chosen to match those already studied for the impact tests where possible, as detailed measurements of internal damage were recorded for the cross-sectioned impact specimens. By choosing similar impact energy levels for both the impact only and CAI panels the amount of damage contained within each CAI panel could be estimated. In addition to testing panels containing impact damage two undamaged panels of each type were also tested. These control panels gave a baseline value for the undamaged compressive strength, which was then used to work out the reduction in residual compressive strength of the impact damaged panels.

7.1. Design methodology for CAI of sandwich panels

7.1.1. Design consideration

From the literature reviewed in Section 1 it is apparent that no internationally approved CAI testing standards exist for composite sandwich structures. As focus is on the compressive response of sandwich panels with only a limited number of tests completed on 16 ply monolithic laminates as a side study, the experimental test set-up was optimised for the sandwich panel specimens. The chosen specimen length and width dimensions and loading arrangement were used for both sandwich panels and laminates to allow a direct comparison of the compressive response without the use of scaling factors.

The NASA, SACMA and CRAG standards for monolithic laminates, reviewed in Section 1.3, have been altered for use with sandwich structures in previous research. ASTM C364 designed for the compression of sandwich struts is occasionally used in CAI testing of sandwich structures because of its simplicity. However, as it is a standard for uni-axial compression only with no support for the unloaded edges it does not apply to large sandwich panels whose unloaded edges need to be supported. To replicate in-service conditions all edges of the panel should be supported, and therefore lead to local buckling rather than global buckling. The NASA, SACMA and CRAG standards which use clamped and simply-supported edges are therefore preferable over the ASTM C364 standard. The CRAG standard is designed for coupon type laminate specimens rather than panels and therefore is not suitable for this research.

The support system selected for this project consisted of 'clamped' loaded edges using epoxy end pots and simply-supported unloaded edges through cylindrical-edged supports. Although the loaded ends of the specimen were not physically clamped the epoxy pots increased the surface area of the panel ends therefore preventing rotation of the panel at low loads, which if allowed to occur could cause premature failure of the panel, whilst also protecting the ends from delamination and end-brooming failure. This method provides a simple way of achieving the effects of a clamped end condition without the problems normally associated with clamping surface pressure and restraints.

The dimensions of the monolithic laminates used in the NASA and SACMA standards vary but are designed to give a width-to-thickness ratio and specimen aspect ratio within a specific range. The width-to-thickness ratio is the dominant factor and ranges from 20-75 for 2-8mm thick panels in the NASA standard and 16-100 for 1-8mm thick panels in the SACMA standard. The specimen aspect ratio is fixed at 2 and 1.5 in the NASA and SACMA standards respectively, whilst it is also recognised that aspect ratios of 1 or less should be avoided. To meet both these ratios would require a sandwich panel with the dimensions of 450mm × 300mm, which would cost a considerable amount in raw materials. Therefore a compromise had to be made to keep the project cost down. Existing literature in Table 1.2 indicate that in the CAI of sandwich panels width-to-thickness ratios of 3-10 with corresponding aspect ratios of 1-3 have been used in previous research. An important issue to consider was the size of the impact damage.

Both standards use a fixed energy level of 27 and 30J, though the SACMA standard does allow alteration of the applied energy value as it is based on plate thickness (6.675J/mm thickness in the original specification) [97]. It is also recognised in the testing of monolithic laminates that the impactor should not penetrate through the laminate and the impact damage should not extend past half the width of the specimen.

The amount of damage encountered during impact testing was greatest at fibre fracture, extending over a 75mm diameter region within the aluminium cored panels, though this did increase to 100mm of core damage upon fibre fracture of the nomex cored panels. Therefore a panel width of 150mm was deemed acceptable. For a 14.7mm thick 8 ply sandwich panel this gave a width-to-thickness ratio of 10, whilst for the 2mm thick 16 ply laminates this increased to 75. A panel length of 200mm was chosen, giving an aspect ratio of 1.33. This was within the levels observed for existing research, whilst also permitting the use of an existing compression jig within the department, although minor modification was required.

Following the guidelines for damage size it was decided to limit the impact energy level to that corresponding to fibre fracture of the top skin. Impact was through a drop weight impact rig equipped with a 20mm diameter impactor with a fixed weight of 1.45kg, dropped from varying heights. This rig has been used extensively in previous research within the department on the impact of monolithic laminates [100,139]. Ultrasonic scanning of the specimen prior to compression is recommend by both NASA and SACMA, however, as C-Scanning is impeded by the honeycomb sandwich structure an alternative method had to be used. To ascertain the level of impact damage present in the panels prior to compression loading a number of diagnostic tests were completed on sandwich panels and laminates impacted to the same level as those subjected to CAI (results presented in Section 6.3). These panels were cross-sectioned and the internal damage measured in the same way as for the panels studied for damage resistance. To be sure that the level of damage in each panel type was similar the residual dent length was compared for both the CAI and diagnostic specimen. The load-displacement curves from each impact were also compared to identify any signs of damage propagation within the panels.

7.1.2. CAI rig design and modification

To execute an in-plane compression test an existing compression jig for composite laminates [100,139] was modified for use with thick sandwich panels. The jig structure comprised of a welded steel frame mounted on a 10mm thick steel base plate, with steel bolts used as horizontal braces, see Fig. 7.1. All surfaces were machined perfectly flat and mounted perpendicular and parallel to the base plate/each other. Simply-supported side edges were provided through cylindrical-edged supports. The previous study on composite laminates used specimens measuring 150mm × 100mm × 4mm. To accommodate the larger 200mm × 150mm × 15mm sandwich panels and 200mm × 150mm × 2mm monolithic specimens, new support plates were manufactured. Two pairs of side edge supports were formed using cylindrical-edged steel support plates with removable 8mm thick shims for use with the thinner monolithic specimens. These support plates slotted into notches machined out of the steel frame and were positioned through the adjustment of 12 bolts. When in the jig these plates provided support to the central 160mm of the panel length with the top and bottom 20mm of the panel left free to accommodate the end pots. The 12 bolts were tightened to finger tightness such that the cylindrical-edged supports were just in contact with the panel surface, preventing forwards and backwards movement but allowing sideways translation and rotation. The compression jig and modified support plates are shown in Fig. 7.1.

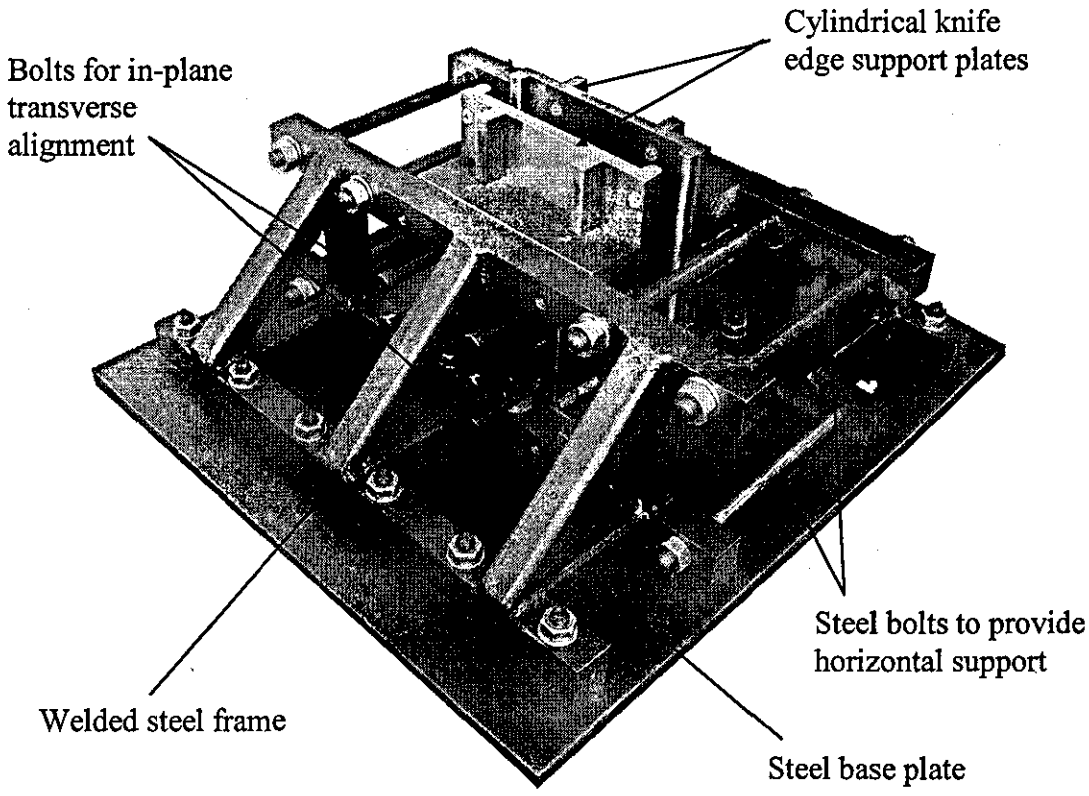

Figure 7.1 Design of compression jig

7.1.3. Test matrix

A test matrix was determined for the impact energies to be used in the damage tolerance study. The impact energies were chosen to range from zero up to the level required for fibre fracture of the top skin, identified from previous impact tests. Where possible impact energy levels were chosen to match those already considered in the previous impact tests. Two to three control panels and four to five impact damaged panels were tested for each core type, with most aluminium panel tests repeated to prove accuracy of results. The control panels were used to find a baseline value for the undamaged compressive strength, which was then used to work out the reduction in residual compressive strength of the impact damaged panels.

Table 7.1 CAI panels to be tested for damage tolerance

Panel ID	Core density (kg/m^3)	IKE level (J)	Testing machine
8/70/CAI(2.5J)	70	2.60	Mand
8/70/CAI(3J)-1	70	3.66	Denison
8/70/CAI(3J)-2	70	3.62	Denison
8/70/CAI(5J)-1	70	5.20	Denison
8/70/CAI(5J)-2	70	5.40	Mand
8/70/CAI(9J)-1	70	9.54	Mand
8/70/CAI(9J)-2	70	9.51	Denison
8/70/CAI(14J)-1	70	13.76	Mand
8/70/CAI(14J)-2	70	13.68	Mand
8/70/CAI(25J)-1	70	24.34	Mand
8/70/CAI(25J)-2	70	25.47	Denison
8/70/CAI(0J)-1	70	0	Mand
8/70/CAI(0J)-2	70	0	Denison
8/70/CAI(0J)-3	70	0	Denison
8/64/CAI(5J)	64	5.13	Denison
8/64/CAI(9J)	64	9.23	Mand
8/64/CAI(16J)	64	16.29	Mand
8/64/CAI(28J)	64	28.20	Mand
8/64/CAI(0J)-1	64	0	Denison
8/64/CAI(0J)-2	64	0	Denison
16/CAI(2.5J)	-	2.51	Denison
16/CAI(5J)	-	5.15	Denison
16/CAI(10J)	-	10.35	Denison
16/CAI(20J)	-	20.26	Mand
16/CAI(0J)-1	-	0	Denison
16/CAI(0J)-2	-	0	Denison

7.2. Specimen preparations

The specimens required for compression-after-impact testing were manufactured in the same way as those used in the damage resistance studies, as discussed in Section 2. However, the dimensions of each specimen were increased to 205mm in the 0° fibre direction, whilst remaining at 150mm in the 90° fibre direction. An extra 5mm was added to the desired length of 200mm to allow for trimming after manufacture and machining of the end pots. Impact damage was introduced into each panel, excluding the control panels, at predetermined levels through drop weight impact testing, as given

in Section 3.3. Each specimen was then potted using an epoxy based mixture and machined to achieve perfectly flat loading surfaces on both ends of the specimen. Each specimen was then strain gauged using the method described in Section 3.1. Prior to testing the dimensions of the panel at various locations were measured for stress and strain calculations.

7.2.1. End-potting

The formulation for the epoxy-based mixture comprised of araldite, hardener, accelerator and slate powder. The slate powder was included to prevent the formulation becoming too brittle. This same formulation was used for making the epoxy disks for polishing, Section 4.2.3, without the addition of slate powder. Proportions of the araldite, hardener and accelerator were carefully measured out according to the mixing ratio given in Table 7.2 and mixed together thoroughly in a disposable container. The slate powder was then added and the formulation was mixed again. It was then left to stand for 15 minutes with occasional 'knocking down' of the container on to the bench to remove any air bubbles. Once ready the formulation was poured into a wooden mould sprayed with CILRELEASE 1711E release wax.

To ensure a good surface finish of the potted ends was achieved the honeycomb cells were depressed by approximately 5mm at the panel ends using a Stanley knife and small steel bar. The specimen was then lowered into the mould such that one corner was placed in first then the rest of the panel lowered into the mixture to allow the epoxy to fill the void left by the honeycomb and any air bubbles trapped beneath the honeycomb to escape. The mould was then clamped together to prevent movement of the panel and left to cure at room temperature for 36 hours. Once cured the panel was removed from the mould and the opposite end of the panel potted in the same manner. The specimen was then machined using a milling machine. When machining it was imperative that both ends were perfectly flat, parallel to each other, perpendicular to the unloaded edges and that the edges of the carbon fibre skins were exposed. The finished panel length was generally 202-204mm.

Table 7.2 Epoxy formulation for end potting for 1 mould with a volume of 84cm^3

Substance	Density	Mass formulation	Volume formulation	Sandwich panel		Laminate panel	
				Mass	Volume	Mass	Volume
	(g/cm^3)	(g)	(cm^3)	(g)	(cm^3)	(g)	(cm^3)
Araldite CY 219	1.175	100	85.11	37.03	31.51	56.18	47.81
Hardener HY 219	1.150	50	43.48	18.52	16.10	28.09	24.43
Accelerator DY 219	1.250	5	4.00	1.84	1.50	2.81	2.25
Slate powder	2.800	20	7.14	7.41	2.65	11.23	4.01
TOTAL	1.252	175	139.73	64.80	51.76	98.31	78.50

7.2.2. Strain gauge locations

Once the specimens were potted strain gauges were bonded to both the front and back faces of the sandwich panel/laminate. The locations of the strain gauges are shown in Fig. 7.2. To obtain a measure of both global and local response the method of back-to-back gauging was selected. To ensure the gauges on the front and back skins were situated exactly back-to-back the top front left corner of the panel was used as a reference point and the panel marked up using a silver pen. The process for attaching the strain gauges was the same as quoted in Section 3.1.

The first strain gauge pair used single element type strain gauges, labelled SG1, aligned with the 0° fibres and located at one sixth of the overall height measured from the top loading edge along the longitudinal mid-section. This is the typical arrangement for measuring far-field response and gave information about the global response of the panel to compressive loading. The second strain gauge pair, labelled SG2, used 2 element strain gauge rosettes and measured the local strain response in both the 0° and 90° fibre directions on the in-plane transverse mid-section, 45mm from the panel centre. This strain gauge pair was accompanied by a similar third strain gauge pair labelled SG3 on Fig. 7.2, located at the centre of the in-plane transverse mid-section in a small number of tests with minimal surface damage, to gain additional information on the local response at the centre of the panel.

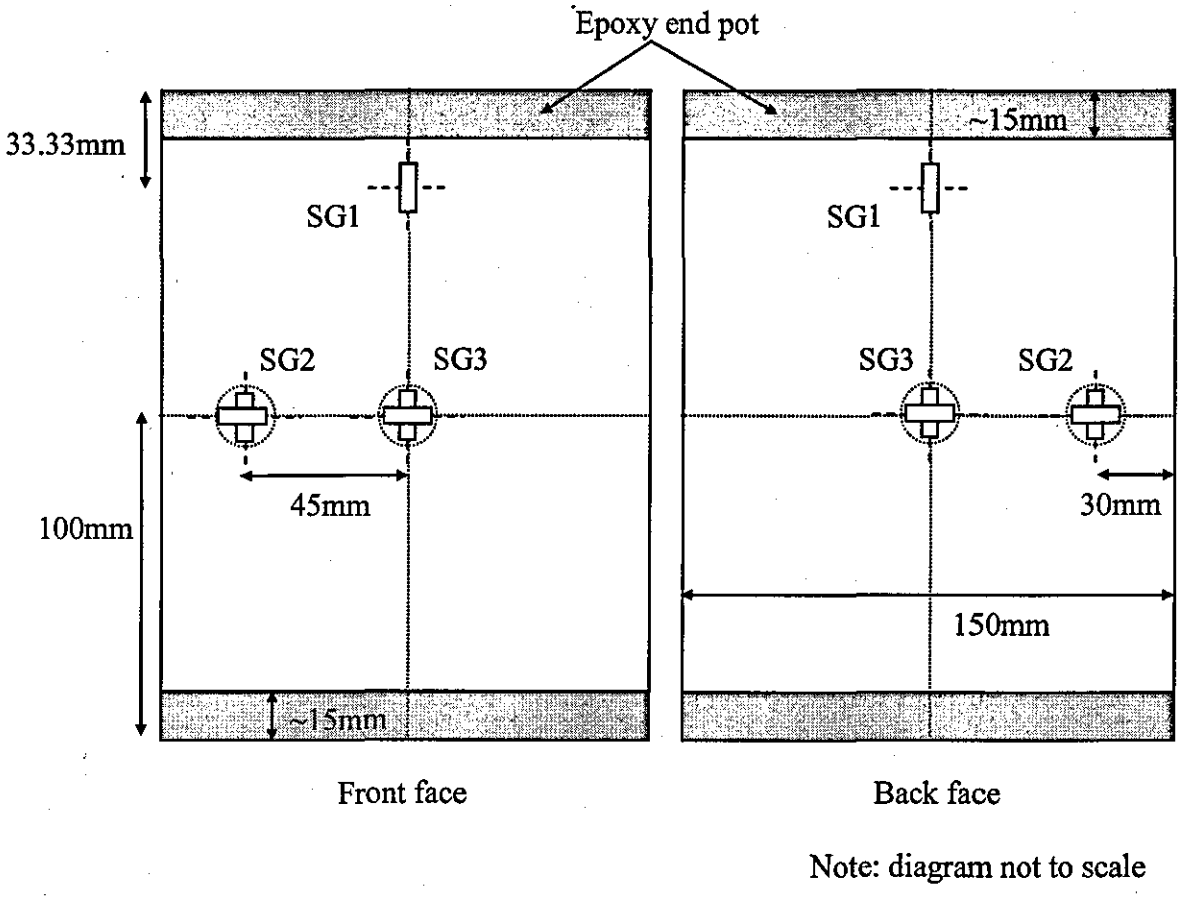

Figure 7.2 Location of strain gauges on front and back faces of compression panels

Normally two pairs of strain gauges are desirable to monitor local response along the in-plane transverse mid-section. The central pair, labelled SG3 on Fig. 7.2, becomes impractical for impact damaged panels because of the presence of dishing and sometimes fibre fracture at the central impact point. Therefore these can only be used on panels with no or minimal surface damage. Ideally these would be accompanied by an off-central pair bonded at the 'front' of the impact damage to see if existing delaminations propagate further. However, due to the presence of the honeycomb core the typical method of ultrasonic scanning could not be used to identify the location of the damage in the sandwich panels. Therefore the location of the SG2 pair in the in-plane transverse direction was chosen based upon the edge of the damage, signified by dishing of the top surface, for the panel with the greatest damage and used for all compression tests on laminates and sandwich panels. The location the SG2 pair was not

varied for each individual panel as the damage resulting from the low energy impacts on the aluminium panels and all impacts on the nomex panels was not visible on the panel surface, and by maintaining a constant location a true comparison of the strain response of each specimen could be made. The aluminium panel subjected to a 25J impact containing fibre fracture and extensive dishing was chosen as the reference panel, with the damage front represented by top skin dishing located at 45mm from the panel centre along the in-plane transverse mid-section.

7.3. Experimental set-up for in-plane compression

In-plane compression testing was carried out using either the Mand machine or a Denison tensile/compressive testing machine. The Denison machine had an upper load limit of 500kN, compared to just 86kN for the Mand machine. However, unlike the Mand machine, which was displacement controlled, the Denison machine was load controlled and driven manually, making it much more difficult to maintain a constant loading rate during testing. Additionally the Denison machine only provided a measurement of load so an LVDT had to be employed to obtain vertical displacement readings, shown in Fig. 7.3. The choice of which machine to use depended on the expected failure load of the panel being tested. All undamaged control panels were tested on the Denison machine. In addition to this some of the repeat tests were also completed on the Denison machine to check consistency of results. A statement of which machine was used for each CAI test is included in Table 7.1.

In a small number of initial tests an LVDT was employed to measure the horizontal displacement in the width-wise direction at the centre of the panel. Using the in-plane transverse displacement in conjunction with the longitudinal displacement measured either directly by the Mand or through another LVDT in the Denison tests, allowed the in-plane transverse response of the panel to be studied. When measuring the width-wise deformation the LVDT was positioned such that it was in contact with the centre line of the back undamaged skin. This position was chosen since the skins were less prone to unstable deformation than the honeycomb and provided a flat surface to mount the LVDT on. However, the amount of in-plane transverse displacement measured was at

most 0.05mm and therefore deemed negligible when compared to the longitudinal displacement, as shown in Fig. 7.4. This coupled with the additional problems encountered with keeping the LVDT head on the 1mm thick skin throughout the test, illustrated in Fig. 7.4, led to this procedure being discontinued for the majority of tests.

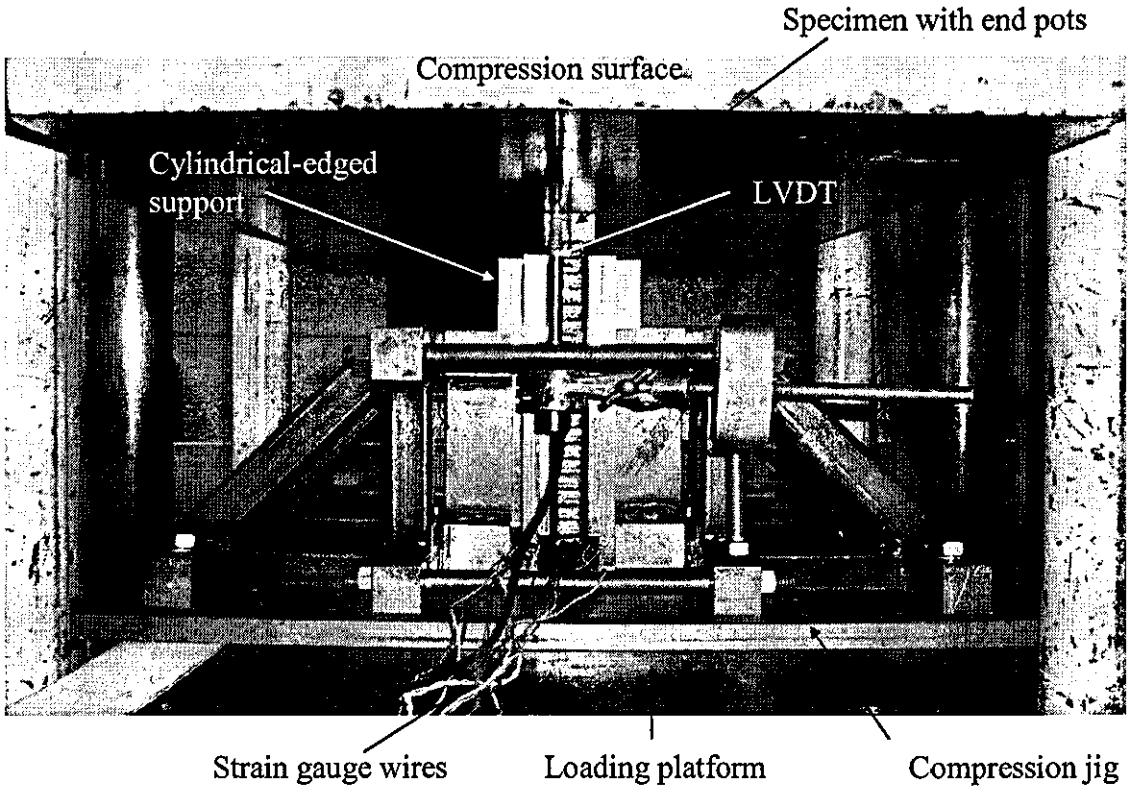

Figure 7.3 Test arrangement in Denison machine

An in-depth description of the testing procedure is given in Appendix D with a summary included here. The specimen was placed in the compression jig, the cylindrical-edged support plates positioned to sit square on the panel surface and the alignment bolts finger driven onto the panel surface. It should be noted that such a minor tightening force does not exert a measurable force on the panel and therefore the panel is free to deform in the in-plane transverse direction due to the Poisson's effect. A set square was used to ensure the panel was perfectly vertical within the jig. The jig was then placed within the Denison/Mand machine and the vertical and horizontal LVDTs, where used, connected to the jig via clamps. The load, displacement and LVDT output cables and strain gauges via a dummy gauge board for temperature compensation, were

connected to the Orion data acquisition system and a sampling rate of 0.5Hz set. The loading head was lowered to approximately 1mm above the panel surface and the panel checked to ensure the loading surface of the specimen and the machine compression surface were completely in parallel, with the aid of a spirit level and thin metal shims. The test was then initiated with load applied at a steady rate of 1mm/min throughout the test until the panel failed, which was signified by a loud bang and large decrease in load carrying ability. Once the test was finished the loading head was raised and the panel removed from the jig.

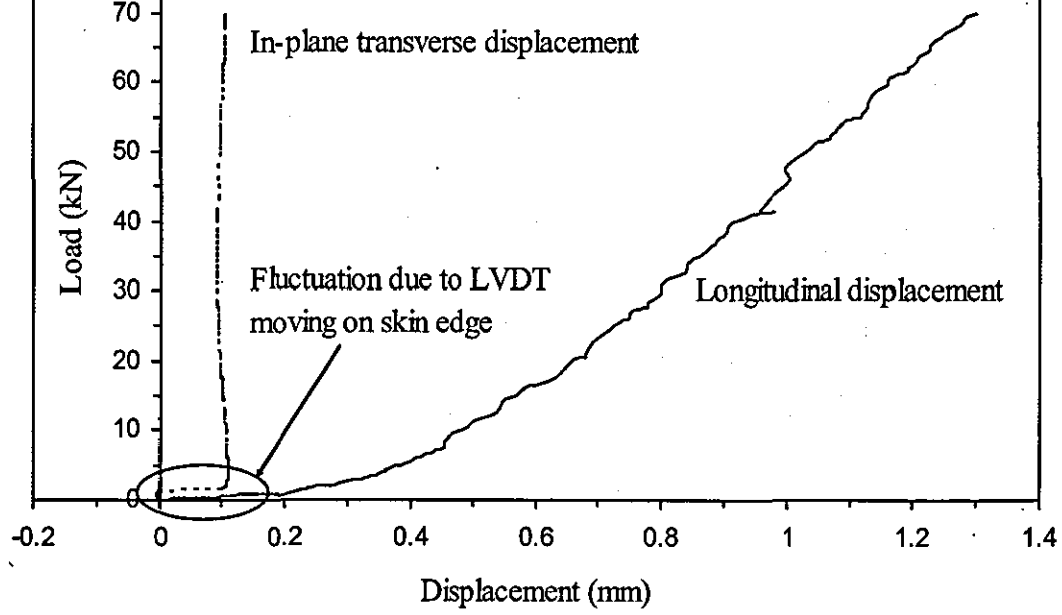

Figure 7.4 Load vs. longitudinal and in-plane transverse displacement for a compression test on 8/70/CAI(14J)-1 panel

The panel was inspected for damage, first through external examination and then internally by cross-sectional examination of the mid-planes. The panel was cross-sectioned using the diamond coated slitting saw with one cut along the longitudinal centre-line and a second cut along the in-plane transverse centre-line of one of the new panel halves. Damage was characterised in terms of skin failure/damage location and

core damage and all panels were photographed for archiving, both prior to and after cross-sectioning.

For the tests conducted on the Denison machine the raw voltage data captured through the Orion data acquisition system was converted into force in kN and displacement in mm using Eqs. 7.1, 7.2 and 7.3 respectively. The strain data was recorded in microstrain, and therefore already in the required format. The equivalent conversion equations for compression tests conducted on the Mand machine were as quoted in Section 3.2.1The processed data was then used to produce load-displacement and load-strain plots using the computer program EXCEL.

$$True\ load = 62.062 \times denison\ output\ voltage + 0.5352 \text{ (kN)} \tag{7.1}$$

$$True\ LVDT\ 1\ \ displacement = LVDT\ output\ voltage \times 1.65 \text{ (mm)} \tag{7.2}$$

$$True\ LVDT\ 2\ \ displacement = LVDT\ output\ voltage \times 3.4 \text{ (mm)} \tag{7.3}$$

8. DISCUSSION OF RESULTS FOR IMPACT DAMAGE TOLERANCE

The impact damage tolerance of composite sandwich panels has been assessed through in-plane compression-after-impact testing. This is achieved by studying the effect of impact damage on the residual compressive strength (RCS) of 8 ply sandwich panels with 70kg/m^3 aluminium honeycomb or 64kg/m^3 nomex honeycomb. A small number of tests have also been completed on 16 ply monolithic laminate panels to understand the role of the core on the compressive response of sandwich panels. In order to understand the type and extent of damage contained within a CAI panel prior to compression loading a duplicate impact test was completed and the specimen cross-sectioned, as reported in Section 6.3. All data are summarised in Tables 8.1 and 8.2. Graphs showing the compressive response of each individual specimen are also included in Appendix C for completeness.

8.1. Damage tolerance assessment of monolithic laminate panels

Two undamaged T700/LTM45-EL cross-ply laminate specimens, termed control laminate panels, and four impact damaged laminate panels were loaded in in-plane compression to failure. The load-displacement response for a selection of tests is shown in Fig. 8.1. Also included where available is the in-plane transverse displacement at the panel mid-section for the benefit of comparison with the response of the sandwich panels.

8.1.1. Compressive response of undamaged laminate panels

The variation of longitudinal displacement with load is non-linear, as shown in Fig. 8.1. The initial non-linear region within the first 2kN is due to bedding in of the panel. From 2 to 16kN loading continues in a stable manner with panel stiffness increasing gradually. After 16kN there is a slight reduction in panel stiffness which continues until failure. The in-plane transverse displacement, representative of an increase in panel width at the mid-section, also begins to increase after 16kN. Failure of the two control panels occurs at 36kN and 41kN respectively, corresponding to an average compressive stress of 135MPa. A photograph of the 16/CAI(0)-1 control panel after compression loading is shown in Fig. 8.2.

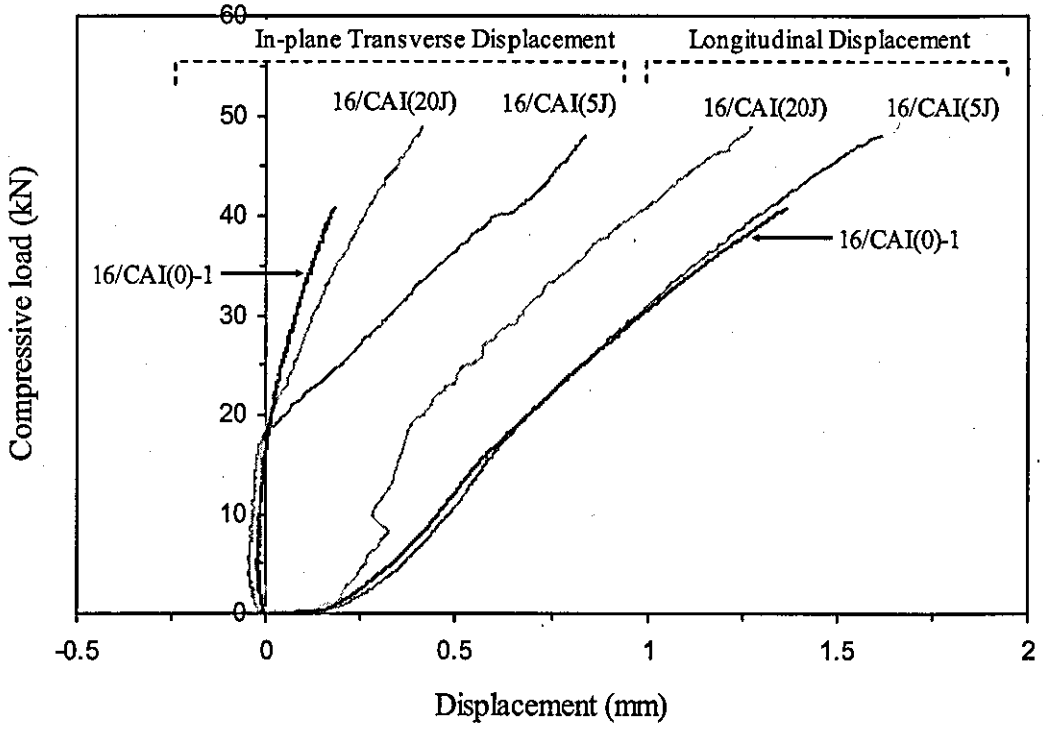

Figure 8.1 Compressive load vs. longitudinal and in-plane transverse displacement for 16 ply laminates with and without impact damage
(fluctuations in 16/CAI(20J) response due to machine vibration)

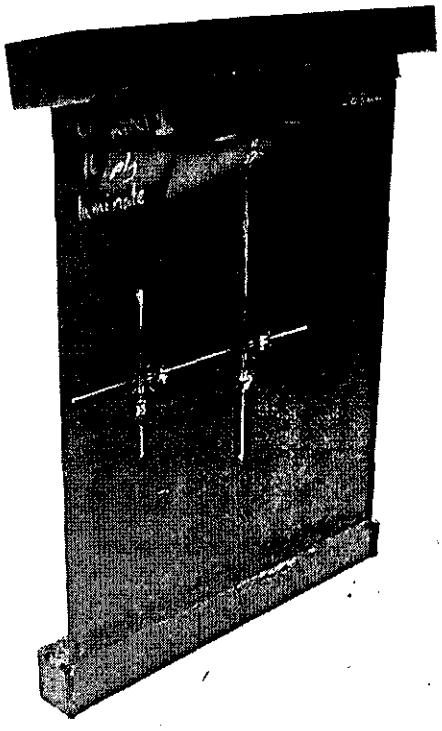

Figure 8.2 Photograph of 16/CAI(0)-1 control panel loaded under in-plane compression

As a panel is compressed in the longitudinal direction it can be expected to spread outwards in the in-plane transverse direction, known as the Poisson's effect. The Poisson's response of the 16/CAI(0J)-1 control panel at the in-plane transverse mid-section can be obtained from the strain gauge readings in the two orthogonal directions. This information could be used as an additional indicator of the panel behaviour, especially when panels are thick [101]. Alternatively, the longitudinal and in-plane transverse displacements can also be used to estimate the Poisson's effect if the panels fail around the mid-section. Both methods are shown in Fig. 8.3. The values estimated by the two approaches differ, most likely due to the value calculated from the SG2 pair of strain gauges representing a local value whilst the value calculated from the displacement readings applies to the whole panel. The value obtained from the SG2 strain gauge pair shows the Poisson's effect to initiate around 13kN and reach a value around 0.24 at failure, which is slightly below the value of 0.3 as predicted by classical lamination theory.

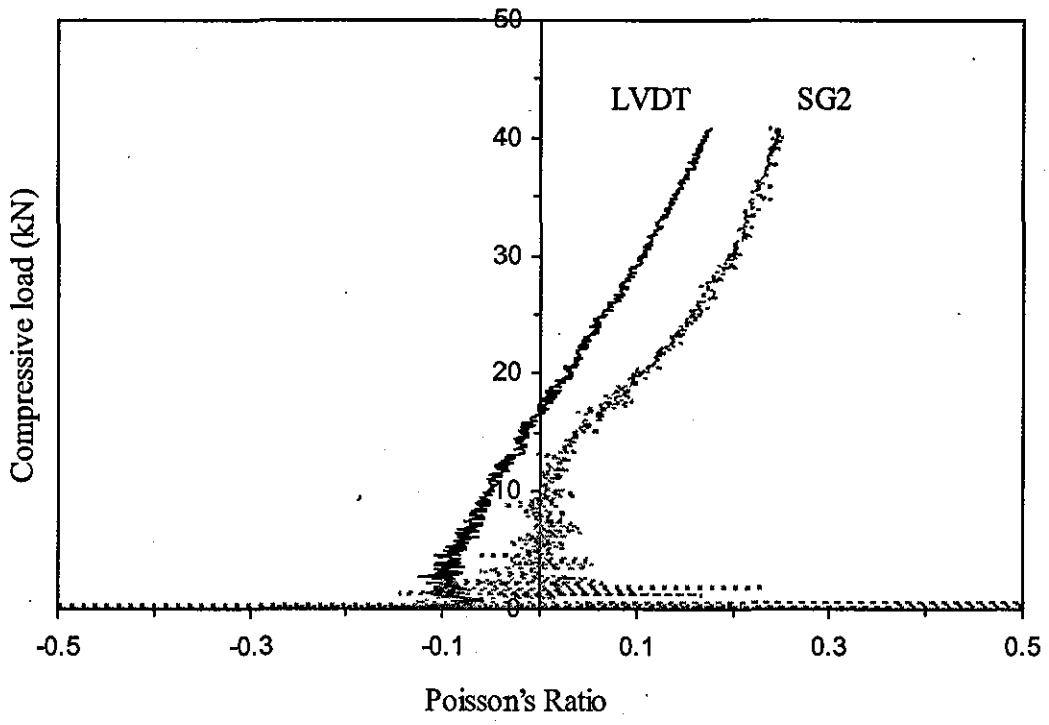

Figure 8.3 Variation of Poisson's ratio with load, calculated from SG2 strain gauge pair and LVDT readings for 16/CAI(0J)-1 panel

Although the individual strain gauge readings provide information about the response at various locations on the panel, an example shown in Fig. 8.4 for the 16/CAI(0J)-1 panel, it is difficult to directly interpret these results in terms of the entire panel movement. Instead, the method of back-to-back strain gauging has been used to obtain the mean strain and bending strain of the panel, calculated using Eq. 8.1. These mean strain and bending strain responses are indicative of the panel behaviour, represented at both the far-field and local mid-section regions, an example shown in Fig. 8.5 for the 16/CAI(0J)-1 panel.

$$\begin{aligned} Mean\ strain &= \frac{\varepsilon_{front} + \varepsilon_{back}}{2} \\ Bending\ strain &= \varepsilon_{front} - \varepsilon_{back} \end{aligned} \tag{8.1}$$

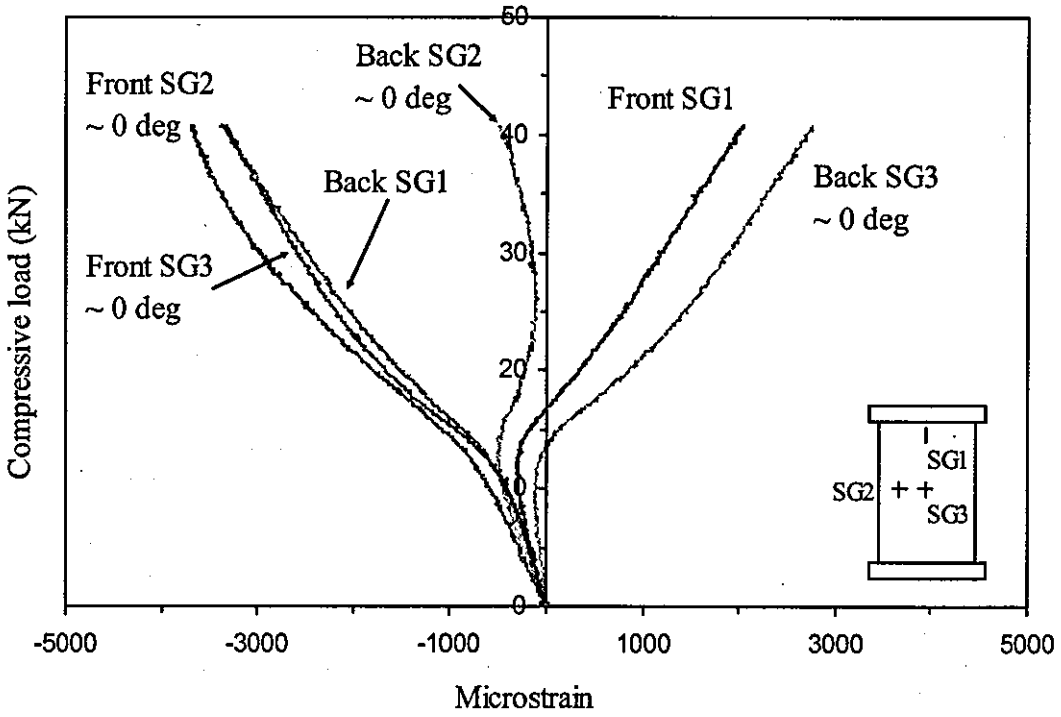

(a)

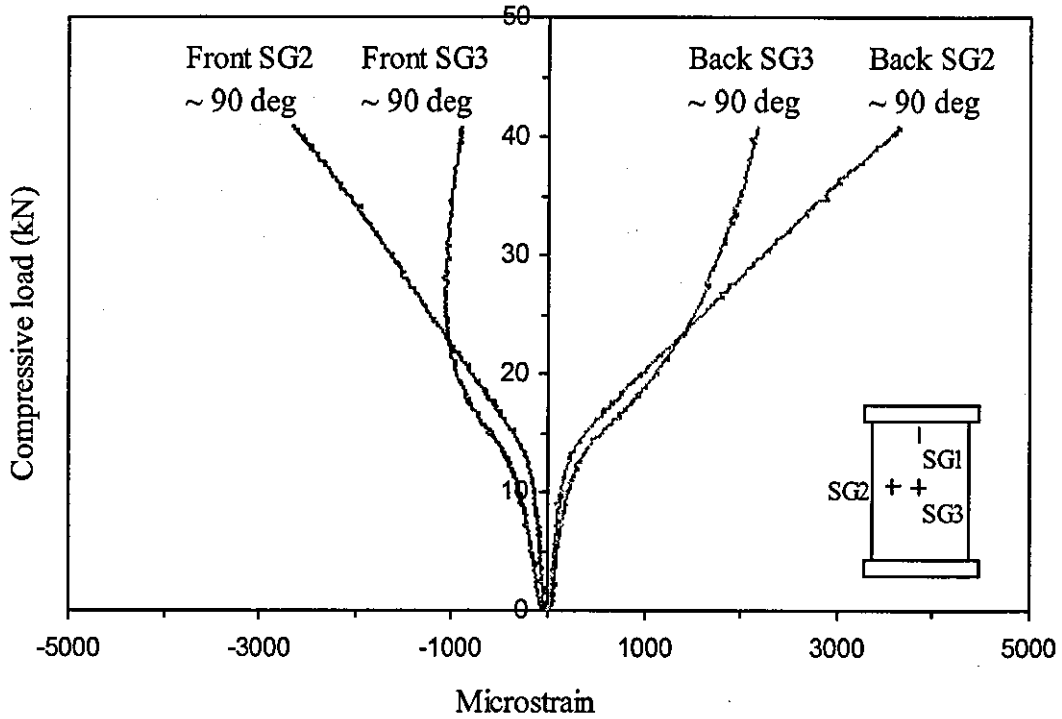

(b)

Figure 8.4 Load-strain response for 16/CAI(0)-1 panel under in-plane compression

(a) individual strain response in 0° fibre direction

(b) individual strain response in 90° fibre direction

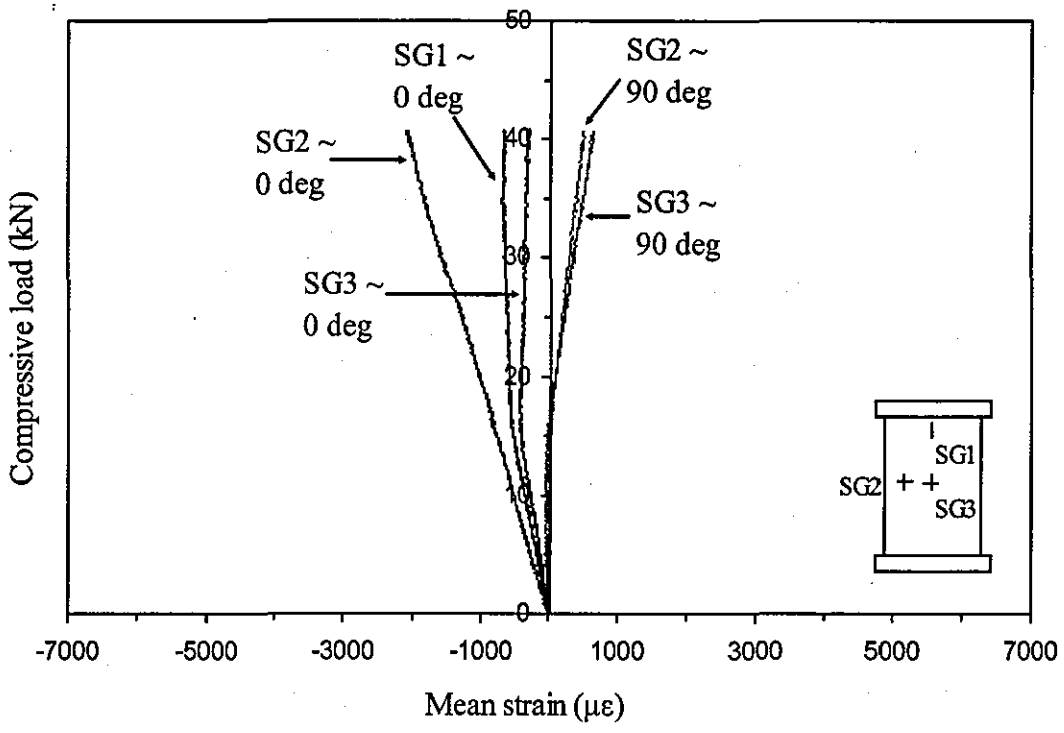

(a)

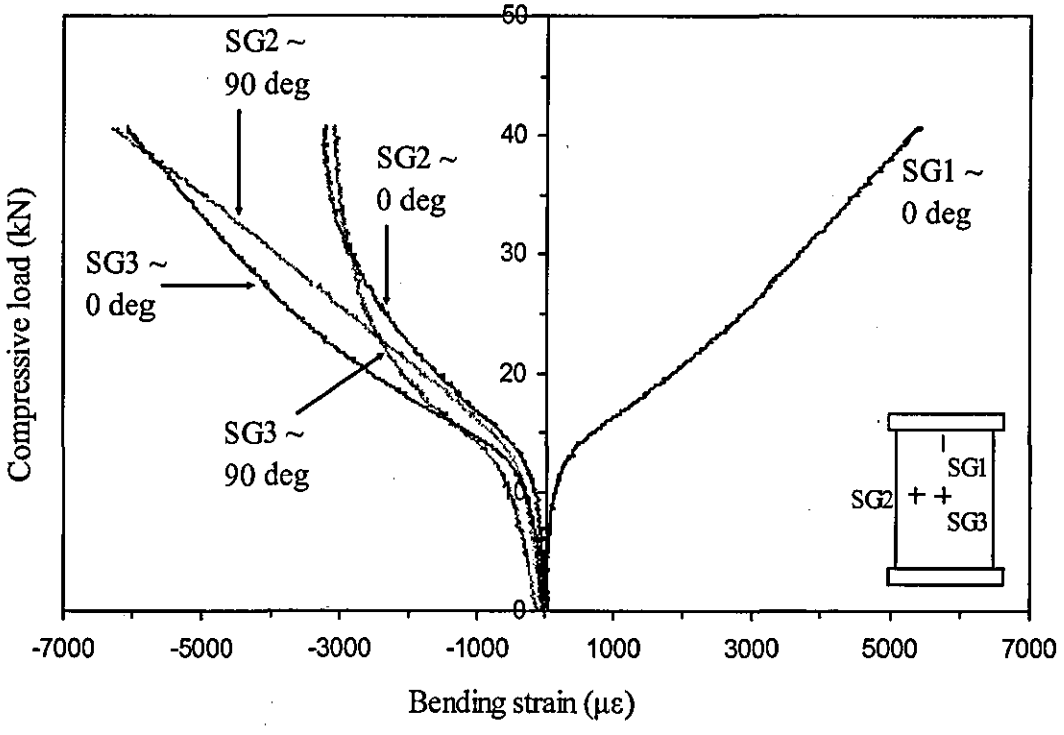

(b)

Figure 8.5 Load-strain response for 16/CAI(0)-1 panel under in-plane compression
(a) Mean strain (b) Bending strain

Theoretically, the use of side supports removes the possibility of Euler global buckling. If the panel undergoes pure local bending to a substantial extent the local mean strain should be zero. If the panel does not bend and responses in a pure in-plane compressive manner both the local and far-field mean strains should be large whilst the bending strains should be zero. The bending strain response can be tensile or compressive depending on which direction the panel bends. Any local buckling should be detected by the local strain gauges and is represented by a deviation of the far-field and local mean and/or bending strain responses. Global buckling will be reflected in both local and far-field strain responses. Panel deformation and subsequent failure should initiate via local buckling at the mid-section, even in cases with no impact damage, as the nodal line where the largest shear stresses occur is within this section. At this location local (mode I) buckling should occur and grow sufficiently leading to mode II buckling, as discussed by Zhou et al. [101] for 2mm thick quasi-isotropic panels with slightly smaller in-plane dimensions. The buckling pattern established by Zhou et al. is depicted in Fig. 8.6 (a-b).

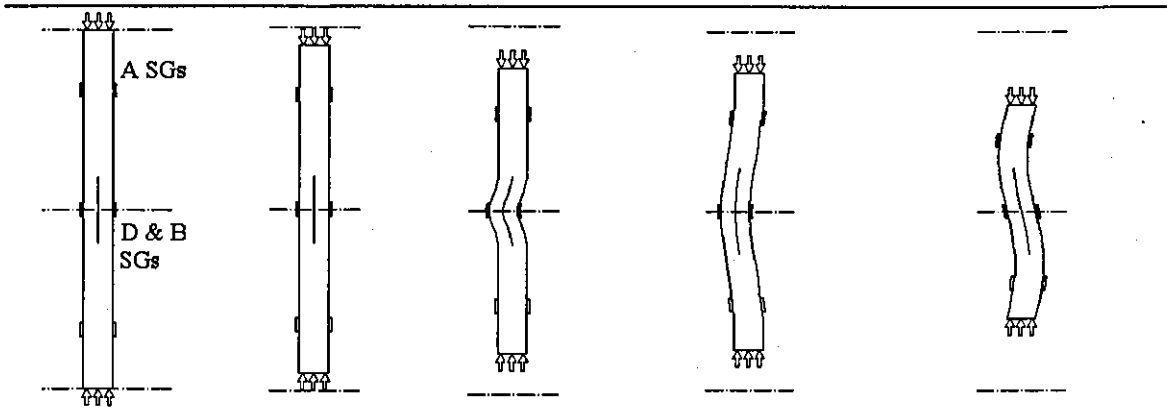

P_{local} — Local buckling load
$P_{global\text{-}II}$ — Global buckling load
ε_b — Bending strain
$P_{global\text{-}I}$ — Incipient global buckling load
$P_{failure}$ — Ultimate failure load
ε_m — Membrane strain

(a)

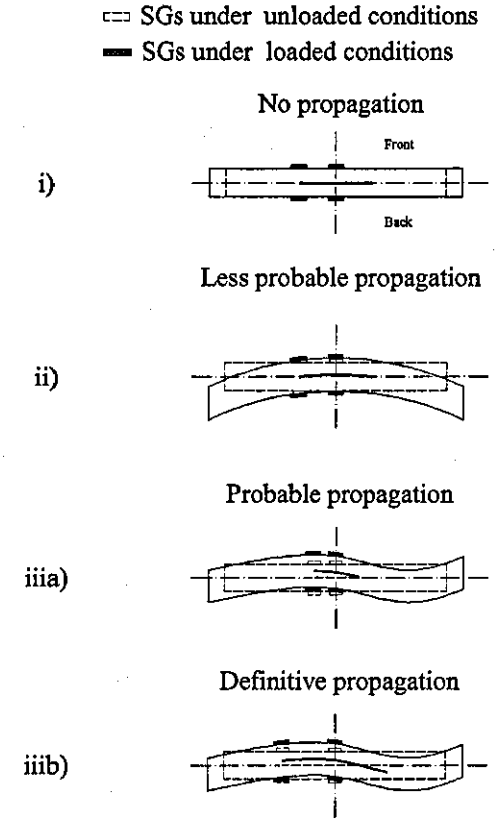

In-plane Transverse strain

	Mean	Bending
i)	$P_{local}>P>0$	$\varepsilon^{i}_{m\,centre}=\varepsilon^{i}_{m\,side}>0$ $\varepsilon^{i}_{b\,centre}=\varepsilon^{i}_{b\,side}=0$
ii)	$P_{global\text{-}II}>P>P_{local}$ or $P_{failure}>P>P_{global\text{-}II}$	$\varepsilon^{ii}_{m\,side}>\varepsilon^{i}_{m\,side}$ $\varepsilon^{ii}_{b\,side}>\varepsilon^{i}_{b\,side}$ $\varepsilon^{ii}_{m\,centre}>\varepsilon^{i}_{m\,centre}$ $\varepsilon^{ii}_{b\,centre}>\varepsilon^{i}_{b\,centre}$ $\varepsilon^{ii}_{m\,side}\doteq\varepsilon^{ii}_{m\,centre}$ $\varepsilon^{ii}_{b\,side}\doteq\varepsilon^{ii}_{b\,centre}$
iiia)	$P_{failure}>P>P_{global\text{-}II}$ $\varepsilon^{iiia}_{m\,side}\doteq\varepsilon^{iiia}_{m\,centre}$	$\varepsilon^{iiia}_{b\,side}>-\varepsilon^{iiia}_{b\,centre}$ or $\varepsilon^{iiia}_{b\,side}>\varepsilon^{iiia}_{b\,centre}$
iiib)	$P_{failure}>P>P_{global\text{-}II}$ $\varepsilon^{iiib}_{m\,side}<\varepsilon^{iiib}_{m\,centre}$, $\varepsilon^{iiib}_{b\,side}<\varepsilon^{iiib}_{b\,centre}$ or $\varepsilon^{iiib}_{m\,side}>\varepsilon^{iiib}_{m\,centre}$, $\varepsilon^{iiib}_{b\,side}>\varepsilon^{iiib}_{b\,centre}$	

(b)

Figure 8.6 The deformation sequence of the compressive and buckling behaviour of 2-mm thick quasi-isotropic preconditioned carbon/epoxy panels in the (a) longitudinal direction (b) in-plane transverse direction [101]

The mean strain and bending strain responses for the 16/CAI(0J)-1 control panel are shown in Fig. 8.5. The longitudinal strain gauges show a uniform panel response until 2kN, at which SG3 shows a negative increase in bending strain. This is indicative of local mode I buckling initiating. At approximately 5kN the bending strain at the SG2 location also begins to increase in a negative manner, followed by a positive increase in the bending strain at the SG1 location at 7kN. This suggests local mode I buckling to have grown and the onset of deformation at the far-field location. Up to this point the buckling pattern is the same for both quasi-isotropic and cross-ply panels. After this

point the quasi-isotropic panels experience a large increase in bending strain prior to a strain reversal detected by all gauges, signifying the rapid extension of local buckling and the transfer from mode I to mode II buckling. In the cross-ply panels the growth of local buckling was moderate and slowed after 17kN, whilst the subsequent strain reversal in the bending strain response did not occur. However, after 17kN the bending strain at the far-field location continued to increase at a steady rate and the trends for mean strain were similar for both panel lay-ups.

Despite the lack of bending strain reversal the positive bending strain at the far-field location combined with the reduction in the negative bending strain at the mid-section suggests the panel deformation to be of a mode II buckling shape. This deformation pattern is composed of local buckling around the mid-section and localised bending at the far-field location. The two deformed regions are independent of each other and do not interact, therefore are not caused by conventional mode II buckling phenomena. The negative rather than zero amount of bending strain at the mid-section indicates an uneven buckling distribution where the buckling nodal line is not in the centre of the panel, instead located closer to the loaded end. The strain response in the in-plane transverse direction during the local mode I and mode II regions also follows the trends identified by Zhou et al. [101] for the quasi-isotropic panels. The longitudinal deformation sequence for the cross-ply panels is depicted in Fig. 8.7.

Failure of the panel occurred in an abrupt manner with little obvious indication of damage initiation, except for the non-linear characteristics of the load-displacement and load-strain curves in Figs. 8.1 and 8.5. Although the strain response indicates the development of local bending both control panels failed just below the loaded end of the panel, due to local compressive failure of the panel and not panel buckling, illustrated in Fig. 8.2. However, a similar 2mm thick panel with a quasi-isotropic lay-up but slightly smaller in-plane dimensions failed at the mid-section [101]. Therefore the failure characteristics of the larger cross-ply panel could be associated with the lay-up. The 50% proportion of fibres in the 0° fibre direction provides a large flexural resistance to local bending development. When the flexural rigidity of a panel is higher than the shear rigidity failure of the panel in a central location through buckling becomes highly

unlikely, and a compressive failure towards the panel ends may be expected [102]. This may also be exasperated by uneven buckling introducing high stresses in the smaller buckling quadrant, which in this instance is where failure occurred in both specimens.

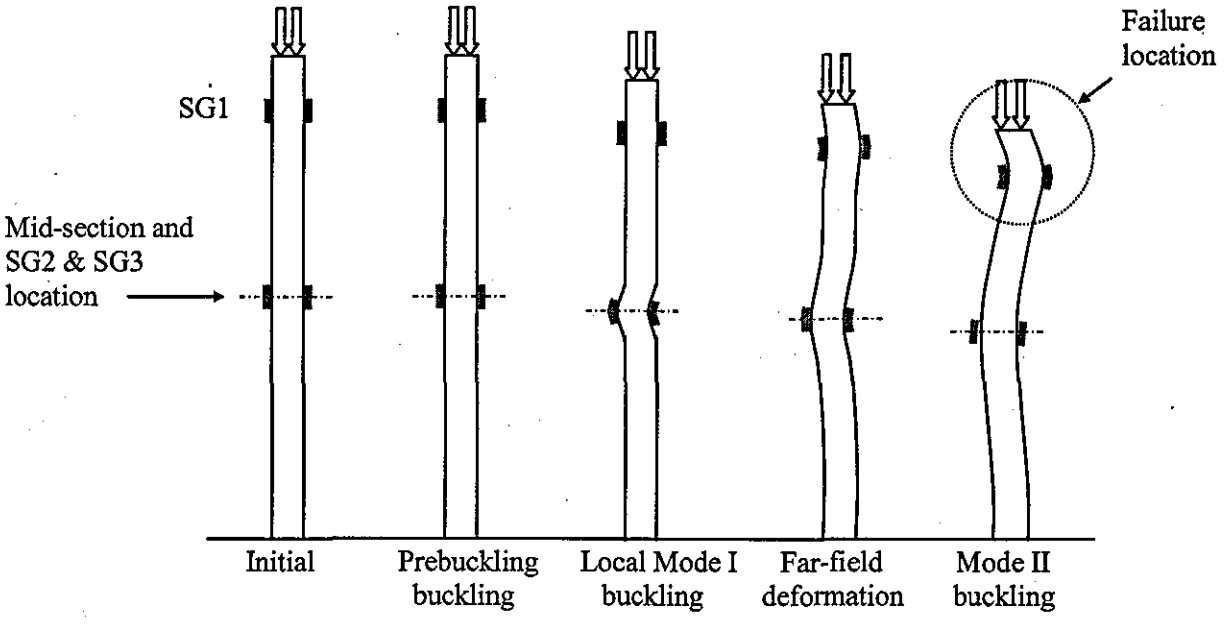

Load	$P = 0$	$P < 2kN$	$2kN < P < 7kN$	$7kN < P < 17kN$	$17kN < P$
Mean strain	$\varepsilon_m^I = 0$	$\varepsilon_m^{II} > 0$	$\varepsilon_m^{III} > \varepsilon_m^{II}$	$\varepsilon_m^{IV} > \varepsilon_m^{III}$	$\varepsilon_m^V < \varepsilon_m^{IV}$
Bending strain	$\varepsilon_b^I = 0$	$\varepsilon_b^{II} = 0$	$\varepsilon_b^{III} = 0\ (farfield)$ $\varepsilon_b^{III} > \varepsilon_b^{II}\ (local)$	$\varepsilon_b^{IV} > \varepsilon_b^{III}$	$\varepsilon_b^V >> \varepsilon_b^{IV}\ (farfield)$ $\varepsilon_b^V > \varepsilon_b^{IV}\ (local)$

Figure 8.7 Illustration of buckling sequence and strain response of 2mm thick cross-ply panels in longitudinal (loading) direction

8.1.2. Compressive response of impact damaged laminate panels

Laminate panels were impacted at 2.5J, 5J, 10J and 20J, respectively. The internal damage was estimated from the cross-sections of duplicate impact tests, as recorded in Table 6.27. The cut specimens contained increasing levels of damage with multiple delaminations spread over 8, 27, 46 and 73mm respectively, accompanied by fibre splitting on the back surface beneath the impact point of the 20J specimen. In all specimens the most significant delaminations were located below the through-the-thickness transverse mid-section between the 9^{th}-10^{th} plies, and immediately above the back face between the 15^{th}-16^{th} plies. When loaded in compression all impact damaged panels failed at a load between 36-49kN. For a given load the trend of the strain responses at the far-field SG1 and local SG2 locations are comparable to those of the control panels, as shown in Fig. 8.8, though the value of the far-field mean strain at failure does vary as indicated in Table 8.1. Despite the panels containing increasing amounts of internal damage, all the impact damaged panels failed in compression at the loaded end, in the same manner as discussed for the undamaged control panels. In addition no reduction in residual compressive strength occurred, with all monolithic laminate panels failing between 36 and 49kN.

At the impact damage location the strain response recorded by the SG3 pair for the 2.5J and 10J specimens shows a different trend to that identified for the 5J impact damaged panel and the control panels, Fig. 8.9. The bending strain response both at the far-field and local locations shows the 5J panel buckled in the same direction as the control panels, as illustrated in Fig. 8.8, with the impacted side of the panel in compression. Conversely, the 2.5J, 10J and 20J panels buckled in the opposite direction, such that the impacted side of the panel was in tension. As a result of this the large delamination between the 15^{th}-16^{th} plies buckled locally, creating a bulge on the back face of the panel as illustrated in Fig. 8.10. This local buckling was detected by the SG3 strain gauge pair as shown in Fig. 8.9 for the 2.5J and 10J panels, by both the individual strain curves for the SG3 pair and corresponding mean and bending strain response. The 20J impact specimen is believed to have behaved in the same manner, though the SG3 strain gauge pair could not be used due to the fibre spitting on the back surface post-impact.

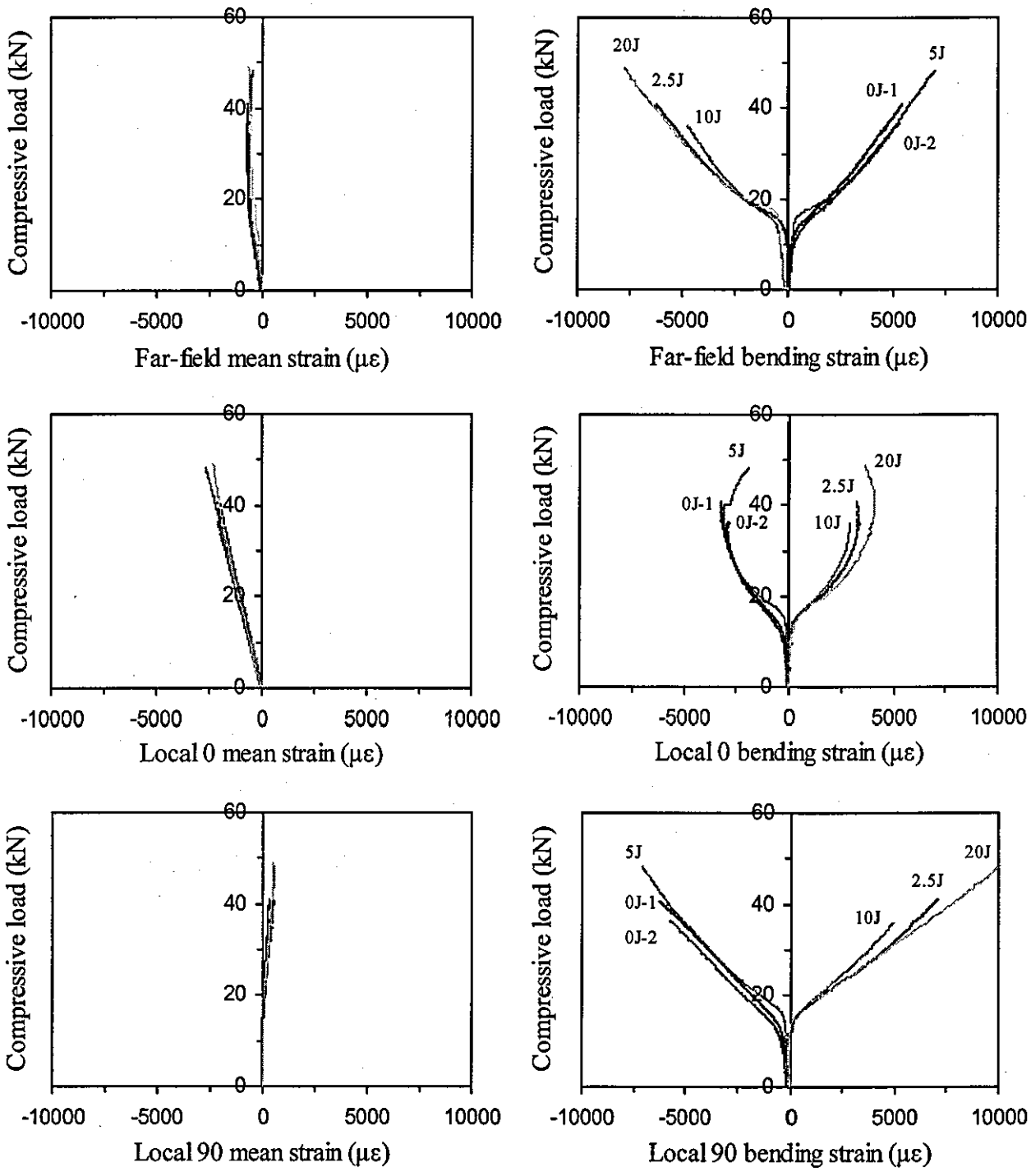

Figure 8.8 Mean and bending strain at far-field (SG1) and local (SG2) locations on undamaged and impacted 16 ply laminates in in-plane compression

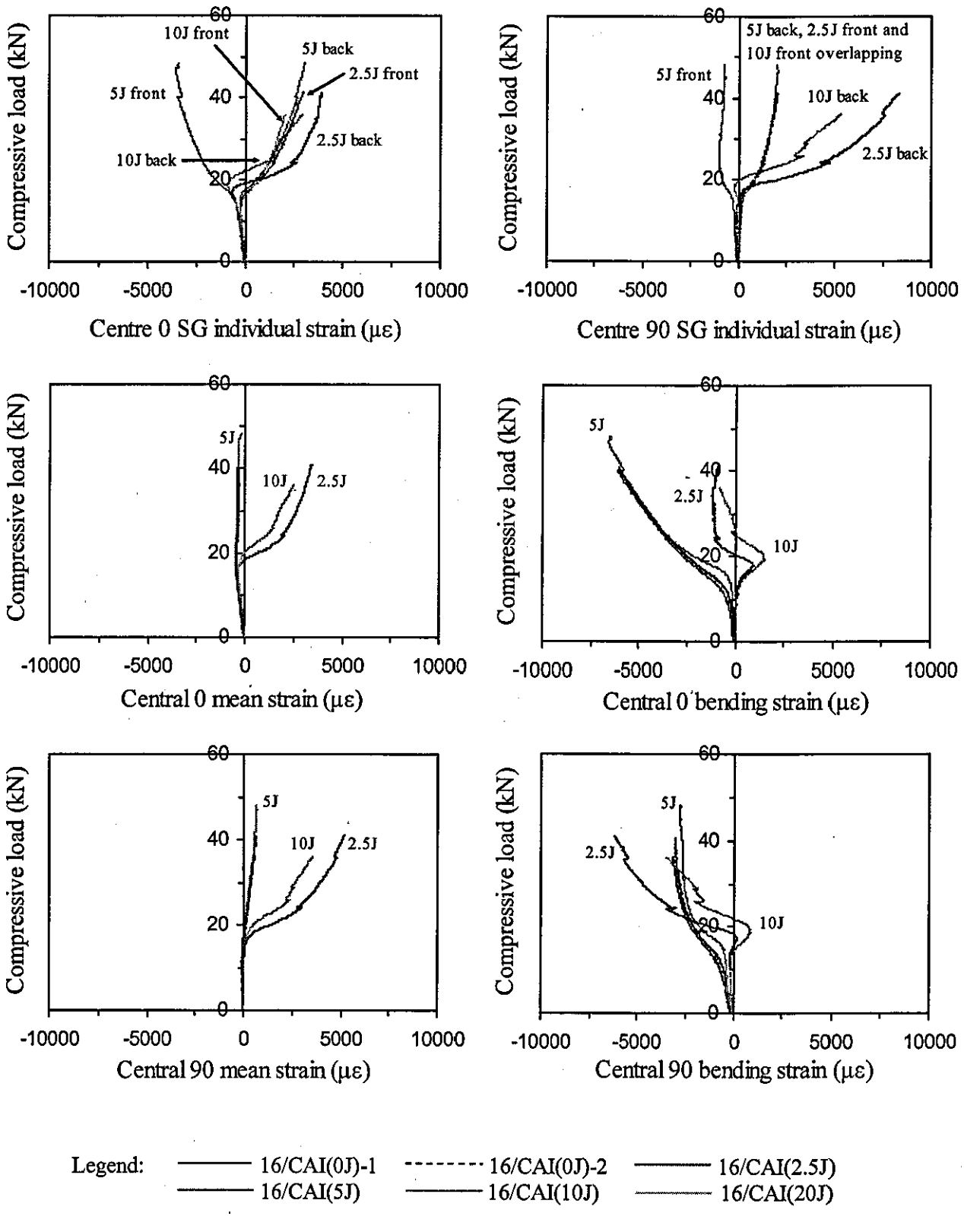

Figure 8.9 Strain variation at central (SG3) location in on undamaged and impacted 16 ply laminates in in-plane compression

Despite local buckling at the impact point mode II buckling of the panel continued to develop and the 2.5J, 10J and 20J panels failed in compression towards the loaded end, shown in Fig. 8.11 for the 16/CAI(20J) panel. This indicates the level of damage was not sufficient to affect the overall panel strength and failure mode, despite delamination damage extending over almost half of the panel width in the 16/CAI(20J) specimen. This suggests a high level of damage tolerance for this type of specimen and is identified in Fig. 8.12 by the constant value of residual compressive strength for increasing IKE levels. The reasoning behind this apparent lack of strength degradation may be due to the fact that the local buckling associated with the impact damaged area was not able to propagate far enough to cause instability and ultimate failure.

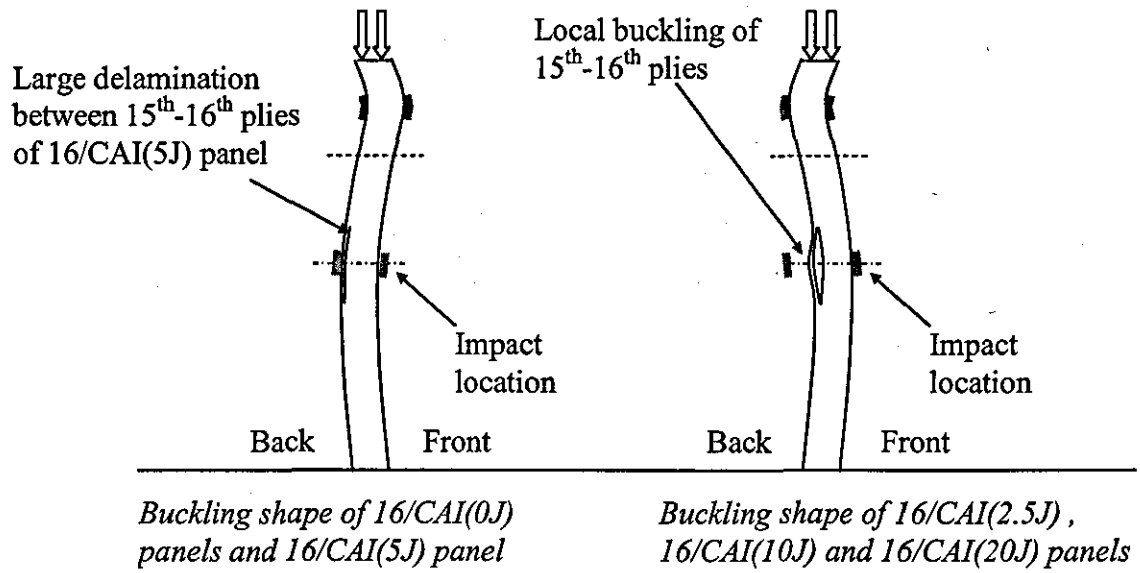

Buckling shape of 16/CAI(0J) panels and 16/CAI(5J) panel

Buckling shape of 16/CAI(2.5J), 16/CAI(10J) and 16/CAI(20J) panels

Figure 8.10 Mode II buckling shape of damaged and undamaged laminate panels

Cross-sectioning of the specimens after testing shows extensive delamination in the vicinity of the failure location. At the panel mid-section the delamination size and pattern are comparable to the damage present in the duplicate impact specimens, as recorded in Table 8.1. This confirms propagation of the delaminations resulting from impact did not occur during compressive loading. This is in agreement with the variation of the Poisson's response throughout loading, illustrated in Fig. 8.13 for the

16/CAI(20J) panel, which does not show any sudden deviations, as have been suggested in existing literature [101] to be indicative of delamination propagation.

Moreover, the concept of effective width, w_e, as often used in metallic plate buckling theory [207], could be used to add understanding. In compression testing of simply-supported thin metallic plates, failure of the plate occurred at a load largely in excess of the theoretical buckling load of the plate. This has been associated to an uneven stress distribution across the plate width. Prior to the buckling load being reached the stress distribution is uniform. As the central section of the plate undergoes local mode I buckling its load carrying ability is reduced. Consequently the two outer edge strips of the plate, which are constrained by the simple supports, are less buckled and continue to support the load. Failure of the panel occurs when the stress within the edge strips reaches the yield stress of the material. The effective width, w_e, for a thin metallic plate can be calculated using Eq. 8.2 [207] and has been estimated for a 16 ply laminate to be 23mm, based upon the mechanical properties given in Chapter 2. Therefore in the case of an impact damaged panel provided the impact damage is not greater than 100mm in diameter a reduction in strength is unlikely to occur. For the 16 ply laminate panels tested even an impact energy of 20J, which caused fibre splitting of the back surface, only contained delaminations less than 75mm in length following impact loading.

$$2w_e = \frac{\pi t}{\sqrt{3}\left(1-\nu_s^{\,2}\right)^{1/2}}\sqrt{\frac{E_{comp}}{\sigma_{comp}}} \tag{8.2}$$

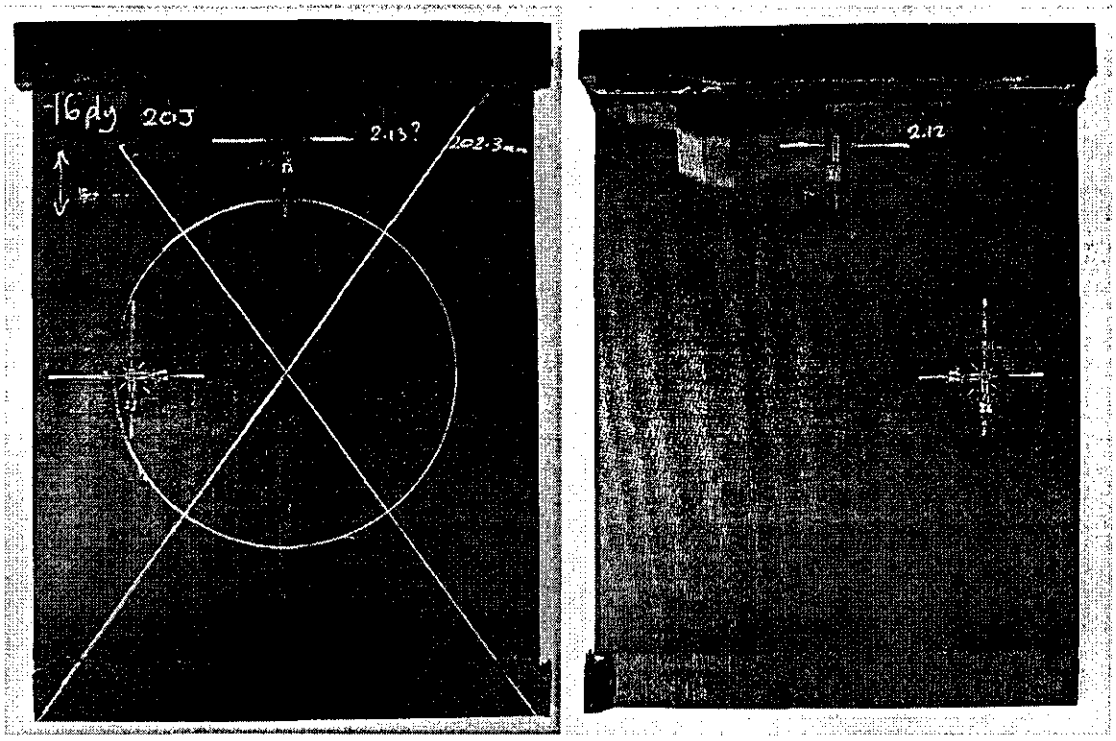

(a) (b)

Figure 8.11 Photograph of 16/CAI(20J) panel after compression loading
(a) front view (impacted side) (b) back view

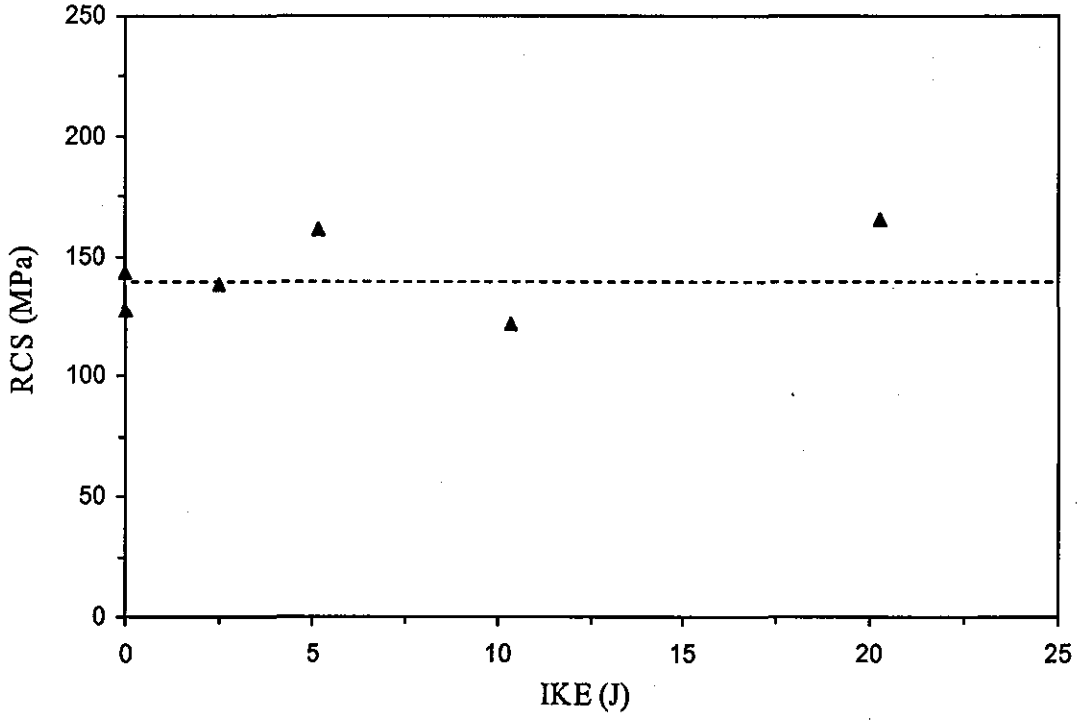

Figure 8.12 Variation of compressive strength with impact energy level for 16 ply monolithic laminates

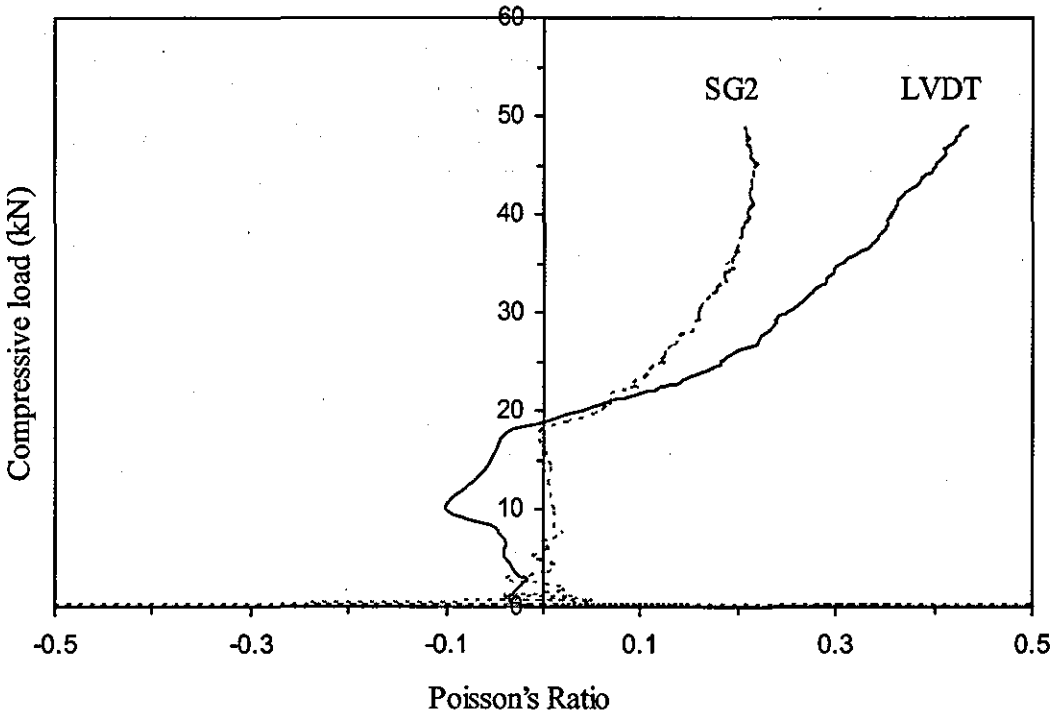

Figure 8.13 Variation of Poisson's ratio with load, calculated from SG2 strain gauge pair and LVDT readings for 16/CAI(20J) panel

8.2. General behavioural characteristics of sandwich panels under in-plane compression

To determine the general behavioural characteristics of sandwich panels under in-plane compression a number of control sandwich panels were loaded until failure, similar to the monolithic laminates discussed in Section 8.1. Being equipped with the findings of the 16 ply monolithic panels in in-plane compression, the only suitable skin thickness was 8 plies, as sandwich panels with any thicker skins would be unlikely to be able to fail around the mid-section region for the chosen aspect and width-to-thickness ratios. Thus, the control panels tested consisted of three 8 ply 70kg/m^3 aluminium honeycomb panels and two 8 ply 64kg/m^3 nomex honeycomb panels. The load-displacement response of all control panels is compared in Fig. 8.14. The initial region of the load-displacement curve is non-linear due to bedding in effects. The length of this region varies slightly due to its dependence on each individual specimen and positioning

within the test rig. Once bedding in has completed, typically around 10kN, the load-displacement response becomes approximately linear until failure.

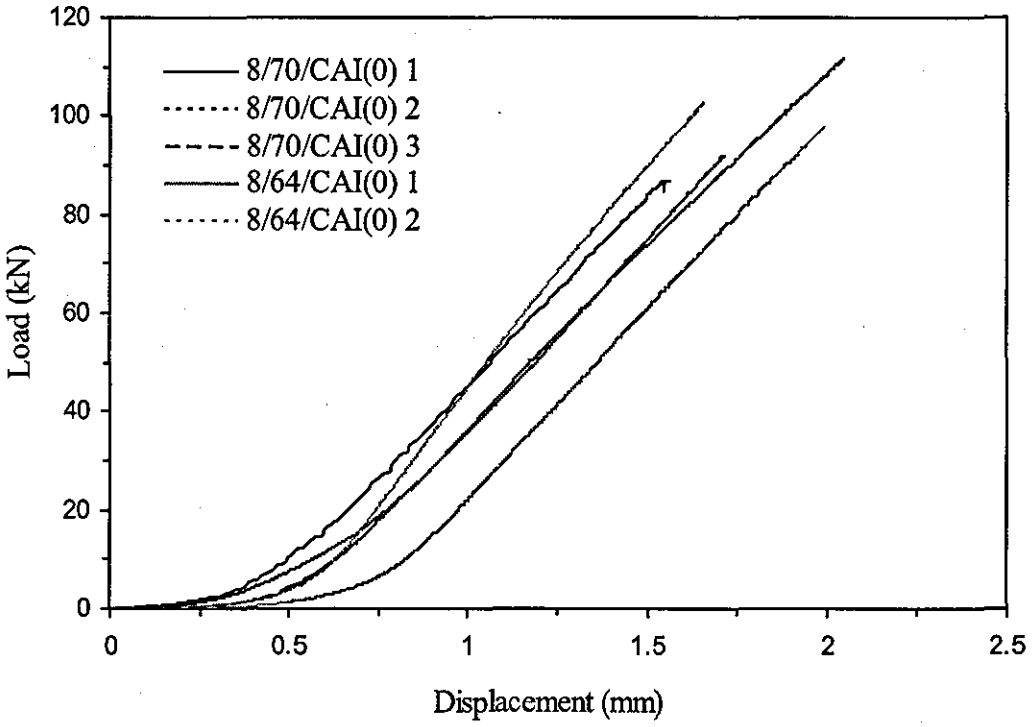

Figure 8.14 Load-displacement response of undamaged 8 ply sandwich panels with aluminium and nomex honeycomb under in-plane compression

During loading the occurrence of damage was signified by cracking sounds generally occurring after 60kN, with failure represented by a sudden loud bang accompanied by a loss of panel strength. The failure loads of all control panels ranged from 92-112kN, with the 20% variation in load typical for compression testing of monolithic laminates. This corresponds to an average stress level of 292MPa when the load is assumed to be supported by the skins alone, which is more than double the strength of the undamaged 16 ply monolithic laminate plates. Analysis of the specimens shows compressive failure of both skins below the epoxy end pot at the loaded end of the panel, an example shown in Fig. 8.15 for the 8/70/CAI(0)-2 panel. The cross-section along the longitudinal mid-section shows only minor delamination and core distortion at the failure location.

An interesting core crushing pattern can be seen on the external edges of the aluminium control panels, as illustrated in Fig. 8.15 for the 8/70/CAI(0J)-2 panel. Crushing occurs near to one face at the failure location. It then shears to the other face for the central section of the panel then either continues or shears back to the original face at the opposite end of the panel. At the panel mid-section this core crushing extends towards the centre of the panel, appearing as a shearing distortion of the cell walls over approximately 6 cells, depicted in Fig. 8.15. The external crushing pattern is not always well defined and can be difficult to identify, especially in the nomex panels where core damage is represented by resin cracking on the cell walls and is only well defined in the vicinity of the failure location.

Videos of the compression tests showed the core damage to occur at the point of failure. As compressive failure of both skins occurred sequentially in a shearing manner beneath the epoxy end pot, the panel tried to bend globally. The side supports prevented through-the-thickness transverse movement of the panel and consequently the core beneath the side supports was crushed. The top and bottom edges of the panel 20cm beneath the epoxy end pots were not supported by the side supports and could move freely in either direction as each skin failed in turn. This created the shearing pattern seen on the panel edge beneath the end pots. However, these crushing patterns only applied to the external edges of the panel as the central region of the panel was unsupported and could move freely so did not suffer core crushing, as shown in Fig. 8.15.

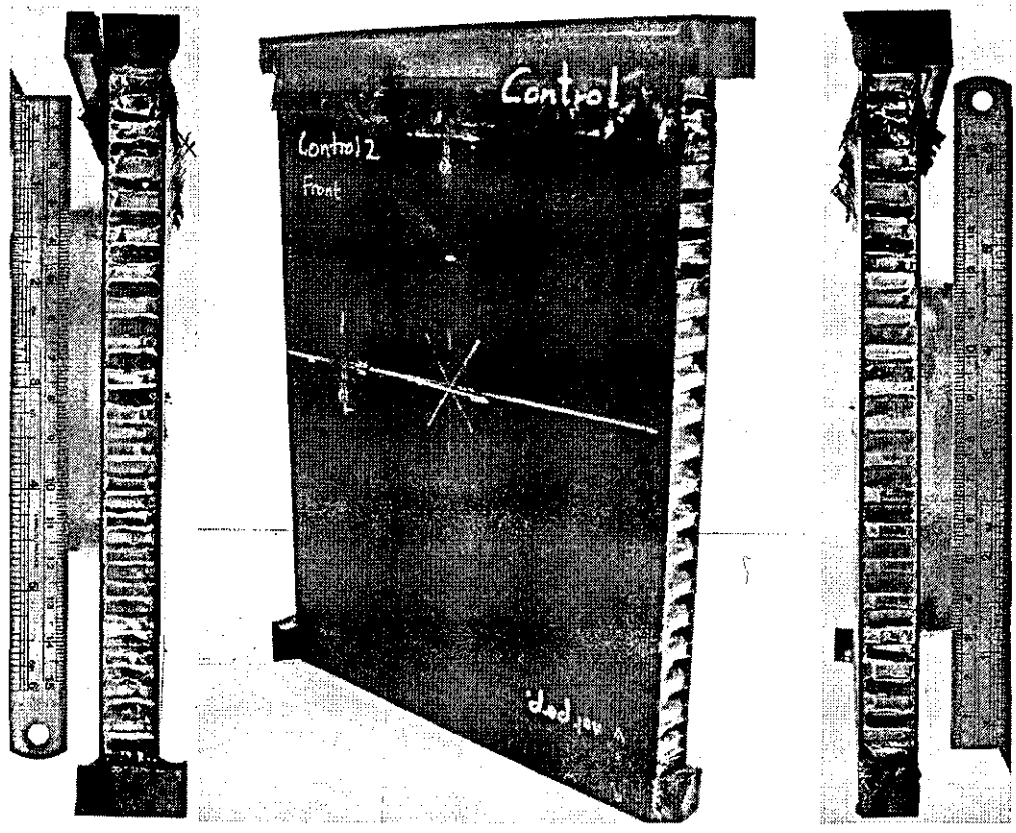

(a) (b) (c)

(d)

(e) Distorted cell walls (f)

Figure 8.15 Photographs of 8/70/CAI(0)-2 panel after in-plane compression: (a) Left external edge (b) Front (c) Right external edge (d) Cross-section of internal damage on longitudinal mid-section (e) Transverse mid-section view of right hand side top quadrant (f) Transverse mid-section view of right hand side bottom quadrant

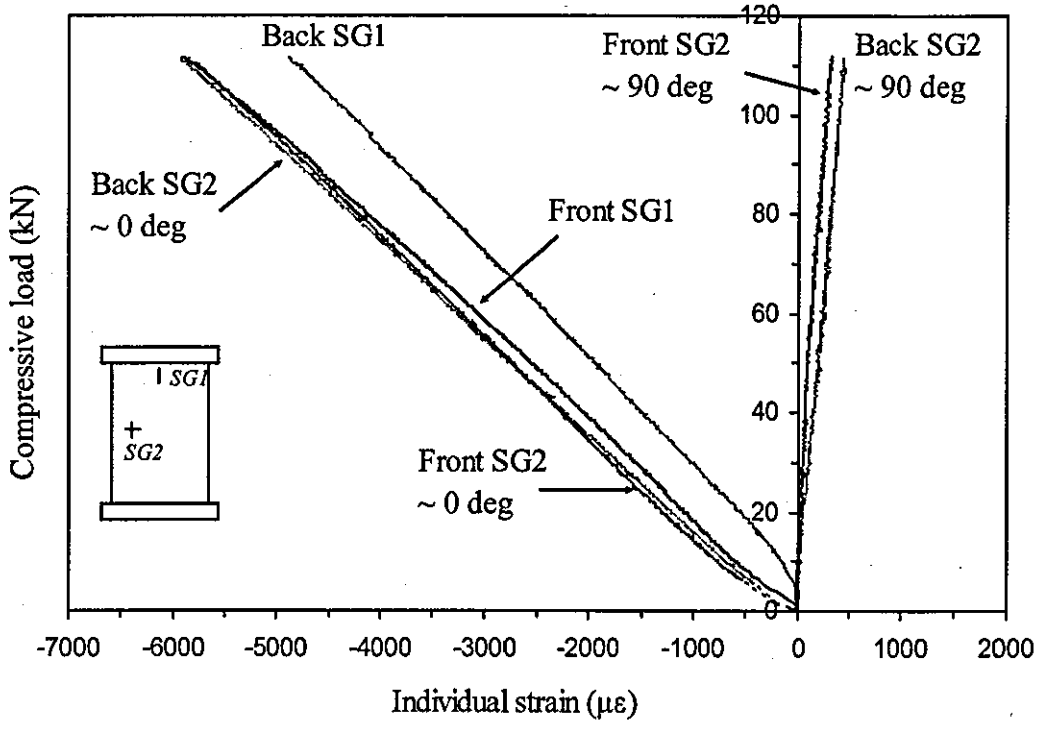

(a)

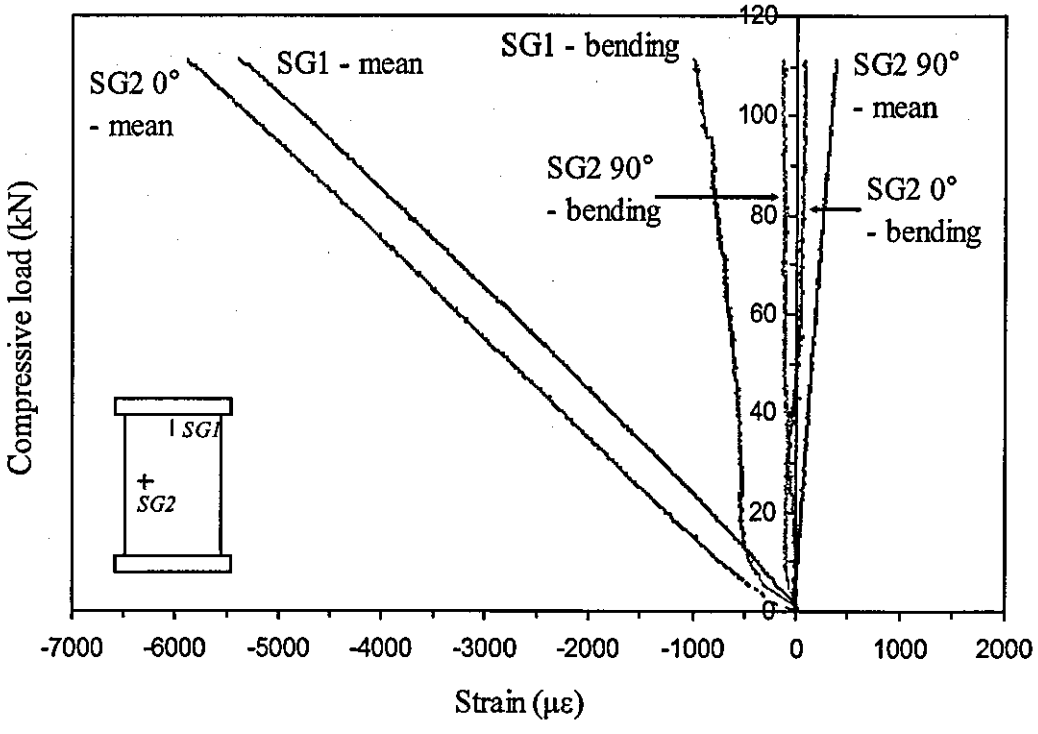

(b)

Figure 8.16 Load-strain response for undamaged 8/70/CAI(0)-3 panel under in-plane compression (a) individual strain response (b) mean and bending strain response

The individual, mean and bending strain responses under in-plane compression are shown in Fig. 8.16 for the 8/70/CAI(0)-3 panel, and are typical of the responses seen in all control panel tests. Once bedding in of the panel has occurred the individual strain responses become linear and show stable compressive behaviour in the 0° fibre direction with slightly tensile behaviour in the 90° fibre direction, shown in Fig. 8.16(a). The similar level of linear increase in mean and bending strain at both the local and far-field locations following bedding in, as shown in Fig. 8.16(b), indicates in-plane compression only with no panel buckling. The strain response at both local and far-field locations remains linear until failure, with no detection of the oncoming compressive failure at the far-field location. The minimal amount of strain in the in-plane transverse direction reflects the minor variation in horizontal displacement as measured by the LVDT at the mid-section, shown previously in Fig. 7.4. This suggests the Poisson's effect, which was visible in the monolithic laminate panels, is negligible in the sandwich panels, as illustrated in Fig. 8.17. This is most likely due to the constraining effect of the core, preventing in-plane transverse movement of the skins.

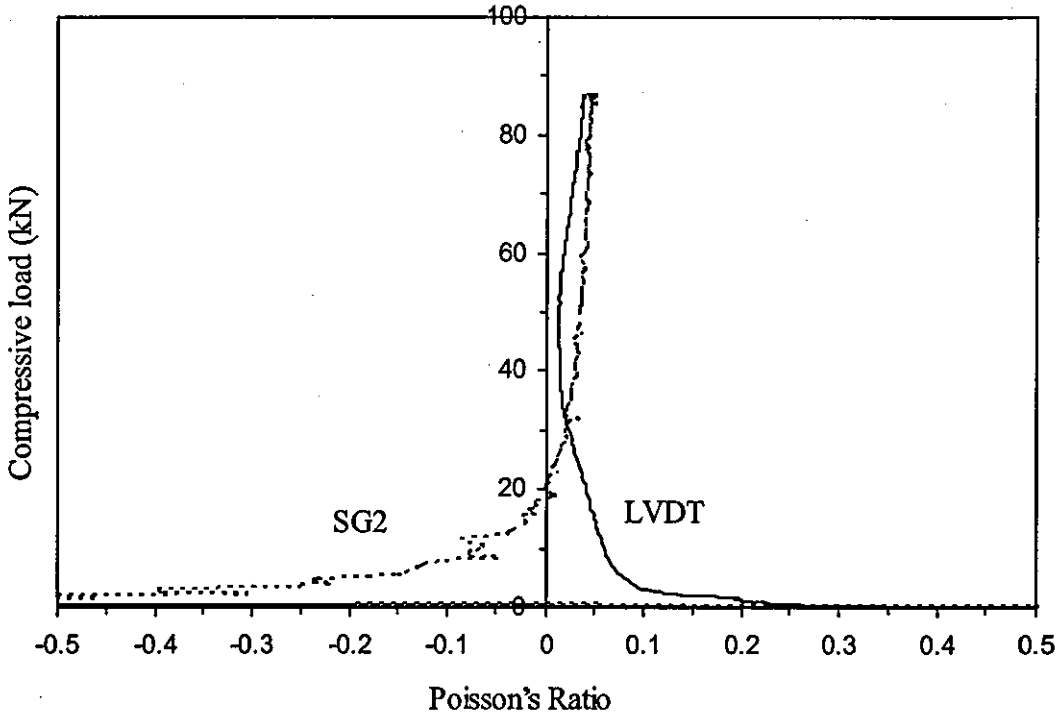

Figure 8.17 Variation of Poisson's ratio with load, calculated from SG2 strain gauge pair and LVDT readings for 8/70/CAI(0J)-1 panel

The failure mechanism seen in the control panels is not typical for compressive panel loading as panel buckling did not develop. Consequently discussion of damage characteristics is difficult. The probable panel deformation process for the control panels is illustrated in Fig. 8.18.

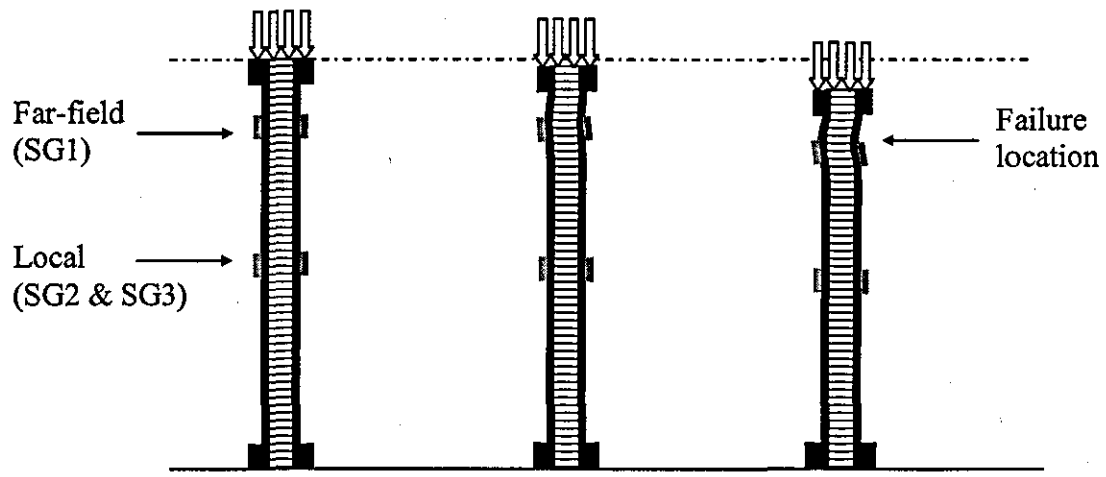

Load	*P=0*	*P<10kN*	*P=96-112kN*
Mean strain	$\varepsilon_m=0$	$\varepsilon_{mf} < \varepsilon_{ml}$	ε_m *linear increase*
Bending strain	$\varepsilon_b=0$	$\varepsilon_{bf} > \varepsilon_{bl}$	ε_b *constant*

Figure 8.18 Illustration of the deformation process of undamaged control panels under in-plane compression

Neither local mode I nor mode II buckling ever developed, indicating the associated buckling stresses to be larger than the in-plane compressive strength of the skins of the panel. It is known from the tests on monolithic laminates that the high number of 0° plies provides the panel with a high flexural strength and that mode II buckling can not occur if the flexural rigidity of the panel is larger than the in-plane shear rigidity [102]. As flexural rigidity is directly linked to panel thickness it is to be expected that the thicker undamaged sandwich panel will not fail in mode II buckling as the undamaged

monolithic laminates did not. However, by splitting the 16 ply skins into two 8 ply laminates with a 12.7mm thick core mode II buckling was completely prevented from developing such that the panel underwent pure in-plane compression.

The core acts as a brace between the two skins and gives the panel not only a high flexural rigidity and through-the-thickness compressive resistance but also provides a local stabilising effect to the skins. Both local and global through-the-thickness transverse deformations of the skins are prevented provided the adhesive bond and compressive strength of the core are sufficient. The adhesive tensile strength of 7MPa (measured by the manufacturer ACG) is approximately double the bare compressive strength of the honeycomb (measured by the manufacturer Hexcel), indicating local skin dimpling as a result of core crushing would occur rather than skin wrinkling due to skin-core debonding. As neither type of deformation occurred the local through-the-thickness transverse stresses were below both the adhesive and core strengths. This highlights the importance of including the effects of not only the skins but also the core in theoretical models. As has been proven experimentally, monolithic laminate compression methodology cannot be directly applied to sandwich structures where the panel thickness is not negligible when compared to the in-plane dimensions.

8.3. Compressive response of impact damaged aluminium honeycomb sandwich panels

Aluminium sandwich panels were impacted at IKE levels ranging from 2.5J to 25J, respectively. The internal damage was estimated from the cross-sections of duplicate impact tests, as recorded in Table 6.24. The damage contained within these specimens consisted of increasing amounts of core crushing and multiple delaminations throughout the skin thickness, accompanied by fibre fracture of the top skin of the 25J specimen. When loaded in compression the panels impacted between 2.5J and 13J failed at a load between 67-84kN. The load-displacement response for a number of the CAI tests are shown in Fig. 8.19, and show close correlation with the 8/70/CAI(0)-1 control panel. A summary of the relevant test data including residual compressive strength, failure location and internal damage before and after compression is contained in Table 8.2.

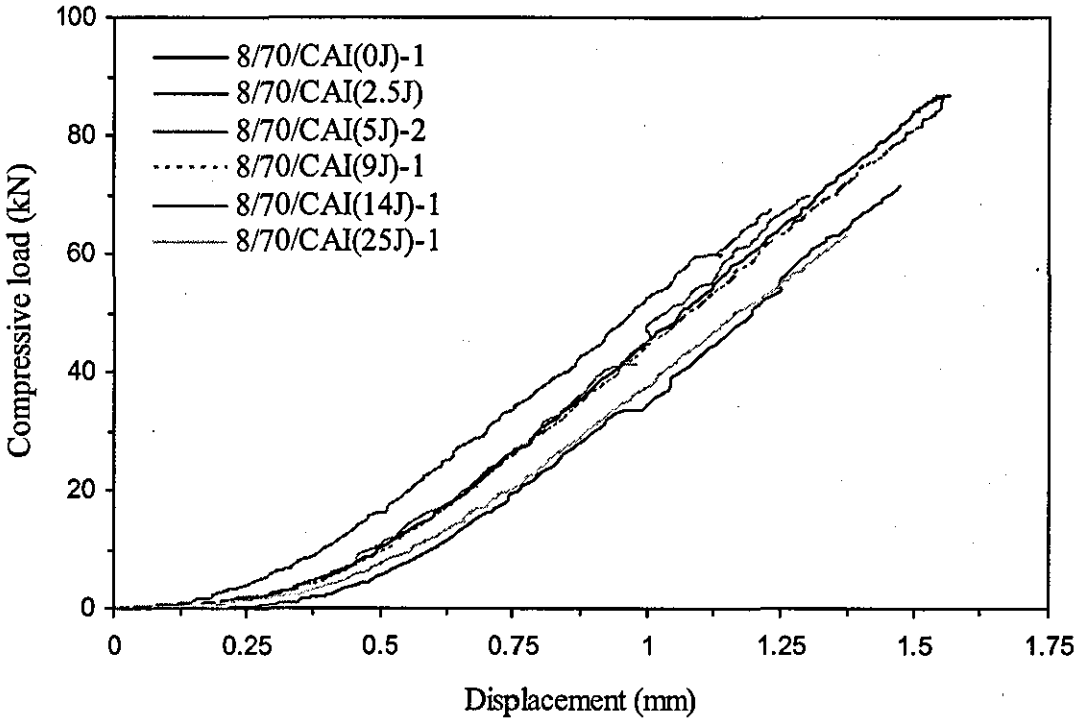

Figure 8.19 Variation of load vs. vertical displacement for panels impacted from 0-25J and loaded in compression on the Mand machine

The mean and bending strain responses for each CAI panel have similar general characteristics to those of the undamaged control panel tests regardless of impact energy, examples shown in Figs. 8.20 & 8.21 with graphs for each individual test included in Appendix C. The strain reversals representative of local buckling of the impact damaged area in the monolithic laminate panels are not present on the strain responses for the impact damaged aluminium sandwich panels. In a number of tests a minor fluctuation in the bending strain, often more prominent at the far-field location, occurred prior to failure. This fluctuation is most distinct for the 8/70/CAI(25J) panels, which contained an 80mm diameter residual dent and top skin fibre fracture, and is accompanied by a reasonably pronounced increase in local bending in both the 0° and 90° fibre directions, shown in Fig. 8.21 for the 8/70/CAI(25J)-2 panel. This suggests the initiation of local buckling around the impacted section, which may be accompanied by some propagation of the impact damage. Although the 8/70/CAI(25J)-2 panel still failed at the loaded end, the 8/70/CAI(25J)-1 panel with a similar amount of impact damage failed at the mid-section.

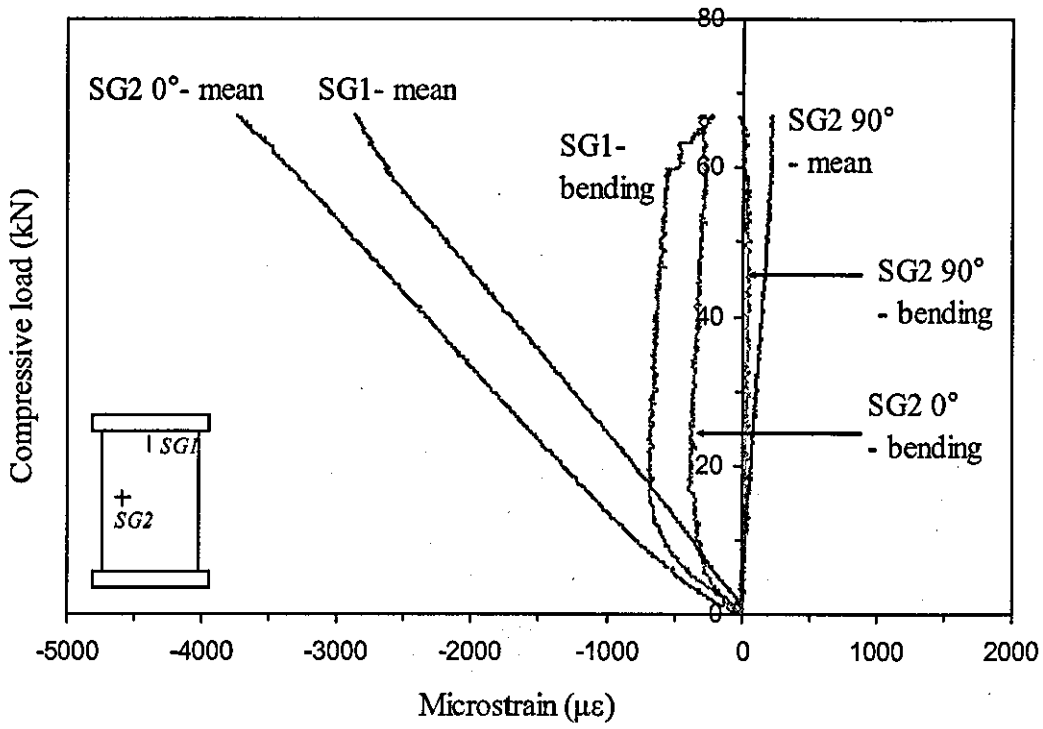

(a)

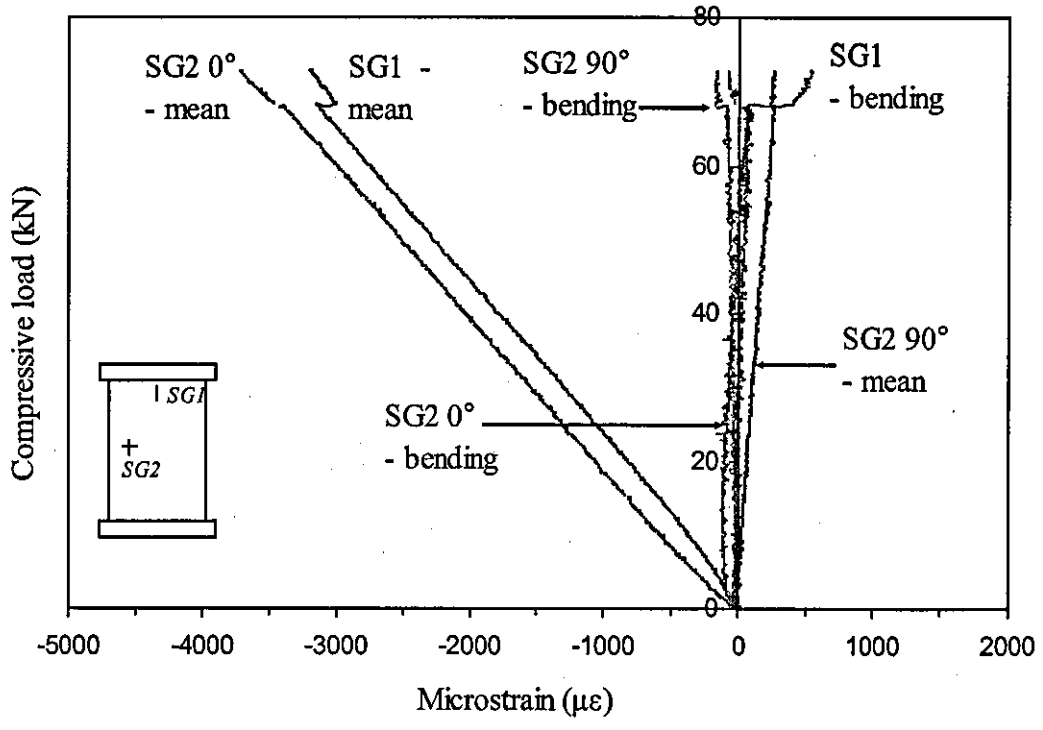

(b)

Figure 8.20 Mean and bending strain response for (a) 8/70/CAI(3J)-1 (failure located at mid-section of panel) (b) 8/70/CAI(3J)-2 (failure located at mid-section of panel)

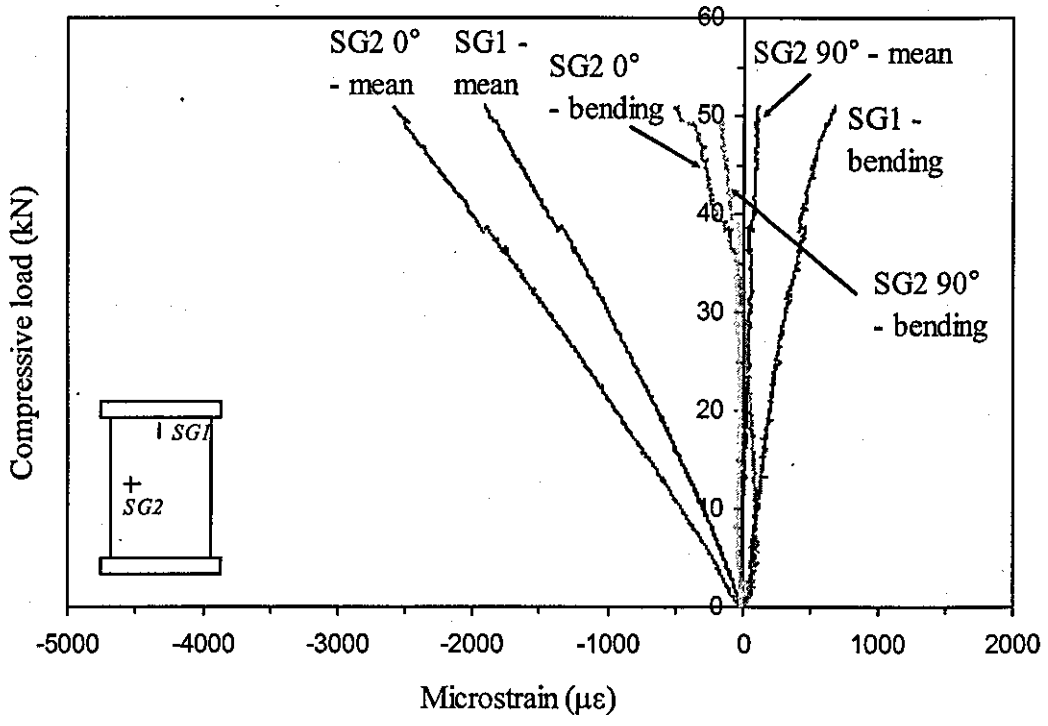

Figure 8.21 Mean and bending strain response for 8/70/CAI(25J)-2 loaded on Denison with failure located at loaded end of panel

The failure location under compression loading would be expected to coincide with the location of the impact damage at the panel mid-section. However, for a number of panels failure occurred at the end of the panel rather than at the mid-section, with no strong correlation between failure location and impact damage level or RCS. In the majority of cases failure occurred near the mid-section with compressive failure of the impacted skin to either side of the impact damage, illustrated in Figs. 8.22 & 8.23. At the panel centre there was local wrinkling/dimpling of the sub-laminates created during the impact event rather than fibre fracture. Only the 8/70/CAI(9J)-1 panel had compressive failure of the back skin combined with local buckling. In the cases where failure occurred close to the end of the panel, failure was through compressive failure of both skins in the same manner as seen for the control panels, shown in Fig. 8.24. In all cases failure occurred just below the epoxy end pot at the top edge of the panel above the SG1 location, except in the 8/70/CAI(5J)-1 panel where the failure location was just above the epoxy end pot at the bottom edge of the panel.

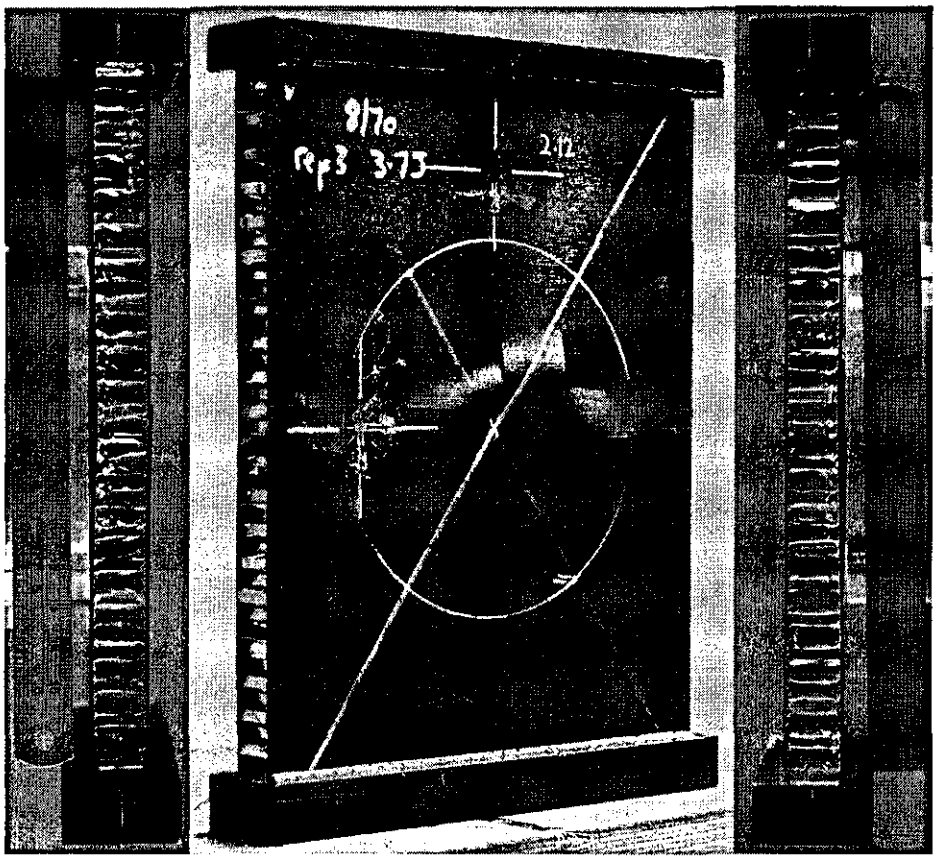

(a) (b) (c)

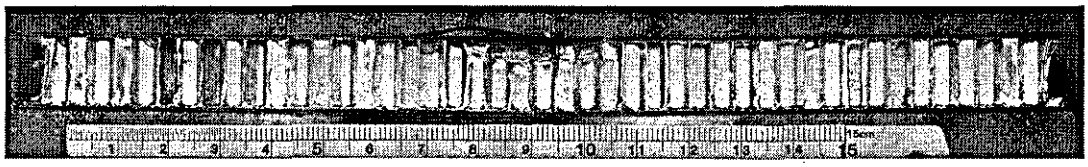

(d)

(e) (f)

Figure 8.22 Photographs of 8/70/CAI(3J)-2 panel after in-plane compression: (a) Left external edge (b) Front (c) Right external edge (d) Cross-section of internal damage on longitudinal mid-section (e) Cross-section of internal damage on transverse mid-section top right quarter and (f) bottom right quarter

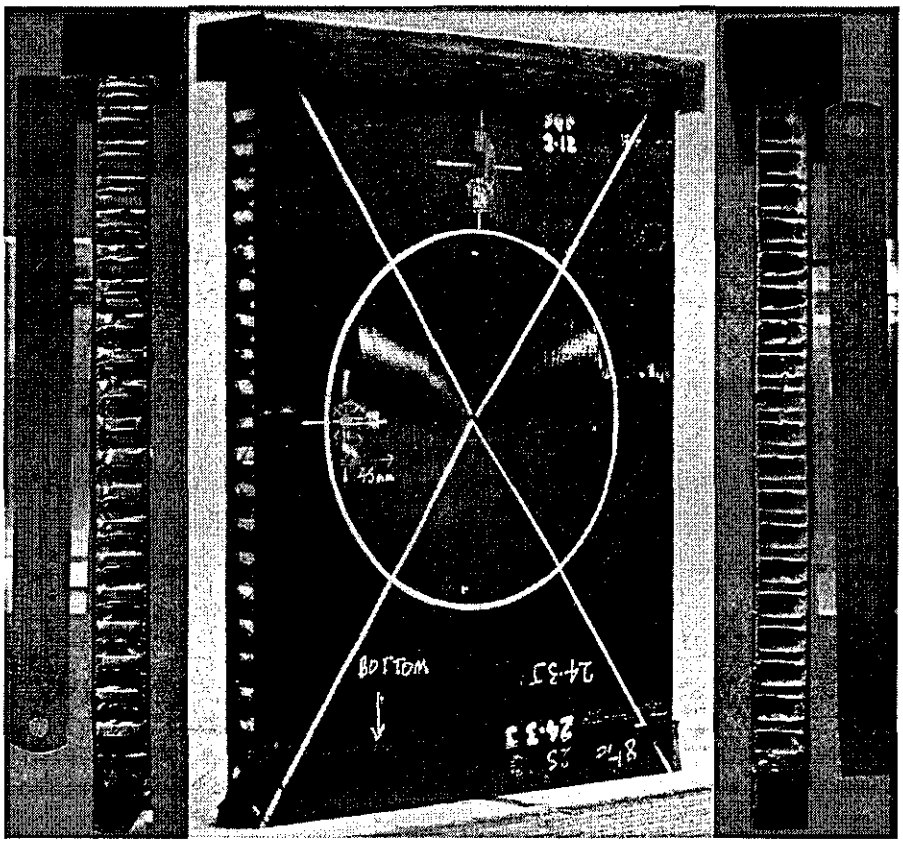

(a) (b) (c)

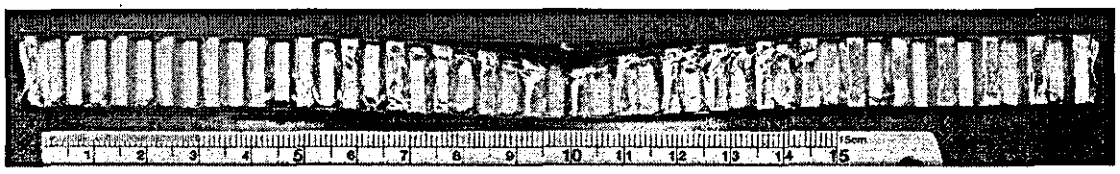

(d)

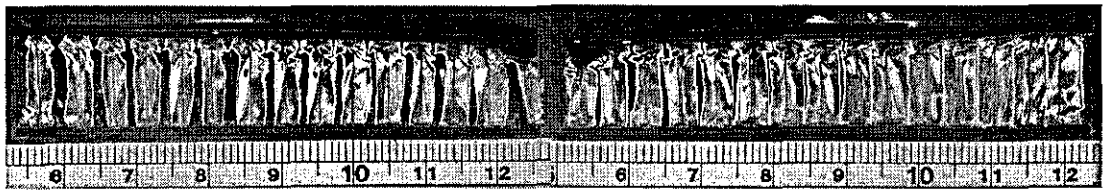

(e) (f)

Figure 8.23 Photographs of 8/70/CAI(25J)-1 panel after in-plane compression: (a) Left external edge (b) Front (c) Right external edge (d) Cross-section of internal damage on longitudinal mid-section (e) Cross-section of internal damage on transverse mid-section top left quarter and (f) bottom left quarter

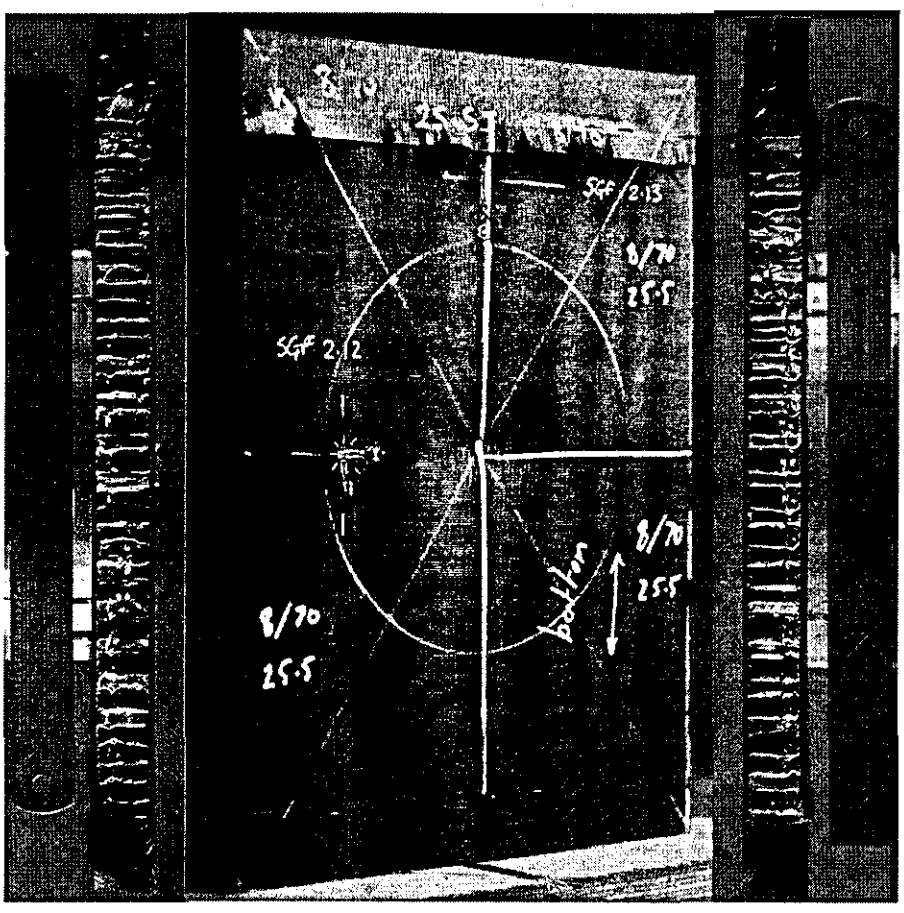

(a) (b) (c)

(d)

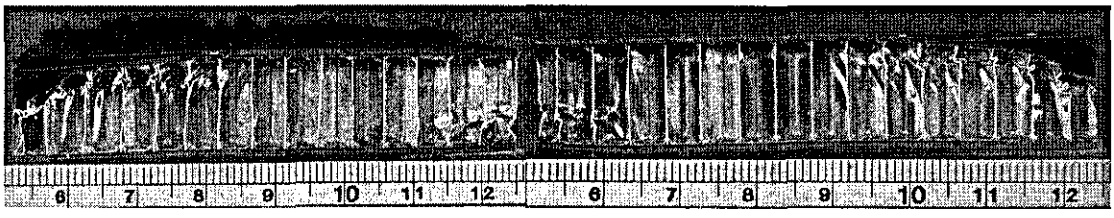

(e) (f)

Figure 8.24 Photographs of 8/70/CAI(25J)-2 panel after in-plane compression: (a) Left external edge (b) Front (c) Right external edge (d) Cross-section of internal damage on longitudinal mid-section (e) Cross-section of internal damage on transverse mid-section top right quarter and (f) bottom right quarter

For those panels which failed close to one of the ends, an additional mechanism could be the giving-in of one of the two skins thereby leading to the occurrence of end rotation during bedding in of the panel, as indicated by a large increase in the far-field bending strain. However, in the panels which failed near the mid-section the level of bending strain measured by the SG1 pair of gauges ceased to increase and became stable once bedding in was complete, illustrated in Fig. 8.20(a) for the 8/70/CAI(3J)-1 panel. If the bending strain becomes stable the failure load and location of failure are as expected for a panel with little or no initial end rotation. This is illustrated graphically in Fig. 8.20(b) for the 8/70/CAI(3J)-2 panel which had almost no end rotation during bedding in but failed at the mid-section and at a similar load to the 8/70/CAI(3J)-1 panel which had considerable end rotation. Conversely, when the far-field bending strain did not become stable and continued to increase throughout loading failure was often located towards the loaded end of the panel, illustrated in Figs. 8.21 & 8.24 for the 8/70/CAI(25J)-2 panel. The increasing amount of bending at the panel end induces stress concentrations that ultimately lead to failure of the panel towards the loaded end despite measurable damage at the panel mid-section.

The core crushing pattern seen on the unloaded edges of the impact damaged panels after compression testing typically take one of two forms. If failure occurs towards the end of the panel the crushing patterns are similar to those described in Section 8.2 for the control panels, shown in Fig. 8.24 for the 8/70/CAI(25J)-2 panel. The alternative crushing pattern is applicable to panels which failed near the mid-section. In this instance the core is crushed next to the back skin in the vicinity of the failure location on the mid-section, illustrated in Fig. 8.23 for the 8/70/CAI(25J)-1 panel. In some cases an amount of cell wall distortion/shearing also occurred towards the epoxy end pots, shown in Fig. 8.22 for the 8/70/CAI(3J)-2 panel. In all instances the cell crushing or distortion only extends towards the panel centre in about 6 cells. The change in crushing pattern can be attributed to localised bending of the back skin at the mid-section when the top skin fails in compression. As the panel tries to bend through-the-thickness transverse movement of the back skin is prevented by the simple supports, inducing localised core crushing at the panel edges. Residual bending of the centre section of the back skin can be seen in the panels once the compressive load is removed.

In Table 8.2 the damage contained within each panel after compression in both the longitudinal and in-plane transverse directions is compared with the damage in the duplicate panels impacted at a similar IKE level and cross-sectioned. It can be seen that in the longitudinal direction the delamination at the centre of the panel is of a similar size prior to and after compression loading, though there is a small increase in the amount of core crushing for panels impacted at higher IKE levels. In the in-plane transverse direction at the mid-section core crushing/cell wall distortion is spread across the width of the panel when compression failure is located at the mid-section. If failure occurs next to the loaded end of the panel no damage propagation occurs in the in-plane transverse direction, substantiated by the repeated tests on panels impacted at 9J or 25J where one panel failed towards the end and the other at the mid-section.

It is difficult to determine for the panels that failed at the mid-section whether the core crushing propagated in the in-plane transverse direction, instigating compressive failure of the impacted skin or if the core crushing was caused when the impacted skin failed. However, any significant propagation should have been detected by the local strain gauges and despite the notable fluctuation in the local mean and bending strain of the 8/70/CAI(25J)-2 panel the internal damage did not grow significantly. Also in some instances, as recorded in Table 8.2, although the core was damaged across the panel width only the central region had core crushing whilst in the remaining section the cell walls were only distorted. Therefore it is most probable that although the impact damaged skin did undergo a small amount of damage propagation and local dimpling at higher loads, represented by the fluctuation in the mean and bending strain, this dimpling did not propagate across the panel width, and the compressive failure of the impacted skin caused core crushing/cell wall distortion at the failure location as it buckled inwards. This implies that the core not only plays a role in supporting the skins and preventing mode II buckling of the panel as discussed in Section 8.2, but also inhibits propagation of the impact damage and local buckling of the damaged area. It can therefore be inferred that the stabilising effect of core opposes de-stabilising effect of the impact damage.

8.4. Compressive response of impact damaged nomex honeycomb sandwich panels

Sandwich panels with 8 ply skins and 64kg/m^3 nomex core are compared with the sandwich panels with a 70kg/m^3 aluminium core. Although the nomex density is 8.6% lower this is the closest pair of densities that could be found for each material type. Impact energy ranged from 5 to 28J, which was sufficient to cause fibre fracture of the impact damaged skin of the nomex panels. Under compression the nomex panels failed at a marginally lower load than for the aluminium panels when impacted at a similar energy level, with an average strength of 185MPa for nomex panels impacted below 25J. This is to be expected as the skins are the primary load bearing constituent of the panel, whilst the core plays only a secondary role in holding the skins in position.

The mean and bending strain response for the nomex panels is compared in Fig. 8.25. The response of the undamaged nomex panels, as discussed previously in Section 8.2, was almost identical to that of the aluminium panels. For the nomex panels containing impact damage the mean strain response is approximately linear until failure and follows similar trends to those identified for the aluminium panels. The bending strain response shows that an amount of panel bending typically occurred in the 0° fibre direction during bedding in of the panel at low loads, as witnessed for the aluminium panels. However, whilst the bending response of the aluminium panels is approximately linear until just prior to failure, at medium to high loads the far-field bending strain in the nomex panels increased in a tensile non-linear fashion until panel failure. This was then followed by a distinct compressive non-linear increase in the local 0° bending strain and tensile non-linear increase in the local 90° bending strain. This bending strain pattern, which is clearly visible in Fig. 8.25, is indicative of the development of local buckling and is more prominent in panels with higher levels of impact damage.

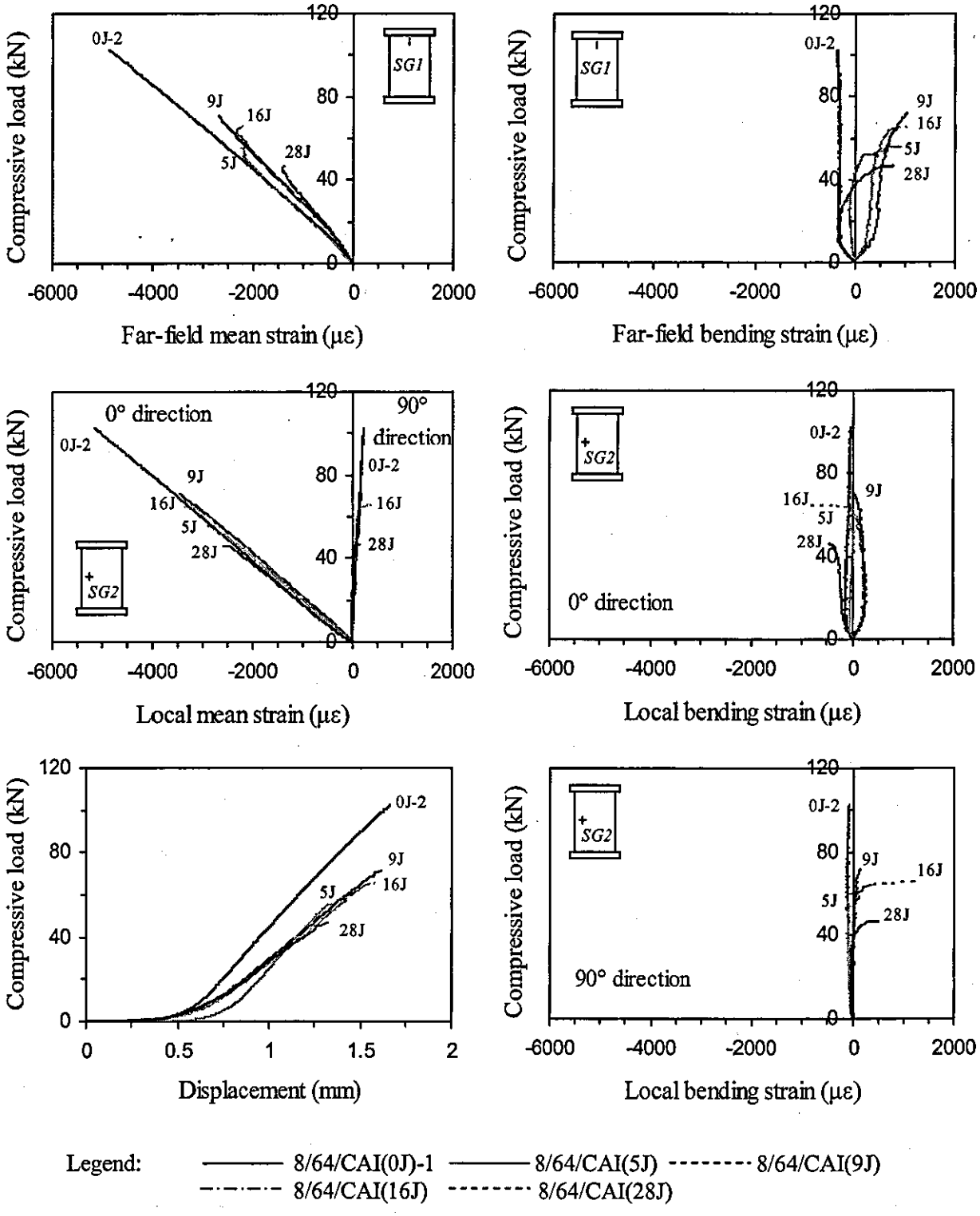

Figure 8.25 Mean and bending strain at far-field (SG1) and local (SG2) locations and load-vertical displacement response of undamaged and impacted 8 ply nomex sandwich panels under in-plane compression

Failure in the undamaged control panels was due to compressive failure of both skins just below the epoxy end pot at the loaded end, whilst all panels containing impact damage failed around the panel mid-section. In the 5J panel compressive failure of the impact damaged skin occurred across the panel width excluding the central impacted region and the back skin remained intact. In all other panels compressive skin failure occurred in both skins of the panel, as illustrated in Fig. 8.26 for the 8/64/CAI(9J) panel, with the extent of back skin damage increasing with impact energy. The effective width theory presented previously does appear to be valid as fibre fracture typically occurs only in the strips at the outer edge of the panel where it is suspected that the stress levels are largest, illustrated in Figs. 8.26 and 8.27. Unlike in the aluminium panels very little residual buckling or bending of either skin was present, due to the elastic nature of the nomex honeycomb allowing complete relaxation of the panel after unloading.

The crushing patterns on the unloaded edges of the panel were similar to those described previously for the aluminium specimens though not so well defined and core crushing, represented by resin cracking, was situated in the middle of the core rather than next to the back skin. Some increase in the extent of the impact damage in the longitudinal direction in terms of both core crushing and top skin delamination was seen from the cross-sectioned specimens after compressive loading, as recorded in Table 8.2. In the in-plane transverse direction both delamination and core damage were spread across the panel width. Interestingly whilst the aluminium panels had core crushing or cell wall distortion located immediately below the impacted skin-core interface, the core of the nomex panel was completely split across the panel width. The location of the split varied through-the-thickness but was generally shifted from the mid-section to the back skin towards the panel edges, shown in Figs. 8.26 and 8.27 for the 8/64/CAI(9J) and 8/64/(16J) panels respectively.

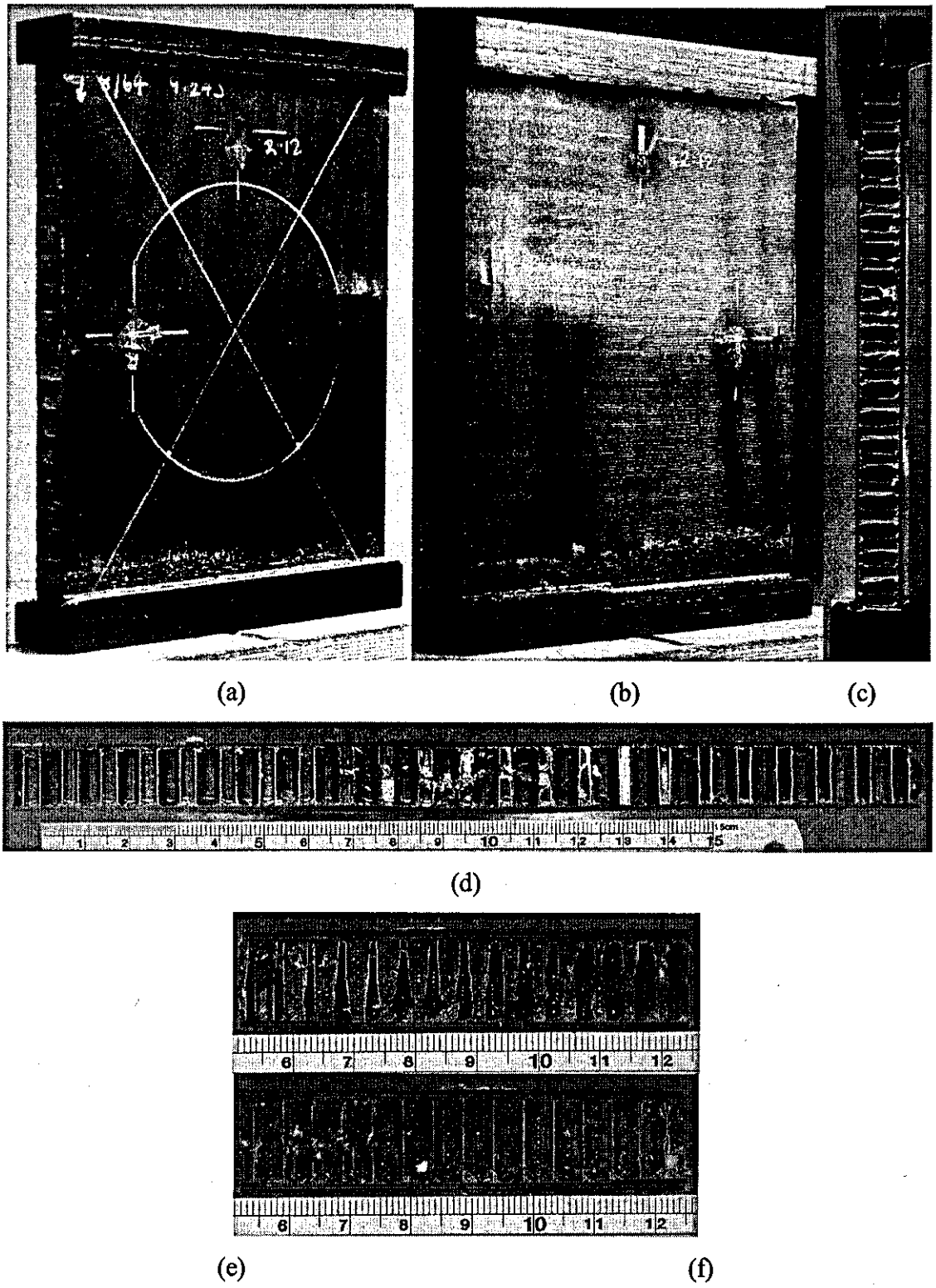

Figure 8.26 Photographs of 8/64/CAI(9J) panel loaded under in-plane compression: (a) Front view (b) Rear view (c) Right hand external edge (d) Cross-section of internal damage on longitudinal mid-section (e) Cross-section of internal damage on transverse mid-section top left quarter and (f) bottom left quarter

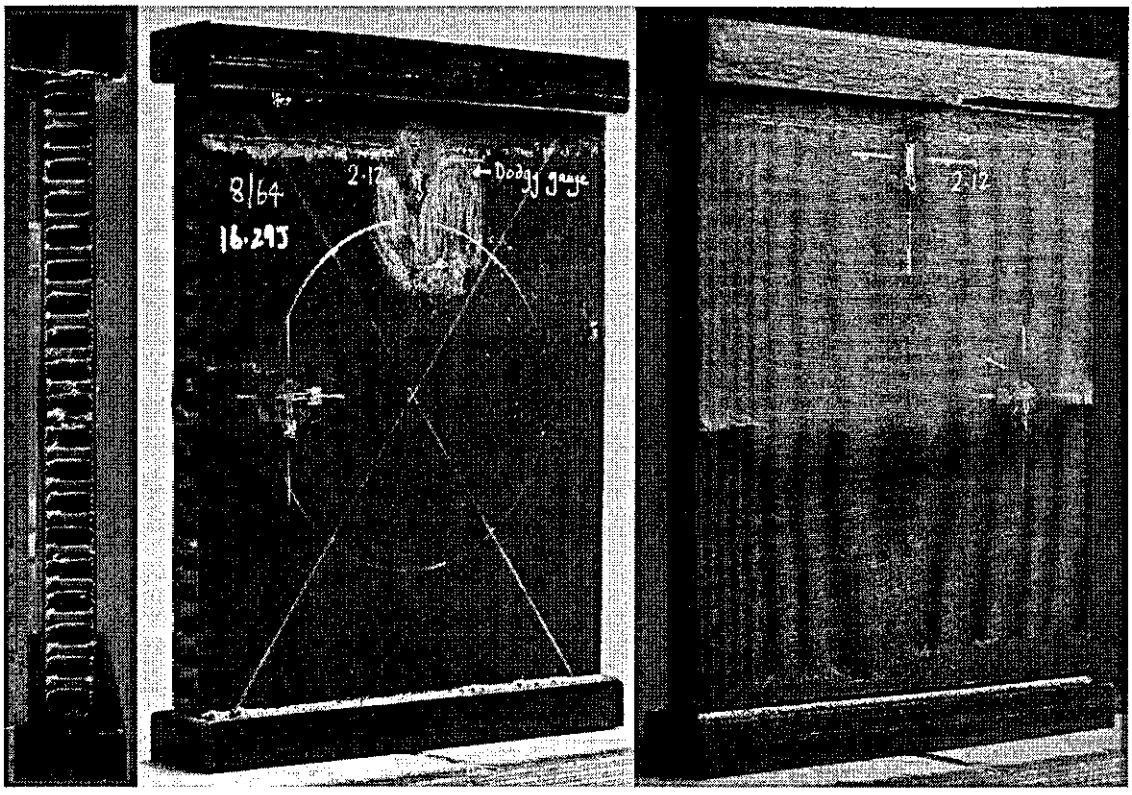

(a) (b) (c)

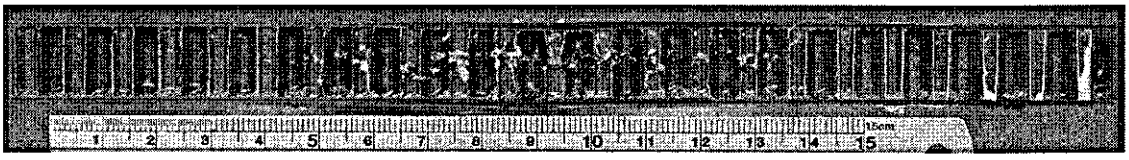

(d)

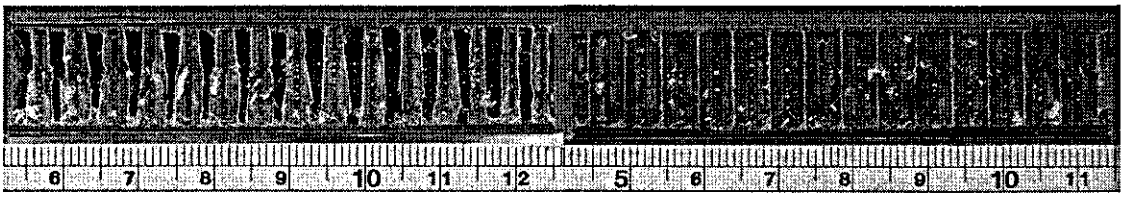

(e) (f)

Figure 8.27 Photographs of 8/64/CAI(16J) panel loaded under in-plane compression: (a) Left hand external edge (b) Front view (c) Rear view (d) Cross-section of internal damage on longitudinal mid-section (e) Cross-section of internal damage on transverse mid-section top right quarter and (f) bottom right quarter

The damage patterns to the core seen on the panel cross-sections suggests the extent of the core crushing caused by the impact propagated in both the longitudinal and in-plane transverse directions, to the point where the core damage moves towards the back skin on the in-plane transverse mid-section. There may also have been a small amount of delamination propagation. The damage propagation was accompanied by local dimpling of the damaged area, and extended far enough to be clearly detected by the local strain gauges for the panels impacted with a higher IKE. As with the aluminium panels prior to the damage propagating across the entire panel width compressive failure of the impact damaged skin occurred. However, once the impact damaged skin failed the nomex honeycomb was incapable of providing sufficient local support to the back skin, which subsequently induced compressive failure of the back skin in quick succession. This caused the tearing of the nomex core across the panel width as seen on the in-plane transverse cross-sections, rather than the controlled core crushing/cell wall distortion present in the aluminium panels. Often the location of the failure in each skin was in differing longitudinal locations, shown in Fig. 8.27 for the 8/64/CAI(16J) panel, indicating the panel to distort in a shearing mode. This type of failure mechanism is often termed panel shear failure and is a direct result of the low shear modulus and strength of the nomex core. This change in failure mechanism is a key difference in the damage tolerance performance of impact damaged nomex and aluminium sandwich panels.

8.5. Damage tolerance assessment of impact damaged panels

It is known that impact damage area increases with IKE level and consequently a reduction in RCS would be expected to occur with increased levels of IKE or damage. The compressive strength retention factor, based upon the average compression strength of the control panels, is plotted against impact energy in Fig. 8.28(a) to form a damage tolerance map. For the monolithic laminates there is no reduction in the RCS of the impact damaged panels as all panels failed at the loaded end rather than the mid-section, with the deviations from the average RCS of the undamaged panels, shown by the dotted line in Fig. 8.28(a), due to normal experimental scatter. However, for the sandwich panels Fig. 8.28(a) shows a clear reduction in compressive strength for

sandwich panels containing impact damage compared to the undamaged sandwich panels. However, the high level of scatter in compressive strength for IKE levels from 2.5J to 16J suggests the sandwich panel is insensitive to small variations in damage area and impacts below that required to cause fibre fracture. Above 25J, corresponding to fibre fracture of the top skin of the sandwich panels, there is a further small reduction in compressive strength. Similar trends are witnessed when the compressive strength retention factor is plotted against absorbed energy and delamination length, as shown in Fig. 8.28(b-c).

An alternative measure often used in damage tolerance assessment is the residual mean compressive strain at the far-field location. Again similar trends are observed with marginally less scatter than seen for RCS, though the amount of strain loss is slightly greater than for the RCS, shown in Fig. 8.29. The damage tolerance maps also show the nomex sandwich panels to undergo marginally larger levels of RCS and strain loss than the aluminium sandwich panels. Conversely the monolithic laminate panels had no reduction in RCS or strain for all levels of impact damage tested in this investigation.

Typically damage tolerance maps for monolithic laminates contain an initial region at low IKE levels where there is no degradation in RCS followed by a steep drop in RCS which levels out at higher IKE levels [102]. This trend even applies to thick laminates which do not undergo local buckling. However, for the sandwich panels tested during this research this initial region appears to be nonexistent as does the steep drop in RCS. This may be as a result of asymmetry in the impact damaged panels and the existence of two load paths, one through each skin, which leads to an uneven load distribution within each skin, accentuated by even the most minor residual dent in the impacted skin. In the monolithic laminates this scenario cannot occur as only one load path exists. The effective width concept discussed in Section 8.1 may also in part be responsible for the insensitivity to impacts with a damage width less than two thirds of the panel width.

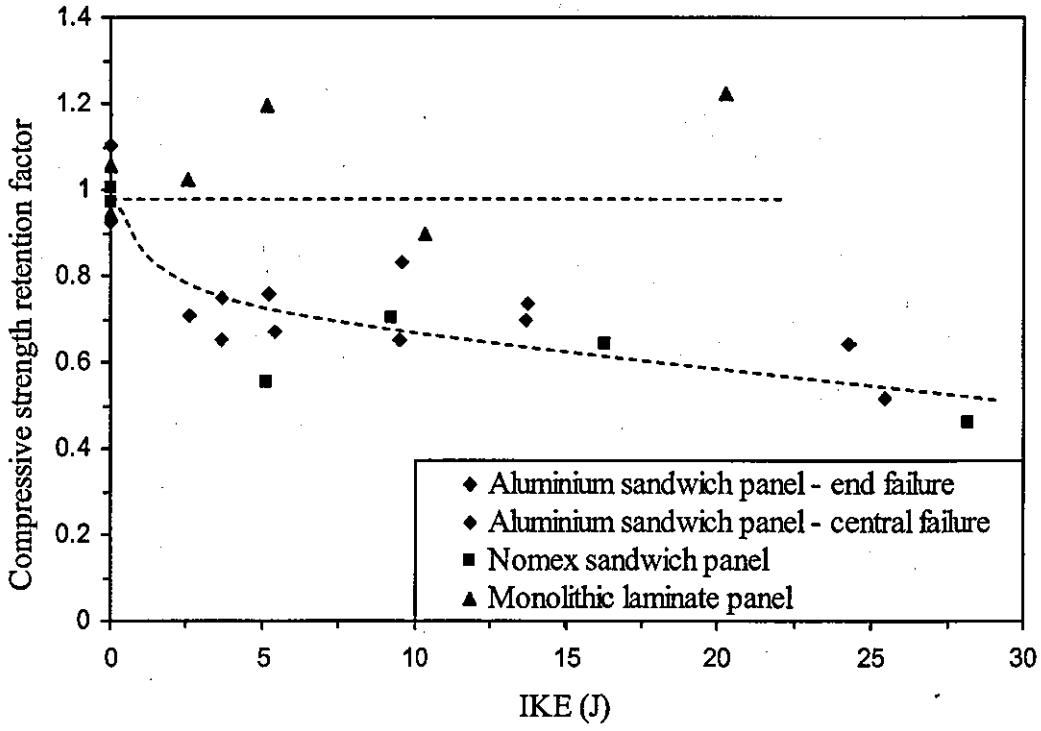
Compressive strength retention factor
1.4
1.2
1
0.8
0.6
0.4
0.2
0
0
5
10
15
20
25
30
IKE (J)
Aluminium sandwich panel - end failure
Aluminium sandwich panel - central failure
Nomex sandwich panel
Monolithic laminate panel

(a)

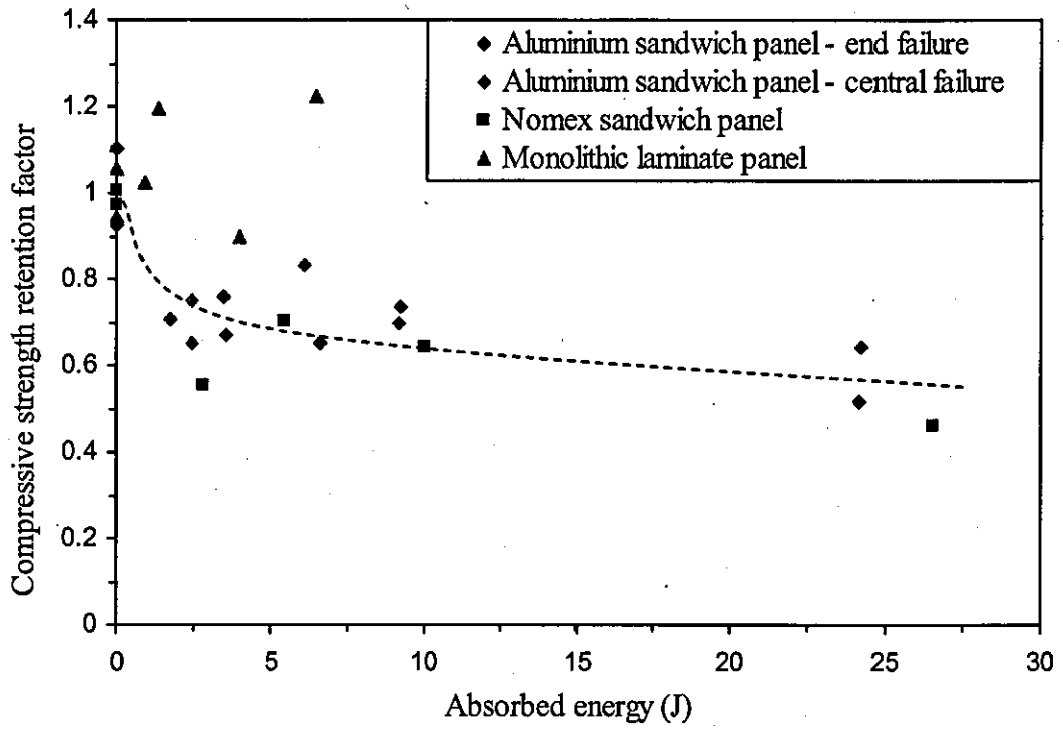
Compressive strength retention factor
1.4
1.2
1
0.8
0.6
0.4
0.2
0
0
5
10
15
20
25
30
Absorbed energy (J)
Aluminium sandwich panel - end failure
Aluminium sandwich panel - central failure
Nomex sandwich panel
Monolithic laminate panel

(b)

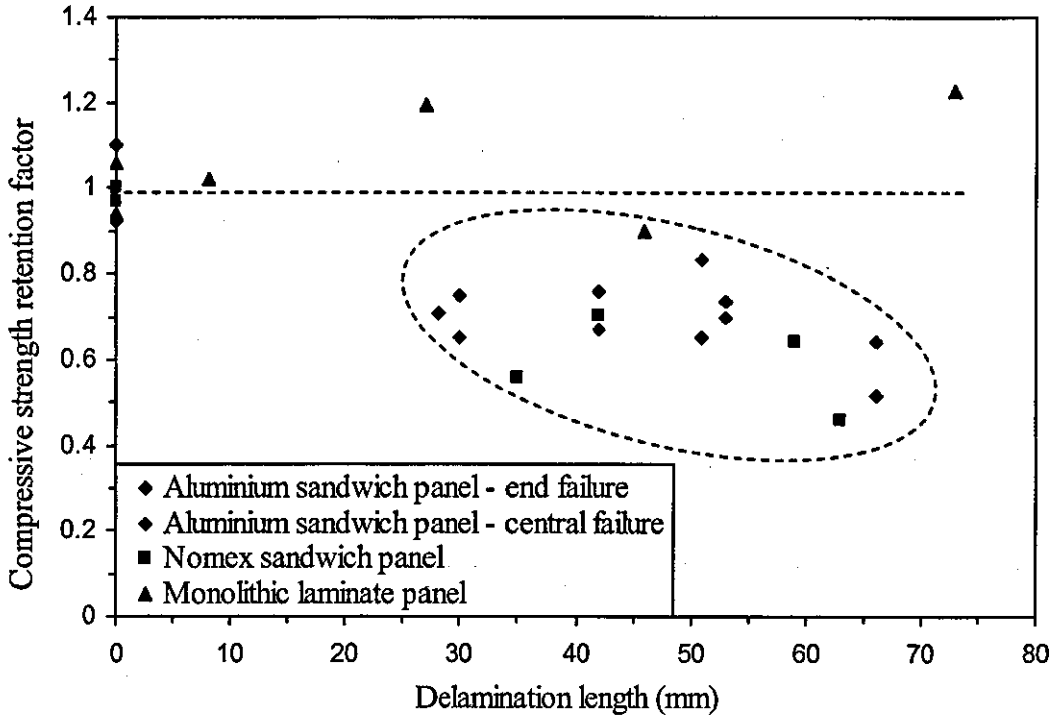

(c)

Figure 8.28 Damage tolerance maps for 8 ply 70kg/m^3 aluminium or 64kg/m^3 nomex sandwich panels and 16 ply monolithic panels based upon compressive strength retention factor (a) Impact energy (b) Absorbed energy (c) Delamination length

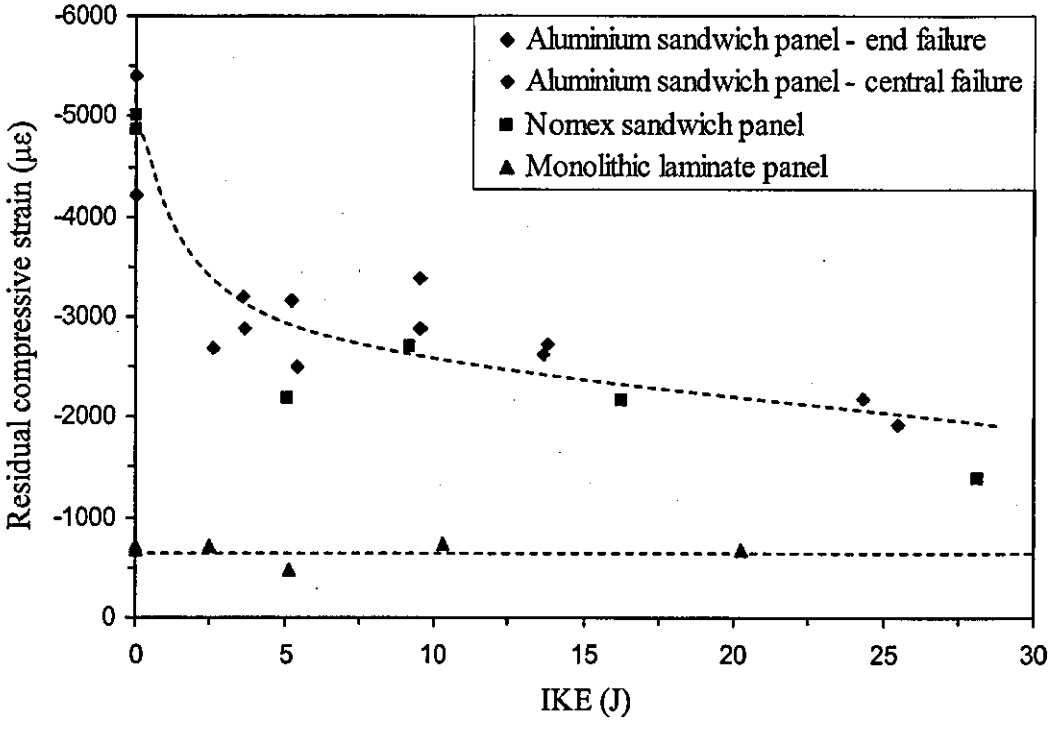

(a)

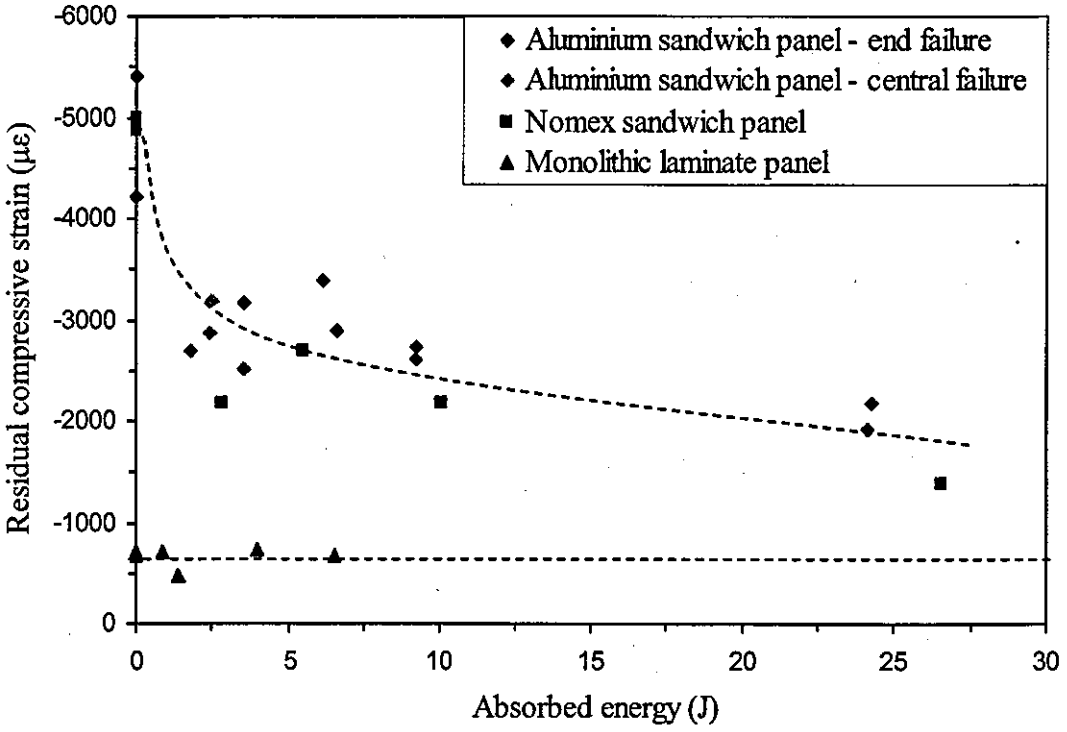

(b)

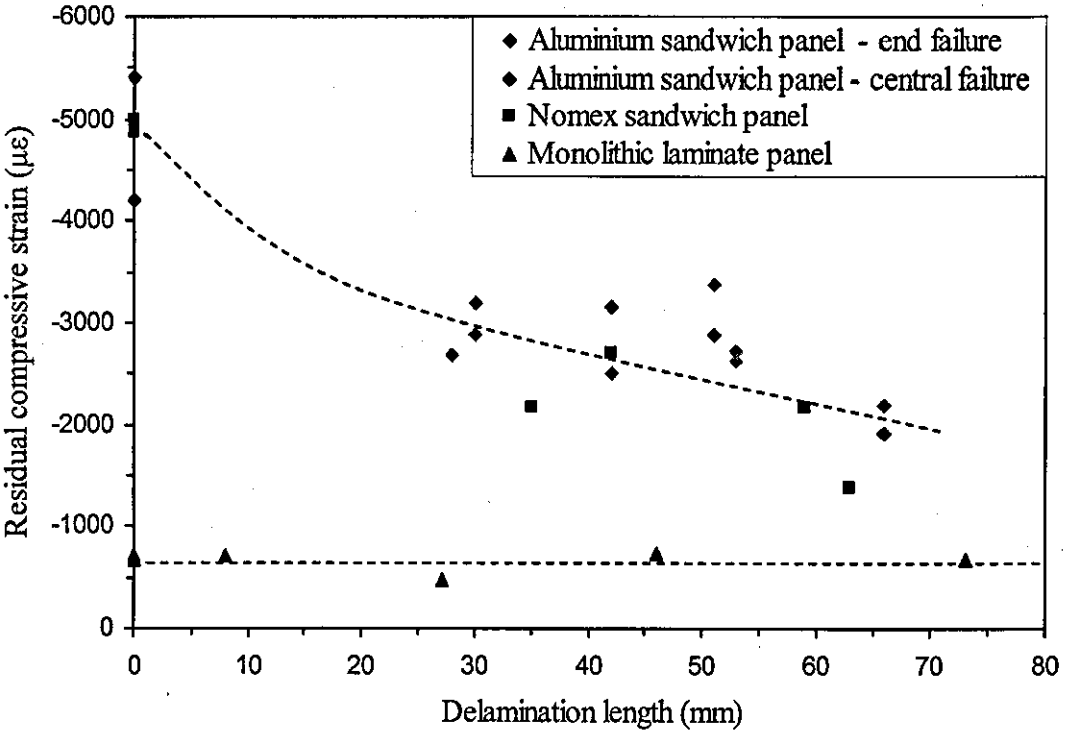

(c)

Figure 8.29 Damage tolerance maps for 8 ply 70kg/m^3 aluminium or 64kg/m^3 nomex sandwich panels and 16 ply monolithic panels based upon residual compressive strain (a) Impact energy (b) Absorbed energy (c) Delamination length

8.6. Concluding remarks

In-plane compression tests have been completed on both monolithic laminate panels and sandwich panels. Each specimen type has been assessed in terms of both residual compressive strength and strain response. The 16 ply laminate panels underwent local mode I buckling, which did not grow sufficiently to develop into mode II buckling. In-plane compressive failure of the panel close to the loaded end occurred prior to the initiation of mode II buckling, due to bending of the panel at the loaded end. The laminate panels show a high level of damage tolerance, indicated by the similar values of compressive strength for both damaged and undamaged specimens, even when the impact damage resulted in visible fibre damage on the back surface of the panel. This is believed to be due to a combination of the high number of 0° fibres providing the panel with a high flexural rigidity and the effective width of the panel not interacting with the impact damaged area.

The introduction of a honeycomb core separating the 16 ply panel into two 8 ply skins provides a high level of flexural support to the specimen. In the undamaged control panels mode II buckling was prevented from developing and panel failure was due to in-plane compressive failure of the skins below the epoxy end pots. In the impact damaged sandwich panels the majority of panels failed around the mid-section whilst the remaining few failed adjacent to the epoxy end pots. The core crushing caused by the impact was seen to propagate in the in-plane transverse direction in both the aluminium and nomex honeycomb specimens impacted at medium to high IKE levels. This resulted in dimpling of the impacted skin, which appeared to be more significant in the nomex panels, as shown by the bending strain response. Despite an amount of damage propagation occurring the cause of failure for the aluminium panels was compressive failure of the impact damaged skin. However, the nomex panels had compressive failure of both skins through panel shear failure. The critical factor in the change of failure mechanism was the low shear modulus and strength of the nomex honeycomb.

The inclusion of the honeycomb core also led to the compressive strength of an undamaged sandwich panel with 8 ply skins to be double that of an undamaged 16 ply laminate panel. A clear decrease in residual compressive strength was found in the damaged sandwich panels when compared to the undamaged sandwich panels. However, for impact energy levels less than required for fibre fracture of the top skin the residual compressive strength was approximately constant, with an average value of 210MPa for the aluminium panels. The nomex sandwich panels had a similar undamaged strength to the aluminium panels but a marginally lower average residual compressive strength of 185MPa for impact energy levels less than required for fibre fracture.

Therefore it can be concluded that just the presence of the core material provides critical support to the panel even though it does not directly support the in-plane load. Despite the impact damaged sandwich panel being asymmetric the local stabilising effect of the core opposes the de-stabilising effect of the impact damage. The mechanical properties of core material also appear to have a direct influence on the ability of the panel to resist local buckling and influence the manner in which compressive skin failure occurs. Consequently it is important that the core material is included in a theoretical model if an accurate model of the behaviour of an impact damaged sandwich panel is to be obtained.

Table 8.1 Summary of damage and failure loads of cross-sectioned T700/LTM45-EL monolithic laminate panels loaded under in-plane compression

Panel ID	IKE (J)	Level of damage in a panel impacted at a similar IKE and cross-sectioned in longitudinal (0°) direction		Test machine	Back-to-back SG's	RCS (kN)	RC strain (με)	Failure location	Internal delamination at impact location after compression in longitudinal (0°) direction (mm)
		Delamination (mm)	Fibre fracture						
16/CAI(0J)-1	0	-	No	Denison	Yes	40.88	-670.5	Top edge, fractured across panel width above SG1	-
16/CAI(0J)-2	0	-	No	Denison	Yes	36.60	-708.5	Top edge, fractured across panel width above SG1	-
16/CAI(2.5J)	2.5	8	No	Denison	Yes	41.03	-708.5	Top edge, fractured across panel width above SG1	17
16/CAI(5J)	5.2	27	No	Denison	Yes	48.59	-480.5	Top edge, fractured across panel width above SG1	25
16/CAI(10J)	10.4	46 (15th-16th plies)	No	Denison	Yes	35.92	-737.5	Top edge fractured above SG1 at left and right edges, delam./buckling spread under SG1	unavailable
16/CAI(20J)	20.3	73 (15th-16th plies)	Partial	Mand	Yes	49.25	-672.5	Top edge, fractured across panel width above SG1	65 (15th-16th plies)

Table 8.2 Summary of damage and failure loads of cross-sectioned T700/LTM45-EL honeycomb sandwich panels loaded under in-plane compression

Panel ID	IKE (J)	Level of damage in a panel impacted at a similar IKE and cross-sectioned in longitudinal (0°) direction			Test machine	Back-to-back SG's	RCS (kN)	RC strain (με)	Failure location	Damage at impact location after compression in longitudinal (0°) direction		Damage length at mid-section in transverse (90°) direction (mm)	Crushing pattern on outer edge of panel
		Delamination (mm)	Core crushing (mm)	Fibre fracture						Delamination (mm)	Core crushing (mm)		
8/70/CAI(0J)-1	0	-	-	-	Mand	No	-	-	No failure as machine reached limit prior to failure	0	0	0	Top edge: Back skin Mid-section: Front skin Bottom edge: Back skin
8/70/CAI(0J)-2	0	-	-	-	Denison	No	91.8	-4209.5	Top edge above SG1, both skins fractured across panel width	0	0	0	Top edge: Back skin Mid-section: Front skin Bottom edge: Front skin
8/70/CAI(0J)-3	0	-	-	-	Denison	Yes	111.6	-5406	Top edge above SG1, both skins fractured across panel width	0	0	0	Top edge: Back skin Mid-section: Middle Bottom edge: None

Panel ID	IKE (J)	Level of damage in a panel impacted at a similar IKE and cross-sectioned in longitudinal (0°) direction			Test machine	Back-to-back SG's	RCS (kN)	RC strain (με)	Failure location	Damage at impact location after compression in longitudinal (0°) direction		Damage length at mid-section in transverse (90°) direction (mm)	Crushing pattern on outer edge of panel
		Delamination (mm)	Core crushing (mm)	Fibre fracture						Delamination (mm)	Core crushing (mm)		
8/70/CAI(2.5J)	2.6	28	28	No	Mand	Yes	71.5	-2685.5	Mid-section, front skin fractured, central region no fracture but local buckling	29	31	Crushing across panel width and some front skin delam	Top edge: None Mid-section: Back skin Bottom edge: None
8/70/CAI(3J)-1	3.7	30	32	No	Denison	Yes	67.1	-2873	Mid-section, front skin fractured, central region no fracture but local buckling	unavailable	unavailable	unavailable	Top edge: Front skin Mid-section: Back skin Bottom edge: None
8/70/CAI(3J)-2	3.6	30	32	No	Denison	Yes	72.9	-3191.5	Mid-section, front skin fractured, central region no fracture but local buckling	42	33	Crushing and front skin delam across panel width	Top edge: Middle Mid-section: Back skin Bottom edge: Back skin
8/70/CAI(5J)-1	5.2	42	39	No	Denison	Yes	75.5	-3162.5	Bottom edge, both skins fractured across panel width	38	38	38	Top edge: Middle Mid-section: None Bottom edge: Front skin
8/70/CAI(5J)-2	5.4	42	39	No	Mand	Yes	67.6	-2510.5	Mid-section, front skin fractured, central region no fracture but local buckling	37	38	Front skin delam and crushing in centre with cell wall distortion to panel edge	Top edge: None Mid-section: Back skin Bottom edge: None
8/70/CAI(9J)-1	9.5	51	50	No	Mand	No	84.5	-3380.5	Mid-section, front skin entirely fractured Back skin fracture at outer edge with local buckling	53	62	Crushing and front and back skin delam across panel width with back skin debonding	Top edge: None Mid-section: Back skin Bottom edge: None
8/70/CAI(9J)-2	9.5	51	50	No	Denison	Yes	68.3	-2885	Top edge above SG1, both skins fractured across panel width	50	54	52	Top edge: Back skin Mid-section: Back skin Bottom edge: None
8/70/CAI(14J)-1	13.8	53	57	No	Mand	No	73.0	-2723	Mid-section, front skin fractured, central region no fracture but local buckling	54	70	Front skin delam and crushing in centre with cell wall distortion to panel edge	Top edge: None Mid-section: Back skin Bottom edge: None
8/70/CAI(14J)-2	13.7	53	57	No	Mand	Yes	71.5	-2618	Mid-section, front skin fractured, central region no fracture but local buckling	55	67	Front skin delam across panel width crushing at centre and edge, in between cell wall distortion	Top edge: None Mid-section: Back skin Bottom edge: None

Panel ID	IKE (J)	Level of damage in a panel impacted at a similar IKE and cross-sectioned in longitudinal (0°) direction			Test machine	Back-to-back SG's	RCS (kN)	RC strain (με)	Failure location	Damage at impact location after compression in longitudinal (0°) direction		Damage length at mid-section in transverse (90°) direction (mm)	Crushing pattern on outer edge of panel
		Delamination (mm)	Core crushing (mm)	Fibre fracture						Delamination (mm)	Core crushing (mm)		
8/70/CAI(25J)-1	24.3	66	74	Yes	Mand	No	63.2	-2188	Mid-section, front skin fractured, central region no fracture but local buckling	50	100	Crushing and front skin delam across panel width	Top edge: None Mid-section: Back skin Bottom edge: None
8/70/CAI(25J)-2	25.5	66	74	Yes	Denison	Yes	51.0	-1919	Top edge above SG1, both skins fractured across panel width. Bottom edge, back skin fractured at outer edges	67	85	72	Top edge: Front skin Mid-section: Back skin Bottom edge: Front skin
8/64/CAI(0J)-1	0	-	-	No	Denison	Yes	97.7	-5000	Top edge at SG1, both skins fractured across panel width, panel buckled forward	0	0	0	Top edge: Middle Mid-section: Back skin Bottom edge: Front skin
8/64/CAI(0J)-2	0	-	-	No	Denison	Yes	102.7	-4869	Top edge at SG1, both skins fractured across panel width, panel buckled backwards	0	0	0	Top edge: Back skin Mid-section: None Bottom edge: None
8/64/CAI(5J)	5.1	35	33	No	Denison	No	55.9	-2176	Mid-section, front skin fractured, central region no fracture	35	34	46mm but fracture point just above mid-section	Top edge: None Mid-section: Middle Bottom edge: None
8/64/CAI(9J)	9.2	42	38	No	Mand	Yes	71.6	-2699	Mid-section, front skin fractured, central region no fracture, back skin fractured at both edges	Front skin 60 Back skin 77	63	Front and back skin delam and core splitting across width	Top edge: None Mid-section: Middle Bottom edge: None
8/64/CAI(16J)	16.3	59	64	No	Mand	Yes	65.0	-2171	Mid-section, front and back skins fractured at left and right edges	Front skin 63 Back skin 50	93	Front and back skin delam and core splitting across width	Top edge: None Mid-section: Middle Bottom edge: None
8/64/CAI(28J)	28.2	63	100	Yes	Mand	Yes	46.5	-1389.5	Mid-section, front skin fractured at both edges, back skin fractured across panel width	Front skin 75 Back skin 10	102	Front and back skin delam and core crushing across width	Top edge: None Mid-section: Middle Bottom edge: None

9. CONCLUSIONS AND RECOMMENDATIONS

The impact damage resistance and damage tolerance of composite honeycomb sandwich panels has been studied experimentally. Sandwich panels consisting of carbon fibre skins and aluminium or nomex honeycomb were manufactured and tested. Material characterisation tests were carried out on both the laminate skin and honeycomb core materials. Damage resistance testing consisted of quasi static and impact loading in the through-the-thickness transverse direction whilst in-plane compressive loading was used to assess damage tolerance. The effect of both intrinsic and extrinsic variables on the sandwich panel performance was studied, with performance assessed in terms of damage mechanisms, strength, stiffness and energy absorption. Intrinsic variables considered included skin thickness, skin material, core material and core density. Under transverse loading the extrinsic variables studied were indenter nose-shape, panel size, support conditions and loading speed. A summary of the major findings is given below.

The damage resistance of composite sandwich panels has been assessed in terms of damage mechanisms, critical loads and energy absorption. Under transverse loading three critical damage levels were identified as; the initial damage threshold, signifying core failure and initiation of matrix cracks and minute delaminations; secondary damage through sudden propagation of delaminations within the top skin; and ultimate failure where top skin fibre fracture occurred and the indenter pierced through the top skin. These general failure mechanisms were applicable to all skin thicknesses and core densities. Skin thickness was found to be the most dominant intrinsic variable, controlling both the critical loads and energy absorption under transverse loading. Core density had a smaller effect on panel performance and both aluminium and nomex honeycomb cores were seen to respond in a similar manner. The elastic nature of the nomex honeycomb permitted larger amounts of global bending and consequently the level of energy absorbed in creating permanent damage was reduced by around 10%. The ability of the nomex to recover elastically also masked the presence of internal impact damage and the residual dents which have frequently been used to measure BVID in aluminium panels were not present.

Of the extrinsic variables indenter nose-shape had a dramatic effect on the critical loads and damage resistance of a sandwich panel, with the panels much more susceptible to damage when the loading area was concentrated as in the case of the HS indenter. The effect of the specimen size and support conditions was minimal and showed the local response to dominate the response of aluminium sandwich panels under concentrated transverse loads. This finding was reflected in the comparison of existing analytical models for transverse loading, which found the theories primarily based upon local indentation theories to be most accurate. However, the ability of these models to accurately predict the response of nomex panels was poor, most likely due to the elastic nature of the nomex material. The large effect of the indenter nose-shape on the panel response also highlighted the need for the contact conditions to be accurately represented in an analytical model, demonstrated by the models with questionable assumptions regarding hemispherical contact conditions often offering poorer estimates of panel response.

The effect of loading rate for impacts up to 8.5m/s was negligible for the epoxy resin systems used in this study, with the damage mechanisms witnessed for impact loading matching those identified for quasi-static loading. Prior to the occurrence of top skin fibre fracture absorbed energy was approximately 65% in the aluminium panels for all skin thicknesses, reducing to 55% for the nomex panels. Following fibre fracture the absorbed energy increased to just below 100% for both core types. The optimum design for sandwich panels in terms of damage resistance and strength was identified to be thick skin-high density core panels, as skin thickness dominated the panel strength. However, when weight was taken into consideration for a concentrated loading area thin skin-high density core panels performed equally well. For optimum energy absorption panels with a low density core generally had a higher amount of energy absorption per gram, as core crushing, the main source of energy absorption, became extensive.

Compression-after-impact testing was selected to assess damage tolerance as in-plane compressive loading represented the most critical loading scenario. The effect of the core material was studied by comparing the response of 16 ply monolithic laminate panels with 8 ply aluminium and nomex honeycomb sandwich panels. Even though the 16 ply laminate panels showed a high level of damage tolerance, the inclusion of a

honeycomb core led to the compressive strength of an undamaged sandwich panel with 8 ply skins to be double that of an undamaged 16 ply laminate panel. The presence of impact damage led to a clear decrease in the compressive strength of both aluminium and nomex sandwich panels; however, for impact energy levels less than required for top skin fibre fracture the residual compressive strength was approximately constant. Despite an amount of core crushing propagation in the sandwich panels impacted at medium to high IKE levels the cause of failure for all aluminium panels was compressive failure of the impact damaged skin; however, the nomex panels suffered compressive failure of both skins through panel shear failure. The low shear modulus and strength of the nomex honeycomb was identified as the critical factor in the change of failure mechanism, suggesting that the mechanical properties of core material have a direct influence on the ability of the panel to resist local buckling and affect the compressive failure mechanisms. Therefore it has been concluded that the core material provides critical support to the panel even though it does not directly support the in-plane load. Despite the impact damaged sandwich panel being asymmetric the local stabilising effect of the core opposed the de-stabilising effect of the impact damage.

As a result of this research a number of recommendations can be made for future work. In terms of damage resistance the effects of the majority of intrinsic and extrinsic variables have been reasonably well understood from the findings of this research combined with previous literature. One aspect that has not been considered previously is the effect of honeycomb cell size. As skin delamination length has been shown to be closely linked to the number of crushed cells increasing or decreasing the cell size for a given density may have a direct effect on the damage area under transverse loading.

The review of the existing analytical models for transverse loading has revealed a lack of simple closed form models for the prediction of critical loads and absorbed energy. Although a few of the models reviewed did give promising results, generally the models were restricted to the initial linear region and failed to provide accurate predictions for nomex sandwich panels. There is a definite need for a universal analytical model which can be applied to all panel types and various boundary conditions. To be of particular use the model should be able to be applied by composite engineers with only a basic knowledge of classical lamination theory and without finite element experience. This

will allow reasonably quick estimations of panel performance to be made at any stage of the design phase of a component.

In terms of understanding the damage tolerance of sandwich panels much work is still required to obtain a comprehensive understanding of the effects of both the intrinsic and extrinsic variables. Whilst this research has provided valuable information on the contribution of the core material it is still quite superficial. The next logical step is to test panels with a range of core thicknesses followed by studying in-depth the effect of core density and material type. Although it is intuitive that the skins are dominant in determining the in-plane compressive strength it has been shown that the core material plays a large role in stabilising the sandwich panel and controlling panel deformation. If larger core thicknesses can be used to obtain superior in-plane strength rather than thicker skins significant weight savings may be achieved.

Another issue directly relevant to in-plane compression is the size of the panels tested. As there are currently no standards for CAI of sandwich panels various panel sizes and support conditions have been used by previous researchers. The effect of specimen size is of particular interest and has received limited attention previously. To obtain true panel buckling responses larger panels may well be required for panels with thicker skins or stronger cores. Therefore the effect of panel size must be understood and scaling factors identified. If panel size is studied at Loughborough University in the future it is suggested that an adjustable in-plane compression support rig is developed, which can accommodate the various LVDTs for displacement measurement and permits the front and rear panel surfaces to be viewed during loading to monitor dimple propagation.

Finally as a long term objective the effect of environmental factors on the damage tolerance of composite sandwich panels should be investigated. Very limited information on hot-wet testing is available in the public domain despite its importance to in-service components. The ingress of water is known to have a detrimental effect on honeycomb sandwich panels in particular, which when combined with the hot and cold air temperatures regularly experienced by aerospace components could have significant consequences on the residual compressive strength.

REFERENCES

1. Bernard, ML and Lagace, PA, Impact resistance of composite sandwich plates, *Journal of Reinforced Plastics Composites,* 8, 432-445, 1989.
2. Herup, EJ and Palazotto, AN, Low-velocity impact damage initiation in graphite/epoxy/nomex honeycomb-sandwich plates, *Composites Science and Technology,* 57, 1581-1598, 1997.
3. Palm, TE, Impact resistance and residual compression strength of composite sandwich panels, *Proceedings of 8th International Conference on Composite Materials (ICCM/8), Honolulu, July 15-19,* 3-G-1-3-G-14, 1991.
4. Raju, KS and Tomblin, JS, Damage characteristics in sandwich panels subjected to static indentation using spherical indentors, *AIAA-2001-1189,* 103-111, 2001.
5. Tomblin, JS, Raju, KS, Liew, J and Smith, BL, Impact damage characterization and damage tolerance of composite sandwich airframe structures, *DOT/FAA/AR-00/44,* 1-181, 2001.
6. Tsotsis, TK and Lee, SM, Characterisation of localized failure modes in honeycomb sandwich panels using indentation, *Composite Materials: Testing and Design,* 12, 139-165, 1996.
7. Wen, HM, Reddy, TY, Reid, SR and Soden, PD, Indentation, penetration and perforation of composite laminates and sandwich panels under quasi-static and projectile loading, *Key Engineering Materials,* 141 - 143, 501-552, 1998.
8. Williamson, JE and Lagace, PA, Response mechanisms in the impact of graphite/epoxy honeycomb sandwich panels, Proceedings of the American Society for Composites, 8th Technical Conference, Cleveland 1993, 287-297, 1994.
9. Abrate, S, Localized impact on sandwich structures with laminated facings, Applied Mechanics Review, 50(2), 69-82, 1997.
10. Allen, HG, Analysis and Design of Structural Sandwich Panels, Pergamon Press, Oxford, 1969.
11. Bull, PH, Damage tolerance and residual strength of composite sandwich structures, *PhD thesis, Royal Institute of Technology, Sweden,* 2004.
12. Kepler, J, Impact penetration of sandwich panels at different velocities - an experimental parameter study: part II - interpretation of results and modelling, *Journal of sandwich structures and materials,* 6, 379-397, 2004.
13. Mines, RAW, Worrall, CM and Gibson, AG, Low velocity perforation behaviour of polymer composite sandwich panels, *International Journal of Impact Engineering,* 21(10), 855-879, 1998.
14. Petras, A and Sutcliffe, MPF, Failure mode maps for honeycomb sandwich panels, *Composite Structures,* 44(4), 237-252, 1999.
15. Triantafillou, TC and Gibson, LJ, Failure mode maps for foam core sandwich beams, *Materials Science and Engineering,* 95, 37-53, 1987.
16. Zhou, G, Hill, M, Loughlan, J and Hookham, N, Damage characteristics of composite honeycomb sandwich panels in bending under quasi-static loading, *Journal of Sandwich Structures and Materials,* 8, 55-90, 2006.
17. Davies, P, Choqueuse, D, Verniolle, P, Prevosto, M, Genin, D and Hamelin, P, Impact behaviour of composite sandwich panels, *Impact and Dynamic Fracture of Polymers and Composites, ESIS,* 19, 341-358, 1995.
18. Rizov, V, Shipsha, A and Zenkert, D, Indentation study of foam core sandwich composite panels, *Composite Structures,* 69, 95-102, 2005.

19. Zhou, G, Hill, M and Hookham, N, Investigation of parameters governing the damage and energy absorption characteristics of honeycomb sandwich panels, *Journal of Sandwich Structures and Materials,* 9(4), 309-342, 2007.
20. Aymerich, F, Priolo, P and Vacca, D, Impact damage of foam core graphite/epoxy sandwich panels, *Proceedings of ECCM-8,* 1, 615-622, 1998.
21. Kepler, J, Impact penetration of sandwich panels at different velocities - an experimental parameter study: Part I - parameters and results, *Journal of Sandwich Structures and Materials,* 6, 357-374, 2004.
22. Kim, CG and Jun, EJ, Impact resistance of composite laminated sandwich plates, *Journal of Composite Materials,* 26(15), 2247-2261, 1992.
23. Hull, D and Shi, YB, Damage mechanism characterization in composite damage tolerance investigations, *Composite Structures,* 23, 99-120, 1993.
24. Tomblin, J, Lacy, T, Smith, B, Hooper, S, Vizzini, A and Lee, S, Review of damage tolerance for composite sandwich airframe structures, *FAA Report, Number DOT/FAA/AR-99/49,* 1-71, 1999.
25. Kassapoglou, C, Compression strength of composite sandwich structures after barely visible impact damage, *Journal of composites technology and research,* 18(4), 274-284, 1996.
26. Moody, RC, Harris, JS and Vizzini, AJ, Scaling and curvature effects on the damage tolerance of impacted composite sandwich panels, *Journal of Sandwich Structures and Materials,* 4, 71-82, 2002.
27. McGowan, DM and Ambur, DR, Damage characteristics and residual strength of composite sandwich panels impacted with and without a compression loading, *AIAA-98-1783,* 713-723, 1998.
28. McGowan, DM and Ambur, DR, Compression response of a sandwich keel panel with and without damage, *NASA TM 110302,* 1-33, 1997.
29. McGowan, DM and Ambur, DR, Damage tolerance characteristics of composite fuselage sandwich structures with thick facesheets, *NASA Technical Memorandum 110303,* 1997.
30. Cvitkovich, MK and Jackson, WC, Compressive failure mechanisms in composite sandwich structures, *Journal of the American Helicopter Society,* 44(4), 260-268, 1999.
31. Levin, K, Damage tolerance of carbon fibre reinforced plastic sandwich panels, *Proceedings of 3rd European Conference on Composite Materials, Bordeaux, France, March 20-23,* 509-514, 1989.
32. Lacy, TE, Samarah, IK and Tomblin, JS, Damage resistance characterisation of sandwich composites using response surfaces, *DOT/FAA/AR-01/71,* 1-67, 2002.
33. Gottesman, T, Bass, M and Samuel, A, Criticality of impact damage in composite sandwich structures, *Proceedings of 6th International Conference on Composite Materials and Second European Conference on Composite Materials, London, England,* 3, 3.27-3.35, 1987.
34. Rhodes, MD, Impact fracture of composite sandwich structures, *AIAA/ASME/SAE 16th Structures, Structural Dynamics, and Materials Conference, Denver, Colorado, May 27-29,* 1975.
35. Auerkari, P, Pankakoski, PH and Kauppinen, P, Effect of impact face damage on the strength of sandwich composites, *Impact and Dynamic Fracture of Polymers and Composites. ESIS,* 19, 423-431, 1995.
36. Shipsha, A and Zenkert, D, Compression-after-impact strength of sandwich panels with core crushing damage, *Applied Composite Materials,* 12, 149-164, 2005.

37. Roach, AM, Evans, KE and Jones, N, Penetration energy of sandwich panel elements under static and dynamic loading. Part I, *Composite Structures,* 42(2), 119-134, 1998.
38. Roach, AM, Jones, N and Evans, KE, Penetration energy of sandwich panel elements under static and dynamic loading. Part II, *Composite Structures,* 42(2), 135-152, 1998.
39. Shih, WK and Jang, BZ, Instrumented impact testing of composite sandwich panels, *Journal of Reinforced Plastics and Composites,* 8, 270-298, 1989.
40. Gustin, J, Joneson, A, Mahinfalah, M and Stone, J, Low velocity impact of combination kevlar/carbon fiber sandwich composites, *Composite Structures,* 69, 396-406, 2005.
41. Kiratisaevee, H and Cantwell, WJ, Low-velocity impact response of high-performance aluminium foam sandwich structures, *Journal of Reinforced Plastics and Composites,* 24(10), 1057-1072, 2005.
42. Nettles, AT and Hodge, AJ, Impact testing of glass/phenolic honeycomb panels with graphite/epoxy facesheets, *35th International SAMPE Symposium,* 35(2), 1430-1440, 1990.
43. Hiel, C and Ishai, O, Design of highly damage-tolerant sandwich panels, *37th International SAMPE Symposium, March 9-12,* 37, 1228-1242, 1992.
44. Ambur, DR and Cruz, J, Low-speed impact response characteristics of composite sandwich panels, *Structures Structural Dynamics and Materials Conference Collection of Technical Papers AIAA/ASME/ASCE/AHS/ASC,* 4, 2681-2689, 1995.
45. Anderson, T and Madenci, E, Experimental investigation of low-velocity impact characteristics of sandwich composites, *Composite Structures,* 50, 239-247, 2000.
46. Aviles, F and Carlsson, LA, Three-dimensional finite element buckling analysis of debonded sandwich panels, *Journal of Composite Materials,* 40(11), 993-1008, 2006.
47. Boyle, MP, Roberts, JC, Wienhold, PD, Bao, G and White, GJ, Experimental, numerical, and analytical results for buckling and post-buckling of orthotropic rectangular sandwich panels, *Composite Structures,* 52(3-4), 375-380, 2001.
48. Shyr, TW and Pan, YH, Low velocity impact response of hollow core sandwich laminates and interply hybrid laminate, *Composite Structures,* 64, 189-198, 2004.
49. Vaidya, UK, Hosur, MV, Earl, D and Jeelani, S, Impact response of integrated hollow core sandwich composite panels, *Composites - Part A: Applied Science and Manufacturing,* 31(8), 761-772, 2000.
50. van Vuure, AW, Ivens, JA and Verpoest, I, Mechanical properties of composite panels based on woven sandwich-fabric preforms, *Composites - Part A: Applied Science and Manufacturing,* 31(7), 671-680, 2000.
51. Christopherson, J, Mahinfalah, M, Nakhaie Jazar, G and Rastgaar Aagaah, M, An investigation on the effect of a small mass impact on sandwich composite plates, *Composite Structures,* 67, 299-306, 2005.
52. Erickson, MD, Kallmeyer, AR and Kellogg, KG, Effect of temperature on the low-velocity impact behaviour of composite sandwich panels, *Journal of Sandwich Structures and Materials,* 7, 245-264, 2005.
53. Freeman, B, Schwingler, E, Mahinfalah, M and Kellogg, K, The effect of low-velocity impact on the fatigue life of sandwich composites, *Composite Structures,* 70, 374-381, 2005.
54. Gustin, J, Mahinfalah, M, Nakhaie Jazar, G and Aagaah, MR, Low-velocity impact of sandwich composite plates, *Experimental Mechanics,* 44(6), 574-583, 2004.
55. Vaidya, UK, Kamath, MV, Mahabaleswara, KS and Jeelani, S, Low velocity impact response of resin infusion molded foam filled honeycomb sandwich composites, *Journal of Reinforced Plastics and Composites,* 17(9), 819-849, 1998.

56. Vaidya, UK, Ulven, C, Pillay, S and Ricks, H, Impact damage of partially foam-filled co-injected honeycomb core sandwich composites, *Journal of Composite Materials,* 37(7), 611-626, 2003.
57. Palazotto, AN, Gummadi, LNB, Vaidya, UK and Herup, EJ, Low velocity impact damage characteristics of Z-fiber reinforced sandwich panels - an experimental study, *Composite Structures,* 43(4), 275-288, 1998.
58. Torre, L and Kenny, JM, Impact testing and simulation of composite sandwich structures for civil transportation, *Composite Structures,* 50(3), 257-267, 2000.
59. Vaidya, UK, Palazotto, AN and Gummadi, LNB, Low velocity impact and compression after impact response of z-pin reinforced core sandwich composites, *Journal of Engineering Materials and Technology,* 122, 434-442, 2000.
60. Akay, M and Hanna, R, A comparison of honeycomb-core and foam-core carbon-fibre/epoxy sandwich panels, *Composites,* 21(4), 325-331, 1990.
61. Wong, R and Abbott, R, Durability and damage tolerance of graphite/epoxy honeycomb structures, *Proceedings 35th International SAMPE Symposium, Society for the Advancement of Materials and Process Engineering, Anaheim, CA, April 2-5,* 35(1), 366-380, 1990.
62. Nguyen, MQ, Jacombs, SS, Thomson, RS, Hachenberg, D and Scott, ML, Simulation of impact on sandwich structures, *Composite Structures,* 67, 217-227, 2005.
63. Caldwell, MS, Borris, PW and Falabella, R, Impact damage tolerance testing of bonded sandwich panels, *Proceedings of the 22nd International SAMPE Technical Conference, November 6-8,* 509-520, 1990.
64. Gibson, LJ and Ashby, MF, *Cellular Solids: Structure and Properties,* Cambridge University Press, 1999.
65. Goldsmith, W and Sackman, JL, An experimental study of energy absorption in impact on sandwich plates, *International Journal of Impact Engineering,* 12(2), 241-262, 1992.
66. Wierzbicki, T, Crushing analysis of metal honeycombs, *International Journal of Impact Engineering,* 1(2), 157-174, 1983.
67. Becker, W, Closed-form analysis of the thickness effect of regular honeycomb core material, *Composite Structures,* 48, 67-70, 2000.
68. Mohr, D and Doyoyo, M, Deformation-induced folding systems in thin-walled monolithic hexagonal metallic honeycomb, *International Journal of Solids and Structures,* 41, 3353-3377, 2004.
69. Mohr, D and Doyoyo, M, Experimental investigation on the plasticity of hexagonal aluminium honeycomb under multiaxial loading, *Journal of Applied Mechanics,* 71, 375-385, 2004.
70. Mohr, D and Doyoyo, M, Large plastic deformation of metallic honeycomb: orthotropic rate-independent constitutive model, *International Journal of Solids and Structures,* 41, 4435-4456, 2004.
71. Mohr, D and Wierzbicki, T, Crushing of soft-core sandwich profiles: experiments and analysis, *International Journal of Mechanical Sciences,* 45, 253-271, 2003.
72. Goswami, S and Becker, W, The effect of facesheet/core delamination in sandwich structures under transverse loading, *Composite Structures,* 54, 515-521, 2001.
73. Wierzbicki, T, de Lacruz Alverez, A. and Hoo Fatt, MS, Impact energy absorption of sandwich plates with crushable core, *AMD-Vol. 205, Impact, Waves and Fracture ASME,* 205, 391-411, 1995.
74. Hazizan, MA and Cantwell, WJ, The low velocity impact response of an aluminium honeycomb sandwich structure, *Composites Part B: Engineering,* 34, 679-687, 2003.

75. Chen, A and Davalos, JF, A solution including skin effect for stiffness and stress field of sandwich honeycomb core, *International Journal of Solids and Structures,* 42, 2711-2739, 2005.
76. Wu, E and Jiang, W-, Axial crush of metallic honeycombs, *International Journal of Impact Engineering,* 19(5-6), 439-456, 1997.
77. Tomblin, JS, Raju, KS and Arosteguy, G, Damage resistance and tolerance of composite sandwich panels - scaling effects, *DOT/FAA/AR-03/75,* 1-70, 2004.
78. Lagace, PA, Williamson, JE and Tsang, PHW, A preliminary proposition for a test method to measure (impact) damage resistance, *Journal of Reinforced Plastics and Composites,* 12, 584-601, 1993.
79. Hoo Fatt, MS and Park, KS, Dynamic models for low-velocity impact damage of composites sandwich panels - Part A: Deformation, *Composite Structures,* 52(3-4), 335-351, 2001.
80. Hoo Fatt, MS and Park, KS, Dynamic models for low-velocity impact damage of composite sandwich panels - Part B: Damage initiation, *Composite Structures,* 52(3-4), 353-364, 2001.
81. Zenkert, D, Shipsha, A, Bull, P and Hayman, B, Damage tolerance assessment of composite sandwich panels with localised damage, *Composites Science and Technology,* 65, 2597-2611, 2005.
82. Horrigan, DPW, Aitken, RR and Moltschaniwskyj, G, Modelling of crushing due to impact in honeycomb sandwiches, *Journal of Sandwich Structures and Materials,* 2, 131-151, 2000.
83. Chen, CH, Chen, MY and Chen, JP, The residual shear strength and compressive strength of C/E composite sandwich structure after low velocity impact, *36th International SAMPE Symposium,* 36(1), 932-943, 1991.
84. Meo, M, Vignjevic, R and Marengo, G, The response of honeycomb sandwich panels under low-velocity impact loading, *International Journal of Mechanical Sciences,* 47, 1301-1325, 2005.
85. Sburlati, R, The effect of a slow impact on sandwich plates, *Journal of Composite Materials,* 36(9), 1079-1092, 2002.
86. Ferri, R and Sankar, BV, Comparative study on the impact resistance of composite laminates and sandwich panels, *Journal of Thermoplastic Composite Materials,* 10(4), 304-315, 1997.
87. Zhao, H and Gary, G, Crushing behaviour of aluminium honeycombs under impact loading, *International Journal of Impact Engineering,* 21(10), 827-836, 1998.
88. Yamashita, M and Gotoh, M, Impact behavior of honeycomb structures with various cell specifications - numerical simulation and experiment, *International Journal of Impact Engineering,* 32, 618-630, 2005.
89. Tomblin, JS, Raju, KS, Liew, J and Smith, BL, Impact damage characterization and damage tolerance of composite sandwich airframe structures - Phase II, *DOT/FAA/AR-02/80,* 1-87, 2002.
90. Tsang, PHW and Lagace, PA, Failure mechanisms of impact-damaged sandwich panels under uniaxial compression, *AIAA-94-1396-CP,* 745-754, 1994.
91. Shyprykevich, P, Tomblin, J, Ilcewicz, L, Vizzini, AJ, Lacy, TE and Hwang, Y, Guidelines for analysis, testing, and nondestructive inspection of impact-damaged composite sandwich structures, *NASA Report,* DOT/FAA/AR-02/121, 1-94, 2003.
92. Hallstrom, S, Shipsha, A and Zenkert, D, Failure of impact damaged foam core sandwich beams, *AD-Vol. 62/AMD-Vol. 245, Mechanics of Sandwich Structures ASME,* 11-19, 2000.

93. Shipsha, A, Hallstrom, S and Zenkert, D, Failure mechanisms and modelling of impact damage in sandwich beams - a 2D approach: part I - experimental investigation, *Journal of Sandwich Structures and Materials,* 5, 7-31, 2003.
94. Shipsha, A, Hallstrom, S and Zenkert, D, Failure mechanisms and modelling of impact damage in sandwich beams - a 2D approach: part II - analysis and modelling, *Journal of Sandwich Structures and Materials,* 5, 33-51, 2003.
95. Mouritz, AP and Thomson, RS, Compression, flexure and shear properties of a sandwich composite containing defects, *Composite Structures,* 44, 263-278, 1999.
96. Gower, MRL and Sims, GD, Damage tolerance testing of composites: a standard procedure for the introduction of impact damage, *NPL Report CMMT(C) 39,* 1998.
97. Anon., Recommended test method for compression after impact properties of oriented fiber-resin composites, *SACMA, SRM 2-88,*
98. Anon., Standard tests for toughened resin composites, *NASA reference publication 1092,* 1983.
99. Anon., Standard test method for edgewise compressive strength of sandwich constructions, *ASTM C364-94,* 1995.
100. Rivera, LA, In-plane compression of preconditioned carbon/epoxy panels, *PhD thesis, Loughborough University,* 2004.
101. Zhou, G and Rivera, LA, Investigation for the reduction of in-plane compressive strength in preconditioned thin composite panels, *Journal of Composite Materials,* 39(5), 391-422, 2005.
102. Zhou, G and Rivera, LA, Investigation for the reduction of in-plane compressive strength in preconditioned thick composite panels, *Journal of Composite Materials,* 41(16), 1961-1994, 2007.
103. Anon., Standard test method for compressive residual strength properties of damaged polymer matrix composite plates, *ASTM D7137-05,* 2005.
104. Fleck, NA and Sridhar, I, End compression of sandwich columns, *Composites - Part A: Applied Science and Manufacturing,* 33, 353-359, 2002.
105. Mamalis, AG, Manolakos, DE, Ioannidis, MB and Papapostolou, DP, On the crushing response of composite sandwich panels subjected to edgewise compression: experimental, *Composite Structures,* 71, 246-257, 2005.
106. Mouring, SE, Barton, O and Joyce, PJ, Mechanical behaviour of composite sandwich structures subjected to impact damage, *Internet.*
107. Vadakke, V and Carlsson, LA, Experimental investigation of compression failure of sandwich specimens with face/core debond, *Composites Part B: Engineering,* 35, 583-590, 2004.
108. Lagace, PA and Mamorini, L, Factors in the compressive strength of composite sandwich panels with thin facesheets, *Journal of Sandwich Structures and Materials,* 2, 315-330, 2000.
109. Schubel, PM, Luo, JJ and Daniel, IM, Impact and post impact behavior of composite sandwich panels, *Composites Part A: Applied Science and Manufacturing,* 38, 1051-1057, 2007.
110. Kassapoglou, C, Jonas, PJ and Abbott, R, Compressive strength of composite sandwich panels after impact damage: an experimental and analytical study, *Journal of Composites Technology and Research,* 10, 65-73, 1988.
111. Frostig, Y, Classical and high-order computational models in the analysis of modern sandwich panels, *Composites Part B: Engineering,* 34(1), 83-100, 2003.

112. Raju, BB, Lui, D and Dang, X, Thickness effects on impact response of composite laminates, *Proceedings of the 13th Annual Technical Conference on Composite Materials September 21-23, 1998 Baltimore, Maryland,* 1998.
113. Roberts, JC, Boyle, MP, Wienhold, PD and White, GJ, Buckling, collapse and failure analysis of FRP sandwich panels, *Composites Part B:Engineering,* 33(4), 315-324, 2002.
114. Aviles, F and Carlsson, LA, Experimental study of debonded sandwich panels under compressive loading, *Journal of Sandwich Structures and Materials,* 8, 7-31, 2006.
115. Davies, GAO, Hitchings, D, Besant, T, Clarke, A and Morgan, C, Compression after impact strength of composite sandwich panels, *Composite structures,* 63(1), 1-9, 2004.
116. Walker, S, Evaluation of composite honeycomb sandwich panels under compressive loads at elevated temperatures, *NASA / TP-1998-207645,* 1-24, 1998.
117. Turner, KM and Vizzini, AJ, Response of impacted sandwich panels with integral stiffeners, *Journal of Sandwich Structures and Materials,* 6, 313-326, 2004.
118. MacDonald, CD and Vizzini, AJ, Response of indented sandwich panels, *Journal of Thermoplastic Composite Materials,* 15, 33-41, 2002.
119. Nokkentved, A, Lundsgaard-Larsen, C and Berggreen, C, Non-uniform compressive strength of debonded sandwich panels - I. Experimental investigation, *Journal of Sandwich Structures and Materials,* 7, 461-482, 2005.
120. Glinecki, GV, Kodali, SP and Curley, RC, The effect of defects on the strength of composite sandwich assemblies, *Proceedings of the 27th National SAMPE Symposium, May 4-6,* 509-518, 1982.
121. Sankar, BV and Narayanan, M, Finite element analysis of debonded sandwich beams under axial compression, *Journal of Sandwich Structures and Materials,* 3, 197-219, 2001.
122. Thomson, RS and Mouritz, AP, Skin wrinkling of impact damaged sandwich composite, *Journal of Sandwich Structures and Materials,* 1, 299-322, 1999.
123. Vadakke, V and Carlsson, LA, Experimental investigation of compression failure mechanisms of composite faced foam core sandwich specimens, *Journal of Sandwich Structures and Materials,* 6, 327-342, 2004.
124. Paik, JK, Thayamballi, AK and Kim, GS, The strength characteristics of aluminium honeycomb sandwich panels, *Thin-Walled Structures,* 35, 205-231, 1999.
125. Soutis, C and Spearing, SM, Compressive response of notched, woven fabric, face sheet honeycomb sandwich panels, *Plastics, Rubber and Composites,* 31(9), 392-397, 2002.
126. Toribio, MG and Spearing, SM, Compressive response of notched glass-fiber epoxy/honeycomb sandwich panels, *Composites - Part A: Applied Science and Manufacturing,* 32(6), 859-870, 2001.
127. Zenkert, D, *An Introduction to Sandwich Construction,* EMAS Publishing, UK, 1997.
128. Fagerberg, L, Wrinkling and compression failure transition in sandwich panels, *Journal of Sandwich Structures and Materials,* 6, 129-144, 2004.
129. Thomsen, OT and Banks, WM, An improved model for the prediction of intra-cell buckling in CFRP sandwich panels under in-plane compressive loading, *Composite Structures,* 65, 259-268, 2004.
130. Wadee, MA, Experimental evaluation of interactive buckle localization in compression sandwich panels, *Journal of Sandwich Structures and Materials,* 1, 230-254, 1999.
131. Edgren, F, Asp, LE and Bull, PH, Compressive failure of impacted NCF composite sandwich panels - characterisation of the failure process, *Journal of Composite Materials,* 38(6), 495-514, 2004.

132. Bull, PH and Edgren, F, Compressive strength after impact of CFRP-foam core sandwich panels in marine applications, *Composites Part B: Engineering,* 35, 535-541, 2004.
133. Bull, PH and Hallstrom, S, High-velocity and quasi-static impact of large sandwich panels, *Journal of Sandwich Structures and Materials,* 6, 97-113, 2004.
134. Mahfuz, H, Islam, S, Saha, M, Carlsson, L and Jeelani, S, Buckling of sandwich composites; effects of core-skin debonding and core density, *Applied Composite Materials,* 12, 73-91, 2005.
135. Greenhalgh, E and Singh, S, Investigation of the failure mechanisms for delamination growth from embedded defects, *ICCM 12, Paris, France,* 1999.
136. Kassapoglou, C, Buckling, post-buckling and failure of elliptical delaminations in laminates under compression, *Composite Structures,* 9, 139-159, 1988.
137. Peck, SO and Springer, GS, The behaviour of delaminations in composite plates - analytical and experimental results, *Journal of Composite Materials,* 1991, 907-929, 25.
138. Lacy, TE, Samarah, IK and Tomblin, JS, Damage tolerance characterization of sandwich composites using response surfaces, *DOT/FAA/AR-02/101,* 1-40, 2002.
139. Lloyd, JC, Impact damage and damage tolerance of fibre reinforced advanced composite laminate structures, *PhD thesis, Loughborough University,* 2002.
140. Anon., Standard test method for tensile properties of polymer matrix composite materials, *ASTM D3039/D3039M-95,* 1995.
141. Anon., Standard test method for compressive properties of polymer matrix composite materials with unsupported gage section by shear loading, *ASTM D3410/D3410M-94,* 1994.
142. Anon., Standard test methods for flexural properties of unreinforced and reinforced plastics and electrical insulating materials, *ASTM D790-99,* 2000.
143. Anon., Standard test method for in-plane shear response of polymer matrix composite materials by tensile test of a ±45° laminate, *ASTM D3518/D3518M 94,* 1995.
144. Anon., Standard test method for apparent interlaminar shear strength of parallel fibre composites by short-beam method, *ASTM D2344-84,* 1984.
145. Zhou, G and Davies, GAO, Characterisation of thick woven roving/polyester laminates: tension, compression and shear, *Composites,* 26, 579-586, 1995.
146. Whitney, JM and Browning, CE, On short-beam shear tests for composite materials, *Experimental Mechanics,* 25, 294-300, 1985.
147. Anon., Standard test method for flatwise compressive properties of sandwich cores, *ASTM C365-94,* 1995.
148. Wu, CL and Sun, CT, Low velocity impact damage in composite sandwich beams, *Composite Structures,* 34, 21-27, 1996.
149. Bitzer, T, *Honeycomb Technology,* Chapman and Hall Publishers, 1997.
150. Noor, AK, Burton, WS and Bert, CW, Computational models for sandwich panels and shells, *Applied Mechanics Review,* 49(3), 155-198, 1996.
151. Carrera, E and Ciuffreda, A, Bending of composites and sandwich plates subjected to localized lateral loadings: a comparison of various theories, *Composite Structures,* 68, 185-202, 2005.
152. Carrera, E and Ciuffreda, A, A unified formulation to assess theories of multilayered plates for various bending problems, *Composite Structures,* 69, 271-293, 2005.
153. Meyer-Piening, H-, Application of the elasticity solution to linear sandwich beam, plate and shell analyses, *Journal of Sandwich Structures and Materials,* 6, 295-312, 2004.
154. Anderson, T and Madenci, E, Graphite/epoxy foam sandwich panels under quasi-static indentation, *Engineering Fracture Mechanics,* 67, 329-344, 2000.

155. Apetre, NA, Sankar, BV and Ambur, DR, Low-velocity impact response of sandwich beams with functionally graded core, *International Journal of Solids and Structures,* 43, 2479-2496, 2006.
156. Pagano, NJ, Exact solutions for rectangular bidirectional composites and sandwich plates, *Journal of Composite Materials,* 4, 20-34, 1970.
157. Barut, A, Madenci, E, Anderson, T and Tessler, A, Equivalent single-layer theory for a complete stress field in sandwich panels under arbitrarily distributed loading, *Composite Structures,* 58(4), 483-495, 2002.
158. Kim, JS and Cho, M, Enhanced first-order shear deformation theory for laminated and sandwich plates, *Journal of Applied Mechanics,* 72, 809-817, 2005.
159. Kim, JS and Cho, M, Enhanced modeling of laminated and sandwich plates via strain energy transformation, *Composite Science and Technology,* 66, 1575-1587, 2006.
160. Nguyen, VT, Caron, JF and Sab, K, A model for thick laminates and sandwich plates, *Composites Science and Technology,* 65, 475-489, 2005.
161. Swaminathan, K, Patil, MS, Nataraja, MS and Mahabaleswara, KS, Bending of sandwich plates with anti-symmetric angle-ply face sheets - analytical evaluation of higher order refined computational models, *Composite Structures,* 75, 114-120, 2006.
162. Swanson, SR, Response of orthotropic sandwich plates to concentrated loading, *Journal of Sandwich Structures and Materials,* 2, 270 287, 2000.
163. Whitney, JM, Stress analysis of thick laminated composite and sandwich plates, *Journal of Composite Materials,* 6, 426-440, 1972.
164. Frostig, Y and Baruch, M, Localized load effects in high-order bending of sandwich panels, *Journal of Engineering Mechanics,* 122(11), 1069-1076, 1996.
165. Frostig, Y, Thomsen, OT and Sheinman, I, On the non-linear high-order theory of unidirectional sandwich panels with a transversely flexible core, *International Journal of Solids and Structures,* 42, 1443-1463, 2005.
166. Saidi, A, Coorevits, P and Guessasma, M, Homogenization of a sandwich structure and validity of the corresponding two-dimensional equivalent model, *Journal of Sandwich Structures and Materials,* 7, 7-30, 2005.
167. Glenn, CE and Hyer, MW, Bending behavior of low-cost sandwich plates, *Composites: Part A,* 36, 1449-1465, 2005.
168. Polyakov, V, Analytical refinement of sandwich plate bending problem considering local effects - I, *Journal of Sandwich Structures and Materials,* 1, 179-194, 1999.
169. Polyakov, V, Zhigun, I, Shlitsa, R and Khitrov, V, Analytical refinement of sandwich plate bending problem considering local effects - II, *Journal of Sandwich Structures and Materials,* 1, 195-213, 1999.
170. Pai, PF and Palazotto, AN, A higher-order sandwich plate theory accounting for 3-D stresses, *International Journal of Solids and Structures,* 38, 5045-5062, 2001.
171. Wu, H, Mu, B and Warnemuende, K, Failure analysis of FRP sandwich bus panels by finite element method, *Composites Part B: Engineering,* 34(1), 51-58, 2003.
172. Di Sciuva, M and Gherlone, M, Quasi-3D static and dynamic analysis of undamaged and damaged sandwich beams, *Journal of Sandwich Structures and Materials,* 7, 31-52, 2005.
173. Cho, YB and Averill, RC, First-order zig-zag sublaminate plate theory and finite element model for laminated composite and sandwich panels, *Composite Structures,* 50(1), 1-15, 2000.
174. Sburlati, R, The contact behaviour between a foam core sandwich plate and a rigid indenter, *Composites - Part B: Engineering,* 33, 325-332, 2002.

175. Choi, IH and Lim, CH, Low-velocity impact analysis of composite laminates using linearized contact law, *Composite Structures,* 66, 125-132, 2004.
176. Yang, M and Qiao, P, Nonlinear impact analysis of fully backed composite sandwich structures, *Composites Science and Technology,* 65, 551-562, 2005.
177. Abot, JL, Daniel, IM and Gdoutos, EE, Contact law for composite sandwich beams, *Journal of Sandwich Structures and Materials,* 4, 157-173, 2002.
178. Olsson, R, Engineering method for prediction of impact response and damage in sandwich panels, *Journal of Sandwich Structures and Materials,* 4, 3-29, 2002.
179. Malekzadeh, K, Khalili, MR and Mittal, RK, Analytical prediction of low-velocity impact response of composite sandwich panels using new TDOF spring-mass damper model, *Journal of Composite Materials,* 40(18), 1671-1689, 2006.
180. Anderson, TA, An investigation of SDOF models for large mass impact on sandwich composites, *Composites: Part B,* 36, 135-142, 2005.
181. Olsson, R and McManus, HL, Improved theory for contact indentation of sandwich panels, *AIAA Journal,* 34(6), 1238-1244, 1996.
182. Lee, SM and Tsotsis, TK, Indentation failure behavior of honeycomb sandwich panels, *Composites Science and Technology,* 60(8), 1147-1159, 2000.
183. Shuaeib, FM and Soden, PD, Indentation failure of composite sandwich beams, *Composites Science and Technology,* 57(9-10), 1249-1259, 1997.
184. Thomsen, OT, Theoretical and experimental investigation of local bending effects in sandwich plates, *Composite Structures,* 30, 85-101, 1995.
185. Greszczuk, LB, *Damage in composite materials due to low velocity impact,* Impact dynamics, John Wiley, New York, 1982.
186. Shivakumar, KN, Elber, W and Illg, W, Prediction of impact force and duration due to low-velocity impact on circular composite laminates, *Journal of Applied Mechanics,* 52, 674-680, 1985.
187. Hoo Fatt, MS and Park, KS, Modelling low-velocity impact damage of composite sandwich panels, *Journal of Sandwich Structures and Materials,* 3, 130-168, 2001.
188. Lin, CL and Hoo Fatt, MS, Perforation of sandwich panels with honeycomb cores by hemispherical nose projectiles, *Journal of Sandwich Structures and Materials,* 7, 133-172, 2005.
189. Khalili, MR, Malekzadeh, K and Mittal, RK, Effect of physical and geometrical parameters on transverse low-velocity impact response of sandwich panels with a transversely flexible core, *Composite Structures,* 77, 430-443, 2007.
190. Frostig, Y and Thomsen, OT, Localized effects in the nonlinear behavior of sandwich panels with a transversely flexible core, *Journal of Sandwich Structures and Materials,* 7, 53-75, 2005.
191. Lovinger, Z and Frostig, Y, High order behaviour of sandwich plates with free edges - edge effects, *International Journal of Solids and Structures,* 41, 979-1004, 2004.
192. Frostig, Y, Geometrically nonlinear response of modern sandwich panels - distributed loads and localized effects, *Journal of Sandwich Structures and Materials,* 8, 539-556, 2006.
193. Thomsen, OT and Frostig, Y, Localized bending effects in sandwich panels: Photoelastic investigation versus high-order sandwich theory results, *Composite Structures,* 37(1), 97-108, 1997.
194. Frostig, Y, Behaviour of delaminated sandwich beam with transversely flexible core - high order theory, *Composite Structures,* 20, 1-16, 1992.
195. Frostig, Y, On stress concentration in the bending of sandwich beams with transversely flexible core, *Composite Structures,* 24, 161-169, 1993.

196. Frostig, Y and Baruch, M, High-order buckling analysis of sandwich beams with transversely flexible core, Journal of Engineering Mechanics, 119(3), 476-495, 1993.
197. Turk, MH and Hoo Fatt, MS, Localized damage response of composite sandwich plates, *Composites: Part B: engineering,* 30, 157-165, 1999.
198. Hoo Fatt, MS and Park, KS, Perforation of honeycomb sandwich plates by projectiles, *Composites - Part A: Applied Science and Manufacturing,* 31(8), 889-899, 2000.
199. Sokolinsky, VS, Shen, H, Vaikhanski, L and Nutt, SR, Experimental and analytical study of nonlinear bending response of sandwich beams, *Composite Structures,* 60, 219-229, 2003.
200. Vinson, JR, *The behaviour of Sandwich Structures of Isotropic and Composite Materials,* Technomic Publishing Company, 1999.
201. Timoshenko, SP and Woinowsky-Krieger, S, *Theory of Plates and Shells, 2nd Edition,* McGraw-Hill International Editions, New York, USA, 1959.
202. Fabrikant, VI, Selvadurai, APS and Xistris, GD, Asymmetric problem of loading under a smooth punch, *Journal of Applied Mechanics,* 52, 681-685, 1985.
203. Fabrikant, VI, Elastic field around a circular punch, *Journal of Applied Mechanics,* 55, 604-610, 1988.
204. Zhou, G, *Principles of Composite Materials and Structures,* Departmental Publication No. 20, Loughborough University, Loughborough, UK, Unpublished, 2002.
205. Riendeau, S, Nemes, JA, Dynamic punch shear behaviour of AS4/3501-6, *Journal of Composite Materials*, 30(13), 1494-1512, 1996.
206. Choe, GH, Finch, WW, Vinson, J.R., Compression testing of composite materials at high strain rates, *Proceedings of 4th Japan-U.S. Conference on Composites*, 1988.
207. Singer, J, Arbocz, J and Weller, T, *Buckling Experiments - Experimental Methods in Buckling of Thin-Walled Structures: Volume 1,* John Wiley & Sons Ltd, Bath, UK, 1998.

Appendix A – Individual response curves for quasi-static transverse loading

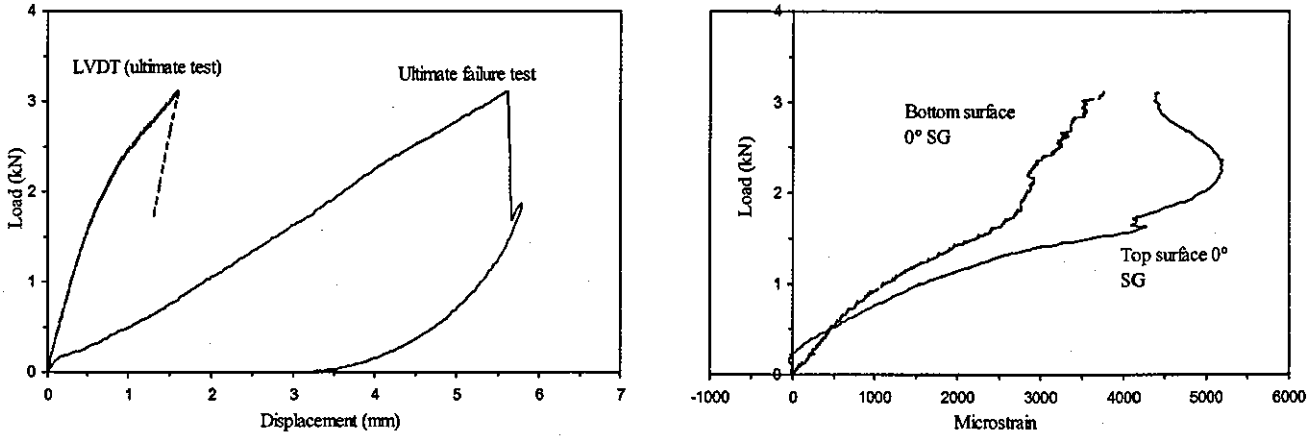

Figure A1 4 ply 50kg/m^3 sandwich panel loaded with HS Indenter

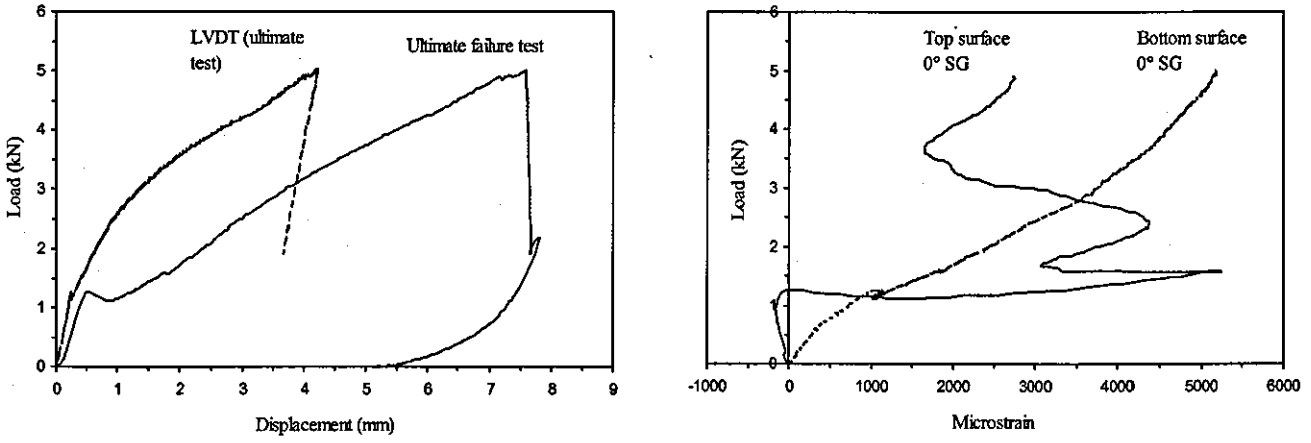

Figure A2 4 ply 50kg/m^3 sandwich panel loaded with FE Indenter

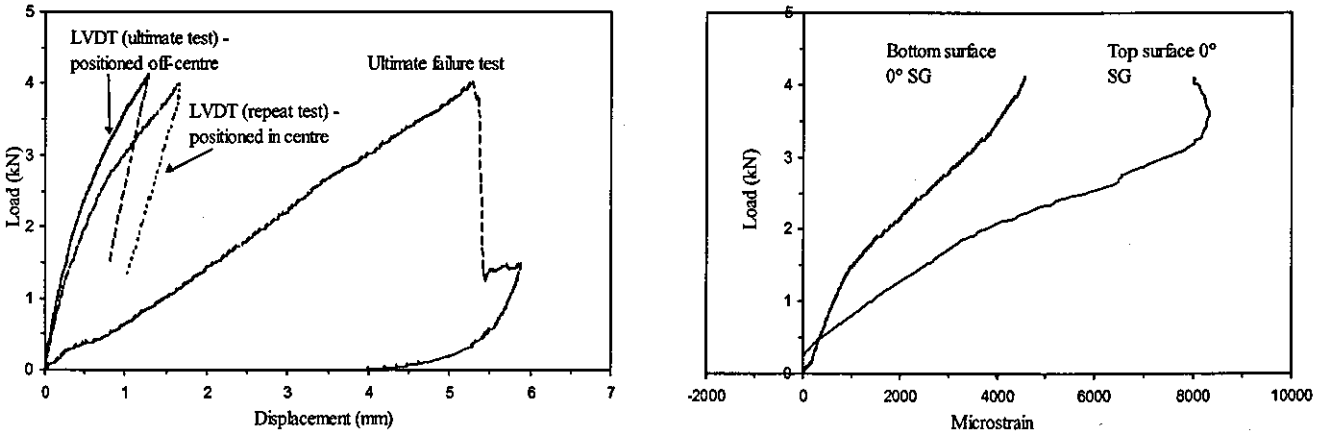

Figure A3 4 ply 70kg/m^3 sandwich panel loaded with HS Indenter

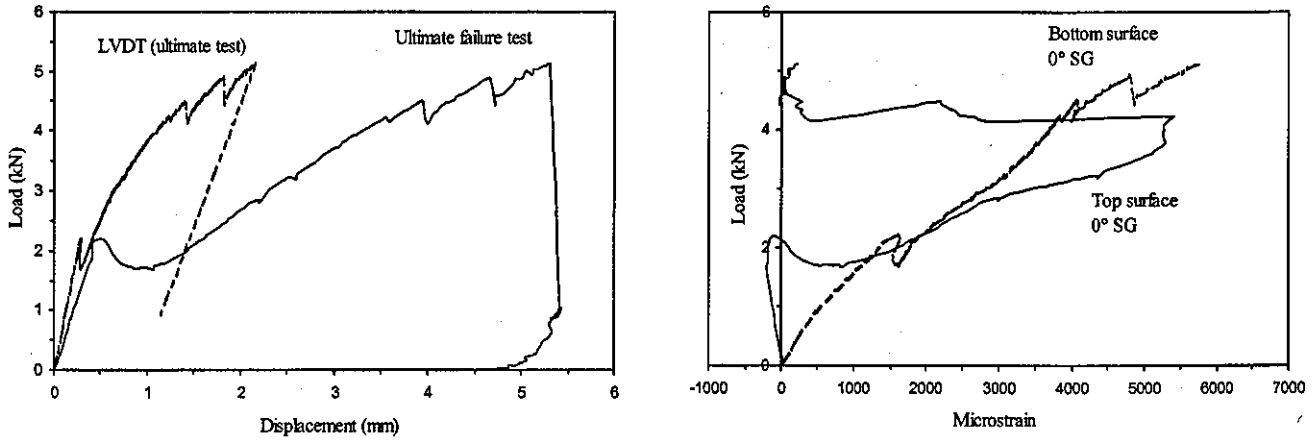

Figure A4 4 ply 70kg/m^3 sandwich panel loaded with FE Indenter

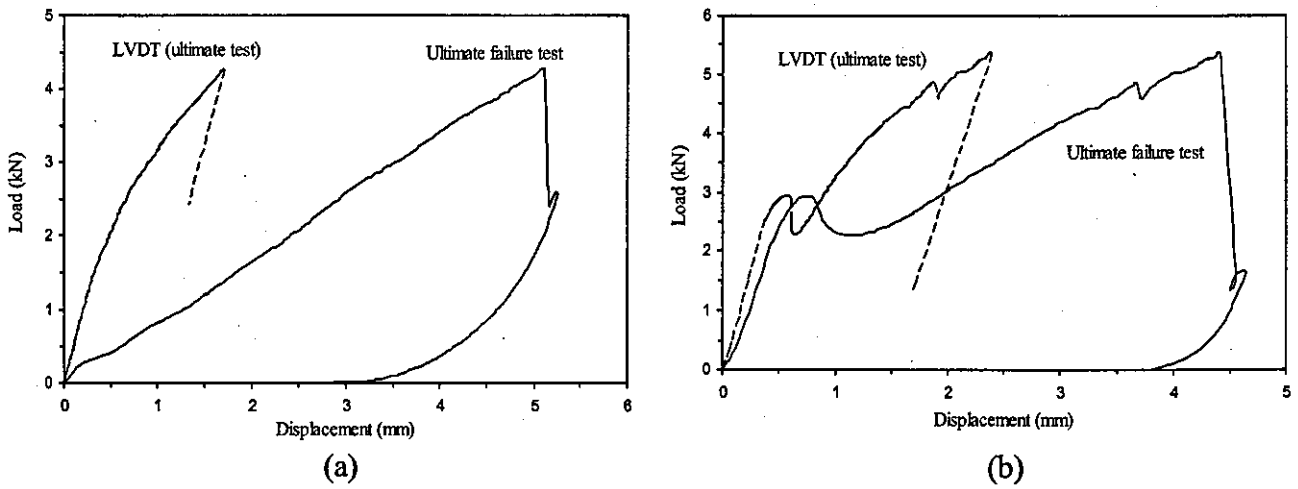

Figure A5 4 ply 90kg/m^3 sandwich panel loaded with (a) HS Indenter (b) FE Indenter

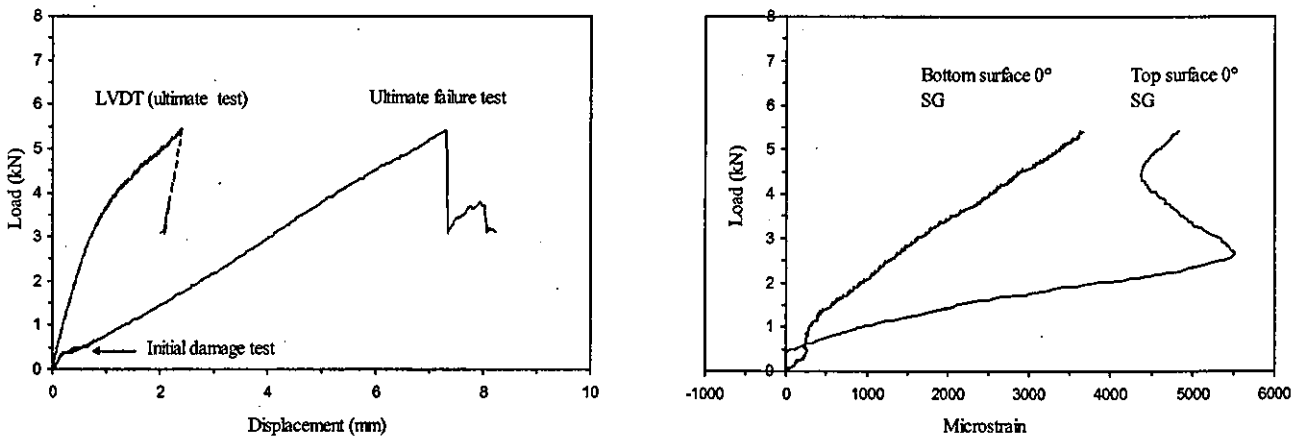

Figure A6 8 ply 50kg/m^3 sandwich panel loaded with HS Indenter

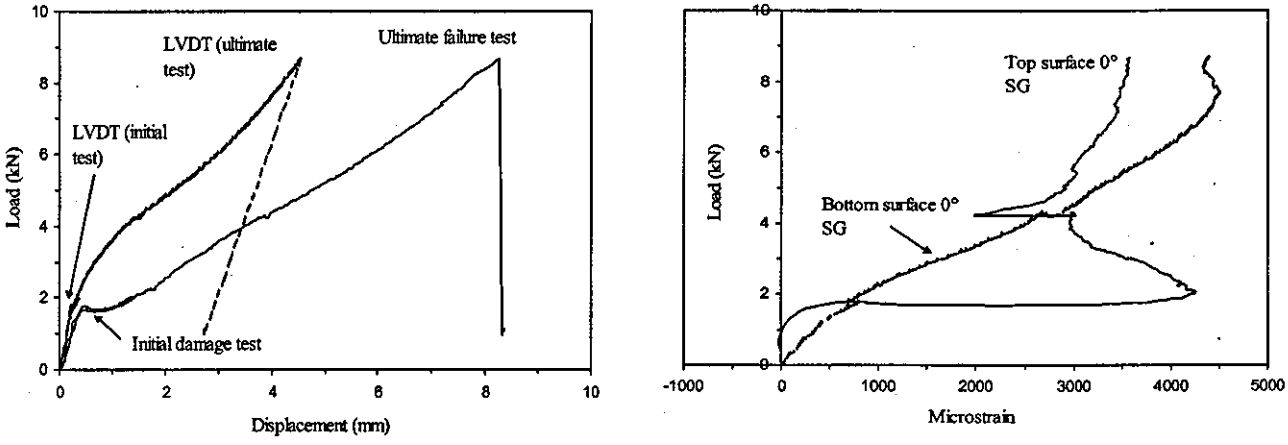

Figure A7 8 ply 50kg/m^3 sandwich panel loaded with FE Indenter

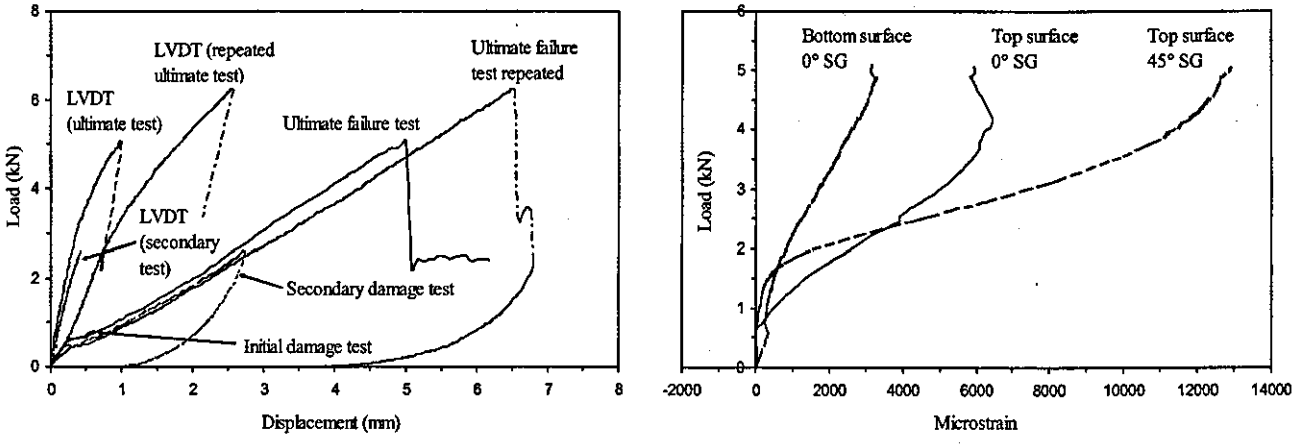

Figure A8 8 ply 70kg/m^3 sandwich panel loaded with HS Indenter

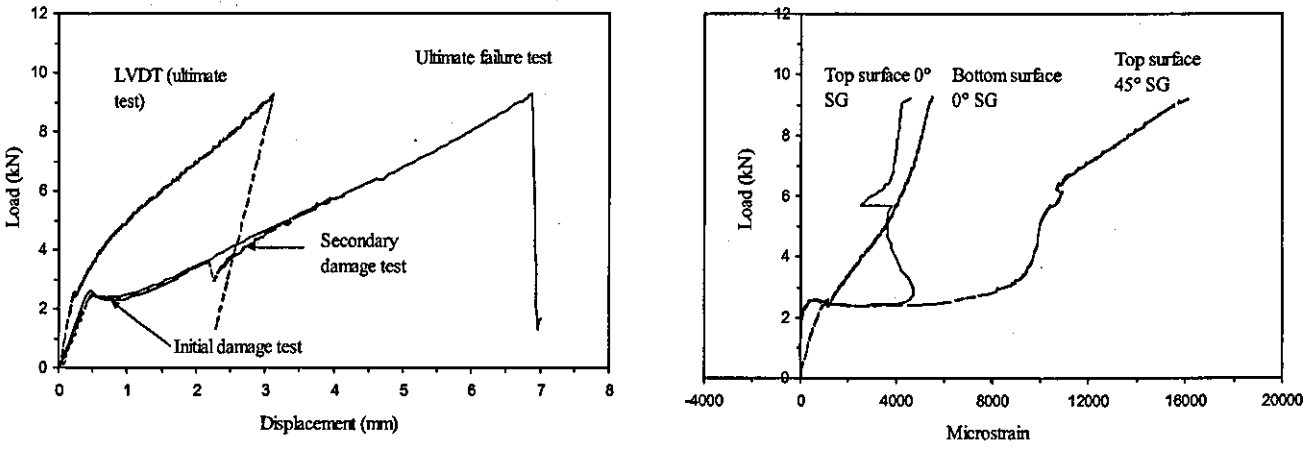

Figure A9 8 ply 70kg/m^3 sandwich panel loaded with FE Indenter

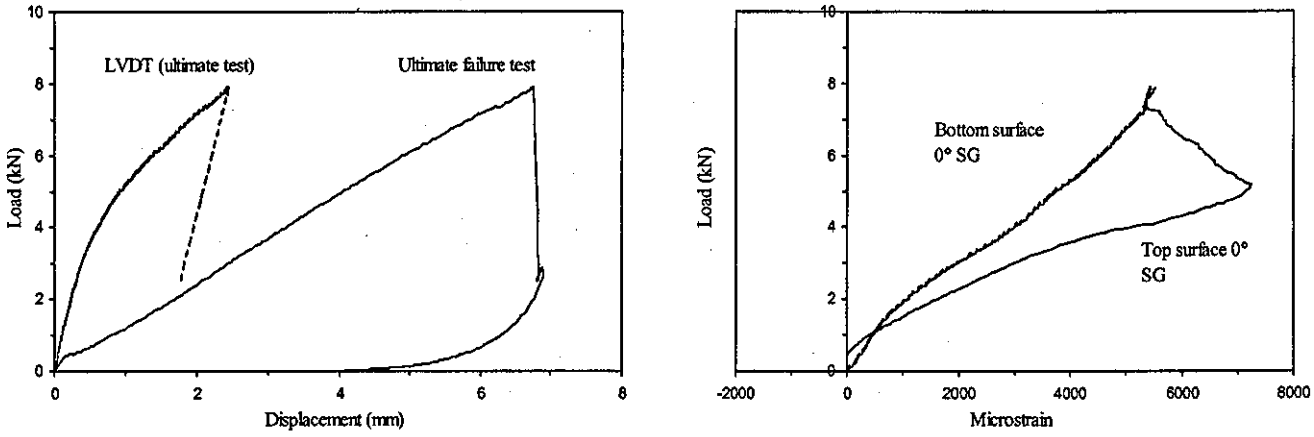

Figure A10 8 ply 90kg/m^3 sandwich panel loaded with HS Indenter

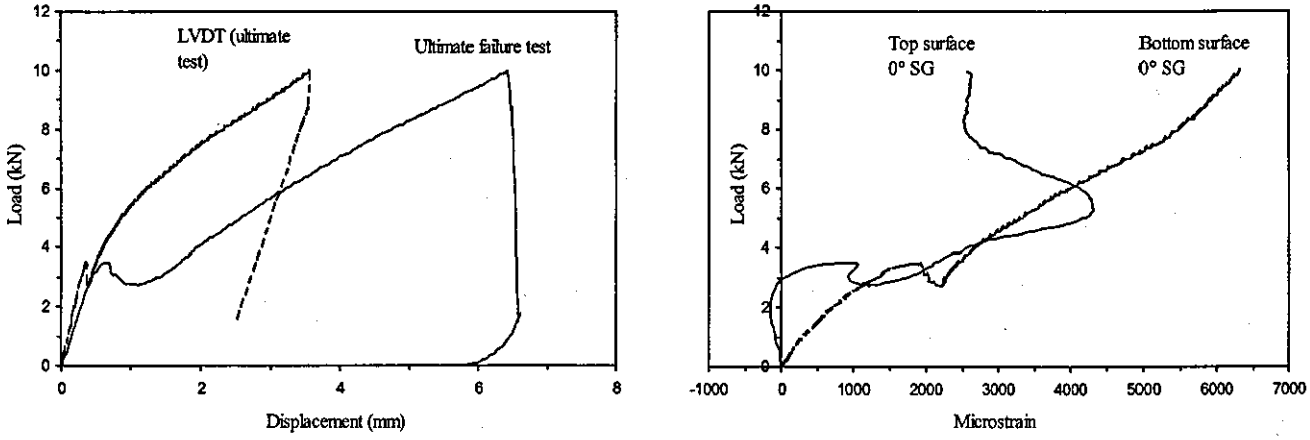

Figure A11 8 ply 90kg/m^3 sandwich panel loaded with FE Indenter

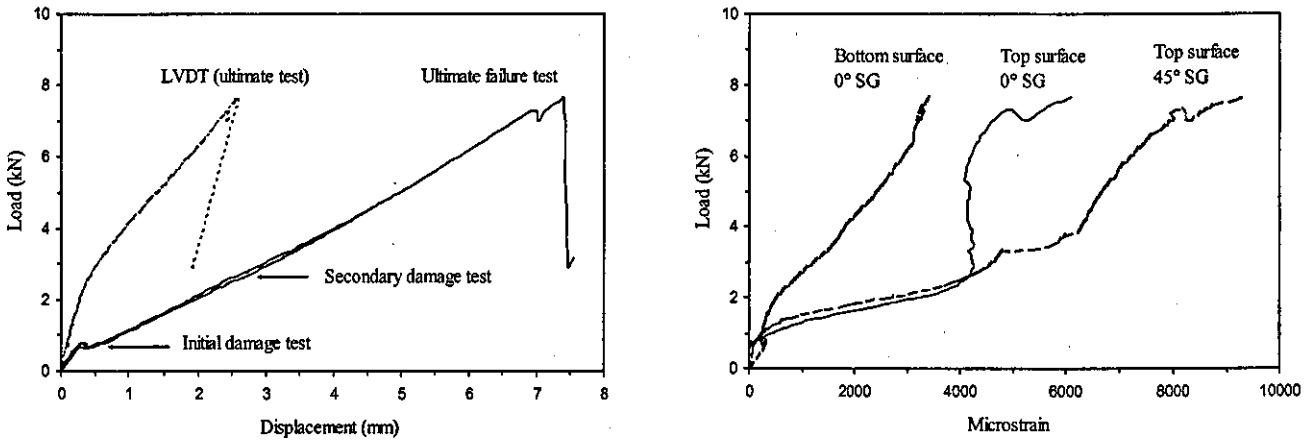

Figure A12 12 Ply 50kg/m^3 sandwich panel loaded with HS indenter

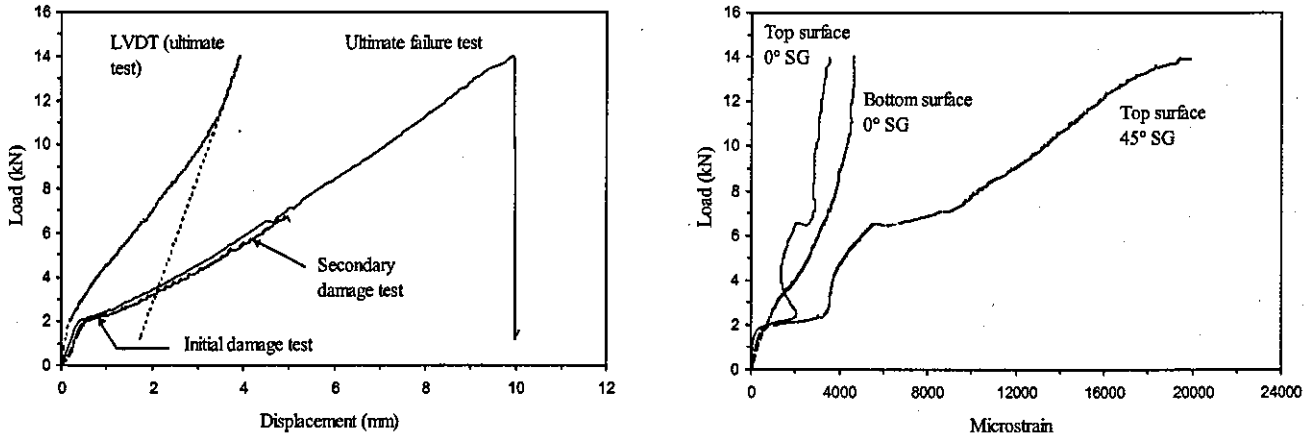

Figure A13 12 ply 50kg/m^3 sandwich panel loaded with FE indenter

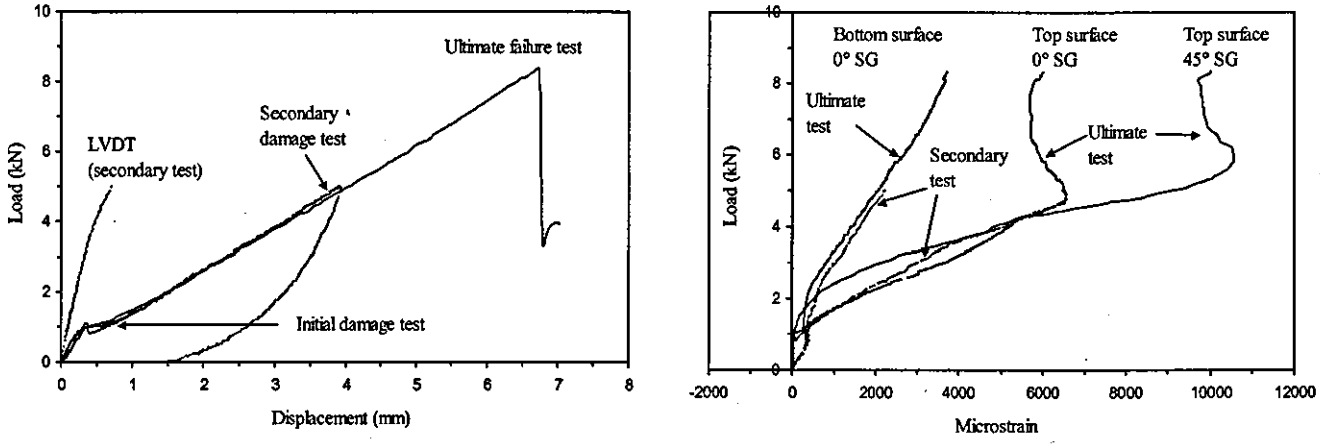

Figure A14 12 ply 70kg/m^3 sandwich panel loaded with HS Indenter

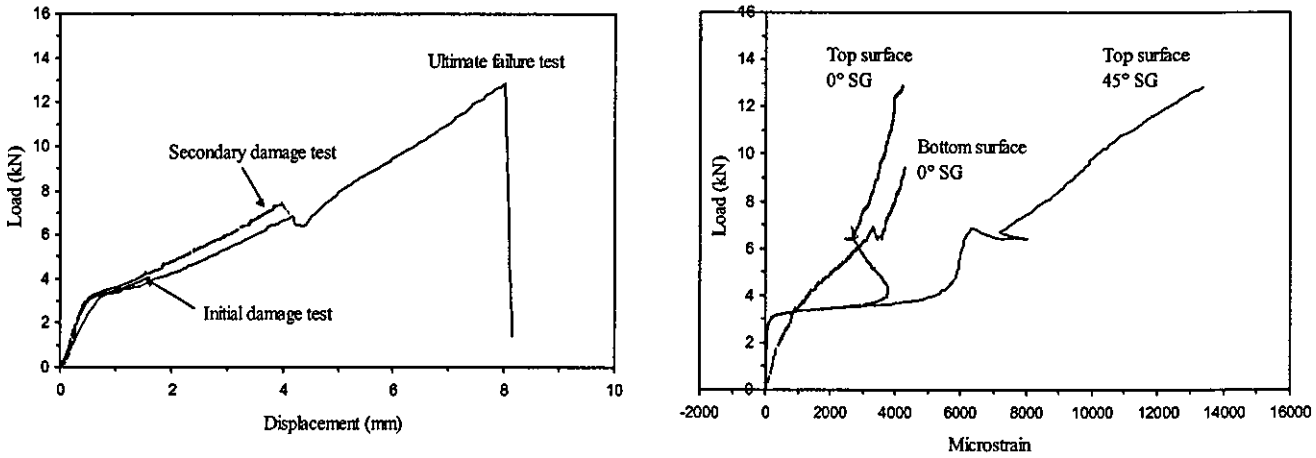

Figure A15 12 ply 70kg/m^3 sandwich panel loaded with FE Indenter

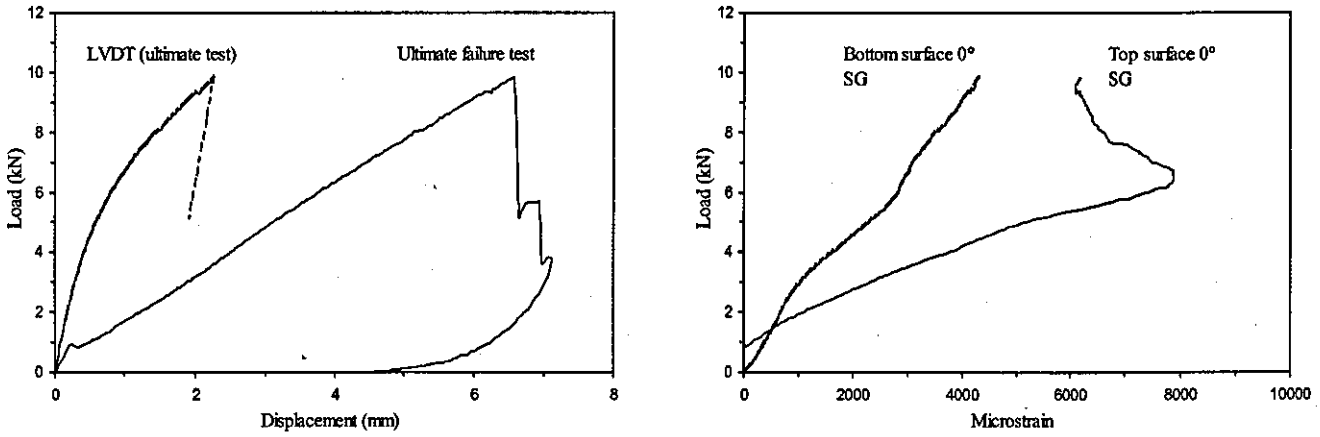

Figure A16 12 ply 90kg/m^3 sandwich panel loaded with HS Indenter

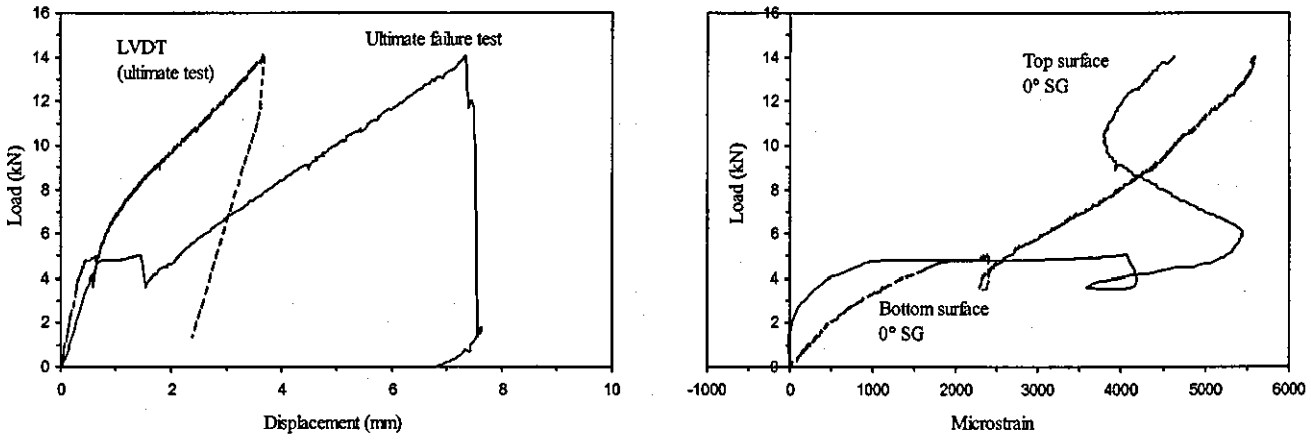

Figure A17 12 ply 90kg/m^3 sandwich panel loaded with FE Indenter

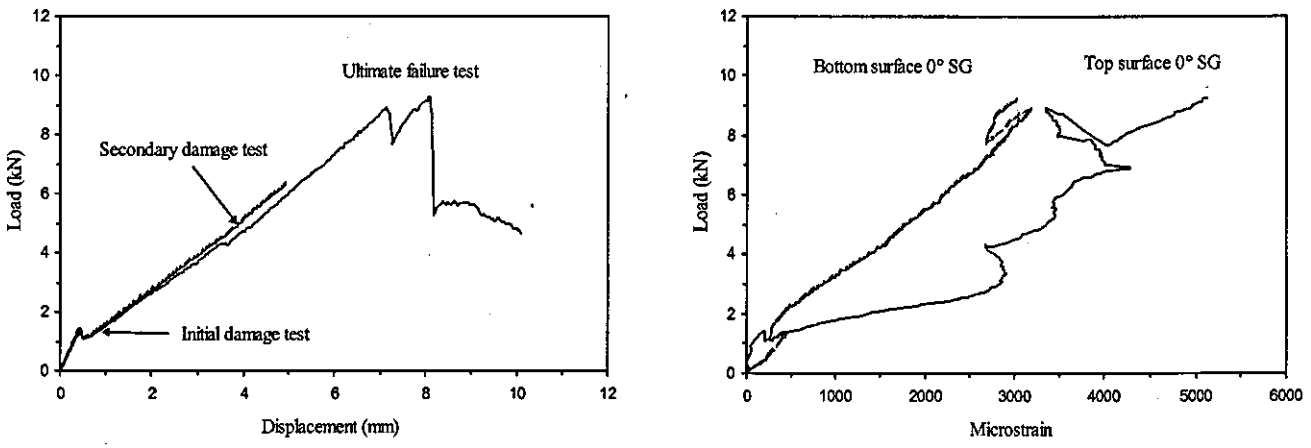

Figure A18 16 ply 50kg/m^3 sandwich panel loaded with HS Indenter

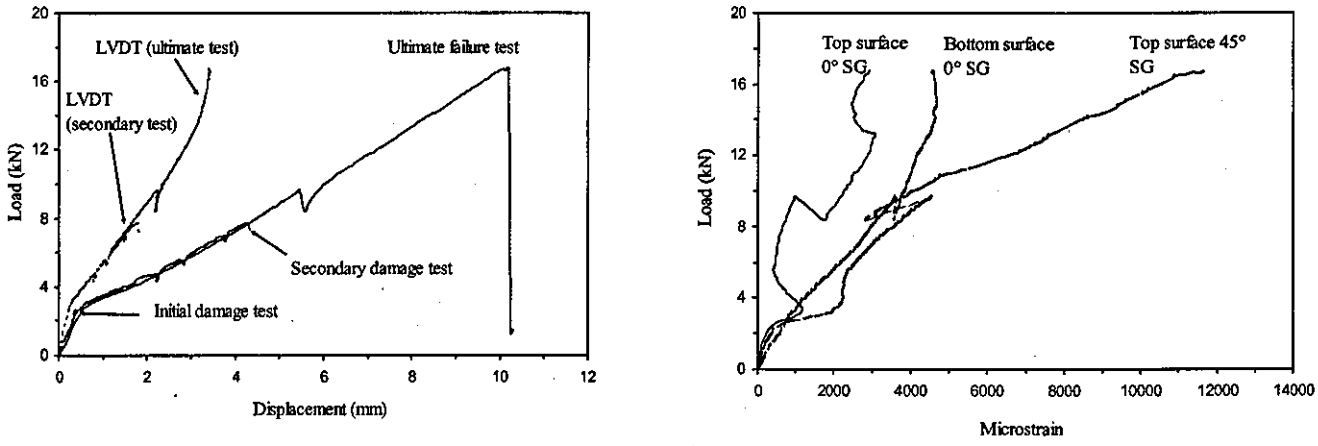

Figure A19 16 ply 50kg/m^3 sandwich panel loaded with FE Indenter

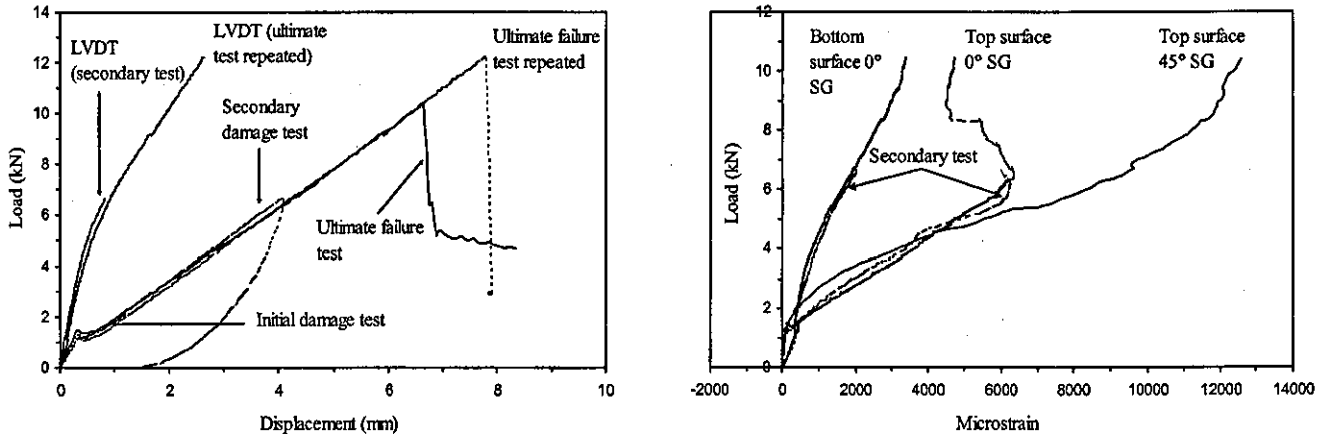

Figure A20 16 ply 70kg/m^3 sandwich panel loaded with HS Indenter

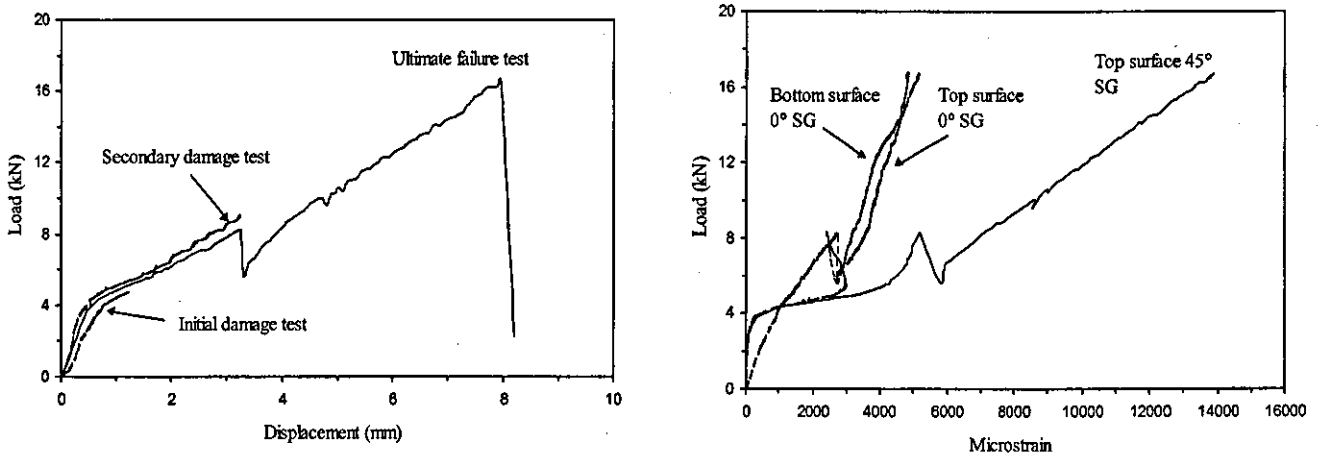

Figure A21 16 ply 70kg/m^3 sandwich panel loaded with FE Indenter

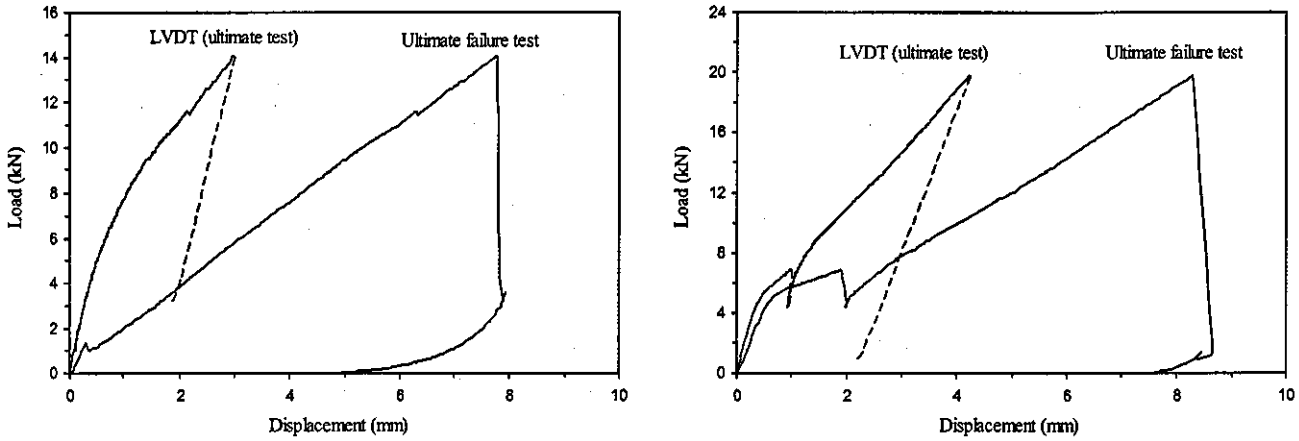

Figure A22 16 ply 90kg/m^3 sandwich panel loaded with (a) HS Indenter (b) FE Indenter

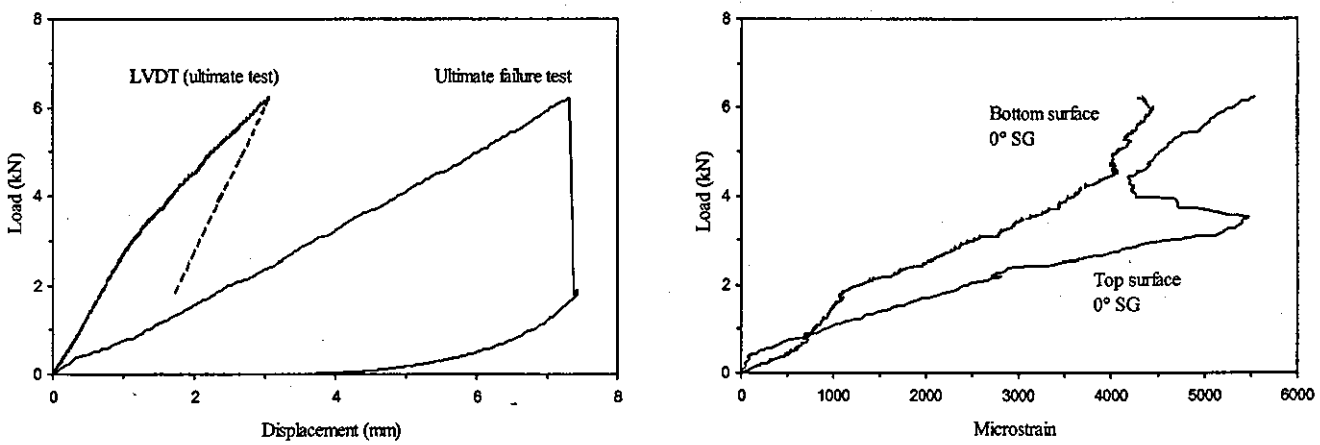

Figure A23 8 ply 64kg/m^3 sandwich panel loaded with HS Indenter

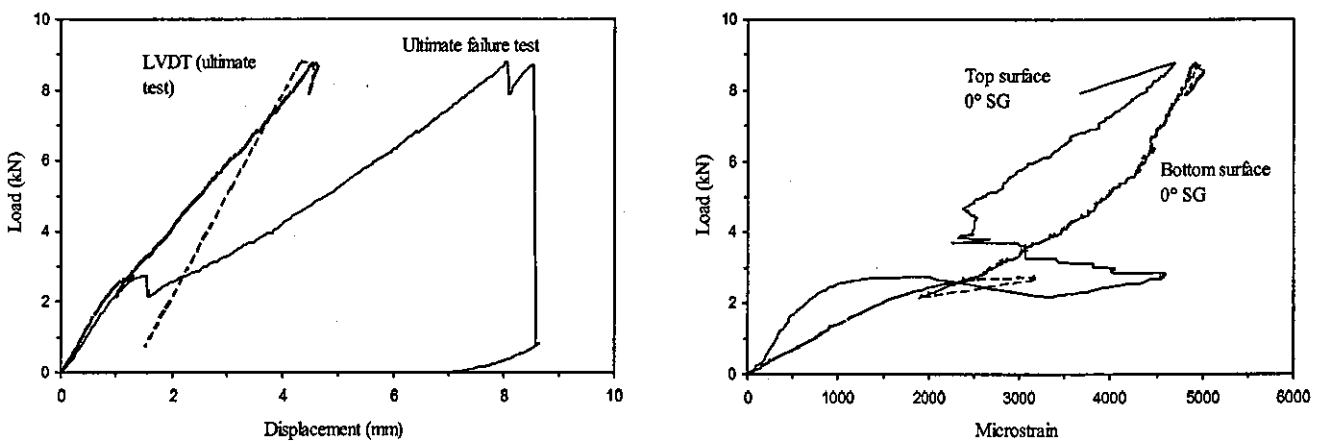

Figure A24 8 ply 64kg/m^3 sandwich panel loaded with FE Indenter

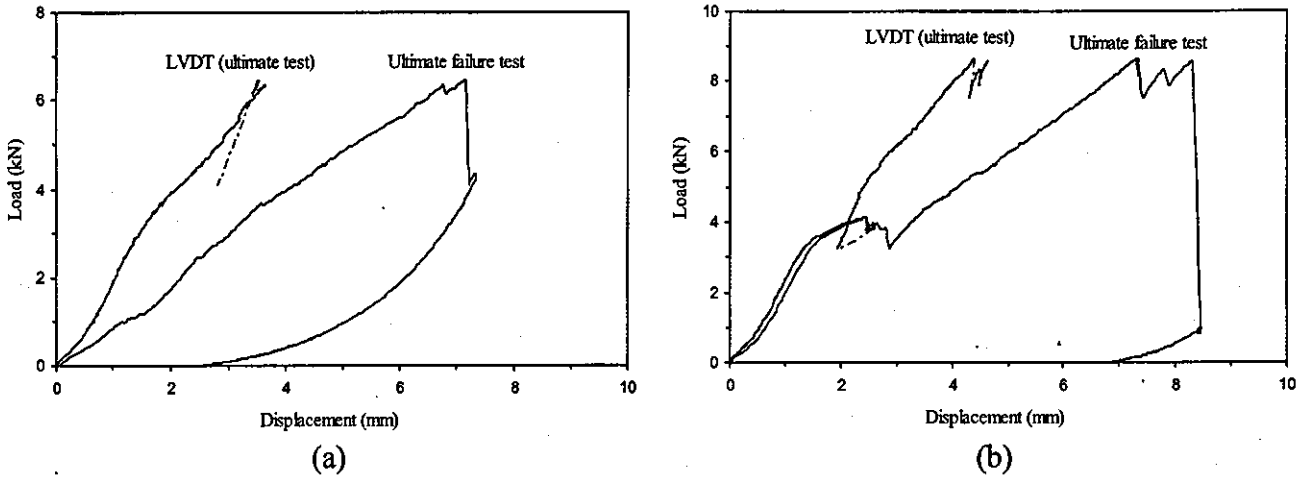

Figure A25 8 ply 96kg/m^3 sandwich panel loaded with (a) HS Indenter (b) FE Indenter

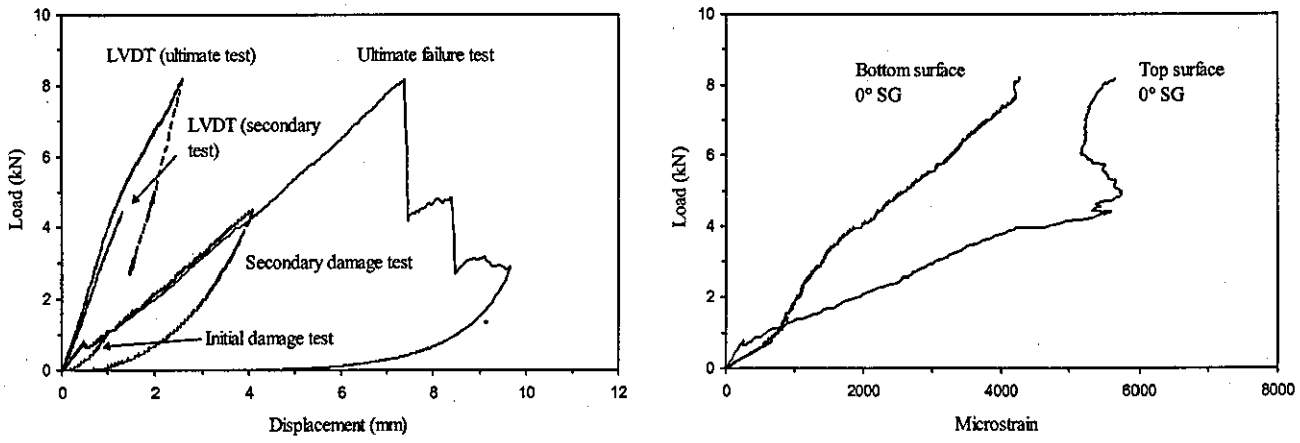

Figure A26 12 ply 64kg/m^3 sandwich panel loaded with HS Indenter

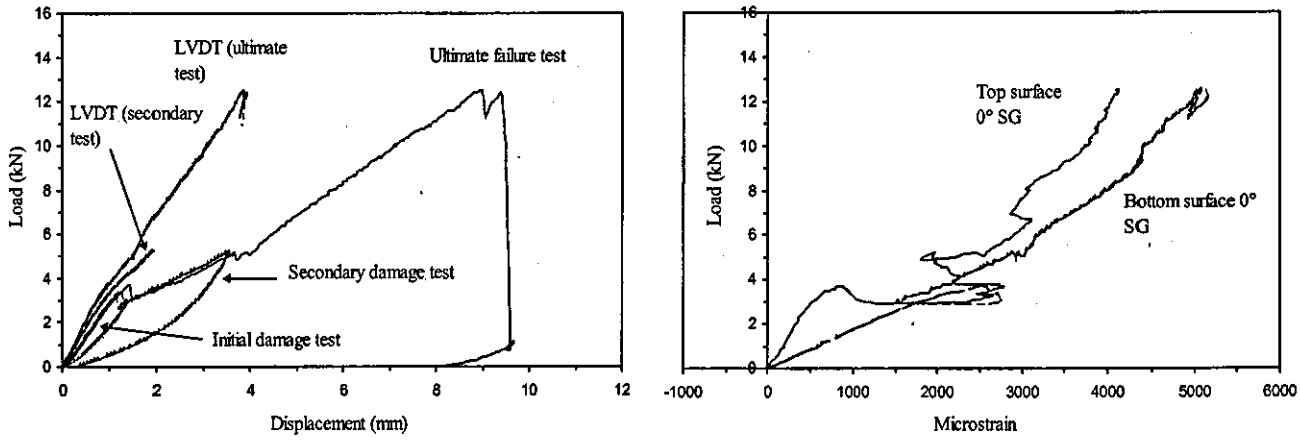

Figure A27 12 ply 64kg/m^3 sandwich panel loaded with FE Indenter

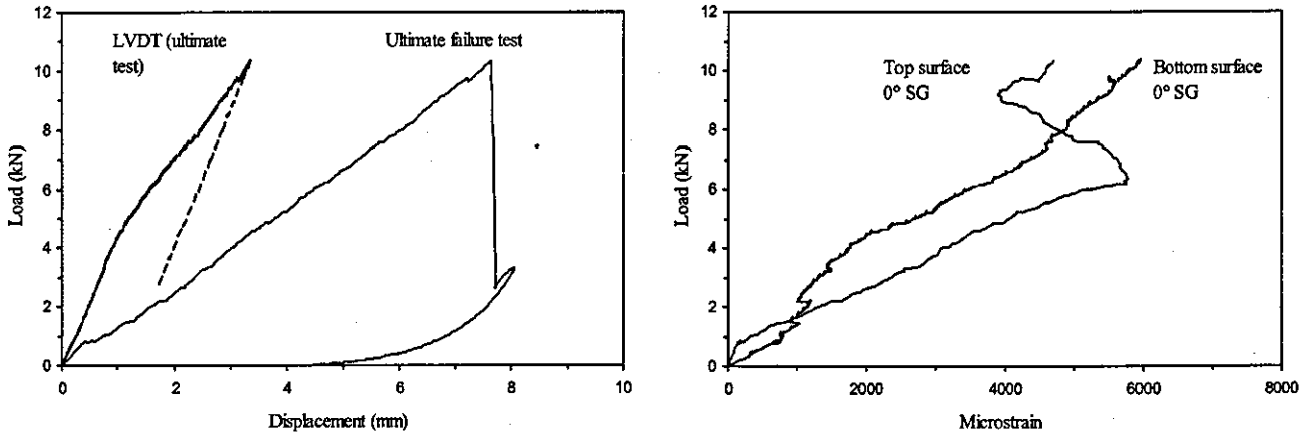

Figure A28 12 ply 96kg/m^3 sandwich panel loaded with HS Indenter

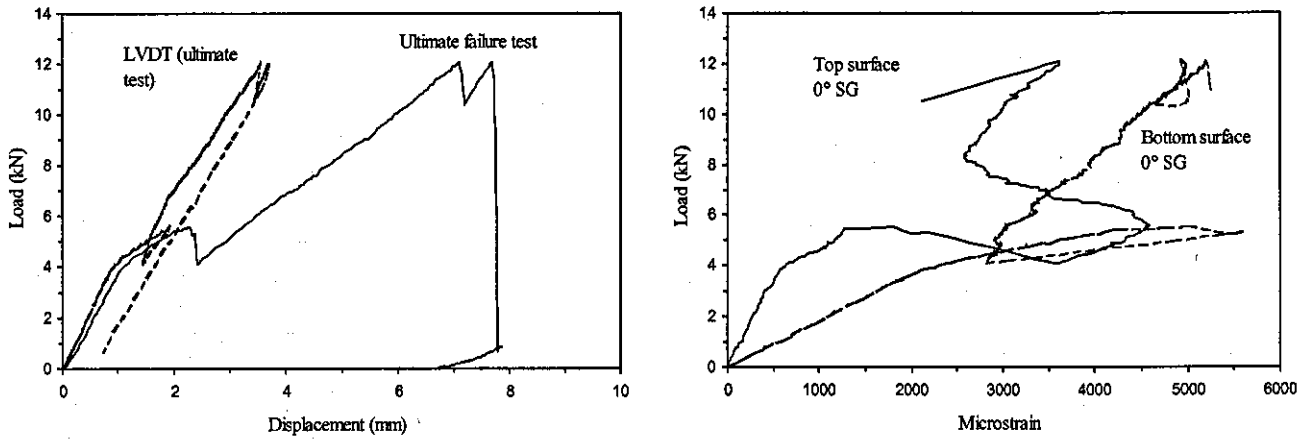

Figure A29 12 ply 96kg/m^3 sandwich panel loaded with FE Indenter

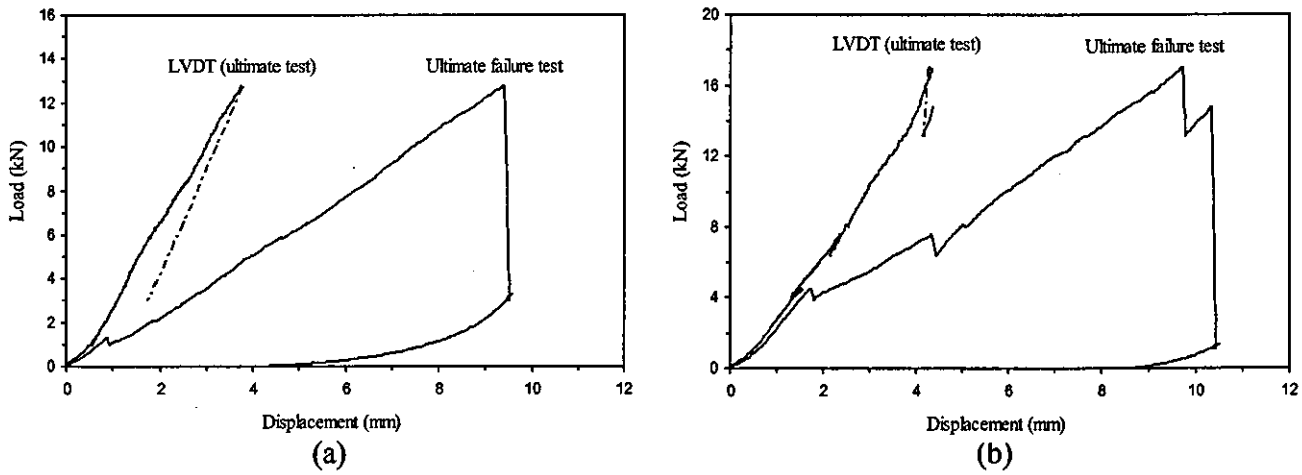

Figure A30 16 ply 64kg/m^3 sandwich panel loaded with (a) HS Indenter (b) FE Indenter

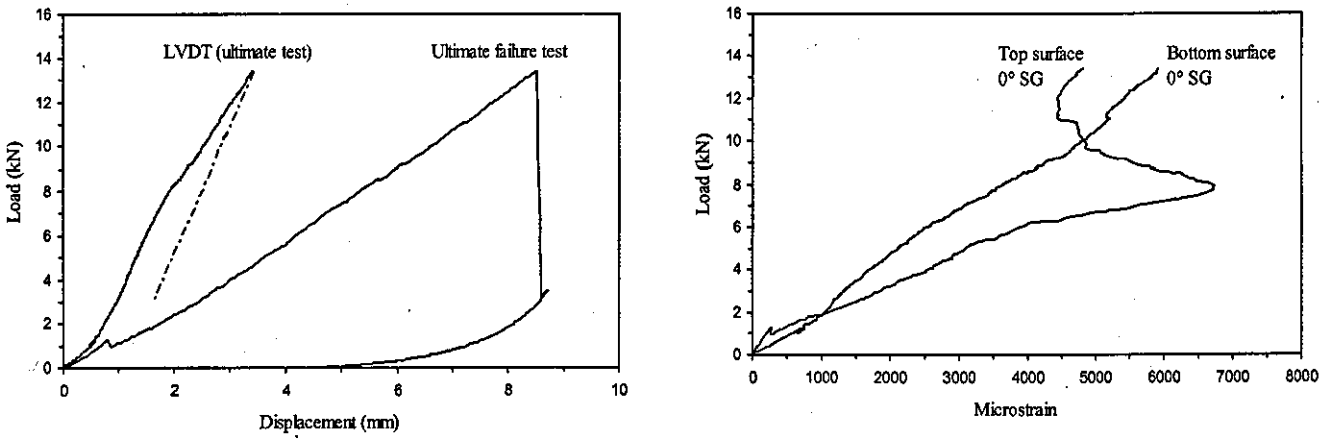

Figure A31 16 ply 96kg/m^3 sandwich panel loaded with HS Indenter

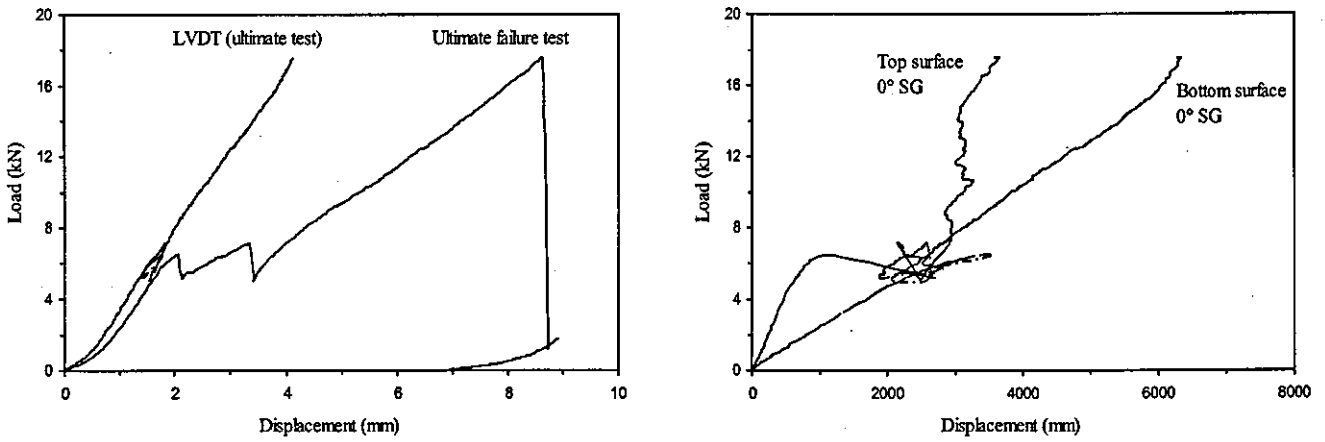

Figure A32 16 ply 96kg/m^3 sandwich panel loaded with FE Indenter

Appendix B – Effect of intrinsic and extrinsic variables on transverse response

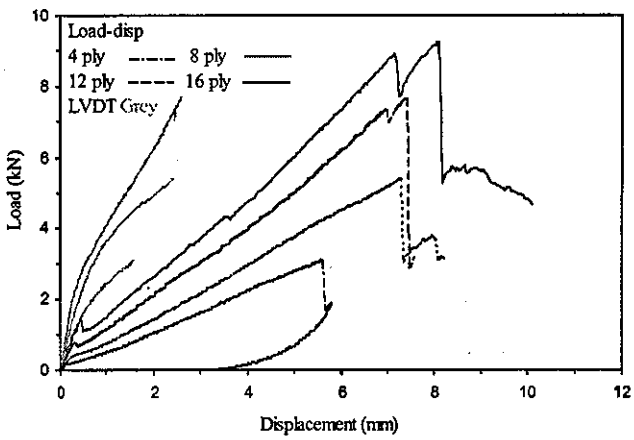

(a)

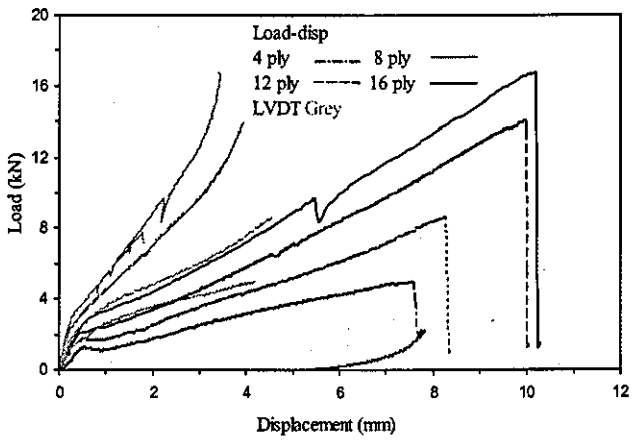

(b)

Figure B1 Effect of skin thickness – 50kg/m^3 honeycomb
(a) HS indenter (b) FE indenter

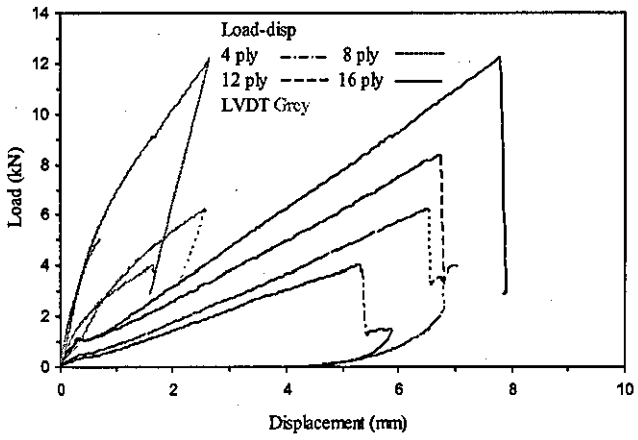

(a)

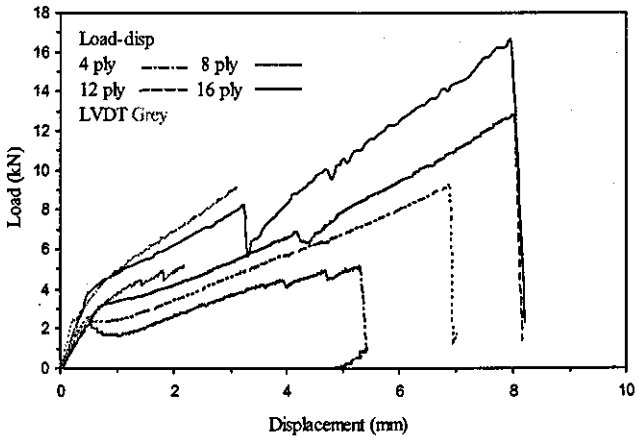

(b)

Figure B2 Effect of skin thickness – 70kg/m^3 honeycomb
(a) HS indenter (b) FE indenter

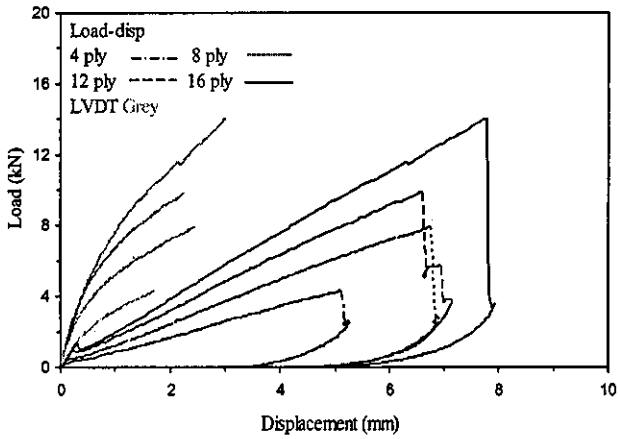

(a)

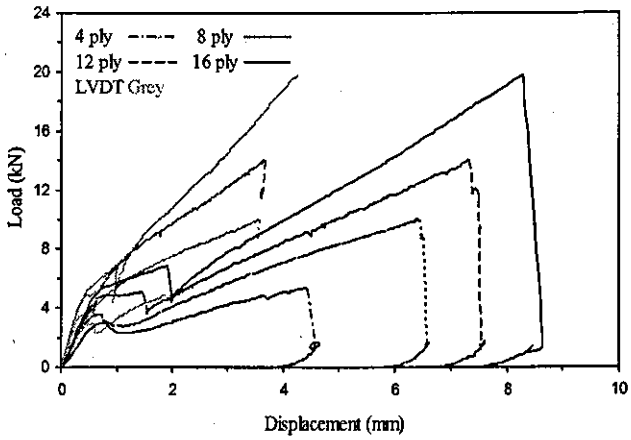

(b)

Figure B3 Effect of skin thickness – 90kg/m^3 honeycomb
(a) HS indenter (b) FE indenter

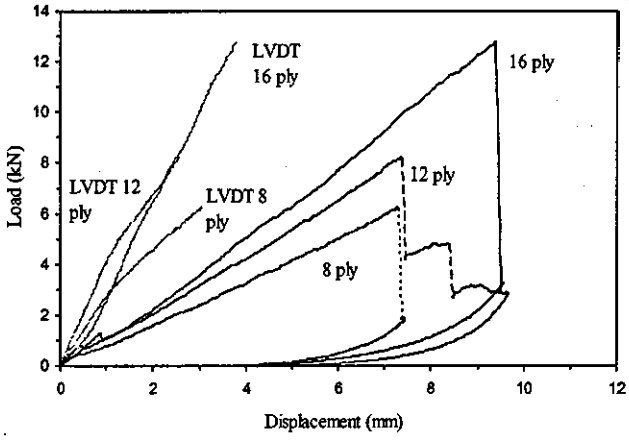

(a)

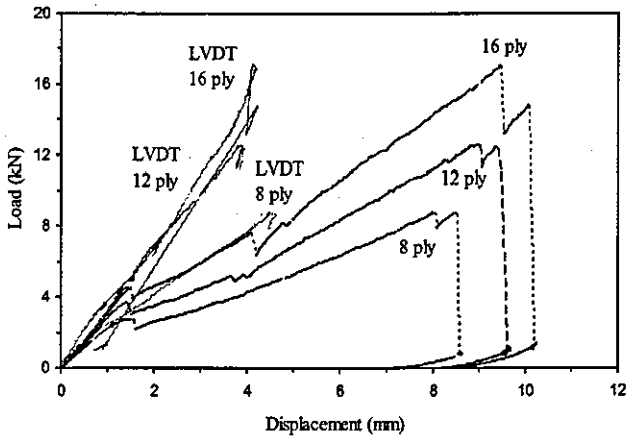

(b)

Figure B4 Effect of skin thickness – 64kg/m^3 honeycomb
(a) HS indenter (b) FE indenter

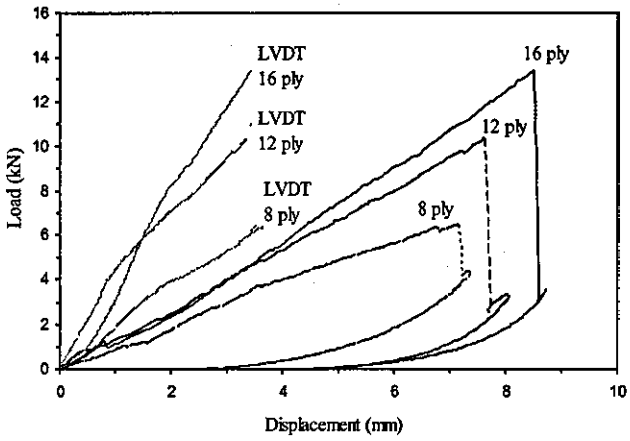

(a)

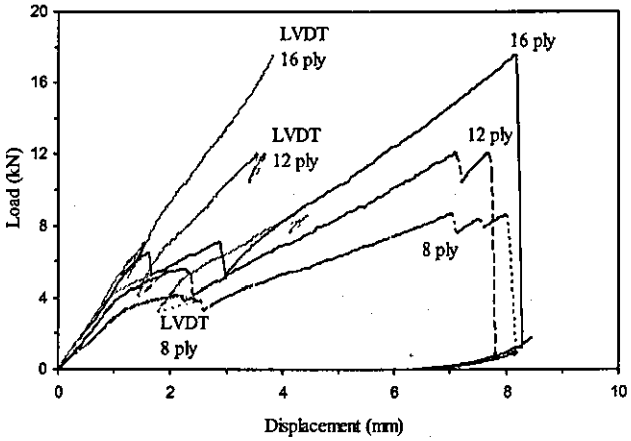

(b)

Figure B5 Effect of skin thickness – 96kg/m^3 honeycomb
(a) HS indenter (b) FE indenter

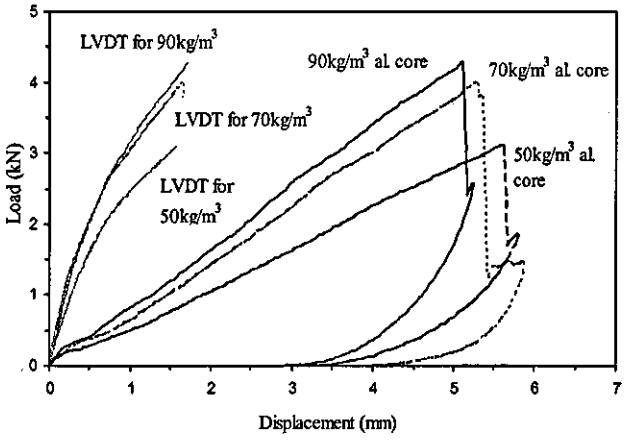

(a)

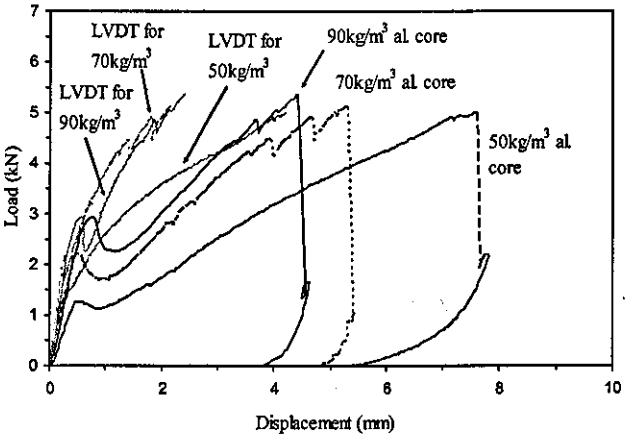

(b)

Figure B6 Effect of honeycomb density (aluminium) – 4 ply skins
(a) HS indenter (b) FE indenter

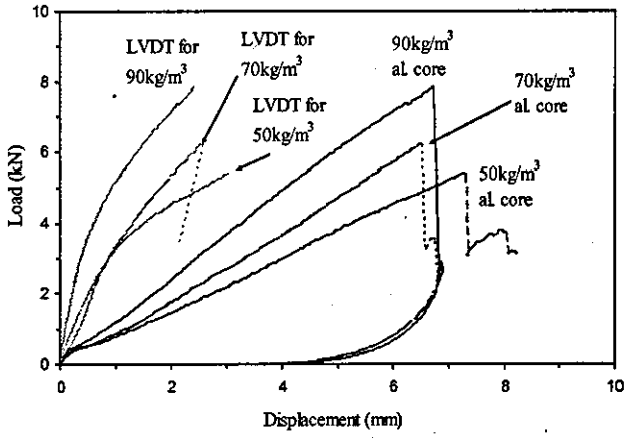

(a)

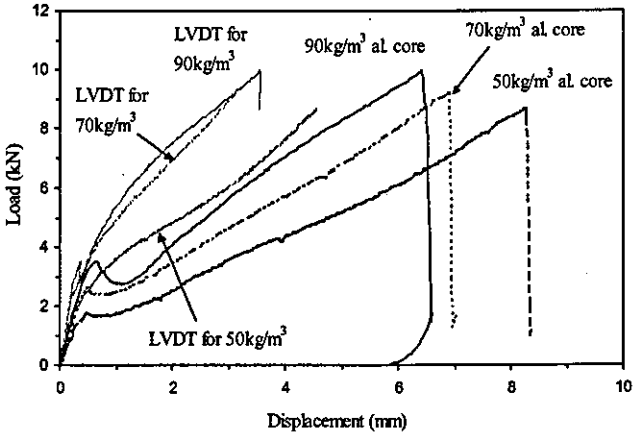

(b)

Figure B7 Effect of honeycomb density (aluminium) – 8 ply skins
(a) HS indenter (b) FE indenter

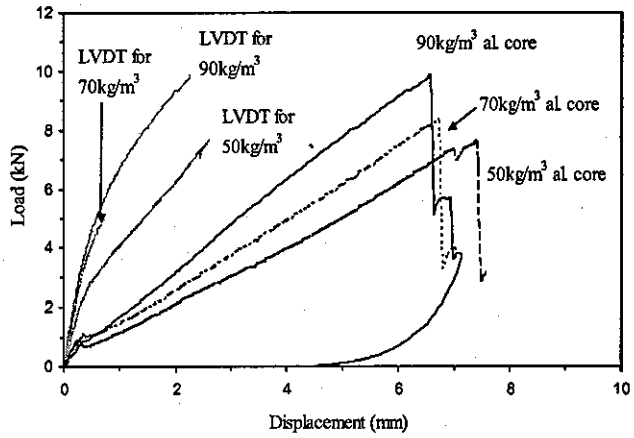

(a)

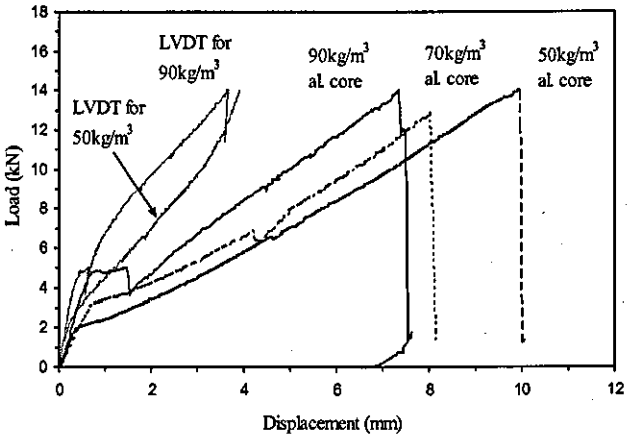

(b)

Figure B8 Effect of honeycomb density (aluminium) – 12 ply skins
(a) HS indenter (b) FE indenter

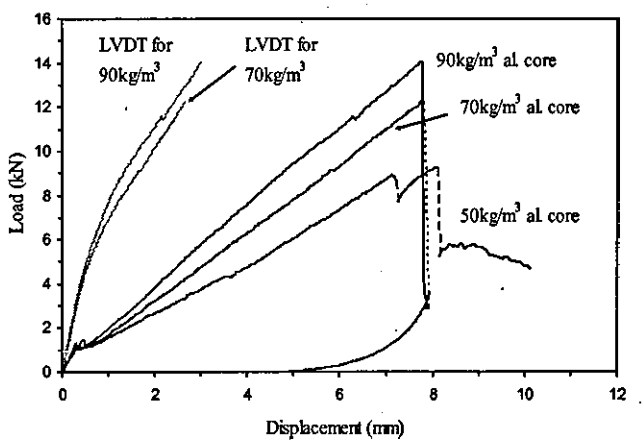

(a)

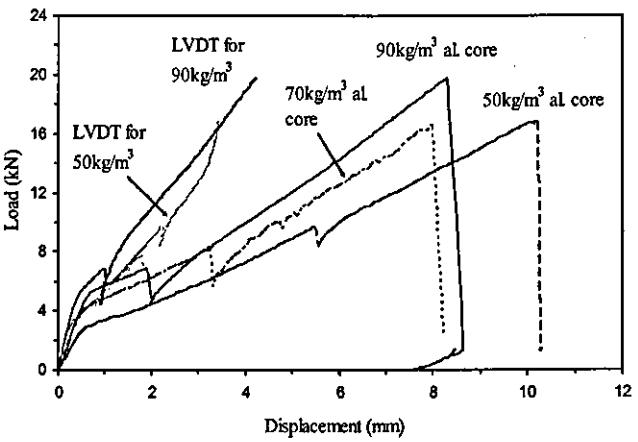

(b)

Figure B9 Effect of honeycomb density (aluminium) – 16 ply skins
(a) HS indenter (b) FE indenter

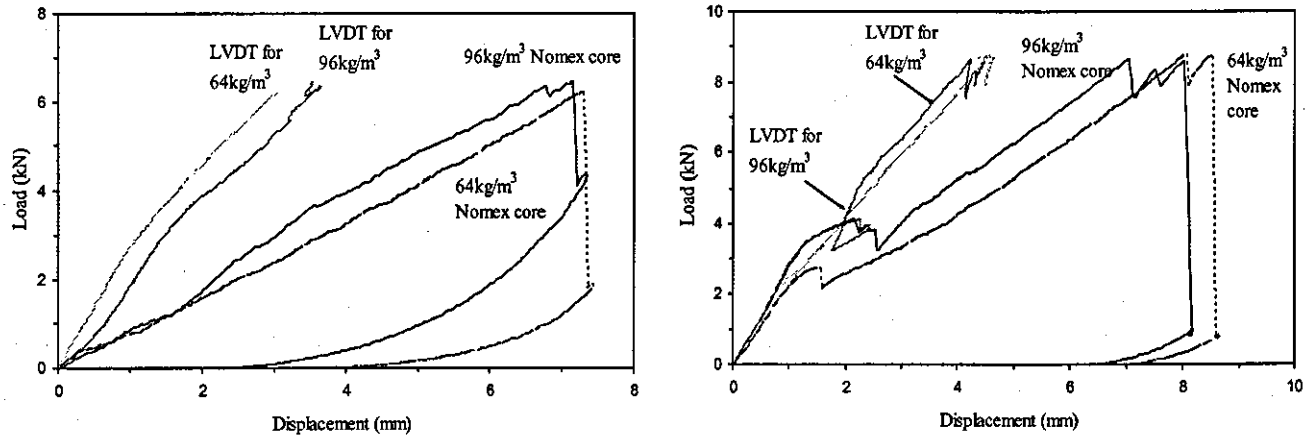

Figure B10 Effect of honeycomb density (nomex) – 8 ply skins
(a) HS indenter (b) FE indenter

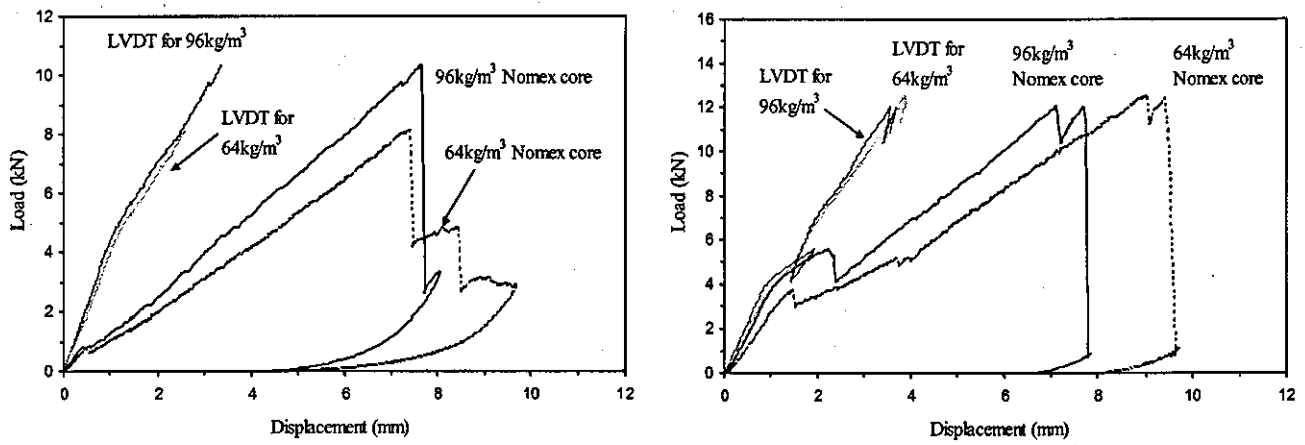

Figure B11 Effect of honeycomb density (nomex) – 12 ply skins
(a) HS indenter (b) FE indenter

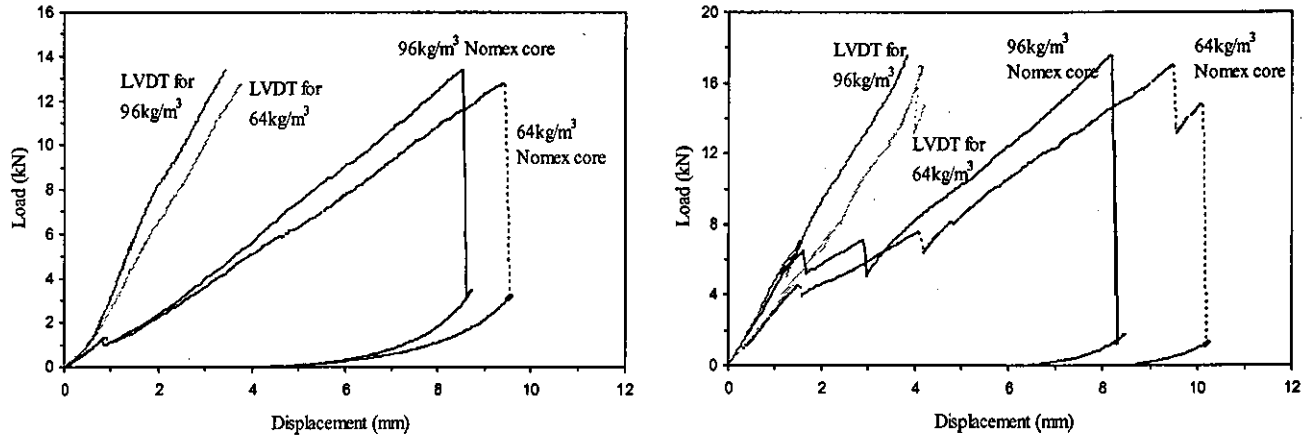

Figure B12 Effect of honeycomb density (nomex) – 16 ply skins
(a) HS indenter (b) FE indenter

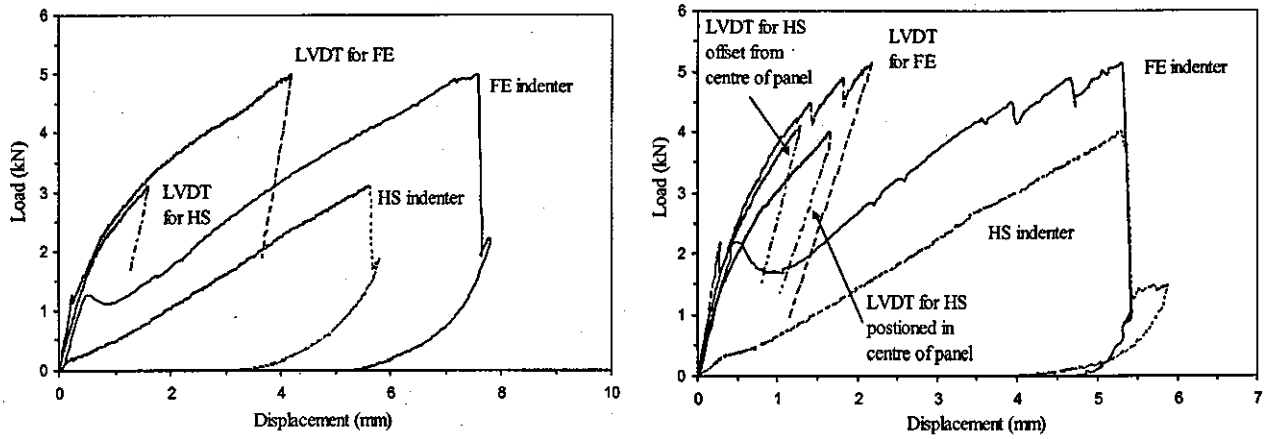

Figure B13 Effect of indenter nose-shape – 4 ply skins with
(a) 50kg/m^3 honeycomb (b) 70kg/m^3 honeycomb

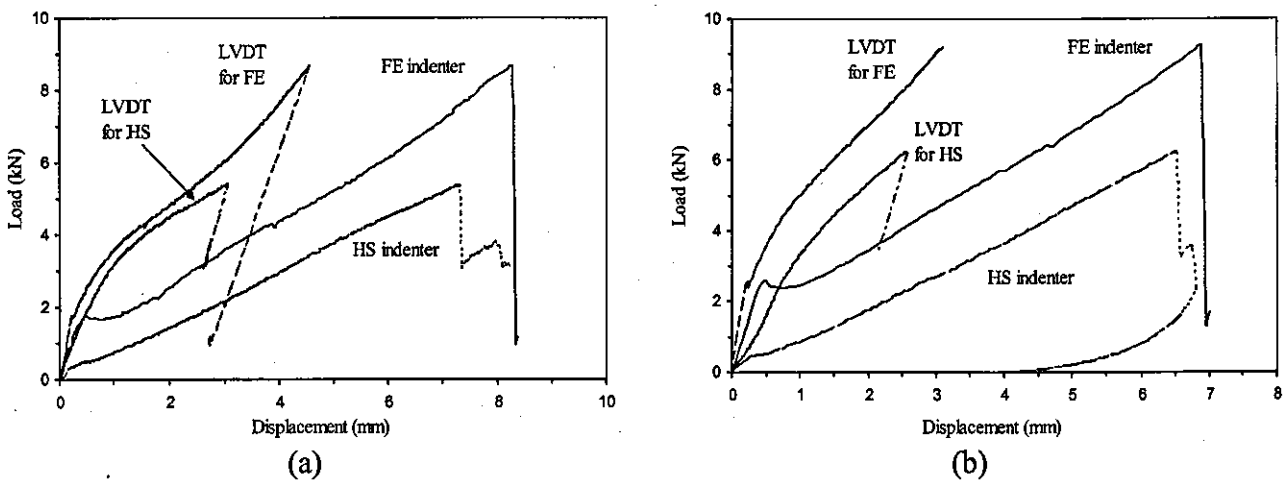

Figure B14 Effect of indenter nose-shape – 8 ply skins with
(a) 50kg/m^3 honeycomb (b) 70kg/m^3 honeycomb

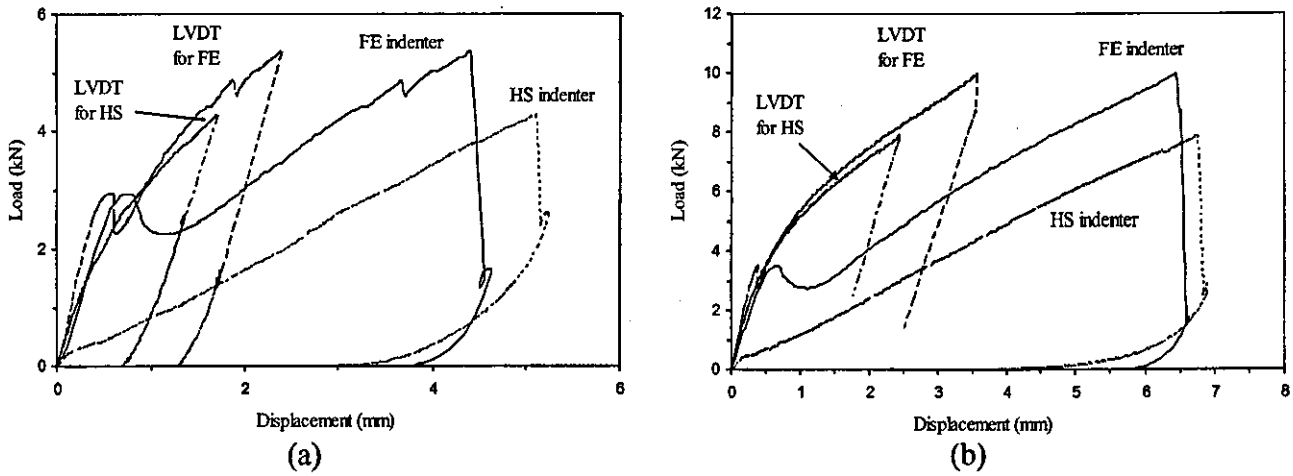

Figure B15 Effect of indenter nose-shape – 90kg/m^3 honeycomb with
(a) 4 ply skins (b) 8 ply skins

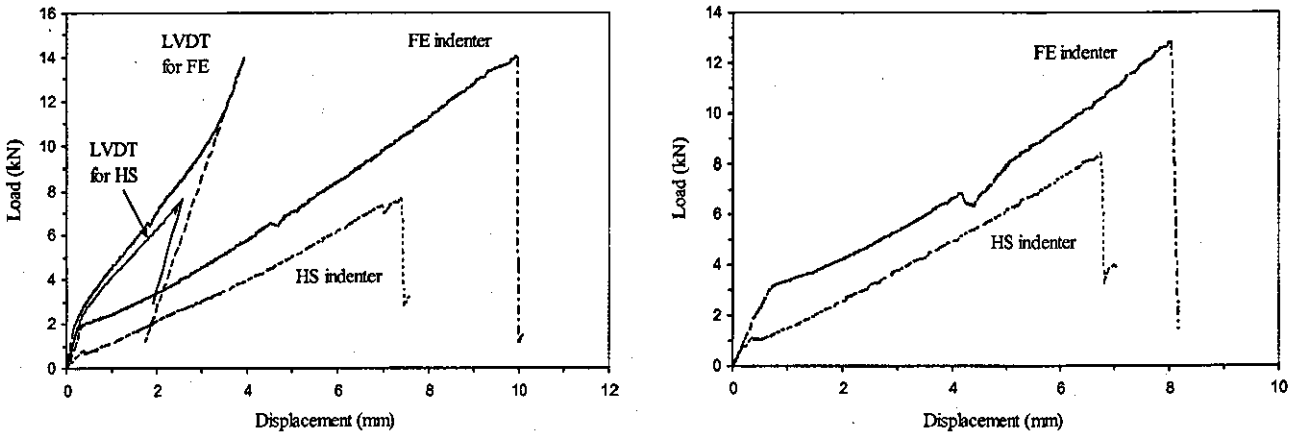

Figure B16 Effect of indenter nose-shape – 12 ply skins with
(a) 50kg/m^3 honeycomb (b) 70kg/m^3 honeycomb

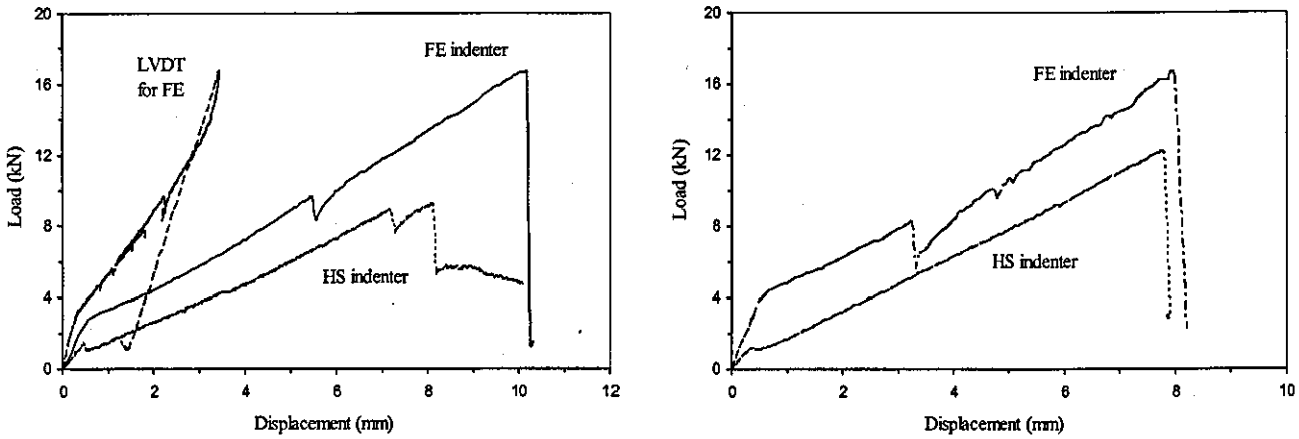

Figure B17 Effect of indenter nose-shape – 16 ply skins with
(a) 50kg/m^3 honeycomb (b) 70kg/m^3 honeycomb

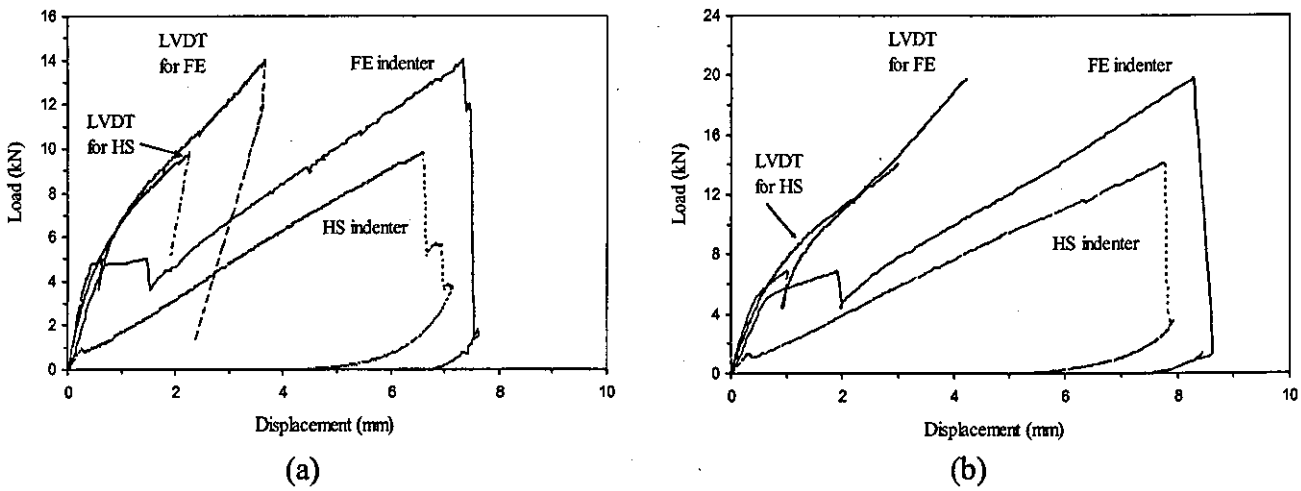

Figure B18 Effect of indenter nose-shape – 90kg/m^3 honeycomb with
(a) 12 ply skins (b) 16 ply skins

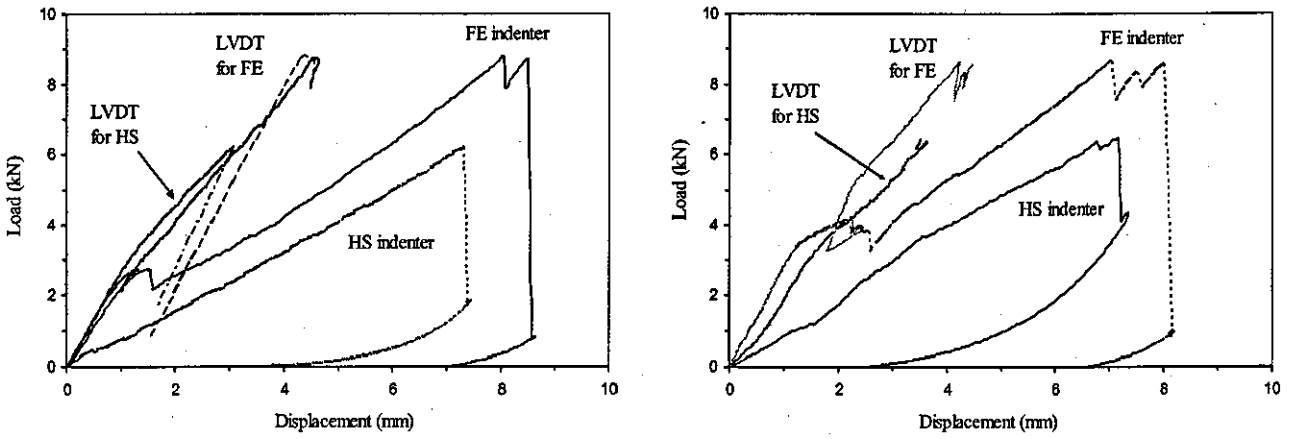

Figure B19 Effect of indenter nose-shape – 8 ply skins with
(a) 64kg/m^3 honeycomb (b) 96kg/m^3 honeycomb

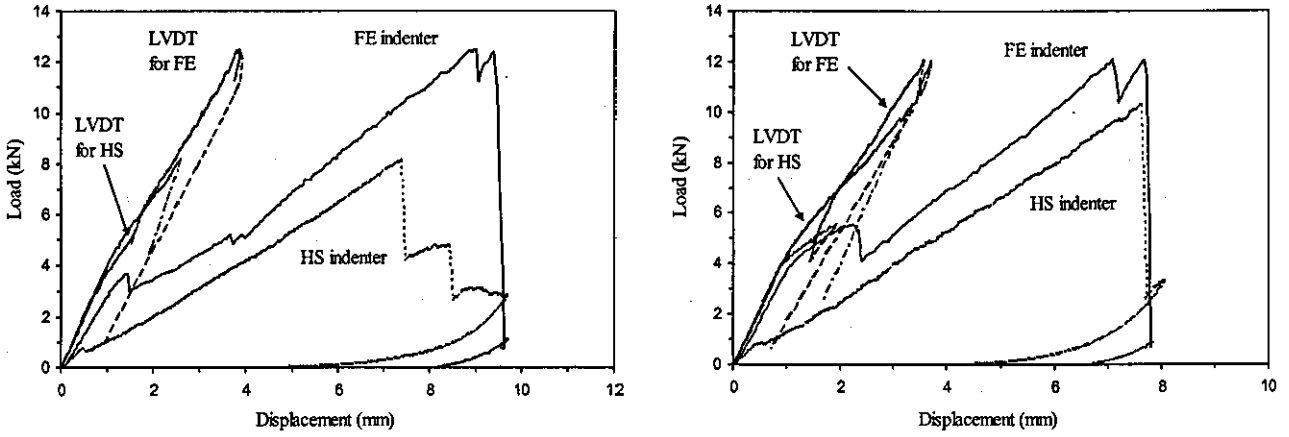

Figure B20 Effect of indenter nose-shape – 12 ply skins with
(a) 64kg/m^3 honeycomb (b) 96kg/m^3 honeycomb

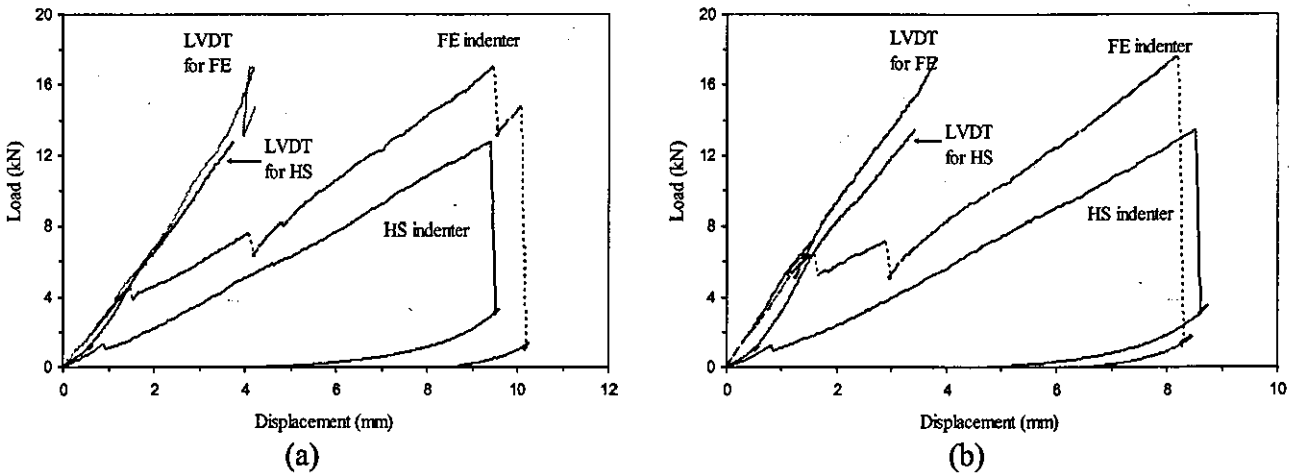

Figure B21 Effect of indenter nose-shape – 16 ply skins with
(a) 64kg/m^3 honeycomb (b) 96kg/m^3 honeycomb

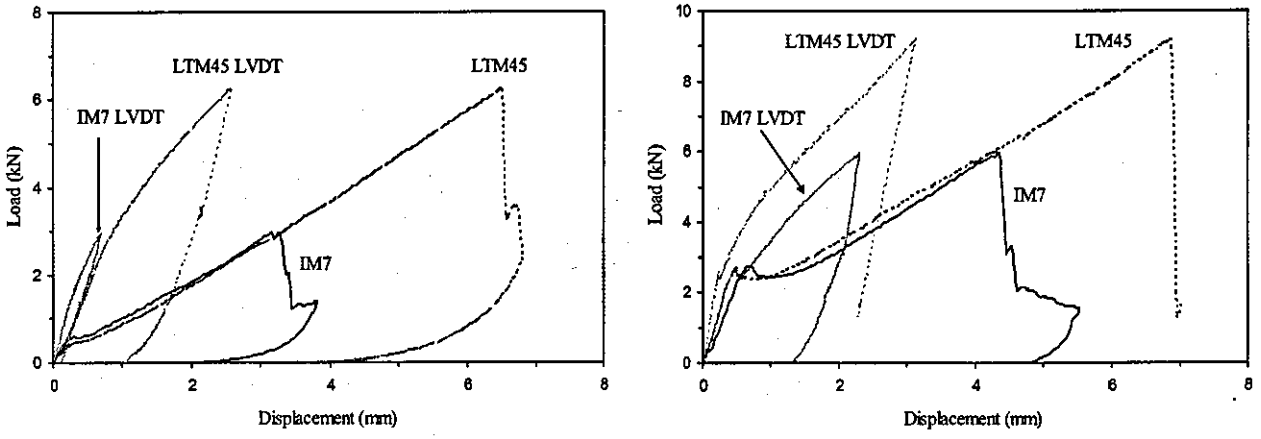

(a) (b)

Figure B22 Effect of skin material - 8 ply skins 70kg/m^3 aluminium core
(a) HS indenter (b) FE indenter

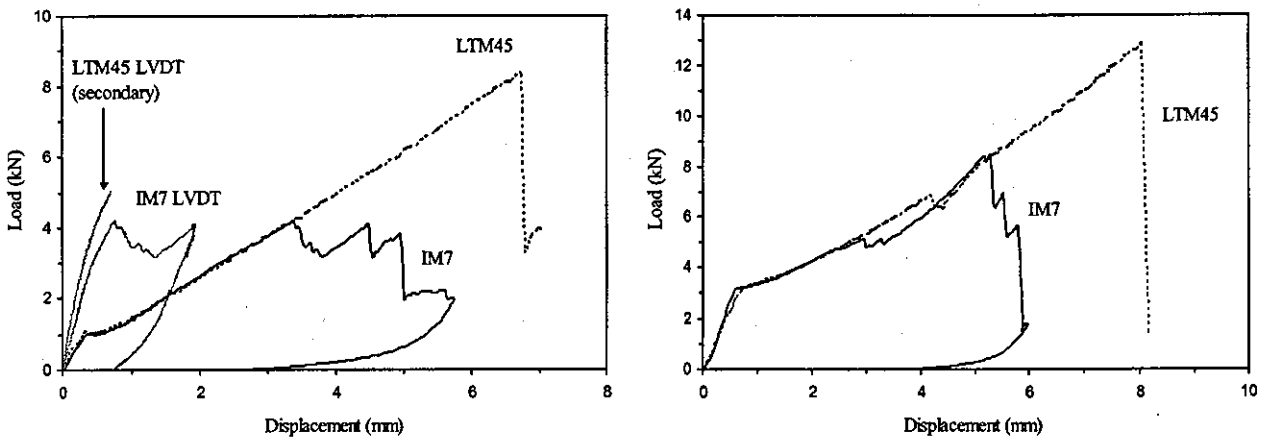

(a) (b)

Figure B23 Effect of skin material - 12 ply skins 70kg/m^3 aluminium core
(a) HS indenter (b) FE indenter

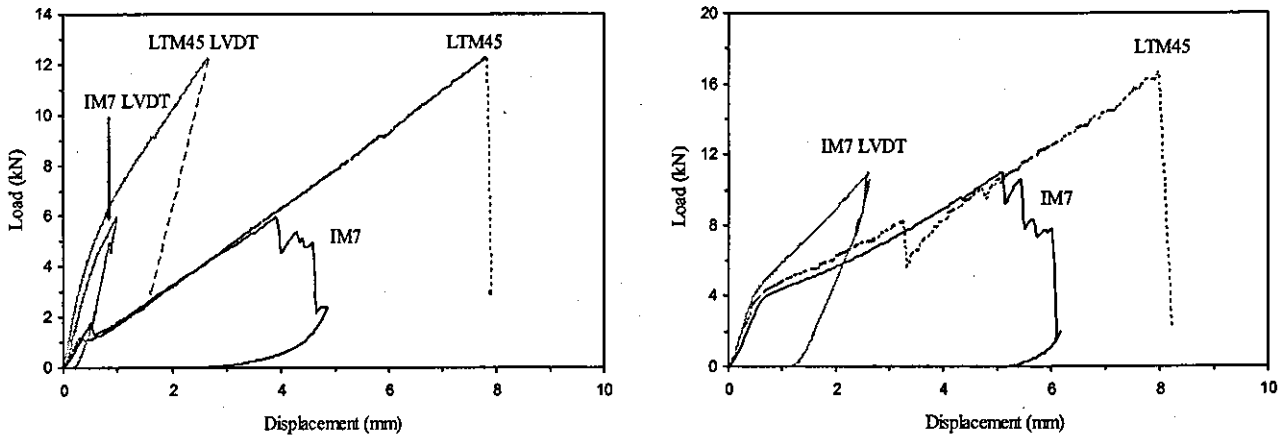

(a) (b)

Figure B24 Effect of skin material - 16 ply skins 70kg/m^3 aluminium core
(a) HS indenter (b) FE indenter

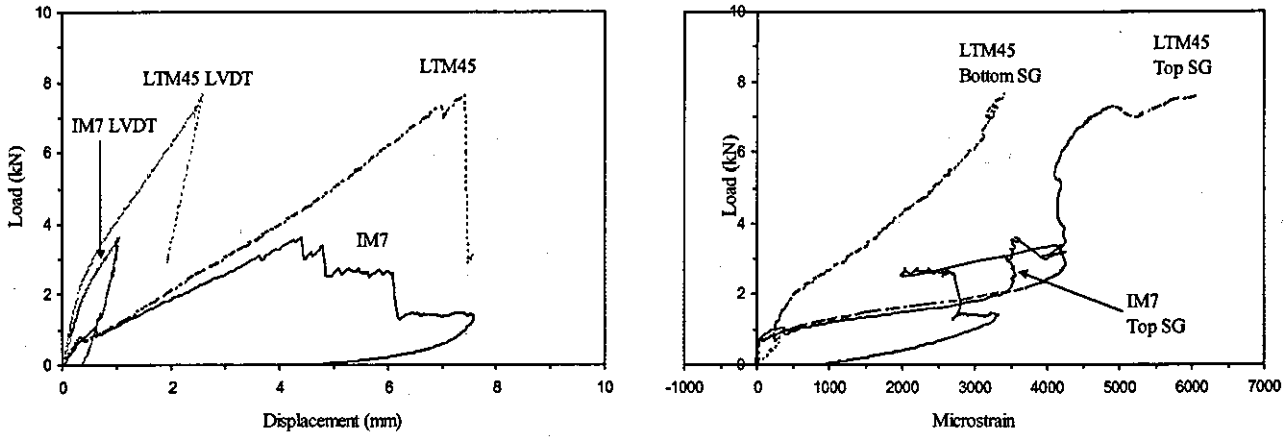

Figure B25 Effect of skin material - 12 ply skins 50kg/m^3 aluminium core loaded with HS indenter

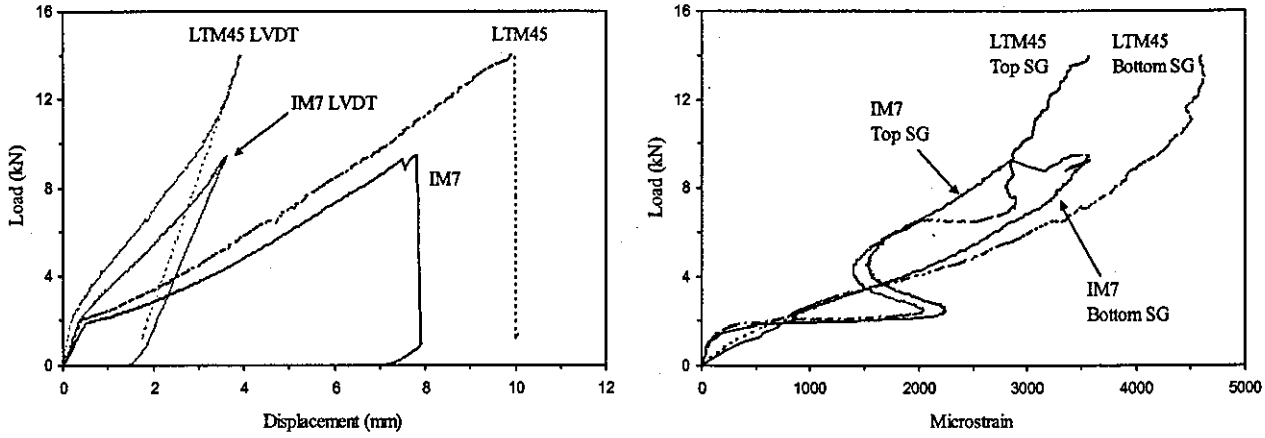

Figure B26 Effect of skin material - 12 ply skins 50kg/m^3 aluminium core loaded with FE indenter

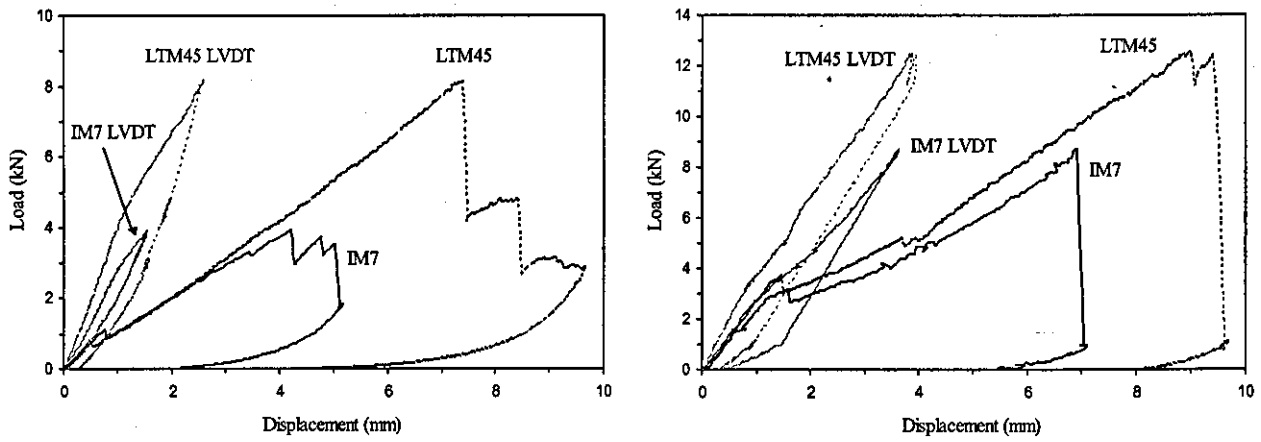

(a) (b)

Figure B27 Effect of skin material - 12 ply skins 64kg/m^3 nomex core
(a) HS indenter (b) FE indenter

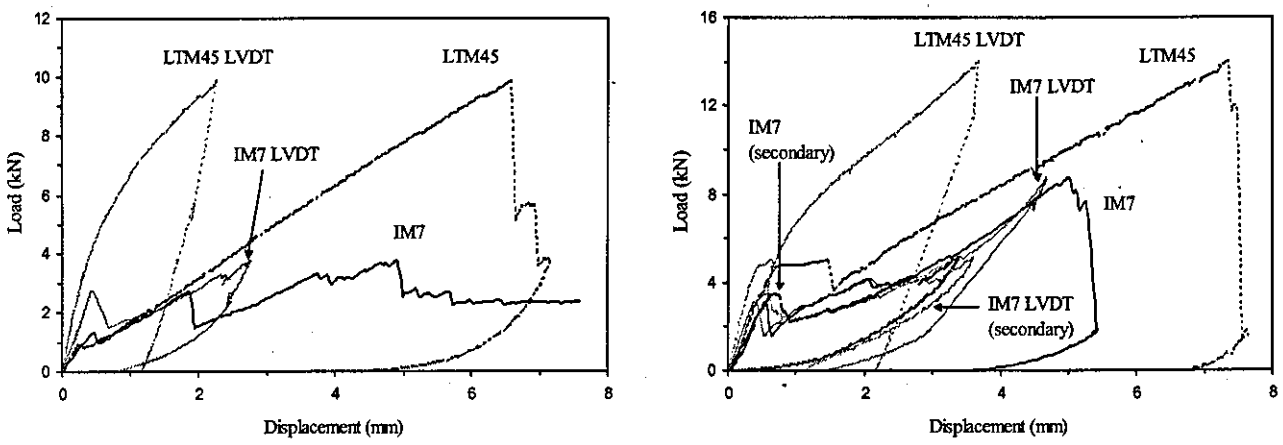

(a) (b)

Figure B28 Effect of skin material - 12 ply skins 90kg/m^3 aluminium core
(a) HS indenter (b) FE indenter

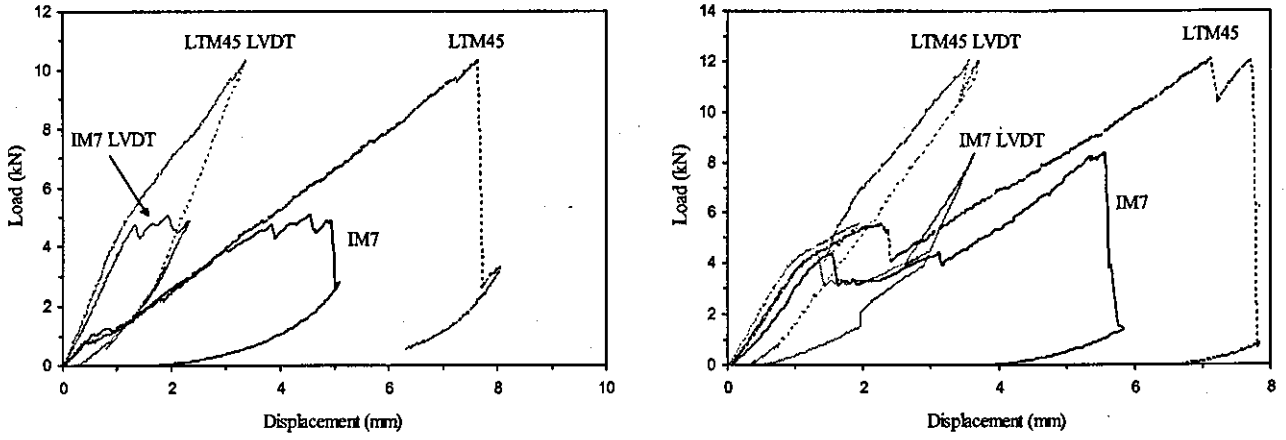

(a) (b)

Figure B29 Effect of skin material - 12 ply skins 96kg/m^3 nomex core
(a) HS indenter (b) FE indenter

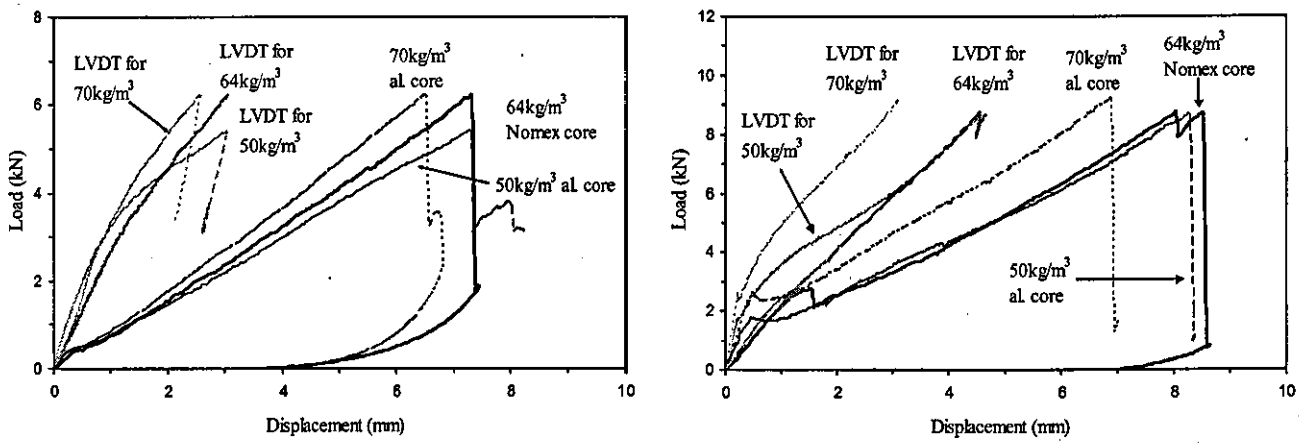

(a) (b)

Figure B30 Effect of core material - 8 ply skins 64kg/m^3 nomex & 50 & 70kg/m^3 aluminium
(a) HS indenter (b) FE indenter

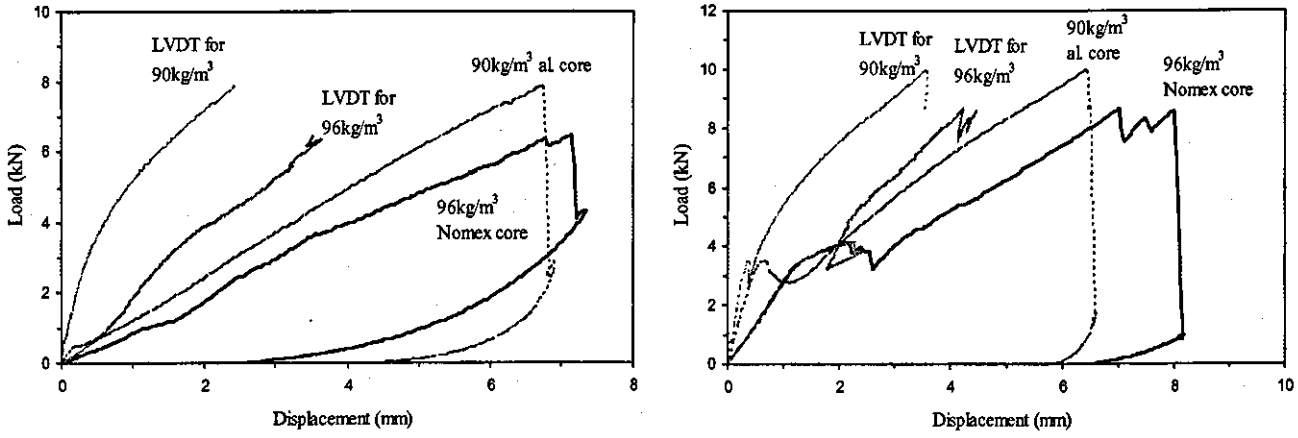

Figure B31 Effect of core material - 8 ply skins 96kg/m^3 nomex & 90kg/m^3 aluminium
(a) HS indenter (b) FE indenter

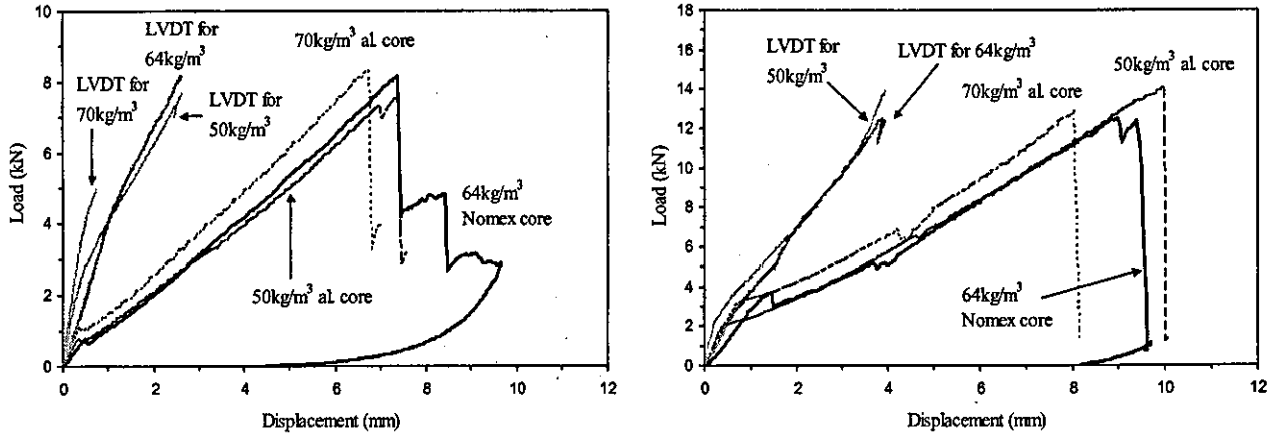

Figure B32 Effect of core material - 12 ply skins 64kg/m^3 nomex & 50 & 70kg/m^3 aluminium
(a) HS indenter (b) FE indenter

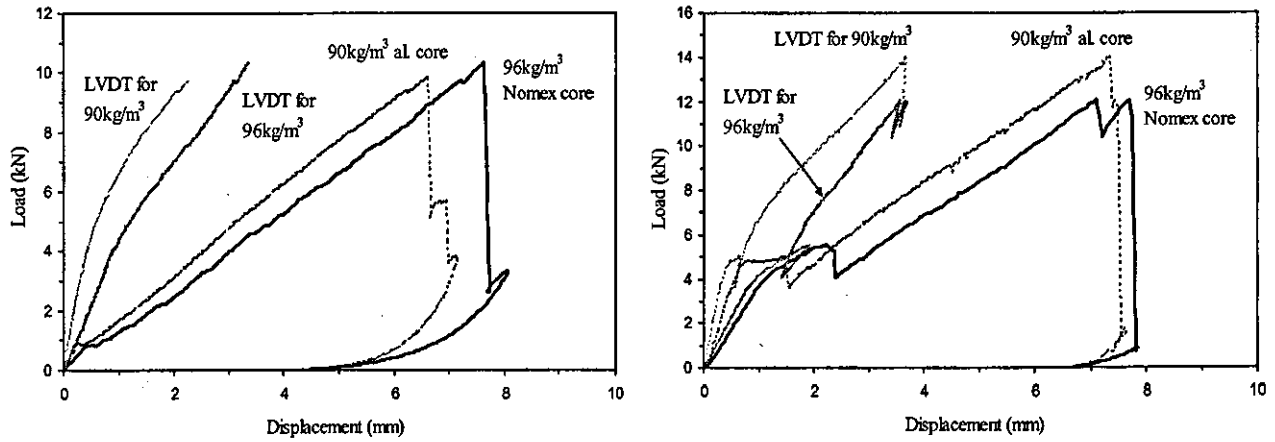

Figure B33 Effect of core material - 12 ply skins 96kg/m^3 nomex & 90kg/m^3 aluminium
(a) HS indenter (b) FE indenter

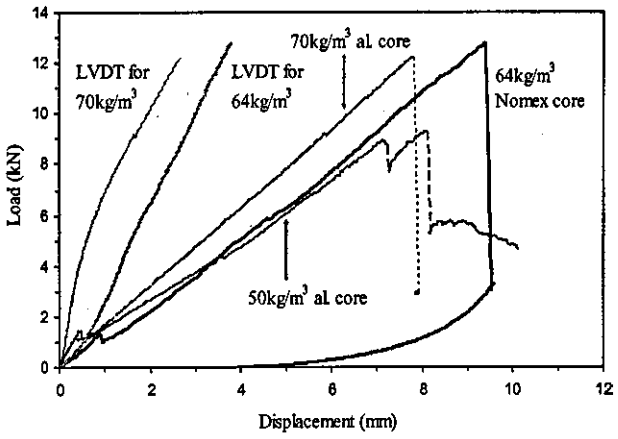

(a)

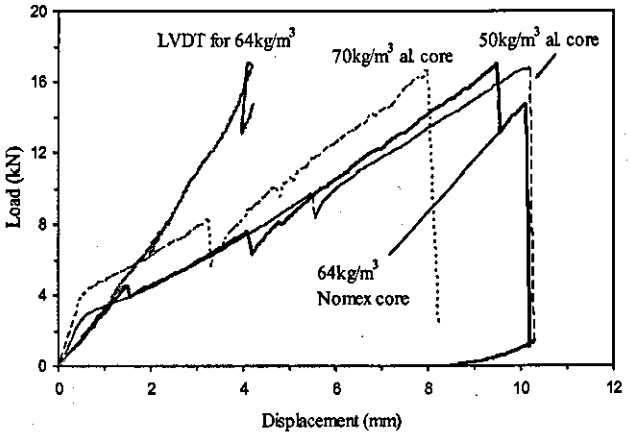

(b)

Figure B34 Effect of core material - 16 ply skins 64kg/m^3 nomex & 50 & 70kg/m^3 aluminium
(a) HS indenter (b) FE indenter

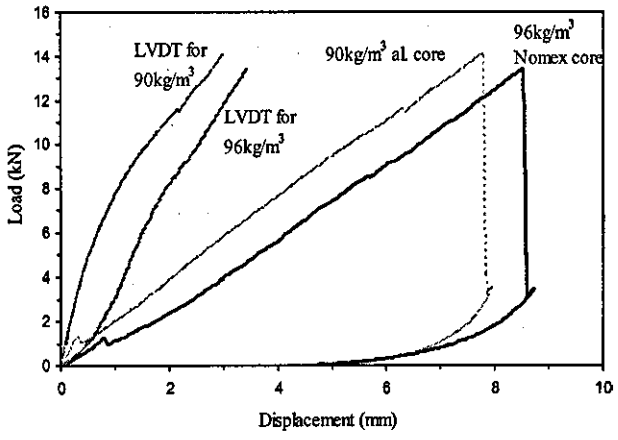

(a)

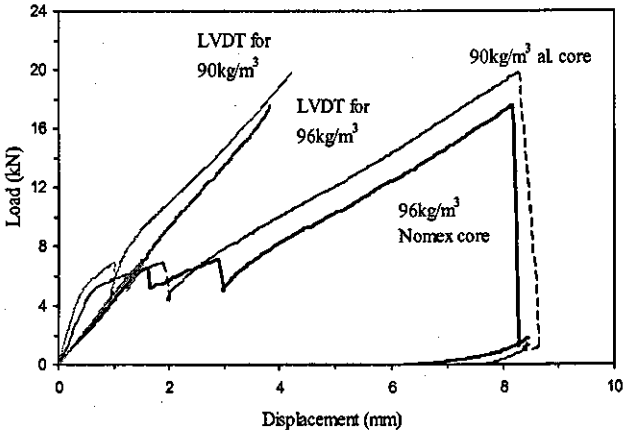

(b)

Figure B35 Effect of core material - 16 ply skins 96kg/m^3 nomex & 90kg/m^3 aluminium
(a) HS indenter (b) FE indenter

Appendix C – In-plane compressive response of individual specimens

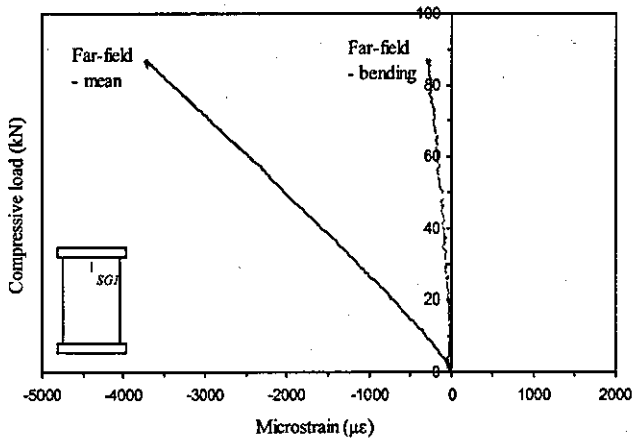

Figure C1 Mean and bending strain response of 8/70/CAI(0J)-1 panel, no failure due to limit of machine being reached prior to panel failure

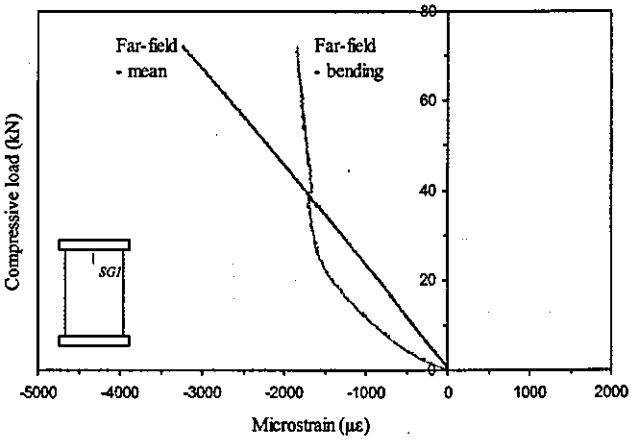

Figure C2 Mean and bending strain response of 8/70/CAI(0J)-2 panel, failure at loaded end

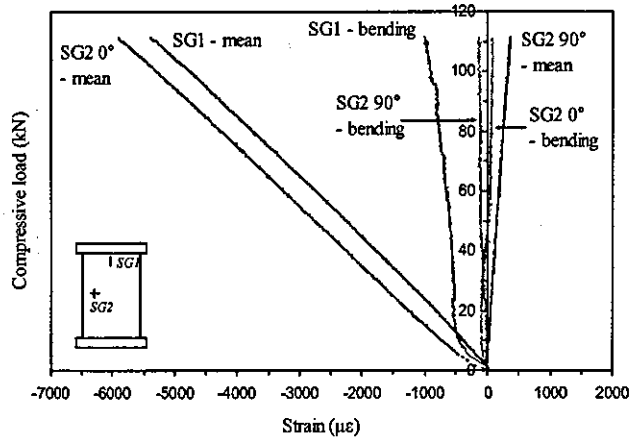

Figure C3 Mean and bending strain response of 8/70/CAI(0J)-3 panel, failure at loaded end

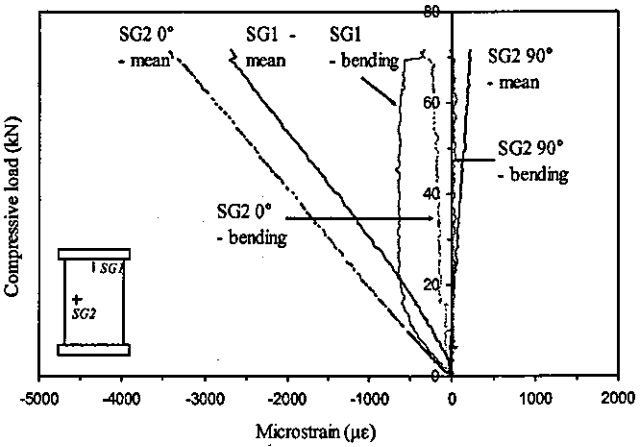

Figure C4 Mean and bending strain response of 8/70/CAI(2.5J) panel, failure at transverse mid-plane

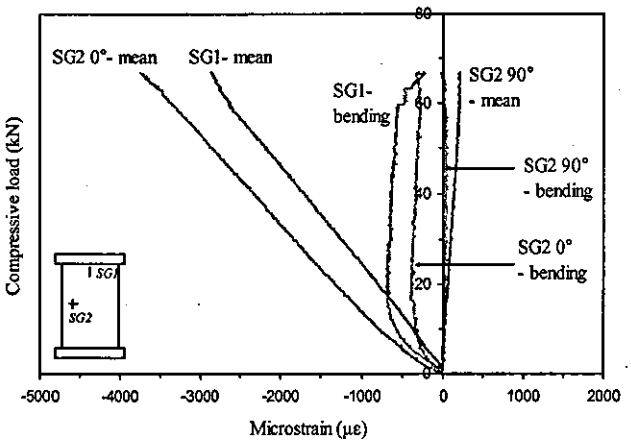

Figure C5 Mean and bending strain response of 8/70/CAI(3J)-1 panel, failure at transverse mid-plane

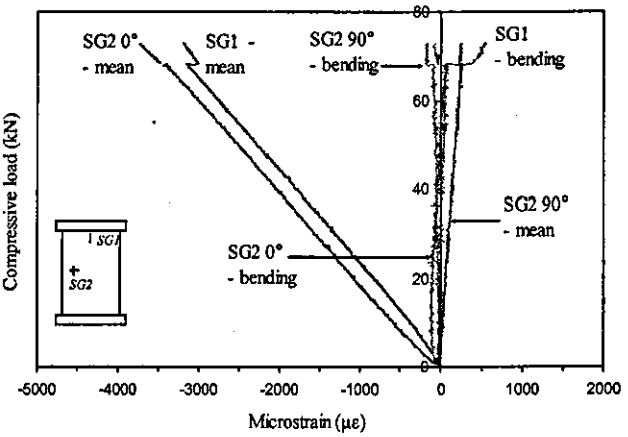

Figure C6 Mean and bending strain response of 8/70/CAI(3J)-2 panel, failure at transverse mid-plane

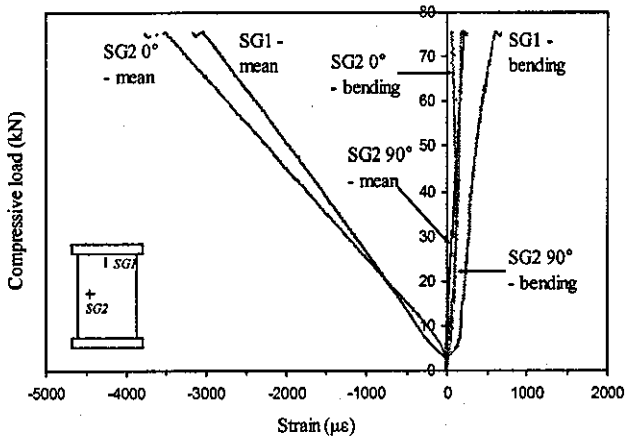

Figure C7 Mean and bending strain response of 8/70/CAI(5J)-1 panel, failure at bottom end of panel

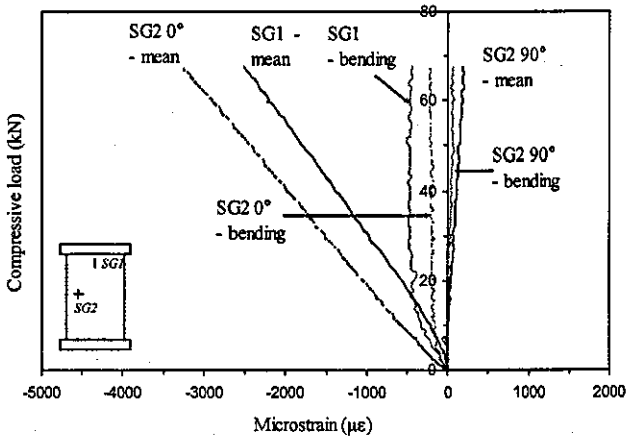

Figure C8 Mean and bending strain response of 8/70/CAI(5J)-2 panel, failure at transverse mid-plane

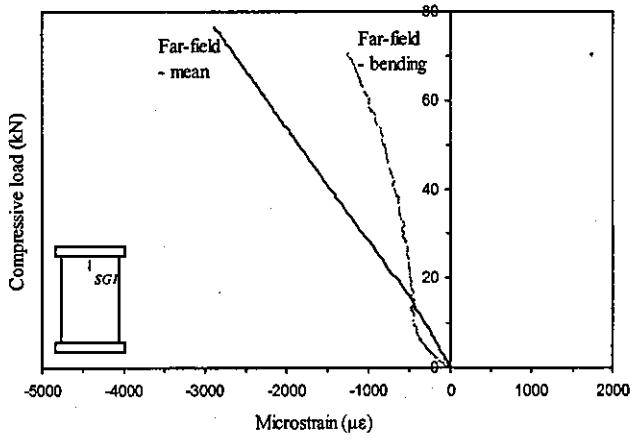

Figure C9 Mean and bending strain response of 8/70/CAI(9J)-1 panel, failure at transverse mid-plane

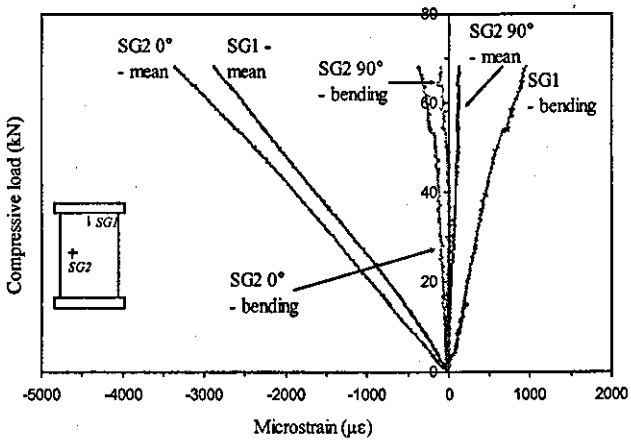

Figure C10 Mean and bending strain response of 8/70/CAI(9J)-2 panel, failure at loaded end

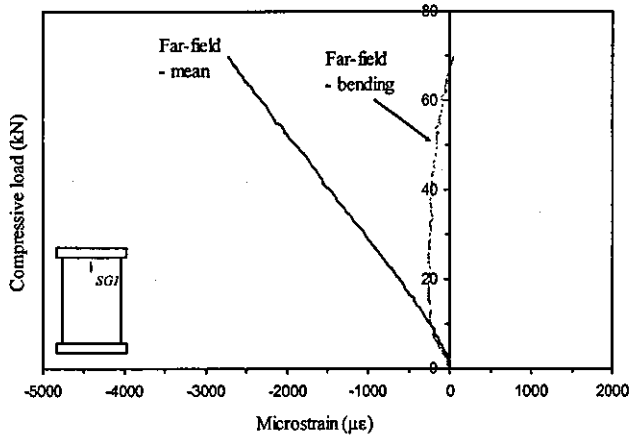

Figure C11 Mean and bending strain response of 8/70/CAI(14J)-1 panel, failure at transverse mid-plane

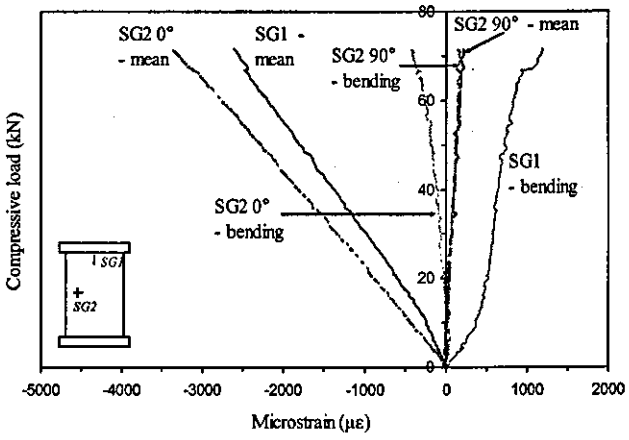

Figure C12 Mean and bending strain response of 8/70/CAI(14J)-2 panel, failure at transverse mid-plane

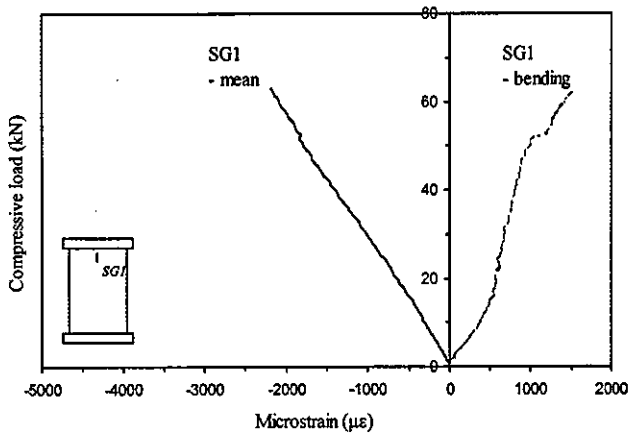

Figure C13 Mean and bending strain response of 8/70/CAI(25J)-1 panel, failure at transverse mid-plane

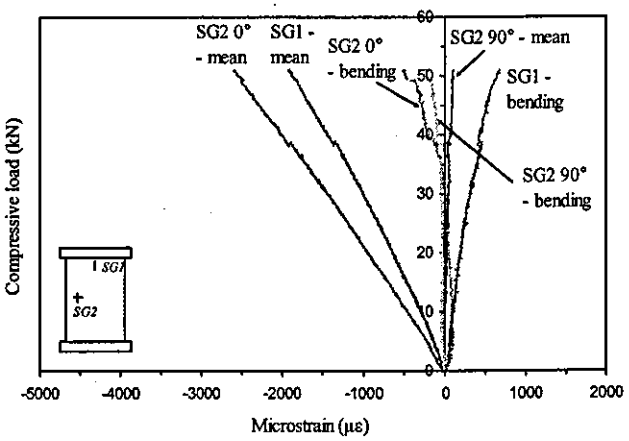

Figure C14 Mean and bending strain response of 8/70/CAI(25J)-2 panel, failure at loaded end

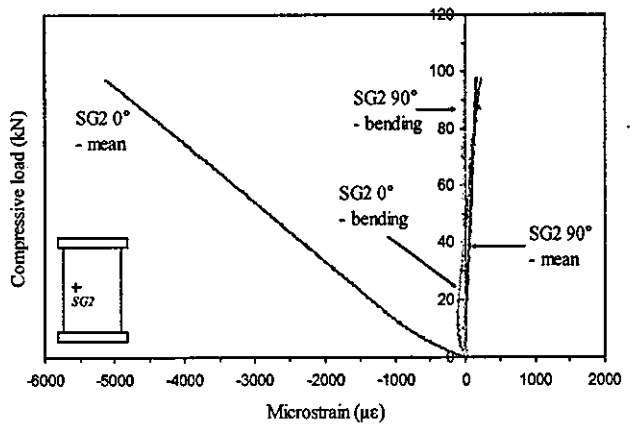

Figure C15 Mean and bending strain response of 8/64/CAI(0J)-1 panel, failure at loaded end

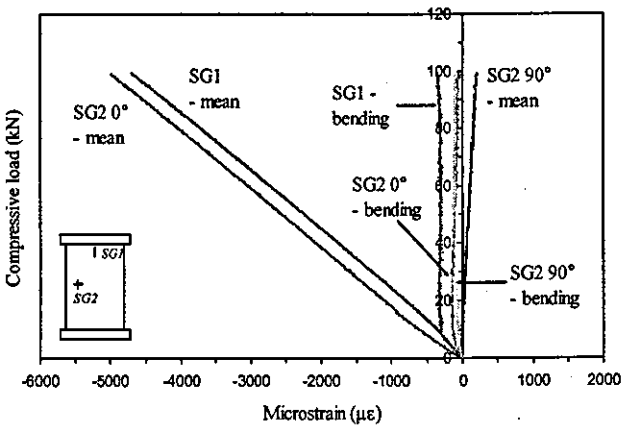

Figure C16 Mean and bending strain response of 8/64/CAI(0J)-2 panel, failure at loaded end

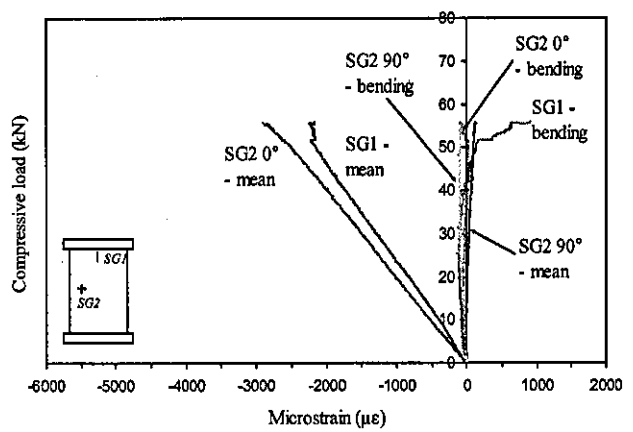

Figure C17 Mean and bending strain response of 8/64/CAI(5J) panel, failure at transverse mid-plane

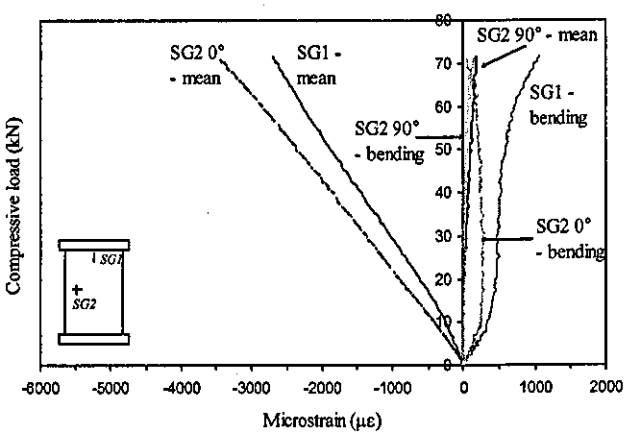

Figure C18 Mean and bending strain response of 8/64/CAI(9J) panel, failure at transverse mid-plane

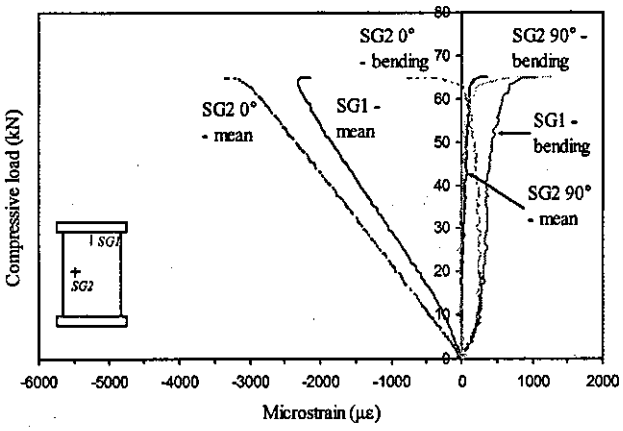

Figure C19 Mean and bending strain response of 8/64/CAI(16J) panel, failure at transverse mid-plane

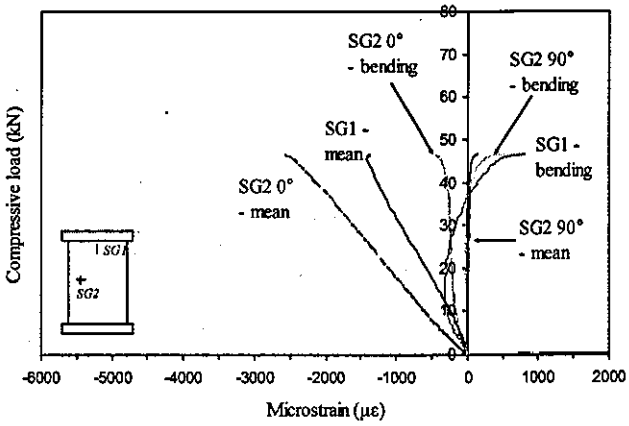

Figure C20 Mean and bending strain response of 8/64/CAI(28J) panel, failure at transverse mid-plane

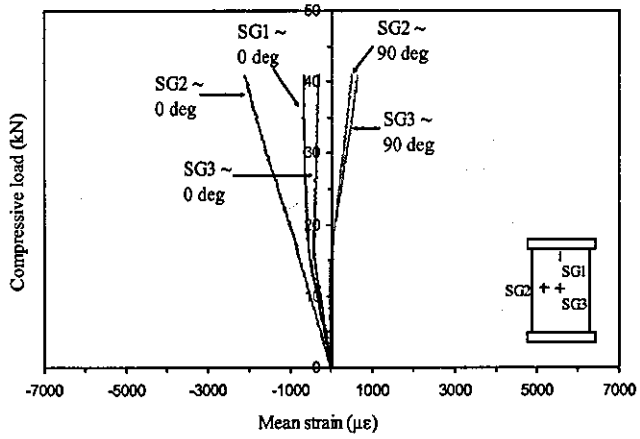

(a)

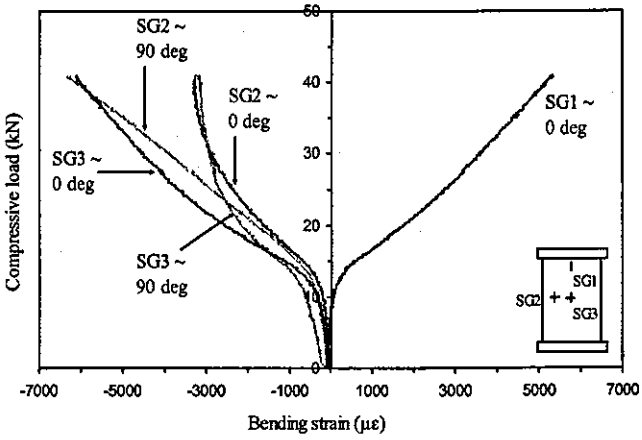

(b)

Figure C21 Strain response of 16/CAI(0J)-1 panel, failure at loaded end
(a) Mean strain (b) Bending strain

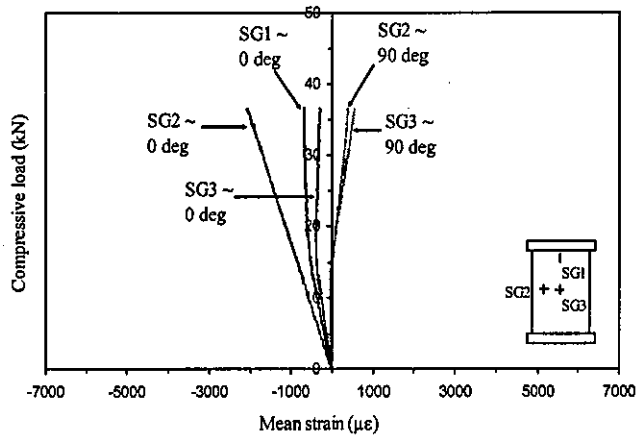

(a)

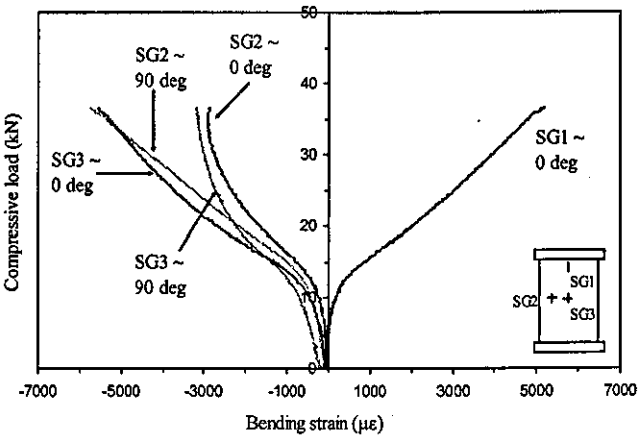

(b)

Figure C22 Strain response of 16/CAI(0J)-2 panel, failure at loaded end
(a) Mean strain (b) Bending strain

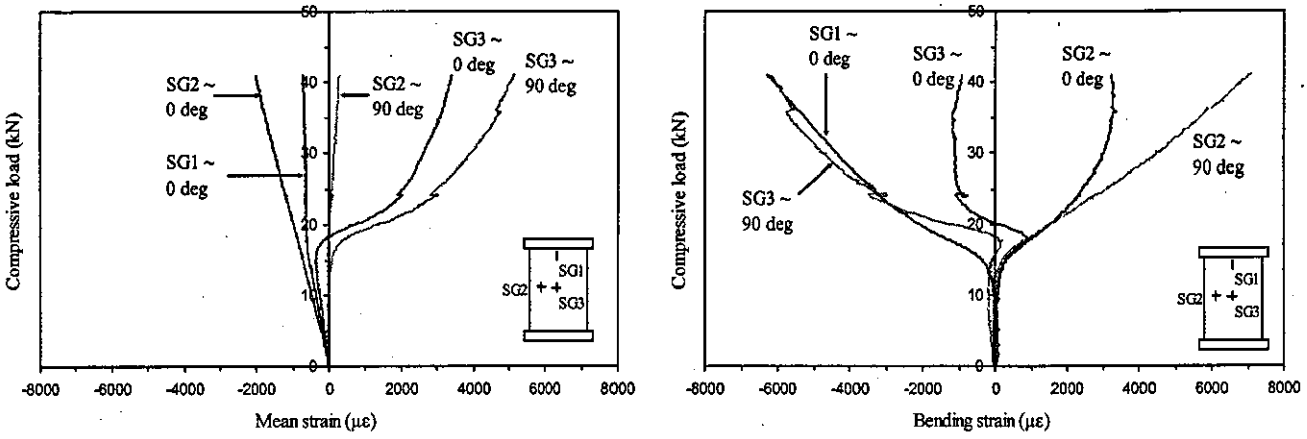

(a) (b)

Figure C23 Strain response of 16/CAI(2.5J) panel, failure at loaded end
(a) Mean strain (b) Bending strain

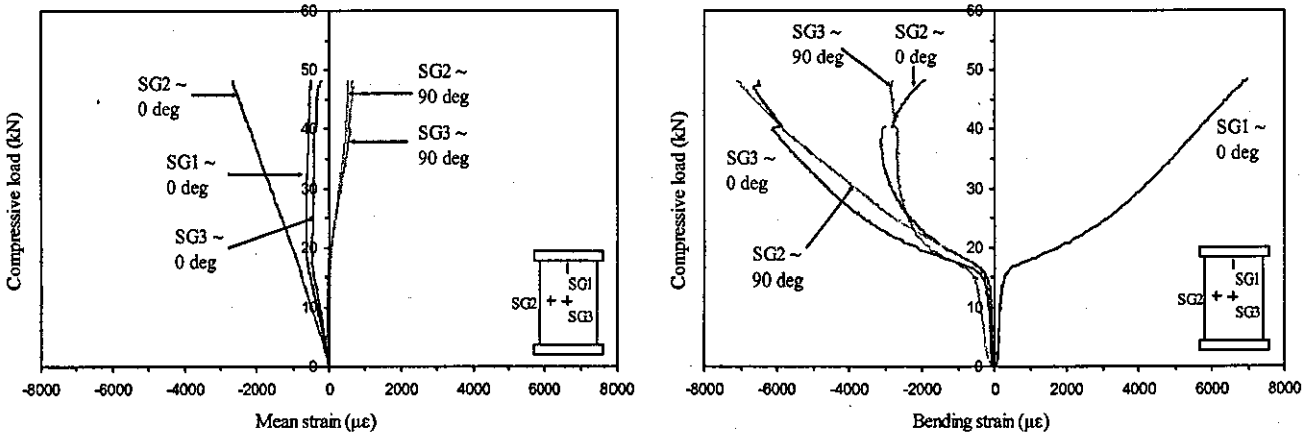

(a) (b)

Figure C24 Strain response of 16/CAI(5J) panel, failure at loaded end
(a) Mean strain (b) Bending strain

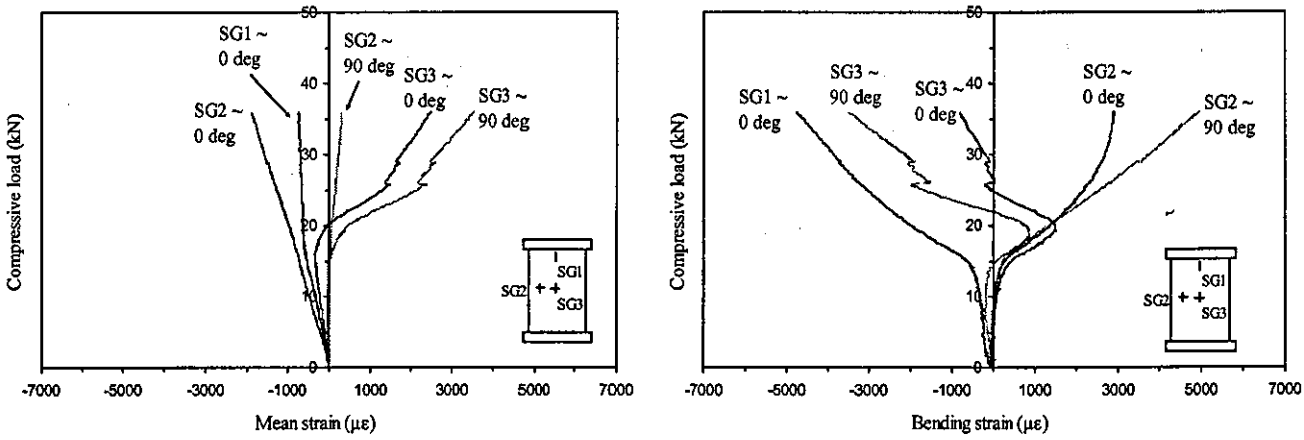

(a) (b)

Figure C25 Strain response of 16/CAI(10J) panel, failure at loaded end
(a) Mean strain (b) Bending strain

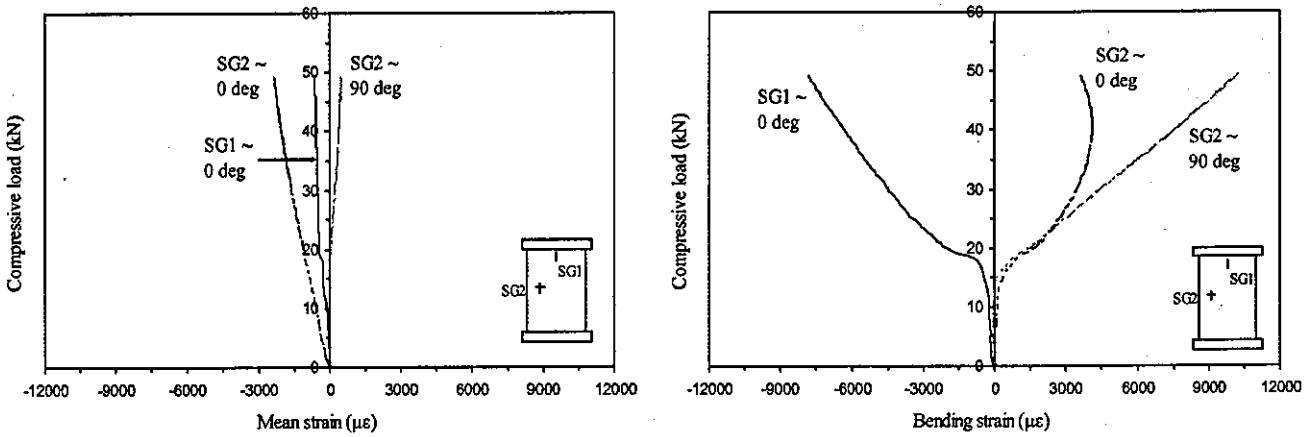

(a) (b)

Figure C26 Strain response of 16/CAI(20J) panel, failure at loaded end
(a) Mean strain (b) Bending strain

Appendix D – Manufacturing and testing procedures

D1 Laminate Skin Manufacture

Lay-up Procedure

1. Clean all work surfaces with acetone to remove grease and dust. Ensure gloves are worn at all times when handling the prepreg to prevent contamination.
2. Remove the carbon fibre prepreg roll from the freezer.
3. Mark and cut a 300mm length from the roll using a sharp knife, ensuring the cut is perpendicular to each edge, mark the fibre direction with a pen and return the cut length to the freezer wrapped in an airtight plastic freezer bag.
4. Repeat the above steps until the required number of layers has been cut and return the prepreg roll to the freezer.
5. To ensure the laminate is laid-up correctly make a simple tick sheet before beginning the lay-up process. An example of a tick sheet is shown in Fig. 2.5.
6. Remove one ply from the freezer and peel off one of the backing sheets.
7. Place the ply on the lay-up table such that the fibres are orientated in the 0° direction (see Fig. 2.4).
8. Remove another ply from the freezer and peel off one of the backing sheets.
9. Carefully place the 2nd ply on top of the 1st ply with the fibres orientated in the 90° direction. When putting the 2nd ply on top of the 1st ply ensure all edges are in line and the plies are perpendicular to each other. Ensure no air bubbles are present
10. Replace the two ply lay-up in the freezer in the plastic bag to refreeze the plies before adding the next ply.
11. Remove the two ply lay-up from the freezer and place back on the lay-up table ensuring the fibres are aligned as before and remove the top backing sheet.
12. Remove another ply from the freezer, peel off one backing sheet and place on top of the two ply lay-up with the fibres orientated in the 0° direction.
13. Repeat the above process until all the plies have been laid-up, as shown in the tick sheet (Fig. 2.5), ensuring the laminate is symmetrical about the mid-plane. (i.e. for the 8 ply laminate the 4th and 5th plies are both orientated in the 90° direction).
14. Once each ply has been laid-up write the number of plies contained in the laminate on one of the backing sheets and place the finished laminate in the freezer sealed in an airtight plastic bag.

Curing Procedure

1. To cure the laminate in the autoclave a number of consumable materials are required. A diagram of the autoclave set-up and material arrangement is shown in Fig. 2.6.
2. Cut out the following materials
   - 2 pieces of porous PTFE 330mm × 330mm
   - 4 pieces of bleeder fabric 400mm × 400mm
   - 1 piece of bagging film 320mm × 320mm
   - 1 piece of bagging film 600mm × 600mm
   - 1 piece of breather fabric 400mm × 400mm
   - 1 piece of non-porous PTFE 450mm × 450mm

3. Remove the laminate from the freezer, place on the lay-up table and remove one of the backing sheets.
4. Place one sheet of porous PTFE on top of the laminate. Starting from the centre and working outwards gently smooth out all of the wrinkles such that the PTFE sticks smoothly to the laminate surface. Any wrinkles or folds in the PTFE will be permanently imprinted onto the laminate surface once it has been cured and may impair its performance and affect any subsequent bonding.
5. Turn the laminate over and repeat the above procedure so the porous PTFE is on both surfaces of the laminate.
6. Place the non-porous PTFE sheet on the autoclave base plate, ensuring it is significantly larger than the laminate to be cured to prevent any excess resin coming into contact with the autoclave base.
7. Place 2 layers of bleeder fabric on top of each other in the centre of the non-porous PTFE on the autoclave base.
8. Place the porous PTFE covered laminate centrally on top of the bleeder fabric ensuring the bleeder fabric is flat.
9. Place the other 2 pieces of bleeder fabric on top of the porous PTFE on the laminate.
10. Place the 320mm × 320mm piece of bagging film on top of the bleeder fabric. This piece must be smaller than the bleeder fabric to allow an air path for the vacuum.
11. Carefully place a caul plate of size 300mm × 300mm on top of the bagging film, ensuring all layers of material placed between the caul plate and the laminate are perfectly flat and the caul plate is directly above and in line with the laminate.
12. Place the breather fabric on top of the caul plate so that all corners and edges of the caul plate are covered to prevent the caul plate piercing a hole in the vacuum bagging film.
13. Cover the vacuum holes at the rear of the autoclave base plate with a piece of breather fabric. This is to prevent any excess resin being sucked into the vacuum holes during curing should excessive resin flow occur. It should also overlap with the breather fabric covering the laminate to allow an air path for the vacuum.
14. Place the 600mm × 600mm piece of bagging film over the autoclave, materials and laminate. Ensure there is plenty of slack in the bagging film around the laminate to prevent tearing when the pressure is applied. Also ensure the bagging film extends past the edges of the autoclave base to allow a perfect seal and vacuum to be formed when the autoclave is switched on.
15. To ease the closing up of the autoclave make 2 small holes in the bagging film over the 2 locator pin holes in the autoclave base corners.
16. Check all rubber seals are intact and in place on the autoclave base and spacer plate and place the spacer plate on the autoclave base, trapping the bagging film between the autoclave base and the spacer plate. Ensure there are no wrinkles or folds in the bagging film as it passes between the seals.
17. Align the spacer plate and insert the locator pins to ensure alignment.
18. Place the autoclave lid on top of the spacer plate at an angle, remove the pins, align lid and re-insert the pins.
19. Connect up the air hose at the rear of the autoclave.
20. Clamp the autoclave firmly shut with the clamping bars and tighten bolts to 25-30Nm. When tightening the clamping bolts tighten opposite corners sequentially. If the bolts are over tightened then there is a risk of damaging both the seals and the bolt threads.

21. Set the autoclave program controller to the desired cycle, as defined below.
22. Switch on the autoclave and the vacuum pump. The vacuum should read around 25mmHg. The vacuum must be switched on before the pressure is applied to prevent damage to the pump by air being forced through it.
23. Slowly apply the required pressure. If a hissing sound can be heard the seal is leaking, most likely due to wrinkles in the bagging film. Release the pressure, remove clamps and identify cause of leak. Replace lid and clamps as stated above.
24. Set the autoclave program controller to 'run'. Check the autoclave periodically during curing.
25. Once the curing cycle is complete allow the autoclave to cool to around 25°C before releasing the pressure and turning off the vacuum.
26. Turn off the autoclave main switch and remove the clamps, lid and seal plate.
27. Take the laminate out of the autoclave and remove all of the consumable materials.

Autoclave Operation

Display

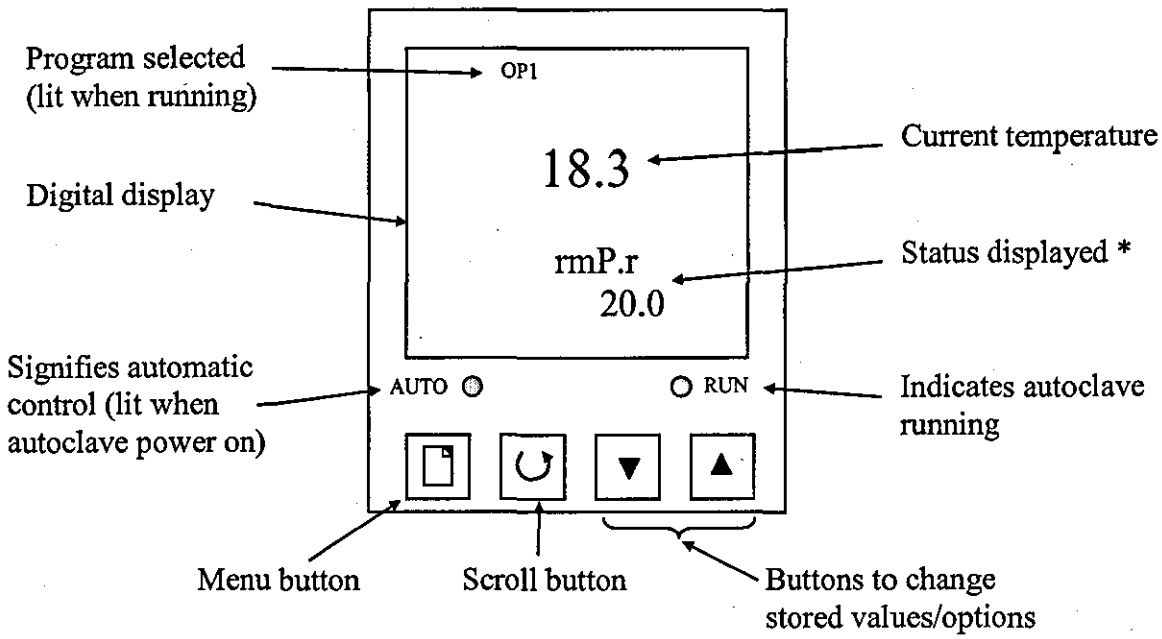

* Status displayed: When ramping *rmP.r* and target temperature (1-2° above current temperature) displayed.
During curing *dwell* and target temperature (as set in program, generally 60°) displayed
During all stages of operation *1LSP* and *2HSP* flash intermittantly.

To run a stored program

1. Press the menu button twice to display: run → List
2. Press the scroll button once to display: Stat → OFF
3. Press the down arrow button once to display: Stat → run
4. The autoclave is now running. *OP1* at the top of the display and the 'run' light in the bottom righthand corner will light up. The digital display will show the current temperature with *rmP.r*, the target temperature, *1LSP* and *2HSP* flashing routinely at the bottom of the display.

To check or change a stored program

1. Press the menu button 3 times to display: ProG → LiSt
2. Press the scroll button to scroll through the options.

   Note: The settings for a 18 hour cure at 60° are shown below. If a different cure cycle is required the settings shown below in bold can be changed by pressing the up and down arrows. If additional segments are required (e.g. when curing IM7/8552) changing segment 3 from *tYPE → End* to *tYPE → rmP.r* will allow additional segments to be programmed. (Please refer to manual for more details).

   When scrolling through the menu if a button is not pressed for several seconds the screen will return to the initial temperature display.

   Hb → OFF
   Hb U → 0.0
   rmP.U → min
   dwL.U → Hour
   CYC.n → 1
   SEG.n → 1
   tYPE → rmP.r
   tGt → **60.0**
   rATE → 2.0
   SEG.n → 2
   tYPE → dwEll
   dur → (hour) **18.0**
   SEG.n → 3
   tYPE → End
   End.t → rSEt

3. Pressing the scroll button again will return the display to: ProG → LiSt
4. If another button is not pressed the display will automatically return to the temperature display screen.

It is imperative that the last segment is an End segment and the *End.t → rSEt* must be selected otherwise the autoclave will not switch off at the end of the cure cycle.

D2 Sandwich Panel Manufacture

1. The honeycomb core material is supplied in 1400mm × 3000mm × 12.7mm sheets, so must be cut to the required size, ensuring the piece is approximately 50mm larger than the laminate skin to ensure good laminate core bonding at the panel edges and to prevent any cells damaged during cutting being contained within the bonding area.
2. Inspect the honeycomb for any existing damage, such as cell wall buckling and cell distortion. Measure out a piece 330mm × 330mm containing no damage such as cell wall buckling or distortion.
3. Using a sharp knife and long metal ruler cut out the piece of honeycomb, do not lean on the honeycomb when cutting and handle with care as the cell walls are easily damaged.
4. If not using the honeycomb immediately cut several pieces of protective bubble wrap (contained in the honeycomb box) and use them to wrap the honeycomb piece. This is to prevent damage through handling and storage.
5. When ready to bond the honeycomb to the skin gently blow the surface to remove any dust. Acetone can be used to remove grease but extreme care must be taken to prevent fibres from the cleaning cloth sticking to the honeycomb cell walls.
6. Clean the surfaces of the laminate skin with acetone to remove dust and grease.
7. Clean the surface of the 5mm thick steel tray kept beneath the oven.
8. Cut 1 piece of bagging film measuring 350mm x 350mm and place on the steel tray.
9. Place the skin to be bonded on the bagging film with the bond surface facing upwards, noting the direction of the fibres
10. Remove the adhesive roll from the freezer and allow to thoroughly defrost prior to unbagging and unrolling, so as not to damage the bonds and mesh material within the adhesive which are brittle when frozen.
11. Cut 2 sheets of adhesive measuring 310mm × 310mm using a pair of sharp scissors. Return one sheet to the freezer wrapped in an airtight plastic bag.
12. Remove the blue plastic backing sheet from one sheet of adhesive, lay face down on top of the laminate and remove the white backing sheet
13. Position the honeycomb on top of the adhesive such that the L-direction of the honeycomb is parallel with the laminate 0° fibre direction, ensuring any damaged cells at the edge of the honeycomb are not contained within the bonding area.
14. Place the second skin on top of the honeycomb. This is to prevent damage to the honeycomb by the steel caul plate used to apply pressure.
15. To provide the required pressure during curing, as stated in Table 2.12, carefully place the steel caul plate on top of the second skin/honeycomb lay-up, and ensure it is aligned directly above the bottom skin.
16. Place the steel tray and lay-up in the oven and check the lay-up is level using a spirit level. The lay-up must be level during curing to prevent the honeycomb sliding on the skin as the adhesive melts and to ensure a consistent bond line thickness.
17. Add steel weights spread evenly across on top of the caul plate if additional weight is needed to obtain the required pressure, as per Table 2.11.
18. Close the oven and heat to the required temperature, as stated in Table 2.12. Once the oven has reached the required temperature start timing, and leave to cure for the required time, see Table 2.12. (As the oven does not automatically switch off a simple plug timer can be used to switch the power off at the required time).

19. Once curing is complete, leave the oven to cool for 1-2 hours before removing the panel, as the cured adhesive must be cooled slowly to prevent damage occurring due to rapid cooling.
20. Once cooled remove from the oven and trim off the excess honeycomb with a Stanley knife taking care not to damage the cell walls. This will make it easier to align the second skin directly above the first skin.
21. The process to bond the second skin is identical to the above except the caul plate can be placed directly on the previously bonded skin.
22. To prevent the second skin becoming misaligned during curing masking tape can be stuck along the corner edges of the first skin then wrapped around the second skin, holding it in place. This will also help to ensure the skins are aligned directly above each other.
23. Once bonded the sandwich panel edge can be trimmed and individual specimens cut using the diamond edged tile cutter.

D3 Specimen Strain Gauging

The strain gauges are positioned in the 0° fibre direction. The strain gauge bonded to the top surface must be positioned 20mm away from the loading centre to prevent the indenter coming into contact with the strain gauge during loading. The second strain gauge is located at the centre of the bottom surface of the panel, directly in-line with the loading point. In a number of the early tests an additional strain gauge was located on the top skin of the panel 20mm away from the loading centre at 45°.

1. Lightly sand the regions where strain gauges are to be bonded and clean with acetone to give a good surface for adhesion.
2. Using a marker pen, locate the centre of the top skin by draw diagonal lines joining each corner together.
3. Using the steel clamping plate draw a circle of 100mm diameter centred in the middle of the panel. This circle is used to centre the panel quickly and easily in the testing apparatus.
4. Draw a 30mm line from the centre of the panel towards the top edge, parallel to the 0° fibres.
5. Measure 20mm along the line away from the centre of the panel and draw a line in the direction of the 90° fibres, creating a cross. This locates the centre of the 0° strain gauge.
6. Turn the panel over and repeat step 2 to identify the centre of the bottom surface.
7. In the centre of the panel draw a short line in the 0° and 90° fibre directions, creating a cross. This marks the centre of the bottom 0° strain gauge. A diagram of how each surface should look is shown in Fig. 3.1.
8. Using tweezers remove the strain gauge from the plastic sheath and place on the panel with the surface to be bonded facing downwards. Do not handle the strain gauge directly as the bonding surface of the gauge is pre-cleaned and will easily pick up grease and dirt.
9. Cut a piece of non-stick paper and position next to the strain gauge such that the edge of the gauge just touches the paper with the terminal wires lying on top of the

paper. The non-stick paper is used to prevent the terminal wires from sticking to the panel surface.

10. To allow the gauge to be moved and positioned easily without direct handling cut a length of sellotape about 8cm long and place over the strain gauge and non-stick paper.
11. Position the gauge over the position markings on the panel, so the silver arrows on the gauge are aligned with the marking lines on the panel and the terminal wires are pointing towards the edge of the panel.
12. Peel back the sellotape until the bonding surface of the strain gauge is accessible.
13. Place one drop of quick-drying isocianate superglue on the bonding surface of the strain gauge. Stick the sellotape back down and gently smooth. Only apply a very small amount of pressure to the gauge to prevent inducing pre-strain in the gauge.
14. Leave to dry for 5 minutes then carefully remove the sellotape, taking care not to pull off the terminal wires. If bonded correctly the strain gauge should be dark red in colour. If any light red patches are visible air is trapped beneath the gauge.
15. Using the tweezers carefully bend the terminal wires back over the gauge.
16. Cut out one terminal from the sheet of terminals.
17. Place one drop of glue on the panel surface next to the end of the strain gauge with the terminal wires. Position the terminal so that it is just touching the strain gauge. Apply a small amount of pressure to the terminal and leave to dry.
18. Bend the terminal wires back down and position above the gold terminal contacts. Cut the terminal wires to the same length as the contacts to prevent the terminal wires coming into contact with the panel surface during testing (as carbon is a good electrical conductor).
19. Using a soldering iron, solder the left terminal wire to the left contact and the right wire to the right contact. The solder on each contact must not touch the other contact else the terminals will be bridged and the strain gauge will give incorrect readings. If bridging does occur the solder can be melted and removed using the soldering iron and the process repeated. When soldering ensure the soldering iron does not touch the panel surface as it can damage the laminate.
20. To enable the strain gauge to be connected to the computer solder a length of insulated electrical wire to each terminal, again ensuring the terminals are not bridged.
21. Check the resistance of the strain gauge using an ohmmeter. The resistance should be $120\Omega \pm 0.3\Omega$ if the gauge has been bonded and soldered correctly. If the resistance differs from this value check the terminals are not bridged and the electrical wires are firmly in place.
22. Stick the electrical wires to the panel surface with a small piece of sellotape to prevent the wires being pulled off accidentally during storage and test set-up. Using masking tape label each wire to avoid confusion during test set-up
23. Make a note of the strain gauge factor written on the packet, as it will need to be used when programming the data logger.

D4 Experimental Testing Procedures

Mand Machine Operating Procedure for Quasi-Static Transverse Loading

1. Turn on the main power supply switch, sockets and the water tap situated behind the Mand machine. This tap allows water to pass through the machine for cooling during operation.
2. Turn on the key at the front of the control panel.
3. Press the following buttons: yellow 'reset' button – 'activate' position button – yellow 'reset' button – blue 'pump' button – green 'pressure on' button.
4. Move the indenter up with the manual up-down dial and ensure a block of wood is positioned beneath the indenter as a safety measure in the event of hydraulic failure.
5. As the machine is hydraulically controlled allow the machine to warm up for 30 minutes prior to commencing testing.
6. Set the loading rate to 5mm/minute (0.033 volts/sec) on the ramp rate switch.
7. Set the loading range on the range switch (10kN, 25kN, or 100kN). This will determine the maximum load the machine can apply.
8. Connect the load and position wires to the data logger and the Mand machine. The displacement connection corresponds to the wire labelled 17 and load to 18. These numbers refer to the data logger channels through which all data is collected.
9. Zero the displacement reading by setting the digital reader switch to 'position' and zero the reading with the actuator set point buttons.
10. Zero the load reading by setting the digital reader switch to 'load' and zero the digital reader with the load set point dial.
11. Place the specimen in the Mand machine and secure it the test rig as described in Section 3.2.1. Tighten bolts to 4Nm with a torque wrench, over tightening can damage the honeycomb and introduce pre-stresses. Reposition the block of wood above the specimen.
12. Connect the strain gauge wires to the data logger through the connection block points 1-6. Use position 1 for the top 0° strain gauge, position 3 for the top 45° strain gauge and position 5 for bottom strain gauge (or position 3 if no 45° strain gauge present). Check the strain gauge resistance is 120Ω±0.3Ω with the multimeter (test at the connection block).
13. Position the LVDT underneath the panel as close to the loading centre as possible without touching the bottom strain gauge or clamping plates. Ensure the LVDT is slightly compressed and not at the extent of its range by gently compressing the head of the LVDT, releasing and listening for a 'ping' as it springs back against the panel.
14. Turn on the LVDT at the control box. The LVDT data will connect to the data logger through channel 38.
15. Program the data logger as described in the instructions provided with the machine. On the computer run the program DATALOGGER 2000.HT. On the menu bar select TRANSFER and CAPTURE TEXT. Enter the file name 'hope.txt' (default name must be used in current software set-up) and path to where the data will be stored. The computer is now ready to run.

16. When ready to test remove the wood from the machine and lower the indenter to a point approximately 1mm above the specimen. Check the load and displacement readings are still zeroed.
17. Press START on the computer, RUN on the data logger and START– on the Mand machine.
18. When the test is complete press START+ on the Mand machine for controlled unloading and RESET when the indenter is no longer in contact with the panel. Stop data collection by pressing RUN on the data logger. Select SAVE on the computer and close the DATALOGGER 2000.HT program.
19. Raise the loading head upwards, remove the specimen from the Mand machine and replace the block of wood.
20. To process the data open the DATASORT.EXE program and type 'reformat'. This will convert the data into a text file which can then be opened through EXCEL. The data which is recorded in volts can then be converted into the correct units using Eqs. 3.1-3.3.
21. Once testing is complete lower the indenter to just above the block of wood and turn off the Mand machine: press the orange 'reset' button – press the red 'pressure off' button – press the big red 'STOP' button and turn off the key. Turn off the water tap and the main power supply switch.

Impact Rig Operating Procedure

1. Raise the indenter away from the impact rig base using the pulley lever.
2. Place the specimen on the rig base over the 100mm circular cut-out.
3. Place the clamping plate with a 100m diameter cut-out on top of the specimen, align with the markings on the impact rig base and secure using the 4 bolts tightened to 4Nm using a torque wrench.
4. Lower the indenter so it is just resting on the specimen, checking that the time marker just completely passes through both time sensor gates else the impact and rebound times will not be recorded.
5. Pick a reference point on the indenter cluster and measure the height of the reference point above the rig base, e.g. 145mm.
6. Raise the indenter to the required height remembering to take into account the specimen height by using the reference height, e.g. required drop height 1m so align the reference point 1.145m above the rig base.
7. Lock the pulley handle to prevent accidental adjustment of the indenter height.
8. If the indenter is raised high enough insert the safety bar to prevent the indenter falling accidentally.
9. Switch on the computer, Microlink 4000 data acquisition unit, strain gauge amplifier and power supply units.
10. Zero the strain gauge amplifier by disconnecting it from the Microlink unit, attaching the small wire with two wire connectors on the end and reading the voltage across the wire connectors using the multimeter. Adjust the amplifier reading to 0±0.1mV by placing and turning a screwdriver in the zeroing hole. Once zeroed reconnect the amplifier to the Microlink unit.
11. Reset the time counters to zero.

12. On the computer open the WAVECAP program.
13. When testing for the first time it is necessary to create your own settings. To do this select SETTINGS from the main menu and select and save under a new set-up the desired settings for the Comparator, Time base, AD0703 and AD0704/5, Trigger and Data file format as shown below.
14. When testing after the initial set-up is complete the above is not necessary. Instead select FILE on the main menu and LOAD the required SET-UP created previously

COMPARATOR:	Output range → 0-500mV (1% taken and excluded as noise so as signal is small can't use a large range. Also maximum received signal must not exceed limit). Coupling → DC
TIMEBASE:	Clock rate → 50μs (Impact lasts approximately 3000 μs but as readings are triggered manually need enough time for indenter to drop, hit and rebound. 50μs gives 1.6s of readings, 32000 samples).
AD0703:	Range → -250-250mV Coupling → DC Engineering units → volts Scale → 1.0 Offset → 0 (Want raw data not adjusted by offsetting or scaling)
AD0704/5	Do not use during test so do not need to set
TRIGGER:	Arm options → using mouse or key press Trigger options → using mouse or key press
DATA FILE FORMAT:	File format → ASCII (Saves file as text file) Units → Engineering units (due to AD0703 setting in this case engineering units and raw analogue data are the same)

15. Select DISPLAY → SUMMARY and DISPLAY → STATUS from the main menu.
16. On SUMMARY check the settings are correct
17. On STATUS click RUN followed by ARM
18. As the data capture must be triggered manually it is necessary to get an assistant to do this whilst you release the indenter.
19. Simultaneously release the indenter whilst the assistant clicks TRIGGER on the computer.
20. Immediately after the indenter has hit the specimen and rebounded slide the wooden impact stopper between the specimen and the indenter to prevent multiple impacts.
21. Write down the incident and rebound times recorded on the time counters.
22. On the computer click SAVE, select directory to save in and create new sub-directory (required for each test).
23. Once data has saved click ABORT on the STATUS program.
24. Six files will be saved in the sub-directory. Only AD0703.asc is required.
25. Open the AD0703.asc file in EXCEL and the raw data will be displayed in Volts with 32000 data points. Load data can be converted using Eq. 3.4.
26. Raise the impact cluster and remove the specimen from the rig.

Denison Operation for In-plane Compression Loading

The Denison machine applies load using hydraulic pressure, which is controlled by 3 valves connected to the oil reservoir. The main valve is used for large movements of the loading head whilst the fine control valve is used for adjustment of the loading head position at higher loads. Both these valves must be turned clockwise to increase the rate of oil delivery. The third valve is a release valve and is used to rapidly return the loading head to its upper most location by moving the lever upwards.

1. Turn on the main power supply.
2. Turn on the power switch lever located at the right hand side of the machine.
3. Turn on the key.
4. Turn on the motor by pressing the button located on the front panel.
5. As the machine is hydraulically controlled allow it to warm up for 30 minutes before using.
6. Remove the cover cage from the machine.
7. Place the loading bed in the machine, ensure the bed is level by using a spirit level and adjusting the 4 screws at the base of the bed as required.
8. Place the specimen into the compression jig taking care not to trap the strain gauge wires and ensure the specimen is level and centred in the jig.
9. Place the jig on the loading bed such that the side edge of the panel faces the front of the machine. Use shims where necessary to get the jig level and check by lowering the loading head to 1mm above the specimen.
10. Press the reset button on the control panel.
11. Turn the fine control valve anti-clockwise until it is fully closed.
12. Turn the main valve clockwise to lower the loading head to approximately 1mm above the specimen. The oil flow rate is displayed on the oil delivery indicator and the main valve should be opened enough to let the oil delivery indicator read between 4 and 5.
13. Place the LVDT on the loading bed such that it is only very slightly compressed. This will allow a maximum amount of travel and therefore displacement measurement to be recorded during the test. Note the LVDT must be removed during the test prior to it being compressed to its limit to prevent it being damaged.
14. Press the store button on the Denison control panel to allow the highest load reached during the test to be captured and stored.
15. Turn on the Orion data logger and computer.
16. Connect the LVDT wires to the RDT cable as indicated in Table D1.

Table D1 LVDT connections

LVDT wire colour	Function	Connects to
White	Positive output	Blue wire in RDT cable of data logger
Green	Reference output	Green wire in RDT cable
Blue	Power supply for LVDT	Black terminal in supply, identified by SENSE label
Red	Power supply for LVDT	Red terminal in supply identified by SENSE label

17. Connect the Load output channel located at the rear of the Denison machine to the Load amplifier using the long black cable through the 'channel 3' input terminal. The load amplifier must be used, as the load signal from the Denison is very weak.
18. Connect the Load amplifier, through output 'channel 3', to the data logger using the grey wire labelled 'Load Channel 18'.
19. Connect the strain gauges to the data logger using the 18 point connection block and check the resistance across the strain gauge wires is 120Ω±0.3Ω.
20. Program the data logger as per the user manual noting the strain gauge factor is generally 2.13 for single FLA-5-11 strain gauges and 2.12 for double FCA-3-11 rosette strain gauges.
21. Open the DATALOGGER 2000.HT program on the computer.
22. From the main menu select TRANSER and CAPTURE TEXT.
23. Enter the file name and path for the test data to be stored; currently default setting of 'hope.txt' must be used.
24. To begin the test press START on the computer and RUN on the data logger.
25. Begin loading the specimen using first the main valve then the control valve when the main valve reaches its limit (at around 50kN). The loading rate should be kept steady throughout loading at a rate around 1mm/min.
26. Remove the LVDT just prior to it reaching its compressive limit and before specimen failure. As loading must be controlled manually throughout the test an assistant will be needed to remove the LVDT.
27. After failure move the release lever upwards to return the loading head to its top most position, and turn both the main and fine control valves anti-clockwise until fully closed.
28. Press RUN on the data logger, select SAVE on the computer and close the DATALOGGER 2000.HT program.
29. Remove the specimen from the Denison machine.